Lehrstuhl für Anorganische Chemie mit Schwerpunkt Neue Materialien

Reactions of $[Ge_9]^{4-}$ Zintl Anions for the Synthesis of New Materials

Manuel Meinrad Bentlohner

Dissertation

Technische Universität München

Lehrstuhl für Anorganische Chemie mit Schwerpunkt Neue Materialien

Reactions of $[Ge_9]^{4-}$ Zintl Anions for the Synthesis of New Materials

Manuel Meinrad Bentlohner

Vollständiger Abdruck der von der Fakultät für Chemie der Technischen Universität München zur Erlangung des akademischen Grades eines

Doktors der Naturwissenschaften (Dr. rer. nat.)

genehmigten Dissertation.

Voristzender:	Univ.-Prof. Dr. Tom Nilges
Prüfer der Dissertation:	1. Univ.-Prof. Dr. Thomas F. Fässler
	2. Univ.-Prof. Dr. Dr. h.c. Hubert Schmidbaur (em.)
	3. Univ.-Prof. Dr. Dr. h.c. Manfred Scheer, Universität Regensburg

Die Dissertation wurde am 20.07.2016 bei der Technischen Universität München eingereicht und durch die Fakultät für Chemie
am 21.10.2016 angenommen.

Felix qui potuit rerum cognoscere causas

Acknowledgements

Mein besonderer Dank gilt meinem Doktorvater

Prof. Dr. Thomas F. Fässler

für die Möglichkeit zur Bearbeitung dieses überaus interessanten Themas im Rahmen einer Promotion, sowie für die stets vertrauensvolle Zusammenarbeit und die unentwegte Unterstützung und Hilfe bei allen anstehenden Fragen während dieser Arbeit.

Überdies danke ich

PD Dr. Dina Fattakhova-Rohlfing
für die Bereitstellung einer Vielzahl von Messgeräten zur Charakterisierung von Nanomaterialien sowie für die stete Unterstützung bei allen Fragen und zahlreichen Ratschlägen darüber hinaus.

Dr. Wilhelm Klein
für die stete Unterstützung zur Lösung kristallographischer Probleme und den stets guten Ratschlägen in allen Teilen meiner Promotion.

M. Sc. Laura-Alice Jantke
für die Durchführung einer Reihe von theoretischen Rechnungen

Manuela Donaubauer für die unentwegte Hilfe bei allen organisatorischen Angelegenheiten.

dem **Arbeitskreis Prof. Dr. Thomas Bein**
für die Unterstützung und Hilfe bei einer Vielzahl von Messungen zur Charakterisierung von Germanium invers Opalen

dem **Arbeitskreis Prof. Dr. Peter Müller-Buschbaum**
für die Unterstützung beim Aufbau von Solarzellen und den Effizienzmessungen, sowie der Durchführung von GISAXS Experimenten am Synchrotron in Triest.

dem **Arbeitskreis Prof. Dr. Paolo Lugli**
für Spin- und Spray-Coating Versuchen zur Herstellung von Germanium invers Opalen

dem **Arbeitskreis Prof. Dr. Thomas F. Fässler**
für das sehr gute Arbeitsklima und die einwandfreie Zusammenarbeit in allen Bereichen

Insbesondere danke ich dabei meinen Laborkolleg(in)en **Sabine Frischhut**, **Michael Giebel** und **Sebastian Geier** für viele fruchtbare Diskussionen, die stets einwandfreie Zusammenarbeit sowie das überaus gute Arbeitsklima im Labor.

Mein ganz besonderer Dank gilt weiterhin:

meinen **Masterstudenten sowie Forschungs- und Synthesepraktikanten**
Sabine Frischhut, Lorenz Schiegerl, Michael Giebel, Sebastian Geier, Alexander Rinkenburger, Christina Fischer, Kim Vetter, Laura Wimberger, Björn Stühmeier, Leon Schuchmann, Mathias Wenari, Tjark Schröder, Tobias Milzarek, Daniel Henschel, Jaroslaw Marciniszyn, Stefanie Mayr

Dr. Markus Waibel für die Einführung in die Herstellung von inversen Opalen und die stets guten Ratschläge, **Dr. Steffen Schmidt**, **Ingrid Werner** und **Katia Rodewald** für die Durchführung einer Vielzahl von REM, TEM und EDX Messungen, **Patrick Zeller** für die Durchführung von XPS Messungen, **Christina Fischer** für die Durchführung von ESI-MS Messungen, **Herta Slavik** für die Durchführung von Raman-Messungen an Einkristallen, **Kristina Peters** und **Dr. Benjamin Mandlmeier** für monodisperses PMMA und der Unterstützung bei Messungen, **Enrico Greul** für die Durchführung von UV-VIS Spektroskopie zur Bandlückenbestimmung, **Stefan Datz** für die Einführung in die Raman-Mikroskopie, **Dr. Benedikt Stoib** und **Alexander Kupijai** für die Einführung in die Bandlückenbestimmung an Halbleitern, **Dr. Michael Zeilinger** und **Dr. Viktor Hlukhyy** für die Unterstützung bei kristallographischen Themen, **Prof. Dr. Florian Kraus** und **Dr. Patrick Woidy** für die Hilfe bei einer Vielzahl von technischen Themen im Labor sowie Glasbläserarbeiten, **Dr. Christian Benda** für Zahlreiche Diskussionen rund um Zintl Anionen und technische Themen, **Dr. Volodymyr Baran** für die Einführung in die Betreuung von Handschuhkästen, **Maria Weindl**, **Jürgen Kudermann** und **Christine Schwarz** für die Durchführung von NMR Messungen, **Dr. Peter Schmidtmüller** für seine Geduld mir die Chemie bereits während meiner Schulzeit näher zu bringen, **Dr. Hemambar Chilukuru** und **Martin Nirschl** für viele gute Ratschläge und unterhaltsame Stunden auch außerhalb der Promotionstätigkeiten.

Schließlich bedanke ich mich noch ganz besonders

bei meiner Frau **Simone** und meinen **Eltern Monika** und **Meinrad**
für Ihren Rückhalt, Ihre unermessliche Geduld sowie die unentwegte Unterstützung während meines gesamten Studiums und dieser Promotion.

Außerdem möchte ich mich noch besonders bei meiner Tochter **Magdalena Sophia Bentlohner** bedanken, deren Geburt, kurz vor Abschluss dieser Arbeit, mich immer wieder zu Höchstleistungen angespornt hat.

Abbreviations

18-crown-6	1,4,7,10,13,16-hexaoxacyclooctadecane
cryptand[2.2.2]	4,7,13,16,21,24-hexaoxa-1,10-diazabicyclo[8.8.8]hexacosane
Å	angstrom
A	alkali metal
A'	1,4-bis(trimethylsilyl)-buta-1-en-3-yne-1-yl
$\mathbf{A}^{\mathbf{E}}$	(1*E*)-4-trimethylsilyl-buta-1-en-3-yne-1-yl
Am	amyl
a	amorphous
α	crystalline
BTS	copper oxide catalys for gas regeneration
^{n}Bu	n-butyl
^{t}Bu	tert-butyl
$^{ZZ}\mathbf{B}$	(1*Z*,3*Z*)-buta-1,3-dien-1,4-diyl
$^{EZ}\mathbf{B}$	(1*E*,3*Z*)-buta-1,3-dien-1,4-diyl
COSY	correlation spectroscopy
cod	cyclooctadiene
Cp	cyclopentadienyl
Cy	cyclohexyl
dmf	N,N-dimethylformamide
dmso	dimethylsulfoxide
E	tetrel element
EDX	energy dispersive X-ray analysis
ESI-MS	electrospray ionization mass spectroscopy
en	ethylenediamine
Et	ethyl
FL	flat
FTO	fluorinated tin oxide
GISAXS	grazing incidence small angle X-ray scattering
HOMO	highest occupied molecular orbital
HSQC	heteronuclear single quantum coherence
HMBC	heteronuclear multiple bond correlation
ITO	indium tin oxide

INOP	inverse opal
K	Kelvin
LUMO	lowest occupied molecular orbital
M	main group element
Me	methyl
MHz	megahertz
MPP	maximum power point
min	minute(s)
mA	milliampere
mg	milligram
ml	millilitre
µ	micro
n	negative
nm	nanometer
NMR	nuclear magnetic resonance spectroscopy
h	hour(s)
P3HT	poly(3-hexylthiophen-2,5-diyl)
p	positive
ppm	parts per million
Ph	phenyl
^{i}Pr	iso-propyl
R	all isomers of 7-amino-5-aza-hepta-2,4-dien-2-yl
^{Z}**R**	(2*Z*)-7-amino-5-aza-hepta-2,4-dien-2-yl
RT	room temperature
r.t.	reaction time
SEM	scanning electron microscopy
s	second(s)
SAED	selected area electron diffraction
T	transition metal
TEM	transmission electron microscopy
TMS	trimethylsilyl (–Si(CH_3)$_3$)
t	time
thf	tetrahydrofurane
UV	ultraviolet

V	volume
Vis	visible light
X	halogen (in chemical formula)
XPS	X-ray photoelectron spectroscopy
Z	number of formula units per unit cell

Abstract

For the development of enhanced photovoltaic concepts, materials with tailored morphology and electronic properties are necessary. Inspired by the versatile reactivity and electronic properties of the $[Ge_9]^{4-}$ Zintl anion, the latter was investigated as precursor for new molecular clusters and porous Ge materials for photovoltaic applications. In particular the chemical properties of $[Ge_9]^{4-}$ Zintl anions with respect to cluster linking and extension as well as controlled oxidation to elemental germanium with tunable morphology and composition, were examined in the course of this thesis.

For the first time Zintl triads **$[Ge_9–CH=CH–CH=CH–Ge_9]^{6-}$** and **$[R–Ge_9–CH=CH–CH=CH–Ge_9–R]^{4-}$** [R = (2*Z*, 4*E*)-7-amino-5-aza-hepta-2,4-dien-2-yl] are described in terms of synthesis, crystal structure and electronic properties. Theoretical calculations reveal that the Zintl triads are conjugated. The Zintl Triads were synthesized by the reaction of 1,4-bis(trimethylsilyl)butadiyne with the Zintl phases A_4Ge_9 (*A* = K, Rb) and ethylenediamine, and by *in situ* investigations their formation was rationalized. Depending on the experimental conditions both $[Ge_9]^{4-}$ and ethylenediamine are able to react with 1,4-bis(trimethylsilyl)butadiyne. A significant influence of water on the reaction of 1,4-bis(trimethylsilyl)butadiyne with ethylenediamine in the absence of clusters was found, and exploited for a new method for qualitative water determination in ethylendiamine.

Additionally reactions allowing the extension and linking of $[Ge_9]^{4-}$ clusters by tetrel elements were investigated. The pristine ***closo*-$[Ge_{10}]^{2-}$** Zintl anion was obtained by reaction of $[Ge_9]^{4-}$ with water-free ethylenediamine and formally arises from the oxidative addition of a Ge^{2+} atomic ion to the open square face of a *nido*-$[Ge_9]^{4-}$ cluster. For the first time *closo*-$[Ge_{10}]^{2-}$ was successfully isolated and fully characterized. Investigations on the synthesis of heteroatomic tetrel clusters, by reaction of $[Ge_9]^{4-}$ with $SnPh_2Cl_2$ in presence of elemental K, yielded crystals containing the **$[(\eta^4\text{-}Ge_9)Sn(\eta^3\text{-}Ge_9)]^{4-}$** Zintl anion, with two Ge_9 clusters linked by a tin atom. Analysis of the bonding situation revealed an adduct of ***closo*-$[Ge_9Sn]^{2-}$** and *closo*-$[Ge_9]^{2-}$ for the latter. Accordingly the series of heteroatomic tetrel clusters was extended.

In another study the utilization of $[Ge_9]^{4-}$ Zintl anions, as source for elemental germanium with tunable composition, was investigated. ***a*-Ge** was obtained by

pumping down a solution of K_4Ge_9 in ethylenediamine with water-traces. For the first time an oxidative potential of ethylenediamine was evidenced by NMR spectroscopic detection of the corresponding amide. An analogous procedure in water-free ethylenediamine yielded a "**K_4Ge_9" phase** with intact clusters. Annealing of both the *a*-Ge and the "K_4Ge_9" phase with intact clusters at 600 °C led to **α-Ge**. The thermal treatment of the "K_4Ge_9"-Phase was accompanied with the release of elemental potassium. Reaction of K_4Ge_9 with MCl_n (M = Ge, Si, n = 4; M = P, n = 3) resulted in ***a*-$Ge_{1-x}M_x$** and potassium chloride as a side product. Thermal annealing of the *a*-$Ge_{1-x}M_x$-phases at 600 °C resulted in **α-$Ge_{1-x}M_x$**.

Finally $[Ge_9]^{4-}$ Zintl anions were used for wet-chemical and template-based fabrication of ***$Ge_{1-x}M_x$-INOP*** with tunable composition and regular volume-porosity. Water-free ethylenediamine was used for the transfer of $[Ge_9]^{4-}$ into a PMMA opal template. Subsequent gas phase reaction of the clusters with MCl_n (M = Ge n = 4; M = P, n = 3) resulted, after removal of the PMMA template and the side product potassium chloride, *a*-$Ge_{1-x}M_x$ inverse opals. Annealing at 600 °C led to α-$Ge_{1-x}M_x$-*INOP*. By spin- and spray-coating extended areas of the inverse opals were established on transparent and conductive substrates. With such films working hybrid solar cells were assembled, by filling the pores with poly(3-hexylthiophen-2,5-diyl) (P3HT) and deposition of gold electrodes.

Inhaltsübersicht

Für die Entwicklung verbesserter photovoltaischer Konzepte sind Materialien mit maßgeschneiderter Morphologie und elektronischen Eigenschaften notwendig. Inspiriert durch die vielfältige Reaktivität und elektronischen Eigenschaften des $[Ge_9]^{4-}$ Zintl Anions, wurde dieses als Vorstufe für neue molekulare Cluster-Verbindungen und poröse Ge Materialien für photovoltaische Anwendungen untersucht. Insbesondere das chemische Verhalten der $[Ge_9]^{4-}$ Zintl-Anionen in Bezug auf deren Verknüpfung und Erweiterung sowie deren kontrollierte Oxidation zu elementaren Germanium mit einstellbarer Zusammensetzung und Morphologie wurden im Rahmen dieser Arbeit beleuchtet.

Erstmalig werden Zintl Triaden **$[Ge_9–CH=CH–CH=CH–Ge_9]^{6-}$** und **$[R–Ge_9–CH=CH–CH=CH–Ge_9–R]^{4-}$** [R = (2*Z*, 4*E*)-7-amino-5-aza-hepta-2,4-dien-2-yl] bezüglich Synthese, Kristallstruktur und elektronischen Eigenschaften beschrieben. Wie theoretische Rechnungen zeigen sind die Zintl Triaden konjugiert. Die Zintl Triaden wurden durch Reaktion von 1,4-Bis(trimethylsilyl)butadiin mit den Zintl-Phasen A_4Ge_9 (*A* = K, Rb) und Ethylendiamin hergestellt, und durch *in situ* Untersuchungen konnte deren Entstehung rationalisiert werden. In Abhängigkeit der Reaktionsbedingungen können sowohl $[Ge_9]^{4-}$ als auch Ethylendiamin mit 1,4-Bis(trimethylsilyl)butadiin reagieren. Auf die Reaktion von 1,4-Bis(trimethylsilyl)butadiin mit Ethylendiamine in Abwesenheit von Clustern wurde ein signifikanter Einfluss von Wasser gefunden und für eine neue Methode zur qualitativen Bestimmung von Wasser in Ethylendiamin ausgenutzt.

Zusätzlich wurden Reaktionen, welche die Erweiterung und Verknüpfung von $[Ge_9]^{4-}$ Clustern durch Tetrel-Elemente ermöglichen, untersucht. Das ungebundene und leere ***closo*-$[Ge_{10}]^{2-}$** Zintl Anion wurde durch Reaktion von $[Ge_9]^{4-}$ mit wasserfreiem Ethylendiamin gewonnen und entsteht formal durch oxidative Addition eines Ge^{2+} Ions an die offene Viereckfläche eines *nido*-$[Ge_9]^{4-}$ Clusters. Zum ersten Mal konnte das freie *closo*-$[Ge_{10}]^{2-}$ erfolgreich isoliert und vollständig charakterisiert werden. Untersuchungen zur Synthese heteroatomarer Tetrel-Cluster, durch Reaktion von $[Ge_9]^{4-}$ mit $SnPh_2Cl_2$ in Anwesenheit von elementaren Kalium, lieferte Kristalle mit dem **$[(\eta^4\text{-}Ge_9)Sn(\eta^3\text{-}Ge_9)]^{4-}$** Zintl Anion, welches aus zwei über ein Zinn Atom verbundenen Ge_9 Clustern besteht. Analyse der Bindungssituation zeigt, dass

es sich bei Letzterem um ein Addukt zwischen ***closo*-[Ge_9Sn]$^{2-}$** und *closo*-[Ge_9]$^{2-}$ handelt. Die Reihe heteroatomarer Tetrel-Cluster konnte damit ergänzt werden.

In einer weiteren Studie wurde die Nutzbarmachung von [Ge_9]$^{4-}$ Zintl-Anionen als nass-chemische Quelle für elementares Germanium mit einstellbarer Zusammensetzung untersucht. ***a*-Ge** wurde durch Einengen einer Lösung von K_4Ge_9 in Ethylendiamin mit Wasser-Spuren, gewonnen. Erstmalig konnte ein oxidatives Potential von Ethylendiamin durch NMR spektroskopische Detektion des korrespondierenden Amids nachgewiesen werden. Eine analoge Prozedur in wasserfreiem Ethylendiamin lieferte eine **„K_4Ge_9"-Phase** mit intakten Clustern zurück. Thermische Behandlung sowohl des amorphen Germaniums als auch der „K_4Ge_9"-Phase mit intakten Clustern bei 600 °C, lieferte in beiden Fällen **α-Ge**. Die thermische Behandlung des „K_4Ge_9" war mit der Freisetzung von elementarem Kalium verbunden. Die Reaktion von K_4Ge_9 mit MCl_n (M = Ge, Si, n = 4; M = P, n = 3) resultierte ***a*-$Ge_{1-x}M_x$** mit Kaliumchlorid als Nebenprodukt. Thermische Behandlung des amorphen $Ge_{1-x}M_x$ bei 600°C erbrachte **α-$Ge_{1-x}M_x$**.

Schließlich wurden [Ge_9]$^{4-}$ Zintl-Anionen zur nass-chemischen und Templat-basierten Herstellung von **$Ge_{1-x}M_x$ inversen Opal Filmen** mit einstellbarer Zusammensetzung und regelmäßiger Volumen-Porosität genutzt. Wasser-freies Ethylendiamin wurde zum Transfer der [Ge_9]$^{4-}$ Zintl-Anionen in ein PMMA Opal Templat verwendet. Anschließende Gasphasen-Reaktion der Cluster mit MCl_n (M = Ge, n = 4; M = P, n = 3) erbrachte nach Entfernen des Templats und des Nebenprodukts Kaliumchlorid, ***a*-$Ge_{1-x}M_x$-*INOP***. Die thermische Behandlung bei 600 °C führte zu **α-$Ge_{1-x}M_x$-*INOP* Filmen**. Durch Spin- und Spray-Coating wurden ausgedehnte Flächen von $Ge_{1-x}M_x$ inversen Opalen auf transparenten und leitfähigen Substraten hergestellt. Daraus wurden funktionierende Hybrid Solarzellen, durch Füllung der Poren mit Poly(3-hexylthiophen-2,5-diyl) (P3HT) und Aufdampfen von Gold Elektroden, hergestellt.

Contents

Declaration

This dissertation is written as a publication based thesis. The bibliographic data of articles published in peer-reviewed journals is compiled in chapter 5. In case of unpublished work, corresponding manuscripts prepared for publication are included. In chapter 5 for each manuscript a one-page summarization with the contents and accentuation of my contributions to the respective work is given. The relevance of the present work for science and research as well as the motivation, scope and outline are presented as introductory part in chapter 1. The experimental section in chapter 2 gives details on the syntheses and characterization of materials as well as computational methods. The results and discussion are presented in chapter 3. The subsections 3.1-3.3 are structured as follows: i) review of relevant literature, ii) results and discussion, iii) references. An overall summary and conclusion is given in the chapter 4.

1 Introduction

1.1 The Element Germanium

Germanium is a member of the 14th group in the periodic table, and occurs in nature in form of seldom sulfidic minerals such as *Agyrodit* Ag_8GeS_6 and *Germanit* $Cu_6FeGe_2S_8$. The element is produced from GeO_2, which is a side product in the production of zinc, by reduction with hydrogen gas. The most common and technical most important modification of the element is α-Ge, which is semiconducting and exhibits cubic diamond structure. Under very high pressures α-Ge transfers into β-Ge, which is an electrical conductor and adopts the structure of β-Sn. α-Ge is a brittle and grey colored solid which is inert to ambient conditions.[1, 2]

In early days germanium was the key semiconducting material for transistors and integrated circuits, but later on the latter was overruled by the more abundant homologue silicon and its mature production technology.[3] Anyhow germanium has regained a lot of attention in material science and in particular for applications in photovoltaics[4-9] and Li-ion batteries[10-13], due to its variable opto-electronic properties and high charge carrier mobility, respectively.[3, 14, 15] A great advantage of germanium is its capability to form solid solutions $Ge_{1-x}E_x$ (E = Si, Sn)[16, 17] with properties depending on the Ge/E ratio.[18-21] Also introduction of group 13 and 15 dopants like boron and gallium as well as phosphorus and arsenic is possible and provides n- and p-type germanium, which can be applied as electron- and hole-conductor in electronics, respectively.[22-24] As for the lighter homologue silicon, the optical properties of germanium not only can be altered by changing the composition but also by shrinking the material's morphology to the nanoscale.[14, 25] In that context (nano)porous forms of germanium have attracted significant attention, due to tunable opto-electronic properties as well as high surface areas suitable for interaction with other molecules or electron transfer processes.[5, 14]

The diversity of germanium and its prospects for a bunch of applications has triggered the search for synthetic methods, allowing the bottom up assembly of functional germanium materials with tailored morphology, composition and properties.[5, 14]

1.2 Group 14 deltahedral $[E_9]^{4-}$ Zintl Anions

1.2.1 Structure and Bonding Situation

Alloying of alkaline or earth alkaline metals (except Be) with group 13-16 elements (except period 2) results in Zintl phases, which comprise polyanions with one, two or three dimensional networks.[1, 2] According to the *Zintl-Klemm* concept the polyanions are formed by transfer of electrons from the electropositive alkaline/earth alkaline metal to the more electronegative group 13-16 elements and adopt structures of isovalent elements in accordance to the "*8–N*" rule.[1, 2, 26-28] Examples in that context are NaTl and KSb, which exhibit $[Tl^-]_x$ and $[Sb^-]_x$ polyanions with diamond- and chain-frameworks, in analogy to the electronically isovalent C and Te, respectively.[26, 28] From group 14 elements, Zintl phases with the nominal composition A_4E_4 (*A* = K, Rb; *E* = Si-Pb), A_4E_9 (*A* = K-Cs, *E* = Ge-Pb) and $A_{12}E_{17}$ (*A* = K–Cs, E = Si-Pb) emerge by heating of stoichiometric amounts of the elements.[29-31] In A_4E_4 isolated $[E_4]^{4-}$ tetrahedra are present, which are electronically isovalent to the P_4 molecules in the white phosphorus, and therefore can be described by the "*8–N*" rule.[32-35] In case of A_4E_9 Zintl phases, $[E_9]^{4-}$ polyanions are present in the solid state[29, 36-40], which require a more demanding description by the Wade rules for electron deficient clusters.[41, 42] According to these rules, $[E_9]^{4-}$ Zintl anions possess 22 skeleton bonding electrons (SE) - two electrons from each tetrel vertex and additional 4 electrons sum up by the charge - and therefore are *nido*-clusters.[41, 42] The $A_{12}E_{17}$ (*A* = K, Rb, Cs; *E* = Si, Ge) Zintl phases consist of a 2:1 mixture of $[E_4]^{4-}$ and $[E_9]^{4-}$ Zintl clusters.[29, 36]

By extraction of A_4E_9 Zintl phases with polar solvents such as *en*, *dmf* or liquid ammonia, solutions containing $[E_9]^{4-}$ Zintl anions are accessible.[30, 31, 43] Even though A_4E_4 and $A_{12}E_{17}$ at least partially dissolve in such solvents and a downstream chemistry is emerging [44-47], the solubility of A_4E_9 is much better and yields stable and highly concentrated solutions with $[E_9]^{4-}$ Zintl anions.[30, 31] Due to the stability of $[E_9]^{4-}$ in solution and the opportunity to crystallize the clusters and their reaction products by addition of sequestering agents such as cryptand[2.2.2][48] or 18-crown-6[49], the structure and reactivity of the latter is well studied.[30, 31, 43, 50] X-ray structure analysis of a bunch of compounds, containing $[E_9]^{4-}$ Zintl anions, reveals that the latter either adopt the structure of C_{4v} symmetric mono-capped square antiprisms (Figure 1.1a) or D_{3h} symmetric tricapped trigonal prisms with elongated prism

heights. E_9 Zintl clusters not only can adopt a charge of –4, but also appear as $[E_9]^{3-}$ and $[E_9]^{2-}$, with 21 and 20 SE, respectively. According to the Wade rules the $[E_9]^{2-}$ clusters (20 SE) are *closo*-deltahedra and adopt the structure of a tricapped trigonal prism (Figure 1.1b). $[E_9]^{3-}$ with 21 SE, evade from that description and adopt structures between those of *nido*-$[E_9]^{4-}$ and *closo*-$[E_9]^{2-}$.[30, 31]

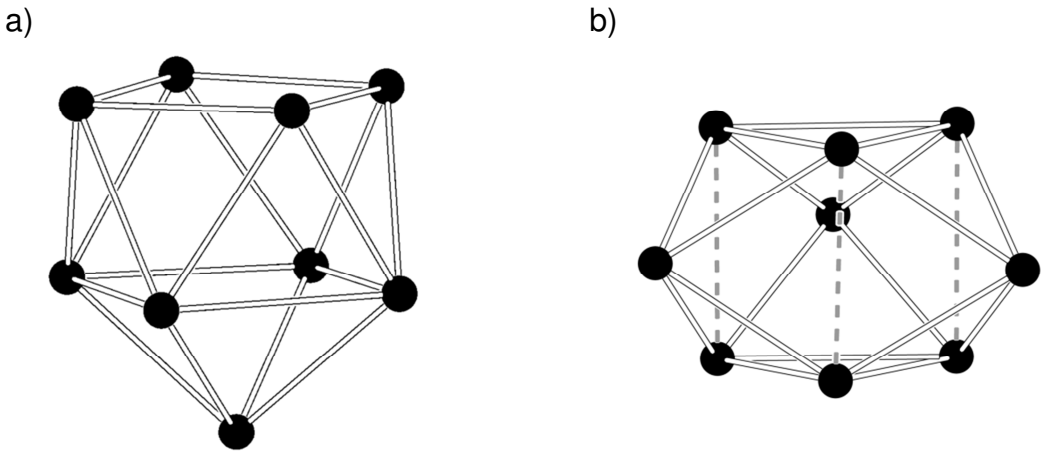

Figure 1.1. Schematic representation of a) *nido*-$[Ge_9]^{4-}$ [40] with C_{4v} symmetry and b) *closo*-$[Ge_9]^{2-}$ [51] with D_{3h} symmetry.

1.2.2 Reactivity in Solution

$[E_9]^{4-}$ Zintl anions show a versatile reactivity in solution. [30, 31] A milestone in Zintl chemistry was the derivatization of E_9 clusters with organic functionalities. With the synthesis of $[Ph\text{-}Ge_9\text{-}SbPh_2]^{2-}$ by reaction of K_4Ge_9 with $SbPh_3$, the first E_9 Zintl cluster comprising a 2c/2e$^-$ covalent cluster-carbon bond was found.[52] Later on it turned out that the reaction of $[E_9]^{4-}$ (E = Ge, Sn) with alkynes R^1–C≡C–R^2 in *en* readily proceeds to alkenylated clusters $[(R^2HC{=}CHR^1)_n(E_9)]^{m-}$ (n = 1, m = 3; n = 2, m = 2) with Ge–C *exo*-bonds, and a multitude of such species has been synthesized so far: R^1/R^2 = -H/-Fc, -H/-Ph, -H/-^{t}Bu, -H/-Ph-OMe, -Ph/-Ph, -$SiMe_3$/-$SiMe_3$, -$SiMe_3$/-Im-Me, -H/-$(CH_2)_4$-C≡CH, -H/-Ph-C≡CH, -H/-Ph-NH_2, -H/-Py, -H/-$(CH_2)_3$-C≡N, -H/-$CH(OEt)_2$, -H/-CH-$(CH_2)_2$, -H/-$C(CH_3)_2$-Cl, -H/-CH_2-NH_2.[53-61] In particular the reaction of K_4Ge_9 with bis(trimethylsilyl)acetylene in *en* is well investigated (details see chapter 3.1.1) and proceeds in very good yields to the mono- and bis-vinylated clusters $[(H_2C{=}CH)(Ge_9)]^{3-}$ and $[(H_2C{=}CH)_2(Ge_9)]^{2-}$, respectively (Figure 1.2)[54, 58].

Also the nucleophilic substitution of alkyl halides RX (R = ^{t}Bu, ^{s}Bu, ^{n}Bu, ^{t}Am; X = halogen) with $[E_9]^{4-}$ is possible and results in several organo-Zintl clusters bearing alkyl groups (Figure 1.2c).[55, 62] Derivatization of clusters with organic functionalities is particularly interesting, as further transformations such as polymerization or π-stacking of the molecules are feasible and point to the development of a supramolecular Zintl chemistry.

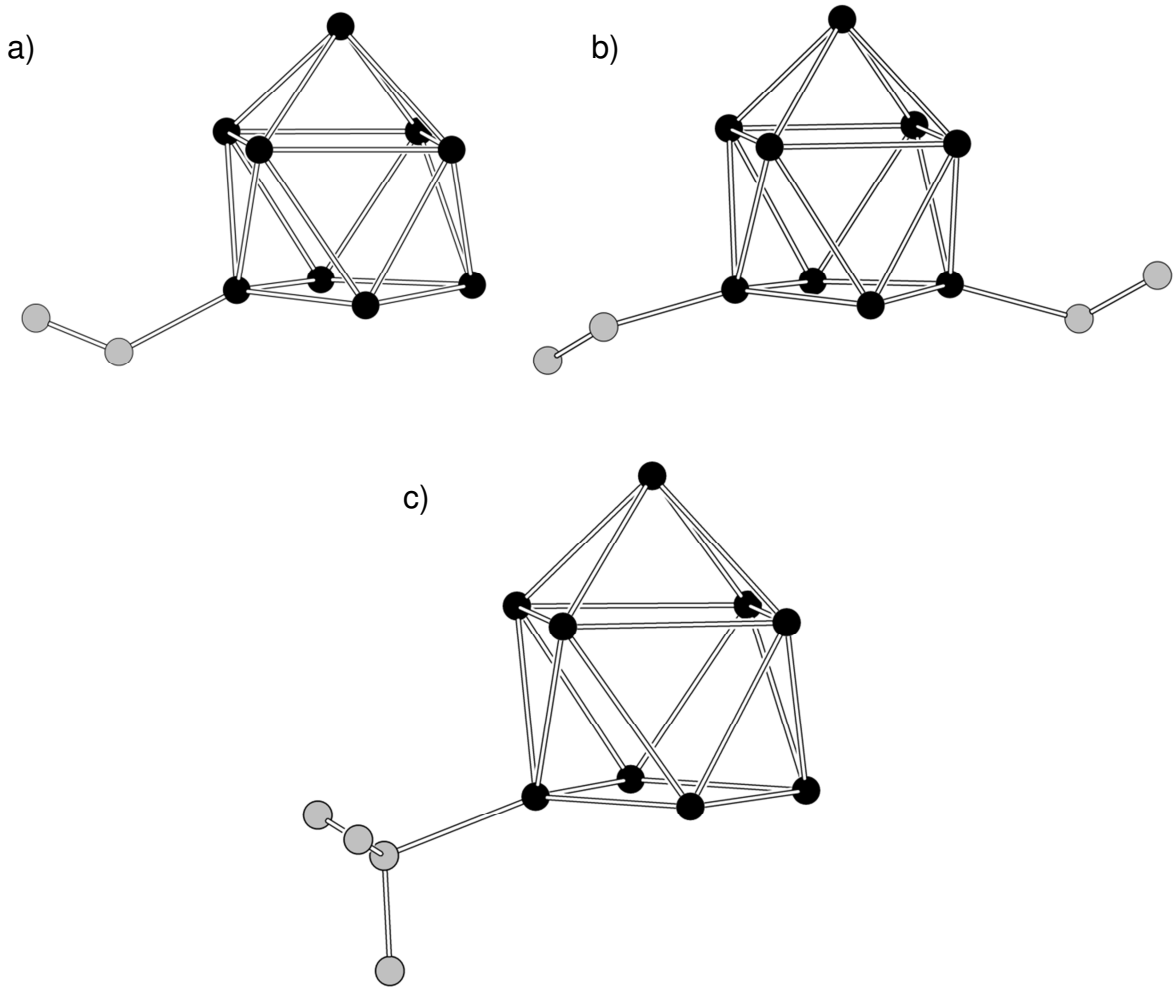

Figure 1.2. Schematic representation of a) $[Ge_9(CH{=}CH_2)]^{3-}$ [63], b) $[Ge_9(CH{=}CH_2)_2]^{2-}$ [54] and c) $[Sn_9{-}^{t}Bu]^{3-}$ [55]. Carbon atoms are shown as grey spheres and hydrogens are omitted for clarity.

E_9 clusters not only can undergo reaction with organic substrates, but are also capable to connect to each other, via Ge–Ge *exo* cluster-bonds, under soft oxidative conditions. From experiments with Zintl phases in *en*, *dmf* and liquid ammonia, oxidatively coupled clusters $[Ge_9{-}Ge_9]^{6-}$ [64, 65] and $^{1}_{\infty}[Ge_9]^{2-}$ [66] as well as $[Ge_9{=}Ge_9{=}Ge_9]^{6-}$ [67] and $[Ge_9{=}Ge_9{=}Ge_9{=}Ge_9]^{8-}$ [68, 69] were obtained (Figure 1.3). As follows from the X-ray structures and electron counts, $[Ge_9{-}Ge_9]^{6-}$ and $^{1}_{\infty}[Ge_9]^{2-}$ exhibit single 2c/2e^{-} Ge–Ge bonds between the clusters [64, 66], whereas for

$[Ge_9{=}Ge_9{=}Ge_9]^{6-}$ and $[Ge_9{=}Ge_9{=}Ge_9{=}Ge_9]^{8-}$ the bond order is lower than one and the electrons are evenly distributed among the clusters.[67, 68] The solvents and in particular *en* have been discussed to trigger the oxidative cluster coupling, as oxidatively coupled clusters are also accessible without explicitly adding an oxididant to the solutions with the Zintl phases.[52, 70] The formation of conjugated cluster-oligomers[67, 68], highlights that soft oxidation of $[Ge_9]^{4-}$ Zintl anions is a powerful approach tofunctional germanium materials, such as molecular wires[69] or (semi)conductive nano-sheets. From theoretical investigations for *E* = Ge follows that full oxidation of $[Ge_9]^{4-}$ Zintl anions to one, two and three-dimensional structures under retention of the polyhedral structures is reasonable, holding out the prospect of carbon analogous graphene sheets and nanotubes.[71]

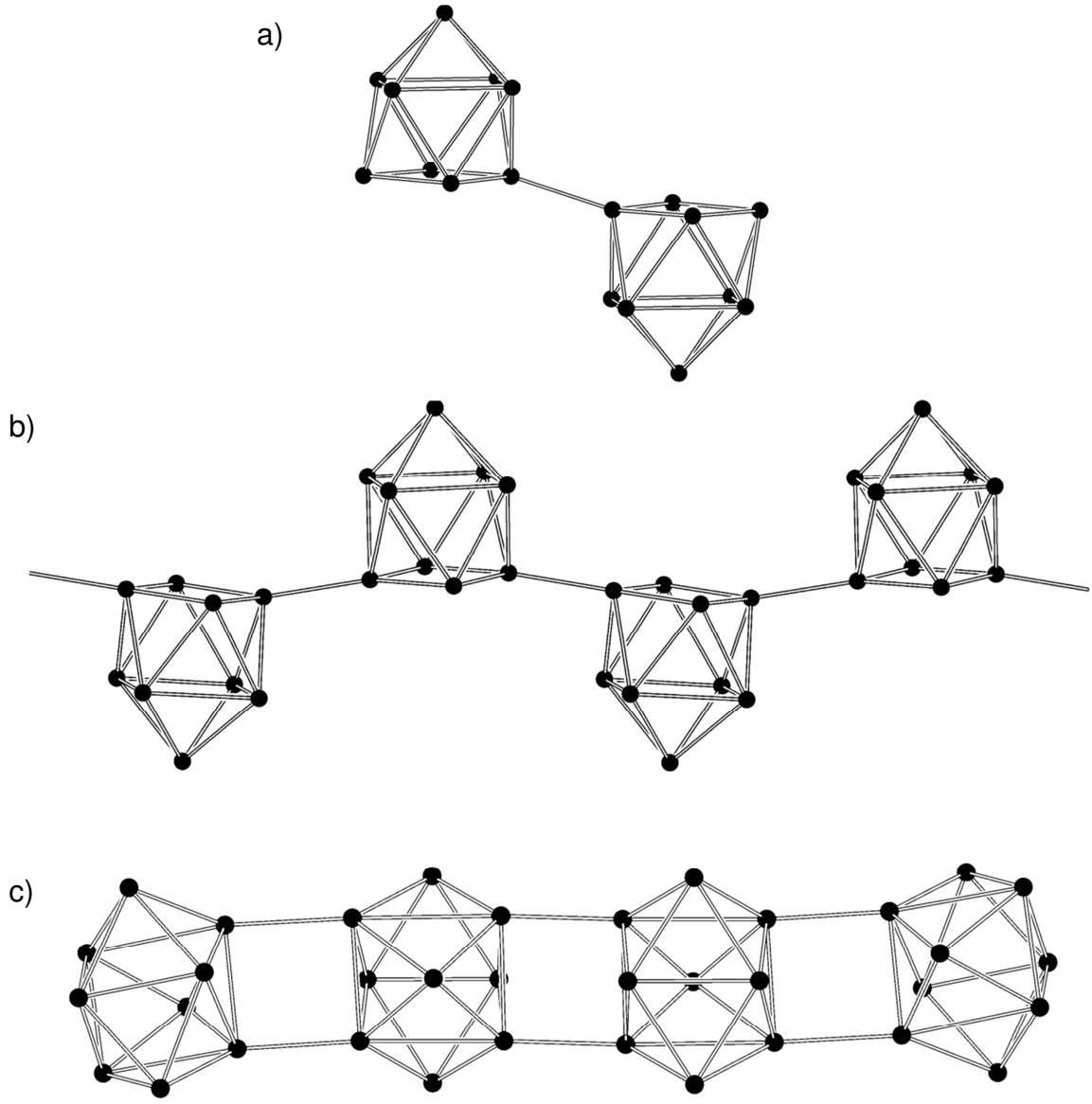

Figure 1.3. Schematic representation of a) $[Ge_9\text{-}Ge_9]^{6-}$ [64], b) $^1_\infty[Ge_9]^{2-}$ [66] and c) $[Ge_9{=}Ge_9{=}Ge_9{=}Ge_9]^{8-}$ [69]

In addition to the organic functionalization and oxidative coupling of E_9 clusters, it is possible to introduce heteroatoms to the deltahedral cages. A plethora of heteroatomic clusters (Figure 1.4) was obtained by the reaction of transition metal organyles TX_xL_y (T = transition metal; X = halogen, $x \geq 0$; L = electron donor ligand, $y > 0$), bearing weakly bonded ligands, with $[E_9]^{4-}$ Zintl anions. The latter are also called *intermetalloids*, as their molecular structures can be seen as molecular excerpts from corresponding intermetallic phases of the respective elements.[30, 31, 72, 73] Triggered by the early syntheses of *closo*-$[(\eta^4\text{-}E_9)Cr(CO)_3]^{4-}$ (E = Sn, Pb) by *Eichhorn* [74, 75] and investigations on the structural dynamics of such clusters in solution[76], the line of transition metal capped clusters was extended with examples, such as $[(\eta^4\text{-}Sn_9)Ir(cod)]^{3-}$ [77], $[(\eta^4\text{-}Ge_9)Ni(CO)]^{3-}$ [78], $[(\eta^4\text{-}Ge_9)Pd(PPh_3)]^{3-}$ [79], $[(\eta^4\text{-}Ge_9)Cu(PR_3)]^{3-}$ [80] and $[(\eta^4\text{-}E_9)Zn(Ph)]^{3-}$ (E = Si, Ge, Sn, Pb)[81] . Also the insertion of the transition metal into the deltahedral cage is possible and yielded a variety of endohedrally filled clusters. Owing to the ability of E_9 cages to undergo oxidative coupling and structural reorganization[57, 59, 82] , endohedral clusters $[T@E_n]^{q-}$ ($n \geq 9$) with extended sizes and different shapes were obtained.[30, 31, 72, 73] A well investigated reaction is that of $[IrCl(cod)]_2$ with $[Sn_9]^{4-}$, yielding $[(\eta^4\text{-}Sn_9)Ir(cod)]^{3-}$ which can be transferred by soft oxidation to $[Ir@Sn_{12}]^{3-}$.[77] A comparable result was also found for the reaction of $Ni(cod)_2$ and/or $Ni(PPh_3)_2(CO)_2$ with $[Ge_9]^{4-}$, proceeding to capped and capped/endohedrally filled clusters $[(\eta^4\text{-}Ge_9)Ni(CO)]^{3-}$ and $\{Ni[Ni@(\eta^4\text{-}Ge_9)](CO)\}^{2-}$, $[Ni@(\eta^4\text{-}Ge_9)]^{3-}$, respectively.[78] Outstanding examples in the series of intermetalloids with germanium are $[Au_3Ge_{45}]^{9-}$ [83], being up to date the largest known cluster of a heavier tetrel element, and $[Co@Ge_{10}]^{3-}$ [84], which has been the first one reported with an archimedean structure. In addition, metal atom bridged clusters $\{[(E_9)T(E_9)]_m\}^{q-}$ (m = 1 - ∞) were obtained from reactions with transition metal organyls.[30, 31] Thereby, reaction of $CuCl(PR_3)$ with $[Ge_9]^{4-}$ yielded $[(\eta^4\text{-}Ge_9)Cu(\eta^1\text{-}Ge_9)]^{7-}$, comprising two Ge_9 units linked by a single copper atom.[85] Similar approaches have also yielded oligomers and polymers such as ${}^1_\infty\{Zn[trans\text{-}\mu_2(\eta^3\text{:}\,\eta^3\text{-}Ge_9)]\}^{2-}$ [63], $[(HgGe_9)_4]^{10-}$ [86] and ${}^1_\infty[HgGe_9]^{2-}$ [87] as well as $[(Ge_9)Au_3(Ge_9)]^{5-}$ [88] and $[(Pb_9)Cd\text{–}Cd(Pb_9)]^{6-}$ [89], with more than one metal bridging atom. Recently a general insight in the formation of intermetalloids was given by the *Fässler* group, with investigations on the reaction of $TiCp_2Cl_2$ with $[Sn_9]^{4-}$ Zintl anions in liquid ammonia.[90]

The introduction of heteroatoms to tetrel clusters by solvent based reactions is not limited to transition metals only, but also possible for main group elements (see chapter 3.2.1).[59, 70, 91-96] Heteroatomic main group clusters are in particular interesting for the bottom up assembly of mixed group 13-16 semiconductor materials (details see chapter 1.3).[5, 97-101] A detailed discussion on larger homo- and heteroatomic tetrel clusters is given in the results chapter 3.2.1.

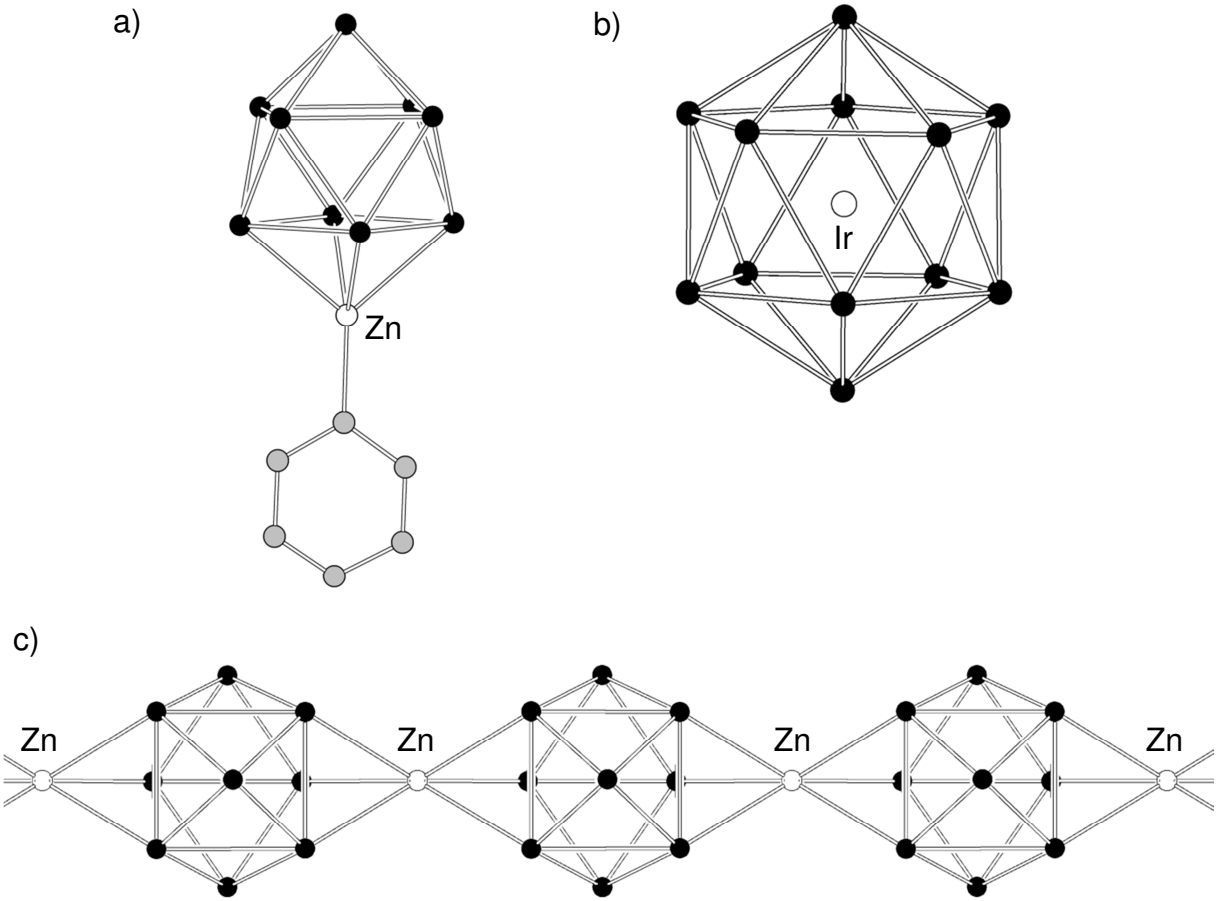

Figure 1.4. Schematic representation of a) $[(Ge_9)Zn(Ph)]^{3-}$ [81], b) $[Ir@Sn_{12}]^{2-}$ [77] and $^1_\infty\{Zn[trans\text{-}\mu_2(\eta^3\text{:}\,\eta^3\text{-}Ge_9)]\}^{2-}$ [63]. Carbon atoms are shown as grey spheres and hydrogens are omitted for clarity.

A series of low charged and neutral heteroatomic clusters, such as $[(Hyp_3Ge_9)Zn(Ge_9Hyp_3)]$ [Hyp = $Si(SiMe_3)_3$][102] (Figure 1.5), with enhanced solubility in less polar solvents was gained by applying $\{Ge_9[Si(SiMe_3)_3]_3\}^-$ instead of $[Ge_9]^{4-}$ as starting material in reactions with metal organyles. $\{Ge_9[Si(SiMe_3)_3]_3\}^-$ can be obtained in good yields by reaction of $[Ge_9]^{4-}$ with $\{(Me_3Si)_3Si\}Cl$.[103]

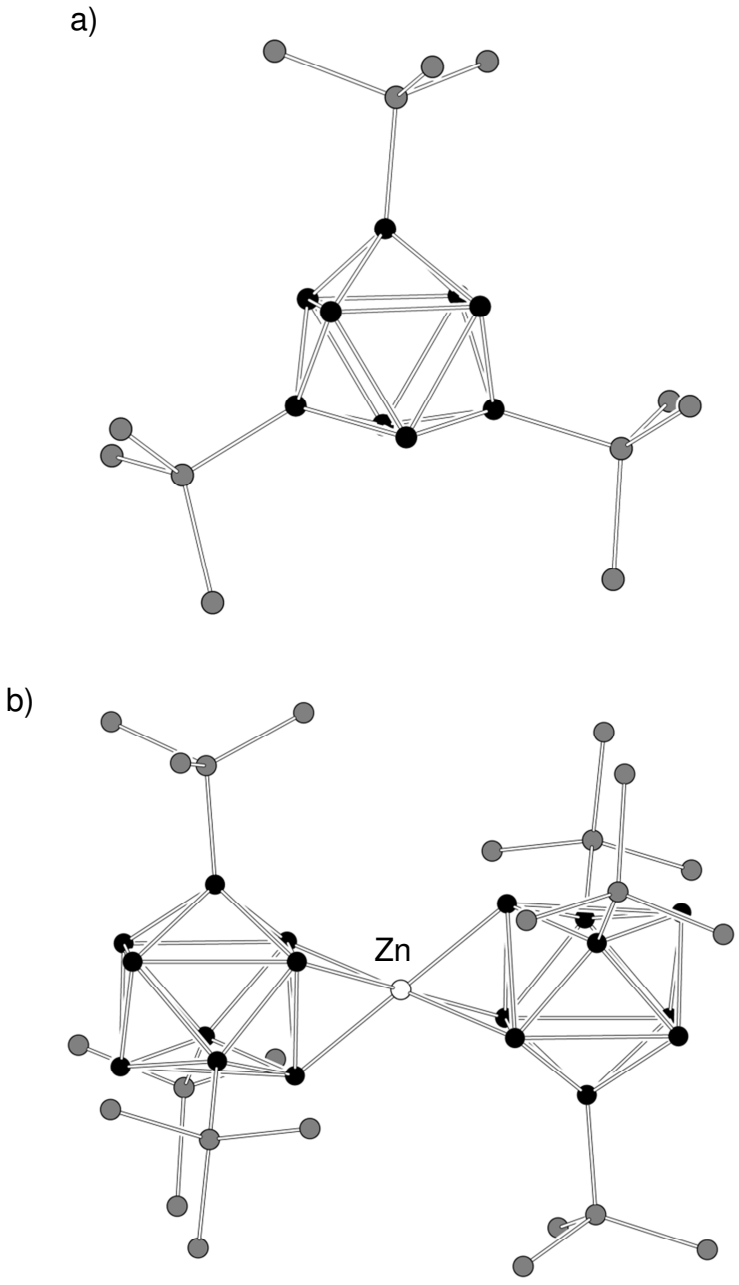

Figure 1.5. Schematic representation of a) $[Hyp_3Ge_9]^-$ [103] and b) $[(Hyp_3Ge_9)Zn(Ge_9Hyp_3)]$ [Hyp = $Si(SiMe)_3$] [102]. Silicon atoms are shown as dark grey spheres. Carbon and hydrogen atoms are omitted for clarity.

1.3 Advantages of $[Ge_9]^{4-}$ Zintl Anions for the Synthesis of Functional Germanium Materials

Several years ago *Kanatzidis* and *Tolbert* have introduced group 14-16 clusters as precursors for nanostructured non-oxide semiconductors. The solubility of Zintl clusters in selected solvents, a rich library of compositions and the opportunity of their oxidation to the elements, makes them attractive precursors for fabrication of non-oxide nanostructures with tunable composition and electronic properties. [5, 97-101] In this context the $[Ge_9]^{4-}$ has been effectively applied as molecular building block and germanium source, for the fabrication of larger molecular clusters [30, 31] as well as (nano)porous germanium powders with tunable composition [104-108] and flat germanium films [109, 110]. The potential of $[Ge_9]^{4-}$ as versatile precursor for new materials is further highlighted by the synthesis of a novel allotrope of germanium.[111, 112] As reviewed in chapter 1.2 the $[Ge_9]^{4-}$ exhibits a versatile reactivity and the formation of organo-tetrel clusters as well as larger tetrel/transition metal and tetrel/main-group clusters is possible with that fascinating Zintl anion. The utilization of $[Ge_9]^{4-}$ and its heteroatomic derivatives as molecular building blocks for the controlled step-by-step assembly of homo- and heteroatomic molecular cluster compounds up to nanomaterials is particularly interesting as an unprecedented control over the material's properties can be expected. However, not only the molecular assembly of such materials is valuable, but also the application of solutions with $[Ge_9]^{4-}$ Zintl anions as an ink like Ge source in the wet-chemical and template based fabrication of elemental germanium with porous structure.[14]

1.4 Prospects for Germanium Materials in Photovoltaics

The tremendously increasing energy consumption of mankind and the shortage of fossil fuels are a central issue of the 21th century. In particular the combustion of fossil fuels for the generation of electricity is associated with fundamental impacts on the global climate and brings severe problems for nature and humans. The sun as an virtually infinite energy reservoir is a long-term and sustainable alternative to the burning of fossil fuels and nuclear power.[113] Accordingly it is essential to develop new materials and photovoltaics concepts for the efficient conversion of solar energy into electricity. From the material's point of view, germanium is interesting for that kind of application due to its diverse opto-electronic properties[5, 14] and its special feature to exist in form of soluble molecular $[Ge_9]^{4-}$ atom clusters.[30, 31]

The fundamental working principle (Figure 1.6) of photovoltaic cells grounds on the photo-generation and dissociation of electron-hole-pairs (excitons) at a p-n heterojunction. Upon dissociation of the excitons, the electrons and holes move via the n- (acceptor) and p-type (donor) semiconductor to metal contacts, respectively, and an electrical potential is generated, which can be used to operate electrical devices. [114]

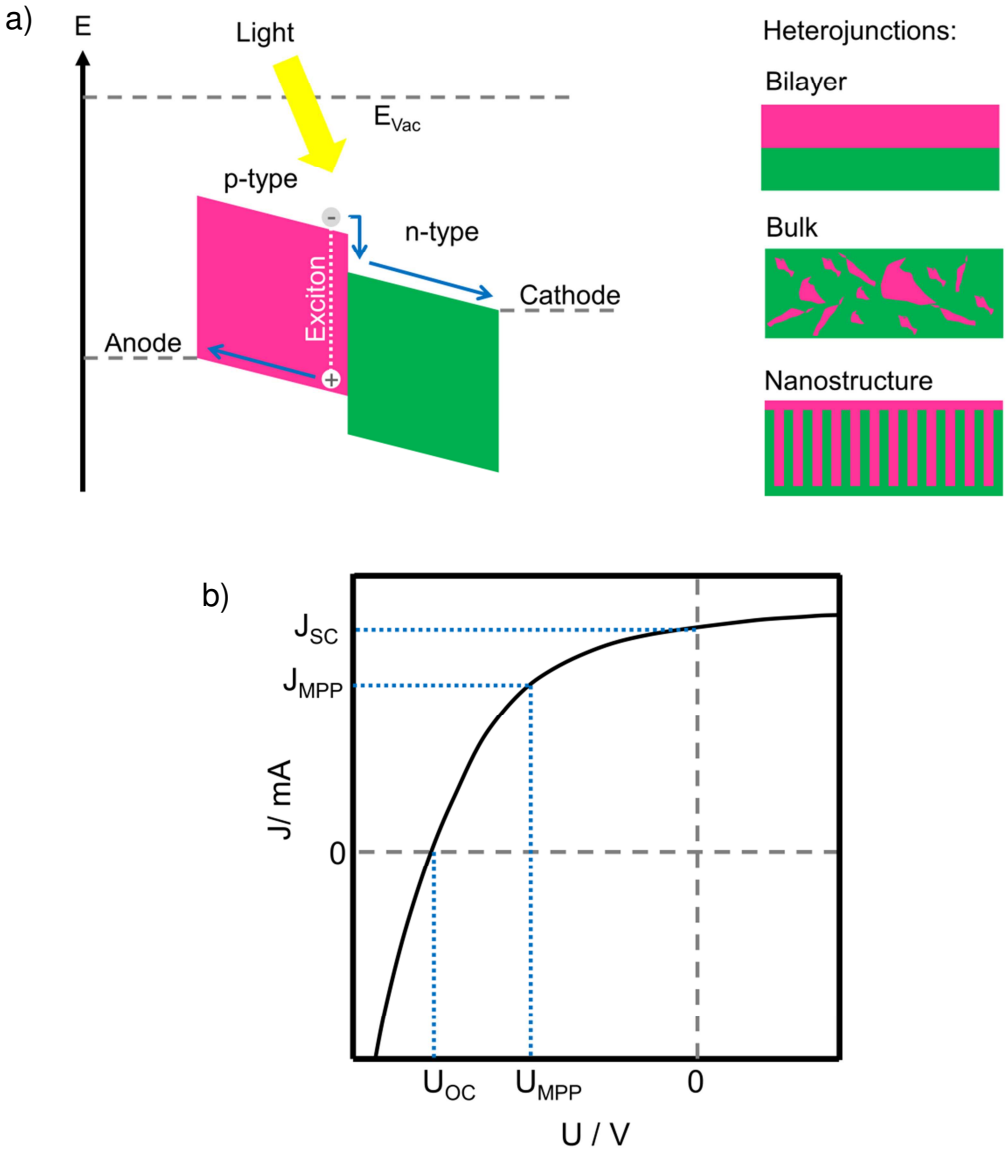

Figure 1.6. a) Schematic representation of a p-n-junction solar cell. p-type (donor) and n-type (acceptor) semiconductor are depicted in pink and green, respectively. The movement of the electrons and holes is illustrated by blue arrows. On the right side of the illustration differently structured heterojunctions are shown. The figure was modified on the basis of ref. [115]. b) J-U-curve of a solar cell under illumination. The intersections of the curve with the abscissa and ordinate characterize the short cut current (J_{SC}) and open circuit voltage (U_{OC}) of the cell. By operating the cell at J_{MPP} and U_{MPP} (MPP = maximum power point) the power output is maximal. The figure and figure caption was modified on the basis of ref. [116].

Established photovoltaic concepts such as n-Si/p-Si based solar cells exhibit high durability and efficiencies up to 24 %.[114, 117] Even though, energy expensive production and rigidity of such solar cells make alternative approaches necessary for the future.[115, 116, 118] Alternative concepts such as organic solar cells, in which the donor and acceptor interfaces are formed by organic molecules with extended π-electron systems, are one focus of research due to their cheap and easy roll-to-roll

production. Commonly used acceptor and donor molecules in that context are [6,6]-phenyl-C61-butyric acid methyl ester (PCBM)[119] and poly(3-hexylthiophen-2,5-diyl (P3HT)[120] (Figure 1.7), respectively. In a typical P3HT/PCBM cell[121], excitons are generated in the P3HT layer and PCBM passes over the electrons from the P3HT to a metal contact. Due to poor exciton diffusion length in the organic polymers of only 10-20 nm, the organic donor-akzeptor-materials are intermixed at the nanoscale in order to achieve efficient charge separation. However, rather low efficiencies and short life times, attributed to fast photo-oxidation of the organic materials, has hindered a large scale commercialization of these cells so far.[118] The capability of Ge_9 clusters to accommodate different numbers of electrons and their close relation to fullerenes [30, 31, 129] as well as the opportunity of their organic functionalization[56], points to the application of organo-Zintl clusters and larger tetrel clusters as molecular donor/acceptor material in photovoltaics.

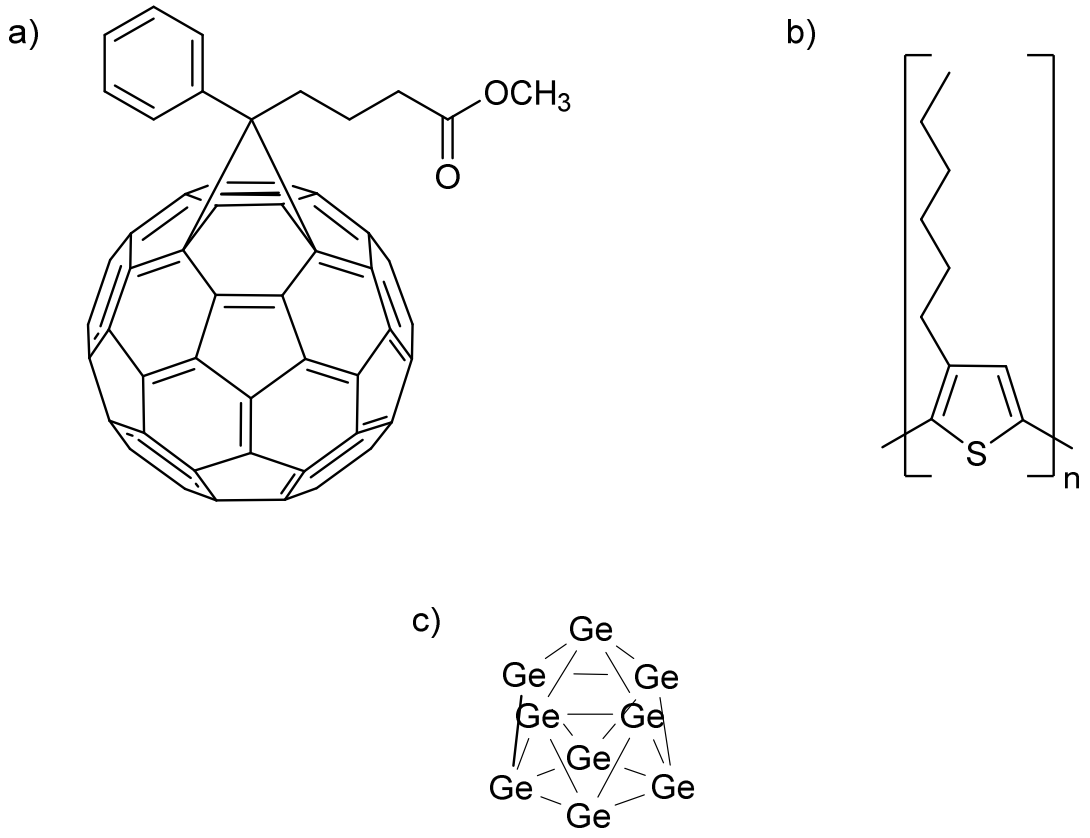

Figure 1.7. a/b) Chemical structures of organic donor and acceptor molecules for organic photovoltaics. a) [6,6]-phenyl-C61-butyric acid methyl ester (PCBM) and b) poly(3-hexylthiophen-2,5-diyl (P3HT). c) Chemical structure of a C_{4v} symmetric $[Ge_9]^{4-}$ Zintl anion for comparison.

An alternative photovoltaic concept grounds on the combination of the unique opportunities of inorganic and organic semiconductor films in inorganic/organic hybrid

solar cells.[115, 116] In particular good photo-stabilities as well as size and composition tunable properties make inorganic materials interesting for such applications. [7, 115, 116, 122] To overcome the problem of short exciton diffusion length in the organic polymers and efficiently harvest the excitons, nanostructuring of the inorganic materials is reasonable.[115] Metal oxide films, which are readily accessible by wet-chemical procedures[123] have been frequently used in hybrid solar cells.[116, 122] As an alternative to metal oxides, porous non-oxide semiconductors such as porous germanium have gained a lot of attention due to high absorption coefficients, tunable opto-electronic properties as well as inherently high charge carrier mobility.[5, 7] The tuning of porous materials by changing their compositions and morphologies enables the harmonization of the electronic properties of the organic and inorganic materials and hold out the prospect of hybrid solar cells with enhanced efficiency.[5, 115] Regular porosity of materials also alters their optical absorption behavior, which can be advantageous for efficient photon harvesting.[14, 124]

1.5 Motivation, Scope and Outline

1.5.1 Motivation and Scope

The opportunity to tailor the opto-electronic properties of germanium, by composition tuning and nanostructuring[14], as well as the close relation of Ge_9 clusters with fullerenes[129], makes both porous forms and molecular cluster compounds of Ge attractive in terms of photovoltaics and other applications such as artificial photosynthesis and spintronics. [30, 31] The high solubility and multifaceted reactivity of the $[Ge_9]^{4-}$ Zintl anion allows its utilization as precursor for the bottom up synthesis of novel clusters [30, 31] and porous forms of germanium with tailored compositions and structures.[104-108, 110] Inspired by these very facts, in the present work the reactivity of $[Ge_9]^{4-}$ Zintl anions was further investigated with respect to their linking and extension to novel molecular cluster compounds as well as their controlled oxidation to elemental germanium with tunable composition and morphology (Figure 1.8).

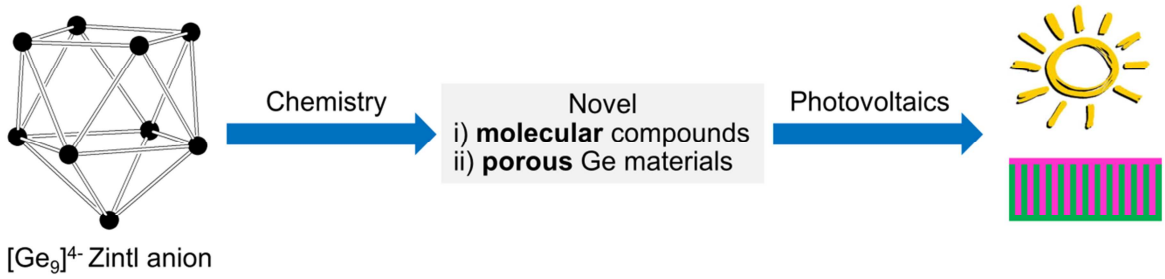

Figure 1.8. Illustration showing the motivation of this work

Linking of Ge_9 clusters by conjugated organic building blocks holds out the prospect of materials which can be reversible oxidized and/or accommodate electrons in different spin states.[125] Also grafting of such molecules to surfaces via additional organic tethers is reasonable[60] and points to the fabrication of electroactive films and particles. In that context the homologous fullerenes have been thoroughly investigated and a bunch of electroactive {fullerene-linker-fullerene} triads has been synthesized.[119, 126, 127] One possible synthetic approach for analogous {Ge_9-linker-Ge_9} Zintl triads represents the reaction of $[Ge_9]^{4-}$ with alkadiynes. Even though the reaction of $[E_9]^{4-}$ with alkynes has been thoroughly investigated before and resulted in a multitude of alkenylated Zintl anions (see chapter 1.2.2)[53-61], {Ge_9-linker-Ge_9} Zintl triads have not been synthesized prior to this work. Accordingly one aim of this thesis was the development of a method allowing the controlled synthesis of {Ge_9-linker-Ge_9} Zintl triads.

The controlled step-by-step assembly of larger homo- and heteroatomic tetrel clusters [30, 31, 72, 73] up to nanoscaled $Ge_{1-x}E_x$ with deltahedral structures, by the atom-wise extension/linking of $[Ge_9]^{4-}$ Zintl anions with tetrel atoms, holds out the prospect of materials with unforeseen properties and new element allotropes [104, 108, 111, 112]. The general suitability of $[Ge_9]^{4-}$ as molecular building block for larger homo- and heteroatomic cage-like materials is highlighted by the variety of oxidatively coupled clusters and intermetalloids which were obtained from solution based reactions of the clusters (see chapter 1.2.2).[30, 31] In view of the controlled assembly of larger, fullerene analogous, tetrel clusters and frameworks with deltahedral structures, reactions allowing the atom-wise extension and linking of $[Ge_9]^{4-}$ Zintl anions with germanium and tin were investigated in the course of this work.

In regard to the application of germanium in hybrid solar cells, flexible wet-chemical procedures for the fabrication of porous film morphologies – such as inverse opals - with tunable composition are necessary.[5, 7, 115] As reviewed in

chapter 1.4, porous germanium is advantageous for hybrid solar cells due to its variable properties.[14] Even though $[Ge_9]^{4-}$ Zintl anions have been used as precursor for porous powders before [104-108, 128], a wet-chemical method for continuous germanium film morphologies has not been described prior to this work. Moreover, the introduction of dopants like phosphorus [23, 24] into the films is also important, as it further enhances electrical conductivities and facilitates charge carrier extraction from a photovoltaic device. Motivated by these very facts, another aim of this thesis was the development of a wet-chemical and template-based method, utilizing $[Ge_9]^{4-}$ Zintl anions as soluble Ge source, for the fabrication of extended inverse opal and flat $Ge_{1-x}M_x$ (*M* = Ge, Si, P) films and their application in P3HT/Ge based hybrid solar cells [4].

1.5.2 Outline

Chapter 3.1 deals with the synthesis of the first {Ge_9-Linker-Ge_9} Zintl triads by reaction of $[Ge_9]^{4-}$ Zintl anions with 1,4-bis(trimethylsilyl)butadiyne in *en*. In **chapter 3.1.2** fundamental investigations on the reaction of *en* with 1,4-bis(trimethylsilyl)butadiyne in the absence of clusters and the role of water are presented. From these experiments a new method for the qualitative determination of water in *en* was derived and is demonstrated. The Zintl triad $[Ge_9–CH=CH–CH=CH–Ge_9]^{6-}$ is presented in **chapter 3.1.3** in terms of synthesis, X-ray structure and Raman spectrum along with an *in situ* NMR study delineating its formation. In **chapter 3.1.4** investigations on the grafting of 7-amino-5-aza-hepta-2,4-dien-2-yl organic tethers at Ge_9 clusters are presented in terms of the synthesis as well as *in situ* ESI-MS and NMR characterization of $[Ge_9–R]^{3-}$ and $[R–Ge_9–R]^{2-}$ (R =7-amino-5-aza-hepta-2,4-dien-2-yl). **Chapter 3.1.5** deals with the Zintl Triad $[R–Ge_9–CH=CH–CH=CH–Ge_9–R]^{4-}$ [R = (2Z,4E)-7-amino-5-aza-hepta-2,4-dien-2-yl] in regard to its synthesis, X-ray structure, spectroscopic characterization and electronic properties.

Investigations on the extension and linking of $[Ge_9]^{4-}$ Zintl anions by addition of tetrel atoms, such as germanium and tin are shown in **chapter 3.2**. In **chapter 3.2.2** the synthesis of *closo*-$[Ge_{10}]^{2-}$, by oxidative extension of $[Ge_9]^{4-}$ through reaction with *en*, as well as its isolation and structural characterization is shown. The latter is described in terms of X-ray structure, ESI-MS and Raman-spectrum. *In situ* ESI-MS investigations, shedding light on the formation of *closo*-$[Ge_{10}]^{2-}$, are additionally

presented. **Chapter 3.2.3** deals with the linking of Ge_9 clusters via tin atoms, by reaction of $SnPh_2Cl_2$ with $[Ge_9]^{4-}$ Zintl anions in the presence of elemental potassium. In that context, the structure and bonding situation of the herein obtained $[(\eta^4\text{-}Ge_9)Sn(\eta^3\text{-}Ge_9)]^{4-}$ Zintl anion are discussed and compared to other group 13/14 clusters.

In **chapter 3.3** the utilization of $[Ge_9]^{4-}$ Zintl anions as soluble Ge source for the wet-chemical and template-based fabrication of germanium inverse opal films with tunable composition and their application in P3HT based hybrid solar cells, is demonstrated. **Chapter 3.3.2** deals with fundamental *ex situ* investigations on the oxidation of $[Ge_9]^{4-}$ Zintl anions to amorphous/crystalline bulk Ge and $Ge_{1-x}M_x$ (M = Si, Ge, n = 4; M = P, n = 3), by reaction with *en* (**chapter 3.3.2.1**) and MCl_n (**chapter 3.3.2.2**), respectively. In **chapter 3.3.3** the wet-chemical and template-based fabrication of amorphous/crystalline Ge and $Ge_{1-x}M_x$ inverse opal films is presented. In that chapter also results on the morphological and electronic characterization of such films are shown. In **chapter 3.3.4** the application of inverse opal and also flat germanium films in P3HT based hybrid solar cells is shown.

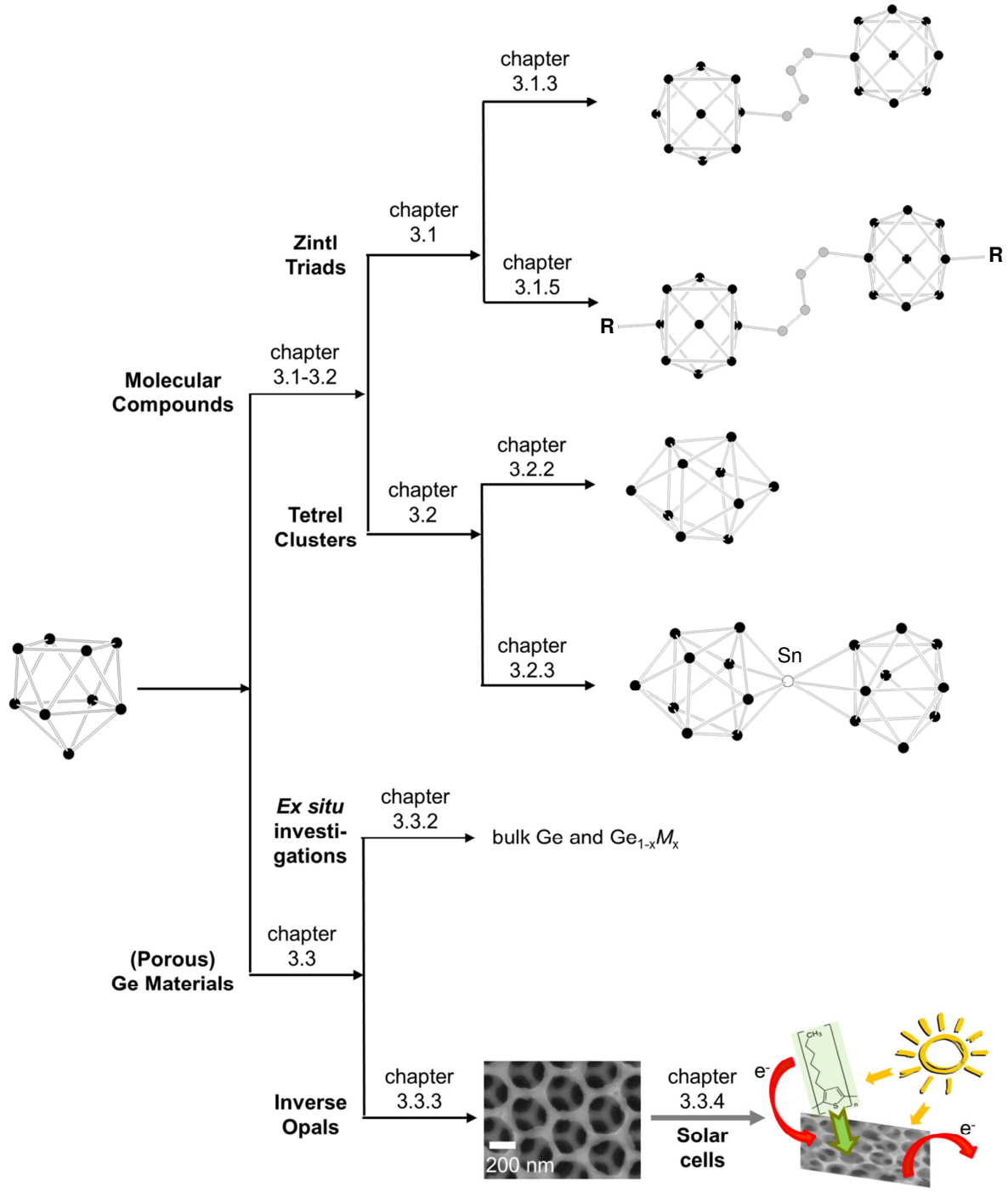

Figure 1.9. Illustration giving an outline to the results of this work. Ge and C atoms are shown as black and grey spheres, respectively.

1.6 Literature

[1] A. F. Holleman, E. Wiberg, N. Wiberg, *Lehrbuch der anorganischen Chemie*, de Gruyter, **1995**.

[2] C. E. Housecroft, A. G. Sharpe, A. Rompel, *Anorganische Chemie*, Pearson Studium, **2006**.

[3] C. Claeys, E. Simoen, *Germanium-Based Technologies: From Materials to Devices*, Elsevier Science, **2011**.

[4] A. Du Pasquier, D. D. T. Mastrogiovanni, L. A. Klein, T. Wang, E. Garfunkel, *Appl. Phys. Lett.* **2007**, *91*, 183501.

[5] M. G. Kanatzidis, *Adv. Mater.* **2007**, *19*, 1165.

[6] W. Guter, J. Schone, S. P. Philipps, M. Steiner, G. Siefer, A. Wekkeli, E. Welser, E. Oliva, A. W. Bett, F. Dimroth, *Appl. Phys. Lett.* **2009**, *94*, 223504.

[7] P.-L. Ong, I. Levitsky, *Energies* **2010**, *3*, 313.

[8] B. Hekmatshoar, D. Shahrjerdi, M. Hopstaken, K. Fogel, D. K. Sadana, *Appl. Phys. Lett.* **2012**, *101*, 032102.

[9] K. Ramasamy, P. G. Kotula, A. F. Fidler, M. T. Brumbach, J. M. Pietryga, S. A. Ivanov, *Chem. Mater.* **2015**, *27*, 4640.

[10] T. Song, Y. Jeon, M. Samal, H. Han, H. Park, J. Ha, D. K. Yi, J.-M. Choi, H. Chang, Y.-M. Choi, U. Paik, *Energy & Environmental Science* **2012**, *5*, 9028.

[11] H. Jia, R. Kloepsch, X. He, J. P. Badillo, P. Gao, O. Fromm, T. Placke, M. Winter, *Chem. Mater.* **2014**, *26*, 5683.

[12] J. Liang, X. Li, Z. Hou, T. Zhang, Y. Zhu, X. Yan, Y. Qian, *Chem. Mater.* **2015**, *27*, 4156.

[13] C. Zhang, Z. Lin, Z. Yang, D. Xiao, P. Hu, H. Xu, Y. Duan, S. Pang, L. Gu, G. Cui, *Chem. Mater.* **2015**, *27*, 2189.

[14] A. Stein, *Nature* **2006**, *441*, 1055.

[15] R. Pillarisetty, *Nature* **2011**, *479*, 324.

[16] R. W. Olesinski, G. J. Abbaschian, *Bull. Alloy Phase Diagr.* **1984**, *5*, 180.

[17] R. W. Olesinski, G. J. Abbaschian, *Bull. Alloy Phase Diagr.* **1984**, *5*, 265.

[18] E. Kasper, *J. Cryst. Growth* **1995**, *150, Part 2*, 921.

[19] A. Gerhard, *Phys. Scripta* **1996**, *1996*, 68.

[20] S. Abedrabbo, D. E. Arafah, S. Salem, *J. Electron. Mater.* **2005**, *34*, 468.

[21] E. Kasper, M. Kittler, M. Oehme, T. Arguirov, *Photonics Research* **2013**, *1*, 69.

[22] A. B. Fowler, W. E. Howard, G. E. Brock, *Phys. Rev.* **1962**, *128*, 1664.

[23] G. Contreras, L. Tapfer, A. K. Sood, M. Cardona, *Phys. Status. Solidi. B.* **1985**, *131*, 475.

[24] N. Fukata, K. Sato, M. Mitome, Y. Bando, T. Sekiguchi, M. Kirkham, J.-i. Hong, Z. L. Wang, R. L. Snyder, *ACS Nano* **2010**, *4*, 3807.

[25] A. G. Cullis, L. T. Canham, P. D. J. Calcott, *J. Appl. Phys.* **1997**, *82*, 909.

[26] E. Zintl, *Angew. Chem.* **1939**, *52*, 1.

[27] F. Laves, *Naturwissenschaften* **1941**, *29*, 244.

[28] E. Busmann, S. Lohmeyer, *Z. Anorg. Allg. Chem.* **1961**, *312*, 53.

[29] C. Hoch, M. Wendorff, C. Röhr, *J. Alloy. Compd.* **2003**, *361*, 206.

[30] S. C. Sevov, J. M. Goicoechea, *Organometallics* **2006**, *25*, 5678.
[31] S. Scharfe, F. Kraus, S. Stegmaier, A. Schier, T. F. Fässler, *Angew. Chem. Int. Ed.* **2011**, *50*, 3630.
[32] E. Busmann, *Z. Anorg. Allg. Chem.* **1961**, *313*, 90.
[33] W. Klemm, E. Busmann, *Z. Anorg. Allg. Chem.* **1963**, *319*, 297.
[34] J. Witte, H. G. Schnering, *Z. Anorg. Allg. Chem.* **1964**, *327*, 260.
[35] H. G. Schnering, S. M., J.-H. Chang, K. Peters, E.-M. Peters, R. Nesper, . *Z. Kristallogr. NCS* **2005**, *220*, 525.
[36] H. G. Von Schnering, M. Baitinger, U. Bolle, W. Carrillo-Cabrera, J. Curda, Y. Grin, F. Heinemann, J. Llanos, K. Peters, A. Schmeding, M. Somer, *Z. Anorg. Allg. Chem.* **1997**, *623*, 1037.
[37] V. Queneau, S. C. Sevov, *Angew. Chem. Int. Ed.* **1997**, *36*, 1754.
[38] V. Queneau, S. C. Sevov, *Inorg. Chem.* **1998**, *37*, 1358.
[39] E. Todorov, S. C. Sevov, *Inorg. Chem.* **1998**, *37*, 3889.
[40] S. Ponou, T. F. Fässler, *Z. Anorg. Allg. Chem.* **2007**, *633*, 393.
[41] K. Wade, *Inorg. Nucl. Chem. Lett.* **1972**, *8*, 559.
[42] K. Wade, *Adv. Inorg. Chem., Vol. Volume 18* (Eds.: H. J. Emeléus, A. G. Sharpe), Academic Press, **1976**, pp. 1.
[43] J. D. Corbett, *Chem. Rev.* **1985**, *85*, 383.
[44] M. Waibel, *Dissertation* **2012**.
[45] J. M. Goicoechea, S. C. Sevov, *J. Am. Chem. Soc.* **2004**, *126*, 6860.
[46] M. Waibel, F. Kraus, S. Scharfe, B. Wahl, T. F. Fässler, *Angew. Chem. Int. Ed.* **2010**, *49*, 6611.
[47] S. Joseph, M. Hamberger, F. Mutzbauer, O. Härtl, M. Meier, N. Korber, *Angew. Chem. Int. Ed.* **2009**, *48*, 8770
[48] J. D. Corbett, D. G. Adolphson, D. J. Merryman, P. A. Edwards, F. J. Armatis, *J. Am. Chem. Soc.* **1975**, *97*, 6267.
[49] T. F. Fässler, R. Hoffmann, *Angew. Chem. Int. Ed.* **1999**, *38*, 543.
[50] T. F. Fässler, *Coordin. Chem. Rev.* **2001**, *215*, 347.
[51] J. Åkerstedt, S. Ponou, L. Kloo, S. Lidin, *Eur. J. Inorg. Chem.* **2011**, *2011*, 3999.
[52] A. Ugrinov, S. C. Sevov, *J. Am. Chem. Soc.* **2003**, *125*, 14059.
[53] M. W. Hull, S. C. Sevov, *Angew. Chem. Int. Ed.* **2007**, *46*, 6695.
[54] M. W. Hull, S. C. Sevov, *Inorg. Chem.* **2007**, *46*, 10953.
[55] D. J. Chapman, S. C. Sevov, *Inorg. Chem.* **2008**, *47*, 6009.
[56] M. W. Hull, S. C. Sevov, *J. Am. Chem. Soc.* **2009**, *131*, 9026.
[57] M. M. Gillett-Kunnath, I. Petrov, S. C. Sevov, *Inorg. Chem.* **2009**, *49*, 721.
[58] C. B. Benda, J.-Q. Wang, B. Wahl, T. F. Fässler, *Eur. J. Inorg. Chem.* **2011**, 4262.
[59] M. M. Gillett-Kunnath, A. G. Oliver, S. C. Sevov, *J. Am. Chem. Soc.* **2011**, *133*, 6560.
[60] M. W. Hull, S. C. Sevov, *J. Organomet. Chem.* **2012**, *721*, 85.
[61] M. W. Hull, S. C. Sevov, *Chem. Commun.* **2012**, *48*, 7720.
[62] M. W. Hull, A. Ugrinov, I. Petrov, S. C. Sevov, *Inorg. Chem.* **2007**, *46*, 2704.

[63] C. B. Benda, R. Schäper, S. Schulz, T. F. Fässler, *Eur. J. Inorg. Chem.* **2013**, *2013*, 5964.
[64] L. Xu, S. C. Sevov, *J. Am. Chem. Soc.* **1999**, *121*, 9245.
[65] A. Nienhaus, S. D. Hoffmann, T. F. Fässler, *Z. Anorg. Allg. Chem.* **2006**, *632*, 1752.
[66] C. Downie, Z. J. Tang, A. M. Guloy, *Angew. Chem. Int. Ed.* **2000**, *39*, 337.
[67] A. Ugrinov, S. C. Sevov, *J. Am. Chem. Soc.* **2002**, *124*, 10990.
[68] A. Ugrinov, S. C. Sevov, *Inorg. Chem.* **2003**, *42*, 5789.
[69] L. Yong, S. D. Hoffmann, T. F. Fässler, *Z. Anorg. Allg. Chem.* **2004**, *630*, 1977.
[70] A. Ugrinov, S. C. Sevov, *Chem. Eur. J.* **2004**, *10*, 3727.
[71] A. J. Karttunen, T. F. Fässler, M. Linnolahti, T. A. Pakkanen, *Chemphyschem* **2010**, *11*, 1944.
[72] T. F. Fässler, S. D. Hoffmann, *Angew. Chem. Int. Ed.* **2004**, *43*, 6242.
[73] S. Scharfe, T. F. Fässler, *Phil. Trans. A Math. Phys. Eng. Sci.* **2010**, *368*, 1265.
[74] B. W. Eichhorn, R. C. Haushalter, W. T. Pennington, *J. Am. Chem. Soc.* **1988**, *110*, 8704.
[75] B. W. Eichhorn, R. C. Haushalter, *J. Chem. Soc., Chem. Comm.* **1990**, 937.
[76] B. Kesanli, J. Fettinger, B. Eichhorn, *Chem. Eur. J.* **2001**, *7*, 5277.
[77] J.-Q. Wang, S. Stegmaier, B. Wahl, T. F. Fässler, *Chem. Eur. J.* **2010**, *16*, 1793.
[78] J. M. Goicoechea, S. C. Sevov, *J. Am. Chem. Soc.* **2006**, *128*, 4155.
[79] Z.-M. Sun, Y.-F. Zhao, J. Li, L.-S. Wang, *J. Clust. Sci.* **2009**, *20*, 601.
[80] S. Scharfe, T. F. Fässler, *Eur. J. Inorg. Chem.* **2010**, *2010*, 1207.
[81] J. M. Goicoechea, S. C. Sevov, *Organometallics* **2006**, *25*, 4530.
[82] D. Rios, S. C. Sevov, *Inorg. Chem.* **2010**, *49*, 6396.
[83] A. Spiekermann, S. D. Hoffmann, T. F. Fässler, I. Krossing, U. Preiss, *Angew. Chem. Int. Ed.* **2007**, *46*, 5310.
[84] J.-Q. Wang, S. Stegmaier, T. F. Fässler, *Angew. Chem. Int. Ed.* **2009**, *48*, 1998.
[85] S. Scharfe, T. F. Fässler, *Eur. J. Inorg. Chem.* **2010**, 1207.
[86] M. S. Denning, J. M. Goicoechea, *Dalton Trans.* **2008**, 5882.
[87] M. B. Boeddinghaus, S. D. Hoffmann, T. F. Fässler, *Z. Anorg. Allg, Chem.* **2007**, *633*, 2338.
[88] A. Spiekermann, S. D. Hoffmann, F. Kraus, T. F. Fässler, *Angew. Chem. Int. Ed.* **2007**, *46*, 1638.
[89] B. Zhou, M. S. Denning, T. A. D. Chapman, J. E. McGrady, J. M. Goicoechea, *Chem. Commun.* **2009**, 7221.
[90] C. B. Benda, M. Waibel, T. F. Fässler, *Angew. Chem. Int. Ed.* **2015**, *54*, 522.
[91] S. C. Critchlow, J. D. Corbett, *Inorg. Chem.* **1982**, *21*, 3286.
[92] M. M. Gillett-Kunnath, I. Petrov, S. C. Sevov, *Inorg. Chem.* **2010**, *49*, 721.
[93] D. Rios, M. M. Gillett-Kunnath, J. D. Taylor, A. G. Oliver, S. C. Sevov, *Inorg. Chem.* **2011**, *50*, 2373.

[94] D. F. Hansen, B. Zhou, J. M. Goicoechea, *J. Organomet. Chem.* **2012**, *721-722*, 53.
[95] M. M. Gillett-Kunnath, A. Muñoz-Castro, S. C. Sevov, *Chem. Commun.* **2012**, *48*, 3524.
[96] C. B. Benda, *Dissertation,* Technical University of Munich, Garching **2013**.
[97] K. K. Rangan, P. N. Trikalitis, M. G. Kanatzidis, *J. Am. Chem. Soc.* **2000**, *122*, 10230.
[98] P. N. Trikalitis, K. K. Rangan, T. Bakas, M. G. Kanatzidis, *Nature* **2001**, *410*, 671.
[99] S. D. Korlann, A. E. Riley, B. L. Kirsch, B. S. Mun, S. H. Tolbert, *J. Am. Chem. Soc.* **2005**, *127*, 12516.
[100] A. E. Riley, S. D. Korlann, E. K. Richman, S. H. Tolbert, *Angew. Chem. Int. Ed.* **2006**, *45*, 235.
[101] S. D. Korlann, A. E. Riley, B. S. Mun, S. H. Tolbert, *J. Phsy. Chem. C* **2009**, *113*, 7697.
[102] F. Henke, C. Schenk, A. Schnepf, *Dalton Trans* **2009**, 9141.
[103] F. Li, S. C. Sevov, *Inorg. Chem.* **2012**, *51*, 2706.
[104] G. S. Armatas, M. G. Kanatzidis, *Science* **2006**, *313*, 817.
[105] G. S. Armatas, M. G. Kanatzidis, *J. Am. Chem. Soc.* **2008**, *130*, 11430.
[106] G. S. Armatas, M. G. Kanatzidis, *Adv. Mater.* **2008**, *20*, 546.
[107] G. S. Armatas, M. G. Kanatzidis, *Nano Lett* **2010**, *10*, 3330.
[108] S. Dong, A. E. Riley, A. J. Cadby, E. K. Richman, S. D. Korlann, S. H. Tolbert, *Nature* **2006**, *441*, 1126.
[109] N. Chandrasekharan, S. C. Sevov, *J. Electrochem. Soc.* **2010**, *157*, C419.
[110] N. Chandrasekharan, S. C. Sevov, *J. Electrochem. Soc.* **2010**, *157*, C140.
[111] A. M. Guloy, R. Ramlau, Z. Tang, W. Schnelle, M. Baitinger, Y. Grin, *Nature* **2006**, *443*, 320.
[112] T. F. Fässler, *Angew. Chem. Int. Ed.* **2007**, *46*, 2572.
[113] Frankfurt School – UNEP Collaboration Centre, *Global Trends in Renewable Energy Investment 2016*, **2016**.
[114] A. Luque, S. Hegedus, *Handbook of Photovoltaic Science and Engineering*, Wiley, **2003**.
[115] M. D. McGehee, *MRS Bulletin* **2009**, *34*, 95.
[116] S. Günes, N. S. Sariciftci, *Inorg. Chim. Acta* **2008**, *361*, 581.
[117] M. A. Green, *Progr. Photovol: Res. Appl.* **2001**, *9*, 123.
[118] S. Günes, H. Neugebauer, N. S. Sariciftci, *Chem. Rev.* **2007**, *107*, 1324.
[119] N. Martín, L. Sánchez, B. Illescas, I. Pérez, *Chem. Rev.* **1998**, *98*, 2527.
[120] T. J. Prosa, M. J. Winokur, J. Moulton, P. Smith, A. J. Heeger, *Macromolecules* **1992**, *25*, 4364.
[121] P. Vanlaeke, A. Swinnen, I. Haeldermans, G. Vanhoyland, T. Aernouts, D. Cheyns, C. Deibel, J. D'Haen, P. Heremans, J. Poortmans, J. V. Manca, *Sol. Energ. Mat. Sol. C.* **2006**, *90*, 2150.
[122] S.-S. Li, C.-W. Chen, *J. Mater. Chem. A* **2013**, *1*, 10574.
[123] D. Fattakhova-Rohlfing, A. Zaleska, T. Bein, *Chem. Rev.* **2014**, *114*, 9487.

[124] S. Guldin, S. Hüttner, M. Kolle, M. E. Welland, P. Müller-Buschbaum, R. H. Friend, U. Steiner, N. Tétreault, *Nano Lett* **2010**, *10*, 2303.
[125] M. M. Bentlohner, W. Klein, Z. H. Fard, L.-A. Jantke, T. F. Fässler, *Angew. Chem. Int. Ed.* **2015**, *54*, 3748.
[126] J. L. Segura, N. Martin, *Chem. Soc. Rev.* **2000**, *29*, 13.
[127] M. A. Lebedeva, T. W. Chamberlain, E. S. Davies, B. E. Thomas, M. Schröder, A. N. Khlobystov, *Beilstein J. Org. Chem.* **2014**, *10*, 332.
[128] G. S. Armatas, M. G. Kanatzidis, *Nature* **2006**, *441*, 1122.
[129] T. F. Fässler, *Angew. Chem. Int. Ed.* **2001**, *40*, 4161.

2 Experimental Section

2.1 General Experimental Procedures

2.1.1 Inert Gas Technique

Most of the precursors and products were moisture and air sensitive and therefore all manipulations were carried out in an argon atmosphere, using standard glove box and Schlenk technique (H_2O < 0.1 ppm, O_2 < 0.1 ppm). The glove boxes (*MBraun*) were filled with argon4.8 (*Westphalen*, purity 99.998%), which was recycled over a copper catalyst and mole sieve in order to remove oxygen and water traces. The copper catalyst was regenerated periodically with forming gas (Westphalen, 95% nitrogen, 5% hydrogen). Solution based reactions were performed under argon4.8 (*Westphalen*, purity 99.998%) by using standard Schlenk technique. Thereby, the argon4.8 was further purified in a gas cleaning unit (BTS catalyst, mole sieve 4 Å, P_4O_{10}) prior to use. Schlenk tubes (10-50 ml) were used as reaction vessels and cleaned in an isopropanol/KOH bath. All glass equipment and spatula were stored in a furnace at 120°C for at least 2 h. The Schlenk tubes were thoroughly dried by heating in fine vacuum (< 10^{-3} mbar) and purging with argon for three times. The vacuum was generated by an oil rotary vane pump and the pressure was measured with a Pirani pressure sensor (*Thyracont VSP841 Vacuum Instruments*). Glass junctions were lubricated with silicon-based high vacuum grease (*Dow Corning*)

2.1.2 Filtration of Reaction Solutions

Reaction solutions were filtered over glass fibers (Whatman GF/D) in order to remove finely dispersed precipitates. Therefore, the glass fiber filters were stuffed into a Pasteur pipette and dried for at least one day at 120 °C under ambient pressure in a furnace. Within a glove box the reaction solution was filtered and the filtrate was collected in a thoroughly dried Schlenk tube.

2.1.3 Annealing of Reaction Residues and Films

Samples for annealing were placed in a Schlenk tube (d = 35 mm) and heated in a tube furnace (*HTM Reetz GmbH Losa 600 40 180*) at temperatures between 100 °C and 600 °C. Powdery samples were additionally filled into a glass tube. The samples were either annealed in fine vacuum (< 10^{-3} mbar) or under argon at ambient pressure. In case of annealing in argon the Schlenk tube was connected to a pressure relief valve to release overpressures.

2.1.4 Reagents

Table 1.1. Overview on reagents used in this thesis

Name	Producer	Morphology	Purity	Storage
Germanium	Chempur	Pieces	99.999%	Glove box
Potassium	Lab inventory	Plastic mass	Liquated	Glove box
Rubidium	Lab inventory	Plastic mass	Liquated	Glove box
K_4Ge_9	Self-made (see 2.1.4.2)	Powder	Phase Pure	Glove box
Rb_4Ge_9	Self-made (see 2.1.4.2)	Powder	Phase Pure	Glove box
Ethylenediamine	Alfa Aesar	Liquid	Stored over CaH_2; Freshly collected (see 2.1.4.1)	Lab
1,4-bis(trimethylsilyl)-butadiyne	Alfa Aesar	Powder	98%	Glove box
1-(trimethylsilyl)-7-amino-5-aza-hepta-3-en-1-yne in ethylenediamine	Self-made	Liquid	-	Freshly prepared prior to use (see 2.1.4.3)
Poly(3-hexylthiophen-2,5-diyl)	Lab inventory	Powder	-	AK Müller-Buschbaum
cryptand[2.2.2]	Merck	Powder	Dried in vacuum	Glove box
18-crown-6	Merck	Powder	Sublimated	Glove box
Dichlorodiphenyltin	Sigma-Aldrich	Powder	96%	Glove box
Germaniumtetrachloride	Sigma-Aldrich	Liquid	99.999%	Glove box

Silicontetrachloride	Lab inventory	Liquid	-	Glove box
Phosphorustrichloride	Merck	Liquid	>99%	Glove box
Triphenlyphosphin	Lab inventory	Powder		Glove box
Toluene	Merck	Liquid	SPS	Lab
Tetrahydrofuran	Merck	Liquid	SPS	Lab
Dimethylsulfoxide	Sigma-Aldrich	Liquid	H_2O <0.005%	Glove box
Acetonitrile-d_3	Deutero GmbH	Liquid	Mole Sieve 4 Å	Glove box
Pyridine-d_5	Deutero GmbH	Liquid	Mole Sieve 4 Å	Glove box
Chloroform-d_1	Deutero GmbH	Liquid	Mole Sieve 4 Å	Lab
Polymethylmethacrylat monodisperse	AK Fattakhova-Rohlfing (Ludwig Maximilian University)	Powder	-	Lab

The solvents *tol* and *thf* were dried over mole sieve (4 Å) in a SPS solvent purificator (*MBraun MB-SPS*). The solvents *py*-d_5, *acn*-d_3 and *dmso* were dried over mole sieve in the original glass bottles. Cryptand[2.2.2] was dried in vacuum for at least 8 h. 18-crown-6 was sublimated in dynamic vacuum at ca. 80°C and further dried in vacuum prior to use.

2.1.4.1 Purification of Ethylenediamine

En (*Merck*) with an initial water content of ≤ 1% was refluxed over calcium hydride (*Merck*) and freshly collected prior to use. Water free *en* (denoted as grade A) was obtained after refluxing for 72 h. For *en* grade A, the sample tubes of the distillation apparatus were thoroughly cleaned and dried at 120°C immediately before the *en* collection. Most importantly, all glass parts of the *en* distillation apparatus have to be free of white residues, which form if *en* is exposed to moisture and ambient air. *En* containing trace amounts of water (denoted as grade B) was obtained after refluxing for 2-6 h. The sample tubes for grade B *en* were stored under ambient conditions. Qualitative analysis of water content was performed using reaction of *en* with 1,4-bis(trimethylsilyl)butadiyne.[1, 2] 1,4-bis(trimethylsilyl)butadiyne readily reacts with *en* to form different reaction products depending on the water content. Reaction in water-free conditions results in formation of 7-amino-1-(trimethylsilyl)-5-aza-hepta-3-

en-1-yne, whereas in presence of trace amounts of water this product further reacts to 2,3-dihydro-5-methyl-*H*-1,4-diazepine. The rate of the 2,3-dihydro-5-methyl-*H*-1,4-diazepine formation increases with the water content. In a typical procedure, 34.9 mg 1,4-bis(trimethylsilyl)butadiyne were dissolved in 3 ml *en*, and ^{1}H NMR spectra were recorded from the obtained solutions (in non-deuterated *en*, see chapter 2.2.11) after different reaction times. In *en* grade A, no 2,3-dihydro-5-methyl-*H*-1,4-diazepine is detectable even after more than 150 h of reaction time, whereas in *en* grade B the formation of 2,3-dihydro-5-methyl-*H*-1,4-diazepine is completed within 100 h.

2.1.4.2 Preparation of A_4Ge_9 (*A* = K, Rb)

K_4Ge_9 was synthesized by heating a stoichiometric mixture of the elements K and Ge (Chempur, 99.999%) at 650 C for 20 h (heating +2 K/min, cooling -1 K/min) in a stainless-steel autoclave.[3, 4] The autoclave was placed in a corundum tube, which was three times evacuated in fine vacuum (< 10^{-3} mbar) and purged with argon. The argon filled corundum tube was heated in a tube furnace (*HTM Reetz GmbH*), equipped with a temperature controller from *Eurotherm Deutschland Gmbh*. Rb_4Ge_9 was prepared by heating stoichiometric mixtures of the elements Rb and Ge at 650°C for 48 h (heating + 1 K/min, cooling -1 K/min) in a sealed tantalum ampoule.[3] Ta ampoules were prepared by cutting small cylinders from Ta tubes (diameter: 10 mm, wall thickness: 0.5 mm). The cylinders were crimped at one side and by arc melting (arc furnace MAM 1 *Edmund Bühler*) the crimp was sealed. The ampoules were cleaned by sonication in acetic acid, water and acetone. Prior to loading, the ampoules were thoroughly dried in an oven at 120°C. Loaded ampoules were placed into a fused silica tube and the silica tube was three times evacuated (< 10^{-3} mbar) and purged with argon. The evacuated silica tube was annealed in a tube furnace (*HTM Reetz GmbH*), equipped with temperature controller from *Eurotherm Deutschland Gmbh*. The obtained reaction products were finely mortared and stored in a glove box. The phase purity was checked by X-ray powder diffraction.

2.1.4.3 Preparation of 7-amino-1-(trimethylsilyl)-5-aza-hepta-3-en-1yne/*en* solutions

Solutions of 7-amino-1-(trimethylsilyl)-5-aza-hepta-3-en-1yne in *en* with concentrations of 60, 120 and 240 µmol/ml were prepared by reacting 23.4 mg (120 µmol), 46.7 mg (240 µmol) and 93.4 mg (480 µmol) of 1,4-bis(trimethylsilyl)butadiyne with each 2 ml *en* grade A in a Schlenk tube for 5-20 h, respectively.[5] Thereby pale yellow colored and transparent solutions were obtained. Prior to application for further syntheses, the solutions were filtered over glass wool in order to remove traces of unreacted 1,4-bis(trimethylsilyl)butadiyne.

2.1.5 Preparation of aqueous PMMA bead Dispersions

Monodisperse PMMA beads were prepared in the group of PD Dr. Dina Fattakhova-Rohlfing *University of Munich (LMU)*. A typical procedure for the synthesis of monodisperse PMMA is described elsewhere.[6] 1.5 g monodisperse PMMA beads were dispersed in 8.5 ml water by intensive stirring. To break up agglomerates, the mixture was stirred for one week and daily treated in an ultrasonicator for at least 15 min. The dispersity and the average PMMA bead size of the dispersion were determined by dynamic light scattering (*Malvern Zetasizer Nanoseries*). The obtained 15 wt% PMMA dispersion was used for fabrication of PMMA opal templates. In order to avoid agglomeration upon storage, the dispersion was continuously stirred.

2.1.6 Coating of Substrates with PMMA beads

PMMA opal films were prepared by depositing PMMA beads by dip-, spin- and spray-coating of substrates (silicon, silica, sapphire, FTO: 1-4 cm^2) with aqueous PMMA dispersions. Prior to coating, the substrates were cleaned by ultrasonication for 15 min in water/Extran, ethanol and acetone, respectively. Silicon, silica and sapphire substrates were additionally treated in an oxygen-plasma (*Diener Electronic*, *Femto Plasma System*, parameters: 10 min, 50 W, 4-5 cm^3/min) to improve the surface wettability.

Dip coating was performed at the chair of Prof. Dr. Thomas Bein (*University of Munich*) with a home-made dip-coater. Thereby, the substrate was clamped vertically at the dip-coater and dipped once (ca. 0.5 cm/s) into the PMMA dispersion. The coated substrate was stored vertically for ca. 10 min in ambient air, in order to evaporate the majority of water.

Spin-coating was performed at the chair of Nanoelectronics Prof. Dr. Paolo Lugli (*Technical University of Munich*) by Marius Loch with a SCC-200 spin coater (*NOVOCONTROL Technologies GmbH & Co. KG*). In a typical procedure, 100 µl of the aqueous PMMA dispersion were dropped onto the stationary substrate, which was subsequently rotated at 1500 rpm for 45 s.

Spray-coating was performed at the chair of Nanoelectronics Prof. Dr. Paolo Lugli (*Technical University of Munich*) by Marius Loch with a self-constructed setup. The deposition setup is composed of a commercially available spray gun (*Krautzberger GmbH, Germany*) connected to a semi-automated pneumatic controller. The atomizing gas is pressurized N_2 and the pressure was always kept below 2 bar in order to obtain smoother depositions. The samples were placed on a hotplate 15 cm below the spray gun and heated at 80 °C during the spray process. An aqueous PMMA dispersion (0.4 wt%, bead diameter: 250-300 nm) was used for spray coating and the spray time was 5-15 s.

2.1.7 Coating of PMMA Opals with K_4Ge_9

For the preparation of germanium inverse opal films, PMMA opal films were thoroughly dried (4 h, 100°C, fine vacuum: < 10^{-3} mbar) and coated with K_4Ge_9/*en* solutions by drop-casting and spin-coating. K_4Ge_9/*en* solutions were prepared by dissolving 50 mg K_4Ge_9 in 1 ml *en* grade A. The red-orange colored solutions were stirred for ca. 1 h and immediately before use filtered over a glass fiber filter in order to remove finely dispersed particles.

For drop casting, the PMMA opal films were horizontally placed in a glove box and by a syringe ca. 50-100 µl of the K_4Ge_9/*en* solution were dropped onto the PMMA opal. Instantaneously the substrate was slightly tilted in order to homogenously distribute the K_4Ge_9/*en* solution over the PMMA opal. Subsequently, the substrate was placed again horizontally in the glove box, whereby *en* evaporated within ca. 10 min and a PMMA/K_4Ge_9 composite formed.

Infiltration of PMMA Opals with K_4Ge_9/*en* by spin coating was performed with a Delta6 RC spin coater (*Süss MicroTec Lithography GmbH*) at the Chair of Nanoelectronics Prof. Dr. Paolo Lugli (*Technical University of Munich*) by Marius Loch. The spin coater was placed in a nitrogen filled glove box (*MBraun*). In a typical procedure, 100 µl of precursor solution were dropped onto the stationary substrate, which was subsequently rotated at 1500 rpm for 40 s

Under thorough exclusion of water the K_4Ge_9/PMMA composites were colored intensively orange, however in presence of water-traces the color was dark-violet.

2.1.8 Assembly of P3HT/Ge Hybrid Solar Cells and Efficiency Tests

Flat and inverse opal structured germanium films were deposited on FTO substrates, covered with a thin layer of TiO_2. Subsequently, the germanium films were coated/infiltrated with P3HT solution (20 mg/ml in chlorobenzene) by spin coating (Delta 6 RC TT, *Süss MicroTec Lithography GmbH*, 2000 rpm, 60 s). After P3HT deposition, a mask was placed on top of the P3HT/Ge/TiO_2/FTO composites and then gold contacts were deposited by physical vapor deposition.

The efficiency of the as prepared hybrid solar cells were tested in a solar simulator (SolarConstant, K. H. *Steuernagel Lichttechnik GmbH*). The light intensity was calibrated to be 1000 W/cm^2 (AM1.5 solar illumination) by using a silicon-based calibration solar cell (WPVS Reference Solar Cell Type RS-ID-3k Fraunhofer ISE). The IV-curves were recorded with a Keithley 2400 sourcemeter and the bias was -1 V to 0.1 V.

P3HT and gold coating of inverse opal films as well as the testing of the assembled cells was done by co-workers of the chair for functional materials Prof. Dr. P. Müller-Buschbaum (*Technical University of Munich*).

2.2 Characterization Methods

2.2.1 Single Crystal X-ray Diffraction

The crystal structures presented in this work were determined by means of single crystal X-ray diffraction methods at the chair of Prof. Dr. Thomas F. Fässler (*Technical University of Munich*). All crystals were prepared and measured under inert gas due to their air and moisture sensitivity. Single crystals were measured with Xcalibur3 (*Oxford*), FR591 APEX II (*Bruker*) and D8 APEX II (*Bruker*) diffractometers comprising goniometers with kappa geometry. The diffractometers were equipped with CCD (charge coupled device) detectors and Mo-radiation was generated either by an X-ray tube or a rotating anode (50 kV/40 mA). By means of graphite the radiation of the X-ray sources was monochromatized to Mo-$K_{\alpha 1}$ (λ = 0.71073 Å). Single crystals were fixed on the top of a glass capillary with perfluorinated ether and positioned in a cold N_2 stream at 100-130 K (*Oxford Cryosystems*). Absorption correction was done empirically.[7] The crystal structures were solved by Direct Methods using the SHELX-97 program-package.[8] The positions of the hydrogen atoms were geometrically calculated and refined using a riding model. All non-hydrogen atoms were treated with anisotropic displacement parameters. In special cases disordered solvent molecules were treated with the SQUEEZE option in PLATON.[9, 10] For raw data processing and visualistion of the crystal structures the programs CrysalisRED[11] and Diamond[12] were used, respectively.

2.2.2 X-ray Powder Diffraction

X-ray powder diffractograms *(XRD)* were recorded on STADI P (*STOE Darmstadt*, Cu-$K_{\alpha 1}$ radiation, Ge monochromator) powder diffractometers. The diffractometers were either equipped with an IP-PSD (imaging plate position sensitive detector) or L-PSD (linear position sensitive detector). Due to air and moisture sensitivity, the finely powdered samples (agate mortar) were filled into glass capillaries (*Hilgenberg*, diameter 0.3-0.5 mm, wall thickness 0.01 mm) and measured in Debye-Scherrer geometry. The capillaries were filled within a glove-box and sealed by fusing with a tungsten-filament. In order to close small leakages a wax droplet was placed at the sealing. Samples which could not be filled into capillaries were put onto a Scotch

tape and placed in a flat-bed sample holder. Flat-bed samples were only short-time measured in transmission geometry, since inert gas conditions could not be maintained by that method. The obtained X-ray powder pattern were compared with theoretical powder diffractograms, calculated from single crystal diffraction data by using the program package *WinXPOW*[13]

2.2.3 Scanning Electron Microscopy

Scanning electron microscopy (SEM) measurements were carried out using *JEOL* JSM-6500F (Group of Prof. Dr. Thomas Bein, *University of Munich*, operator: Dr. Steffen Schmidt) and JSM-7500F (Group of Prof. Dr. Bernhard Rieger, *Technical University of Munich*: operator Katia Rodewald) scanning electron microscopes equipped with field emission guns operated at 1-30 kV. For PMMA films acceleration voltages of 1-5 kV were most suitable, whereas in case of Ge films 5-30 kV were used. Powdery samples and substrates with films were stuck onto a conductive carbon tape (*Plano Gmbh*) which was fixed at a SEM sample holder. In order to avoid charging the lower surface and edges of the substrates were coated with a conductive silver lacquer (*Plano GmbH*) and in selected cases films were coated with carbon.

2.2.4 Energy Dispersive X-ray Analysis

Energy dispersive X-ray (EDX) analysis on powders and single crystals was performed on a SEM 5900LV (*JEOL*) equipped with an INCA energy dispersive X-ray analyzer (*Oxford Instruments*) in the group of Prof. Dr. Sevil Weinkauf (*Technical University of Munich*) by Ingrid Werner and Maria Müller. EDX analysis of films was done at *JEOL* scanning electron microscopes JSM-6500F (Prof. Dr. Thomas Bein, *University of Munich*, operator: Dr. Steffen Schmidt) and JSM-7500F (Prof. Dr. Bernhard Rieger, *Technical University of Munich*, operator: Katia Rodewald) (*JEOL*) equipped with an Oxford analysis system (*Oxford Instruments*) (JSM-6500F: cross section = 10 mm², ATW2 window; JSM-7500F: X-Max Detector)

2.2.5 Transmission Electron Microscopy

Transmission electron microscopy (TEM) was carried out at the University of Munich (*Prof. Dr. Thomas Bein*) by Dr. Steffen Schmidt on a JEM-2010 (*JEOL*) with a high resolution pole piece at an operation voltage of 200 kV. For the sample preparation material was scraped from the substrate with the film and deposited on a perforated carbon coated copper grid. The TEM was equipped with an EDX system Apollo XLT SUTW (*Co. AMETEK/EDAX*) with a cross section of 30 mm^2.

2.2.6 UV/Vis-Spectrsocopy

UV/Vis spectra of porous Ge films were recorded at the *University of Munich* (Prof. Dr. Thomas Bein) by Enrico Greul on a Lambda 1050 UV/VIS-spectrometer (*PerkinElmer*) equipped with GaInAs integrating sphere detector.

2.2.7 X-ray Photoelectron Spectroscopy

X-ray photoelectron spectroscopy (XPS) on films was conducted by Patrick Zeller (Group of Prof. Dr. Joost Wintterlin, *University of Munich*) using a VSW HA 100 hemispherical analyzer and a VSW TA10 X-ray source providing non monochromatized Al K_α radiation (Al K_α = 1486.6 eV). The films were cleaned by argon sputtering using a VSW AS10 ion source (E = 1 keV). XPS peaks were fitted with Gaussians convoluted with Doniach-Sunjic functions.[14]

2.2.8 Raman-Spectroscopy

Raman spectroscopy measurements on single-crystals were carried out by Herta Slavik (*Technical University of Munich*) using a Senterra Raman microscopy spectrometer (*Bruker Corporation*) equipped with a diode laser (785 nm, 1 mW). Films and powdery reaction residues were investigated with a LabRAM HR UV-Vis (*HORIBA JOBIN YVON*) Raman Microscope (OLYMPUS BX41) with a SYMPHONY CCD detection system and a He-Ne laser (λ = 633 nm) (spot size 4.5 µm) (Prof. Dr.

Thomas Bein, *University of Munich*). In standard cases the spectrometer was operated at a laser power of 0.17 mW. Moisture and air sensitive powders and single-crystals were sealed in glass capillaries (*Hilgenberg*, diameter 0.3-0.5 mm, wall thickness 0.01 mm).

2.2.9 Infrared-Spectroscopy

IR spectra were recorded within a glove box on a Bruker Alpha spectrometer, comprising a diamond ATR unit.

2.2.10 Gracing Incidence Small Angle X-ray Scattering

Gracing incidence small angle X-ray scattering (GISAXS)[15, 16] was performed on porous Ge films at the SAXS beamline of the Elettra synchrotron at Trieste, Italy by co-workers of the group of Prof. Dr. Peter Müller-Buschbaum (*Technical University of Munich*). The incident angle for the measurements was chosen well-above the critical angle of the material (0.3°), thereby ensuring penetration of the X-ray beam into the film volume and decoupling of the specular and the Yoneda peak positions in the scattering signal. The wavelength of the synchrotron radiation used was 1.5 Å (X-ray energy of 8.26 keV). A sample-detector distance of 2.047 m was fixed for the measurements using vertical horizontal beam dimensions of 200 µm ^{x} 3 mm. The scattered signal was detected by a Pilatus 1M detector with pixel dimensions of (172 ^{x} 172) µm^2. It is a noise-free detector with a signal readout time of 2.3 ms. A semi-transparent beamstop was used for the data acquisition in order to shield the detector from high intensity specular and off-specular scattering. Careful adjustment of the counting time was done in order to prevent beam damage to the film. The horizontal line cut from the 2D GISAXS data is performed by averaging over seven pixels along the q_z direction (from 0.53 – 0.58 nm^{-1}).

2.2.11 Nuclear Magnetic Resonance Spectroscopy

Nuclear magnetic resonance spectroscopy (NMR) was performed at 500 MHz (AV 500: *Bruker*) and 400 MHz (AV 400: *Bruker*) NMR spectrometers, equipped with auto sampling units. For clarification of organic structures ^{1}H, ^{13}C, COSY, HMBC and HSQC were recorded. Measurements under special experimental conditions were assisted by Maria Weindl and Christine Schwarz (*Technical University of Munich*). For the characterization of isolated reaction products (powders, single-crystals and liquids) ca. 10 mg of the sample was dissolved in 0.6 ml deuterated solvent under inert gas conditions and the solutions were filled into NMR-tubes with an inner diameter of 4 mm. For *in situ* investigation on reactions in ethylenediamine an aliquot of ca. 150 µl of the filtered reaction solution (solvent: non-deuterated *en*) was filled into Norell® NMR tube (*Deutero Gmbh*, outer diameter: 3 mm) under inert gas conditions. The Norell® NMR tube was tightened with a plastic stopper and stuck into a NMR tube with an inner diameter of 4 mm (denoted as outer tube). The outer NMR tube was filled with 0.4 ml of chloroform-d_1. Due to the application of non-deuterated *en*, the spectra show dominant signals at. 2.5-3.0 ppm (s, *en*, -CH_2-) and 1.3-1.9 ppm (s, *en*, -NH_2-), respectively. Samples for time-resolved ^{1}H-NMR-spectroscopy were taken immediately after the reactants had entirely dissolved (ca. 15 min) and the NMR measurements immediately were started. Spectra were evaluated by MestreNova 8.1.0[15]

2.2.12 Electrospray Mass Spectroscopy

Electrospray ionization mass spectroscopy (ESI-MS) was done at a HCT mass spectrometer (*Bruker Daltronic*) in the negative ion mode (-). The measurements were assisted by Christina Fischer (*Technical University of Munich*). Solutions of the samples in the solvents *acn* and *en* were used for measurement. Depending on the solvent different measurement conditions were applied. Acetonitrile: capillary voltage: 4.5 kV, capillary exit: -166 V, drying gas temperature: 125 °C, injection rate: 240 µL/h; *En*: capillary voltage: 4.5 kV, capillary exit: -166 V, drying gas temperature: 125 °C, injection rate: 240 µL/h.

2.2.13 Quantumchemical Methods

DFT calculations were performed by Laura-Alice Jantke (group of Prof. Dr. Thomas F. Fässler, *Technical University of Munich*) with Gaussian09 program package [18] using the Perdew-Burke-Ernzerhof hybrid functional (PBE0)[19, 20] and def2-TZVPP basis sets for germanium [21] and tin [22]. For tin, a pseudopotential (ESP) was estimated.[23] and the charge was compensated with a solvation model (polarizable continuum model, PCM).[24]

2.3 Literature

[1] M. M. Bentlohner, M. Waibel, P. Zeller, K. Sarkar, P. Müller-Buschbaum, D. Fattakhova-Rohlfing, T. F. Fässler, *Angew. Chem. Int. Ed.*, **2016**, *55*, 2441.

[2] M. M. Bentlohner, S. Frischhut, T. F. Fässler, **2016**, *manuscript for publication.*

[3] C. Hoch, M. Wendorff, C. Röhr, *J. Alloy. Compd,* **2003**, *361*, 206.

[4] S. Ponou, T. F. Faessler, *Z. Anorg. Allg. Chem.,* **2007**, *633*, 393.

[5] M. M. Bentlohner, W. Klein, Z. H. Fard, L.-A. Jantke, T. F. Fässler, *Angew. Chem. Int. Ed.* **2015**, *54*, 3748.

[6] T. Wang, O. Sel, I. Djerdj, B. Smarsly, *Colloid Polym Sci* **2006**, *285*, 1-9.

[7] Scale3/ABSPACK, *Oxford Diffraction Ltd.*, Crysalis RED, Version 1.171.322007

[8] G. M. Sheldrick, *Acta Crystallogr* **2008**, *A64*, 112.

[9] A. L. S. P. van der Sluis, *Acta Crystallogr* **1990**, *A46*, 194.

[10] A. L. Spek, *Acta Crystallogr* **2009**, *D65*, 148.

[11] Version 1.171.33.34d ed., Oxford Diffraction, Abingdon, UK, **2009**.

[12] K. Brandenburg, Version 3.2k ed., *Crystal Impact Gbr*, Bonn, Germany, **2014**.

[13] WinXPow, *Stoe & Cie GmbH*, Version 2.08. **2003**.

[14] S. Doniach, M. Sunjic, *J. Phys. C: Solid State* **1970**, *3*, 285.

[15] P. Müller-Buschbaum, *Anal. Bioanal. Chem.* **2003**, *376*, 3-10.

[16] G. Renaud, R. Lazzari, F. Leroy, *Surf. Sci. Rep.,* **2009**, *64*, 255-380.

[17] MestReNova, *Mestrelab Research S. L.*, *Version 8.1.0-11315*, **2012**.

[18] Gaussian 09, Revision B.01, M. J. Frisch, G. W. Trucks, H. B. Schlegel, G. E. Scuseria, M. A. Robb, J. R. Cheeseman, G. Scalmani, V. Barone, B. Mennucci, G. A. Petersson, H. Nakatsuji, M. Caricato, X. Li, H. P. Hratchian, A. F. Izmaylov, J. Bloino, G. Zheng, J. L. Sonnenberg, M. Hada, M. Ehara, K. Toyota, R. Fukuda, J. Hasegawa, M. Ishida, T. Nakajima, Y. Honda, O. Kitao, H. Nakai, T. Vreven, J. A. Montgomery, Jr., J. E. Peralta, F. Ogliaro, M. Bearpark, J. J. Heyd, E. Brothers, K. N. Kudin, V. N. Staroverov, T. Keith, R. Kobayashi, J. Normand, K. Raghavachari, A. Rendell, J. C. Burant, S. S. Iyengar, J. Tomasi, M. Cossi, N. Rega, J. M. Millam, M. Klene, J. E. Knox, J.

B. Cross, V. Bakken, C. Adamo, J. Jaramillo, R. Gomperts, R. E. Stratmann, O. Yazyev, A. J. Austin, R. Cammi, C. Pomelli, J. W. Ochterski, R. L. Martin, K. Morokuma, V. G. Zakrzewski, G. A. Voth, P. Salvador, J. J. Dannenberg, S. Dapprich, A. D. Daniels, O. Farkas, J. B. Foresman, J. V. Ortiz, J. Cioslowski, and D. J. Fox, Gaussian, Inc., Wallingford CT, **2010**.

[19] J. P. Perdew, K. Burke, M. Ernzerhof, *Phys. Rev. Lett*. **1996**, *77*, 3865–3868;

[20] C. Adamo, V. Barone, *J. Chem. Phys*. **1999**, *110*, 6158-6170.

[21] F. Weigend, M. Häser, H. Patzelt, R. Ahlrichs, *Chem. Phys. Lett*. **1998**, *294*, 143.

[22] F. Weigend, R. Ahlrichs, *Phys. Chem. Phys. Lett*., **2005**, 7, 3297.

[23] S. Miertus, E. Scorcco, J. Tomasi, *Chem. Phys*., **1981**, 55, 117.

[24] V. Barone, M. Cossi, *J. Phys. Chem. A* **1998**, *102*, 1995–2001.

3 Results and Discussion

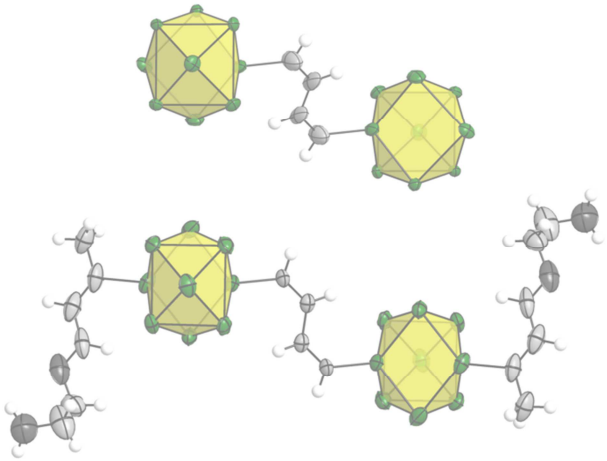

3.1 Linking of $[Ge_9]^{4-}$ Zintl Anions with Organic Building Blocks

3.1.1 Review of Relevant Literature

3.1.1.1 Fullerene- and Zintl-Cluster based Triad Systems

Fullerenes and Zintl anions are closely related and show similarities in their physical and chemical properties. Both compound classes can be seen as electron reservoirs and are interesting for electronic applications.[1] A commercially used fullerene derivate is [6,6]-phenyl-C61-butyric acid methyl ester (PCBM), and serves as an electron acceptor molecule in organic photovoltaics.[2-4] Covalent connection of two fullerene cages by reaction with bi-functional organic molecules led to a variety of electroactive {fullerene-linker-fullerene} triads (Figure 3.1), which can accommodate different numbers of electrons in different spin states.[5, 6]

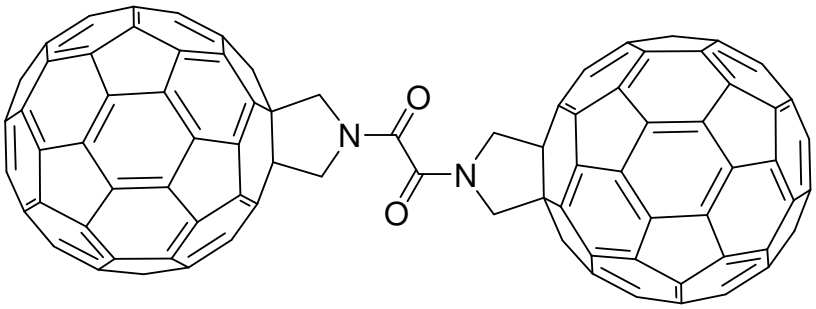

Figure 3.1. {fullerene-linker-fullerene} triad. The structure is drawn on the basis of ref. [6]

The synthesis of analogous {Ge_9-linker-Ge_9} Zintl triads is also reasonable as organic functionalities can be attached to $[E_9]^{4-}$ (E = Ge, Sn) by reaction with organic halides and alkynes as reviewed in chapter 1.2.2.[7-10] The reaction of $[Ge_9]^{4-}$ Zintl anions with alkynes $R^1–C≡C–R^2$, which so far was successfully conducted only in *en*, resulted in a large diversity of alkenylated Zintl clusters $[(R^2HC=CHR^1)_n(Ge_9)]^{m-}$.[7, 11-15] In particular the reaction of $[Ge_9]^{4-}$ with bis(trimethylsilyl)acetylene was intensively studied by *Sevov* and proceeds with very good yields to $[(H_2C=CH)_2Ge_9]^{2-}$.[7, 12] Even though di-ynes such as, $HC≡C–(CH_2)_4–C≡CH$ and $HC≡C–(C_6H_4)–C≡CH$ were also applied in such syntheses [14], the linking of two clusters via an organic functionality has not been reported prior to this work.

3.1.1.2 The Reaction of $[Ge_9]^{4-}$ and Amines with Alkynes

Due to their electron rich carbon triple bond, the preferred reaction of alkynes is the addition of electrophiles. However, low lying and unoccupied π*-orbitals also allow the addition of nucleophiles [16, 17] such as $[Ge_9]^{4-}$ Zintl anions[7] and amines.[18, 19]

The mechanism of the reaction of $[Ge_9]^{4-}$ Zintl anions with alkynes is described in the following according to *Sevov* (Scheme 3.1a).[7] In the first step of the reaction the nucleophile $[Ge_9]^{4-}$ regioselectively adds to the most electropositive and sterically less demanding carbon atom of the alkyne's triple bond, forming an alkenyl-anion. Due to electrostatic repulsion between the cluster and the carbanion the addition proceeds in *anti*-fashion, and the resulting alkenyl-anion adopts *trans*-geometry. Through the protonation of the *trans*-alkenyl-anion the $[(R^2HC=CHR^1)(Ge_9)]^{3-}$ is formed. It has been proposed that *en* is the proton source for the alkenyl-anion, however an evidence for amide formation has not been given in these former investigations. In case of $R^{1/2}$ = TMS, the TMS-groups are quickly exchanged by protons from *en*, and $H_2N(CH_2)_2NH(TMS)$ is formed as a side product. The driving force for that reaction is the nitrophilicity of the TMS group. For alkynes with an extended π-electronic system, the alkenyl-anion can change from *trans*- to *cis*-geometry due to delocalization of the negative charge. In such cases, instead of *anti*-products, the corresponding *syn*-products can be formed.[10] By analogous reactions of $[(R^2HC=CR^1)(Ge_9)]^{3-}$ with another alkyne, the bis-alkenylated species $[(R^2HC=CR^1)_2(Ge_9)]^{2-}$ is formed. The formation of mono- and bis-alkenylated products can be controlled via the stoichiometric ratio between alkyne and $[Ge_9]^{4-}$. As

a rule of thumb, a surplus of clusters leads to mono-alkenylated species and *vice versa* to bis-alkenylation.[7]

Even though their nucleophilic character is less pronounced, also amines can nucleophilically add to an alkyne's triple bond (Scheme 3.1b).[18, 19] Thereby C–N bonds are formed and depending on the type of amine, different products are obtained. Application of primary amines yields enamines, which tautomerize to the corresponding imines by a prototropic shift. By using instead secondary amines, the reaction stops at the enamine. Additions of amines to alkynes - also called hydroaminations - are of high technical relevance as enamines and imines are important intermediates for the synthesis of commercially available chemicals and pharmaceuticals. Accordingly, a bunch of catalysts has been developed to enhance the yield and selectivity of such reactions. [18, 19]

Motivated by the multifaceted reaction possibilities of alkynes towards clusters and amines, the reaction of 1,4-bis(trimethylsilyl)butadiyne (**1**) with $[Ge_9]^{4-}$ and *en* was investigated in regard to the synthesis of {Ge_9-Linker-Ge_9} Zintl triads.

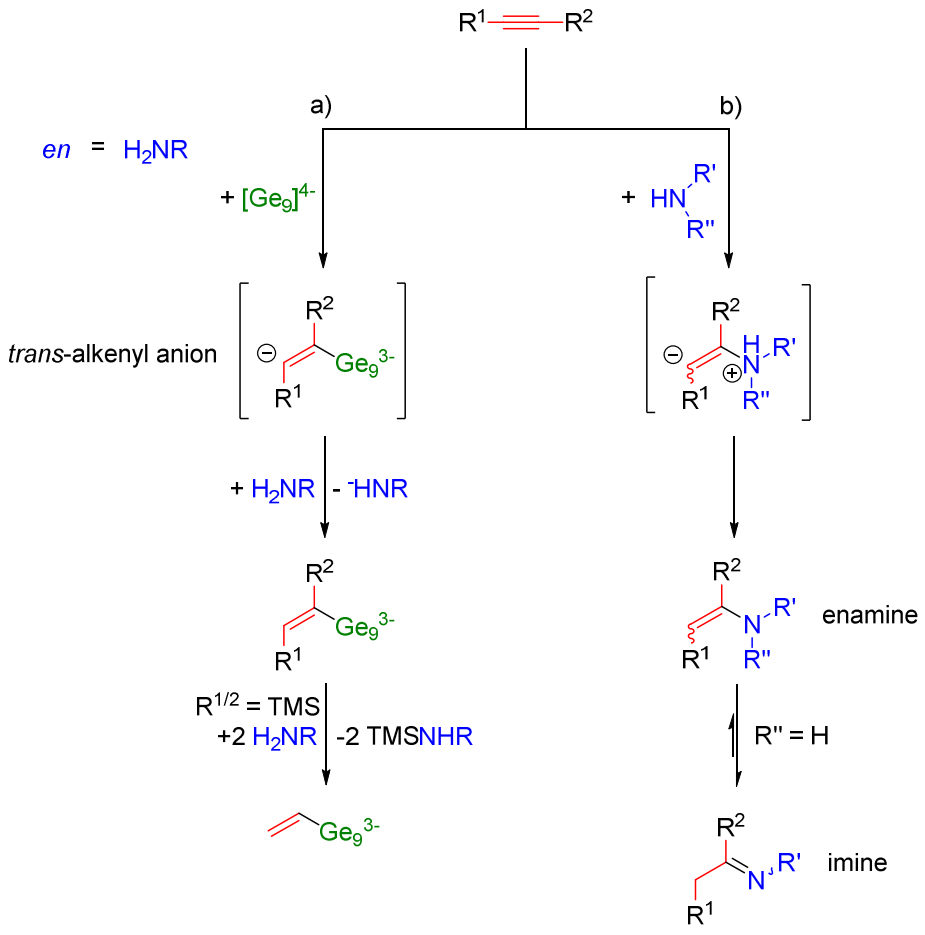

Scheme 3.1. General mechanism of the nucleophilic addition of a) $[Ge_9]^{4-}$ Zintl anions[7] and b) amines to alkynes.[18, 19] Red: carbon backbone of the alkyne, blue: *en*-substituent, green: Ge_9 Zintl cluster.

3.1.2 The Reaction of 1,4-bis(trimethylsilyl)butadiyne with Ethylenediamine and the Role of Water

see chapter 5.1 M. M. Bentlohner, W. Klein, Z. H. Fard, L.-A. Jantke, T. F. Fässler, *Angew. Chem. Int. Ed.* **2015**, *54*, 3748.

see chapter 5.2 M. M. Bentlohner, S. Frischhut, T. F. Fässler, *manuscript for publication*, **2016**.

As discussed in chapter 3.1.1.2 both $[Ge_9]^{4-}$ Zintl anions and amines are able to react with alkynes.[18, 19] Aiming for the definition of a rational synthetic protocol for {Ge_9-Linker-Ge_9} Zintl triads, the reaction of the solvent *en* with **1** in the absence of clusters was clarified.

As monitored by NMR, the reaction of **1** with water-free *en* quantitatively forms (3*Z*)- and (3*E*)-1-trimethylsilyl-7-amino-5-aza-hepta-3-en-1-yne (**2**) in an approximate isomers ratio of *Z*/*E* = 30/70 (Scheme 3.2). Under water-free conditions, **2** is the final product, emerging from the nucleophilic addition of *en* to the terminal carbon of **1**. The alkyne-functionality of **2** is suitable for further reaction with $[Ge_9]^{4-}$, which is presented in chapter 3.1.4.

In the presence of water, **2** reacts further to 2,3-dihydro-5-methyl-*H*-1,4-diazepine (**3**) and 1,9-di-amino-4-methyl-3,7-di-aza-nonadien (**4**). In an earlier described synthesis, **3** was obtained by reaction of *en* with 1,3-butadiyne, however the role of water has not been discussed.[20] Obviously, **3** and **4** arise from water-catalyzed intramolecular amine addition and addition of another *en* molecule to carbon γ, respectively. According to ^{13}C chemical shifts the electrophilicity of the γ carbons for both (3E)-**2** and (3Z)-**2** is higher than for the δ carbons {^{13}C chemical shifts [ppm] (3*E*)-**2**: 109.1 (γ), 86.1 (δ); (3*Z*)-**2**: 105.8 (γ), 93.9 (δ)}. Hence, addition of a second amino group to **2**, preferentially proceeds at the γ carbon. A catalytic effect of water in hydroaminations has also been reported in previous publications dealing with the synthesis of imidazo[1,2-a]pyridines.[21, 22]

The influence of water on the reaction of **1** with *en* was exploited for the qualitative determination of water in the solvent. Due to moisture sensitivity, the chemistry of $[E_9]^{4-}$ in solution requires thoroughly dried reactants and solvents in order to achieve reproducible results. For *en* the determination of the water content by classical Karl-Fischer titration methods is difficult, due to side reactions of the

solvent with the titration-reagents.[23] In the course of this thesis, each freshly distilled *en*-batch was qualitatively tested according to its water-content by mixing an aliquot of the solvent with **1** and monitoring the reaction with ^{1}H NMR for at least 24 h. As long as **2** was the only product after 24 h, the *en* was considered as water-free and used for further reactions.

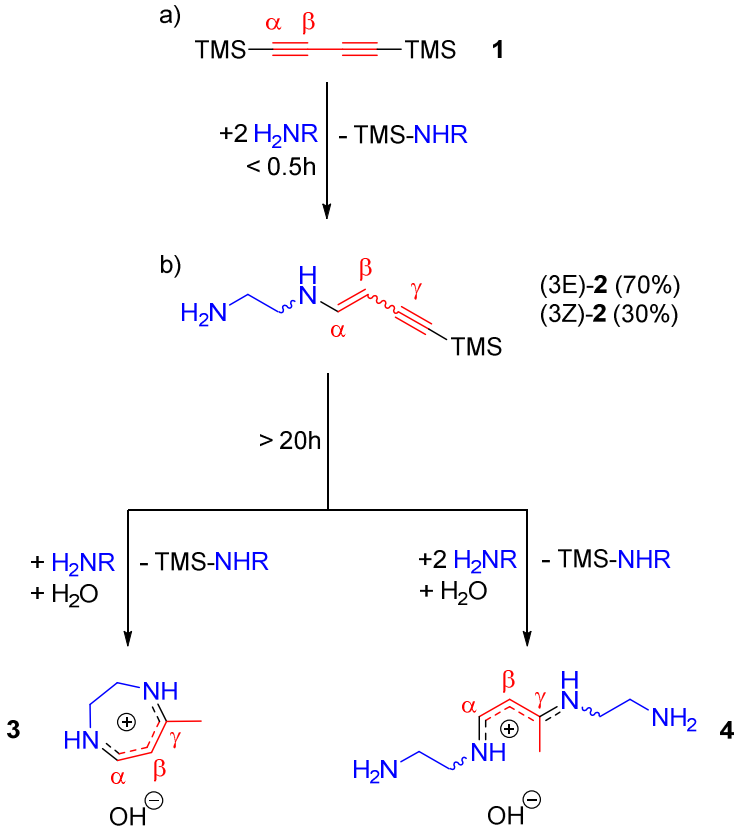

Scheme 3.2. Reaction of 1,4-bis(trimethylsilyl)butadiyne (**1**) with *en* in the absence of $[Ge_9]^{4-}$ Zintl anions and the influence of water. a) Independently whether water is present **2** is formed by addition of one *en* molecule to **1**. b) Only in presence of water **2** further reacts to **3** and **4**. With regard to the NMR time-scale **3**/**4** quickly isomerize/tautomerize in presence of water, as can be seen by a signal broadening.

3.1.3 The Zintl Triad $[Ge_9–CH=CH–CH=CH–Ge_9]^{6–}$

see Chapter 5.2 M. M. Bentlohner, S. Frischhut, T. F. Fässler, **2016**, *manuscript for publication*.

The results in chapter 3.1.2 show that **1** readily reacts with *en* in the absence of clusters. On the other hand, both **1** and *en* are required simultaneously for the linking of two Ge_9 entities. It turned out, that a suitable way for reacting $[Ge_9]^{4–}$ with **1** but avoiding reaction with the solvent *en*, is the dissolution of pre-mixtures of the neat solids A_4Ge_9 (*A* = K or Rb) and **1** in *en*. In the course of experiments with **1** and an excess of clusters, the $[(Ge_9)–(^{ZZ}\mathbf{B})–(Ge_9)]^{6–}$ (**5a**) [^{ZZ}**B** = (1*Z*,3*Z*)-buta-1,3-dien-1,4-diyl] Zintl triad was crystallized with cryptand[2.2.2] as $\{A(222\text{-crypt})]_6$ **5a**$\}\cdot(tol)_2\cdot(en)_2$ with *A* = K or Rb (Scheme 3.3).

a)

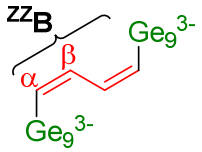

5a

b) $\underbrace{A_4Ge_9 + 0.5\text{ eq. }\mathbf{1}}_{\text{pre-mixture of solids}}$ —(i) *en*/20 h; (ii) tol/crypt[2.2.2]→ $\{[A(222\text{-crypt})]_6\,\mathbf{5a}\}(tol)_2(en)_2$

Scheme 3.3. a) The chemical structure of **5a**. b) Synthesis of $\{[A(222\text{-crypt})]_6$ **5a**$\}(tol)_2(en)_2$. *A* = K or Rb. Red: C_4 backbone of **1**, blue: *en*-substituent, green: Ge_9 Zintl cluster. The scheme was adopted from ref. [24]

In the crystal structures of $\{A(222\text{-crypt})]_6$ **5a**$\}\cdot(tol)_2\cdot(en)_2$, the centrosymmetric entity **5a** is disordered and appears by three superimposing conformers (**5a**^{I}, **5a**^{II}, **5a**^{III}), differing by the orientation of the Ge_9 units with respect to the s-*trans* [Ge–(^{ZZ}**B**)–Ge] plane and their spatial location around the inversion center (Figure 3.2). Even though the ^{ZZ}**B** functionality of conformer **5a**^{III} could not be derived from the X-ray data, a bare $[Ge_9]^{3–}$ can be excluded, due to an analogous Raman pattern for the disorded $\{Rb(222\text{-crypt})]_6$ **5a**$\}\cdot(tol)_2\cdot(en)_2$ (Figure 3.3) and ordered $\{Rb(222\text{-crypt})]_4$ [^{Z}**R**–(Ge_9)–(^{ZZ}**B**)–(Ge_9)–^{Z}**R**]}(tol) (see chapter 3.1.5 Figure 3.6), for which the absence of $[Ge_9]^{3–}$ is evidenced by X-ray structure analysis. Due to very similar spatial orientations of **5a**^{I} and **5a**^{II}, solely a superposition of the ^{ZZ}**B** bridges of both

conformers can be resolved in the crystal structure. The Ge_9 entities of the three conformers adopt C_s symmetry, attributed to a one-side compression of the cluster's open square face at the germanium atoms (Ge1, Ge10, Ge19) bearing the ^{ZZ}**B** functionality. A similar situation was also found for the mono-vinylated $[(H_2C{=}CH)(Ge_9)]^{3-}$ Zintl anion.[13]

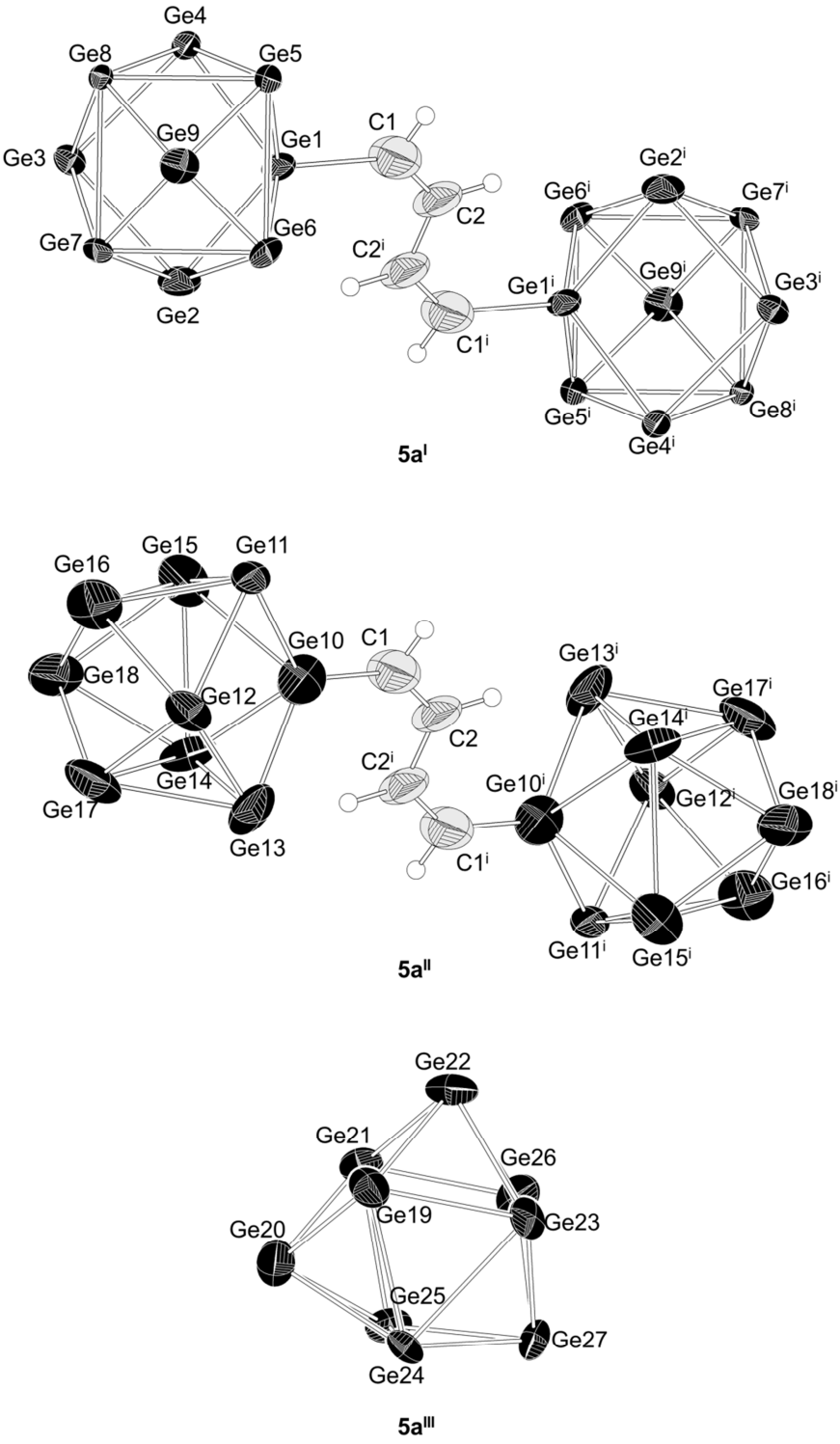

Figure 3.2. Illustration of the components **I**-**III** of the disordered **5a**. Carbon atoms are shown as light grey spheres. Ellipsoids are set at 50% probability. Symmetry code: (*i*) –x, -y, 1-z. The figure and figure caption was modified on the basis of ref. [24]

The Raman spectrum of {Rb(222-crypt)]$_6$ **5a**}·(tol)$_2$·(en)$_2$ shows a typical pattern for *cis*,*cis*-1,4-di-substituted buta-1,3-dienes.[25, 26] The modes of the carbon single and double bonds appear at 1554 and 1225 cm^{-1}, whereas the Ge–C bond valence vibration appears at 506 cm^{-1}, which was also found similarily for the [(H$_2$C=CH)$_2$(Ge$_9$)]$^{2-}$ Zintl anion.[27] Intensive signals at 142 and 221 cm^{-1} correspond to the Ge$_9$ units of **5a**.[28, 29] Solubility tests of {*A*(222-crypt)]$_6$ **5a**}·(tol)$_2$·(en)$_2$ in *py*, *acn*, *thf* and dichloromethane led to the decomposition of the compound.

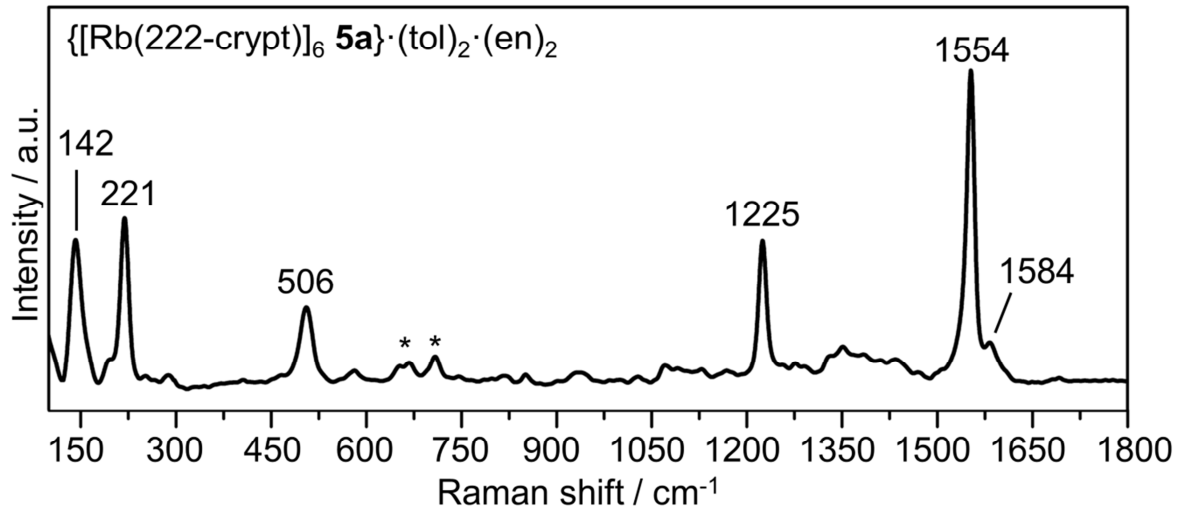

Figure 3.3. The Raman spectrum of single-crystals of {Rb(222-crypt)]$_6$ **5a**}·(tol)$_2$·(en)$_2$. Characteristic signals are labeled with the wavenumbers.Unknown signals are marked with * The figure was modified on the basis of ref. [24]

In reaction solutions from which **5a** was isolated, **2** is not present, evidencing that under the applied conditions **1** solely reacts with [Ge$_9$]$^{4-}$ but not with *en*. *In situ* NMR studies further revealed fast formation (<0.5 h) of [(Ge$_9$)–(**A'**)]$^{3-}$ (**5'a**; *anti*-product) [**A'** = 1,4-bis(trimethylsilyl)-buta-1-en-3-yne-1-yl] and [(Ge$_9$)–(**^{E}A**)]$^{3-}$ (**6'a**; *syn*-product) [**^{E}A** = (1*E*)-4-trimethylsilyl-buta-1-en-3-yne-1-yl] upon dissolution of *A*$_4$Ge$_9$/**1** (1 eq./0.5 eq.) in *en* (Scheme 3.4). In a slow consecutive reaction the **5'a** and **6'a** slowly add (ca. 20 h) another [Ge$_9$]$^{4-}$ cluster in δ position, resulting in the Zintl triads [(Ge$_9$)–(**^{ZZ}B**)–(Ge$_9$)]$^{6-}$ (**5a**; *anti*/*anti*-product) and [(Ge$_9$)–(**^{EZ}B**)–(Ge$_9$)]$^{6-}$ (**6a**; *syn*/*anti*-product) [**^{EZ}B** = (1*E*,3*Z*)-buta-1,3-dien-1,4-diyl] (**5a**/**6a** = 20/80), respectively. Even though for **5'a** and **6'a** the electropositivities of the γ carbons are higher than for the δ carbons {**5'a** [ppm]: 108.6 (γ), 89.4 (δ); **6'a** [ppm]: 108.9 (γ), 86.8 (δ)}, the cluster additions proceed regioselectively in the δ positions. That behavior can be attributed to steric reasons and electronic repulsion between the Ge$_9$ cages[7], and also explains the low velocity of a second cluster addition to **1**. Compared to other

alkenylated Zintl clusters, which almost exclusively occur as *anti*-products, **6'a** and **6a** are scarce examples of *syn*-products. The only literature reported example for a *syn*-product is *trans*-$[(PhHC{=}C(CH_3))(Ge_9)]^{3-}$, which was obtained by the reaction of $[Ge_9]^{4-}$ with MeC≡CPh.[10]

Regarding the influence of the stoichiometry, solely a surplus of clusters led to the formation of Zintl triads. In a control experiment a surplus of **1** was applied, however in that case no Zintl triads formed and $[(Ge_9)–(^{E}\mathbf{A})]^{3-}$ and/or $[(^{E}\mathbf{A})–(Ge_9)–(^{E}\mathbf{A})]^{2-}$ were the only products. This is attributed to fast addition of the first cluster to **1**, leading in presence of an excess of **1** to the entire consumption of $[Ge_9]^{4-}$ and therefore hinders the formation of Zintl triads.

The presented results emphasize, that the critical parameters for the linking of two $[Ge_9]^{4-}$ Zintl anions by reaction with **1** are the stoichiometry and reaction time. In literature reported reactions involving alkadiynes solely a surplus of the latter was applied, resulting in the bi-functionalization but not the linking of clusters.[14]

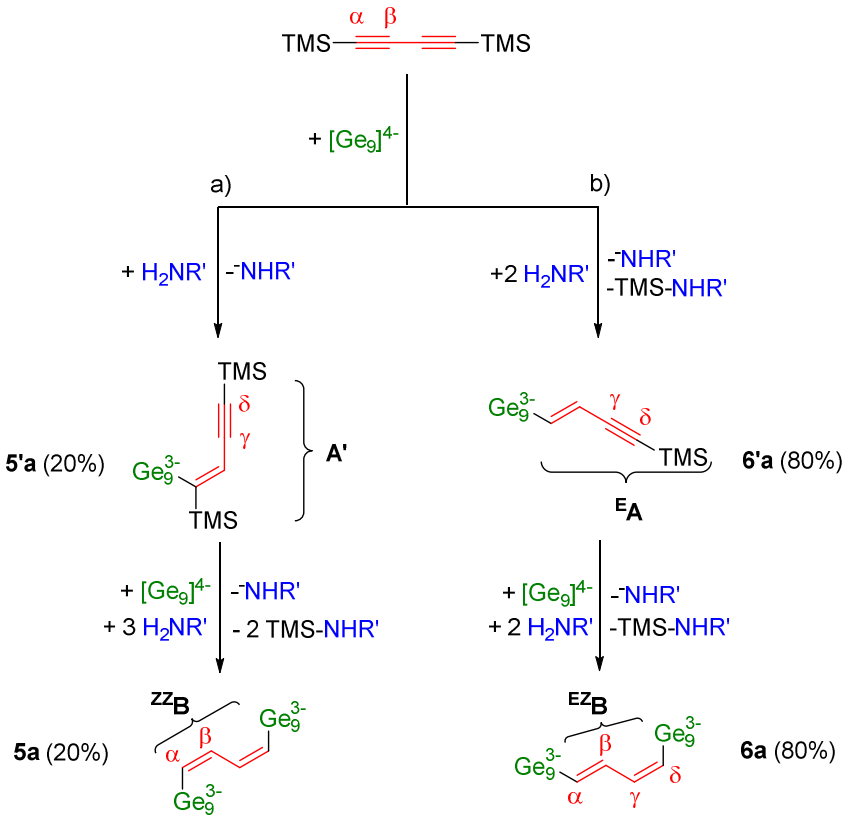

Scheme 3.4. Formation of Zintl triads a) $[(Ge_9)–(^{ZZ}\mathbf{B})–(Ge_9)]^{6-}$(**5a**) and b) $[(Ge_9)–(^{EZ}\mathbf{B})–(Ge_9)]^{6-}$ (**6a**). Intermediates were derived from *in situ* studies. The figure was modified on the basis of ref. [24]

3.1.4 The organo Zintl Anions $[Ge_9–R]^{3–}$ and $[R–Ge_9–R]^{2–}$ (R = 7-amino-5-aza-hepta-2,4-dien-2-yl)

see Chapter 5.2 M. M. Bentlohner, S. Frischhut, T. F. Fässler, **2016**, *manuscript for publication*.

Covalent grafting of Zintl triads to surfaces and nanoparticles requires functionalities at the clusters suitable for further organic transformations.[14, 15] In that context enamine **2** is interesting due to its terminal amino- and alkinyl-group. In the course of this work, reaction of A_4Ge_9 (*A* = K or Rb) with **2**/*en* solutions was investigated and yielded $[(Ge_9)–(\mathbf{R})]^{3–}$ (**7a**) and $[(\mathbf{R})–(Ge_9)–(\mathbf{R})]^{2–}$ (**8a**) (**R** = 7-amino-5-aza-hepta-2,4-dien-2-yl) (Scheme 3.5) The organo-Zintl anions were identified *in situ* by ESI-MS and NMR (Figure 3.4).

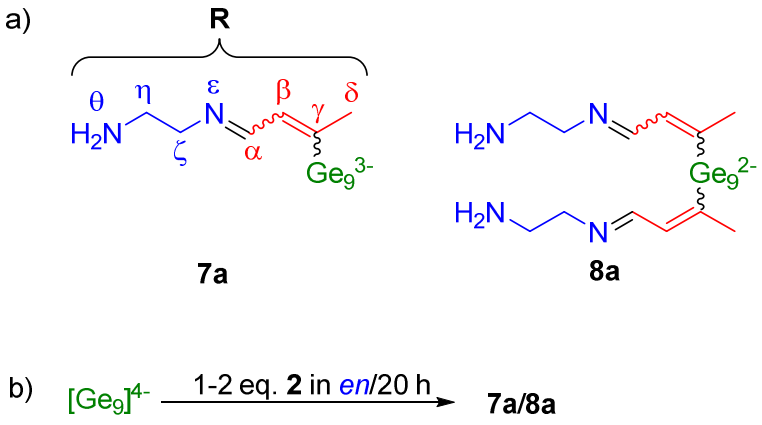

Scheme 3.5. a) Chemical structure as well as b) synthesis of $[(Ge_9)–(\mathbf{R})]^{3–}$ (**7a**) and $[(\mathbf{R})–(Ge_9)–(\mathbf{R})]^{2–}$ (**8a**).

In the mass-spectrum of a reaction mixture obtained by dissolving 1 eq. Rb_4Ge_9 in 1 eq. **2**/*en*, species **7a**/**8a** are indicated by dominant signals of $Ge_9\mathbf{R}^–$ (m/z = 764), $Ge_8\mathbf{R}^–$ (m/z = 692) and $Ge_7\mathbf{R}^–$ (m/z = 618) as well as weaker signals of $(\mathbf{R}Ge_9\mathbf{R})^–$ (m/z = 875). Even though **7a** and **8a** did not crystallize by layering with cryptand[2.2.2]/*tol*, it was possible to isolate the first salt of the $[Ge_{10}]^{2–}$ Zintl anion from such a solution. For details on the results see chapter 3.2.2.[30]

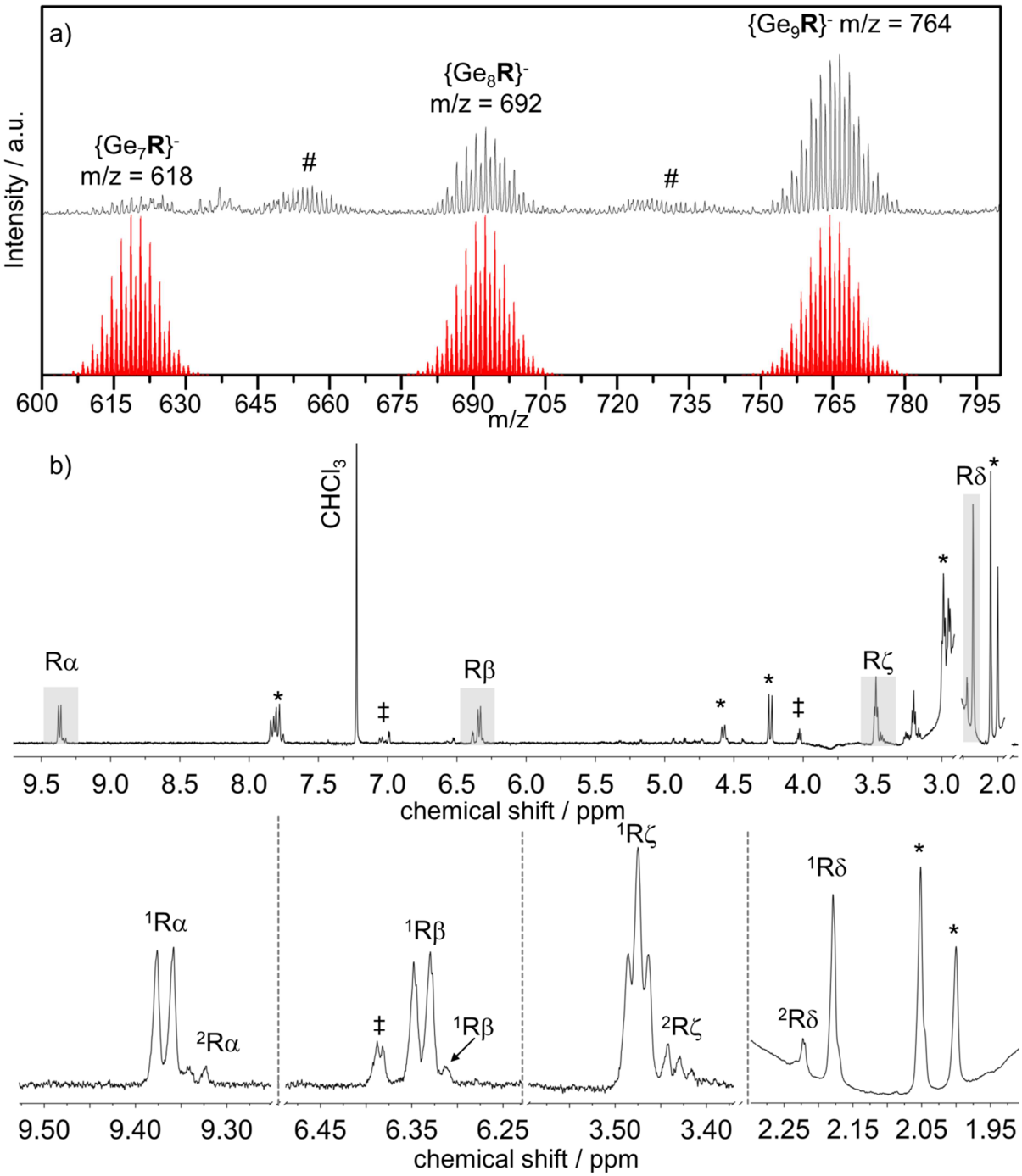

Figure 3.4. a) ESI-MS and b) ^{1}H NMR of solutions obtained by reacting A_4Ge_9 (A = K, Rb) with 1 eq. **2**. a) Red: simulated mass peaks, grey: references for unfunctionalized Ge_9/Ge_{10} clusters. Signals marked with # are discussed in chapter 3.2.2 b) Signals highlighted in grey are magnified in the lower part of the illustration. For assignment of the signals see the labeled chemical structure in Scheme 3.5. For a detailed description as well as additional NMR data see ref. [24]. Signals * correspond to different isomers of **4**. Due to the absence of water isomerization/tautomerization of **4** is slow with respect to NMR time-scale. Signals ‡ are unknown. The figures a) and b) were modified on the basis of ref. [24]

The formation of **7a** is due to the nucleophilic addition of $[Ge_9]^{4-}$ to the most electropositive position γ of **2** (Scheme 3.6 left). As follows from NMR the formation of **7a**/**8a** is accompanied by the formation of **4** as a dominant side product. The

formation of **4** by simple reaction of **1** with water-free *en* was ruled out as shown in chapter 3.1.2. In a control experiment it turned out that **4** forms by reaction of **2** with $KNH(CH_2)_2NHK$, which has been proposed to originate from the deprotonation of *en* in reactions of $[Ge_9]^{4-}$ with alkynes.[7] Accordingly, in this thesis the first evidence for amide formation in additions of $[Ge_9]^{4-}$ Zintl anions to alkynes was provided (Scheme 3.6 right).

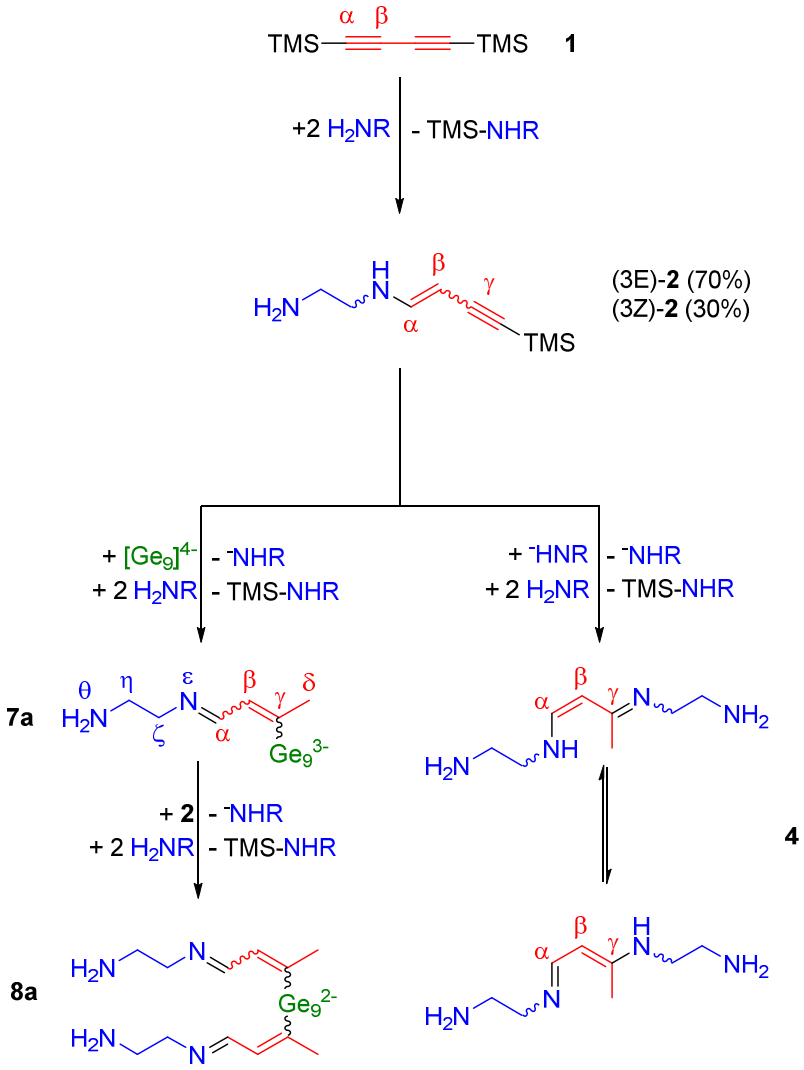

Scheme 3.6. Formation of (left)$[(Ge_9)–(\mathbf{R})]^{3-}$ (**7a**) and $[(\mathbf{R})–(Ge_9)–(\mathbf{R})]^{2-}$ (**8a**) as well as (right) the side product **4**. The reactions were derived from *in situ* studies.

Sevov et al. synthesized the similar $[Ge_9–(CH{=}CH–CH_2–NH_2)_2]^{2-}$ by reaction of $[Ge_9]^{4-}$ with propargylamin. In that case it was demonstrated that the terminal amino-group of $[Ge_9–(CH{=}CH–CH_2–NH_2)_2]^{2-}$ is able to undergo reaction with carbonyls such as ferrocene carboxaldehyd.[15] The latter highlights the potential of organic tethers with terminal amino groups for the attachment of Zintl clusters at functionalized surfaces.

3.1.5 The Zintl Triad [R–Ge_9–CH=CH–CH=CH–Ge_9–R]$^{4-}$ (R = 7-amino-5-aza-hepta-2,4-dien-2-yl)

see chapter 5.1 — M. M. Bentlohner, W. Klein, Z. H. Fard, L.-A. Jantke, T. F. Fässler, *Angew. Chem. Int. Ed.* **2015**, *54*, 3748.

see chapter 5.2 — M. M. Bentlohner, S. Frischhut, T. F. Fässler, **2016**, *manuscript for publication*.

The opportunity to establish 7-amino-5-aza-hepta-2,4-dien-2-yl organic tethers at Zintl clusters is further reflected in the synthesis of the [^{Z}**R**–(Ge_9)–(^{ZZ}**B**)–(Ge_9)–^{Z}**R**]$^{4-}$ (**9a**) Zintl triad. Simultaneous exposition of alkynes **1** and **2** to [Ge_9]$^{4-}$, by dissolving pre-mixtures of the neat solids A_4Ge_9 (*A* = K or Rb) and **1** (1 eq./0.5 eq.) in (2 eq) **2**/*en* solutions, leads to the formation of **9a**. Layering of such solutions with cryptand[2.2.2]/*tol* yielded orange plates of {*A*(222-crypt)]$_4$ **9a**}·(tol) with *A* = K or Rb (Scheme 3.7).

a)

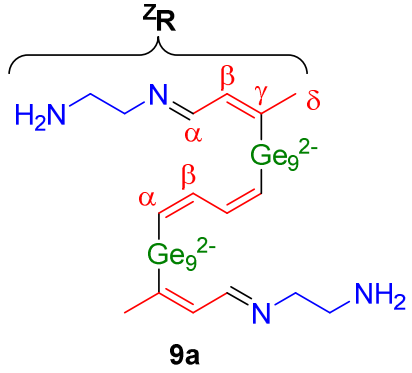

9a

b) A_4Ge_9 + 0.5 eq. **1** → (i) 2 eq. **2** in *en*/20 h; (ii) tol/crypt[2.2.2] → {[*A*(222-crypt)]$_4$ **9a**}(tol)

Scheme 3.7. a) Chemical structure of [**R**–(Ge_9)–(^{ZZ}**B**)–(Ge_9)–**R**]$^{4-}$(**9a**) and b) synthesis of {[*A*(222-crypt)]$_6$ **9a**}(tol)$_2$(en)$_2$ (*A* = K or Rb)

X-ray structure analysis shows that **9a** is composed of two C_{2v} symmetric Ge_9 units, which are connected by the ^{ZZ}**B** functionality and each cluster bearing a ^{Z}**R** side chain (Figure 3.5). In contrast to **5a**, **9a** is not disordered and solely one conformer appears in the crystal structure. Similar to other bis-functionalized clusters, the Ge_9 units adopt C_{2v} symmetry, which is due to a compression of the open square face at

the Ge1 and Ge3 atoms bearing the organic functionalities ^{zz}**B** and ^{z}**R**. Also for other bis-alkenylated species C_{2v} symmetric Ge_9 entities are observed.[12]

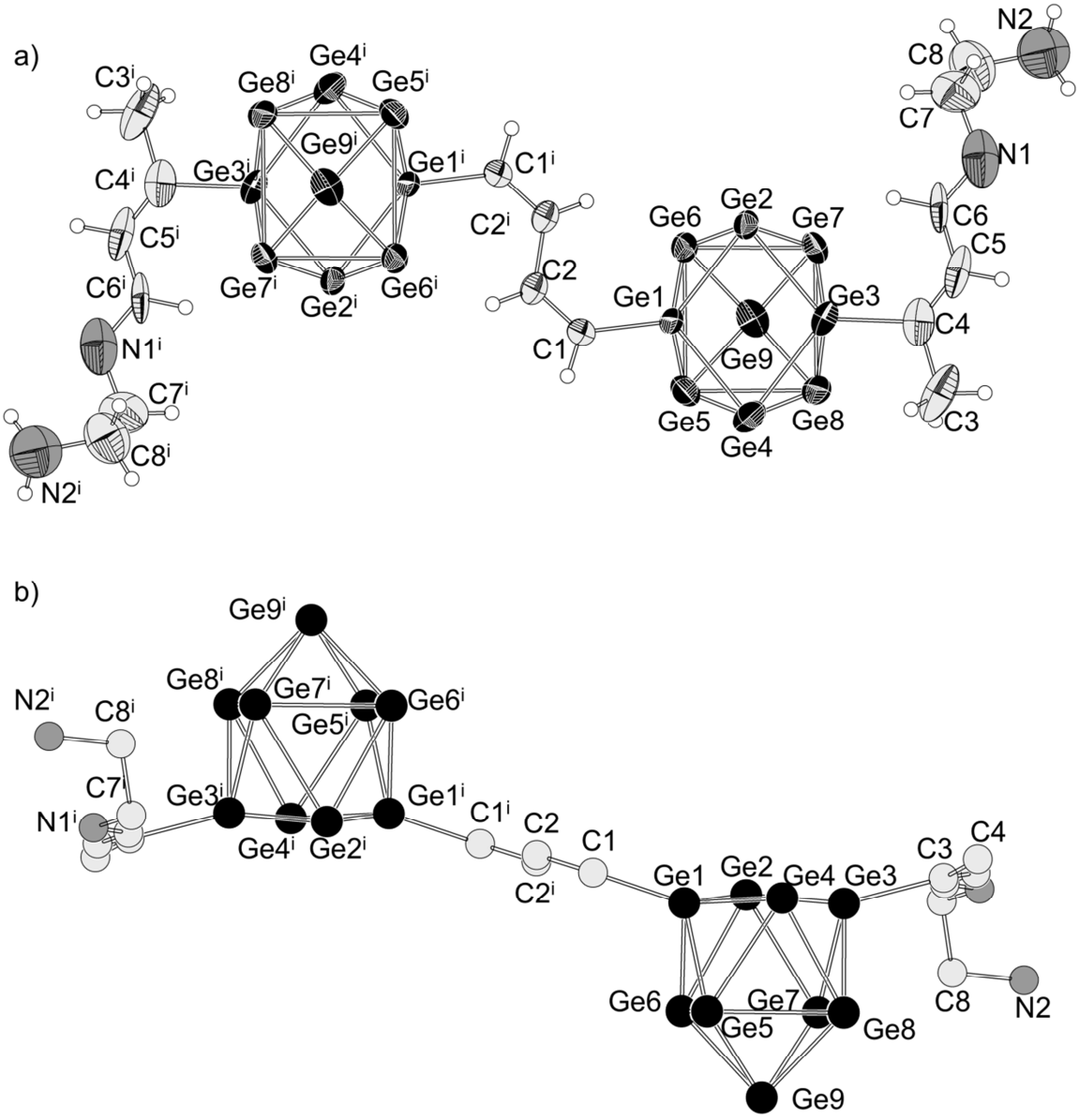

Figure 3.5. Two views of the molecular structure of **9a**, a) perpendicular and b) parallel to the plane of the connecting ^{zz}**B** unit. a) For reasons of clarity hydrogen atoms are omitted. Ellipsoids are set at 50% probability. b) For reasons of clarity the atoms are shown as colored spheres. Ge (black), C (light grey) and N (dark grey). Symmetry code: (*i*) –x, -y, 1-z. The figure and figure caption was modified on the basis of ref. [24, 31]

The compounds {*A*(222-crypt)]$_4$ **9a**}·(tol)$_2$ were additionally characterized by Raman for *A* = Rb and NMR-spectroscopy for *A* = K, Rb (Figure 3.6 and manuscript in chapter 5.2). The Raman spectra of {Rb(222-crypt)]$_4$ **9a**}·(tol) and {Rb(222-crypt)]$_6$ **5a**}·(tol)$_2$·(en)$_2$ (chapter 3.1.3) are analogous and show pattern characteristic for

cis,*cis*-1,4-di-substituted buta-1,3-dienes.[25, 26] and Ge_9 clusters [28, 29]. In case of {Rb(222-crypt)]$_4$ **9a**}·(tol) additional signals at 1180 and 1614 cm^{-1}, indicate C–C as well as C=C and C=N valence vibrations of the ^{z}**R** side chain.[32] In NMR characteristic signal patterns for the ^{zz}**B** and **R** functionalities are visible. For a detailed discussion of the NMR data see reference [24, 31]

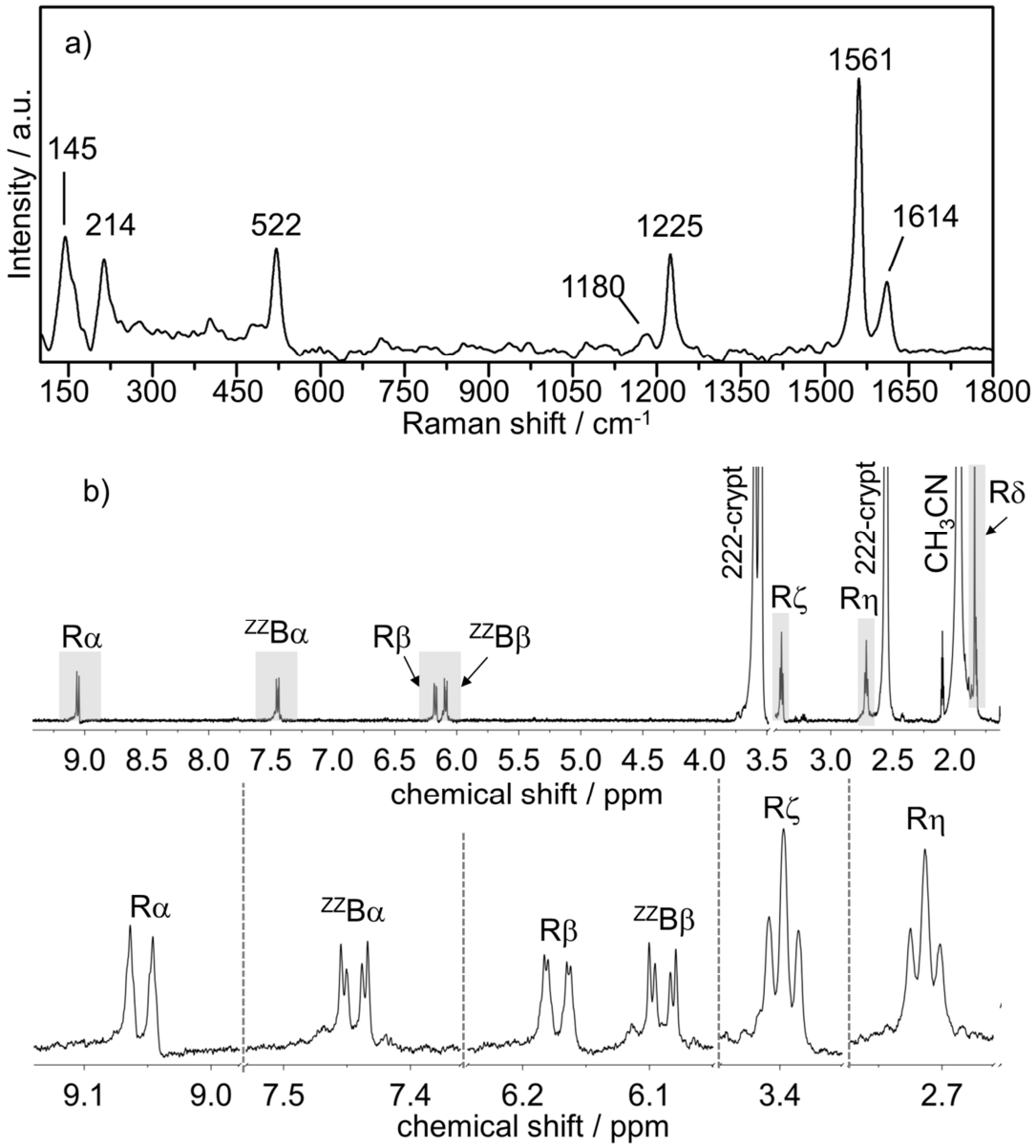

Figure 3.6. a) The Raman spectrum of {Rb(222-crypt)]$_4$ **9a**}·(tol). b) ^{1}H NMR resonances of **9a** in *acn*-d_3. For assignment of the signals see the labeled chemical structure in Scheme 3.7.Crystals of {K(222-crypt)]$_4$ **9a**}·(tol) were recrystallized from py-d_5 and re-dissolved in *acn*-d_3. Thus the ^{1}H NMR spectrum in *acn*-d_3 does not show signals of toluene, whereas the ^{1}H NMR spectrum of {[K(222-crypt)]$_4$**9a**}(toluene) in pyridine-d_5 displays the signals of toluene. Resonances originating from **9a** labeled with letters. The figures and figure captions were modified on the basis of ref. [24, 31]

The structure of **9a** and its electronic structure were quantum chemically investigated on a PBE0/def2-TZVPP/PCM level of theory by using [H_2C=HC–(Ge_9)–

([ZZ]**B**)–(Ge_9)–CH=CH_2] as a model compound. The calculations were conducted by Laura-Alice Jantke (*Technical University of Munich*, group of Prof. Dr. T. F. Fässler) and indicate a delocalized electronic system which is extended over the whole Zintl triad. Time dependent NMR investigation on reaction solutions from which {*A*(222-crypt)]$_4$ **9a**}·(tol) was obtained, shows that **9a** forms much faster (<0.5 h) compared to the Zintl triads **5a** and **6a** (ca. 20 h). Due to the fast formation of **9a**, intermediates could not be clarified. However, it is feasible that intermediately formed **5a** and **7a** play a role in the formation of **9a**.[31]

3.1.6 Literature

[1] T. F. Fässler, *Angew. Chem. Int. Ed.* **2001**, *40*, 4161.
[2] N. Martín, L. Sánchez, B. Illescas, I. Pérez, *Chem. Rev.* **1998**, *98*, 2527.
[3] P. Vanlaeke, A. Swinnen, I. Haeldermans, G. Vanhoyland, T. Aernouts, D. Cheyns, C. Deibel, J. D'Haen, P. Heremans, J. Poortmans, J. V. Manca, *Sol. Energ. Mat. Sol. C.* **2006**, *90*, 2150.
[4] Y. Kanai, J. C. Grossman, *Nano Lett.* **2007**, *7*, 1967.
[5] J. L. Segura, N. Martin, *Chem. Soc. Rev.* **2000**, *29*, 13.
[6] M. A. Lebedeva, T. W. Chamberlain, E. S. Davies, B. E. Thomas, M. Schröder, A. N. Khlobystov, *Beilstein J. Org. Chem.* **2014**, *10*, 332.
[7] M. W. Hull, S. C. Sevov, *J. Am. Chem. Soc.* **2009**, *131*, 9026.
[8] M. W. Hull, A. Ugrinov, I. Petrov, S. C. Sevov, *Inorg. Chem.* **2007**, *46*, 2704.
[9] D. J. Chapman, S. C. Sevov, *Inorg. Chem.* **2008**, *47*, 6009.
[10] M. M. Gillett-Kunnath, I. Petrov, S. C. Sevov, *Inorg. Chem.* **2009**, *49*, 721.
[11] M. W. Hull, S. C. Sevov, *Angew. Chem. Int. Ed.* **2007**, *46*, 6695.
[12] M. W. Hull, S. C. Sevov, *Inorg. Chem.* **2007**, *46*, 10953.
[13] C. B. Benda, J.-Q. Wang, B. Wahl, T. F. Fässler, *Eur. J. Inorg. Chem.* **2011**, 4262.
[14] M. W. Hull, S. C. Sevov, *J. Organomet. Chem.* **2012**, *721*, 85.
[15] M. W. Hull, S. C. Sevov, *Chem. Commun.* **2012**, *48*, 7720.
[16] R. Brückner, *Reaktionsmechanismen: Organische Reaktionen, Stereochemie, Moderne Synthesemethoden*, Spektrum Akademischer Verlag, **2009**.
[17] K. P. C. Vollhardt, H. Butenschön, N. E. Schore, *Organische Chemie*, VCH [Imprint], **2011**.
[18] T. E. Müller, M. Beller, *Chem. Rev.* **1998**, *98*, 675.
[19] T. E. Müller, K. C. Hultzsch, M. Yus, F. Foubelo, M. Tada, *Chem. Rev.* **2008**, *108*, 3795.
[20] W. W. Paudler, A. G. Zeiler, *J. Org. Chem.* **1969**, *34*, 999.
[21] D. Chandra Mohan, N. B. Sarang, S. Adimurthy, *Tetrahedron Lett.* **2013**, *54*, 6077.

[22] D. Chandra Mohan, S. Nageswara Rao, S. Adimurthy, *J. Org. Chem.* **2013**, *78*, 1266.
[23] M. Conceicao, P. Lima, M. Spiro, *Anal. Chim. Acta.* **1976**, *81*, 429.
[24] M. M. Bentlohner, S. Frischhut, T. F. Fässler, *manuscript for publication* **2016**.
[25] E. Benedetti, M. Aglietto, S. Pucci, Y. N. Panchenko, Y. A. Pentin, O. T. Nikitin, *J. Mol. Struct.* **1978**, *49*, 293.
[26] G. Gundersen, P. Klaeboe, A. Borg, Z. Smith, *Spectrochim. Acta Mol. Biomol. Spectrosc.* **1980**, *36*, 843.
[27] C. B. Benda, *Dissertation,* Technical University of Munich, Garching **2013**.
[28] H. G. Von Schnering, M. Baitinger, U. Bolle, W. Carrillo-Cabrera, J. Curda, Y. Grin, F. Heinemann, J. Llanos, K. Peters, A. Schmeding, M. Somer, *Z. Anorg. Allg. Chem.* **1997**, *623*, 1037-1039;
[29] M. Somer, W. Carrillo-Cabrera, E. M. Peters, K. Peters, H. G. v. Schnering, *Z. Anorg. Allg. Chem.* **1998**, *624*, 1915-1921.
[30] M. M. Bentlohner, C. Fischer, T. F. Fässler, *Chem. Commun.* **2016**, *52*, 9841.
[31] M. M. Bentlohner, W. Klein, Z. H. Fard, L.-A. Jantke, T. F. Fässler, *Angew. Chem. Int. Ed.* **2015**, *54*, 3748.
[32] M. Hesse, H. Meier, B. Zeeh, *Spektroskopische Methoden in der organischen Chemie*, Thieme, **2005**.

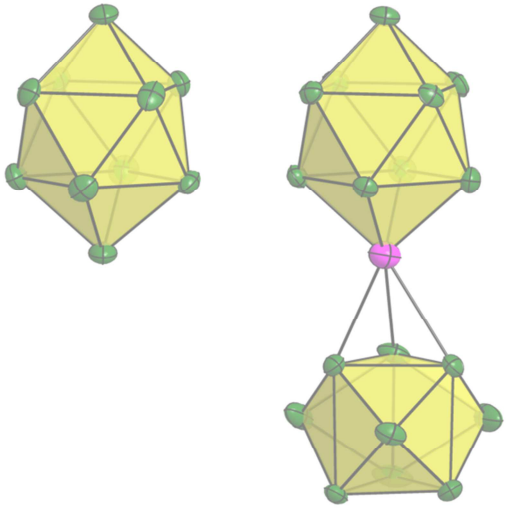

3.2 Extension and Linking of $[Ge_9]^{4-}$ Zintl Anions with Tetrel Atoms

3.2.1 Review of Relevant Literature

The bottom up assembly of larger homo- and heteratomic tetrel clusters, up to nanoscaled $Ge_{1-x}E_x$ with polyhedral structures, holds out the prospect of novel materials, such as element allotropes, with unforeseen properties [1-7]. The extension and linking of $[Ge_9]^{4-}$ clusters by tetrel atomic ions under retention of the deltahedral structures is one possible strategy in that context (Figure 3.7). Even though some papers deal with the assembly of porous frameworks with intact Ge_9 entities by crosslinking of $[Ge_9]^{4-}$ Zintl anions, the procedures are rather empirical and need further clarification. [8-14] Accordingly, general examinations on reactions allowing the addition of *E* atoms to $[Ge_9]^{4-}$ Zintl anions as well as investigations on the nature of the bonding modes of Ge_9 clusters to *exo*-(semi)metal atoms are required.

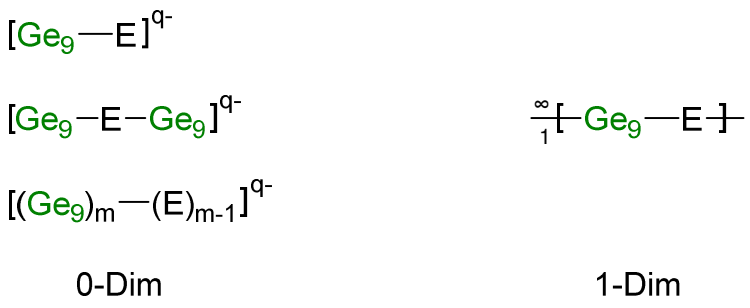

Figure 3.7. Schematic representation of zero and one dimensional structures composed of deltahedral Ge_9 clusters linked via *E* atoms. By the formal crosslinking of Ge_9 entities via tetrahedral E atoms, also the formation of three dimensional structures is theoretically possible .

The formally simplest extension of $[E_9]^{4-}$ Zintl anions to ligand-free clusters is the addition of a tetrel atom of the same sort to the cluster's open square face in η^4 mode. Examples in that context are $[(Ge_{10})Mn(CO)_3]^{3-}$ [15] and $[Pb_{10}]^{2-}$ [16] (Figure 3.8), which were obtained by reactions of $[E_9]^{4-}$ (*E* = Ge, Pb) with $Mn_2(CO)_{10}$ and $[PPh_3AuCl]$ in *en*, respectively. The tetrel clusters of $[(Ge_{10})Mn(CO)_3]^{3-}$ and $[Pb_{10}]^{2-}$ adopt the shape of a bi-capped quadratic antiprism with D_{4d} symmetry and exhibit bond lengths in the range of covalent multicenter *E*–*E* interactions. The structural parameters and charges of the latter two examples allow a description by the Wade rules as 22 SE *closo*-clusters.[17, 18] So far, $[(Ge_{10})Mn(CO)_3]^{3-}$ and $[Pb_{10}]^{2-}$ have been the only representatives of empty ten vertex group 14 *closo*-clusters and their formation also suggests the existence of an unbound $[Ge_{10}]^{2-}$ Zintl anion. Moreover, $[Ge_{10}]$ is a frequently observed species in mass spectra obtained by laser desorption experiments or from solutions of Zintl phases in polar organic solvents. [15, 19-21] An earlier report on a $[Ge_{10}]^{2-}$ cluster turned out to be erroneous as actually a disordered *closo*-$[Ge_9]^{2-}$ cluster was unequivocally characterized.[22, 23]

Even though the reaction of $[E_9]^{4-}$ with metal organyles in *en* mostly has led to capped $[(E_9)(TL_a)]^{q-}$, bridged $\{[(E_9)T(E_9)]_m\}^{q-}$ (m = 1 - ∞) and endohedral $[T@E_n]^{q-}$ ($n \geq 9$) clusters [1, 4, 6, 7], $[(Ge_{10})Mn(CO)_3]^{3-}$ and $[Pb_{10}]^{2-}$ demonstrate that formation of larger empty homoatomic clusters is also possible in the solvent *en*. As reviewed in chapter 1.2.2, *en* is supposed to have a mild oxidative potential towards $[E_9]^{4-}$ Zintl anions.[5, 24, 25] and promotes structural reorganization of clusters.[15, 26] These facts call for a detailed investigation of *en* as a reactant for the homoatomic expansion of $[Ge_9]^{4-}$ Zintl anions. Accordingly, in the course of this thesis solutions of $[Ge_9]^{4-}$ Zintl anions in water-free *en* were investigated in regard to the formation of larger homoatomic germanium clusters.

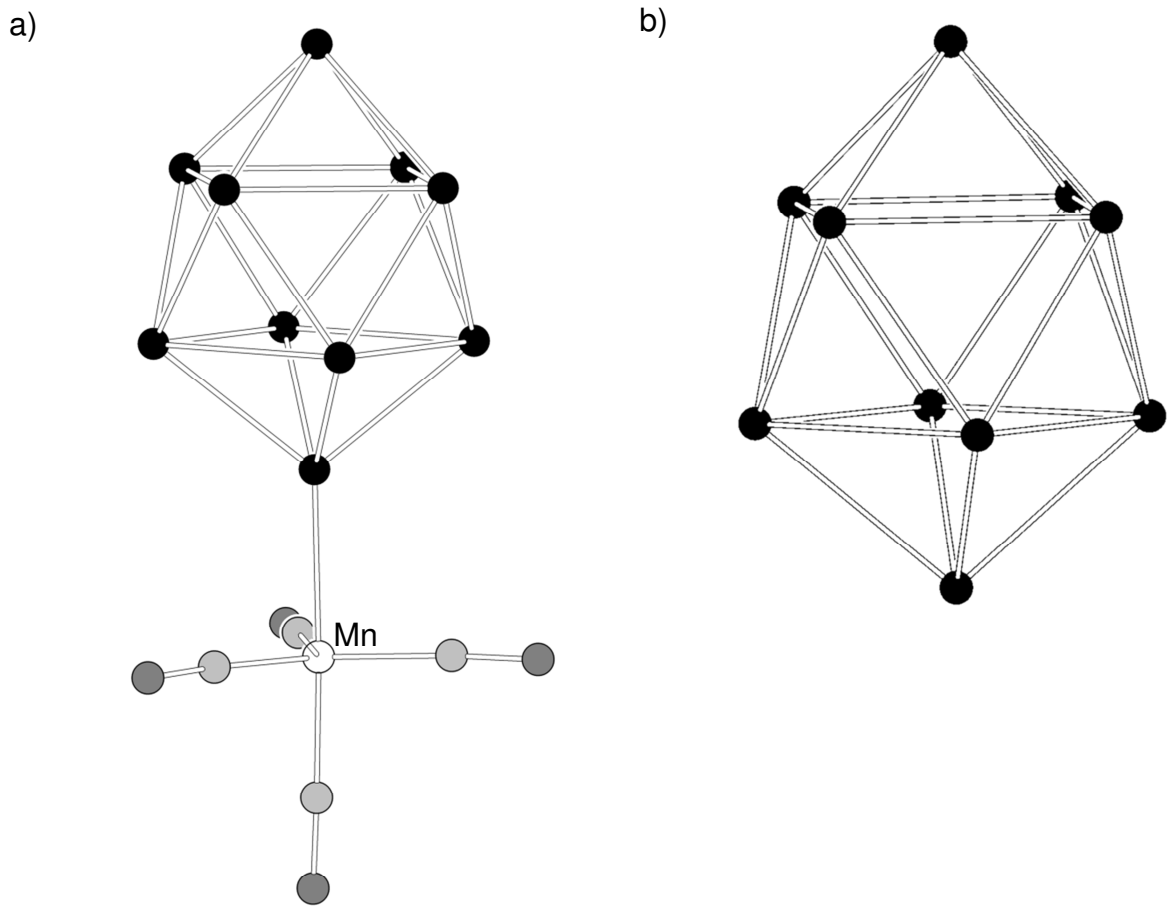

Figure 3.8. Schematic representation of a) $[Ge_{10}Mn(CO)_3]^{3-}$ [15] and $[Pb_{10}]^{2-}$ [16]. a) Carbon and oxygen atoms are shown as light and dark grey spheres, respectively.

An example for the heteroatomic expansion of a tetrel cluster with a main group element is the reaction of TlCp with $[E_9]^{4-}$ (E = Ge, Sn), resulting in $[E_9Tl]^{3-}$, with a Tl^+ atomic ion formally bonded in η^4 mode to the open square face of $[E_9]^{4-}$ (Figure 3.9a). The structural parameters of the $[E_9Tl]^{3-}$ indicate that the Tl atom is bonded by strong covalent multicenter bonds to the open square face of E_9, giving a ten vertex *closo*-cluster with 22 SE. [27]

Selected examples in the context of main group elements with a η^3 bonding mode are $[(\eta^3\text{-}Ge_9)In(\eta^3\text{-}Ge_9)]^{5-}$ [28] and $[(\eta^3\text{-}Ge_9)(SnPh_3)]^{3-}$ [29]. For the synthesis of $[(\eta^3\text{-}Ge_9)In(\eta^3\text{-}Ge_9)]^{5-}$, $[Ge_9]^{4-}$ Zintl anions were reacted with $InPh_3$ in *en* solution. The structural parameters of the cluster entities in $[(\eta^3\text{-}Ge_9)In(\eta^3\text{-}Ge_9)]^{5-}$ are indicative of 22 SE *nido*-$[Ge_9]^{4-}$ clusters, adopting the structure of D_{3h} symmetric tricapped trigonal prisms with elongated prism heights. Accordingly the $[(\eta^3\text{-}Ge_9)In(\eta^3\text{-}Ge_9)]^{5-}$ can be rationalized by the η^3 coordinative interaction of a triangular face of $[Ge_9]^{4-}$

(HOMO) with an acceptor orbital at the linking In^{3+} atomic ion. The coordinative cluster-indium interaction can also be seen on the Ge–In distances, which are considerably longer than expected for covalent bonds.[28]

In contrast to the previous example, the situation for $[(\eta^3\text{-}Ge_9)(SnPh_3)]^{3-}$ is reverse and the Zintl anion emerges from the coordination of the tin atom (HOMO) to a triangular face of *closo*-$[Ge_9]^{2-}$ (LUMO). The synthetic protocol for $[(\eta^3\text{-}Ge_9)(SnPh_3)]^{3-}$ grounds on the reaction of $(SnPh_3)^-$, which was separately prepared by reduction of $SnPh_3Cl$ with elemental K [30, 31], with K_4Ge_9 in *en*.[29] The possibility to attach tin atoms at Ge_9 entities by reaction of Sn(II)organyles with K_4Ge_9/*en* solutions, points to the utilization of that method for the linking of clusters.

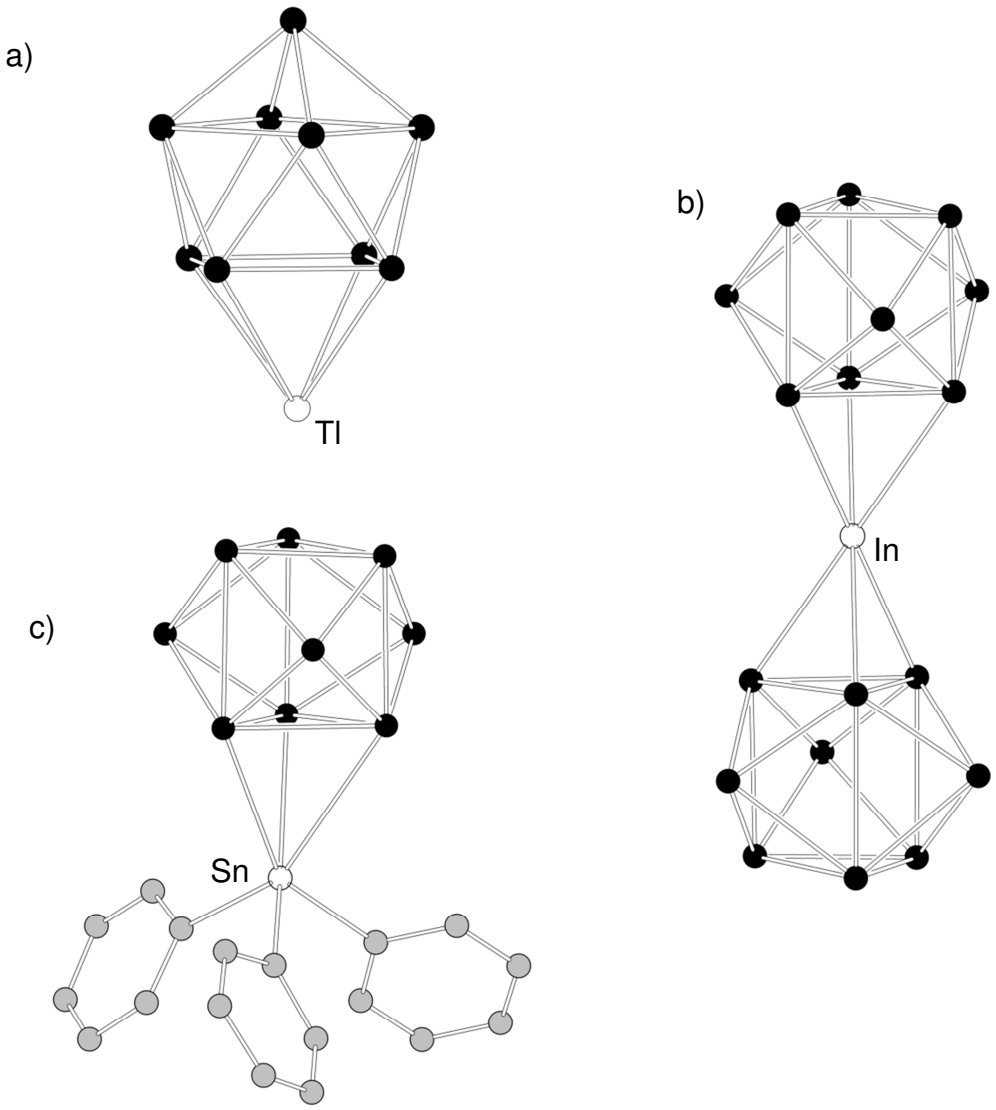

Figure 3.9. Schematic representation of a) $[Ge_9Tl]^{3-}$ [27], b) $[(\eta^3\text{-}Ge_9)In(\eta^3\text{-}Ge_9)]^{5-}$ [28] and c) $[(Ge_9)(SnPh_3)]^{3-}$ [29]. Carbon atoms are shown as grey spheres. Hydrogens are omitted for clarity.

3.2.2 The pristine $[Ge_{10}]^{2-}$ Zintl Anion

see chapter 5.3

M. M. Bentlohner, C. Fischer, T. F. Fässler, *Chem. Commun.* **2016**, *52*, 9841.

As reviewed in chapter 3.2.1 *en* is supposed to have a mild oxidative potential towards $[Ge_9]^{4-}$ Zintl anions and promotes reorganization of clusters into different sizes and shapes.[15, 26] In this work, reaction of water-free *en* with Rb_4Ge_9 was investigated in regard to oxidative extension of the clusters by addition of germanium. For these investigations water-free *en* was applied in order to exclude influences of water-traces. The water-content of the solvent was qualitatively checked by the method described in chapter 3.1.2.[32, 33]

Upon dissolution of Rb_4Ge_9 in water-free *en*, within a few minutes a deep orange-green solution with plenty of yellow precipitate formed.[34] After stirring the mixture for 20 h the precipitate entirely dissolved and a deep green solution was obtained. In the ESI-MS of the Rb_4Ge_9/*en* solution (Figure 3.10) solely $\{H_xGe_9\}^-$ (x = 0-2, m/z = 653-655), $\{HGe_{10}\}^-$ (m/z = 726) and $\{Ge_9Rb\}^-$ (m/z = 738) are visible. The high dominance of the $\{HGe_{10}\}^-$ in the ESI-MS reveals that $[Ge_{10}]^{2-}$ (**10a**) readily forms upon simple dissolution of Rb_4Ge_9 in *en*, by oxidative growth of $[Ge_9]^{4-}$ clusters. Even though $[Ge_{10}]$ has been observed in MS before, so far crystallization of the dianion has been unsuccessful and layering of A_4Ge_9/*en* solutions with different sequestering agents in toluene led solely to products comprising (coupled) $[Ge_9]_n$ units (n = 2-4).[24]

In the course of this work crystallization of Ge_9 clusters from Rb_4Ge_9/*en* solution was inhibited by chemical "masking" of the latter with 1-trimethylsilyl-7-amino-5-aza-hepta-3-en-1-yne (**2**) (chapter 3.1.4), and **10a** for the first time could be isolated and structurally characterized as $\{[Rb(222\text{-crypt})]_2$ **10a**$\}\cdot(en)_{1.5}$ salt. As presented in chapter 3.1.4 $[Ge_9]^{4-}$ Zintl anions readily react with **2** to $[Ge_9\text{-}\mathbf{R}]^{3-}$ and $[\mathbf{R}\text{-}Ge_9\text{-}\mathbf{R}]^{2-}$ (**R** = 7-amino-5-aza-hepta-2,4-dien-2-yl), which do not crystallize by layering with cryptand[2.2.2]/*tol*.[33] In the ESI-MS, of a reaction solution from which $\{[Rb(222\text{-crypt})]_2$ **10a**$\}\cdot(en)_{1.5}$ was isolated (Figure 3.10), dominant signals originating from $[Ge_9\text{-}\mathbf{R}]^{3-}$ and $[\mathbf{R}\text{-}Ge_9\text{-}\mathbf{R}]^{2-}$ appear together with weaker signals of $\{H_xGe_9\}^-$ (x = 0-2), $\{Ge_9Rb\}^-$ and $\{HGe_{10}\}^-$. The high abundance of clusters bearing organic functionality **R** documents the higher reactivity of the $[Ge_9]^{4-}$ unit towards **2**, compared to that of **10a**. The appearance of $\{HGe_{10}\}^-$ suggests that a fraction of the

initial $[Ge_9]^{4-}$ clusters reacts to **10a** prior to the reaction with **2**, whereas the occurrence of Ge_9^- and $(Ge_9Rb)^-$ most likely is attributed to the cleavage of the Ge–C bonds of $[Ge_9\text{-}\mathbf{R}]^{3-}$ and $[\mathbf{R}\text{-}Ge_9\text{-}\mathbf{R}]^{2-}$ under ESI-MS conditions.[35].

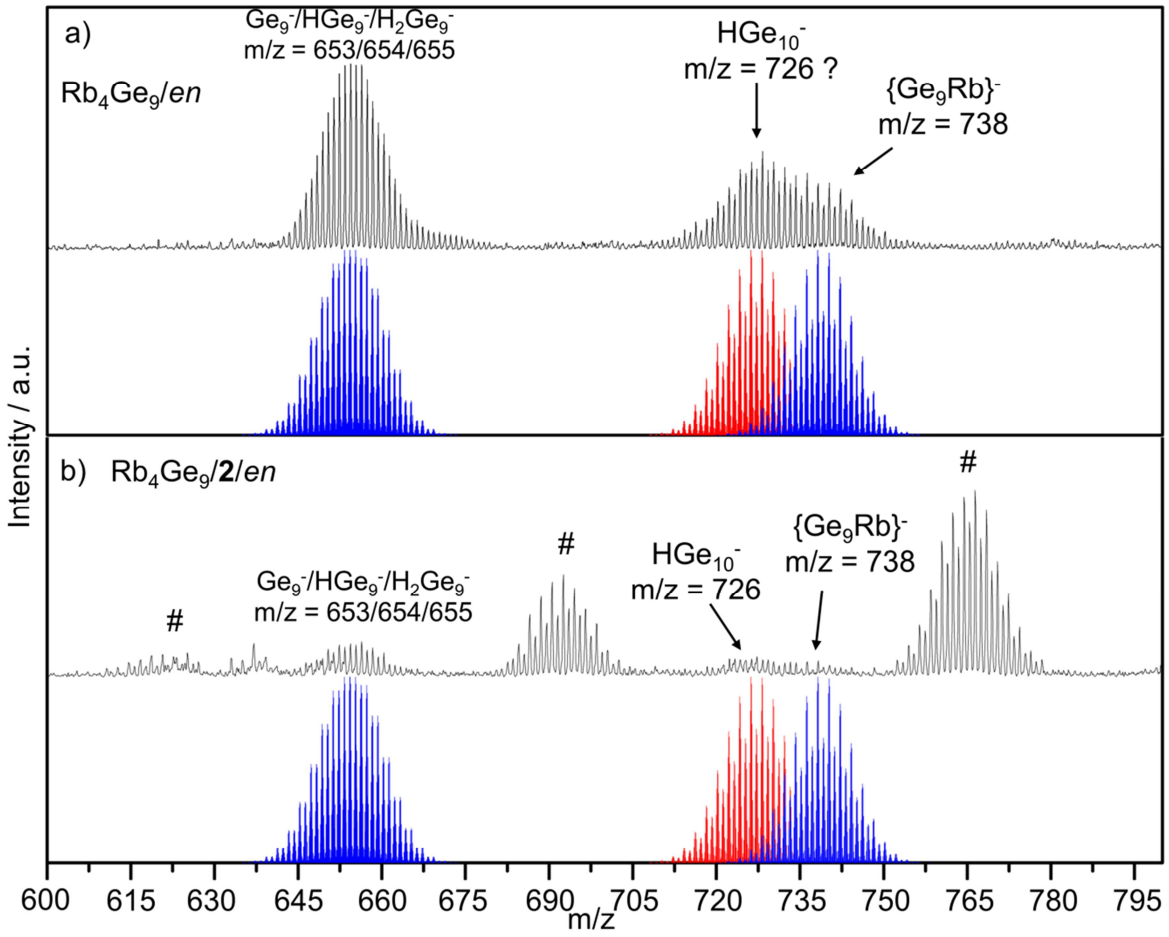

Figure 3.10. ESI-MS (-) of the reaction solutions a) Rb_4Ge_9/*en* and b/c) Rb_4Ge_9/**2**/*en*. The measured spectra (black) and simulated patterns (coloured) are stacked **R** = 7-amino-5-aza-hepta-2,4-dien-2-yl = $C_6H_{11}N_2$. Signals marked with # are discussed in chapter 3.1.4. The figure and figure caption were adopted from [20] by the permission of The Royal Society of Chemistry.

According to X-ray structure analysis, **10a** adopts the shape of a bicapped square anti-prism with D_{4d} symmetry (Figure 3.11) which is build up by ten symmetry independent fully occupied Ge positions. The squares of the cluster are significantly widened compared to the open square of a *nido*-$[Ge_9]^{4-}$ Zintl cluster. According to the Wade rules, **10a** possesses 22 SE and is a *closo*-cluster[17, 18], which is consistent with the descriptions of $[(Ge_{10})Mn(CO_3)]^{3-}$ and $[Pb_{10}]^{2-}$.[15, 16]

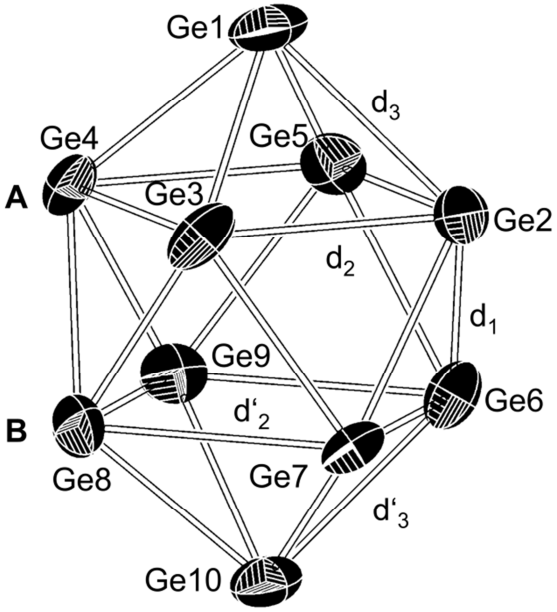

Figure 3.11. X-ray structure of *closo*-$[Ge_{10}]^{2-}$. The ellipsoids are shown at a probability level of 50%. The figure and figure caption were adopted from [20] by the permission of The Royal Society of Chemistry.

The successful isolation of **10a** was further confirmed by ESI-MS (Figure 3.12a). In the Raman spectrum of {[Rb(222-crypt)]$_2$ **10a**}·$(en)_{1.5}$ (Figure 3.12b) a very strong signal appears at 209 cm^{-1}, beside several very weak bands in the range of 95 to 166 cm^{-1}, respectively. Comparison of the latter with the spectra of *nido*-$[Ge_9]^{4-}$ (Figure 3.12c) [34, 36, 37] and *closo*-$[Ge_9]^{2-}$[22] points that the signal at 209 cm^{-1} corresponds to the "breathing mode" of **10a**.

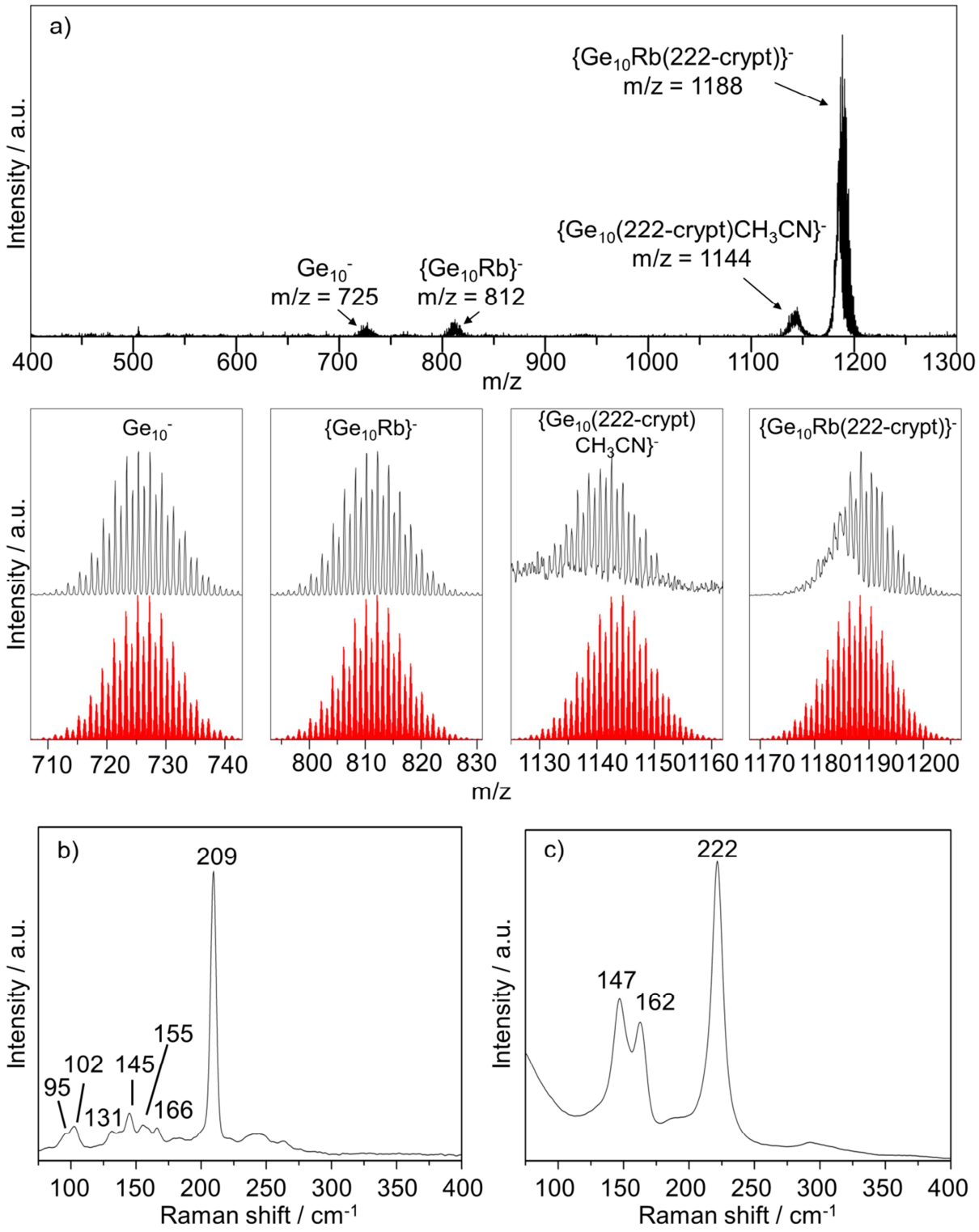

Figure 3.12. a) ESI-MS of a solution of {[Rb(222-crypt)]$_2$ **10a**}·(en)$_{1.5}$ in *acn*. The signals are magnified in the lower row. b/c) Raman spectra of b) {[Rb(222-crypt)]$_2$ **10a**}·(en)$_{1.5}$ and c) Rb_4Ge_9. Characteristic modes are labeled with the corresponding Raman shifts. The figures a-c) were adopted from [20] by the permission of The Royal Society of Chemistry.

3.2.3 The $[(\eta^4\text{-}Ge_9)Sn(\eta^3\text{-}Ge_9)]^{4-}$ Zintl Anion

see chapter 5.4

M. M. Bentlohner, L.-A. Jantke, T. Henneberger, C. Fischer, K. Mayer, W. Klein, T. F. Fässler, *Chem. Eur. J.* **2016**, *22*, 13946.

In addition to the homoatomic extension of $[Ge_9]^{4-}$ Zintl anions, reactions allowing addition of tin to the clusters, were searched. As reviewed in chapter 3.2.1 the reaction of $(SnPh_3)^-$ with K_4Ge_9 in *en*, results in the $[(\eta^3\text{-}Ge_9)(SnPh_3)]^{3-}$. Thereby, the $(SnPh_3)^-$ was synthesized separately by reduction of $SnPh_3Cl$ with elemental potassium.[29] Catching up this idea, reaction of $[Ge_9]^{4-}$ with $SnPh_2Cl_2$ in presence of elemental potassium was tested. From fundamental chemistry it is known, that reduction of SnR_2Cl_2 with alkaline metals leads to stannylenes "SnR_2" which quickly polymerize.[30, 31] To overcome the problem of polymerization, the reduction of the Sn(IV)organyle was done *in situ* by adding a $SnPh_2Cl_2$/*en* suspension to a mixture of K_4Ge_9 and elemental potassium in *en*. After stirring for several hours and layering of the reaction mixture with 18-crown-6/*tol*, crystals of $\{K(18\text{-crown-6})]_4$ $[(\eta^4\text{-}Ge_9)Sn(\eta^3\text{-}Ge_9)]\}(en)_{4.5}$ were obtained.

The $[(\eta^4\text{-}Ge_9)Sn(\eta^3\text{-}Ge_9)]^{4-}$ (**11a**) consists of two Ge_9 entities (denoted in the following by **1A** and **1B**), which are linked by a Sn atom (Figure 3.13). Cluster **1A** is an idealized monocapped square antiprism (the ratio of the diagonal lengths of the open square is 1.0) and thus corresponds to a C_{4v}-symmetric cluster, whereas **1B** adopts D_{3h}-symmetry and corresponds to a tri-capped trigonal prism. The bridging Sn atom coordinates to the atoms Ge1 to Ge4 of the open square of **1A**, with Sn–Ge distances [2.630(1) Å - 2.709(1) Å] being slightly above the sum of covalent radii. The Sn atom further coordinates to the three atoms Ge10, Ge11 and Ge12 of the triangular face of **1B**, with considerably longer Sn–Ge distances [2.770(1) Å - 3.151(1) Å]. The structural parameters of the C_{4v}- and D_{3h}-symmetric clusters **1A** and **1B** are in full agreement with 22 SE and 20 SE *nido*- and *closo*-cluster, respectively.

In the ESI MS of a reaction solution from which $\{K(18\text{-crown-6})]_4$ **11a**$\}(en)_{4.5}$ was isolated the occurrence of $\{Ge_9Sn\}^-$ (m/z = 771) as the only fragment of **11a** indicates stronger bonds between the Sn atom and the Ge atoms of the open square of **1A**. The ESI-MS spectra were recorded by Christina Fischer (*Technical University of Munich*, group Prof. Dr. T. F. Fässler).

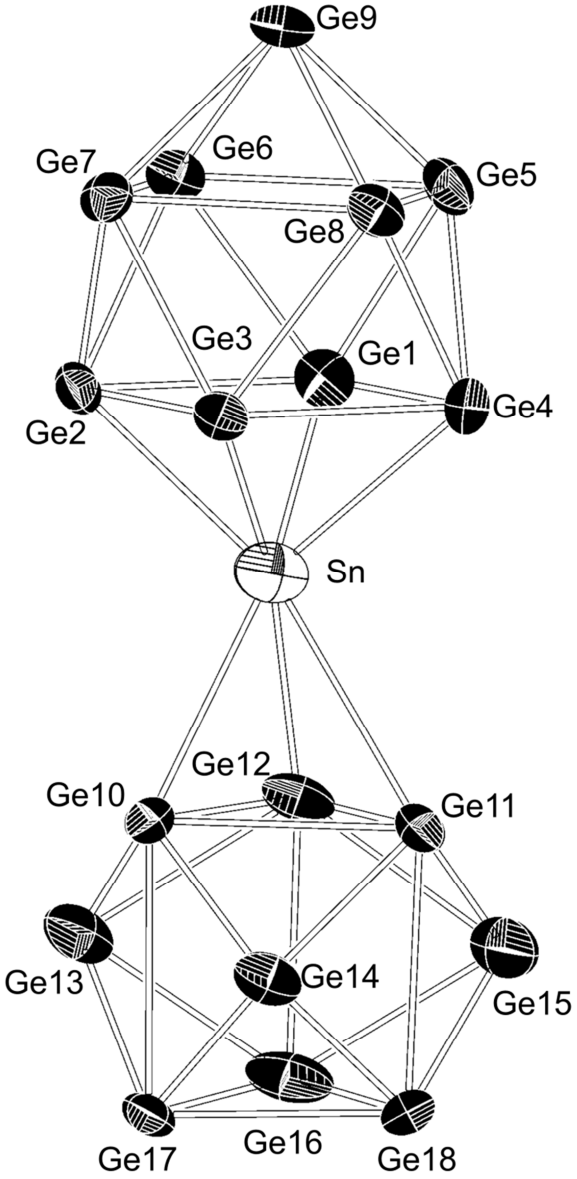

Figure 3.13. The X-ray structure of $[(\eta^4\text{-}Ge_9)Sn(\eta^3\text{-}Ge_9)]^{4-}$ (**11a**). The figure was modified on the basis of ref. [38]

Shorter average Sn-Ge distances to the atoms of the η^4-coordinated cluster, in the range of covalent bonds, and widening of the open square face of **1A** (Figure 3.14 and Table 3.1) in the same order of magnitude as observed for *closo*-$[Ge_{10}]^{2-}$ [20], allow the formulation of a ten-vertex 22 SE *closo*-$[Ge_9Sn]^{2-}$, with one lone pair at each vertex pointing radially to the outside of the cluster. Similar to the formal description of *closo*-$[Ge_9Tl]^{3-}$ [27] as a covalent combination of *nido*-$[Ge_9]^{4-}$ with Tl^+, *closo*-$[Ge_9Sn]^{2-}$ can be interpreted as the covalent combination of Sn^{2+} with a *nido*-$[Ge_9]^{4-}$ cluster. The coordinative interaction of the lone pair at the Sn atom of *closo*-$[Ge_9Sn]^{2-}$ with an acceptor orbital of *closo*-$[Ge_9]^{2-}$ (**1B**), in analogy to the $[(\eta^3\text{-}$

$Ge_9)(SnPh_3)]^{3-}$ Zintl anion, can be seen on the considerably longer Ge–Sn distances and only slight widening of the coordinated triangular face of **1B** (Figure 3.14 and Table 3.2). Overall, **11a** can be interpreted as a Lewis base/Lewis acid pair of the fragments *closo*-$[Ge_9Sn]^{2-}$ (**1A**) and *closo*-$[Ge_9]^{2-}$ (**1B**). This description is supported by a molecular orbital analysis on a PBE0/def2-TZVPP/PCM level of theory for **11a**, which was conducted by Laura-Alice Jantke (*Technical University of Munich*, group Prof. Dr. T. F. Fässler)

Similar investigations were also engaged with zinc bridged clusters $[(Ge_9)Zn(Ge_9)]^{6-}$, which were synthesized by Kerstin Mayer and Thomas Henneberger (*Technical University of Munich*, group Prof. Dr. T. F. Fässler), and therefore are out of the scope of the present work. From investigations on both the tin and zinc containing species followed the general concept, that metal atoms coordinating to the open square of a C_{4v}-symmetric Ge_9 cluster form strong covalent multicenter bonds, which is in contrast to metal atoms coordinating to triangular cluster faces.

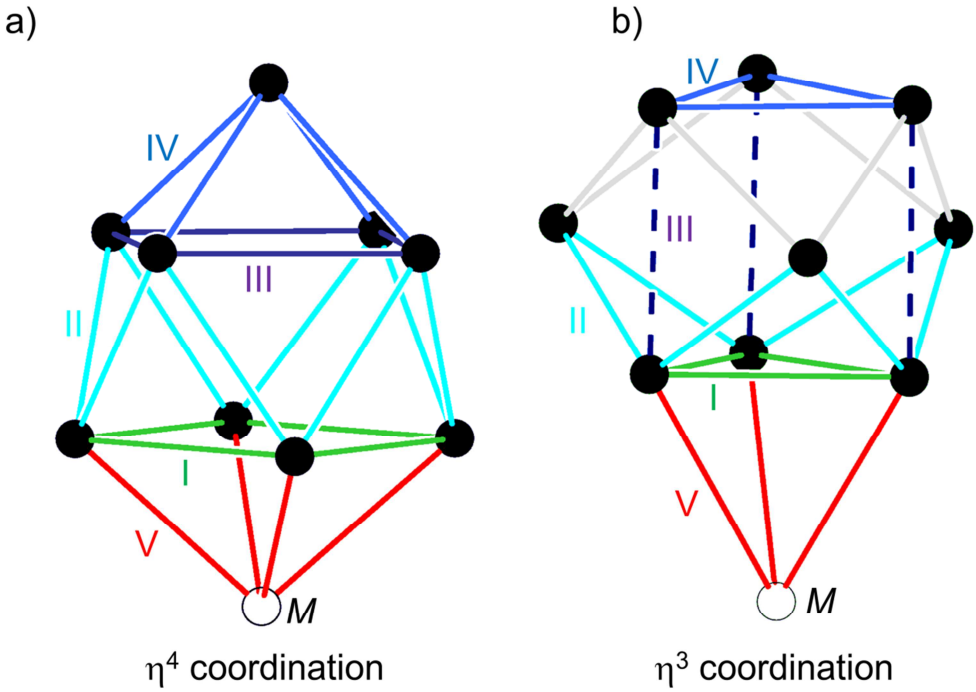

Figure 3.14. a) η^4 and b) η^3 coordinated Ge_9 clusters. Different classes of bonds are depicted in different colores and denoted with roman numbers. In Table 3.1-3.2 the average bond lengths for each bond class are shown for selected examples. The figure and figure caption was modified on the basis of ref. [38]

Table 3.1. Influence on bond length through η^4-coordination of an additional atom. Average bond lenghts [Å] for a) bare *nido*-$[Ge_9]^{4-}$ [39], b) $[Ge_{10}]^{2-}$ [20] being formally $[(\eta^4\text{-}Ge_9)Ge]^{2-}$ and c) **11a.** The table and caption was modified on the basis of ref. [38]

	a) -	b) Ge	c) Sn
I	2.57	2.80	2.84
II	2.58	2.55	2.56
III	2.83	2.79	2.79
IV	2.57	2.58	2.59
V	-	2.59	2.67

Table 3.2. Influence on bond length through η^3-coordination of an additional atom. Average bond lenghts [Å] for a) **11a**, b) $[K(222\text{-crypt})]_3[(\eta^3\text{-}Ge_9)(SnMe_3)]^{3-}$ [29], c) $[K(18\text{-crown-}6)]_3[(\eta^3\text{-}Ge_9)(SnMe_3)]\cdot(thf)\cdot(en)_2$ [29], d) $[K(222\text{-crypt})]_3[(\eta^3\text{-}Ge_9)(SnPh_3)]\cdot en$ [29], e) $[K(222\text{-crypt})]_3[(\eta^3\text{-}Ge_9)(SnPh_3)]\cdot(NH_3)_7$ [40] and f) $[K(18\text{-crown-}6)(NH_3)_2]_2K[(\eta^3\text{-}Ge_9)(SnPh_3)]\cdot(NH_3)_{15}$ [40] . The table and caption was modified on the basis of ref. [38]

	a) η^3-Sn	b) η^3-$SnMe_3$	c) η^3-$SnMe_3$	d) η^3-$SnPh_3$	e) η^3-$SnPh_3$	f) η^3-$SnPh_3$	g) η^3-In
I	2.73	2.74	2.71	2.73	2.74	2.76	2.73
II	2.55	2.57	2.59	2.60	2.57	2.57	2.54
III	2.88	2.97	2.98	2.93	2.92	2.93	2.95
IV	2.65	2.68	2.70	2.64	2.65	2.64	2.63
V	2.97	3.32	3.18	3.07	3.04	3.01	2.90

3.2.4 Literature

[1] T. F. Fässler, S. D. Hoffmann, *Angew. Chem. Int. Ed.* **2004**, *43*, 6242.
[2] A. M. Guloy, R. Ramlau, Z. Tang, W. Schnelle, M. Baitinger, Y. Grin, *Nature* **2006**, *443*, 320.
[3] A. Stein, *Nature* **2006**, *441*, 1055.
[4] S. C. Sevov, J. M. Goicoechea, *Organometallics* **2006**, *25*, 5678.
[5] T. F. Fässler, *Angew. Chem. Int. Ed.* **2007**, *46*, 2572.
[6] S. Scharfe, T. F. Fässler, *Phil. Trans. A Math. Phys. Eng. Sci.* **2010**, *368*, 1265.
[7] S. Scharfe, F. Kraus, S. Stegmaier, A. Schier, T. F. Fässler, *Angew. Chem. Int. Ed.* **2011**, *50*, 3630.
[8] G. S. Armatas, M. G. Kanatzidis, *Science* **2006**, *313*, 817.
[9] S. Dong, A. E. Riley, A. J. Cadby, E. K. Richman, S. D. Korlann, S. H. Tolbert, *Nature* **2006**, *441*, 1126.
[10] G. S. Armatas, M. G. Kanatzidis, *Nature* **2006**, *441*, 1122.
[11] M. G. Kanatzidis, *Adv. Mater.* **2007**, *19*, 1165.
[12] G. S. Armatas, M. G. Kanatzidis, *J. Am. Chem. Soc.* **2008**, *130*, 11430.
[13] G. S. Armatas, M. G. Kanatzidis, *Adv. Mater.* **2008**, *20*, 546.
[14] G. S. Armatas, M. G. Kanatzidis, *Nano Lett.* **2010**, *10*, 3330.
[15] D. Rios, S. C. Sevov, *Inorg. Chem.* **2010**, *49*, 6396.
[16] A. Spiekermann, S. D. Hoffmann, T. F. Fässler, *Angew. Chem. Int. Ed.* **2006**, *45*, 3459.
[17] K. Wade, *Inorg. Nucl. Chem. Lett.* **1972**, *8*, 559.
[18] K. Wade, in *Advances in Inorganic Chemistry and Radiochemistry, Vol. Volume 18* (Eds.: H. J. Emeléus, A. G. Sharpe), Academic Press, **1976**, pp. 1.
[19] T. F. Fässler, H.-J. Muhr, M. Hunziker, *Eur. J. Inorg. Chem.* **1998**, *1998*, 1433.
[20] M. M. Bentlohner, C. Fischer, T. F. Fässler, *Chem. Commun.* **2016**, *52*, 9841.
[21] S. Mitzinger, L. Broeckaert, W. Massa, F. Weigend, S. Dehnen, *Nat. Commun.* **2016**, *7, 10480*.
[22] J. Åkerstedt, S. Ponou, L. Kloo, S. Lidin, *Eur. J. Inorg. Chem.* **2011**, *2011*, 3999.
[23] C. Belin, H. Mercier, V. Angilella, *New J. Chem.* **1991**, *15*, 931.
[24] A. Ugrinov, S. C. Sevov, *J. Am. Chem. Soc.* **2003**, *125*, 14059.
[25] A. Ugrinov, S. C. Sevov, *Inorg. Chem.* **2003**, *42*, 5789.
[26] M. M. Gillett-Kunnath, A. G. Oliver, S. C. Sevov, *J. Am. Chem. Soc.* **2011**, *133*, 6560.
[27] D. Rios, M. M. Gillett-Kunnath, J. D. Taylor, A. G. Oliver, S. C. Sevov, *Inorg. Chem.* **2011**, *50*, 2373.
[28] D. F. Hansen, B. Zhou, J. M. Goicoechea, *J. Organomet. Chem.* **2012**, *721–722*, 53.
[29] A. Ugrinov, S. C. Sevov, *Chem. Eur. J.* **2004**, *10*, 3727.
[30] R. E. Dessy, W. Kitching, T. Chivers, *J. Am. Chem. Soc.* **1966**, *88*, 453.
[31] A. F. Holleman, E. Wiberg, N. Wiberg, *Lehrbuch der anorganischen Chemie*, de Gruyter, **1995**.
[32] M. M. Bentlohner, M. Waibel, P. Zeller, K. Sarkar, P. Müller-Buschbaum, D. Fattakhova-Rohlfing, T. F. Fässler, *Angew. Chem. Int. Ed.* **2016**, *55*, 2441.
[33] M. M. Bentlohner, S. Frischhut, T. F. Fässler, *manuscript for publication* **2016**.
[34] M. Somer, W. Carrillo-Cabrera, E. M. Peters, K. Peters, H. G. v. Schnering, *Z. Anorg. Allg. Chem.* **1998**, *624*, 1915.
[35] M. W. Hull, S. C. Sevov, *J. Am. Chem. Soc.* **2009**, *131*, 9026.

[36] H. G. Von Schnering, M. Baitinger, U. Bolle, W. Carrillo-Cabrera, J. Curda, Y. Grin, F. Heinemann, J. Llanos, K. Peters, A. Schmeding, M. Somer, *Z. Anorg. Allg. Chem.* **1997**, *623*, 1037.
[37] V. Hlukhyy, T. F. Fässler, S. Ponou, S. Lidin, N. P. Ivleva, R. Niessner, *Inorg. Chem.* **2012**, *51*, 4058.
[38] M. M. Bentlohner, L.-A. Jantke, T. Henneberger, C. Fischer, K. Mayer, W. Klein, T. F. Fässler, *Chem. Eur. J.* **2016**, *22*, 13946. [39] S. Ponou, T. F. Fässler, *Z. Anorg. Allg. Chem.* **2007**, *633*, 393.
[40] C. B. Benda, *Dissertation,* Technical University of Munich, Garching **2013**.

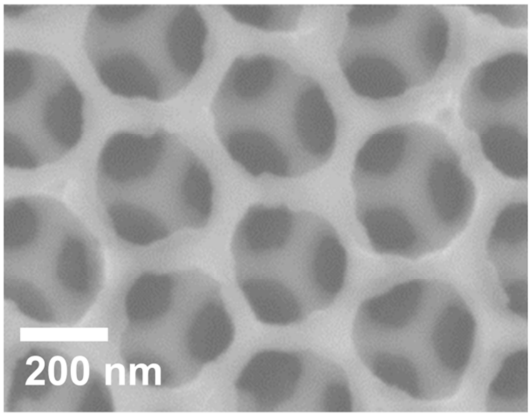

3.3 Germanium Inverse Opals by the Oxidation of $[Ge_9]^{4-}$ Zintl Anions and their Application in Hybrid Solar Cells

3.3.1 Review of Relevant Literature

3.3.1.1 Fabrication of porous Ge Materials

Porous forms of germanium, such as inverse opals, have attracted significant attention due to a broad range of potential applications in photovoltaics, electrochemical energy storage, sensing, microelectronics and photonics.[1-5]

The synthetic approaches for porous germanium are less developed [6], compared to the synthesis of corresponding nanoparticles [7-9] and nanowires [10]. A top down approach (Figure 3.14a) for porous germanium layers grounds on the chemical or electrochemical etching of corresponding bulk germanium, providing a good control over the composition and crystallinity, however only a limited control over the porous structure and the surface chemistry[11]. Bottom-up approaches, which ground on molecular precursors are more beneficial for fabricating periodic porous materials due to a better control over the shape, size and spatial arrangement of the pores (Figure 3.14b).[12] Examples in regard to the fabrication of germanium inverse opals are chemical vapor deposition (CVD) involving silanes/germanes [13, 14],

electrochemical reduction of group 14 halides [15-17] and reduction of germanium(IV)oxide with hydrogen [18] in presence of an opal template. Even though these examples provide a good control over the composition, morphology and crystallinity, the set-ups are technically demanding and less flexible, which hinders fabrication of the inverse opals on a larger area.

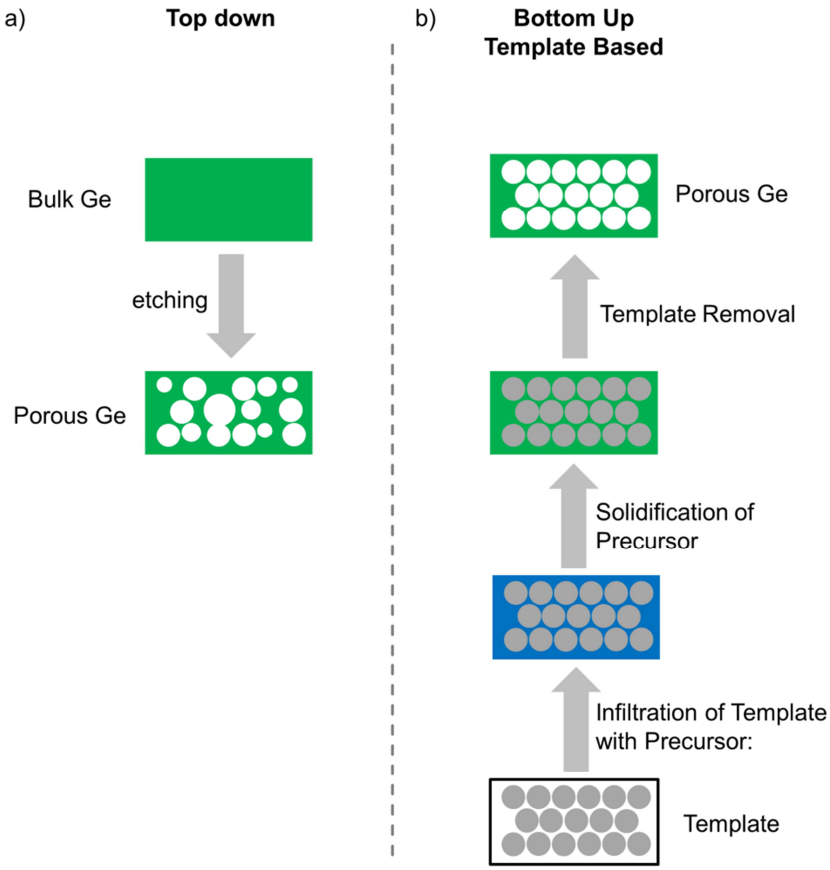

Figure 3.15. Schematic representation of a) top down and b) template based bottom up approaches for the fabrication of porous germanium layers.

In contrast to physico-chemical methods, wet chemical bottom-up approaches, grounding on soluble precursors, are in high demand due to their general potential of simplicity, scalability and applicability in printing or spray processes.[19] A multitude of wet-chemical bottom-up approaches has been developed for metal oxides resulting in a large variety of periodic porous morphologies with different compositions.[12] A transfer of these methods to the fabrication of porous germanium morphologies has been started just recently by the introduction of $[Ge_9]^{4-}$ as soluble Ge source.[20, 21] In that context $[Ge_9]^{4-}$ Zintl anions were used for electrodeposition of dense germanium layers[22] as well as for fabrication of mesoporous powders using surfactant templating approaches [20, 21, 23-25]. Strongly Lewis acidic main-group halides and

nitrates (*M* = Ge, Sb, In, Sn, Pb) as well as cadmium chloride have been applied to trigger the full oxidation of the clusters, and a bunch of germanium materials with different compositions have been obtained.[20, 24] Also the reaction of $[Ge_9]^{4-}$ in presence of a surfactant template and *en* has led to mesoporous germanium. Even though the involved reactions were not clearly evidenced, *en* has been attributed to be the oxidizer for the clusters. [23, 25] Although $[Ge_9]^{4-}$ Zintl anions have been successfully used as precursors for porous germanium powders [20, 21, 23-25], requires application of the latter in photovoltaics their fabrication in form of continuous films over extended areas. However, largely unclear oxidation reactions of the clusters restrict the generalization of these methods to alternative template morphologies and fabrication scales.

In the course of this thesis methods for the controlled oxidation of $[Ge_9]^{4-}$ to germanium with tunable composition and inverse opal structure were searched. The herein presented approach grounds on the transfer of Ge_9 clusters, by the solvent *en*, into an opal template and their controlled oxidation to elemental germanium. For using *en* as a transfer medium, a mature understanding of the oxdative potential of that solvent towards $[Ge_9]^{4-}$ is necessary and ways for the recovery of intact clusters from K_4Ge_9/*en* solutions are required. Therefore reaction of $[Ge_9]^{4-}$ with *en* and the role of water was investigated. Targeting towards fabrication of germanium phases with tunable composition, the oxidation of $[Ge_9]^{4-}$ with MCl_n (*M* = Si, Ge, P) has been examined.

3.3.1.2 Nanostructured Non-Oxide Semiconductors in Organic/Inorganic Hybrid Solar Cells

As reviewed in chapter 1.4 nanostructured inorganic materials enhance the performance of organic/inorganic hybrid solar cells. Due to quantum confinement, opto-electronic properties such as band gaps, light absorption behavior and electrical conductivites significantly alter with the size of the nanostructures. That circumstance provides an additional parameter to harmonize the organic and inorganic counterparts of the photovoltaic device. Nanostructuring also provides high interface areas suitable for efficient exciton harvesting as well as enhanced light absorption due to lower reflectance and photonic band structures.[26-29]

Progresses in the nanostructuring of group 14 and 13/15 semiconductors and their inherently advantageous electronic properties, such as inherently high charge carrier mobility and optical absorption coefficients, fuels the implementation of such materials in hybrid solar cells.[29] The architecture of one class of hybrid solar cells grounds on the combination of the hole conductor P3HT with Si [30], Ge [31], InP [32] or GaAs [33] nanowires/nanopillars, which are generated by laser ablation, vapor-liquid-solid method, chemical vapor deposition (CVD) and molecular beam epitaxy, respectively. Investigations on the application of Ge nanowires in P3HT based hybrid solar cells (Figure 3.16) revealed that germanium can efficiently take up electrons from the donor polymer P3HT and therefore enhances the performance of the photovoltaic device.[31] Investigations with differently sized Si nanowires in P3HT solar cells demonstrated that with decreasing diameter of the wires the efficiency of the device increases.[30] A major improvement of that type of cells was also achieved by the direct growth of the nanowires on ITO substrates. Due to direct contacts of the wires to the substrate, ohmic resistances are minimized and continous pathways for the electrons are established in the photovoltaic device.[32] Also porous Si and GaAs, which were fabricated by electrochemical etching, have been investigated in hybrid solar cells.[34-35] Investigations on the influence of the pore dimensions revealed that both smaller pore diameters and deeper pores positively influence the efficiency of the hybrid solar cell, due to enhanced exciton harvesting and lowering of the device's reflectance, respectively.[36] Among nanostructured group 14 semiconductors silicon is the one which is most intensively investigated, whereas germanium despite of its valuable properties (see chapter 1.4) is only little studied.[29]

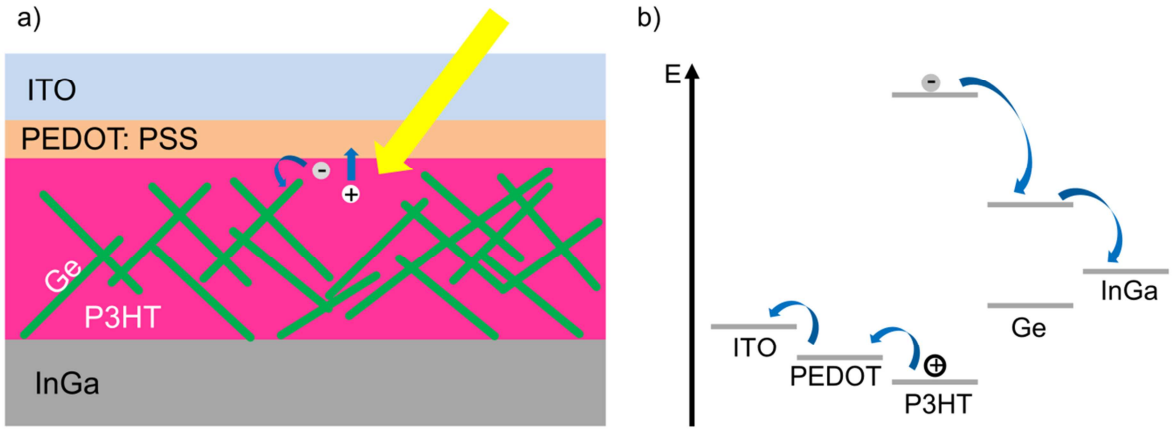

Figure 3.16. a) Schematic representation and b) energy band diagram of a Ge-NW/P3HT hybrid solar cell. The figure was drawn on the basis of ref. [31]

3.3.2 *Ex Situ* Investigations on the Oxidation of $[Ge_9]^{4-}$ Zintl Anions to Elemental Germanium

3.3.2.1 The Reaction of $[Ge_9]^{4-}$ with Ethylenediamine and the Role of Water

see chapter 5.5

M. M. Bentlohner, M. Waibel, P. Zeller, K. Sarkar, P. Müller-Buschbaum, D. Fattakhova-Rohlfing, T. F. Fässler, *Angew. Chem. Int. Ed.* **2016**, 55, 2441.

For the development of a wet-chemical fabrication method for Ge inverse opals using *en* as transfer-medium, the oxidative potential of *en* and ways for the recovery of intact clusters from K_4Ge_9/*en* solutions had to be investigated. As highlighted in chapter 3.2.2 water-free *en* is a mild oxidizer for $[Ge_9]^{4-}$ Zintl anions and can trigger oxidative reorganization and growth of clusters under retention of the deltahedral structures.[37] Despite this, *en* has also been proposed to be able to fully oxidize $[Ge_9]^{4-}$ clusters to elemental germanium, however so far this has never been evidenced.[23, 25] In particular the role of water on the oxidative potential of *en* towards clusters is only less studied. For shedding light on this, K_4Ge_9/*en* and K_4Ge_9/*en*/$[H_2O]$ solutions were pumped down in vacuum and the obtained reaction residues were investigated by Raman and powder X-ray diffractometry. Water-free *en* (denoted by grade A) and *en* containing water-traces (denoted by grade B) were prepared according to chapter 2.1.4.1.[38, 39]

Solutions of K_4Ge_9 in *en* with the different water contents show different colors – orange-red in case of K_4Ge_9/*en* and deep-green in case of K_4Ge_9/*en*/$[H_2O]$. As follows from Raman (Figure 3.17) is it possible to recover a "K_4Ge_9"-phase with intact germanium clusters from K_4Ge_9/*en* solutions in the absence of water (residue denoted by **A-RT**) by evaporation of the solvent. In contrast to that, the removal of *en* from K_4Ge_9/*en*/$[H_2O]$ solutions results in a residue (denoted by **B-RT**), which shows in Raman no clusters [40] but signals of *a*-Ge.[41, 42]

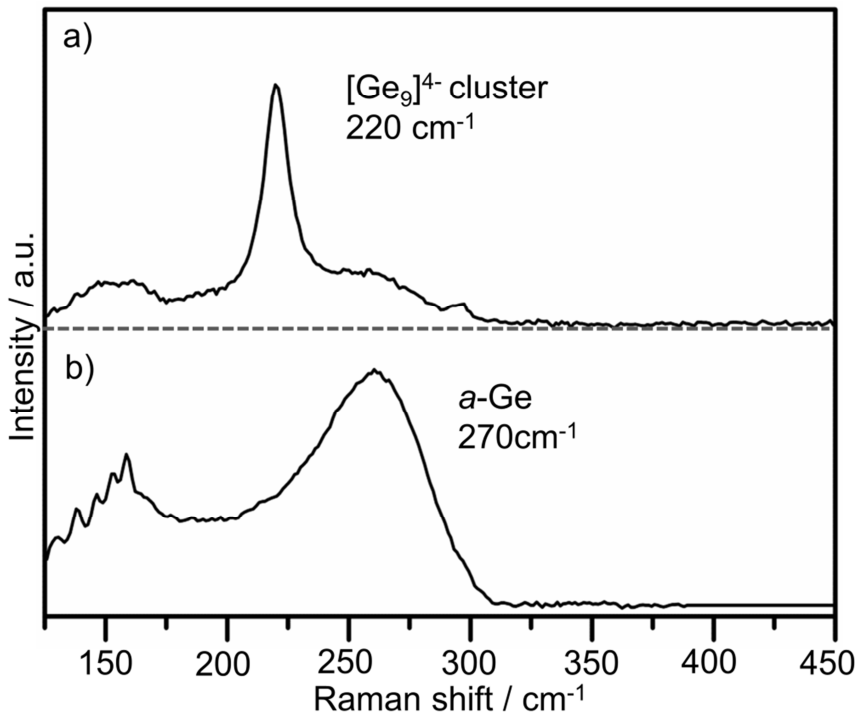

Figure 3.17. Raman spectra of residues obtained by pumping down K_4Ge_9/*en* solution a) in the absence of water (**A-RT**) and b) in the presence of water (**B-RT**). The figure was modified on the basis of Ref. [38]

Extraction of the residue **B-RT** with *acn*-d_3 and the NMR spectroscopic investigation of the extract revealed that ethylene(di)amide is formed as a side product, evidencing that *en* is able to fully oxidize $[Ge_9]^{4-}$ Zintl clusters to elemental germanium in the presence of water.

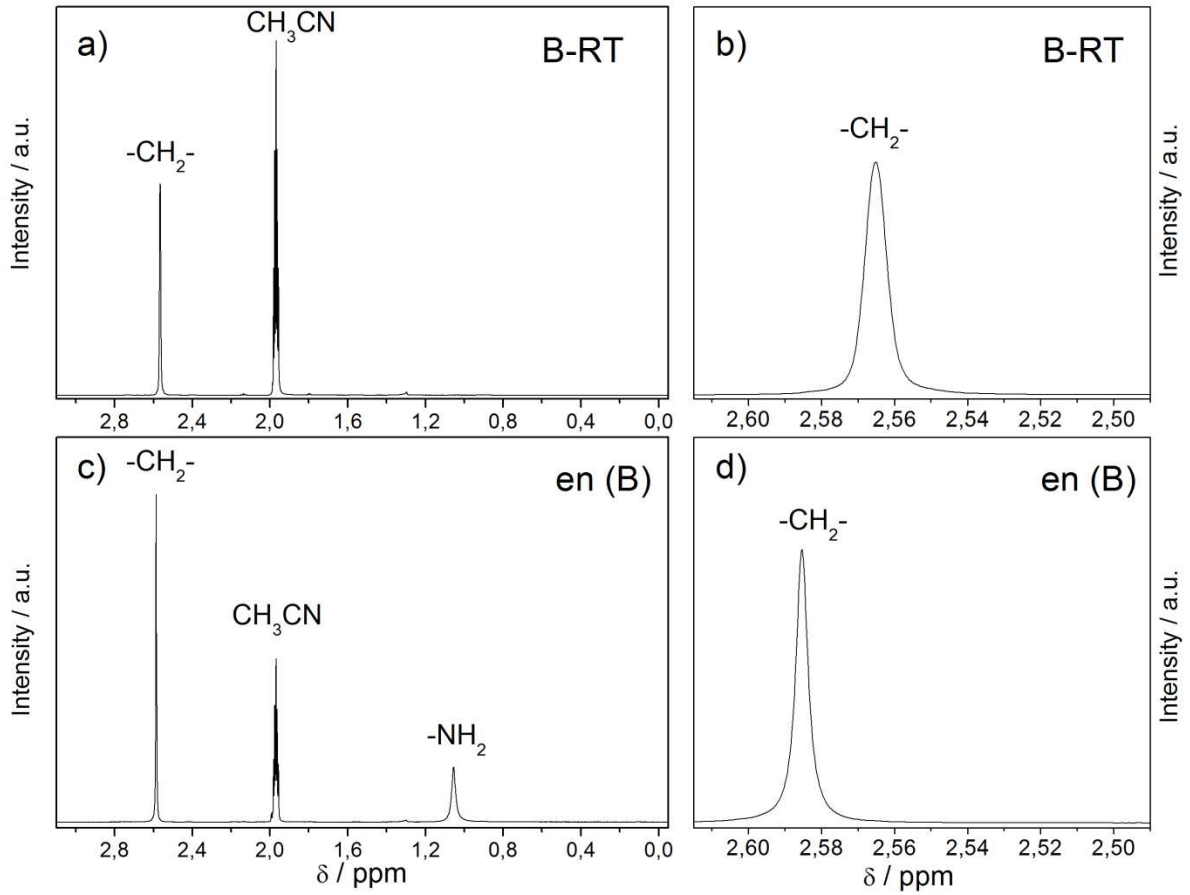

Figure 3.18. a/b) ^{1}H-NMR spectrum of the extract obtained by stirring sample **B-RT** for one hour with *acn*-d_3 and subsequent filtration over glass-wool. c/d) ^{1}H-NMR spectrum of *en* grade B dissolved in *acn*-d_3. Figure b) and d) show magnified sections of the spectra a) and c). The ^{1}H NMR spectrum of *en* in *acn*-d_3 shows two signals, corresponding to the methylene groups (2.555 ppm) and the amino functionality (1.02 ppm). For the extract the signal for the amino functionality is absent and exclusively a signal corresponding to methylene groups appears, indicating deprotonated *en*.[43] As expected for a deprotonated *en*, the signal of the methylene groups is high field shifted due to a shielding effect of the negatively charged –NH^- functionalities. The figure and figure caption was modified on the basis of ref. [38]

By thermal annealing of the *a*-Ge (residue **B-RT**) at 600°C for one hour α-Ge is formed (Figure 3.19a). An analogous procedure with "K_4Ge_9" (residue **A-RT**), which was recovered from water-free *en*, also yielded α-Ge, however in that case accompanied by the release of elemental potassium (Figure 3.19b).

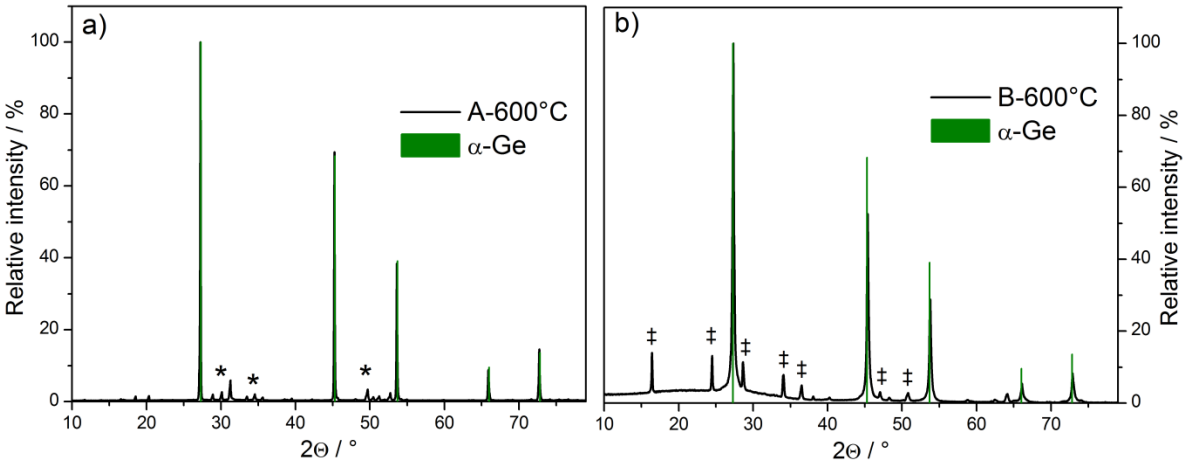

Figure 3.19. Powder X-ray diffractograms of the drying residues a) **A-RT** and b) **B-RT** after annealing at 600°C. The measurements were performed on the samples placed in Ar-sealed glass capillaries. Unknown reflections are marked with *. Reflections marked with ‡ are similar to the reflections of K_8Ge_{44}.[44] The figure and figure caption was modified on the basis of ref. [38]

The results demonstrate that *en* is a suitable transfer-medium for the transport of clusters into a mold and enables further chemical transformations with the clusters if water is thoroughly excluded. On the other hand *en* can be also used to trigger the oxidation of $[Ge_9]^{4-}$ to an undoped germanium phase if water traces are present (Scheme 3.8).

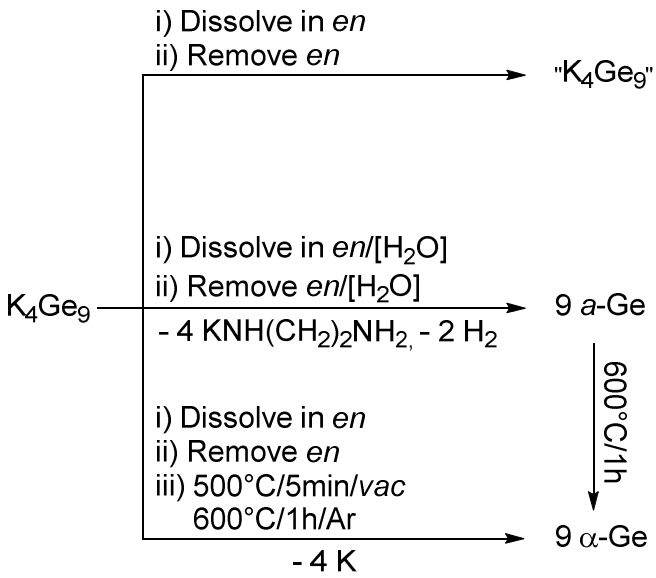

Scheme 3.8. Reaction of K_4Ge_9 with the solvent *en* and the influence of water. The scheme was modified on the basis of ref. [38]

3.3.2.2 The Reaction of $[Ge_9]^{4-}$ with MCl_n (M = Ge, Si, n = 4; E = P, n = 3)

see chapter 5.5

M. M. Bentlohner, M. Waibel, P. Zeller, K. Sarkar, P. Müller-Buschbaum, D. Fattakhova-Rohlfing, T. F. Fässler, *Angew. Chem. Int. Ed.* **2016**, 55, 2441.

As shown in chapter 3.2.3 it is possible to synthesize heteroatomic tetrel clusters by the reaction of $[Ge_9]^{4-}$ with $SnPh_2Cl_2$/K. Following this idea in regard to germanium phases with tunable composition, the strongly Lewis acidic MCl_n (M = Ge, Si, n = 4; M = P, n = 3) have been applied as oxidizers for $[Ge_9]^{4-}$ Zintl anions. The principal investigations on the reactivity of $[Ge_9]^{4-}$ towards MCl_n were conducted in toluene which is inert towards the halides. *En* vigorously reacts with MCl_n by the formation of a white precipitate and therefore has to be thoroughly removed prior to reactions of clusters with the halides. According to powder XRD and Raman, the reaction of K_4Ge_9 with MCl_n yields an *a*-$Ge_{1-x}M_x$ phase as well as potassium chloride as a side product. The amorphous phase crystallizes by annealing at 600°C for one hour (Figure 3.20 and Scheme 3.9).

$$K_4Ge_9 \xrightarrow[-\ 4\ KCl]{4/n\ MCl_n} m\ a\text{-}Ge_{1-x}E_x \xrightarrow{600°C/1h} m\ \alpha\text{-}Ge_{1-x}E_x$$

x=4/(9n+4); m=(9n+4)/n
E = Si/Ge (n=4), E = P (n=3)

Scheme 3.9. The reaction of K_4Ge_9 with MCl_n. The Scheme was modified on the basis of ref. [38]

By applying $SiCl_4$ for cluster oxidation, the XRD reflections of the crystalline product are shifted to higher angles, and in Raman an additional signal at ~ 390 cm^{-1} arises, which corresponds to the Ge-Si vibrational mode.[45] For the product reacted with PCl_3, the Ge-P mode at ~345 cm^{-1} is visible in the Raman spectra.[46] Energy dispersive X-ray analysis (EDX) of the amorphous and crystallized products confirmed the formation of $Ge_{1-x}M_x$ solid phases (see supporting information ref. [38]).

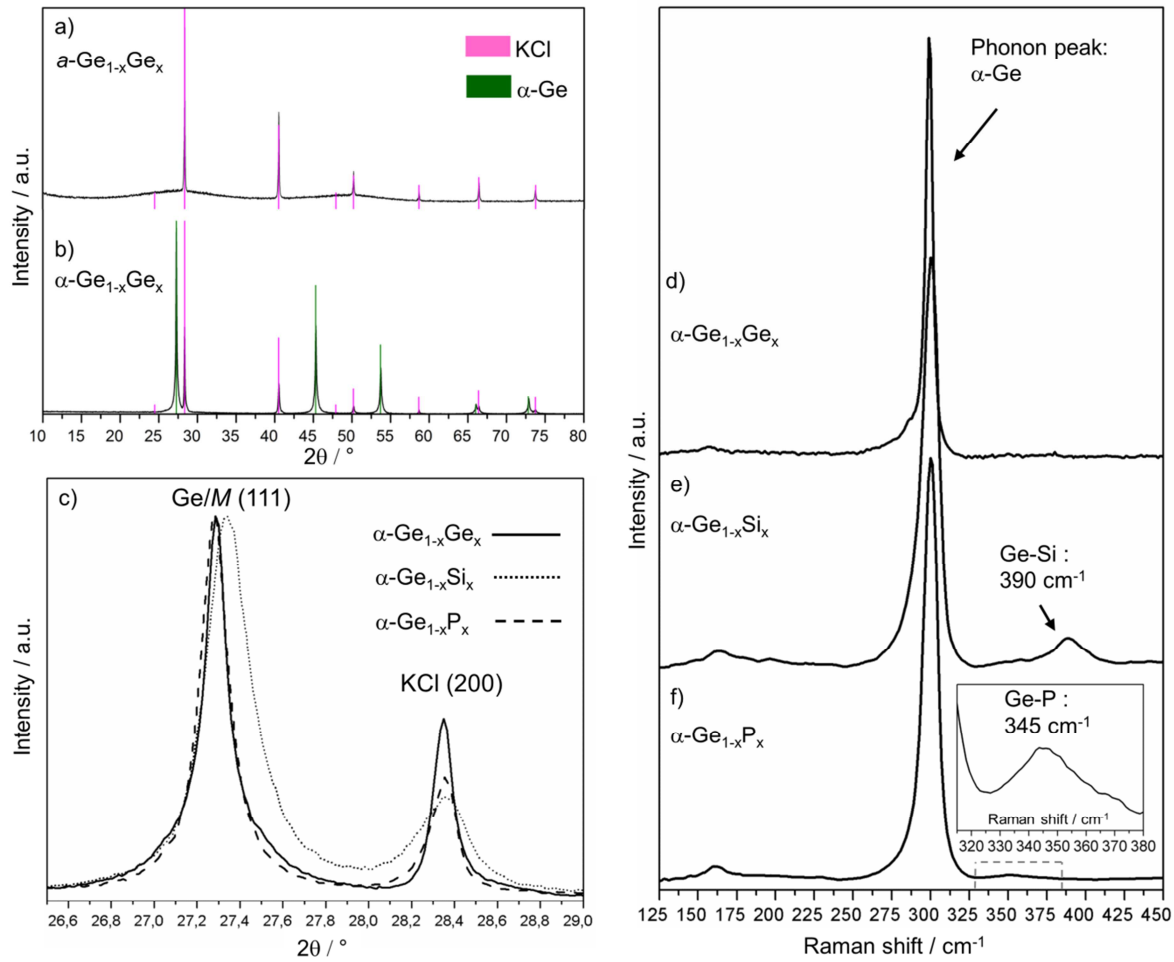

Figure 3.20. Powder X-ray diffractograms and Raman spectra of the products obtained by reacting K_4Ge_9 with MCl_n in toluene. a/b) Powder XRD of the a) *a*-$Ge_{1-x}Ge_x$ and b) α-$Ge_{1-x}Ge_x$. The reflections of potassium chloride and α-Ge are labelled with the corresponding *hkl* indices. c) Magnified section of the diffractograms recorded from α-$Ge_{1-x}Ge_x$ (solid line), α-$Ge_{1-x}Si_x$ (dotted line) and α-$Ge_{1-x}P_x$ (dashed line), respectively. Potassium chloride formed as a side product was used as internal standard. The (111) reflection is shown and a shift to higher diffraction angles can be observed in case of α-$Ge_{1-x}Si_x$ d-f) Raman spectra of the crystallized products obtained with MCl_n. The figure and figure caption was modified on the basis of ref. [38]

Due to the high Lewis acidity of the positively polarized *M* atom, MCl_n readily reacts with the highly Lewis basic $[Ge_9]^{4-}$ clusters in an oxidation reaction. In particular the use of $SiCl_4$ and PCl_3 for oxidation of the clusters is valuable as it enables incorporation of silicon or phosphorus into the Ge structure, and thus tuning of the electronic properties.

In addition the reaction of gaseous MCl_n with $[Ge_9]^{4-}$ also yields a $Ge_{1-x}M_x$ phase. With respect to the fabrication of inherently fragile nanostructures the oxidation of clusters by gaseous MCl_n is valuable, as the mechanical stress is much less compared to the application of solutions.

3.3.3 Fabrication and Characterization of Germanium Inverse Opal Films with Tunable Composition

see chapter 5.5 M. M. Bentlohner, M. Waibel, P. Zeller, K. Sarkar, P. Müller-Buschbaum, D. Fattakhova-Rohlfing, T. F. Fässler, *Angew. Chem. Int. Ed.* **2016**, 55, 2441.

see chapter 5.6 M. M. Bentlohner, S. Geier, M. Giebel, M. Loch, L. Song, P. Lugli, P. Müller-Buschbaum, D. Fattakhova-Rohlfing, T. F. Fässler, **2016**, *manuscript for publication*

By the *ex situ* investigations presented in chapter 3.3.2 a detailed knowledge on the reaction behavior of $[Ge_9]^{4-}$ towards *en* and MCl_n was gained. That knowledge was exploited for the definition of a controllable wet-chemical and template-based fabrication method for Ge inverse opals with tunable composition.[38]

Germanium films with inverse opal structure were prepared via colloidal crystal templating using periodic arrays of PMMA beads as the templates for porosity as well as solutions of K_4Ge_9 in *en* as the Ge source (Figure 3.21 and 3.22). PMMA opals were assembled, by dip-, spin- or spray-coating of substrates (Si, SiO_2, TiO_2/FTO; area = 1-4 cm^2) with a suspension of monodisperse PMMA beads (250-300 nm) in water (experimental details see chapter 2.1.6). $[Ge_9]^{4-}$ Zintl anions were transported to the thoroughly dried PMMA opal by infiltration with a solution of K_4Ge_9 in water-free *en*, and entire removal of the solvent in an argon atmosphere under ambient pressure (experimental details see chapter 2.1.7). The K_4Ge_9/*en* solutions were applied by drop-casting and spin-coating. Thermal treatment of the as prepared K_4Ge_9/PMMA composites at 600°C resulted in pyrolysis of the PMMA and formation of crystalline germanium inverse opal accompanied by the release of elemental potassium, which is in analogy to the results shown in chapter 3.3.2.1. In case of using K_4Ge_9/*en*[H_2O] as the Ge source, the clusters directly oxidize to *a*-Ge upon removal of the solvent *en,* according to the reactions described in chapter 3.3.2.1. In the following, films prepared by full oxidation of clusters with *en* or thermal treatment are denoted with Ge-*INOP*

The oxidation of $[Ge_9]^{4-}$ Zintl anions by reaction with gaseous MCl_n (M = Ge, n = 4; M = P, n = 3), shown in chapter 3.3.2.2, was applied for the oxidation of the clusters to germanium inverse opals with tunable composition. Treatment of the dried

K_4Ge_9/PMMA composites in gaseous MCl_n (M = Ge, P) resulted in the formation of 3D-Ge/M networks distributed in the PMMA bead matrix as follows from Raman and EDX. The PMMA either was removed by dissolution in *thf* or pyrolysis at 500°C/5min in vacuum. In the following, films prepared by oxidation of clusters with MCl_n are denoted with $Ge_{1-x}M_x$-*INOP*.

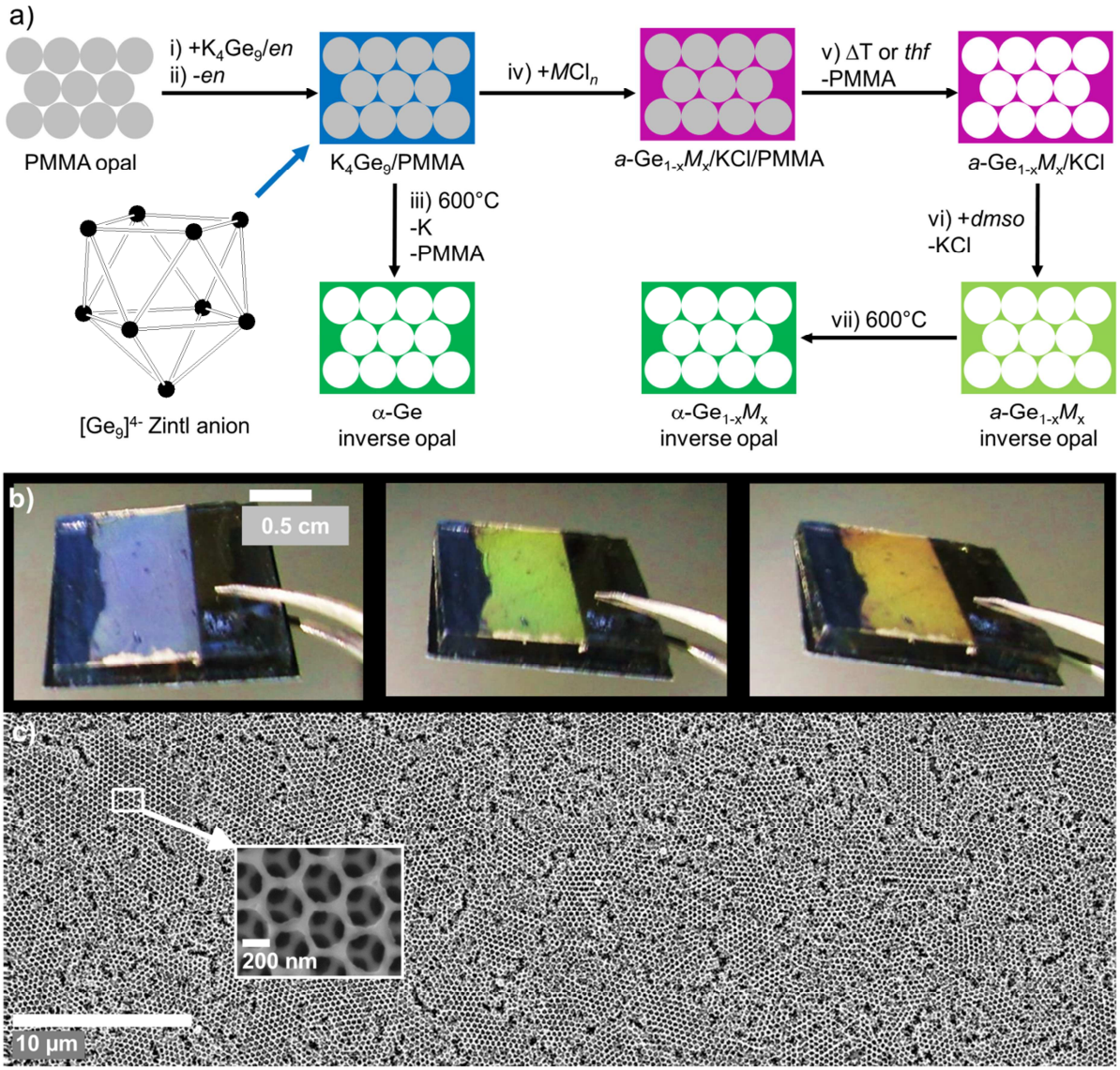

Figure 3.21. a) Fabrication of germanium inverse opals by controlled oxidation of $[Ge_9]^{4-}$ Zintl anions, i) Infiltration of a PMMA opal (grey spheres) with K_4Ge_9/*en*, ii) evaporation of *en*, iii) annealing of the K_4Ge_9/PMMA composite at 600°C and formation of α-Ge *INOP* and K vapor, iv) impregnation of K_4Ge_9/PMMA composite with MCl_n (M = Ge, P) and formation of *a*-$Ge_{1-x}M_x$/KCl/PMMA composite (purple), v) removal of PMMA by flash-annealing or dissolution in *thf*, vi) removal of KCl with *dmso,* vii) annealing of *a*-$Ge_{1-x}M_x$-INOP and formation of α-$Ge_{1-x}E_x$ INOP. b) Photography of *a*-$Ge_{1-x}Ge_x$-*INOP*, fabricated by the *MCln*-method (Oxidizer: $GeCl_4$). Coating: spray (PMMA)/spin (K_4Ge_9). The film was illuminated with white light at different incident angles.c) Scanning electron micrographs of *a*-$Ge_{1-x}Ge_x$ *INOP*-and magnified section of the film as inlay. The figures and figure captions were modified on the basis of ref. [38, 47]

Perfect ordering of the inverse opal films was validated by grazing incidence small angle X-ray scattering (GISAXS) experiments [48, 49] as well as transmission electron microscopy (TEM) (Figure 3.22). Both methods show uniformly sized periodic pores with diameters of ca. 150 nm and 200-250 nm. The obtained germanium inverse opals are amorphous up to 500 °C, as follows from Raman spectroscopy, high resolution TEM images and selected area electron diffraction (SAED). Inverse opal germanium films with enhanced crystallinity were prepared by annealing of the amorphous films for one hour at 600 °C in an argon atmosphere (α-$Ge_{1-x}Ge_x$-*INOP*). TEM micrographs, SAED pattern as well as Raman revealed that the pore walls of such films consist of α-Ge nanoparticles embedded in an amorphous matrix. Powder XRD patterns of the films scraped off the substrate display broadened reflections of α-Ge. The size of the crystallites calculated from the broadening of XRD reflections by using the Scherrer equation confirms the TEM results.

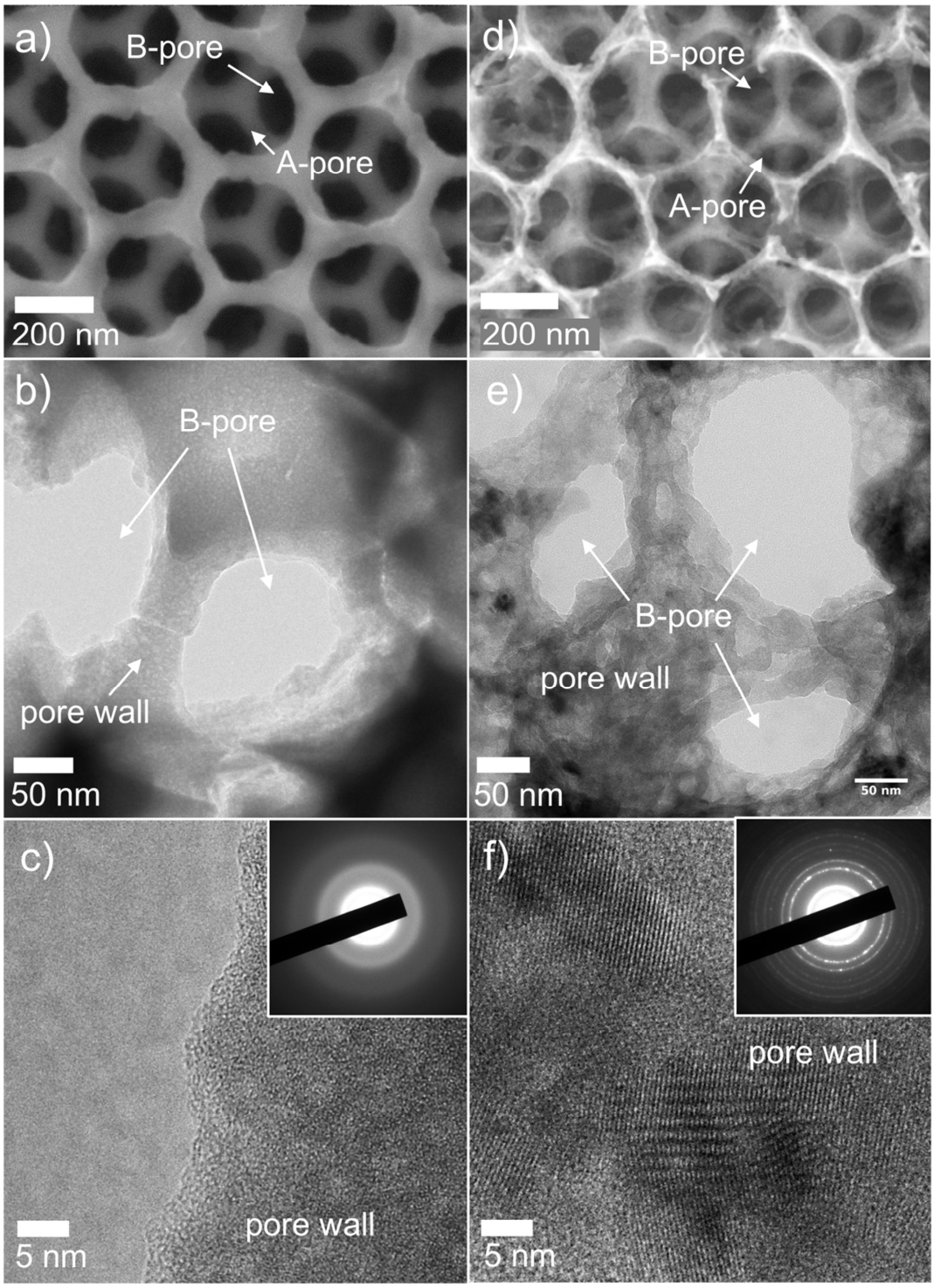

Figure 3.22. SEM and TEM micrographs of a-c) *a*-$Ge_{1-x}Ge_x$-*INOP* and d-f) α-$Ge_{1-x}Ge_x$-*INOP*; a) and d) SEM (pore types A and B are depicted); b) and e) Low magnification TEM; c) and f) High resolution TEM; insets c) and f): Selected area electron diffraction pattern. The figure and figure caption was adopted from ref. [38]

X-ray photoelectron spectra of as prepared *a*-$Ge_{1-x}Ge_x$-*INOP* films reveal that the latter consist of elemental germanium with rather low oxygen content (Figure

3.23). This is in contrast to electrodeposited germanium morphologies, which comprise significant contributions of germanium oxides.[16]

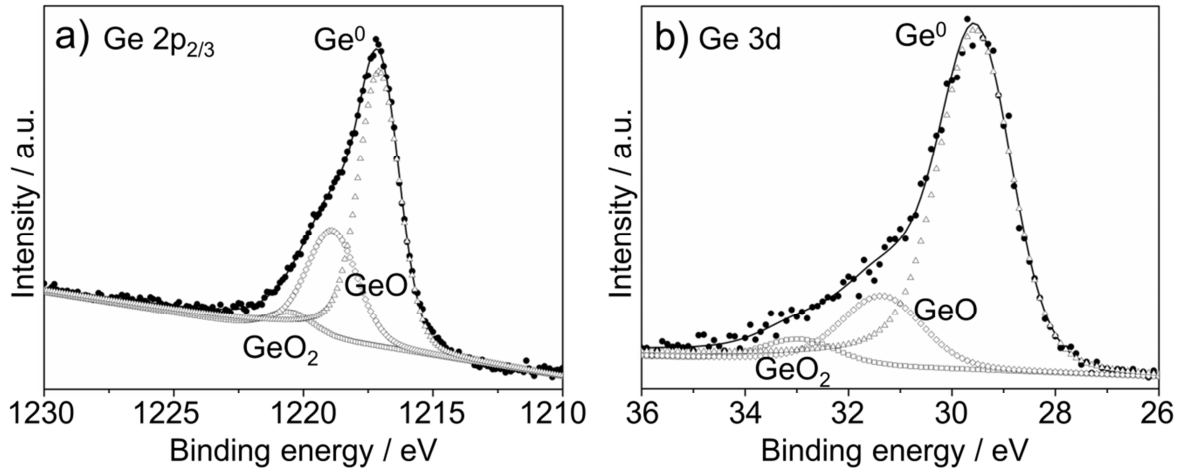

Figure 3.23. XPS spectra of *a*-$Ge_{1-x}Ge_x$-*INOP*. a) Ge $2p_{2/3}$ and b) Ge 3d signal. Data points (circles), fitted curve (solid line); Contributions of Ge (triangles), GeO (rhombs), GeO_2 (squares). The figure and figure caption were modified on the basis of ref. [38]

The germanium inverse opals were further characterized by UV-VIS-spectroscopy. In case of *a*-Ge_{1-x}*Ge*$_x$-*INOP* a band gap of ca. 1.1-1.2 eV was found, which is close to literature reported values for *a*-Ge films.[50] For the annealed and phosphorus containing films a shrinkage of the optical gaps below 1 eV is observed.[51]

3.3.4 P3HT/Germanium based Hybrid Solar Cells

see chapter 5.6

M. M. Bentlohner, S. Geier, M. Giebel, M. Loch, L. Song, P. Lugli, P. Müller-Buschbaum, D. Fattakhova-Rohlfing, T. F. Fässler, **2016**, *manuscript for publication*

As reviewed in chapter 1.4 and 3.3.1.1 porous materials are advantageous for the performance of hybrid solar cells. Therefore, the inverse opal germanium films presented in chapter 3.3.3 were tested in P3HT based hybrid solar cells.[31] Also flat films were tested in the cells. For both solar cells with inverse opal and flat films, FTO/TiO_2 was used as transparent and conductive substrate. Flat germanium films were prepared following the method described in chapter 3.3.3 (Figure 3.24). In the

first step a thin germanium inverse opal film was established on a FTO/TiO_2. Secondly the inverse opal germanium was filled up with germanium by repeated infiltration with K_4Ge_9/*en* and oxidation of the $[Ge_9]^{4-}$ Zintl anions. For introduction of phosphorus into the germanium morphologies besides PCl_3 also the weaker Lewis acid PPh_3 was tested as P-source.[25, 52] A more detailed investigation of the reaction of K_4Ge_9 with PPh_3 was out of the scope of this work and is conducted by Sebastian Geier (*Technical University of Munich*, group of Prof. Dr. T. F. Fässler).

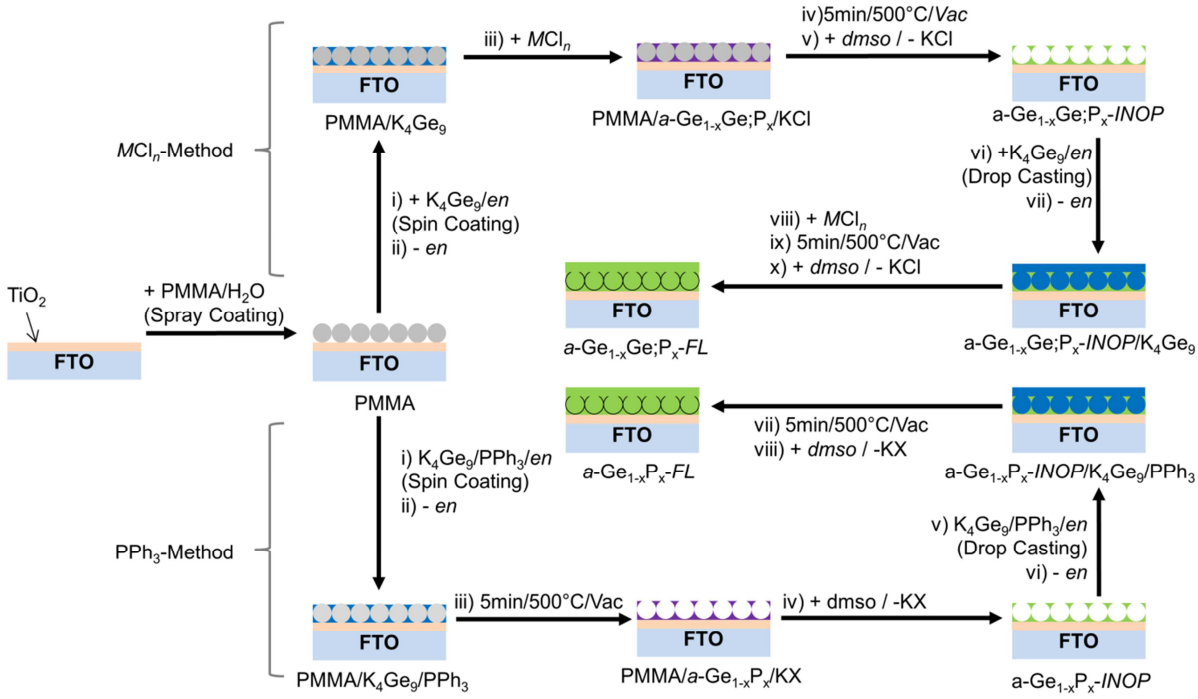

Figure 3.24. Fabrication of flat germanium films (Ge-*FL*). The clusters are oxidized either by *M*Cl_n or PPh_3. A PMMA bead monolayer is deposited on a FTO substrate by spray-coatingspray-coating and the template voids are filled with the germanium precursor solutions by spin-coating. After oxidation of clusters and removal of PMMA the porous germanium monolayer is filled with the germanium-precursor by drop-casting. The clusters are analogously oxidized as in the first oxidation step. The porous Ge layer acts as bonding agent and enables the fabrication of thicker germanium layers on FTO substrates, which do not delaminate. The figure and figure caption was modified on the basis of ref. [47]

Au/P3HT/Ge/TiO_2/FTO hybrid solar cells were assembled by spin-coating of Ge-*INOP*/TiO_2/FTO and Ge-*FL*/TiO_2/FTO with a solution of P3HT in chlorobenzene and deposition of gold contacts by physical vapor deposition (Figure 3.25). As can be seen from SEM is it possible to fill the pores of the Ge-*INOP* by spin coating with P3HT/chlorobenzene. However, SEM also showed that only a fraction of the available pores is filled with P3HT. Moreover, in some areas P3HT only covers the walls of the porous framework. The Au/P3HT/Ge/TiO_2/FTO hybrid solar cells were

tested in regard to their efficiency in a solar simulator. The J-U curves show that in the course of this work it was possible to assemble working hybrid solar cells both with Ge-*INOP* and Ge-*FL* films (Figure 3.25). In order to enhance the efficiency of future Au/P3HT/Ge/TiO_2/FTO hybrid solar cells both the homogeneity of the Ge-*INOP* films as well as the filling of the pores with P3HT has to be improved.

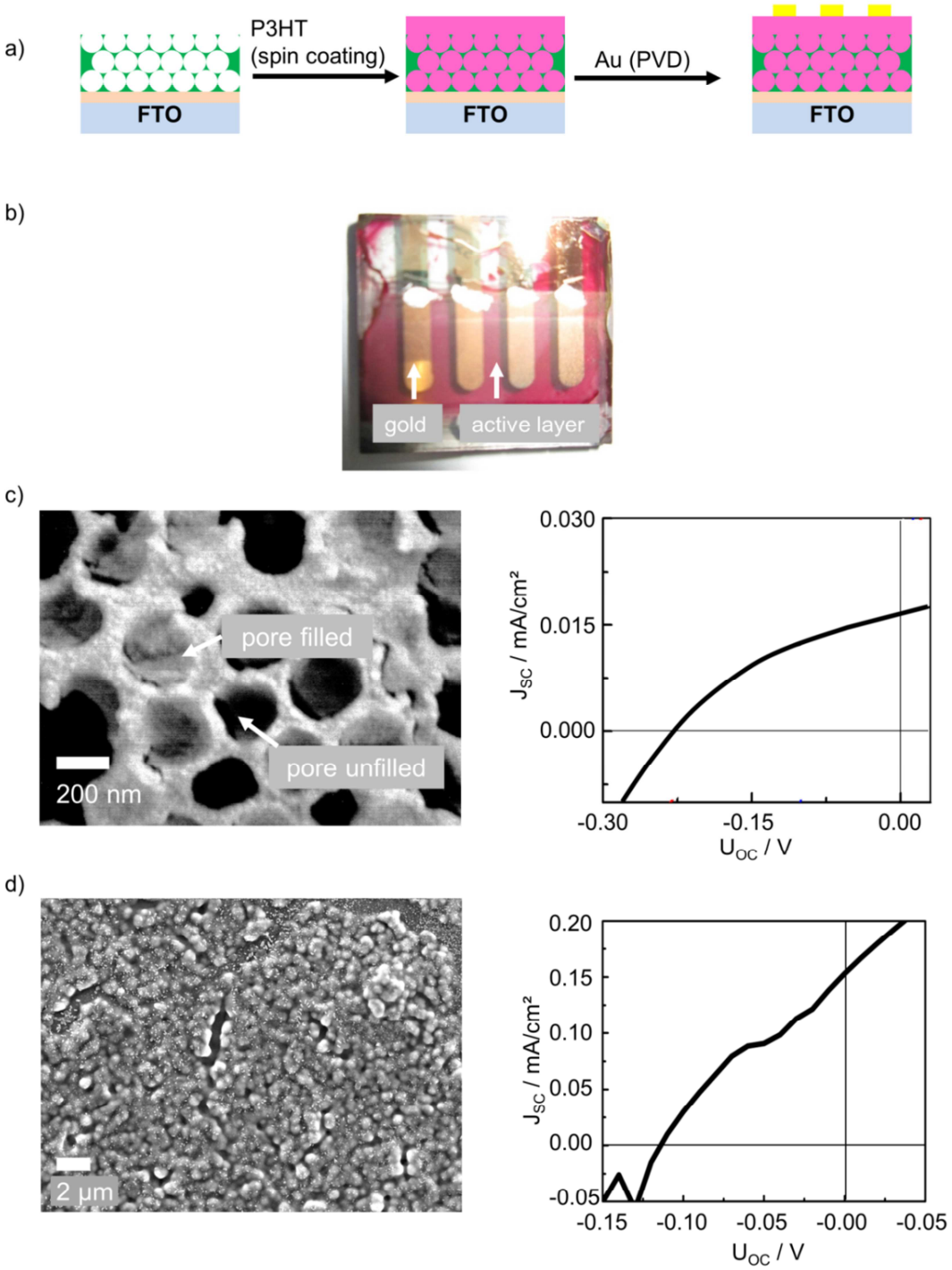

Figure 3.25. a) Assembly and b) photography of Au/P3HT/Ge-*INOP*/TiO_2/FTO hybrid solar cells. c-d) SEM micrographs (left) and J-U-curves (right) of c) Au/P3HT/Ge-*INOP*/TiO_2/FTO and d) Au/P3HT/Ge-*FL*/TiO_2/FTO solar cells assembled in the course of this work. The figures and figure captions were modified on the basis of ref. [47]

3.3.5 Literature

[1] S. Park, *Bull. Korean Chem. Soc.* **2001**, *22*, 15.
[2] M. G. Kanatzidis Adv. Mater. **2007**, *19*, 1165.
[3] R. Pillarisetty, *Nature* **2011**, *479*, 324.
[4] D. D. Vaughn Ii, R. E. Schaak, *Chem. Soc. Rev.* **2013**, *42*, 2861.
[5] K. Ramasamy, P. G. Kotula, A. F. Fidler, M. T. Brumbach, J. M. Pietryga, S. A. Ivanov, *Chem. Mater.* **2015**, *27*, 4640.
[6] A. Stein, *Nature* **2006**, *441*, 1055.
[7] A. Dowd, R. G. Elliman, B. Luther-Davies, *Appl. Phys. Lett.* **2001**, *79*, 2327.
[8] X. D. Pi, U. Kortshagen, *Nanotechnology* **2009**, *20*.
[9] J. A. Kelly, E. J. Henderson, J. G. C. Veinot, *Chem. Commun.* **2010**, *46*, 8704.
[10] M. Amato, M. Palummo, R. Rurali, S. Ossicini, *Chem. Rev.* **2014**, *114*, 1371.
[11] H. C. Choi, J. M. Buriak, *Chem. Commun.* **2000**, 1669.
[12] D. Fattakhova-Rohlfing, A. Zaleska, T. Bein, *Chem. Rev.* **2014**, *114*, 9487.
[13] H. Miguez, E. Chomski, F. Garcia-Santamaria, M. Ibisate, S. John, C. Lopez, F. Meseguer, J. P. Mondia, G. A. Ozin, O. Toader, H. M. van Driel, *Adv. Mater.* **2001**, *13*, 1634.
[14] M. Seino, E. J. Henderson, D. P. Puzzo, N. Kadota, G. A. Ozin, *J. Mater. Chem.* **2011**, *21*, 15895.
[15] L. K. van Vugt, A. F. van Driel, R. W. Tjerkstra, L. Bechger, W. L. Vos, D. Vanmaekelbergh, J. J. Kelly, *Chem. Commun.* **2002**, 2054.
[16] X. Meng, R. Al-Salman, J. Zhao, N. Borissenko, Y. Li, F. Endres, *Angw. Chem. Int. Ed.* **2009**, *48*, 2703.
[17] W. Xin, J. Zhao, D. Ge, Y. Ding, Y. Li, F. Endres, *Phys. Chem. Chem. Phys.* **2013**, *15*, 2421.
[18] H. Miguez, F. Meseguer, C. Lopez, M. Holgado, G. Andreasen, A. Mifsud, V. Fornes, *Langmuir* **2000**, *16*, 4405.
[19] B. Weintraub, Z. Zhou, Y. Li, Y. Deng, *Nanoscale* **2010**, *2*, 1573.
[20] G. S. Armatas, M. G. Kanatzidis, *Science* **2006**, *313*, 817.
[21] S. Dong, A. E. Riley, A. J. Cadby, E. K. Richman, S. D. Korlann, S. H. Tolbert, *Nature* **2006**, *441*, 1126.
[22] N. Chandrasekharan, S. C. Sevov, *J. Electrochem. Soc.* **2010**, *157*, C140.
[23] G. S. Armatas, M. G. Kanatzidis, *Adv. Mater.* **2008**, *20*, 546.
[24] G. S. Armatas, M. G. Kanatzidis, *J. Am. Chem. Soc.* **2008**, *130*, 11430.
[25] G. S. Armatas, M. G. Kanatzidis, *Nano Lett.* **2010**, *10*, 3330.
[26] S. Günes, N. S. Sariciftci, *Inorg. Chim. Acta* **2008**, *361*, 581.
[27] M. D. McGehee, *MRS Bull.* **2009**, *34*, 95.
[28] S. Guldin, S. Hüttner, M. Kolle, M. E. Welland, P. Müller-Buschbaum, R. H. Friend, U. Steiner, N. Tétreault, *Nano Lett.* **2010**, *10*, 2303.
[29] P.-L. Ong, I. Levitsky, *Energies* **2010**, *3*, 313.
[30] C. Y. Kuo, C. Gau, Appl. Phys. Lett. **2009**, *95*, 053302.
[31] A. Du Pasquier, D. D. T. Mastrogiovanni, L. A. Klein, T. Wang, E. Garfunkel, *Appl. Phys. Lett.* **2007**, *91*, 183501.

[32] C. J. Novotny, E. T. Yu, P. K. L. Yu, *Nano. Lett.* **2008**, *8*, 775.
[33] H. Bi, R. R. LaPierre, Nanotechnology **2009**, *20*, 465205.
[34] M. Christophersen, S. Langa, J. Carstensen, I. M. Tiginyanu, H. A. Foll, Phys. Status Solid. A **2003**, *197*, 197.
[35] L. T. Canham, London, UK, 1997.
[36] N. Tokranova, I. A. Levitsky, B. Xu, J. Castracane, W. B. Euler, In Proceedings of the SPIE: Organic Photonic Materials and Devices VII, San Jose, CA. USA, January **2005**, 183.
[37] M. M. Bentlohner, C. Fischer, T. F. Fässler, *Chem. Commun.* **2016**, *52*, 9841.
[38] M. M. Bentlohner, M. Waibel, P. Zeller, K. Sarkar, P. Müller-Buschbaum, D. Fattakhova-Rohlfing, T. F. Fässler, *Angew. Chem. Int. Ed.* **2016**, *55*, 2441.
[39] M. M. Bentlohner, S. Frischhut, T. F. Fässler, *manuscript for publication,* **2016**.
[40] H. G. Von Schnering, M. Baitinger, U. Bolle, W. Carrillo-Cabrera, J. Curda, Y. Grin, F. Heinemann, J. Llanos, K. Peters, A. Schmeding, M. Somer, *Z. Anorg. Allg. Chem.* **1997**, *623*, 1037.
[41] S. Schlecht, M. Yosef, M. Froba, *Z. Anorg. Allg. Chem.* **2004**, *630*, 864.
[42] J. Fortner, R. Q. Yu, J. S. Lannin, *J. Vac. Sci. Technol. A* **1990**, *8*, 3493.
[43] B.-Y. Tay, C. Wang, L. P. Stubbs, C. Jacob, M. van Meurs, *J. Organomet. Chem.* **2011**, *696*, 3431.
[44] A. M. Guloy, R. Ramlau, Z. Tang, W. Schnelle, M. Baitinger, Y. Grin, *Nature* **2006**, *443*, 320.
[45] H. H. Burke, I. P. Herman, *Phys. Rev. B* **1993**, *48*, 15016.
[46] N. Fukata, K. Sato, M. Mitome, Y. Bando, T. Sekiguchi, M. Kirkham, J.-i. Hong, Z. L. Wang, R. L. Snyder, *ACS Nano* **2010**, *4*, 3807.
[47] M. M. Bentlohner, S. Geier, M. A. Giebel, M. Loch, L. Song, P. Lugli, P. Müller-Buschbaum, D. Fattakhova-Rohlfing, T. F. Fässler, *manuscript for publication* **2016**.
[48] P. Müller-Buschbaum, *Anal. Bioanal. Chem.* **2003**, *376*, 3.
[49] G. Renaud, R. Lazzari, F. Leroy, *Surf. Sci. Rep.* **2009**, *64*, 255.
[50] A. Y. Mkrtchyan, *Int. J. Mod. Phys.: Conference Series* **2012**, *15*, 219.
[51] R. W. Lechner, *Dissertation,*Technical University of Munich, Garching **2009**.
[52] C. Belin, H. Mercier, V. Angilella, *New J. Chem.* **1991**, *15*, 931.

4 Conclusion

4.1 On the $[Ge_9]^{4-}$ Zintl Anion as Versatile Precursor for the Fabrication of Novel Molecular Cluster Compounds and Porous Ge Materials

The need for enhanced renwable energy conversion and storage concepts drives chemists and material scientists to search for new chemical procedures for the bottom up assembly of functional materials. As reviewed in the introduction of this work, germanium materials are advantageous for applications in photovoltaics.[1-5] The existence of discrete and soluble $[Ge_9]^{4-}$ atom clusters enables the assembly of novel materials, starting from the clusters with only few atoms up to extended solid state compounds.[6-9] In the present work the reactivity of deltahedral $[Ge_9]^{4-}$ Zintl anions has been thoroughly investigated with the aim to apply the latter as molecular and soluble precursor for both novel molecular cluster compounds and periodic porous materials with tunable composition.

The close relation of the deltahedral Ge_9 cages with the fullerenes was further emphasized with the synthesis of the first {Ge_9-Linker-Ge_9} Zintl triads $[Ge_9–CH=CH–CH=CH–Ge_9]^{6-}$ and $[R–Ge_9–CH=CH–CH=CH–Ge_9–R]^{4-}$, by the reaction of 1,4-bis(trimethylsilyl)butadiyne with $[Ge_9]^{4-}$ and *en*.[10, 11] Analogous fullerene triad systems have been known for longer times and emerged as valuable electroactive materials, with delocalized HOMOs.[12-14] As follows from theoretical calculations the newly described Zintl triads are conjugated, highlighting the potential of such compounds in terms of organic photovoltaics as electron transfer material.[10] Detailed *in situ* investigations on the reaction of 1,4-bis(trimethylsilyl)butadiyne with $[Ge_9]^{4-}$ and *en* led to a deeper understanding of the formation of the Zintl triads. In the course of these examinations it was possible to find a method to rationally establish 7-amino-5-aza-hepta-2,4-dien-2-yl side chains at Ge_9 clusters, which are potential tethers for grafting of the organo-Zintl cluster to surfaces.[10, 11] As has been shown by the *Sevov* group, is it possible to use terminal amino-groups of alkenylated Ge_9 clusters for further transformations, such as reaction with aldehydes.[15] A future field of investigations therefore might be the targeted grafting of Zintl triads such as $[R–Ge_9–CH=CH–CH=CH–Ge_9–R]^{4-}$ to other semiconducting materials in order to establish harmonized donor-acceptor-interfaces suitable for efficient exciton dissociation in photovoltaic cells.[3, 16, 17]

The *in situ* investigations not only shed light on the formation of organic cluster linkages but also on fundamentals in the reaction of alkynes with $[Ge_9]^{4-}$ Zintl anions in *en*.[18] For the first time the deprotonation of *en* in that type of reactions was evidenced and it turned out that both $[Ge_9]^{4-}$ and *en* behave very similar in the reaction with 1,4-bis(trimethylsilyl)butadiyne. Moreover, a new qualitative method for the determination of water in *en* was derived [11, 19] and successfully applied in the course of this work in regard to the investigation of the oxidative behavior of *en* towards $[Ge_9]^{4-}$.[19, 20]

The use of Ge_9 clusters as building blocks in electroactive triad systems highlights their potential for the assembly of functional molecular structures at the border between organic and inorganic materials. By cation exchange it is feasible to bring Zintl triads also into less polar solvents [21], which is the basis for the development of a multifaceted downstream chemistry, such as a supramolecular Zintl chemistry in analogy to metal organic frameworks (MOFs).[22] Future investigations therefore might also target on the establishment of nanoporous inorganic/organic bulk materials using Ge_9 as inorganic building block and alkynes as organic linkers for the clusters.

In addition to molecular inorganic/organic germanium hybrid materials the extension and linking of $[Ge_9]^{4-}$ clusters by germanium [20] and tin [23] has been demonstrated, respectively. Reactions which allow the addition of homo- and heteroatoms to $[Ge_9]^{4-}$ Zintl anions are a major research field of Zintl chemistry since they hold out the prospect of larger fullerene analogous tetrel clusters up to purely inorganic homo- and heteroatomic networks with polyhedral structures and novel properties.[6, 8, 9, 24-26]

It was demonstrated that reaction of $[Ge_9]^{4-}$ with the commonly used solvent *en* can lead to the formation of larger homoatomic clusters, such as the *closo*-$[Ge_{10}]^{2-}$ Zintl anion. The results highlight that also water-free *en* acts as a mild oxidizer and triggers the growth of the clusters. Successful isolation of the pristine *closo*-$[Ge_{10}]^{2-}$ was realized by chemical masking of the Ge_9 clusters with 1-trimethylsilyl-7-amino-5-aza-hepta-3-en-1-yne. The successful synthesis and isolation of *closo*-$[Ge_{10}]^{2-}$ by the method presented in this work, hold out the prospectof a solution based synthesis and isolation of the still missing "*closo*-$[Sn_{10}]^{2-}$" Zintl anion. [20]

In addition to the pristine *closo*-$[Ge_{10}]^{2-}$ a method for linking of clusters via a tin atom was provided, with the synthesis of $[(\eta^4\text{-}Ge_9)Sn(\eta^3\text{-}Ge_9)]^{6-}$ by the reaction of

$[Ge_9]^{4-}$ with $SnPh_2Cl_2$ and K in *en*.[23, 27]. A detailed analysis of the bonding situation in $[(\eta^4\text{-}Ge_9)Sn(\eta^3\text{-}Ge_9)]^{6-}$ and the comparison with other metal bridged clusters, such as $[(\eta^3\text{-}Ge_9)In(\eta^3\text{-}Ge_9)]^{5-}$ [28], led to a generalized description of η^4 and η^3 bonding of Ge_9 cluster to metal atoms. The results herein clearly contribute to the definition of a rational method for the enlargement of tetrel clusters and the assembly of inorganic Ge/*E* networks comprising deltahedral Ge_9 entities.[23]

Not only utilization of $[Ge_9]^{4-}$ Zintl anions in the synthesis of novel molecular cluster compounds with polyhedral structures was investigated, but also ways to solidify the clusters to elemental germanium with tunable composition and morphology. Again the solvent *en* turned out to be a versatile reactant towards $[Ge_9]^{4-}$ clusters, and it was shown that in presence of water traces *en* is able to fully oxidize the clusters to *a*-Ge. For the first time this was proven by the detection of ethylene(di)amide as side product in the reaction of water-containing *en* with $[Ge_9]^{4-}$.[25, 29] In view of the formation of *closo*-$[Ge_{10}]^{2-}$ in water-free Rb_4Ge_9/*en* solution, it manifests that the solvent in general has a mild oxidative potential towards clusters [30], which however decisively depends on the water content.

In analogy to the synthesis of molecular heteroatomic Ge/Sn clusters, possibilities for the oxidation of $[Ge_9]^{4-}$ to elemental germanium containing other tetrel elements such as silicon [31] and also phosphorus as a dopant [32] were shown. The synthesis of $Ge_{1-x}M_x$ phases was achieved by oxidation of the Lewis basic $[Ge_9]^{4-}$ cluster with the strong Lewis acids MCl_n (*M* = Si, Ge, n = 4; *M* = P, n = 3). From the *ex situ* investigations on the controlled oxidation of the clusters and the recovery of intact clusters from K_4Ge_9/*en* solutions, finally a template based and wet-chemical method [33] for the fabrication of germanium inverse opal films with tunable composition and low oxygen content was developed. The inverse opals were fabricated by spray- and spin-techniques over extended areas, being a clear advantage to formerly described methods, which are less flexible [34-38] or deal with the fabrication of powdery products.[7, 8, 25, 29, 39] Correspondingly this work demonstrates the potential of $[Ge_9]^{4-}$ Zintl anions as a soluble Ge source in flexible wet-chemical procedures for porous Ge morphologies. The advantages of $[Ge_9]^{4-}$ for material science and photovoltaics in special were further substantiated by the fabrication of working P3HT based hybrid solar cells [40] with the wet-chemically prepared germanium inverse opals as well as flat films.

In Conclusion this work provides new chemical methods for the synthesis of functional germanium materials and therefore contributes to the development of regenerative energy conversion concepts which are necessary to solve the energy-problems of mankind.

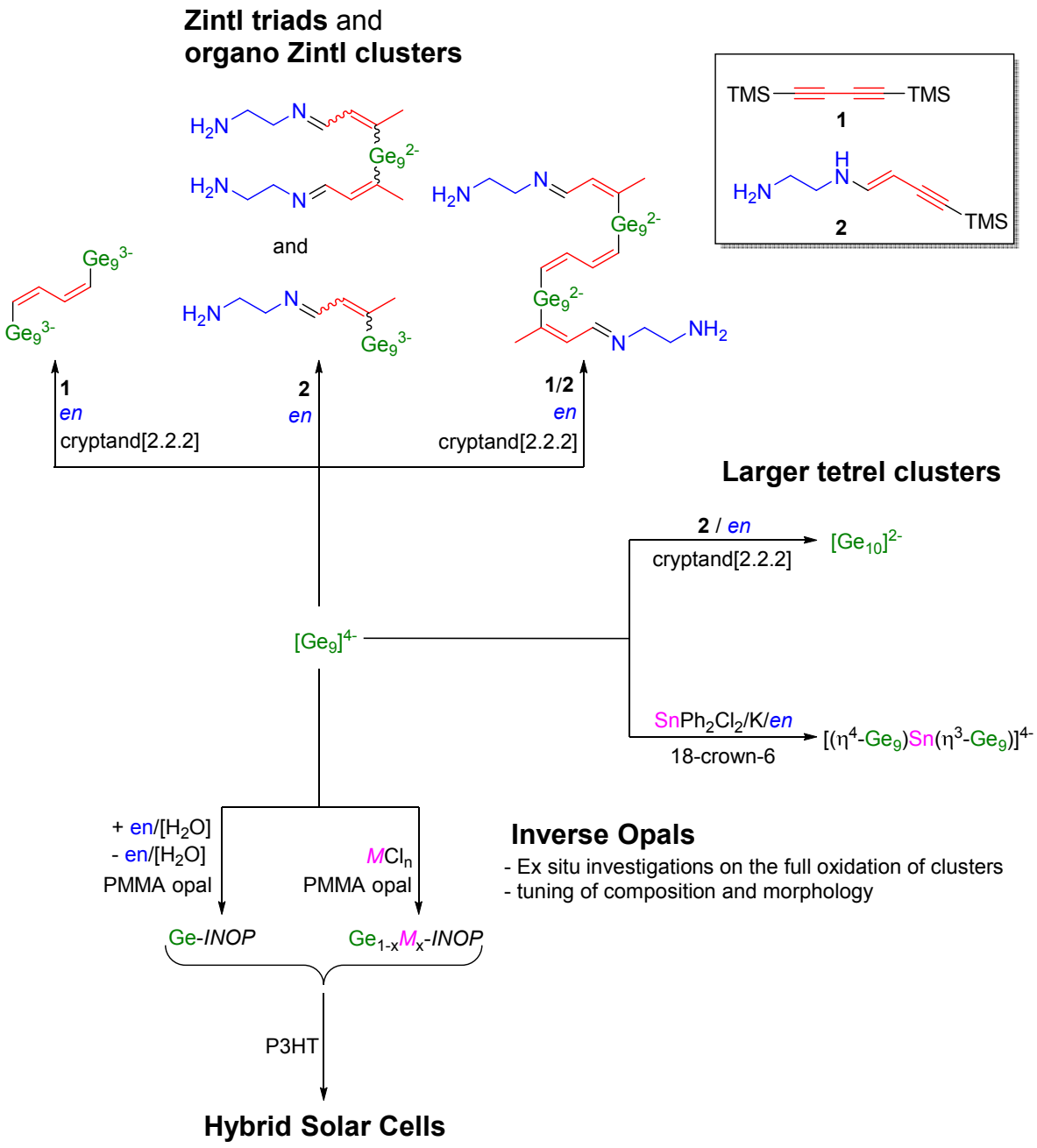

Scheme 3.10. Overview on the reactions carried out in this work for the synthesis of novel molecular cluster compounds and porous Ge materials. [10, 11, 20, 23]

4.2 Literature

[1] A. Stein, *Nature* **2006**, *441*, 1055.
[2] M. G. Kanatzidis, *Adv. Mater.* **2007**, *19*, 1165.
[3] M. D. McGehee, *MRS Bulletin* **2009**, *34*, 95.
[4] P.-L. Ong, I. Levitsky, *Energies* **2010**, *3*, 313.
[5] Frankfurt School – UNEP Collaboration Centre, *Global Trends in Renewable Energy Investment 2016*, **2016**.
[6] S. C. Sevov, J. M. Goicoechea, *Organometallics* **2006**, *25*, 5678.
[7] S. Dong, A. E. Riley, A. J. Cadby, E. K. Richman, S. D. Korlann, S. H. Tolbert, *Nature* **2006**, *441*, 1126.
[8] G. S. Armatas, M. G. Kanatzidis, *Science* **2006**, *313*, 817.
[9] S. Scharfe, F. Kraus, S. Stegmaier, A. Schier, T. F. Fässler, *Angew. Chem. Int. Ed.* **2011**, *50*, 3630.
[10] M. M. Bentlohner, W. Klein, Z. H. Fard, L.-A. Jantke, T. F. Fässler, *Angew. Chem. Int. Ed.* **2015**, *54*, 3748.
[11] M. M. Bentlohner, S. Frischhut, T. F. Fässler, *manuscript for publication* **2016**.
[12] N. Martín, L. Sánchez, B. Illescas, I. Pérez, *Chem. Rev.* **1998**, *98*, 2527.
[13] J. L. Segura, N. Martin, *Chem. Soc. Rev.* **2000**, *29*, 13.
[14] M. A. Lebedeva, T. W. Chamberlain, E. S. Davies, B. E. Thomas, M. Schröder, A. N. Khlobystov, *Beilstein J. Org. Chem.* **2014**, *10*, 332.
[15] M. W. Hull, S. C. Sevov, *Chem. Commun.* **2012**, *48*, 7720.
[16] S. Günes, H. Neugebauer, N. S. Sariciftci, *Chem. Rev.* **2007**, *107*, 1324.
[17] S. Günes, N. S. Sariciftci, *Inorg. Chim. Acta* **2008**, *361*, 581.
[18] M. W. Hull, S. C. Sevov, *J. Am. Chem. Soc.* **2009**, *131*, 9026.
[19] M. M. Bentlohner, M. Waibel, P. Zeller, K. Sarkar, P. Müller-Buschbaum, D. Fattakhova-Rohlfing, T. F. Fässler, *Angew. Chem. Int. Ed.* **2016**, *55*, 2441.
[20] M. M. Bentlohner, C. Fischer, T. F. Fässler, *Chem. Commun.* **2016**, *52*, 9841.
[21] M. W. Hull, S. C. Sevov, *Inorg. Chem.* **2007**, *46*, 10953.
[22] L. E. Kreno, K. Leong, O. K. Farha, M. Allendorf, R. P. Van Duyne, J. T. Hupp, *Chem. Rev.* **2012**, *112*, 1105.
[23] M. M. Bentlohner, L.-A. Jantke, T. Henneberger, C. Fischer, K. Mayer, W. Klein, T. F. Fässler, *Chem. Eur. J.* **2016**, *22*, 13946.
[24] T. F. Fässler, S. D. Hoffmann, *Angew. Chem. Int. Ed.* **2004**, *43*, 6242.
[25] G. S. Armatas, M. G. Kanatzidis, *Adv. Mater.* **2008**, *20*, 546.
[26] S. Scharfe, T. F. Fässler, *Phil. Trans. A Math. Phys. Eng. Sci.* **2010**, *368*, 1265.
[27] A. Ugrinov, S. C. Sevov, *Chem. Eur. J.* **2004**, *10*, 3727.
[28] D. F. Hansen, B. Zhou, J. M. Goicoechea, *J Organomet. Chem.* **2012**, *721–722*, 53.
[29] G. S. Armatas, M. G. Kanatzidis, *Nano Lett.* **2010**, *10*, 3330.
[30] A. Ugrinov, S. C. Sevov, *J. Am. Chem. Soc.* **2003**, *125*, 14059.
[31] R. W. Olesinski, G. J. Abbaschian, *Bull. Alloy Phase Diagr* **1984**, *5*, 180.

[32] G. Contreras, L. Tapfer, A. K. Sood, M. Cardona, *Phys. Status Solidi B* **1985**, *131*, 475.
[33] D. Fattakhova-Rohlfing, A. Zaleska, T. Bein, *Chem. Rev.* **2014**, *114*, 9487.
[34] H. Miguez, F. Meseguer, C. Lopez, M. Holgado, G. Andreasen, A. Mifsud, V. Fornes, *Langmuir* **2000**, *16*, 4405.
[35] L. K. van Vugt, A. F. van Driel, R. W. Tjerkstra, L. Bechger, W. L. Vos, D. Vanmaekelbergh, J. J. Kelly, *Chem. Commun.* **2002**, 2054.
[36] M. Seino, E. J. Henderson, D. P. Puzzo, N. Kadota, G. A. Ozin, *J. Mater. Chem.* **2011**, *21*, 15895.
[37] W. Xin, J. Zhao, D. Ge, Y. Ding, Y. Li, F. Endres, *Phys. Chem. Chem. Phsy.* **2013**, *15*, 2421.
[38] X. Meng, R. Al-Salman, J. Zhao, N. Borissenko, Y. Li, F. Endres, *Angew. Chem. Int. Ed.* **2009**, *48*, 2703.
[39] G. S. Armatas, M. G. Kanatzidis, *J. Am. Chem. Soc.* **2008**, *130*, 11430.
[40] A. Du Pasquier, D. D. T. Mastrogiovanni, L. A. Klein, T. Wang, E. Garfunkel, *Appl. Phys. Lett.* **2007**, *91*, 183501.

5 Publications and Manuscripts

5.1 Linking Deltahedral Zintl Clusters with Conjugated Organic Building Blocks: Synthesis and Characterization of the Zintl Triad $[R\text{-}Ge_9\text{-}CH{=}CH\text{-}CH{=}CH\text{-}Ge_9\text{-}R]^{4-}$

M. M. Bentlohner, W. Klein, Z. H. Fard, L.-A. Jantke, T. F. Fässler*

published in:

Angew. Chem. Int. Ed. **2015**, *54*, 3748-3753; *Angew. Chem.* **2015**, 127, 3819-3824.

Content and Contributions

In the scope of the publication “Linking Deltahedral Zintl Clusters with Conjugated Organic Building Blocks: Synthesis and Characterization of the Zintl Triad [R-Ge_9-CH=CH-CH=CH-Ge_9-R]$^{4-}$“, the accessibility of triads with deltahedral Zintl clusters in analogy to fullerene-linker-fullerene triads is shown as another example for the close relationship between fullerenes and Zintl clusters.

The publication was authored in the course of this thesis. Text contributions to the description of the X-ray crystal structure as well as theoretical investigations were given by Dr. Wilhelm Klein and Laura-Alice Jantke, respectively. In the scope of this thesis the compound {[K(2.2.2-crypt)]$_4$[RGe_9–CH=CH–CH=CH–Ge_9R]}(toluene) (R = (2*Z*,4*E*)-7-amino-5-aza-hepta-2,4-dien-2-yl), which comprises the first Zintl triad [RGe_9–CH=CH–CH=CH–Ge_9R]$^{4-}$, was synthesized by the reaction of 1,4-bis(trimethylsilyl)butadiyne with K_4Ge_9 in ethylenediamine, and crystallized after the addition of cryptand[2.2.2] in toluene. Crystals of the compound were reproduced by Dr. Zohreh Fard and single-crystal X-ray data for publication were recorded from the latter. X-ray structure analysis revealed that the Zintl triad [RGe_9–CH=CH–CH=CH–Ge_9R]$^{4-}$ comprises two deltahedral Ge_9 clusters linked by a conjugated (1*Z*,3*Z*)-buta-1,3-dien-1,4-diyl bridge and additionally bearing (2*Z*,4*E*)-7-amino-5-aza-hepta-2,4-dien-2-yl side chains. Solving of the crystal structure was leadingly done in the scope of this thesis and assisted by Dr. Wilhelm Klein. NMR (^{1}H, COSY, HMBC, HSQC) and IR spectroscopic measurements were conducted and confirmed the results of X-ray structure analysis. The NMR and IR spectroscopic measurements as well as data evaluation were conducted in this thesis. Theoretical calculations on the model compound [(H_2C=CH)–Ge_9–CH=CH–CH=CH–Ge_9–(CH=CH_2)]$^{4-}$ show that the reported Zintl triads are conjugated. The calculations and the interpretation of the data, was done by Laura-Alice Jantke. *In situ* NMR investigations show that reaction of ethylenediamine with 1,4-bis(trimethylsilyl)butadiyne in the absence of clusters plays an important role on the formation of the (2*Z*,4*E*)-7-amino-5-aza-hepta-2,4-dien-2-yl side chains of [RGe_9–CH=CH–CH=CH–Ge_9R]$^{4-}$. In the course of this thesis these investigations were conducted and data were interpreted.

Zintl Clusters

DOI: 10.1002/anie.201410199

Linking Deltahedral Zintl Clusters with Conjugated Organic Building Blocks: Synthesis and Characterization of the Zintl Triad [R-Ge_9-CH=CH−CH=CH-Ge_9-R]$^{4-}$**

*Manuel M. Bentlohner, Wilhelm Klein, Zohreh H. Fard, Laura-Alice Jantke, and Thomas F. Fässler**

Dedicated to Professor Hans-Jörg Deiseroth on the occasion of his 70th birthday

Abstract: *The accessibility of triads with deltahedral Zintl clusters in analogy to fullerene–linker–fullerene triads is another example for the close relationship between fullerenes and Zintl clusters. The compound {[K(2.2.2-crypt)]$_4$[RGe_9-CH=CH−CH=CH-Ge_9R]}(toluene)$_2$ (R = (2Z,4E)-7-amino-5-aza-hepta-2,4-dien-2-yl), containing two deltahedral [Ge_9] clusters linked by a conjugated (1Z,3Z)-buta-1,3-dien-1,4-diyl bridge, was synthesized through the reaction of 1,4-bis(trimethylsilyl)butadiyne with K_4Ge_9 in ethylenediamine and crystallized after the addition of 2.2.2-cryptand and toluene. The compound was characterized by single-crystal structure analysis as well asNMR and IR spectroscopy.*

Molecular spintronics and electron spin-based quantum computing have a demand for molecules that can accommodate a variable number of electrons and/or can form stable radicals. Dyads bearing covalently linked electron-donating moieties in close proximity to such molecules offer a valuable approach to novel molecular electronics as well as to artificial photosynthesis. Besides, triads with electroactive spacers are of special interest as the total spin-carrying capacity can be increased, and spins are tunable. Most prominent examples are the fullerenes, and there exists a large variety of C_{60} donor dyads and triads (Figure 1a) with the C_{60} core being covalently linked to an electron-donating unit, and alternatively, two C_{60} molecules might be connected by organic spacers. Such complex molecules are promising candidates for electron-transfer systems, and the electronic interactions between two C_{60} units has been the subject of different studies.[1,2]

As pointed out earlier, C_{60} molecules show a close relationship to homoatomic deltahedral Zintl ions of Group 14 elements $[E_m]^{n-}$ (E = Si, Ge, Sn, Pb; m = 9, 10, 12).[3] Both kinds of basic polyhedral building units feature delocalized electronic systems such as the conjugated π electrons in the former case and an electron-deficient bonding system, according to Wade's rules, which can also be

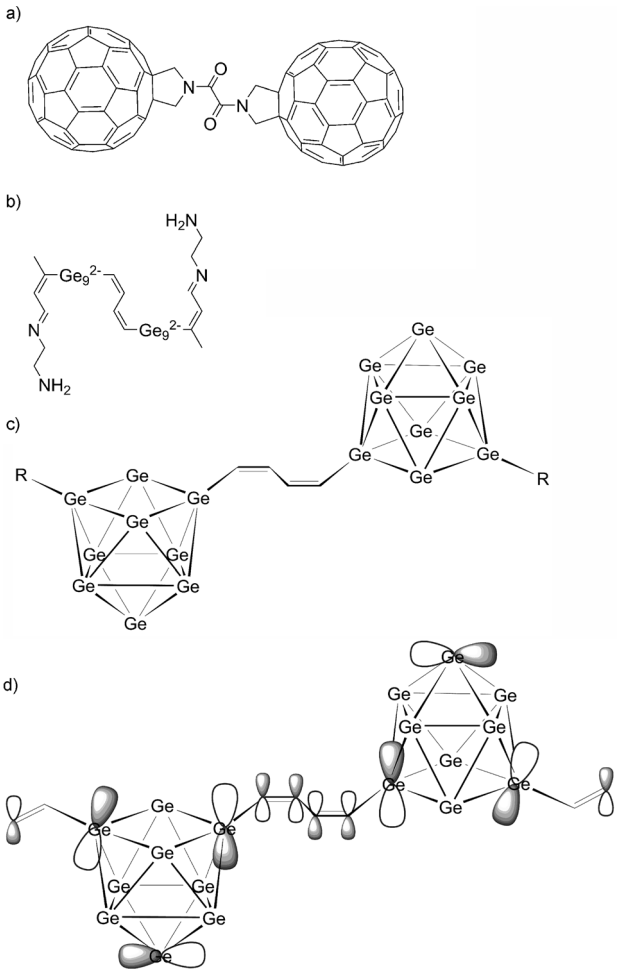

Figure 1. a) A fullerene-linker-fullerene triad. b), c) The organo Zintl triad [R-Ge_9-CH=CH−CH=CH-Ge_9-R]$^{4-}$, R = (2Z,4E)-7-amino-5-aza-hepta-2,4-dien-2-yl comprising a conjugated C_4 linkage between two [Ge_9] Zintl clusters. d) View of the HOMO of **1**. The corresponding wave functions of the HOMO and LUMO as well as that of HOMO−25 reflecting π-type interactions within the C_4 chain are shown in the Supporting Information.

[*] M. M. Bentlohner, Dr. W. Klein, Dr. Z. H. Fard, L.-A. Jantke, Prof. Dr. T. F. Fässler
Department Chemie, Technische Universität München
Lichtenbergstrasse 4, 85747 Garching (Germany)
E-mail: thomas.faessler@lrz.tu-muenchen.de

[**] We would like to thank Dr. Michael Zeilinger for assistance during XRD measurements and to Michael Giebel for fruitful discussions. We thank Prof. Manfred Scheer, University of Regensburg, for cyclic voltammetry measurements. R = (2Z,4E)-7-Amino-5-aza-hepta-2,4-dien-2-yl.

Supporting information for this article is available on the WWW under http://dx.doi.org/10.1002/anie.201410199.

considered as resonance-delocalized σ bonds (spherical aromaticity),[4] in the latter. Furthermore, both polyhedral molecules can adopt different charges (C_{60}^{n-} for $n = 0$–6 and E_9^{n-} for $n = 2$–4). As a further parallel, both clusters form endohedral species with a heteroatom trapped inside the fullerene or Zintl cage, respectively.[5,6b]

Deltahedral Zintl cluster ions $[E_9]^{4-}$ (E = Si, Ge, Sn, Pb) are conveniently accessible as binary alkali metal phases A_4E_9 (A = Na–Cs) obtained from solid-state reactions of the respective elements. Using sequestering agents like cryptands or crown ethers, such phases can be dissolved in a fairly limited selection of organic solvents to investigate the reactivity of these Zintl ions in solution.[6]

The solution chemistry of such homoatomic clusters is well-developed for E = Ge. $[Ge_9\text{-}Ge_9]^{6-}$ dimers,[7] $[Ge_9]_n^{(2n)-}$ ($n = 3$, 4) oligomers[8] and $^1_\infty[Ge_9]^{2-}$ polymers[9] occur with classical (2c/2e) as well as non-classical Ge–Ge *exo* bonds. These examples are manifestations of a rational assembly of molecular structures with valuable electronic and optical properties.[10] Besides directly coupled clusters, a few examples are known in which *exo*-bonded main-group element fragments have been attached.[11–13] $[Ph\text{-}Ge_9\text{-}SbPh_2]^{2-}$ was the first $[E_9]$ Zintl anion containing a covalent 2c/2e cluster–carbon bond.[12] Later, alkylated species $[E_9\text{-}R]^{3-}$ and $[R\text{-}(E_9)_2\text{-}R]^{4-}$ have been obtained by the reaction of $[E_9]^{4-}$ (E = Ge, Sn) with alkyl halides RX.[14,15] Furthermore, $[E_9]^{4-}$ (E = Ge, Sn) was found to readily react with alkynes $R^1\text{-}C{\equiv}C\text{-}R^2$ leading to alkenylated Zintl anions, $[E_9(R^{1/2}CH{=}CR^{1/2})_n]^{(4-n)-}$ ($n = 1$–2; R = H, organic residue; a list of known compounds is given in the Supporting Information).[15–19]

Whereas many of these products are only available in rather low yields, the vinylation of $[Ge_9]^{4-}$ by bis(trimethylsilyl)acetylene in ethylenediamine leads to good quantities of the bis-vinylated clusters $[Ge_9\text{-}(CH{=}CH_2)_2]^{2-}$[17] besides minor amounts of mono- and, in that case, even tris-vinylated species, $[Ge_9\text{-}(CH{=}CH_2)]^{3-}$ and $[Ge_9\text{-}(CH{=}CH_2)_3]^-$, respectively.[15,16] Although it is obvious to link such $[Ge_9\text{-}(CR{=}CHR)_n]^{(4-n)-}$ ($n = 1$–2) species via their olefinic substituents,[20] as successfully applied for fullerenes,[1] such reactions have not been reported to date.

Herein we present the synthesis and the structure of the first deltahedral Zintl cluster anions that are covalently linked by a conjugated C_4 unit. The anion $[RGe_9\text{-}CH{=}CH{-}CH{=}CH\text{-}Ge_9R]^{4-}$ (R = (2*Z*,4*E*)-7-amino-5-aza-hepta-2,4-dien-2-yl) (**1**) is also interesting because it features side chains with an imine functionality, which further enlarge the delocalized π-electron system (Figure 1b).

The anion **1** (Figure 1b) was obtained by adding K_4Ge_9 to a mixture of 1,4-bis(trimethylsilyl)butadiyne (**2**) with ethylenediamine and crystallized in presence of the sequestering agent 2.2.2-cryptand and toluene as $\{[K(2.2.2\text{-crypt})]_4\mathbf{1}\}(toluene)_2$. The new compound was characterized by single-crystal X-ray analysis and NMR and IR spectroscopy.

The crystal structure of $\{[K(2.2.2\text{-crypt})]_4\mathbf{1}\}(toluene)_2$ contains four $[K(2.2.2)\text{-crypt}]^+$ complexes, the title anion **1**, and two disordered toluene molecules. The anion **1** consists of two Ge_9 clusters, which are linked by a zigzag chain of four carbon atoms, and each cluster carries an eight-atom side chain (Figure 1b and Figure 2).

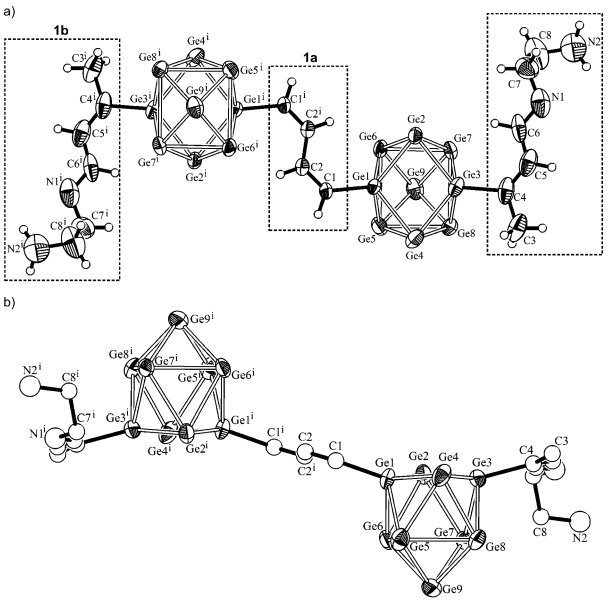

Figure 2. Two views of the molecular structure of the anion **1**, viewed a) perpendicular and b) parallel to the plane of the connecting C_4 unit. a) Cluster bridge (**1a**) and side chains (**1b**) are emphasized with a dashed frame. For reasons of clarity hydrogen atoms are omitted; in (b), C and N atoms are shown as empty spheres. Ellipsoids are set at 50% probability. Symmetry code: (*i*) −*x*, −*y*, 1−*z*.

The molecular anion is located around a crystallographic inversion center, which lies in the middle of the C2–C2^i bond. The Ge1–C1 distance of 1.950(7) Å is indicative of a covalent Ge–C(sp^2) single bond and is in the range of other observed Ge_9–C bonds.[16] Bond lengths of 1.47(2) Å for the central C2–C2^i bond and of 1.33(1) Å for the C1–C2 bond clearly indicate single and double bonds, respectively.[21] Consequently all C atoms of the C_4 chain and the atoms Ge1 and Ge1^i are in plane (Figure 2b, maximum deviation of all atoms of 0.0146 Å from an idealized plane through the atoms Ge1, C1, C2, C2^i, C1^i, and Ge1^i). Both double bonds of the C_4 chain are in *Z* configuration, giving a (1*Z*,3*Z*)-buta-1,3-dien-1,4-diyl (**1a**) cluster linkage.

The Ge_9 unit adopts almost perfect C_{2v} point symmetry and contains two planes including the atoms Ge1 to Ge4 and Ge5 to Ge8, with maximum torsion angles of each set of 4 atoms of 7.5° and 0.01°, respectively. The Ge–Ge bond lengths in the cluster are in the narrow range from 2.519(1) to 2.691(1) Å, except for two distances which are significantly longer (d(Ge5–Ge6) = 2.966(1) Å and d(Ge7–Ge8) = 2.932(1) Å). The shortest bonds are observed in the Ge1/Ge2/Ge3/Ge4 plane, forming a rhombus with one significantly shortened diagonal (3.15 Å compared to 3.95 Å) between the atoms Ge1 and Ge3 that are covalently bonded to C atoms.[22] Consequently, a distinct deviation of the cluster shape from a monocapped square antiprism with C_{4v} symmetry, as expected for a 22 skeletal electron cluster, is shown by the ratio of 1.26 between the diagonal lengths of the uncapped Ge1/Ge2/Ge3/Ge4 plane. The deviation from a tricapped trigonal prism with D_{3h} symmetry is indicated by the ratio of the three heights of the central trigonal prism of 1:1.01:1.18 for Ge6–Ge7, Ge5–Ge8, and Ge2–Ge4, respectively. The

observed shape and distances correspond well to other Ge_9 clusters with 22 skeletal electrons and covalently bonded organic groups.[16–19]

The second organic side chain (atoms C3 to N2, **1b**) form a conjugated electron system with C4–C5 and C6–N1 double bonds.[23] Consequently, the atoms C3 to C7 and Ge3 are in plane with a maximum deviation of 0.074 Å. In summary each cluster is bisubstituted, at Ge1 by the conjugated C_4 linkage and at Ge3 by (2*Z*,4*E*)-7-amino-5-aza-hepta-2,4-dien-2-yl side chains (**1b**).[23]

The structure of **1** is confirmed by the ^{1}H NMR spectrum of {[K(2.2.2-crypt)]$_4$**1**} in [D_3]acetonitrile (Figure 3 and Experimental Section). The signals of the linking unit **1a** are observed as doublets of doublets 1aα$^{(\prime)}$ and 1aβ$^{(\prime)}$, with a major coupling constant of 8.3 Hz typical of *cis*-orientated olefinic hydrogen atoms. For the signals 1aα$^{(\prime)}$ and 1aβ$^{(\prime)}$ a characteristic fine structure is visible, which can be attributed to the magnetically non-equivalent protons 1aα/1aα′ and 1aβ/1aβ′, respectively, analogous to other 1,4-disubstituted *cis*,*cis*-buta-1,3-dienes.[24] The imine functionality of the dangling unit **1b** appears as a strongly down-field shifted signal 1bδ, which corresponds to other reported ^{1}H chemical shift values of imines.[24,25] Furthermore, crystals of {[K(2.2.2-crypt)]$_4$**1**}-(toluene)$_2$ were analyzed by ATR-FTIR spectroscopy. Apart from bands in the spectral range 2729–2949 cm^{-1} indicative of ν(C-H) stretching modes, ν_s(N-H) and ν_{as}(N-H) stretching modes, which are typical of primary amines R-NH_2, are observed at 3347 and 3269 cm^{-1}, respectively. Furthermore, the presence of amine and imine functionalities in **1** is indicated by a strong band at 1609 cm^{-1} and a weaker band at 1582 cm^{-1}.[24,25]

The structure of **1** and its electronic structure were quantum chemically investigated on a PBE0/def2-TZVPP/PCM level of theory by using the bis-vinylated derivative [H_2C=CH-Ge_9-CH=CH–CH=CH-Ge_9-H_2C=CH]$^{4-}$ as a model structure. All Ge–Ge distances are in the range of the experimental values (2.54–2.95 Å). The central C_4 unit (**1a**) reveals two shorter bonds (1.37 Å, cp. exp.1.33 Å) and a longer bond (1.44 Å cp. exp.1.47 Å.), reflecting double and single bonds, respectively. The HOMO–LUMO gap of 3.43 eV confirms the high stability of **1**. The HOMO reflects that the main orbital contributions bear the typical electronic structure for a conjugated π-system extending over the whole molecule (Figure 1 d). Similarly the LUMO shows for all four C atoms of **1a** contribution of the p-orbitals perpendicular to the plane of the C atoms with an additional nodal plane and neglecting contributions of the Ge atoms (see isosurfaces of the wave functions in the Supporting Information).

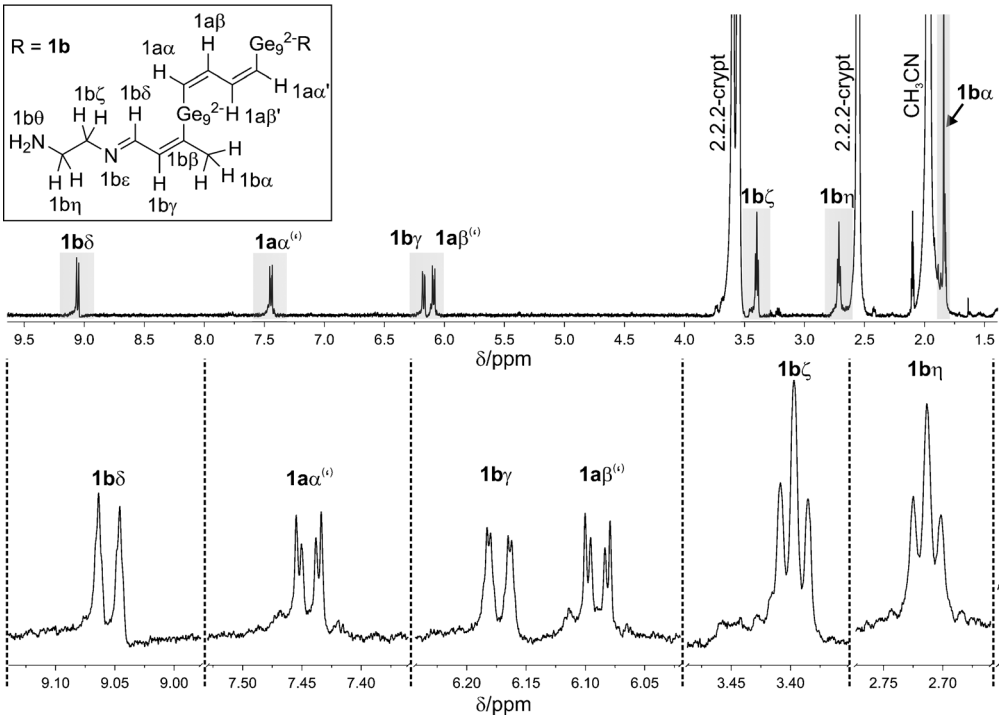

Figure 3. ^{1}H NMR resonances of the anion **1** in [D_3]acetonitrile. Crystals of {[K(2.2.2-crypt)]$_4$**1**}(toluene)$_2$ were recrystallized from [D_5]pyridine in a vacuum and redissolved in [D_3]acetontrile. Thus the ^{1}H NMR spectrum in [D_3]acetontrile does not show signals of toluene, whereas the ^{1}H NMR spectrum of {[K(2.2.2-crypt)]$_4$**1**}-(toluene)$_2$ in [D_5]pyridine displays the signals of toluene (see the Supporting Information). Resonances originating from **1** are highlighted in gray and magnified below. Assignments are given in the Experimental Section.

From the applied synthetic procedure, it would be expected at a first glance that there is a simple connection of two clusters via the bridge **1a**; however, the imine side chain **1b** is also formed, which was unforeseen. Formally the formation of the organic bridge **1a** can be rationalized by an addition of two $[Ge_9]^{4-}$ or $[Ge_9R]^{3-}$ at **2** on its terminal 1,4-positions (Scheme 1). The overall *cis* configuration of **1a** is consistent with observations of Sevov that the alkenylation of $[E_9]^{4-}$ with alkynes selectively proceeds via an *anti*-addition of a cluster unit and a proton to the alkyne triple bond.[18] The role of ethylenediamine as proton source for the hydrogenation of the triple bond has been emphasized before; however, without confirmation of the direct transfer of the proton from ethylenediamine and the formation of the respective anion K[NHR].[18] According to NMR experiments on reaction mixtures involving **2**, ethylenediamine and K_4Ge_9, the formation of the side chain **1b** entails a reaction of the solvent ethylendiamine with **2**.

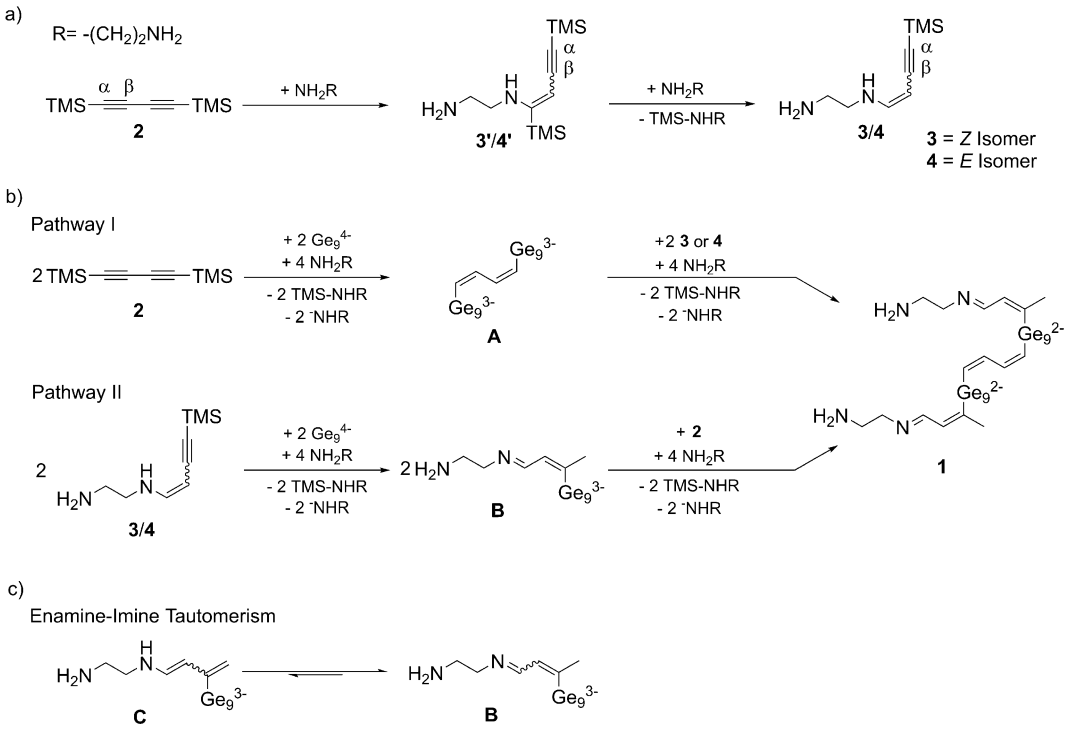

Scheme 1. a) Reaction of 1,4-bis(trimethylsilyl)butadiyne with ethylenediamine leading to (3*Z*)- and (3*E*)-7-amino-5-aza-hepta-3-en-1-yne (**3**/**4**) intermediates, which seem to play a key role in the formation of **1** and its side chain **1b**. b) Possible reaction pathways leading to anion **1**. c) Supposed enamine–imine tautomerizm involved in the formation of side chain **1b**.

The reaction of **2** with ethylenediamine in the absence of clusters forms both (3*Z*)- and (3*E*)-7-amino-5-aza-hepta-3-en-1-yne (**3**/**4**) in an approximate isomer ratio of $Z/E = 30:70$ and $(TMS)NH(CH_2)_2NH_2$ according to NMR spectra. In ethylenediamine, owing to a fast exchange of TMS^+ and H^+, **3′**/**4′** were not observed.[26] Such hydroamination reactions that occur by nucleophilic addition of amines to alkynes or alkenes via their amino functionality are well-known.[28] Given that **2** undergoes fast reaction with ethylenediamine, pre-mixing of **2** and ethylenediamine has a crucial influence on the entire reaction. Owing to their alkyne functionality, the resulting enamines **3** and **4** are also reactants towards the clusters with a preferred cluster addition at the more positively polarized β position.[29]

For the synthesis of **1**, a suspension of **2** in ethylenediamine is mixed with K_4Ge_9, thus **3**/**4** and **2** are both potential reactants for $[Ge_9]^{4-}$. To follow this synthesis by NMR spectroscopy, we added a solution of **3**/**4** to a mixture of K_4Ge_9 and **2**, so that **2** and **3**/**4** were present in a stoichiometric ratio with respect to **1**. The ^1H NMR spectrum (see the Supporting Information) of the mixture does not show signals of **3**/**4**, but resonances assignable to the organic fragments **1a** and **1b** (Figure 3).[30]

In conclusion, we can derive two possible pathways leading to **1** (Scheme 1): Pathway I involves first an addition of $[Ge_9]^{4-}$ at **2** giving intermediate **A**, and a subsequent reaction of **A** with **3** or **4** to the final product **1**. Alternatively, pathway II is in the reverse order and starts with the addition of $[Ge_9]^{4-}$ to **3** or **4**, forming intermediate **B**. The subsequent reaction of **B** with **2** gives rise to **1**. Thereby, further intermediates on the way to **1** are conceivable.[31]

We have shown the synthesis of {[E_9]-linker-[E_9]} triads comprising two deltahedral Zintl clusters and a conjugated organic linker, which are analogous to {fullerene-linker-fullerene} triads. As the (1*Z*,3*Z*)-buta-1,3-dien-1,4-diyl cluster linkage and the (2*Z*,4*E*)-7-amino-5-aza-hepta-2,4-dien-2-yl side chains in the anion **1** are π-delocalized conjugated systems, intramolecular cluster-to-cluster electron transfer processes are conceivable. Thus, a further characterization of **1** concerning its physical and chemical properties is needed, including its redox behavior and optical properties. Preliminary cyclic voltametric measurements in acetonitrile show an irreversible oxidation at approximately 1 V.

An appropriate adjustment of the reaction conditions should also allow for the synthesis of oligomers and polymers with alternating Ge_9 and conjugated (1*Z*,3*Z*)-buta-1,3-dien-1,4-diyl subunits.

Experimental Section

All manipulations were carried out under a purified argon atmosphere using a glove box and standard Schlenk techniques. The Zintl compound of the nominal composition K_4Ge_9 was synthesized by heating a stoichiometric mixture of the elements K and Ge.[6d]

Synthesis of {[K(2.2.2-crypt)]$_4$**1**}(toluene)$_2$: In a glove box, 1,4-bis(trimethylsilyl)butadiyne (Alfa Aesar, 98%, 93.3 mg, 0.48 mmol) was filled into a Schlenk tube and suspended in ethylenediamine (2 mL), whereby within 30 min a pale yellow solution with undissolved bis(trimethylsilyl)butadiyne was obtained. The mixture was

dropped onto solid K_4Ge_9 (97.2 mg, 0.12 mmol) under vigorous stirring. The reaction mixture was further stirred for 3 h at room temperature, resulting in a deep-red solution. After careful layering the filtrate with a solution of 2.2.2-crypt (180.7 mg, 0.48 mmol) in toluene (8 mL), red plates of {[K(2.2.2-crypt)]$_4$**1**}(toluene)$_2$ suitable for single-crystal X-ray diffraction were obtained after two weeks (yield 30%, based on K_4Ge_9) beside reddish-black blocks of {[K(2.2.2-crypt)]$_2$[Ge_9]} (yield ca. 10%).[32] Crystals of {[K(2.2.2-crypt)]$_4$**1**}(toluene)$_2$ were separated from side products by hand and washed with toluene and dried at ambient pressure.

Crystal data: $M_r = 3243.38$, triclinic space group $P\bar{1}$, $a = 11.8949(4)$, $b = 12.8395(4)$, $c = 24.5578(7)$ Å, $\alpha = 104.112(2)$, $\beta = 92.007(2)$, $\gamma = 109.831(2)°$, $V = 3393.1(2)$ Å^3, $Z = 1$, $\rho_{calcd} = 1.59$ g cm^{-3}, $\mu = 4.1$ mm^{-1}; 45570 measured and 11865 independent reflections, $R_{int} = 0.064$; $R_1 = 0.065$ and $wR_2 = 0.186$ for $I > 2\sigma(I)$, $R_1 = 0.099$ and $wR_2 = 0.201$ for all data. Min/max residual electron density: −0.96/2.66 e Å^{-3}. The positions of the hydrogen atoms were calculated and refined using a riding model. All non-hydrogen atoms were treated with anisotropic displacement parameters. Disordered solvent molecules were treated with the SQUEEZE option in PLATON.[33,34] CCDC 1025862 contains the supplementary crystallographic data for this paper. These data can be obtained free of charge from The Cambridge Crystallographic Data Centre via www.ccdc.cam.ac.uk/data_request/cif.

DFT calculations were performed with Gaussian 09 program package[35] using the exchange correlation hybrid functional after Perdew, Burke, and Ernzerhof (PBE0)[36] and a def2-TZVPP basis set for C, H, and Ge.[37] For the compensation of the negative charge, a solvation model (polarizable continuum model, PCM) was estimated.[38] The structure of the compound was optimized under preservation of the C_i point symmetry (keyword symm = loose). Harmonic frequencies were calculated numerically to confirm the nature of the stationary point on the potential-energy surface as a true minimum. As starting input structure, the experimentally determined atom positions were used keeping point group symmetry C_i.

For additional illustrations and a list of known alkenyl functionalities attached to [Ge_9] Zintl-clusters, a detailed experimental section and crystallographic data including selected bond lengths and angles, NMR data and the ATR-FTIR data of {[K(2.2.2-crypt)]$_4$**1**}(toluene)$_2$, and in situ NMR spectroscopy data on reaction solutions involving **2**, ethylenediamine, and K_4Ge_9, see the Supporting Information.

Received: October 20, 2014
Revised: November 20, 2014
Published online: January 29, 2015

Keywords: conjugated π-systems · electronic communication · organically linked clusters · triads · Zintl clusters

[1] a) N. Martín, L. Sánchez, B. Illescas, I. Pérez, *Chem. Rev.* **1998**, *98*, 2527 – 2548; b) J. L. Segura, N. Martin, *Chem. Soc. Rev.* **2000**, *29*, 13 – 25; c) M. A. Lebedeva, T. W. Chamberlain, E. S. Davies, B. E. Thomas, M. Schröder, A. N. Khlobystov, *Beilstein J. Org. Chem.* **2014**, *10*, 332 – 343.

[2] Y. Kanai, J. C. Grossman, *Nano Lett.* **2007**, *7*, 1967 – 1972.

[3] a) T. F. Fässler, *Angew. Chem. Int. Ed.* **2001**, *40*, 4161 – 4165; *Angew. Chem.* **2001**, *113*, 4289 – 4293; b) T. F. Fässler in *Metal Clusters in Chemistry*, Wiley-VCH, Weinheim, **2008**, pp. 1612 – 1642.

[4] a) M. J. S. Dewar, R. Pettit, *J. Chem. Soc. (Resumed)* **1954**, 1625 – 1634; b) K. Exner, P. v. R. Schleyer, *J. Phys. Chem. A* **2001**, *105*, 3407 – 3416; c) R. B. King, T. Heine, C. Corminboeuf, P. v. R. Schleyer, *J. Am. Chem. Soc.* **2004**, *126*, 430 – 431; d) A. Hirsch, Z. Chen, H. Jiao, *Angew. Chem. Int. Ed.* **2000**, *39*, 3915 – 3917; *Angew. Chem.* **2000**, *112*, 4079 – 4081.

[5] S. Scharfe, F. Kraus, S. Stegmaier, A. Schier, T. F. Fässler, *Angew. Chem. Int. Ed.* **2011**, *50*, 3630 – 3670; *Angew. Chem.* **2011**, *123*, 3712 – 3754.

[6] a) J. D. Corbett, *Chem. Rev.* **1985**, *85*, 383 – 397; b) J. D. Corbett in *Structural and Electronic Paradigms in Cluster Chemistry*, *Vol. 87* (Ed.: D. M. P. Mingos), **1997**, pp. 157 – 193; c) T. F. Fässler, R. Hoffmann, *Angew. Chem. Int. Ed.* **1999**, *38*, 543 – 546; *Angew. Chem.* **1999**, *111*, 526 – 529; d) T. F. Fässler, *Coord. Chem. Rev.* **2001**, *215*, 347 – 377; e) S. C. Sevov, J. M. Goicoechea, *Organometallics* **2006**, *25*, 5678 – 5692; f) S. Scharfe, T. F. Fässler, *Philos. Trans. R. Soc. London Ser. A* **2010**, *368*, 1265 – 1284.

[7] a) L. Xu, S. C. Sevov, *J. Am. Chem. Soc.* **1999**, *121*, 9245 – 9246; b) A. Nienhaus, S. D. Hoffmann, T. F. Fässler, *Z. Anorg. Allg. Chem.* **2006**, *632*, 1752 – 1758; c) S. Scharfe, T. F. Fässler, *Z. Anorg. Allg. Chem.* **2011**, *637*, 901 – 906.

[8] a) A. Ugrinov, S. C. Sevov, *J. Am. Chem. Soc.* **2002**, *124*, 10990 – 10991; b) A. Ugrinov, S. C. Sevov, *Inorg. Chem.* **2003**, *42*, 5789 – 5791.

[9] a) C. Downie, Z. J. Tang, A. M. Guloy, *Angew. Chem. Int. Ed.* **2000**, *39*, 337 – 340; *Angew. Chem.* **2000**, *112*, 346 – 348; b) A. Ugrinov, S. C. Sevov, *C. R. Chim.* **2005**, *8*, 1878 – 1882.

[10] A. J. Karttunen, T. F. Fässler, M. Linnolahti, T. A. Pakkanen, *ChemPhysChem* **2010**, *11*, 1944 – 1950.

[11] A. Ugrinov, S. C. Sevov, *J. Am. Chem. Soc.* **2002**, *124*, 2442 – 2443.

[12] A. Ugrinov, S. C. Sevov, *J. Am. Chem. Soc.* **2003**, *125*, 14059 – 14064.

[13] A. Ugrinov, S. C. Sevov, *Chem. Eur. J.* **2004**, *10*, 3727 – 3733.

[14] M. W. Hull, A. Ugrinov, I. Petrov, S. C. Sevov, *Inorg. Chem.* **2007**, *46*, 2704 – 2708.

[15] D. J. Chapman, S. C. Sevov, *Inorg. Chem.* **2008**, *47*, 6009 – 6013.

[16] M. W. Hull, S. C. Sevov, *Inorg. Chem.* **2007**, *46*, 10953 – 10955.

[17] C. B. Benda, J.-Q. Wang, B. Wahl, T. F. Fässler, *Eur. J. Inorg. Chem.* **2011**, 4262 – 4269.

[18] M. W. Hull, S. C. Sevov, *J. Am. Chem. Soc.* **2009**, *131*, 9026 – 9037.

[19] a) M. W. Hull, S. C. Sevov, *Angew. Chem. Int. Ed.* **2007**, *46*, 6695 – 6698; *Angew. Chem.* **2007**, *119*, 6815 – 6818; b) M. M. Gillett-Kunnath, I. Petrov, S. C. Sevov, *Inorg. Chem.* **2009**, *49*, 721 – 729; c) M. M. Gillett-Kunnath, A. G. Oliver, S. C. Sevov, *J. Am. Chem. Soc.* **2011**, *133*, 6560 – 6562; d) M. W. Hull, S. C. Sevov, *Chem. Commun.* **2012**, *48*, 7720 – 7722; e) M. W. Hull, S. C. Sevov, *J. Organomet. Chem.* **2012**, *721*, 85 – 91.

[20] F. A. Carey, R. J. Sundberg, *Advanced Organic Chemistry: Part A: Structure and Mechanisms*, Springer, Heidelberg, **2007**.

[21] E. V. Anslyn, D. A. Dougherty, *Modern Physical Organic Chemistry*, University Science, Sausalito, CA, **2006**.

[22] R. Hauptmann, T. F. Fässler, *Z. Anorg. Allg. Chem.* **2002**, *628*, 1500 – 1504.

[23] Selected bond lengths in Å: Ge1–C1 1.950(7), C1–C2 1.33(1), C2–C2^i 1.47(2), Ge3–C4 1.99(1), C4–C3 1.53(2), C4–C5 1.37(2), C5–C6 1.40(2), C6–N1 1.28(1), N1–C7 1.45(2), C7–C8 1.56(2), C8–N2 1.43(2), Ge1–Ge2 2.519(1), Ge2–Ge3 2.520(1), Ge3–Ge4 2.544 (2), Ge4–Ge1 2.537(1), Ge1–Ge5 2.563(1), Ge1–Ge6 2.595(1), Ge2–Ge6 2.668(1), Ge2–Ge7 2.678(1), Ge3–Ge7 2.584(1), Ge3–Ge8 2.593(1), Ge4–Ge8 2.633(1), Ge4–Ge5 2.652(2), Ge5–Ge6 2.966(1), Ge6–Ge7 2.676(1), Ge7–Ge8 2932(1), Ge8–Ge5 2.691(1), Ge5–Ge9 2.590(1), Ge6–Ge9 2.589(1), Ge7–Ge9 2.580(1), Ge8–Ge9 2.595 (2).

[24] M. Hesse, H. Meier, B. Zeeh, *Spektroskopische Methoden in der organischen Chemie*, Thieme, Stuttgart, **2005**.

[25] R. Escudero, M. Gomez-Gallego, S. Romano, I. Fernandez, A. Gutierrez-Alonso, M. A. Sierra, S. Lopez-Rayo, P. Nadal, J. J. Lucena, *Org. Biomol. Chem.* **2012**, *10*, 2272 – 2281.

[26] The TMS cleavage for the formation of **3**/**4** occurs most probably through intermediates **3′**/**4′**, still bearing TMS groups, in analogy to the reaction of bis(trimethylsilyl)acetylene with [Ge_9]$^{4-}$ in

ethylenediamine. It was found that TMS-substituted alkenes are able to quickly undergo a TMS^+/H^+ exchange reaction with ethylenediamine under formation of $(TMS)NH(CH_2)_2NH_2$. The ^1H NMR spectrum of the solution containing **3/4** shows an intense singlet around 0.1 ppm, which can be attributed to the TMS groups of both **2** and/or $(TMS)NH(CH_2)_2NH_2$. According to ^{13}C NMR spectra, **2** is not present in the solution (for NMR data, see the Supporting Information).[18,27]

[27] N. Kakusawa, K. Yamaguchi, J. Kurita, *J. Organomet. Chem.* **2005**, *690*, 2956 – 2966.

[28] T. E. Müller, K. C. Hultzsch, M. Yus, F. Foubelo, M. Tada, *Chem. Rev.* **2008**, *108*, 3795 – 3892.

[29] In the ^{13}C NMR spectrum, stronger downfield shifts of the β-C atoms of **3/4** when compared to those of the α-C atoms indicate that the β-C atoms are more positively polarized and therefore easier accessible for nucleophiles.

[30] It is not yet fully established whether the resonances of the fragments **1a** and **1b** found in this reaction mixture belong to the same molecule or arise from independent species. Furthermore it is possible that the signals assigned to fragment **1b** arise from a cluster bearing two side chain **1b**. Investigations concerning these questions are still ongoing.

[31] The addition of $[Ge_9]^{4-}$ to **3/4** should involve also enamine intermediate **C**, which might tautomerize to the corresponding imine (Scheme 1). Furthermore it is unclear at this point whether there is a preference of clusters to react either with **3** or **4.** Currently we also investigating which parameters determine the configuration of the double bonds in the side chain **1b**.

[32] J. Åkerstedt, S. Ponou, L. Kloo, S. Lidin, *Eur. J. Inorg. Chem.* **2011**, 3999 – 4005.

[33] P. van der Sluis, A. L. Spek, *Acta Crystallogr. Sect. A* **1990**, *46*, 194 – 201.

[34] A. L. Spek, *Acta Crystallogr. Sect. D* **2009**, *65*, 148 – 155.

[35] Gaussian 09, Revision B.01, M. J. Frisch, G. W. Trucks, H. B. Schlegel, G. E. Scuseria, M. A. Robb, J. R. Cheeseman, G. Scalmani, V. Barone, B. Mennucci, G. A. Petersson, H. Nakatsuji, M. Caricato, X. Li, H. P. Hratchian, A. F. Izmaylov, J. Bloino, G. Zheng, J. L. Sonnenberg, M. Hada, M. Ehara, K. Toyota, R. Fukuda, J. Hasegawa, M. Ishida, T. Nakajima, Y. Honda, O. Kitao, H. Nakai, T. Vreven, J. A. Montgomery, Jr., J. E. Peralta, F. Ogliaro, M. Bearpark, J. J. Heyd, E. Brothers, K. N. Kudin, V. N. Staroverov, T. Keith, R. Kobayashi, J. Normand, K. Raghavachari, A. Rendell, J. C. Burant, S. S. Iyengar, J. Tomasi, M. Cossi, N. Rega, J. M. Millam, M. Klene, J. E. Knox, J. B. Cross, V. Bakken, C. Adamo, J. Jaramillo, R. Gomperts, R. E. Stratmann, O. Yazyev, A. J. Austin, R. Cammi, C. Pomelli, J. W. Ochterski, R. L. Martin, K. Morokuma, V. G. Zakrzewski, G. A. Voth, P. Salvador, J. J. Dannenberg, S. Dapprich, A. D. Daniels, O. Farkas, J. B. Foresman, J. V. Ortiz, J. Cioslowski, and D. J. Fox, Gaussian, Inc., Wallingford CT, **2010**.

[36] a) J. P. Perdew, K. Burke, M. Ernzerhof, *Phys. Rev. Lett.* **1996**, *77*, 3865 – 3868; b) C. Adamo, V. Barone, *J. Chem. Phys.* **1999**, *110*, 6158 – 6170.

[37] F. Weigend, M. Häser, H. Patzelt, R. Ahlrichs, *Chem. Phys. Lett.* **1998**, *294*, 143.

[38] V. Barone, M. Cossi, *J. Phys. Chem. A* **1998**, *102*, 1995 – 2001.

Angewandte Chemie
Eine Zeitschrift der Gesellschaft Deutscher Chemiker

Supporting Information

Linking Deltahedral Zintl Clusters with Conjugated Organic Building Blocks: Synthesis and Characterization of the Zintl Triad [R-Ge_9-CH=CH−CH=CH-Ge_9-R]$^{4-}$**

*Manuel M. Bentlohner, Wilhelm Klein, Zohreh H. Fard, Laura-Alice Jantke, and Thomas F. Fässler**

anie_201410199_sm_miscellaneous_information.pdf

Supporting Information

Contents

Figures and Tables

List of known alkenyl functionalities attached to $[Ge_9]^{4-}$ Zintl anions

$[Ge_9(R^{1/2}C{=}CHR^{1/2})_n]^{(4-n)-}$ (n = 1-2) [1]

Abbreviations:

Fc = Ferrocenyl

Ph = Phenyl

Bu = Butyl

Me = Methyl

Im = Imidazol

Py = Pyridine

Et = Ethyl

R^1/R^2 = H/Fc, H/Ph, H/^{t}Bu, H/PhOMe, Ph/Ph, $SiMe_3/SiMe_3$, $SiMe_3$/ImMe, $H/(CH_2)_4$-C≡CH, H/Ph-C≡CH, H/Ph-NH_2, H/Py, $H/(CH_2)_3$-C≡N, $H/CH(OEt)_2$, $H/CHMe_2$, H/CMe_2Cl, H/CH_2-NH_2 [1]

General experimental procedures

All manipulations were carried out under a purified argon atmosphere using a glove box and standard Schlenk techniques. The Zintl compound of the nominal composition K_4Ge_9 was synthesized by heating a stoichiometric mixture of the elements K and Ge (Chempur, 99.999%) at 650 °C for 20 h in a stainless-steel tube.[2] K was purified by liquation. Ethylenediamine (Merck) was refluxed with calcium hydride (Merck) and freshly collected before use. Toluene was dried over molecular sieve (4 Å) in a solvent purificator (MBraun MB-SPS). 2.2.2-Crypt (Merck) was dried in a vacuum for 8 h. 1,4-bis(trimethylsilyl)butadiyne (Alfa Aesar 98%) was used as received. For Single-crystal X-ray analysis, the crystal was fixed on the top of a glas fiber with perfluorinated ether. The single-crystal X-ray diffraction data were recorded at 120 K on a Bruker APEX II diffractometer equipped with a rotating anode (MoK_α radiation) and a CCD-detector. The crystal structure was solved by Direct Methods using the SHELX software.[3] ^{1}H NMR and 2D-NMR spectra were recorded on Bruker a 500 MHz spectrometer (Bruker AV-500, Bruker AV-500C). NMR solvents, pyridine-d_5 (Deutero GmbH >99.5%) and acetonitrile-d_3 (Deutero GmbH 99.8%) were dried over molecular sieve (4 Å) for at least one day and stored in a

glove box. IR spectra were recorded within a glove box on a Bruker Alpha spectrometer, comprising a diamond ATR unit.

Synthesis and Characterization of {[K(2.2.2-crypt)]$_4$1}(toluene)$_2$

Synthesis of {[K(2.2.2-crypt)]$_4$1}(toluene)$_2$. In a glove box 1,4-bis(trimethylsilyl)butadiyne (Alfa Aesar, 98%, 93.3 mg, 0.48 mmol) was filled into a Schlenk tube and suspended in ethylenediamine (2 mL), whereby within 30 min a pale yellow solution with undissolved bis(trimethylsilyl)butadiyne was obtained. The mixture was dropped onto solid K_4Ge_9 (97.2 mg, 0.12 mmol) under vigorous stirring. The reaction mixture was further stirred for 3 h at room temperature, resulting in a deep-red solution. After careful layering the filtrate with a solution of 2.2.2-crypt (180.7 mg, 0.48 mmol) in toluene (8 mL) red plates of {[K(2.2.2-crypt)]$_4$**1**}(toluene)$_2$ suitable for single-crystal X-ray diffraction were obtained after two weeks (yield 30 %, based on K_4Ge_9) beside reddish-black blocks of {[K(2.2.2-crypt)]$_2$[Ge_9]} (yield ca. 10%).[4] Crystals of {[K(2.2.2-crypt)]$_4$**1**}(toluene)$_2$ were separated from side products by hand and washed with toluene and dried at ambient pressure.

**Crystal data of {[K(2.2.2-crypt)]$_4$1}(toluene)$_2$.** For building units of {[K(2.2.2-crypt)]$_4$**1**}(toluene)$_2$ see Figure S1, for bond length and bond angles see Table S1 and S2. M_r = 3243.38, triclinic space group $P\bar{1}$, a = 11.8949(4), b = 12.8395(4), c = 24.5578(7) Å, α = 104.112(2)°, β = 92.007(2)°, γ = 109.831(2)°, V = 3393.1(2) Å^3, Z = 1, $\rho_{calcd.}$ = 1.59 g cm^{-3}, μ = 4.1 mm^{-1}; 45570 measured and 11865 independent reflections, R_{int} = 0.064; R_1 = 0.065 and wR_2 = 0.186 for $I > 2\,\sigma(I)$, R_1 = 0.099 and wR_2 = 0.201 for all data. Min/max residual electron density: -0.96/2.66 e Å^{-3}. The positions of the hydrogen atoms were calculated and refined using a riding model. All non-hydrogen atoms were refined with anisotropic displacement parameters. Disordered solvent molecules were taken care of with the SQUEEZE option in PLATON.[5,6] CCDC-1025862 contains the supplementary crystallographic data for this paper. These data can be obtained free of charge from The Cambridge Crystallographic Data Centre via www.ccdc.cam.ac.uk/data_request/cif. Higher

standard deviations for carbon atoms are due to their lower scattering power compared to the heavier Ge atoms.

Figure S1. Building units of the crystal structure of {[K(2.2.2-crypt)]$_4$**1**}(toluene)$_2$; ellipsoids are shown at the 50% probability level, symmetry code: (i) *–x*, *-y*, 1-*z*.

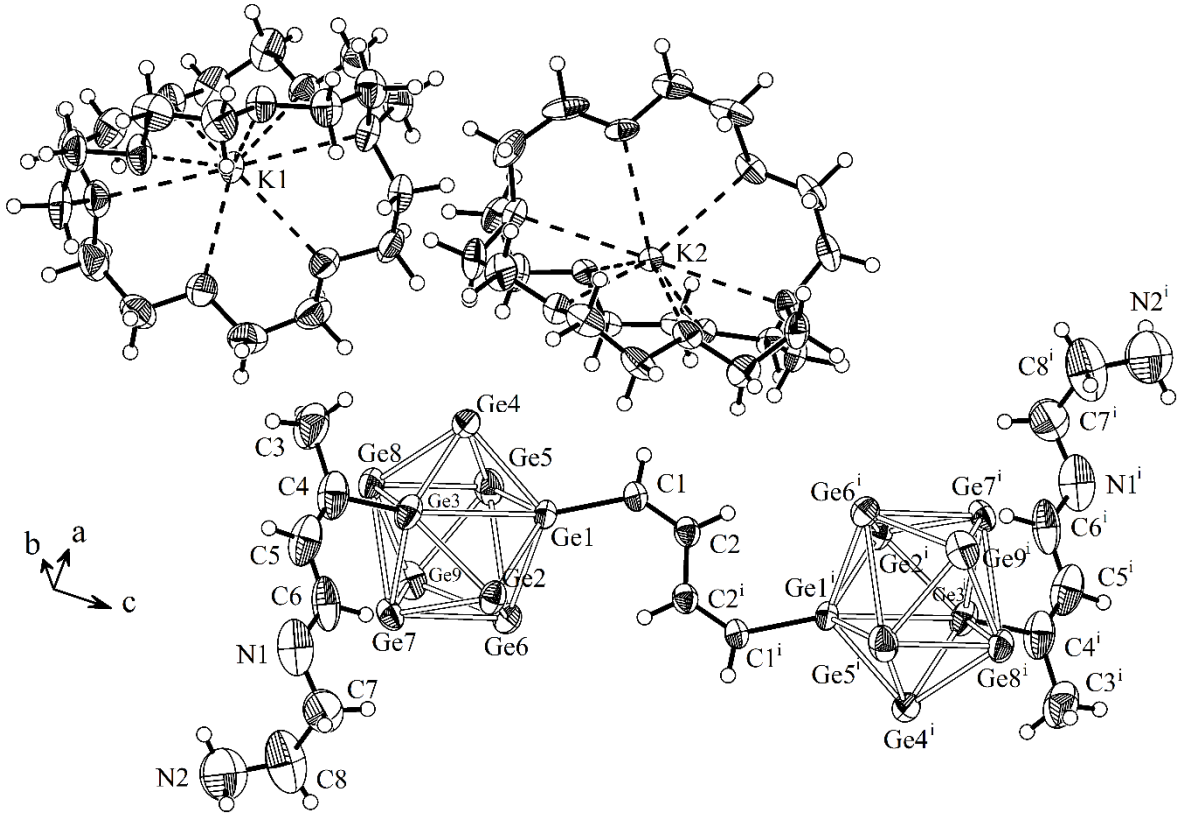

Table S1. Selected bond lengths [Å] of {[K(2.2.2-crypt)]$_4$**1**}(toluene)$_2$.

Atoms	Distances	Atoms	Distances	Atoms	Distances
Ge1 - C1	1.950(7)	C7 - H7B	0.9900	O6 - C25	1.447(10)
C1 - C2	1.327(11)	C8 - N2	1.429(15)	C25 - C26	1.496(14)
C1 - H1	0.95	C8 - H8A	0.9900	C26 - N4	1.450(12)
C2 - C2^{i}	1.470(16)	C8 - H8B	0.9900	K2 - N5	3.026(6)
C2 - H2	0.95	N2 - H2A	0.9800	K2 - N6	3.000(6)
Ge1 - Ge2	2.5189(12)	N2 - H2B	0.9800	K2 - O7	2.907(5)
Ge2 - Ge3	2.5201(12)	K1 - N3	3.010(6)	K2 - O8	2.822(5)
Ge3 - Ge4	2.5444(15)	K1 - N4	2.978(7)	K2 - O9	2.825(5)
Ge4 - Ge1	2.5365(12)	K1 - O1	2.886(6)	K2 - O10	2.845(5)
Ge1 - Ge5	2.5626(13)	K1 - O2	2.830(6)	K2 - O11	2.838(5)
Ge1 - Ge6	2.5954(13)	K1 - O3	2.788(5)	K2 - O12	2.749(5)
Ge2 - Ge6	2.6678(13)	K1 - O4	2.839(6)	N5 - C27	1.445(10)
Ge2 - Ge7	2.6778(12)	K1 - O5	2.832(6)	C27 - C28	1.483(12)
Ge3 - Ge7	2.5841(13)	K1 - O6	2.835(5)	C28 - O7	1.447(9)
Ge3 - Ge8	2.5925(13)	N3 - C9	1.455(11)	O7 - C29	1.402(9)
Ge4 - Ge8	2.6332(13)	C9 - C10	1.529(13)	C29 - C30	1.480(10)
Ge4 - Ge5	2.6518(16)	C10 - O1	1.441(10)	C30 - O8	1.422(8)
Ge5 - Ge6	2.9663(14)	O1 - C11	1.422(10)	O8 - C31	1.411(8)
Ge6 - Ge7	2.6762(12)	C11 - C12	1.482(13)	C31 - C32	1.501(11)
Ge7 - Ge8	2.9318(13)	C12 - O2	1.418(11)	C32 - N6	1.463(10)
Ge8 - Ge5	2.6905(13)	O2 - C13	1.420(10)	N5 - C33	1.471(11)
Ge5 - Ge9	2.5899(14)	C13 - C14	1.534(14)	C33 - C34	1.493(13)
Ge6 - Ge9	2.5890(14)	C14 - N4	1.505(13)	C34 - O9	1.418(10)
Ge7 - Ge9	2.5799(14)	N3 - C15	1.486(11)	O9 - C35	1.407(10)
Ge8 - Ge9	2.5950(15)	C15 - C16	1.483(12)	C35 - C36	1.460(13)
Ge3 - C4	1.992(10)	C16 - O3	1.433(9)	C36 - O10	1.439(9)
C3 - C4	1.529(16)	O3 - C17	1.425(11)	O10 - C37	1.433(10)
C3 - H3A	0.9800	C17 - C18	1.490(13)	C37 - C38	1.484(12)
C3 - H3B	0.9800	C18 - O4	1.443(11)	C38 - N6	1.448(10)
C3 - H3C	0.9800	O4 - C19	1.428(11)	N5 - C39	1.500(11)
C4 - C5	1.367(16)	C19 - C20	1.540(14)	C39 - C40	1.494(12)
C5 - C6	1.396(16)	C20 - N4	1.461(13)	C40 - O11	1.411(10)
C5 - H5	0.9500	N3 - C21	1.453(11)	O11 - C41	1.421(9)
C6 - N1	1.275(14)	C21 - C22	1.483(12)	C41 - C42	1.445(12)
C6 - H6	0.9500	C22 - O5	1.395(10)	C42 - O12	1.425(9)
N1 - C7	1.452(15)	O5 - C23	1.445(10)	O12 - C43	1.408(10)
C7 - C8	1.560(17)	C23 - C24	1.513(13)	C43 - C44	1.507(12)
C7 - H7A	0.9900	C24 - O6	1.416(11)	C44 - N6	1.475(10)

Table S2: Selected bond angles [deg] of {[K(2.2.2-crypt)]$_4$**1**} (toluene)$_2$.

Atoms	Angles	Atoms	Angles
Ge1 - C1 - C2	131.2(6)	Ge4 - Ge5 - Ge6	101.33(4)
C2 - C1 - H1	114.4	Ge2 - Ge6 - Ge5	100.02(4)
Ge1 - C1 - H1	114.4	Ge2 - Ge7 - Ge8	100.64(4)
C1 - C2 - C2	123.8(9)	Ge4 - Ge8 - Ge7	101.51(4)
C1 - C2 - H2	118.1	Ge1 - Ge5 - Ge6	55.42(3)
C2 - C2 - H2	118.1	Ge1 - Ge6 - Ge5	54.38(3)
C1 - Ge1 - Ge2	130.0(3)	Ge3 - Ge7 - Ge8	55.64(3)
C1 - Ge1 - Ge4	119.5(2)	Ge3 - Ge8 - Ge7	55.37(3)
C1 - Ge1 - Ge5	106.3(3)	Ge4 - Ge5 - Ge8	59.06(4)
C1 - Ge1 - Ge6	113.5(3)	Ge2 - Ge6 - Ge7	60.14(3)
Ge4 - Ge1 - Ge2	102.85(4)	Ge2 - Ge7 - Ge6	59.77(3)
Ge1 - Ge2 - Ge3	77.35(4)	Ge4 - Ge8 - Ge5	59.74(4)
Ge2 - Ge3 - Ge4	102.59(4)	Ge1 - Ge5 - Ge9	103.95(4)
Ge3 - Ge4 - Ge1	76.60(4)	Ge1 - Ge6 - Ge9	103.06(4)
Ge8 - Ge5 - Ge6	89.76(4)	Ge3 - Ge7 - Ge9	104.86(4)
Ge5 - Ge6 - Ge7	89.50(4)	Ge3 - Ge8 - Ge9	104.19(4)
Ge6 - Ge7 - Ge8	90.78(4)	Ge4 - Ge5 - Ge9	112.28(5)
Ge7 - Ge8 - Ge5	89.96(4)	Ge2 - Ge6 - Ge9	112.56(4)
Ge2 - Ge1 - Ge5	116.50(4)	Ge2 - Ge7 - Ge9	112.52(4)
Ge4 - Ge1 - Ge6	115.90(4)	Ge4 - Ge8 - Ge9	112.73(4)
Ge2 - Ge3 - Ge8	115.35(4)	Ge6 - Ge5 - Ge9	55.04(4)
Ge4 - Ge3 - Ge7	114.52(5)	Ge5 - Ge6 - Ge9	55.07(4)
Ge1 - Ge2 - Ge7	96.36(4)	Ge8 - Ge7 - Ge9	55.73(4)
Ge3 - Ge2 - Ge6	97.64(4)	Ge7 - Ge8 - Ge9	55.25(3)
Ge1 - Ge4 - Ge8	96.86(4)	Ge8 - Ge5 - Ge9	58.83(4)
Ge3 - Ge4 - Ge5	97.51(4)	Ge7 - Ge6 - Ge9	58.65(3)
Ge2 - Ge1 - Ge6	62.86(4)	Ge6 - Ge7 - Ge9	58.98(4)
Ge4 - Ge1 - Ge5	62.67(4)	Ge5 - Ge8 - Ge9	58.65(4)
Ge2 - Ge3 - Ge7	63.27(4)	Ge5 - Ge9 - Ge6	69.89(4)
Ge4 - Ge3 - Ge8	61.67(4)	Ge6 - Ge9 - Ge7	62.36(4)
Ge1 - Ge2 - Ge6	59.97(3)	Ge7 - Ge9 - Ge8	69.02(4)
Ge3 - Ge2 - Ge7	59.53(3)	Ge8 - Ge9 - Ge5	62.52(4)
Ge1 - Ge4 - Ge5	59.15(4)	Ge5 - Ge9 - Ge7	100.60(5)
Ge3 - Ge4 - Ge8	60.07(4)	Ge6 - Ge9 - Ge8	100.87(4)
Ge5 - Ge1 - Ge6	70.21(4)	C4 - Ge3 - Ge2	130.1(4)
Ge6 - Ge2 - Ge7	60.08(3)	C4 - Ge3 - Ge4	122.1(4)
Ge7 - Ge3 - Ge8	68.99(4)	C4 - Ge3 - Ge7	110.0(3)
Ge8 - Ge4 - Ge5	61.20(4)	C4 - Ge3 - Ge8	105.3(3)
Ge4 - Ge5 - Ge1	58.18(4)	C5 - C4 - C3	122.6(10)
Ge1 - Ge6 - Ge2	57.17(3)	C5 - C4 - Ge3	123.8(9)
Ge2 - Ge7 - Ge3	57.20(3)	C3 - C4 - Ge3	113.5(8)
Ge3 - Ge8 - Ge4	58.27(4)	C4 - C5 - C6	124.8(10)
Ge1 - Ge5 - Ge8	94.81(4)	N1 - C6 - C5	124.5(11)
Ge1 - Ge6 - Ge7	94.59(4)	C6 - N1 - C7	118.5(10)
Ge3 - Ge7 - Ge6	95.87(4)	N1 - C7 - C8	113.6(10)
Ge3 - Ge8 - Ge5	95.39(4)	N2 - C8 - C7	113.3(12)

NMR data of {[K(2.2.2-crypt)]$_4$1}(toluene)$_2$.

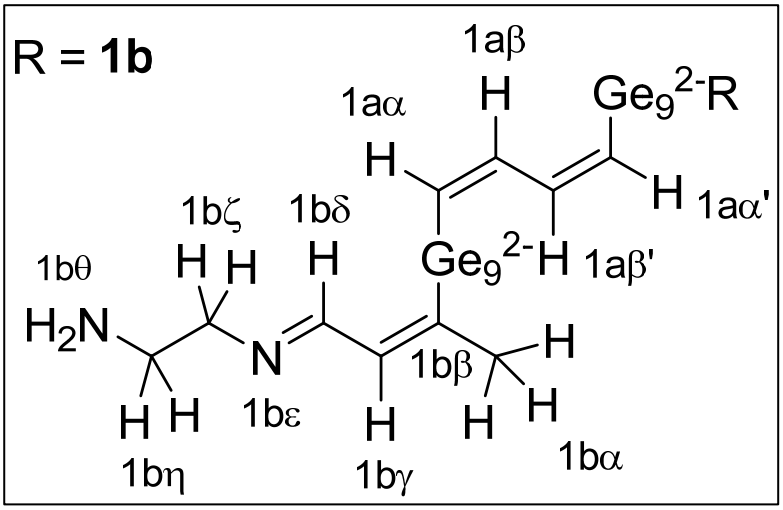

Scheme S1. The Zintl-triad [RGe9–CH═CH–CH═CH–Ge9R]$^{4-}$ (R = (2Z,4E)-7-amino-5-aza-hepta-2,4-dien-2-yl) including the hydrogen atoms labelled depending on their affiliation either with the number of the cluster-bridge (**1a**) or the side chain (**1b**) as well as greek letters, respectively.

For NMR spectra see Figures S2 and S3.

Solvent pyridine-d$_5$

^{1}H NMR (500 MHz, pyridine-d$_5$, 296 K), δ (ppm): 10.14 (d, *J* = 9.0 Hz, 1H, 1bδ), 8.79 (dd, *J* = 8.4 Hz, 2.3 Hz, covered by py, 1aα), 7.23 (covered by py and revealed by COSY, 1aβ), 6.94 (dd, *J* = 9.0 Hz, 1.0 Hz, 1H, 1bγ), 3.82 (t, *J* = 5.8 Hz, 2H, 1bζ), 3.01 (tt, *J* = 7.5 Hz, 5.8 Hz, 2H, 1bη), 2.48 (s, 3H, 1bα), 1.45 (t, *J* = 7.5 Hz, 2H, 1bθ), 7.29 (m, Ar*H*, tol), 7.19 (m, Ar*H*, tol), 2.24 (s, 6H, -CH$_3$, tol), 3.49 (s, crypt), 3.43 (s, crypt), 2.43 (s, crypt); COSY (500 MHz, pyridine-d$_5$, 296 K), δ (ppm): 10.14/6.94 (^{3}*J*, 1bδ/1bγ), 10.15/3.82 (^{4}*J*, 1bδ/1bζ), 8.79/7.22 (^{3}*J*, 1aα/1aβ), 6.93/2.49 (^{4}*J*, 1bγ/1bα), 3.83/3.01 (^{3}*J*, 1bζ/1bη), 3.01/1.45 (^{3}*J*, 1bη/1bθ).

Solvent acetonitrile-d$_3$[*]

* From the solution of {[K(2.2.2-crypt)]$_4$**1**}(toluene)$_2$ in pyridine-d$_5$ the solvent was evaporated in vacuum and the obtained orange residue was redissolved in acetonitrile-d$_3$, thus toluene is not visible in the NMR-spectra in acetonitrile-d$_3$.

^{1}H NMR (500 MHz, acetonitrile-d$_3$, 296 K), δ (ppm): 9.03 (dt, *J* = 8.9 Hz, 1.4 Hz, 1H, 1bδ), 7.41 (dd, *J* = 8.3 Hz, 2.3 Hz, 1H, 1aα), 6.15 (dq, *J* = 8.9 Hz, 1.4 Hz, 1H, 1bγ),

6.06 (dd, *J* = 8.3 Hz, 2.3 Hz, 1H, 1aβ), 3.52 (t, *J* = 5.9 Hz, 1H, 1bζ), 2.53 (t, *J* = 5.9 Hz, 1H, 1bη), 1.81 (s, 3H, 1bα), 3.60 (s, crypt), 3.55 (s, crypt), 2.55 (s, crypt); COSY (500 MHz, acetonitrile-d_3, 296 K), δ (ppm): 9.03/6.15 (^3J, 1bδ/1bγ), 9.03/3.35 (^4J, 1bδ/1bζ), 7.41/6.03 (^3J, 1aα/1aβ), 6.15/1.77 (^4J, 1bγ/1bα), 3.38/2.66 (^3J, 1bζ/1bη).

Description of NMR data

In acetonitrile-d_3 the unit **1a** generates two resonances, namely 1aβ$^{(')}$ at 6.06 ppm and 1aα$^{(')}$ at 7.41 ppm. Both signals 1aα$^{(')}$ and 1aβ$^{(')}$ feature doublet of doublet structures with coupling constants of 8.3 Hz/2.3 Hz. The major coupling constant of 8.3 Hz is typical of *cis*-orientated olefinic protons and proves an overall *cis*-configuration of the protons in the C_4-bridge. Besides, for signals 1aα$^{(')}$ and 1aβ$^{(')}$ a characteristic fine structure is visible, which can be attributed to the magnetically non-equivalent protons 1aα/1aα‘ and 1aβ/1aβ‘, analogous to other 1,4-disubstitueted *cis*,*cis*-buta-1,3-dienes.[7]

For the side chains **1b**, the methyl protons 1bα are observed as a singlet at 1.81 ppm. The olefinic proton 1bγ appears as a doublet of quartets at 6.15 ppm as a result of an 8.9 Hz three bond coupling to the proton 1bδ and a 1.4 Hz four bond coupling to the methyl protons 1bα. At 9.03 ppm the proton 1bδ is detected as a doublet of triplets, due to an 8.9 Hz three bond coupling with the adjacent olefinic proton 1bγ and a 1.4 Hz four bond coupling to the protons 1bζ. The strong deep-field shift of 1bδ is in good agreement with values for imine protons -*H*C=N- as reported in the literature.[7,8] Triplets at 2.53 and 3.52 ppm can be attributed to the adjacent methylene protons 1bζ and 1bη. For so far unknown reasons, the amine protons 1bθ and, and as a consequence, the coupling of the methylene protons 1bη with 1bθ, are not observed in the NMR spectrum taken in acetonitrile-d_3. However, the amine protons 1bθ and the coupling with 1bη was observed when the NMR spectrum was taken in pyridine-d_5. The amine protons 1bθ showed a triplet at 1.45 ppm, with a coupling constant of 7.5 Hz, and the methylene protons 1bη a triplet of triplets at 3.01 ppm, with coupling constants of 7.5 Hz and 5.8 Hz, respectively. The chemical shifts are in good agreement with the values reported for an amine-functionalized Zintl ion {[K(2.2.2-crypt)]$_2$[Ge_9-(CH=CHCH$_2$NH$_2$)$_2$]} in pyridine-d_5.[1e]

Figure S2. a) ^{1}H NMR and b) ^{1}H ^{1}H COSY spectra of {[K(2.2.2-crypt)]$_4$**1**}(toluene)$_2$ in pyridine-d$_5$ recorded at room temperature.

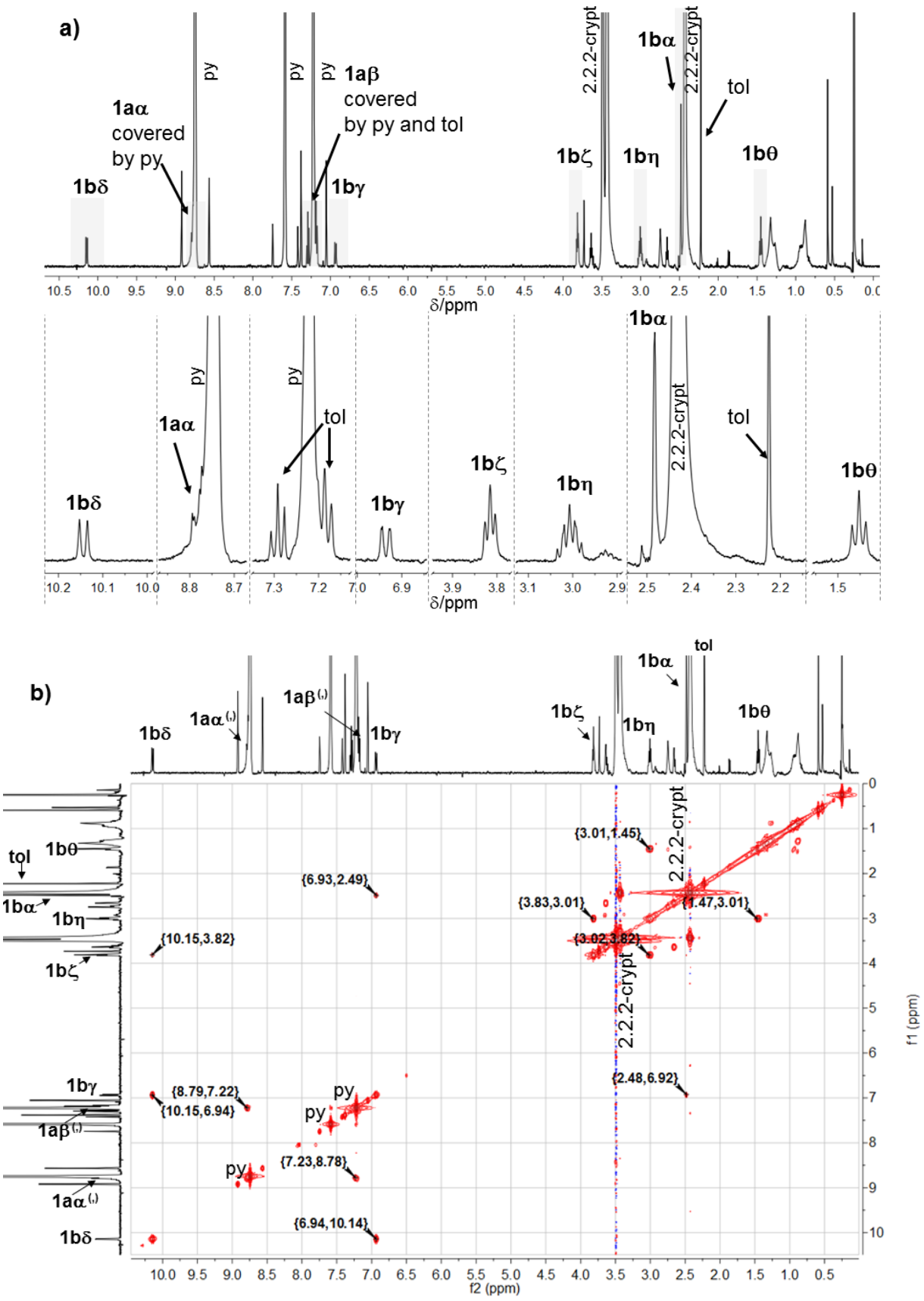

Figure S3. a) ^{1}H-NMR and b) COSY resonances of {[K(2.2.2-crypt)]$_4$**1**} in acetonitrile-d$_3$ recorded at room temperature.

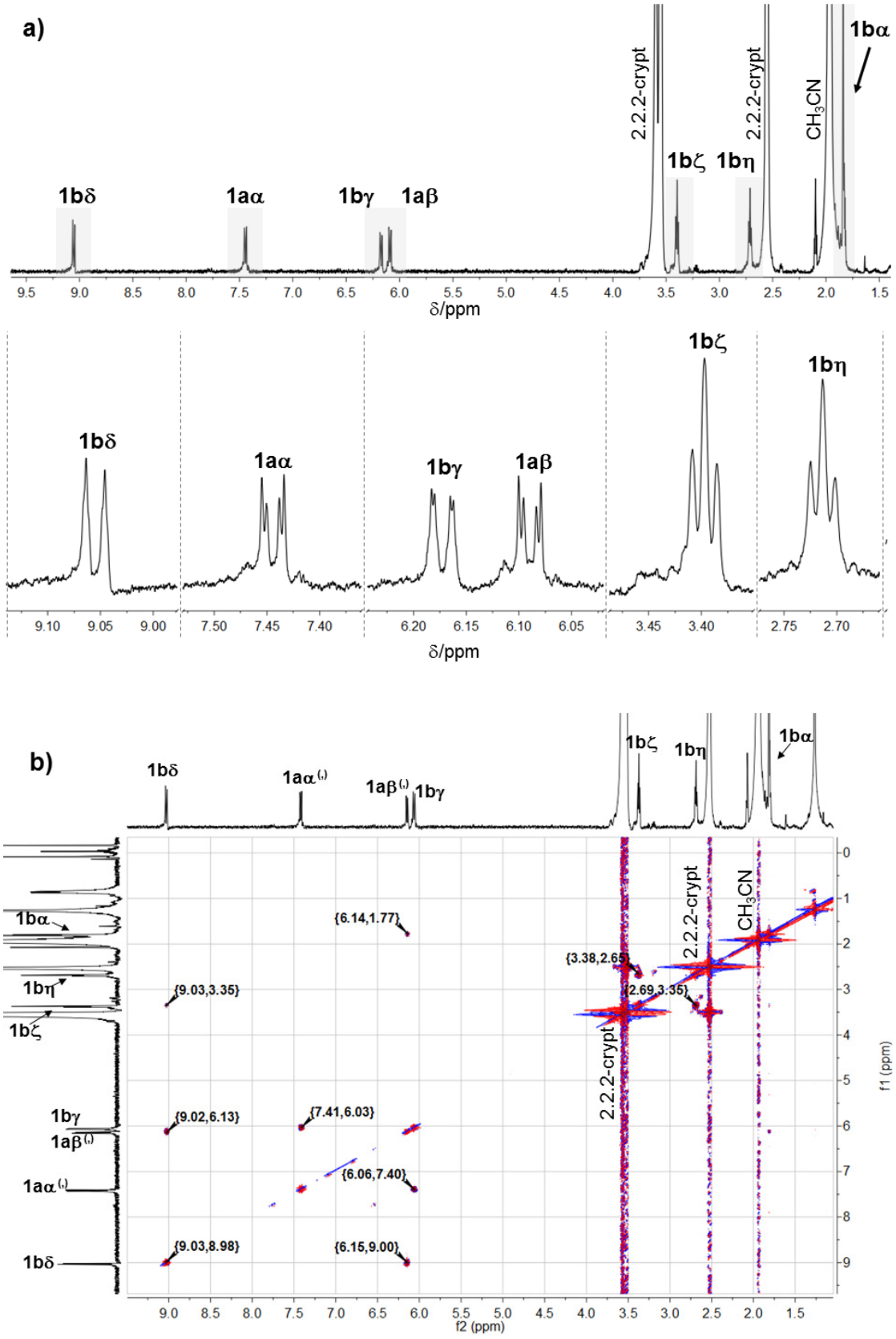

IR data of {[K(2.2.2-crypt)]$_4$1}(toluene)$_2$. For IR-spectrum see Figure S4. IR (diamond ATR) [cm^{-1}]: 3347 (ν_s(N-H)), 3269 (ν_{as}(N-H)), ν_s(C-H) and/or ν_{as}(C-H): 2949, 2873, 2806, 2762, 2729; 1731; 1609 (ν(C=C), ν(C=N)), 1582 ($\delta_{in\text{-}plane}$ (NH_2)); 1540, 1470, 1438, 1352, 1291, 1258, 1173, 1130, 1095, 1075, 942, 930, 824, 738.

Figure S4. ATR-FTIR spectrum of {[K(2.2.2-crypt)]$_4$**1**}(toluene)$_2$. Vibrational bands are labelled with corresponding wavenumbers.

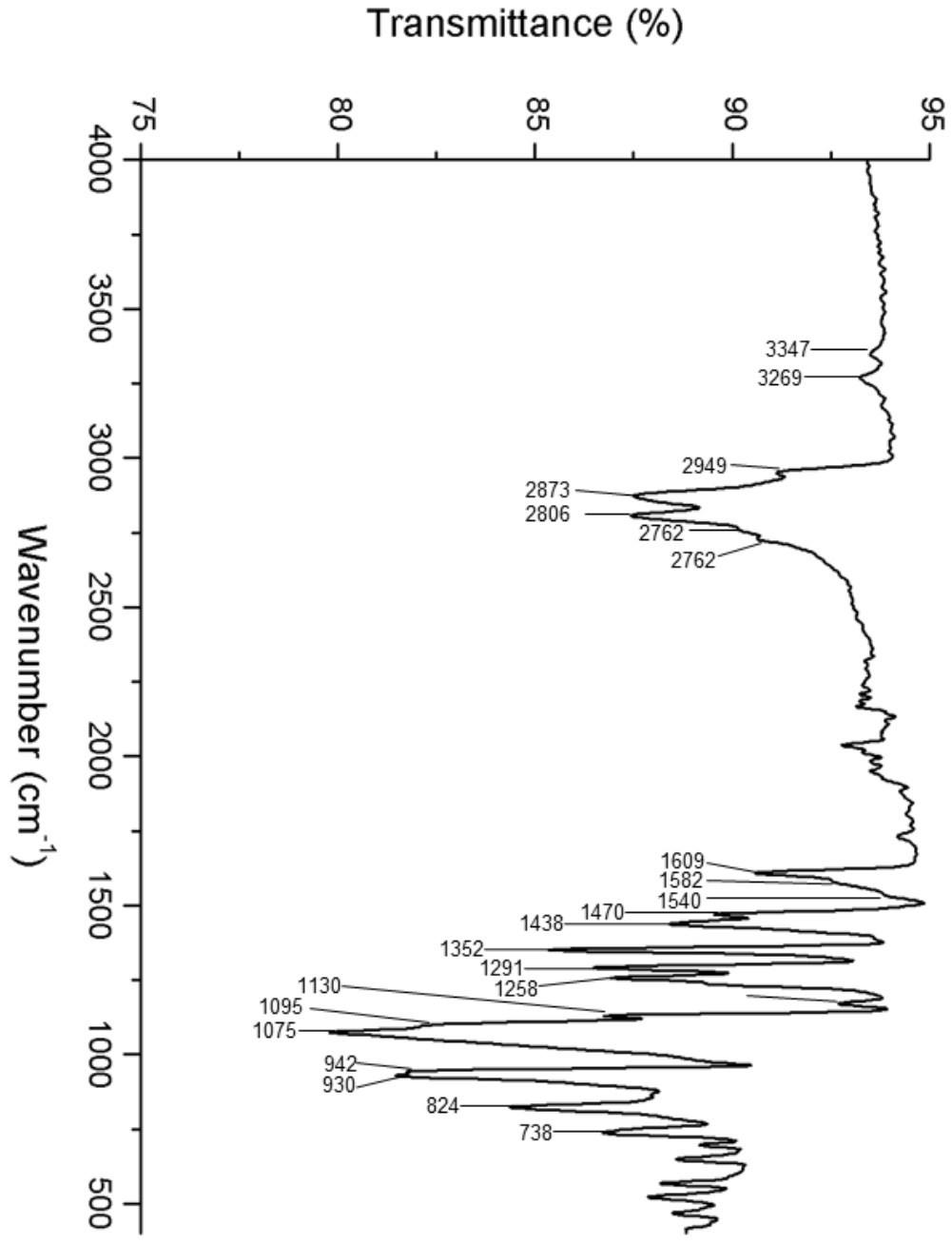

***In situ* NMR studies concerning the formation of molecule 1**

Studies on the reaction between 1,4-bis(trimethylsilyl)butadiyne and ethylenediamine. In a glovebox 1,4-bis(trimethylsilyl)butadiyne (93.6 mg; 0.48 mmol) was dissolved in 2 ml ethylenediamine. The obtained solution was filtered and filled in a glovebox into a Norell® NMR tube, with an outer diameter of 3 mm. Subsequently, the Norell® NMR tube was put into a NMR tube with an inner diameter of 4 mm (denoted as outer tube). Into the outer NMR tube chloroform-d_1 was filled.

NMR data of identified species

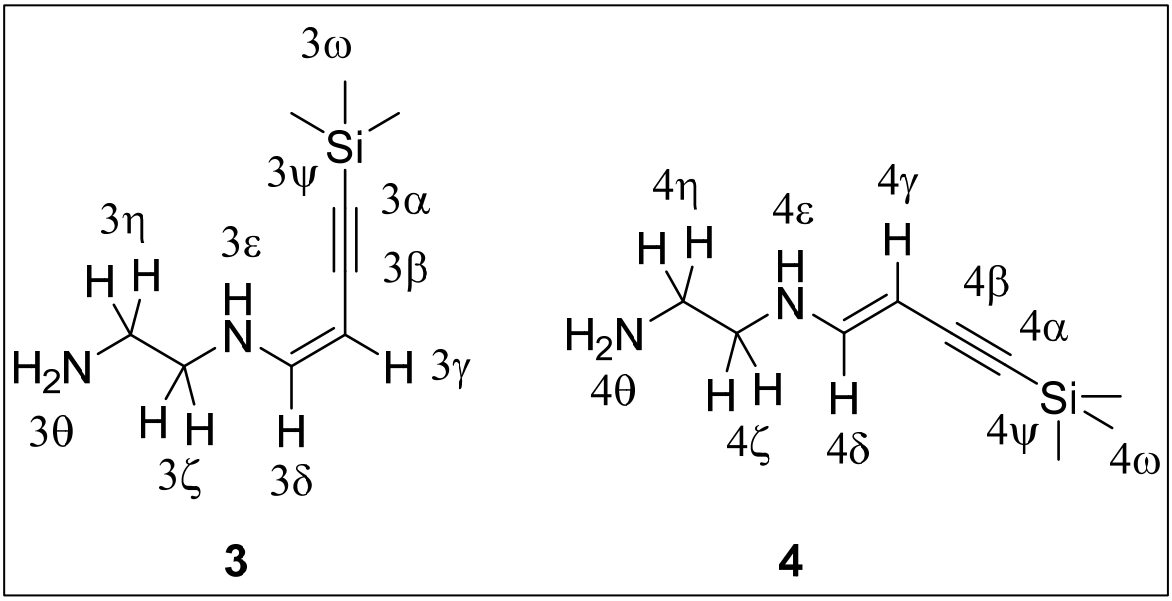

Scheme S2. The (3*Z*) and (3*E*) isomer of the product 7-amino-1-(trimethylsilyl)-5-aza-hepta-3-en-1-yne originating from the reaction between 1,4-bis(trimethylsilyl)butadiyne and ethylenediamine. The hydrogen atoms are labelled with the corresponding compound number as well as greek letters, respectively.

For NMR-spectra see Figure S5

(3*Z*)-7-amino-1-(trimethylsilyl)-5-aza-hepta-3-en-1-yne (3). ^{1}H NMR (500 MHz, chloroform-d_1 (outer tube), ethylendiamine (inner tube), 296 K), δ(ppm): 6.40 (dd, J = 8.6 Hz, 12.2 Hz, 1H, 3δ), 3.96 (d, J = 8.6 Hz, 1H, 3γ), 6.67 (s(broad), 3ε), 3.21 (pseudo q, J = 6.0 Hz, 2H, 3ζ), 2.76 (3η, covered by en and revealed by COSY), 0.23 (s, 9H, 3ω); COSY (500 MHz, chloroform-d_1, 296 K), δ(ppm): 6.67/3.22 (^3J, 3ε/3ζ), 6.39/6.67 (^3J, 3δ/3ε), 6.40/3.98 (^3J, 3δ/3γ), 3.21/2.76 (^3J, 3ζ/3η); ^{13}C NMR (400 MHz, chloroform-d_1, 296 K): 146.9 (3δ), 105.8 (3β), 93.9 (3α, not detectable but revealed

with HMBC), 70.1 (3γ), 49.7 (3ζ), 42.7 (3η); HMBC (500 MHz, chloroform-d_1, 296 K), δ(ppm): 6.41/105.7 (^3J, 3δ/3β), 6.42/70.5 (^2J, 3δ/3γ), 6.42/49.7 (^2J, 3δ/3ζ), 3.98/93.9 (^3J, 3γ/3α), 3.22/146.7 (^3J, 3ζ/3δ), 3.23/42.4 (^2J, 3ζ/3η), 0.24/93.8 (^3J, 3ω/3α); HSQC (500 MHz, chloroform-d_1, 296 K), δ(ppm): 6.4/146.9 (^1J, 3δ/3δ), 4.0/70.1 (^1J, 3γ/3γ), 3.2/49.7 (^1J, 3ζ/3ζ)

(3*E*)-7-amino-1-(trimethylsilyl)-5-aza-hepta-3-en-1-yne (4). ^{1}H NMR (500 MHz, chloroform-d_1 (outer tube), ethylendiamine (inner tube), 296 K), δ(ppm): 6.91 (dd, *J* = 13.6 Hz, 7.4 Hz, 1H, 4δ), 4.23 (d, *J* = 13.6 Hz, 1H, 4γ), 7.54 (s(broad), 1H, 4ε), 2.96 (pseudo q, *J* = 6.0 Hz, 2H, 4ζ), 2.79 (revealed by COSY, 4η), 0.19 (s, 9H, 4ω); COSY (500 MHz, chloroform-d_1, 296 K), δ(ppm): 6.91/7.48 (^3J, 4δ/4ε), 6.92/4.25 (^3J, 4δ/4γ), 7.48/2.98 (^3J, 4ε/4ζ), 2.97/2.79 (^3J, 4ζ/4η); ^{13}C NMR (400 MHz, chloroform-d_1, 296 K), δ(ppm): 147.6 (4δ), 109.1 (4β), 86.1 (4α), 70.7 (4γ), 46.3 (4ζ), 40.3 (4η); HMBC (500 MHz, chloroform-d_1, 296 K), δ(ppm): 6.92/109.2 (^3J, 4δ/4β), 6.92/70.8 (^3J, 4δ/4γ), 6.92/46.3 (^2J, 4δ/4ζ), 4.27/86.1 (^3J, 4γ/4α), 2.98/40.0 (^3J, 4ζ/4η), 0.20/86.2 (^3J, 4ω/4α); HSQC (500 MHz, chloroform-d_1, 296 K), δ(ppm): 6.9/147.6 (^1J, 4δ/4δ), 4.3/70.7 (^1J, 4γ/4γ)

Description of NMR data

Both isomers **3** and **4** show an identical NMR patter and only differ concerning their chemical shifts and coupling constants. For isomer **3** the 3*Z* configuration is indicated by an 8.6 Hz coupling between protons 3δ and 3γ, which is typical for *cis* orientated protons.[7] A coupling of 13.6 Hz between protons 4δ and 4γ indicates *trans* orientated protons and thus the 3*E* configuration of isomer **4**. [7] In sum the doublet of doublet structure of 3δ and 4δ results from the above mentioned coupling to 3γ and 4γ as well as the coupling to -NH protons 3ε and 4ε with 12.2 Hz and 7.4 Hz, respectively. Since NMR measurements were done in non deuterated ethylenediamine and chemical shifts of protons ζ, η and θ are very similar to those of ethylendiamine, strong overlaps occur. Assisted by 2D-NMR techniques (COSY, HMBC, HSQC) the detection of those protons was possible. With HMBC moreover the assignment of methyl protons ω in the ^{1}H NMR spectrum was possible, as a ^3J coupling between carbon atoms α and methyl protons ω is clearly visible.

Figure S5. a) ^{1}H-NMR, b/c) COSY, d) ^{13}C-NMR, e) HMBC and f) HSQC spectra of the reaction solution containing 1,4-bis(trimethylsilyl)-butadiyne in ethylenediamine and the (3*Z*)- and (3*E*)-7-amino-1-(trimethylsilyl)-5-aza-hepta-3-en-1-yne. The ^{1}H-NMR traces in the 2D spectra were measured directly before recording the corresponding 2D spectra in order to see if there are changes in the reaction solution compared to the ^{1}H-NMR spectrum measured after 2.5 h reaction time. In case of HMBC an HSQC spectra the ^{13}C-NMR shown in d) was used as corresponding 1D trace. Unknown peaks are marked with ‡. For 1,4-bis(trimethylsilyl)butadiyne in ^{1}H-NMR a signal around 0 ppm and in ^{13}C-NMR signals at 85.9, 88.0 and -0.5 ppm would be expected.[9]

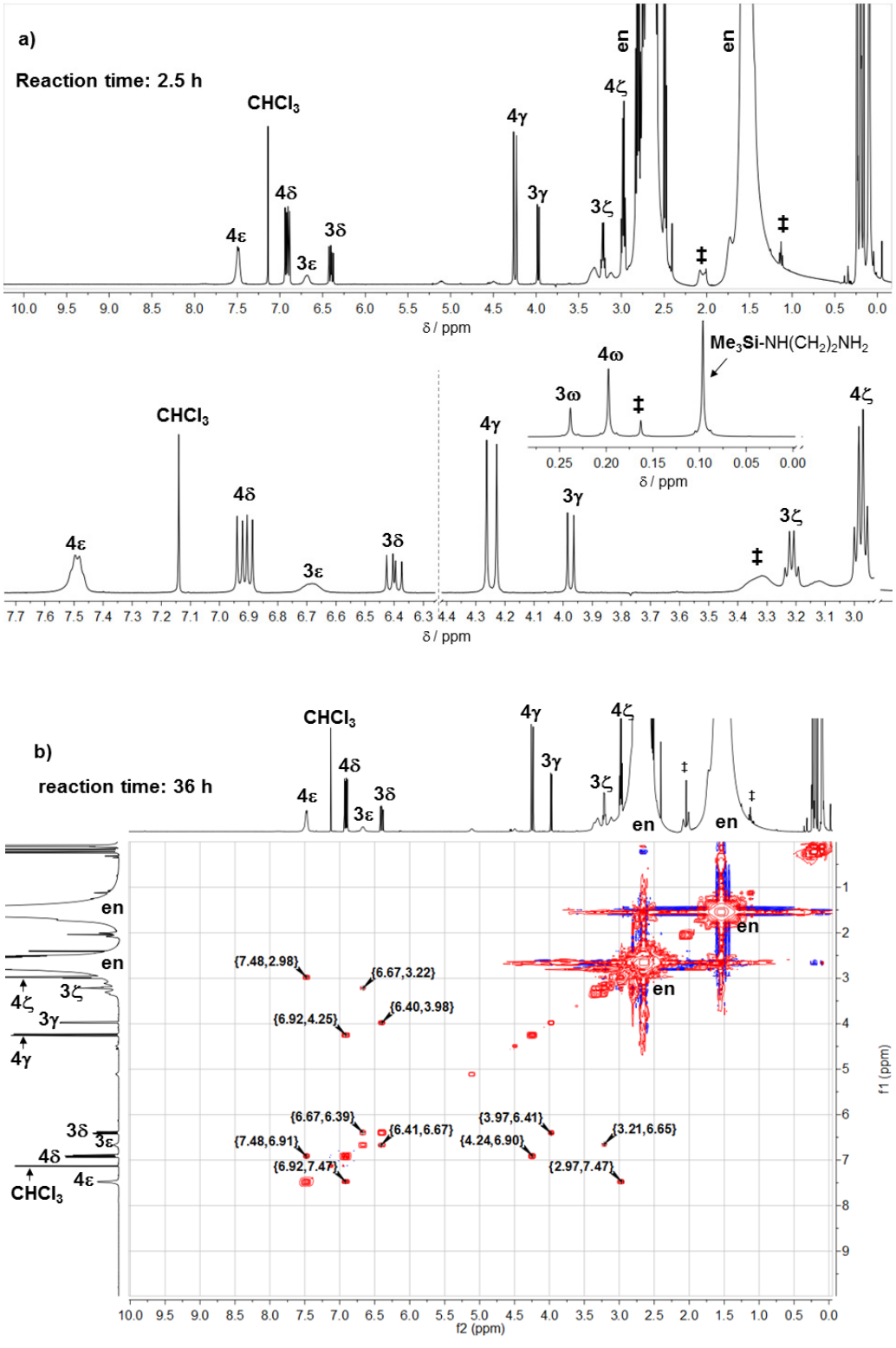

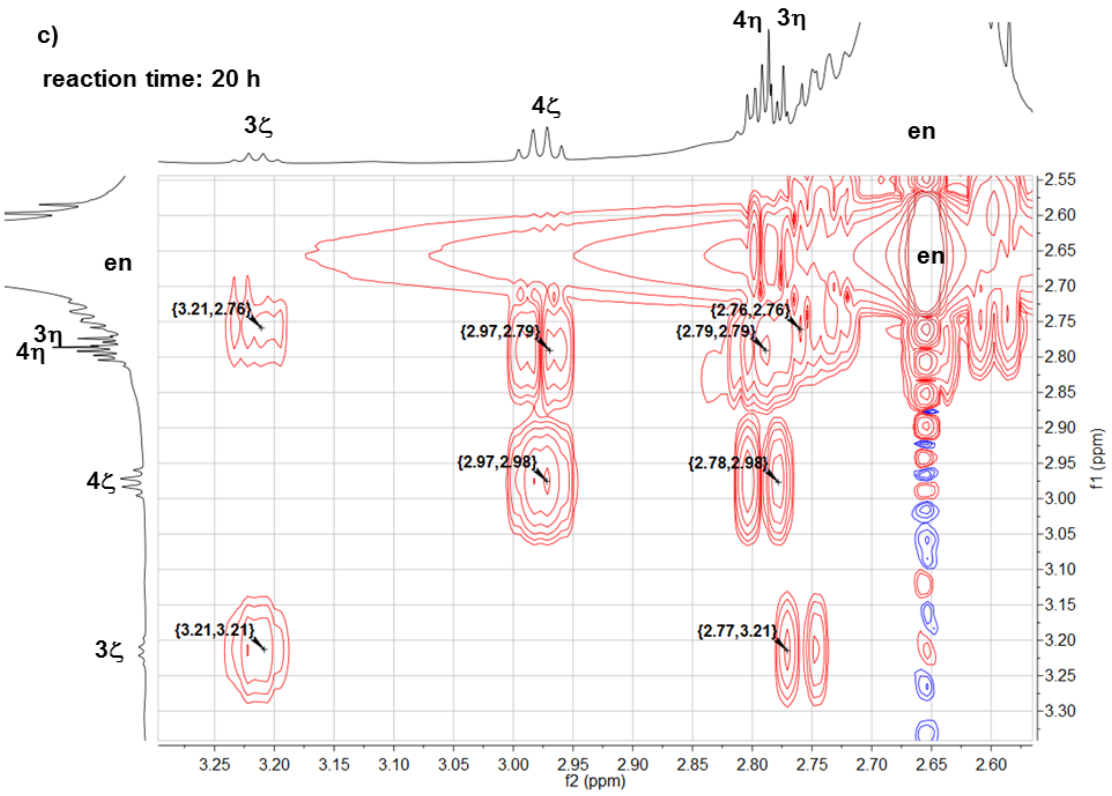
c)
reaction time: 20 h
4η
3η
3ζ
4ζ
en
en
en
3η
4η
4ζ
3ζ
{3.21,2.76}
{2.97,2.79}
{2.76,2.76}
{2.79,2.79}
{2.97,2.98}
{2.78,2.98}
{3.21,3.21}
{2.77,3.21}
f1 (ppm)
f2 (ppm)

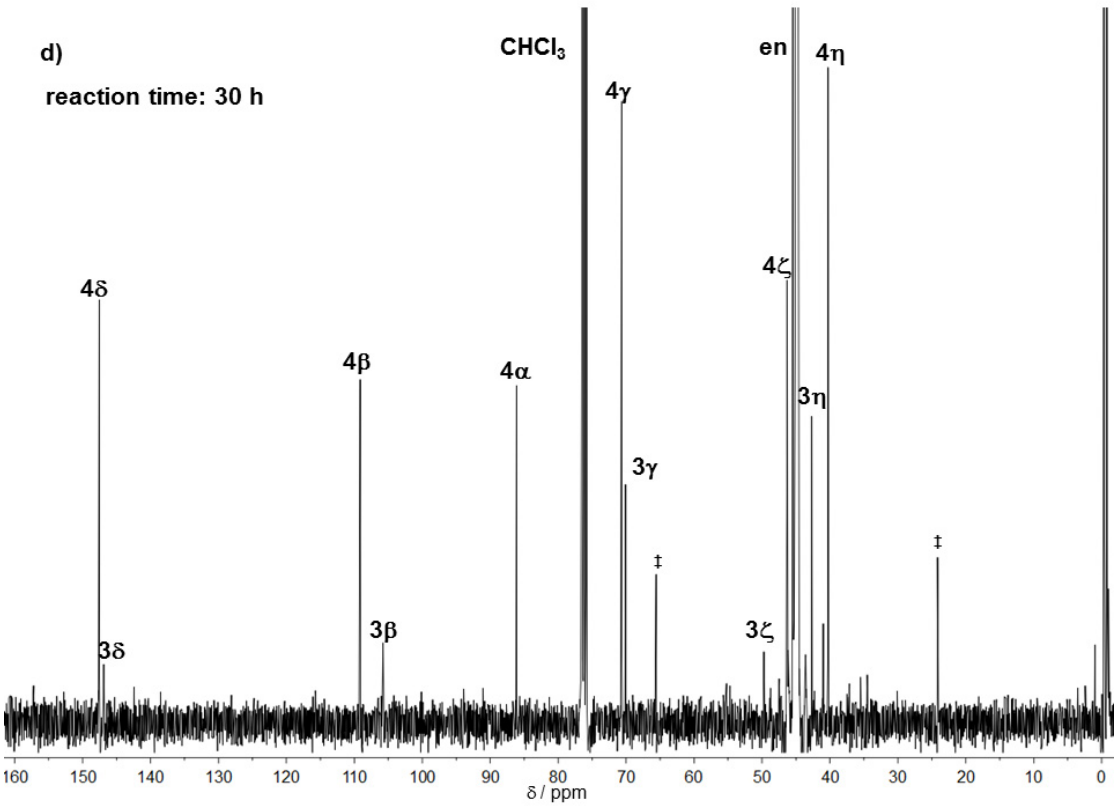
d)
reaction time: 30 h
CHCl3
en
4η
4γ
4ζ
4δ
4β
4α
3η
3γ
‡
‡
3δ
3β
3ζ
δ / ppm

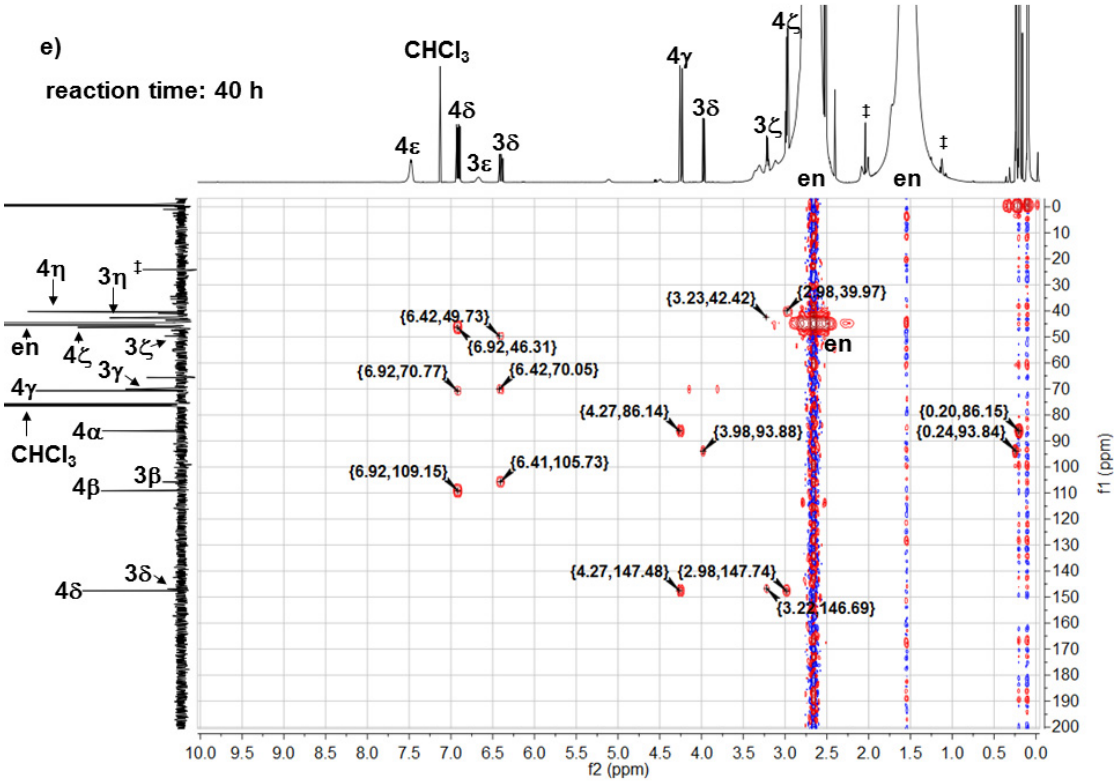
e)
reaction time: 40 h
CHCl3
4ε
4δ
3ε
3δ
4γ
3δ
3ζ
4ζ
‡
‡
en
en
4η
3η
‡
en
4ζ
3ζ
3γ
4γ
4α
CHCl3
4β
3β
4δ
3δ
{3.23,42.42}
{2.98,39.97}
en
{6.42,49.73}
{6.92,46.31}
{6.92,70.77}
{6.42,70.05}
{4.27,86.14}
{3.98,93.88}
{0.20,86.15}
{0.24,93.84}
{6.92,109.15}
{6.41,105.73}
{4.27,147.48}
{2.98,147.74}
{3.22,146.69}
f1 (ppm)
f2 (ppm)

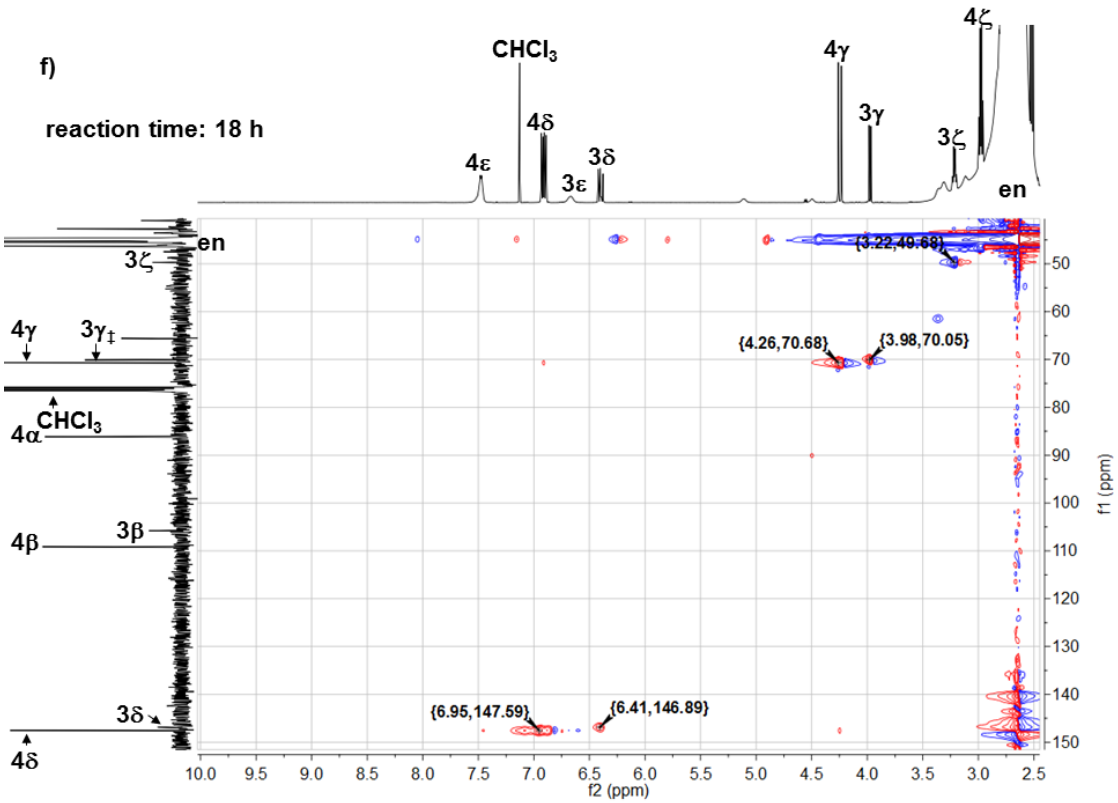
f)
reaction time: 18 h
CHCl3
4ε
4δ
3ε
3δ
4γ
3γ
3ζ
4ζ
en
en
3ζ
4γ
3γ‡
4α
CHCl3
4β
3β
3δ
4δ
{3.22,49.68}
{4.26,70.68}
{3.98,70.05}
{6.95,147.59}
{6.41,146.89}
f1 (ppm)
f2 (ppm)

Studies on the reaction between (3*Z*)- and (3*E*)-7-amino-1-(trimethylsilyl)-5-aza-hepta-3-en-1-yne, 1,4-bis(trimethylsilyl)butadiyne and K_4Ge_9 in ethylene-diamine. In a glovebox 1,4-bis(trimethylsilyl)butadiyne (10.5 mg; 0.054 mmol) was dissolved in 0.9 ml ethylenediamine and stirred for 2.5 hours. The pale yellow solution was mixed with a batch containing solid K_4Ge_9 (43.7 mg; 0.054 mmol) and 1,4-bis(trimethylsilyl)butadiyne (5.3 mg; 0.027 mmol) and stirred for 21 hours. The obtained deep red colored solution was filtered and filled in a glovebox into a Norell® NMR tube, with an outer diameter of 3 mm. Subsequently, the Norell® NMR tube was put into a NMR tube with an inner diameter of 4 mm (denoted as outer tube). Into the outer NMR tube chloroform-d_1 was filled.

NMR data of identified species

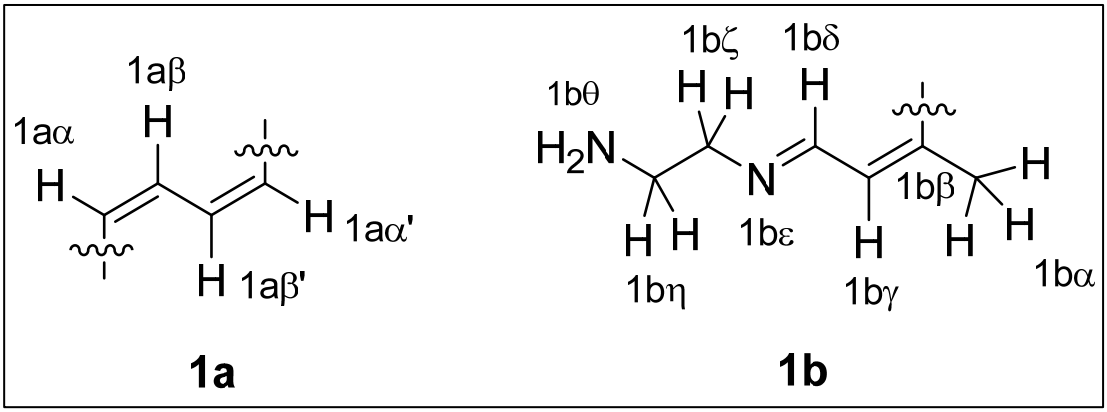

Scheme S3. The organic fragments identified in a solution containing (3*Z*)- and (3*E*)-7-amino-1-(trimethylsilyl)-5-aza-hepta-3-en-1-yne, 1,4-bis(trimethylsilyl)butadiyne, K_4Ge_9 and ethylenediamine. The hydrogen atoms are labelled with the corresponding compound number as well as greek letters, respectively.

For NMR-spectra see Figure S6

^{1}H NMR (500 MHz, chloroform-d_1 (outer tube), ethylendiamine (inner tube), 296 K), δ (ppm): 9.36 (d, J = 9.0 Hz, 1bδ), 7.72 (dd, J = 8.7 Hz, 2.0 Hz, 1aα), 6.78 (dd, J = 8.7 Hz, 2.0 Hz, 1aβ), 6.34 (d, J = 9.0 Hz, 1bγ), 3.48 (t, J = 5.8 Hz, 1bζ), 2.21 (s, 1bα); COSY (500 MHz, chloroform-d_1 (outer tube), ethylendiamine (inner tube), 296 K), δ (ppm): 9.37/6.34 (^3J, 1bδ/1bγ), 9.34/3.44 (^4J, 1bδ/1bζ), 7.72/6.75 (^3J, 1aα/1aβ), 6.33/2.14 (^4J, 1bγ/1bα); Signals 1b$\eta\xi$ and 1bθ covered by peaks of ethylenediamine.

Figure S6. a) ^{1}H-NMR, b) COSY spectra of a reaction solution obtained after mixing 1,4-bis(trimethylsilyl)butadiyne and K_4Ge_9 with a solution of (*3Z*)- and (3*E*)-*7*-amino-5-aza-hepta-3-en-1-yne in ethylenediamine.

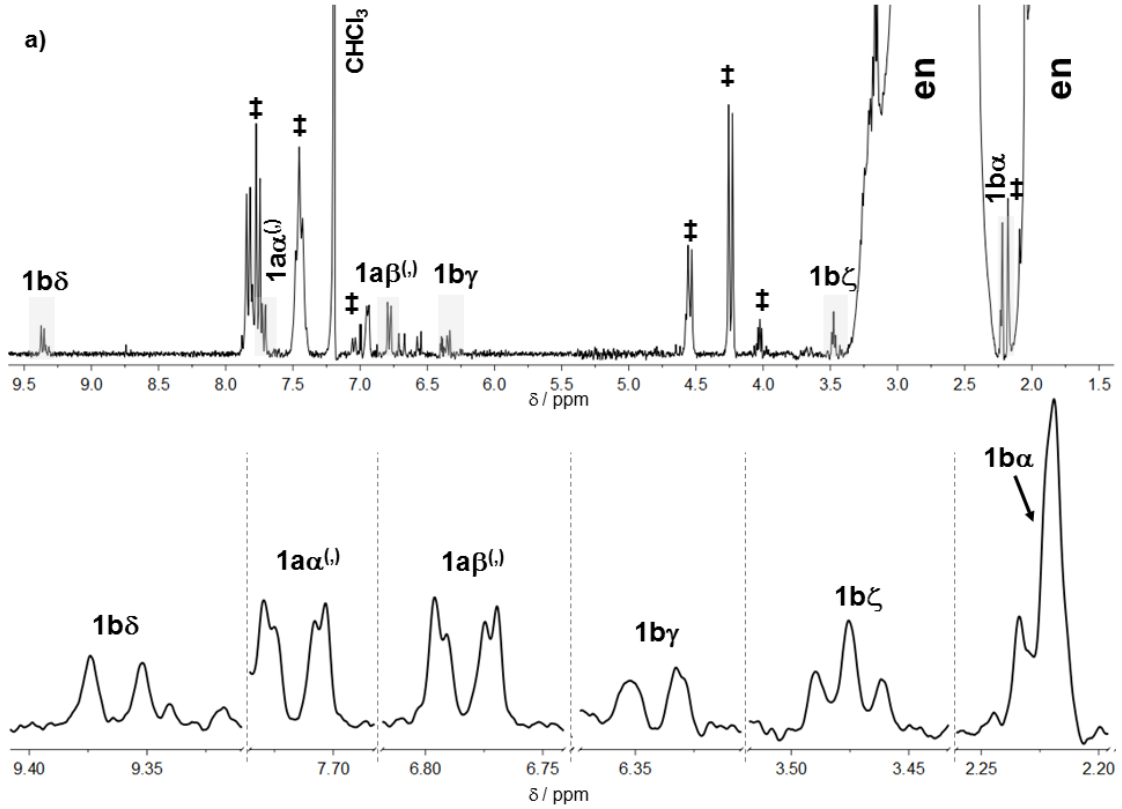

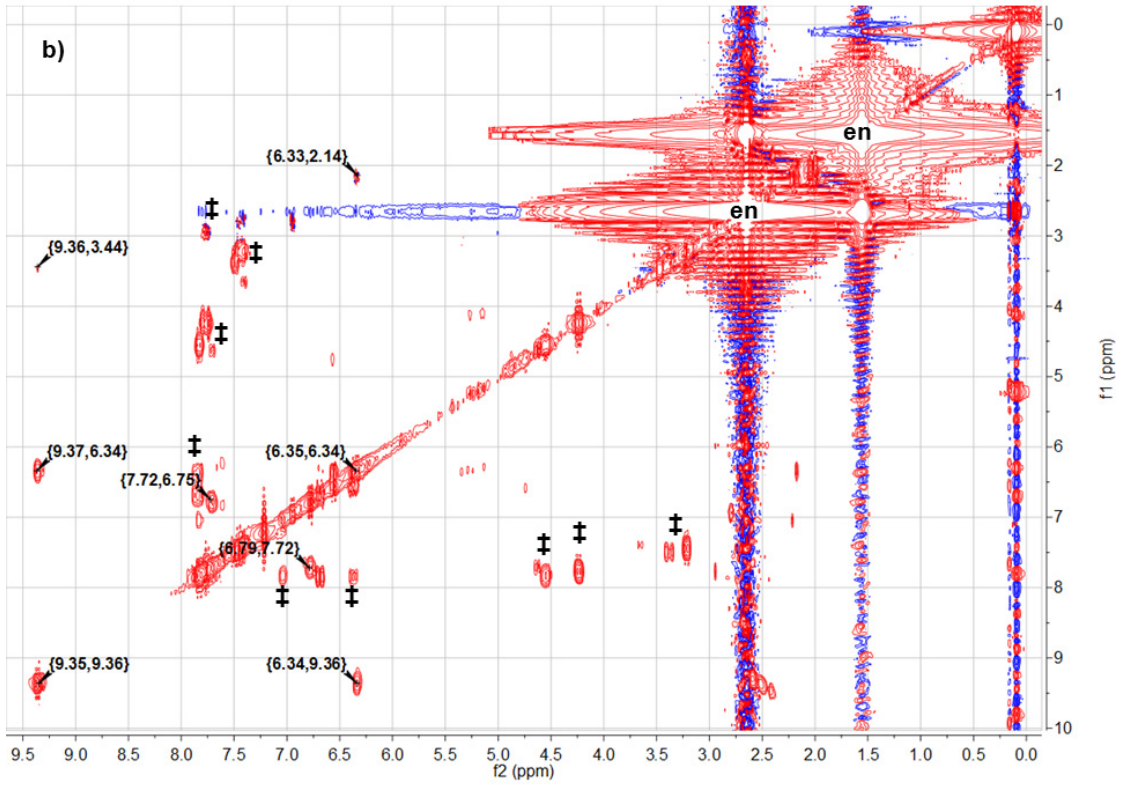

Quantum Chemical Calculations

Figure S7. The molecular orbitals with contributions of the conjugated π-system of the central bridging unit **1a** for the structurally optimized compound $[H_2C{=}CH{-}Ge_9{-}CH{=}CH{-}CH{=}CH{-}Ge_9{-}H_2C{=}CH]^{4-}$. The calculated energy levels of each molecular orbital are shown as dashes. The levels of the relevant molecular orbitals shown on the left side are marked with circles. Iso-surfaces of the wave functions are shown for the value 0.03.

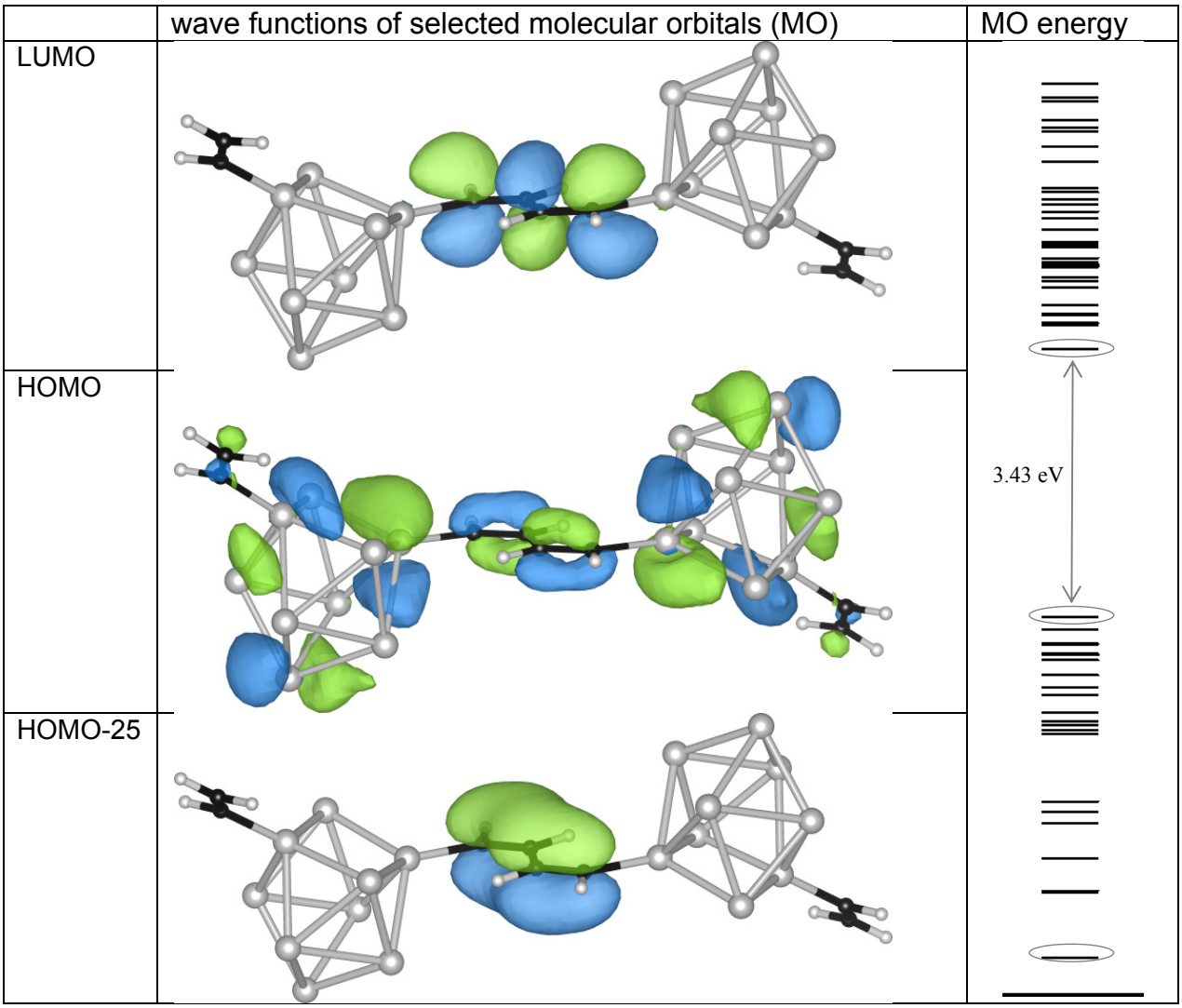

References.

[1] a) M. W. Hull, S. C. Sevov, *Angew. Chem.* **2007**, *119*, 6815-6818; *Angew. Chem. Int. Ed.* **2007**, *46*, 6695-6698; b) M. W. Hull, S. C. Sevov, *Inorg. Chem.* **2007**, *46*, 10953-10955; c) M. W. Hull, S. C. Sevov, *J. Am. Chem. Soc.* **2009**, *131*, 9026-9037; d) C. B. Benda, J.-Q. Wang, B. Wahl, T. F. Fässler, *Eur. J. Inorg. Chem.* **2011**, 4262-4269; e) M. W. Hull, S. C. Sevov, *Chemical Commun.* **2012**, *48*, 7720-7722; f) M. W. Hull, S. C. Sevov, *J. Organomet. Chem.* **2012**, *721*, 85-91.

[2] T. F. Fässler, *Coord. Chem. Rev.* **2001**, *215*, 347-377.

[3] G. M. Sheldrick, *Acta Crystallogr.* **2008**, *A64*, 112-122.

[4] J. Åkerstedt, S. Ponou, L. Kloo, S. Lidin, *Eur. J. Inorg. Chem.* **2011**, *2011*, 3999-4005.

[5] P. van der Sluis, A. L. Spek, *Acta Crystallogr.* **1990**, *A46*, 194-201.

[6] A. L. Spek, *Acta Crystallogr.* **2009**, *D65*, 148-155.

[7] M. Hesse, H. Meier, B. Zeeh, *Spektroskopische Methoden in der organischen Chemie*, Thieme, **2005**.

[8] a) L. Hintermann, *Beilstein J. Org. Chem.* **2007**, *3*, 22; b) R. Escudero, M. Gomez-Gallego, S. Romano, I. Fernandez, A. Gutierrez-Alonso, M. A. Sierra, S. Lopez-Rayo, P. Nadal, J. J. Lucena, *Org. Biomol. Chem.* **2012**, *10*, 2272-2281.

[9] N. Kakusawa, K. Yamaguchi, J. Kurita, J. Organomet. Chem. **2005**, *690*, 2956-2966.

5.2 On the formation of Ge_9-Linker-Ge_9 Zintl Triads - Syntheses and structures of $[Ge_9–CH{=}CH–CH{=}CH–Ge_9]^{6–}$ and $[R–Ge_9–CH{=}CH–CH{=}CH–Ge_9–R]^{4–}$

M. M. Bentlohner, S. Frischhut, T. F. Fässler

Manuscript for publication

5.2.1 Content and Contributions

In the scope of the publication "On the formation of Ge_9-Linker-Ge_9 Zintl Triads - Syntheses and structures of $[Ge_9–CH=CH–CH=CH–Ge_9]^{6–}$ and $[R–Ge_9–CH=CH–CH=CH–Ge_9–R]^{4–}$", the syntheses, X-ray structures and Raman-spectra of the first Zintl triad $[Ge_9–CH=CH–CH=CH–Ge_9]^{6–}$ as well as reproduced $[R–Ge_9–CH=CH–CH=CH–Ge_9–R]^{4–}$ [*R* = (2*Z*,4*E*)-7-amino-5-aza-hepta-2,4-dien-2-yl] are presented along with *in situ* studies on their formation.

The present publication was authored in the course of this Ph.D. thesis. The compounds $\{A(222\text{-crypt})]_6[Ge_9–CH=CH–CH=CH–Ge_9]\}\cdot(tol)_2\cdot(en)_2$ (*A* = K, Rb) and $\{Rb(222\text{-crypt})]_4[R\text{-}Ge_9–CH=CH–CH=CH–Ge_9–R]\}\cdot(tol)$ (R = (2*Z*, 4*E*)-7-amino-5-aza-hepta-2,4-dien-2-yl) were synthesized by reactions of 1,4-bis(trimethylsilyl)butadiyne and 1-trimethylsilyl-7-amino-5-aza-hepta-3-en-1-yne with A_4Ge_9 (*A* = K, Rb) in *en*, and crystallized after the addition of cryptand[2.2.2]/*tol*. Synthesis and isolation of $\{A(222\text{-crypt})]_6[Ge_9–CH=CH–CH=CH–Ge_9]\}\cdot(tol)_2\cdot(en)_2$ was assisted by Sabine Frischhut in the scope of a practical training. According to the X-ray structures, $\{A(222\text{-crypt})]_6[Ge_9–CH=CH–CH=CH–Ge_9]\}\cdot(tol)_2\cdot(en)_2$ (*A* = K, Rb) and $\{Rb(222\text{-crypt})]_4[R\text{-}Ge_9–CH=CH–CH=CH–Ge_9–R]\}\cdot(tol)$ comprise Zintl triads with two Ge_9 clusters linked by a conjugated (1Z, 3Z)-buta-1,3-dien-1,4-diyl functionality and bearing additionally conjugated side chains in the latter case. The $[Ge_9–CH=CH–CH=CH–Ge_9]^{6–}$ anion is disordered and appears in the crystal structure as three different conformers, whereas only one conformer appears for $[R\text{-}Ge_9–CH=CH–CH=CH–Ge_9–R]^{4–}$. X-ray structure analysis, including the development of a model for the disorder of $[Ge_9–CH=CH–CH=CH–Ge_9]^{6–}$, was conducted in the course of this thesis. Raman investigations on both compounds revealed signal patterns typical for 1,4-di-substituted *cis*,*cis*-buta-1,3-dienes and confirmed the X-ray structure analysis. The Raman spectra were measured by Herta Slavik and the interpretation of the data was done in the scope of this thesis. By an *in situ* NMR and ESI-MS study, the formation of Zintl triads was delineated and for the first time the postulated deprotonation of *en* in the reaction of clusters with alkynes was indirectly evidenced by NMR. From these results also a new method for qualitative determination of water in *en* was derived. *In situ* measurements and data evaluation were conducted in the scope of this work and in a practical training of Sabine Frischhut.

5.2.2. Manuscript for Publication

On the formation of Ge_9-Linker-Ge_9 Zintl Triads - Syntheses and structures of $[Ge_9–CH=CH–CH=CH–Ge_9]^{6–}$ and $[R–Ge_9–CH=CH–CH=CH–Ge_9–R]^{4–}$

Manuel M. Bentlohner, Sabine Frischhut and Thomas F. Fässler*

[*]
Manuel M. Bentlohner, Sabine Frischhut, Prof. Dr. T. F. Fässler
Department Chemie, Technische Universität München
Lichtenbergstraße 4, 85747 Garching, Germany
E-mail: thomas.faessler@lrz.tum.de

Keywords

Zintl triads / Germanium / Raman-spectroscopy / crystal structure / *in-situ* NMR

Abstract

The potential of $[E_9]^{4-}$ Zintl anions to form, in analogy to fullerenes, dyads and triads with extended π-electron systems is highlighted. We present the syntheses, X-ray structures and Raman-spectra of the compounds $\{A(222\text{-crypt})]_6[Ge_9–CH=CH–CH=CH–Ge_9]\}\cdot(tol)_2\cdot(en)_2$ (*A* = K, Rb) and $\{Rb(222\text{-crypt})]_4[R\text{-}Ge_9–CH=CH–CH=CH–Ge_9–R]\}\cdot(tol)$ (R = (2*Z*, 4*E*)-7-amino-5-aza-hepta-2,4-dien-2-yl) (cryptand[2.2.2] = 4,7,13,16,21,24-hexaoxa-1,10-diazabicyclo-[8.8.8]hexacosan), comprising anionic entities with two Ge_9 clusters linked by a conjugated (1*Z*, 3*Z*)-buta-1,3-dien-1,4-diyl functionality and bearing additional conjugated side chains in the latter case. $\{A(222\text{-crypt})]_6[Ge_9–CH=CH–CH=CH–Ge_9]\}\cdot(tol)_2\cdot(en)_2$ and $\{Rb(222\text{-crypt})]_4[R\text{-}Ge_9–CH=CH–CH=CH–Ge_9–R]\}\cdot(tol)$ were synthesized by reactions of 1,4-bis(trimethylsilyl)butadiyne with $[Ge_9]^{4-}$ and *en* followed by layering with toluene/cryptand[2.2.2]. Single crystal X-ray structure analysis reveals that $[Ge_9–CH=CH–CH=CH–Ge_9]^{6-}$ appears in the crystal structure as three different conformers, whereas only one conformer appears for $[R\text{-}Ge_9–CH=CH–CH=CH–Ge_9–R]^{4-}$. By an *in situ* NMR and ESI-MS study we shed light on the formation of the Zintl triads $[Ge_9–CH=CH–CH=CH–Ge_9]^{6-}$ and $[R\text{-}Ge_9–CH=CH–CH=CH–Ge_9–R]^{4-}$. For the first time the postulated deprotonation of ethylenediamine in additions of clusters to alkynes was indirectly evidenced by NMR.

Introduction

$[E_9]^{4-}$ Zintl anions (*E* = tetrel element) show a multifaceted redox chemistry, and are accessible by dissolution of the Zintl phases A_4E_9 (*A* = K, Rb, Cs; *E* = Ge, Sn, Pb) and $A_{12}E_{17}$ (*A* = K, Rb, Cs; *E* = Si, Ge) in ethylenediamine (*en*), N,N-dimethylformamide (*dmf*) or liquid ammonia.[1-2] Like the closely related fullerenes [3], E_9 cages are reversibly oxidizable and occur as $[E_9]^{2-}$, $[E_9]^{3-}$ and $[E_9]^{4-}$ Zintl anions, holding 20, 21 and 22 skeleton-bonding electrons (*SE*), respectively. [4-5] According to the Wade-Mingos-rules $[E_9]^{4-}$ (22 *SE*) and $[E_9]^{2-}$ (20 *SE*) are *nido* and *closo* clusters, whereas the paramagnetic $[E_9]^{3-}$ radical anion evades from that description, respectively.[1-2]

The flexibility of E_9 cages to accommodate different numbers of electrons makes these molecules interesting in terms of artificial photosynthesis, spintronics and photovoltaics.[5-6] In that context, the homologous fullerenes have been thoroughly investigated. By covalent grafting of fullerenes to organic donor and acceptor molecules as well as by coupling of two fullerene entities by organic spacers a variety of electroactive dyads and triads has been synthesized, respectively.[3, 7-8] An outstanding example is [6,6]-phenyl-C_{61}-butyric acid methyl ester (PCBM) which is applied in organic photovoltaics as an electron acceptor molecule.[3, 9]

The possibility to functionalize E_9 cages with organic tethers by nucleophilic addition to alkynes [10-14] or substitutions with alkyl halides [15], points to the synthesis of fullerene analogous Zintl dyads and triads. Recently, we reported on the synthesis and characterization of the conjugated Zintl triad $[(^{\mathbf{Z}}\mathbf{R})–(Ge_9)–(^{\mathbf{ZZ}}\mathbf{B})–(Ge_9)–(^{\mathbf{Z}}\mathbf{R})]^{4-}$ [$^{\mathbf{ZZ}}\mathbf{B}$ = (1*Z*, 3*Z*)-buta-1,3-dien-1,4-diyl; $^{\mathbf{Z}}\mathbf{R}$ = (2*Z*, 4*E*)-7-amino-5-aza-hepta-2,4-dien-2-yl] (Scheme 1a). The latter can be obtained by reaction of a mixture of 1,4-bis(trimethylsilyl)butadiyne and 1-trimethylsilyl-7-amino-5-aza-hepta-3-en-1-yne with K_4Ge_9 in *en.*[6] In order to establish E_9-Linker-E_9 Zintl triads in a broader field of chemistry and enable further chemical transformations, it is necessary to get a deeper understanding on their formation.

Herein we present the new Zintl triad $[(Ge_9)–(^{\mathbf{ZZ}}\mathbf{B})–(Ge_9)]^{6-}$ (**1a**) (Scheme 1a) in terms of synthesis, X-ray structure and Raman-spectrum. The anionic entity **1a** crystallizes as {*A*(222-crypt)]$_6$ **1a**}·$(tol)_2$·$(en)_2$ (*A* = K, Rb) salts and is compared with $[(^{\mathbf{Z}}\mathbf{R})–(Ge_9)–(^{\mathbf{ZZ}}\mathbf{B})–(Ge_9)–(^{\mathbf{Z}}\mathbf{R})]^{4-}$ (**2a**) [6], which was repeatedly isolated as {*A*(222-crypt)]$_4$ **2a**}·(tol) salt [6, 16] by a rational synthetic method. An *in situ* NMR and ESI-MS study on reaction solutions containing A_4Ge_9 (*A* = K, Rb), 1,4-

bis(trimethylsilyl)butadiyne (**3**) and/or 1-trimethylsilyl-7-amino-5-aza-hepta-3-en-1-yne (**4**)[6] sheds light on the formation of **1a** and **2a**, respectively.

Results and Discussion

Syntheses

{*A*(222-crypt)]$_6$ **1a**}·(tol)$_2$·(en)$_2$ (*A* = K, Rb) were synthesized (Scheme 1b) by stirring pre-mixtures of the solids A_4Ge_9 (1 eq.) and **3** (0.25-0.5 eq.) with water-free *en* for 20 h, and layering of the resulting dark-brown solutions with cryptand[2.2.2] in toluene. Within 1-2 weeks bundles of dark red crystals of {*A*(222-crypt)]$_6$ **1a**}·(tol)$_2$·(en)$_2$ formed (yield ca. 10%).

In another synthesis we reproduced {K(222-crypt)]$_4$ **2a**}·(tol) and obtained the new compound {Rb(222-crypt)]$_4$ **2a**}·(tol) (Scheme 1c). Thereby, in step A a **4**/*en* solution was prepared by reacting **3** with water-free *en* in the absence of clusters.[6] In step B, the **4**/*en*-solution, which contained 2 eq. **4** with respect to A_4Ge_9, was added to a pre-mixture of the neat solids A_4Ge_9 (1 eq.) and **3** (0.5 eq.). After stirring the mixtures for 20 h, orange-red reaction solutions were obtained and layered with cryptand[2.2.2] in toluene. Orange plates of {*A*(222-crypt)]$_4$ **2a**}·(tol) grew within several weeks (yield ca. 30%).

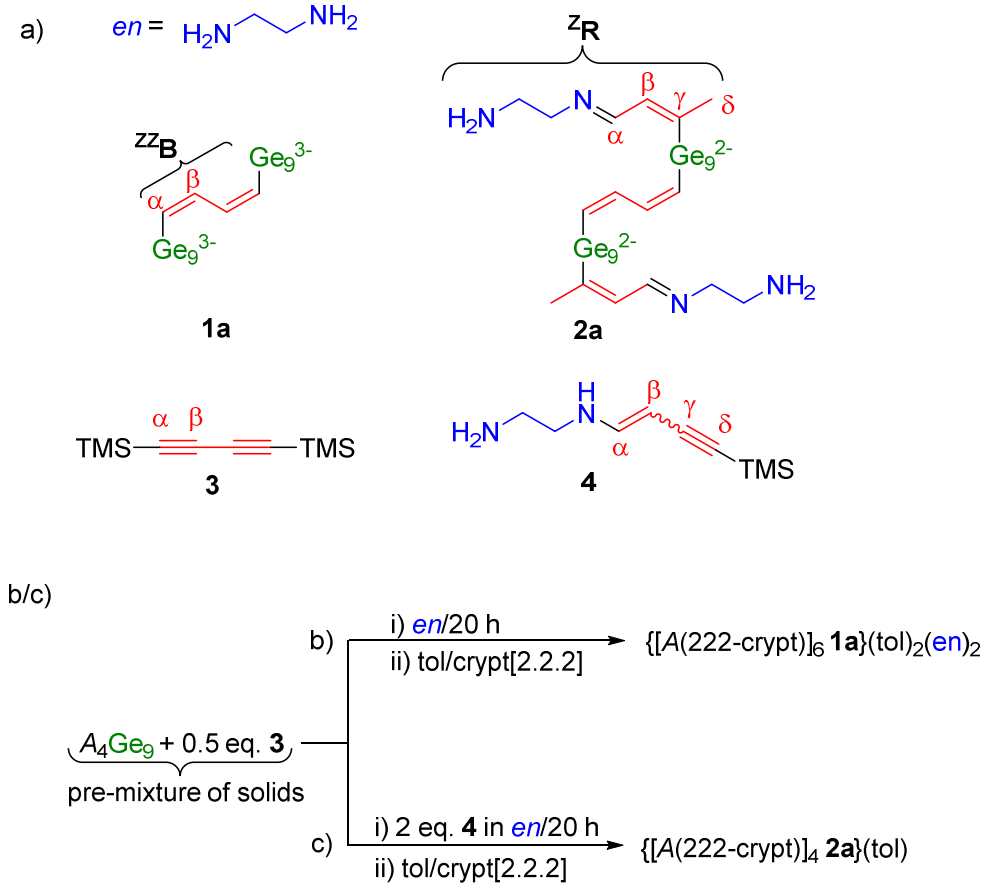

Scheme 1. a) The chemical structures of $[(Ge_9)–(^{ZZ}\mathbf{B})–(Ge_9)]^{6–}$ (**1a**), $[(^{Z}\mathbf{R})–(Ge_9)–(^{ZZ}\mathbf{B})–(Ge_9)–(^{Z}\mathbf{R})]^{4–}$ (**2a**), 1,4-bis(trimethylsilyl)butadiyne (**3**) and 1-trimethylsilyl-7-amino-5-aza-hepta-3-en-1-yne (**4**). b/c) Synthetic protocols for b) $\{A(222\text{-crypt})]_6$ **1a**$\}\cdot(tol)_2\cdot(en)_2$ and c) $\{A(222\text{-crypt})]_4$ **2a**$\}\cdot(tol)$. c) The solution of **4** in *en* was prepared by reacting **3** with water-free *en* for 5 h according to [6].

Crystal structures.

In the crystal structure of $\{Rb(222\text{-crypt})]_6$ **1a**$\}\cdot(tol)_2\cdot(en)_2$, six $[Rb(222\text{-crypt})]^+$ complexes formally assign a six fold negative charge to the cluster anion (Table 1 and Figure S1).[17] The anionic entity **1a** appears in the crystal structure as disordered Ge_9 units, between which a zigzag-chain of four carbon atoms (C1/C2/C2^i/C1^i, occupancy 87%) is located (Figure S2a). The anionic entity is arranged around a crystallographic inversion center, which is located in the middle of the central C2-C2^i bond. For the C1/C2/C2^i/C1^i-chain, bond lengths of 1.343(1) Å (C1-C2) and 1.447(2) Å (C2-C2^i), indicate double and single bonds, respectively.[18-19] The double bonds are in *Z* configuration, giving a (1Z,3Z)-buta-1,3-dien-1,4-diyl functionality (^{ZZ}**B**) with s-*trans* conformation.

For the disordered Ge_9 units, three superimposing and differently orientated components were identified: **I** (61.9%), **II** (25.1%) and **III** (13%) (Figure S2b).

Between the cluster-pairs **I/I^{i}**, **II/II^{i}** and **III/III^{i}**, the shortest Ge-Ge^{i} distances are 6.376 Å (Ge1-Ge1^{i}), 6.583 Å (Ge10-Ge10^{i}) and 6.582 Å (Ge19-Ge19^{i}), respectively (Figure S3). Ge-Ge distances in that range are typical for planar s-*trans* [Ge-(**^{ZZ}B**)-Ge$_9$] fragments [20], pointing to a superposition of three conformers of **1a**, differing by the cluster orientations and spatial location around the inversion center.

Ge–C distances of 2.001(9) Å (Ge1-C1) and 1.918(9) Å (Ge1-C10) (covalent Ge-C(sp^2) single bonds: 1.9-2.0 Å[10, 19]) as well as Ge1/C1/C2 and Ge10/C1/C2 angles of 130.1° and 139.1° indicate that **I** (61.9%) and **II** (25.1%) are connected to the C1/C2/C2^{i}/C1^{i} chain (87%), which is not the case for **III** [d(Ge19-C1) = 2.703 Å, ∢(Ge19/C1/C2) = 109°] (further structural parameters see Table S1). Correspondingly, the Ge1/Ge1^{i} (61.9%) and Ge10/Ge10^{i} (25.7%) atoms of **I/I^{i}** and **II/II^{i}** together with the C1/C2/C2^{i}/C1^{i} chain (87%) correspond to the s-*trans* [Ge–(**^{ZZ}B**)–Ge] subunits of the conformers **1a^{I}** (61.9%) (Figure 1a/b) and **1a^{II}** (25.1%) (Figure S2/3), respectively.[21] The **^{ZZ}B** bridges of **1a^{I}** and **1a^{II}** are almost identically located around the inversion center, and in the crystal structure solely a superposition, which is the C1/C2/C2^{i}/C1^{i} chain, appears.[22]

For the majority component **1a^{I}** the Ge–Ge distances of cluster **I** are in the range from 2.476(2) Å to 2.857(5) Å, (details see Table S1/S3). Cluster **I** is best described as a distorted monocapped quadratic antiprism with the square planes being defined by the atoms Ge1 to Ge4 [d(Ge-Ge) = 2.476(2) – 2.673(5) Å] and Ge5 to Ge8 [d(Ge-Ge) = 2.757(5) – 2.857(5) Å]. The deviation of the cluster shape from a tricapped trigonal prism with D_{3h} symmetry is indicated by maximum torsion angles of 178.8° and 179.8° for square planes Ge1 to Ge4 and Ge5 to Ge8 as well as the heights of the central trigonal prism of 3.390 Å (Ge1-Ge3), 2.767 Å (Ge6-Ge7) and 2.757 Å (Ge5-Ge8), respectively. The square plane Ge1 to Ge4 is significantly compressed at the atom Ge1, which bears the **^{ZZ}B** functionality: d(Ge1-Ge2)= 2.476(2) Å and d(Ge1-Ge4) = 2.499(4) Å *versus* d(Ge3-Ge2) = 2.656(6) Å and d(Ge3-Ge4) = 2.673(5) Å. Correspondingly, **I** adopts C_S symmetry and derives from a C_{4v} symmetric mono-capped square antiprism with 22 skeleton-electrons, by compression of the Ge1/Ge2/Ge3/Ge4 square plane at Ge1.[14, 23]

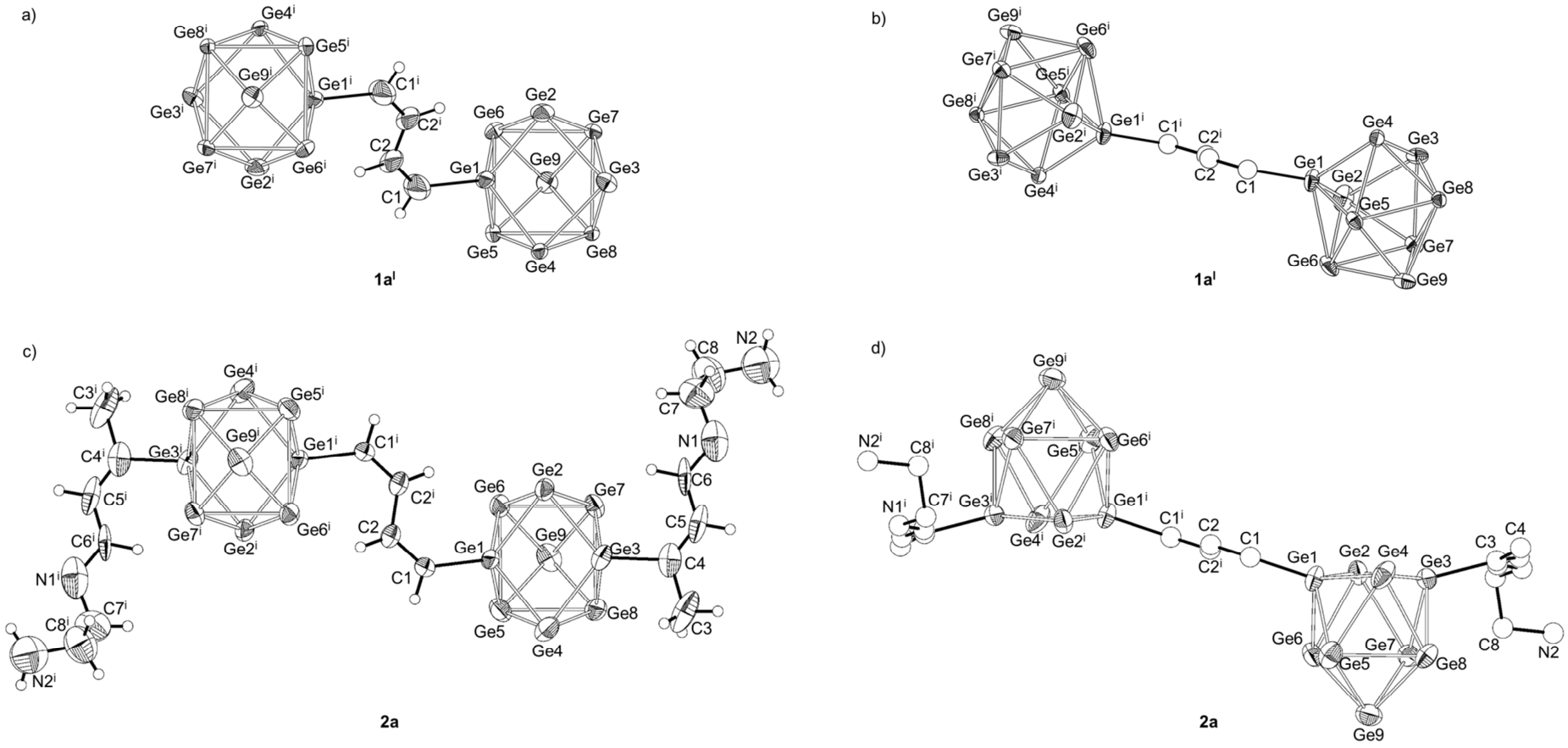

Figure 1. X-ray structures of a/b) **1a**^{I} and c/d) **2a**. Views: a/c) perpendicular and b/d) parallel to the [Ge-^{zz}**B**-Ge] plane. Thermal ellipsoids are shown at a probability level of 50%. b/c) carbon and nitrogen atoms are shown as empty spheres. Hydrogen atoms are omitted for clarity.

In addition, orange crystals of the compound {Rb(222-crypt)]$_4$ **2a**}·(tol) (Scheme 1c) were characterized by X-ray structure analysis. Thereby it turned out that {Rb(222-crypt)]$_4$ **2a**}·(tol) is isotypic to the previously reported structure of {K(222-crypt)]$_4$ **2a**}·(tol).[6, 16] Both compounds contain molecule **2a** (Figure 1c/d), which is four fold negatively charged and located around a crystallographic inversion center. The anion consists of two Ge_9 units, which are connected by a ^{ZZ}**B** bridge and each cluster bears a ^{Z}**R** side chain. The structural parameters of **2a** in both {Rb(222-crypt)]$_4$ **2a**}·(tol) and {K(222-crypt)]$_4$ **2a**}·(tol) are almost identical (Table S1). The open square Ge1 to Ge4 of the Ge_9 unit is compressed at the atoms Ge1 and Ge3, which bear the ^{ZZ}**B** and ^{Z}**R** functionalities. Accordingly the cluster adopts C_{2v} symmetry and derives from a C_{4v} symmetric monocapped square antiprism with 22 skeleton-electrons which is compressed at the atoms Ge1 and Ge3 of the open square face. In comparison to **1a**, the anionic entity **2a** is not disordered. It is reasonable to attribute the lack of disorder in case of molecule **2a** to its ^{Z}**R** side chains, prohibiting free rotation of the clusters around the s-*trans*-[Ge–^{ZZ}**B**–Ge] subunit.

Raman spectroscopy.

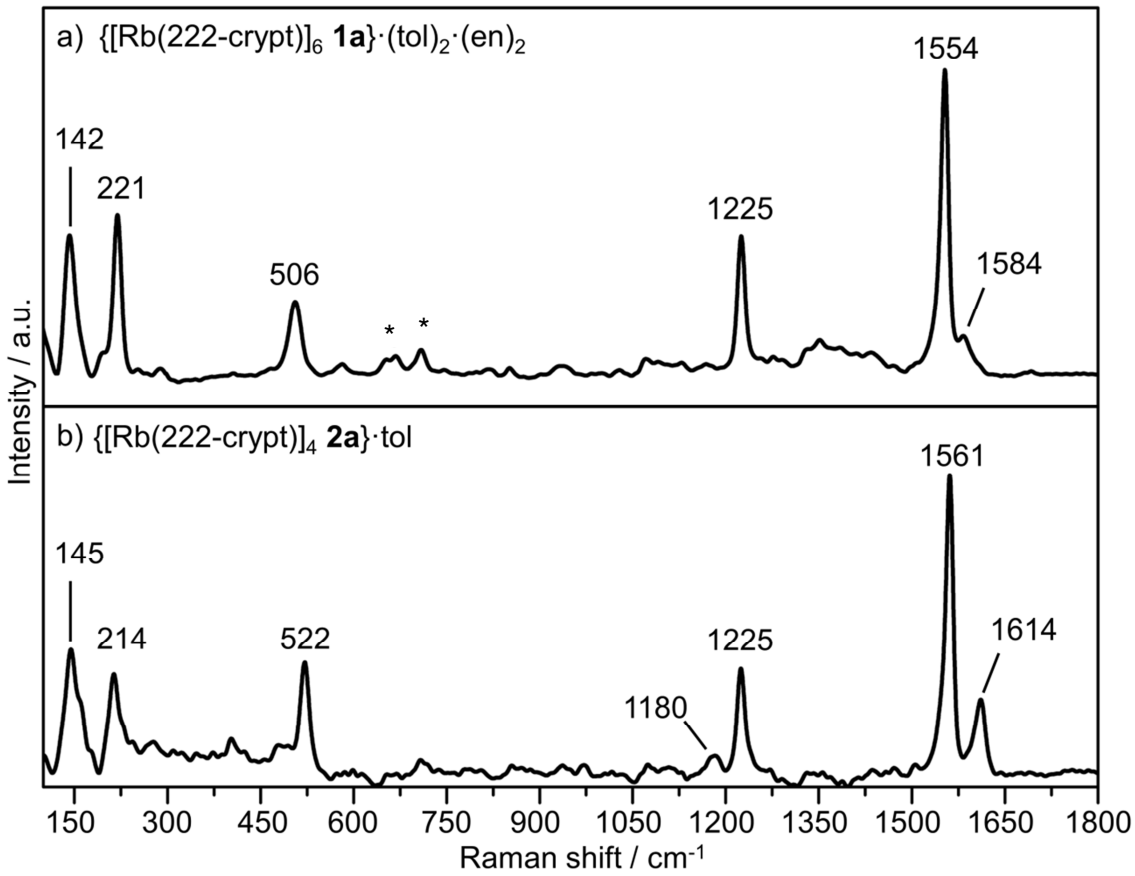

Figure 2. The Raman spectra of single crystals of a) {Rb(222-crypt)]$_6$ **1a**}·(tol)$_2$·(en)$_2$ and b) {Rb(222-crypt)]$_4$ **2a**}·(tol). The most intensive signals are labeled with the corresponding Raman shift. Unknown signals are marked with *

To obtain the vibrational spectra of **1a** and **2a**, single crystals of {Rb(222-crypt)]$_6$ **1a**}·(tol)$_2$·(en)$_2$ and {Rb(222-crypt)]$_4$ **2a**}·(tol) were investigated by Raman spectroscopy (Figure 2). Intensive signals at 142, 221 cm^{-1} and 145, 214 cm^{-1} correspond to the Ge_9 units of the anionic entities **1a** and **2a**, respectively.[24-26] The covalent connections of the Ge_9 units to carbon atoms are displayed by signals at 506 and 522 cm^{-1}, which are typical for Ge–C valence vibrations.[27-30] Moreover, intensive signals at 1225 and 1554 cm^{-1} as well as 1225 and 1561 cm^{-1} are indicative for symmetric C=C and C–C valence vibrations of the ^{ZZ}**B** functionality, respectively.[31-32] In case of {Rb(222-crypt)]$_4$ **2a**}·(tol) additional signals at 1180 and 1614 cm^{-1}, indicate C–C as well as C=C and C=N valence vibrations of the ^{Z}**R** side chain.

***In situ* Studies.**

In order to shed more light on the formation of **1a** and **2a** we performed *in situ* NMR and ESI-MS investigations on mixtures containing A_4Ge_9, **3** and/or **4** in water-free *en*.[33] In the first step reaction mixtures analogous to those, leading to the isolation of {*A*(222-crypt)]$_6$ **1a**}·(tol)$_2$·(en)$_2$ (Scheme 1b) were investigated in dependence of reaction time and stoichiometric ratio between A_4Ge_9 and **3** (Figure S9-S11). According to these investigations the reaction of **3** with an excess of clusters (A_4Ge_9/**3** = 1/0.25, 1/0.5) in water-free *en* results in the formation of the Zintl dyads [(Ge$_9$)–**A'**]$^{3-}$ (**5a**) (**A'** = 1,4-bis(trimethylsilyl)-buta-1-en-3-yne-1-yl)[34] and [(Ge$_9$)–(**^{E}A**)]$^{3-}$ (**6a**) (**^{E}A** = (1*E*)-4-trimethylsilyl-buta-1-en-3-yne-1-yl)] in a 20/80 ratio within less than 30 min (Scheme 2a). With increasing reaction time the concentration of **5a** and **6a** decreases, whereas species [(Ge$_9$)-(**^{ZZ}B**)-(Ge$_9$)]$^{6-}$ (**1a**) and [(Ge$_9$)-(**^{EZ}B**)-(Ge$_9$)]$^{6-}$ (**7a**) emerge. After 20 h, **5a** and **6a** are completely transformed to **1a** and **7a** (**1a**/**7a** = 20/80), respectively. Evaluation of ^{1}H NMR integrals (Figure S11a) indicates that **1a** originates from **5a**, whereas **7a** arises from **6a**. Even though **7a** is the major product, the latter does not crystallize under the applied conditions.

From a mechanistic point of view, **1a** forms by a step by step addition of two [Ge$_9$]$^{4-}$ clusters in *anti*-fashion to the terminal carbon atoms of **3**.[12, 35] According to time resolved ^{1}H NMR, the first cluster-addition in α position proceeds very fast and results in **5a** (*anti*-product). In a much slower consecutive reaction, **5a** adds a second cluster at the δ carbon atom, giving **1a** (*anti*, *anti*-product).[36]

The formation of the *anti*-products **5a** and **1a** is expected [12], whereas the more dominant occurrence of *syn*-products **6a** and **7a** seems contradictory at first glance. Even though examples are scarce, reactions of [E_9]$^{4-}$ with conjugated alkynes can lead to *syn*-products.[37] It is feasible that the addition of a single [Ge$_9$]$^{4-}$ to **3** results in a *trans*-configurated alkenyl-anion (Scheme 2a: **Int-1**), which switches into *cis*-geometry (Scheme 2a: **Int-2**) and forms **6a** after protonation and TMS exchange. Subsequently, slow addition of a second cluster in *anti*-fashion to the δ carbon atom of **6a** and TMS exchange result in the final *syn*, *anti*-product **7a**.

The formation of **1a** and **7a** requires an excess of clusters, as two [Ge$_9$]$^{4-}$ units per one molecule **3** are added. Indeed **1a** and **7a** do not form in mixtures with an excess of **3** (A_4Ge_9/**3** = 1/2) (Figure S11b) and solely species **6a** and/or [(**^{E}A**)–(Ge$_9$)–(**^{E}A**)]$^{2-}$ (**8a**) are present. Layering of such mixtures with toluene/cryptand[2.2.2] did not yield crystals.

The absence of **4** in reaction mixtures prepared according to Scheme 1b points out, that nucleophilic addition of $[Ge_9]^{4-}$ to **3** is favored over *en*-addition, and formation of side chains **R** is not possible under such conditions. To shed also more light on the formation of **2a** and in particular its side chains ^{Z}**R** we performed investigations on the reactivity of $[Ge_9]^{4-}$ towards **4**, which was separately prepared by the reaction of **3** with water-free *en* in the absence of clusters.[6, 38] According to NMR and ESI-MS the reaction of $[Ge_9]^{4-}$ with **4** in water-free *en* (Figure S13/14/18) leads to the Zintl anions $[(Ge_9)–(\mathbf{R})]^{3-}$ (**12a**) and $[(\mathbf{R})–(Ge_9)–(\mathbf{R})]^{2-}$ (**13a**) (**R** = 7-amino-5-aza-hepta-2,4-dien-2-yl) as well as species **10** (Scheme 2b) [39]. The formation of **12a** is attributed to regioselective addition of $[Ge_9]^{4-}$ to the most electrophilic carbon atom γ of **4**. [40] In an analogous reaction **13a** is formed by addition of the clusters of **12a** to the γ carbon of **4**. In contrast to the reaction of $[Ge_9]^{4-}$ with **3** (Scheme 1b), species **10** arises as a dominant side product from the reaction of clusters with **4**. **10** is the formal result of a twofold *en*-addition to **3** in α and γ position. However, in the absence of water, *en* is unable to add to **4** [6, 38], pointing to the addition of the stronger nucleophile ethylenediamide, which has been postulated as a side product in additions of clusters to alkynes. Indeed the reaction of potassium ethylenediamide (preparation see experimental section) with **4** quantitatively forms species **10** in water-free en.[41] Hence, the latter provides the first evidence for the postulated *en* deprotonation in additions of $[E_9]^{4-}$ Zintl clusters to alkynes.

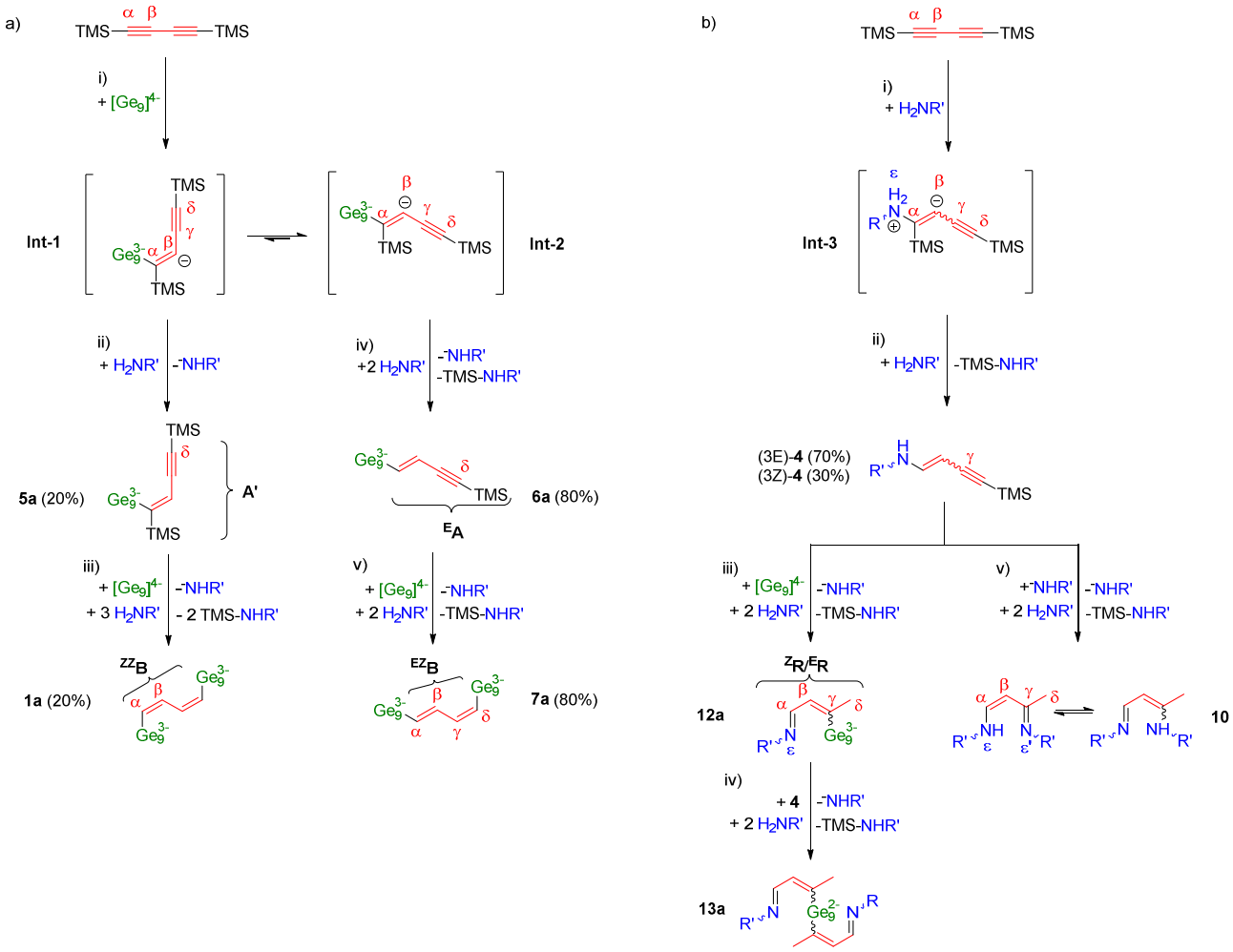

Scheme 2. a) Formation of the buta-1,3-dien-1,4-diyl (**B**) bridge: i) Addition of $[Ge_9]^{4-}$ to the α carbon of **3** in *anti*-fashion, leading to the alkenyl-anion **Int-1** (*trans*-geometry), which is supposed to be in equilibrium with **Int-2** (*cis*-geometry). ii/iv) Protonation of the alkenyl-anions **Int-1** and **Int-2** by *en* as well as TMS exchange in case of **Int-2**, leading to **5a** and **6a**, respectively. iii/vi) Addition of a second $[Ge_9]^{4-}$ cluster to the δ carbon of **5a** and **6a** in *anti*-fashion (intermediate alkenyl-anions are not shown), resulting the Zintl triads **1a** (*anti*,*anti*-product) and **7a** (*syn*,*anti*-product); b) Formation of the 7-amino-5-aza-hepta-2,4-dien-2-yl (**R**) side chains and the 1,9-di-amino-4-methyl-3,7-di-aza-nonadien (**10**) side product: i) Addition of the amino-functionality of *en* in *anti* and *syn*-fashion to the α carbon of **3** giving the alkenyl-anions **Int-3** (*cis* and *trans*-geometry). ii) Assumed protonation of the alkenyl-anions **Int-3** by a prototropic shift from the ε nitrogen to the β carbon, resulting in **4**. iii/iv) Addition of $[Ge_9]^{4-}$ and **12a** to the γ carbon of **4**, resulting in **12a** and **13a**, respectively. It is reasonable that first the enamine-forms of **12a** and **13a** are formed which tautomerize to the corresponding imines [6]. v) Self-sustaining formation of **10** by addition of an amide to the γ position of **4** under release of another amide.

The Zintl anions $[(Ge_9)–(^{ZZ}\mathbf{B})–(Ge_9)]^{6-}$ (**1a**) and $[(Ge_9)–(\mathbf{R})]^{3-}$ (**12a**) can be considered as building blocks for Zintl triad **2a**, and we tested whether it is possible to stepwise build up the latter by addition of **4** and **3** to reaction solutions containing **1a** and **12a**, respectively. However, none of the mixtures showed NMR signals of **2a** (Table S9/S10 and Figure S12/16a) [42] and also layering of such solutions with toluene/cryptand[2.2.2] did not yield crystals of {*A*(222-crypt)]$_4$ **2a**}·(tol). As these

experiments deal with reaction solutions a stepwise formation of **2a** with intermediately occurring **1a** and/or **12a** cannot be excluded.

On the other hand from the synthetic protocol for {*A*(222-crypt)]$_4$ **2a**}·(tol) (Scheme 1c) it follows that **2a** readily forms if the [Ge$_9$]$^{4-}$ clusters are exposed simultaneously to **3** (0.5 eq.) and **4** (2 eq.). In the NMR spectrum of such reaction solutions (Figure S16b/17) signals of ^{ZZ}**B** and **R** are visible in the expected 1/1 integral ratio besides dominant signals of **10**. By applying instead 1 eq. of **4** the integral ratio between ^{ZZ}**B** and **R** becomes > 1 and from the corresponding reaction solutions with *A* = Rb both {*A*(222-crypt)]$_6$ **1a**}·(tol)$_2$·(en)$_2$ and {*A*(222-crypt)]$_6$ **2a**}·(tol) crystallize by layering with cryptand[2.2.2]. Due to consumption of **4** by the self-sustaining formation of **10**, a surplus of **4** is necessary to promote formation of **2a** and avoid formation of **1a**. The time dependent NMR spectra show that formation of **2a** proceeds within < 30 min and is therefore much faster than formation of **1a**. From the experimental results we conclude that in the reaction **3** and **4** compete for [Ge$_9$]$^{4-}$ Zintl anions, and only if both alkynes are simultaneously present, **2a** can form. A bunch of intermediates including also **1a** and **12a** are imaginable, however due to the fast formation of **2a** their observation was not possible by means of *in situ* NMR.

Conclusion

Our investigations emphasize the diversity of Ge$_9$ clusters as building blocks for the rational syntheses of Zintl anions with extended delocalized π-electron systems. Similar to fullerenes Zintl clusters are able to form a bunch of Zintl dyads and triads, pointing to potential applications in spintronics and catalysis. In particular the 7-amino-5-aza-hepta-2,4-dien-2-yl side chains might be used as tethers for grafting the triads to functionalized surfaces. Besides, it is feasible to introduce such molecules in metal organic reactions and coordinate transition metal centers at the π-bonds. From such compounds a multifaceted and valuable redox-chemistry can be expected. In the next step it is necessary to transfer the Zintl triads into less polar solvents in order to further increase the field of possible organic transformations.

Experimental Section

General Methods. All manipulations were carried out under a purified argon atmosphere using a glove box and standard Schlenk technique. The Zintl compounds of the nominal composition A_4Ge_9 (A = K, Rb) were synthesized by heating a stoichiometric mixture of the elements K, Rb and Ge (99.999% Chempur) at 650°C for 48 h in an iron autoclave.[43] 1,4-bis(trimethylsilyl)butadiyne (Alfa Aesar 98%) was used as received. Toluene was dried over molecular sieve (4 Å) in a solvent purificator (MBraun MB-SPS). Cryptand[2.2.2] (Merck) was dried in vacuum for 8 h.

Purification of *en*. *En* (Merck) with an initial water content of ≤ 1% was refluxed over calcium hydride (Merck) and freshly collected prior to use. Water free *en* was obtained after refluxing for 72 h. The sample tubes were thoroughly cleaned and dried at 120°C immediately before the *en* collection. *En* containing trace amounts of water was obtained after refluxing for 2-6 h. The sample tubes were stored under ambient conditions. The finding that water significantly influences the reaction of **3** with *en* was exploited to qualitatively test its water-content. Therefore, from each freshly distilled *en*-batch an aliquot was mixed with **3** and the reaction was monitored by NMR. If **10**/**11** did not form within 24 h the *en* was considered as water-free.

Preparation of (3*Z*/3*E*)-7-amino-1-(trimethylsilyl)-5-aza-hepta-3-en-1yne (4) [6]. Solutions with 60, 120, 240 µmol **4**/ml *en* were obtained by reacting 23.4 mg (120 µmol), 46.7 mg (240 µmol) and 93.4 mg (480 µmol) of **3** each with 2 ml *en* in a Schlenk tube for 5-20 h. Thereby pale yellow colored transparent solutions were obtained. Prior to application of **4** for further syntheses the solutions were filtered over glass wool in order to remove traces of unreacted **3**. ^{1}H NMR (500 MHz, ethylenediamine (non-deuterated), 296 K): Isomer ^{Z}**4** δ(ppm) 6.40 (dd, *J* = 8.6 Hz, 12.2 Hz, 1H, -NH-C*H*=CH-), 3.96 (d, *J* = 8.6 Hz, 1H, -NH-CH=C*H*-), 6.67 (s(broad), -N*H*-CH=CH-), 3.21 (pseudo q, *J* = 6.0 Hz, 2H, NH_2-CH_2-CH_2-), 2.76 (NH_2-CH_2-CH_2-, covered by en and revealed by COSY), 0.23 (s, 9H, C-Si-(CH_3)$_3$-); Isomer ^{E}**4**: δ(ppm) 6.91 (dd, *J* = 13.6 Hz, 7.4 Hz, 1H, -NH-C*H*=CH-), 4.23 (d, *J* = 13.6 Hz, 1H, -NH-CH=C*H*-), 7.54 (s(broad), 1H, -N*H*-CH=CH-), 2.96 (pseudo q, *J* = 6.0 Hz, 2H, NH_2-CH_2-CH_2-), 2.79 (covered by *en* and revealed by COSY, NH_2-CH_2-CH_2-), 0.19 (s, 9H, C-Si-(CH_3)$_3$-);

Synthesis of [Rb(222-crypt)]$_6$[Ge$_9$–CH=CH-CH=CH–Ge$_9$]·(tol)$_2$·(en)$_2$. A mixture of Rb_4Ge_9 (74.7 mg, 75 µmol) and **3** (3.7 mg, 19 µmol, 0.25 eq.) was dissolved in 1.25 ml *en* and stirred for 23 h. The dark brown reaction solution was filtered over glass fibers and an aliquot of 0.8 ml was layered with a solution of cryptand[2.2.2] (72.3 mg, 192µmol, 4 eq.) in toluene (3.2 ml). Bundles of red crystals of {Rb(222-crypt)]$_6$ **1a**}·(tol)$_2$·(en)$_2$ were obtained after two weeks and used for X-ray structure analysis (Table 1) and Raman-spectroscopy. Raman υ [cm^{-1}]: 142 (s, Ge$_9$-cluster), 221 (s, Ge$_9$-cluster, breathing mode), 506 (m, *exo*-Ge–C), 658 (w), 709 (w), 1225 (s, ^{ZZ}**B**, C–C valence), 1554 (vs, ^{ZZ}**B**, C=C valence), 1584 (w).

Synthesis of [Rb(222-crypt)]$_4$[RGe$_9$-CH=CH-CH=CH-Ge$_9$R]·tol (R = (2Z,4E)-7-amino-5-aza-hepta-2,4-dien-2-yl). In a Schlenk tube 1.3 ml of **4**/*en*-solution (120 µmol/ml, 156 µmol, 2 eq.) was dropped onto a mixture of Rb_4Ge_9 (77.6 mg, 78 µmol, 1 eq.) and **3** (7.6 mg, 39 µmol, 0.5 eq.). Immediately, a dark-red suspension formed, which was stirred for 18 h. After stirring, an orange-red reaction solution was obtained and filtered over glass fibers. An aliquot of 1 ml was layered with a solution of cryptand[2.2.2] (90.4 mg, 240µmol, 4 eq.) in toluene (4 ml). After one week many orange crystals of {Rb(222-crypt)]$_4$ **2a**}·tol were found in the Schlenk tube and used for X-ray structure analysis (Table 1), Raman- and NMR-spectroscopy. Raman υ [cm^{-1}]: 145 (s, Ge$_9$-cluster), 214 (s, Ge$_9$-cluster, breathing), 522 (m, *exo*-Ge-C), 1180 (w, ^{Z}**R**, C-C valence), 1225 (s, ^{ZZ}**B**, C-C valence), 1561 (vs, ^{ZZ}**B**, C=C valence), 1614 (m, ^{Z}**R**, C=N/C=C valence). ^{1}H NMR (500 MHz, acetontirile-d$_3$, 296 K), δ (ppm): 10.15 (d, *J* = 8.9 Hz, 2H, ^{Z}**R**: H$_3$C-C(Ge$_9$)-CH=C*H*-C=N-), 8.78 (covered by py revealed by COSY, ^{ZZ}**B**: (Ge$_9$)-C*H*=CH-CH=C*H*-(Ge$_9$)), 7.22 (covered by py revealed by COSY, ^{ZZ}**B**: (Ge$_9$)-CH=C*H*-C*H*=CH-(Ge$_9$)), 6.93 (d, *J* = 8.9 Hz, 2H, ^{Z}**R**: H$_3$C-C(Ge$_9$)-C*H*=CH-C=N-), 3.81 (t, *J* = 5.6 Hz, 4H, ^{Z}**R**: H$_2$N-CH$_2$-C*H*$_2$-N=C-), 3.0 (pseudo q, *J* = 6.1/7.3 Hz, 4H, ^{Z}**R**: H$_2$N-C*H*$_2$-CH$_2$-N=C-), 2.48 (s, 6H, ^{Z}**R**: *H*$_3$C-C(Ge$_9$)-CH=CH-C=N-), 1.43 (covered and revealed by COSY, ^{Z}**R**: *H*$_2$N-CH$_2$-CH$_2$-N=C-), 7.2-7.3 (m, tol, Ar*H*), 2.23 (s, tol, -C*H*$_3$), 3.49 (m, crypt), 3.42 (m, crypt), 2.43 (m, crypt);

Synthesis of [K(222-crypt)]$_6$[Ge$_9$–CH=CH-CH=CH–Ge$_9$]·(tol)$_2$·(en)$_2$. A mixture of K_4Ge_9 (85.0 mg, 105 µmol) and **3** (5.1 mg, 26.3 µmol, 0.25 eq.) was dissolved in 1.75 ml *en* and stirred for 24 h. The dark red-brown reaction solution was filtered over glass fibers and an aliquot of 0.75 ml was layered with a solution of cryptand[2.2.2]

(67.8 mg, 180µmol, 4 eq.) in toluene (3 ml). After one week red crystals of {K(222-crypt)]$_6$ **1a**}·(tol)$_2$·(en)$_2$ were obtained and used for X-ray structure analysis (Table 1).

Synthesis of [K(222-crypt)]$_4$[RGe$_9$–CH=CH-CH=CH–Ge$_9$R]·tol (R = (2Z,4E)-7-amino-5-aza-hepta-2,4-dien-2-yl). In a Schlenk tube 1.3 ml of **4**/*en*-solution (120 µmol/ml, 156 µmol, 2 eq.) was dropped onto a mixture of K_4Ge_9 (63.2 mg, 78 µmol, 1 eq.) and **3** (7.6 mg, 39 µmol, 0.5 eq.). Immediately after addition of the reactants, a brown suspension formed which turned into a deep-red solution after stirring for 18 h. The reaction solution was filtered over glass fibers and an aliquot of 1 ml was layered with a solution of cryptand[2.2.2] (90.4 mg, 240µmol, 4 eq.) in toluene (4 ml). After three weeks many orange crystals of {K(222-crypt)]$_4$ **2a**}·tol [6] were found besides low amounts of black crystals of [K(222-crypt)]$_2$[Ge$_9$] [44]. The crystals were identified by unit cell determination.

Synthesis of KNH(CH$_2$)$_2$NHK. In a Schlenk tube elemental K (100 mg, 256 µmol) was added to a catalytical amount of Fe_2O_3. Subsequently, 2 ml thoroughly dried *en* were added slowly. The mixture was stirred for 17 h, whereupon the potassium completely dissolved under gas formation and a brownish-yellow colored solution was obtained. The unreacted solvent was removed in vacuum and a brownish-white powder was obtained. The powder is very moisture sensitive and immediately deliquesces if it is brought to ambient air. CHN-Analysis (weight-%): 18.2 (C), 3.8 (H), 19.6 (N), 58.4 (K, calculated); ^{1}H NMR (400 MHz, acetonitrile-d$_3$, 296 K), δ(ppm): 2.53 (s, -C*H*$_2$); The protons of the –N*H* groups are invisible.[45] ^{13}C NMR (400 MHz, acetonitrile-d$_3$, 296 K), δ(ppm): 45.7 (-*C*H$_2$); NMR data of *en* in acetonitrile-d$_3$: ^{1}H NMR (400 MHz, acetonitrile-d$_3$, 296 K), δ(ppm): 2.55 (s, -C*H*$_2$), 1.04 (s(broad), -N*H*$_2$); ^{13}C NMR (400 MHz, acetonitrile-d$_3$, 296 K), δ(ppm): 46.2 (-*C*H$_2$);

Table 1. Crystallographic data of compounds

Compound	{[Rb(222-crypt)]$_6$1a}·(en)$_2$(tol)$_2$	{[K(222-crypt)]$_6$1a}·(en)$_2$(tol)$_2$	{[Rb(222-crypt)]$_4$2a}·tol
Formula	$C_{129.45}H_{251.45}N_{16}O_{36}Ge_{18}Rb_6$	$C_{129.37}H_{251.37}N_{16}O_{36}Ge_{18}K_6$	$C_{92.91}H_{175.82}N_{11.3}O_{24}Ge_{18}Rb_4$
fw (g·mol^{-1})	4427.8	4148.5	3520.99
space group (no)	$P\bar{1}$ (2)	$P\bar{1}$ (2)	$P\bar{1}$ (2)
a (Å)	14.5699(4)	14.5799(2)	11.9068(2)
b (Å)	15.5121(4)	15.4866(2)	12.8103(2)
c (Å)	22.1316(6)	22.1328(3)	24.5724(6)
α (deg)	75.148(2)	75.386(1)	104.534(2)
β (deg)	84.305(2)	84.145(1)	92.040(2)
γ (deg)	66.769(2)	66.815(2)	109.352(2)
V (Å^3)	4442.8(2)	4445.2(1)	3394.0(1)
Z	1	1	1
T (K)	100(2)	123(2)	123(2)
λ (Å)	0.71073	0.71073	0.71073
ρ_{calcd} (g·cm^{-3})	1.655	1.550	1.723
μ (mm^{-1})	4.70	3.20	5.41
collected reflections	143971	85505	69836
independent reflections	17443	16516	11894
R_{int}	0.050	0.075	0.094
parameters / restraints	1039 / 118	1039 / 125	688 / 30
R_1 [all data / $I>2\sigma(I)$]	0.080 / 0.049	0.106 / 0.055	0.136 / 0.085
wR_2 [all data / $I>2\sigma(I)$]	0.147 / 0.128	0.142 / 0.129	0.242 / 0.218
goodness of fit	1.062	0.935	1.036
max. / min. diff. el. density	1.34 / -1.24	0.99 / -0.72	2.91 / -1.31

X-ray Data Collection and Structure Determination: Single crystals were fixed on the top of a glas fiber with perfluorinated ether and positioned in a cold N_2 stream at 123 K. The single crystal X-ray diffraction data were recorded on an Oxford-Diffraction Xcalibur3 diffractometer (Mo-K_α radiation). All crystal structures were solved by Direct Methods using the SHELX software.[46] The positions of the hydrogen atoms were geometrically calculated and refined using a riding model. All non-hydrogen atoms were treated with anisotropic displacement parameters. CCDC-

xxx contains the supplementary crystallographic data for this paper. These data can be obtained free of charge from The Cambridge Crystallographic Data Centre via www.ccdc.cam.ac.uk/data_request/cif.

Raman spectroscopy: Raman measurements were performed on single crystals sealed in glass capillaries with a Raman microscopy spectrometer (Senterra Raman spectrometer: Bruker Corporation; diode laser: 785 nm, 1 mW).

Electrospray Ionization Mass Spectrometry (ESI-MS) Investigation: ESI-MS was done on a HCT mass spectrometer (Bruker Daltronic) in the negative ion mode (-). Measurement conditions: capillary voltage: 2.5kV, capillary exit: -180 V, drying gas temperature: 125 °C, injection rate: 240 µL/h.

Supporting Information. The Supporting Information contains detailed crystallographic material on the compounds {*A*(222-crypt)]$_6$ **1a**}·(tol)$_2$·(en)$_2$ and {*A*(222-crypt)]$_4$ **2a**}·(tol). Moreover, details on the *in situ* studies and detailed descriptions of NMR-data are given.

References

[1] S. C. Sevov, J. M. Goicoechea, *Organometallics* **2006**, *25*, 5678-5692;

[2] S. Scharfe, F. Kraus, S. Stegmaier, A. Schier, T. F. Fässler, *Angew. Chem. Int. Ed.* **2011**, *50*, 3630-3670; *Angew. Chem.* **2011**, *123*, 3712-3754;

[3] N. Martín, L. Sánchez, B. Illescas, I. Pérez, *Chem. Rev.* **1998**, *98*, 2527-2548;

[4] T. F. Fässler, *Angew. Chem. Int. Ed.* **2001**, *40*, 4161-4165; *Angew. Chem.* **2001**, *113*, 4289.

[5] J. M. Goicoechea, S. C. Sevov, *Inorg. Chem.* **2005**, *44*, 2654-2658.

[6] M. M. Bentlohner, W. Klein, Z. H. Fard, L.-A. Jantke, T. F. Fässler, *Angew. Chem. Int. Ed.* **2015**, *54*, 3748-3753; *Angew. Chem.* **2015**, *127*, 3819-3824.

[7] J. L. Segura, N. Martin, *Chem. Soc. Rev.* **2000**, *29*, 13-25;

[8] M. A. Lebedeva, T. W. Chamberlain, E. S. Davies, B. E. Thomas, M. Schröder, A. N. Khlobystov, *Beilstein J. Org. Chem.* **2014**, *10*, 332-343.

[9] Y. Kanai, J. C. Grossman, *Nano Lett.* **2007**, *7*, 1967-1972.

[10] M. W. Hull, S. C. Sevov, *Angew. Chem. Int. Ed.* **2007**, *46*, 6695-6698; *Angew. Chem.* **2007**, *119*, 6815-6818;

[11] M. W. Hull, S. C. Sevov, *Inorg. Chem.* **2007**, *46*, 10953-10955;

[12] M. W. Hull, S. C. Sevov, *J. Am. Chem. Soc.* **2009**, *131*, 9026-9037;

[13] M. W. Hull, S. C. Sevov, *Chem. Commun.* **2012**, *48*, 7720-7722;

[14] C. B. Benda, J.-Q. Wang, B. Wahl, T. F. Fässler, *Eur. J. Inorg. Chem.* **2011**, 4262-4269.

[15] M. W. Hull, A. Ugrinov, I. Petrov, S. C. Sevov, *Inorg. Chem.* **2007**, *46*, 2704-2708.

[16] Regarding the better quality of the present crystals, we assume that the potassium analogue of the same compound as reported in [6], {K(222-crypt)]$_4$ **2a**}·(tol)$_2$, does also contain one solvent molecule.

[17] The crystal structures of {K(222-crypt)]$_6$ **1a**}·(tol)$_2$·(en)$_2$ and {Rb(222-crypt)]$_6$ **1a**}·(tol)$_2$·(en)$_2$ are isotypic. In the main paper the structure of {Rb(222-crypt)]$_6$ **1a**}·(tol)$_2$·(en)$_2$ is discussed and for details on {K(222-crypt)]$_6$ **1a**}·(tol)$_2$·(en)$_2$ see supporting information chapter 1.

[18] E. V. Anslyn, D. A. Dougherty, *Modern Physical Organic Chemistry*, University Science, **2006**.

[19] B. Cordero, V. Gomez, A. E. Platero-Prats, M. Reves, J. Echeverria, E. Cremades, F. Barragan, S. Alvarez, *Dalton Trans.* **2008**, 2832-2838.

[20] In [K(222-crypt)]$_4$[RGe$_9$-CH=CH-CH=CH-Ge$_9$R]·(tol) [6] the distance between the Ge atoms of the s-*trans*[(Ge)-(**^{ZZ}B**)-(Ge)] building unit is 6.281 Å.

[21] The orientations of the Ge$_9$ clusters of **1a^{I}** and **1a^{II}** differ by 165.4° with respect to the s-*trans* [(Ge)-(**^{ZZ}B**)-(Ge)] plane. Consequently **1a^{I}** and **1a^{II}** are rotational isomers. For details see Figure S4.

[22] Due to low contribution of **III** (13%) it is unclear from X-ray data whether there is another differently orientated **^{ZZ}B** bridge (giving conformer **1a^{III}**) or if **III** is a [Ge$_9$]$^{3-}$ clusters. (Figure S2/3). Comparison of the Raman spectra (Figure 2) of the disorderd {Rb(222-crypt)]$_6$ **1a**}·(tol)$_2$·(en)$_2$with the ordered {Rb(222-crypt)]$_4$ **2a**}·(tol) reveales, despite of additional signals from side chains **R** in the latter case, analogous signal patterns for both compounds. If also [Ge$_9$]$^{3-}$ was present in {Rb(222-crypt)]$_6$ **1a**}·(tol)$_2$·(en)$_2$ a distinct signal pattern should appear in comparison to {Rb(222-crypt)]$_4$ **2a**}·(tol), for which [Ge$_9$]$^{3-}$ is excluded by X-ray data. Therefore we conclude that cluster **III** corresponds to a third rotamer of **1a** and no [Ge$_9$]$^{3-}$ clusters are present in the crystal structure.

[23] For the clusters **II** and **III** of the minority components **1a^{II}** and **1a^{III}** the structural parameters are analogous to the majority component **1a^{I}** as these clusters were refined by the SAME instruction with Shelx97[46]. For details see Table S1.

[24] Signals of cryptand[2.2.2] are expected at 1040-1080 cm^{-1} (C-O-C, valence), 1374 cm^{-1} (C-N valence) and 1425-1475 cm^{-1} (C-C, valence) [30]

[25] H. G. Von Schnering, M. Baitinger, U. Bolle, W. Carrillo-Cabrera, J. Curda, Y. Grin, F. Heinemann, J. Llanos, K. Peters, A. Schmeding, M. Somer, *Z. Anorg. Allg. Chem.* **1997**, *623*, 1037-1039;

[26] M. Somer, W. Carrillo-Cabrera, E. M. Peters, K. Peters, H. G. v. Schnering, *Z. Anorg. Allg. Chem.* **1998**, *624*, 1915-1921.

[27] H. Siebert, *Z. Anorg. Allg. Chem.* **1952**, *271*, 75-75;
[28] E. R. Lippincott, M. C. Tobin, *J. Am. Chem. Soc.* **1953**, *75*, 4141-4147;
[29] L. A. Leites, S. S. Bukalov, A. V. Zabula, D. V. Lyubetskii, I. V. Krylova, M. P. Egorov, *Russ. Chem. B.* **2004**, *53*, 33-44;
[30] C. Benda, *Dissertation* Garching **2013**.
[31] E. Benedetti, M. Aglietto, S. Pucci, Y. N. Panchenko, Y. A. Pentin, O. T. Nikitin, *J. of Mol. Struct.* **1978**, *49*, 293-299;
[32] G. Gundersen, P. Klaeboe, A. Borg, Z. Smith, *Spectrochim. Acta A* **1980**, *36*, 843-852.
[33] Details on the *in situ* studies as well as detailed descriptions of the NMR data are given in the supporting information chapter 2.
[34] The double-bond configuration of **A'** cannot be clarified from NMR as no couplings to proton α are visible due to non-hydrogen atoms at the neighboring β and ε positions.
[35] As follows from mechanistic studies of *Sevov en* acts as a proton source in additions of clusters to alkynes and formation of amide as a side product has been postulated but not evidenced so far. Moreover, TMS groups are exchanged by protons from *en* and $NH_2(CH_2)_2NH$-TMS is formed as a second side product.[12]
[36] According to the ^{13}C chemical shifts for **A'** and ^{E}**A** {^{13}C chemical shifts [ppm] **A'**: 108.6 (γ), 89.4 (δ); ^{E}**A**: 108.9 (γ), 86.8 (δ)} (Table S5) the electrophilicity of the γ carbon is higher than for the δ carbon and nucleophilic additions are expected to proceed in γ position. However, it is feasible that steric demands and repulsive interactions between the negatively charged clusters prohibit cluster-addition to the more electrophilic γ position.
[37] M. M. Gillett-Kunnath, I. Petrov, S. C. Sevov, *Inorg. Chem.* **2010**, *49*, 721-729.
[38] In the absence of clusters the reaction of **3** with *en* quantitatively forms (3*Z*)-**4** and (3*E*)-**4** (*Z*/*E* = 30/70) by *anti*- and *syn*-addition of the amino-functionality of *en* to the α C-atom of **3** and exchange of TMS by protons (Figure S5).[6] The addition of *en* to **3** does not form amide as a side product since the proton which is required for protonation of the intermediate alkenyl-anion is provided by the incoming *en* itself (Scheme 2b: **Int-3**). Under water-free conditions **4** is the final product, whereas in presence of water-traces the reaction proceeds further to 1,9-di-amino-4-methyl-3,7-di-aza-nonadien (**10**) and 2,3-Dihydro-5-methyl-*H*-1,4-diazepine (**11**) [W. W. Paudler, A. G. Zeiler, J. Org. Chem., *34*, 999] (Figure S6/7) . Species **10** quickly isomerizes/tautomerizes in presence of water (Scheme S3), which can be derived from the broadened signals of the corresponding ^{1}H NMR spectrum.
[39] In the NMR spectrum four different isomers/tautomers of **10** appear by four distinct signals sets, which show characteristic coupling pattern (Figure S8/S13). That is in contrast to solutions of **10** in *en* containing water-traces, where the latter fast isomerizes/tautomerizes and only broadened ^{1}H NMR signals are visible (Figure S15). Under water-free conditions isomerization/tautomerization might be possible however is slow with respect to NMR time scale.
[40] According to the ^{13}C chemical shifts for **4** [^{13}C chemical shifts [ppm] (3*E*)-**4**: 109.1 (γ), 86.1 (δ); (3*Z*)-**2**: 109.1 (γ), 86.1 (δ)] (Table S5) the electrophilicity of the γ position is higher than for the δ position and nucleophilic additions preferably take place at the γ C atom.
[41] For the nucleophilic addition of ethylenediamide to **4** additional protons from *en* are required for protonation of the intermediate alkenyl-anion. Consequently the reaction itself forms another amide and the formation of **10** is self-sustaining and triggered by trace amounts of amide.
[42] In NMR spectra **2a** appears by signals of the **B** and **R** functionalities and the ratio of integrals for the olefinic protons is 1/1
[43] C. Hoch, M. Wendorff, C. Röhr, *J. Alloys Compd.* **2003**, *361*, 206-221.
[44] J. Åkerstedt, S. Ponou, L. Kloo, S. Lidin, *Eur. J. Inorg. Chem.* **2011**, *2011*, 3999-4005.
[45] B.-Y. Tay, C. Wang, L. P. Stubbs, C. Jacob, M. van Meurs, *J. Organomet. Chem.* **2011**, *696*, 3431-3435.
[46] G. M. Sheldrick, *Acta Crystallogr.* **2008**, *A64*, 112.

Acknowledgment

The authors are grateful to the SolTech (Solar Technologies go Hybrid) program of the State of Bavaria for its financial support. For the help with single crystal X-ray structure analysis and treating disorder in the crystal structures the authors are grateful to Dr. Wilhelm Klein and Dr. Viktor Hlukhyy. Moreover, the authors thank M. Sc. Herta Slavik for Raman-spectroscopic measurements as well as M. Sc. Lorenz Schiegerl for helping with the preparation of reaction solutions and NMR-investigations. The authors also thank Maria Weindl for NMR measurements and M. Sc. Christina Fischer for the help with ESI-MS.

TOC

Ge_9-Linker-Ge_9 Zintl Triads. The synthesis and characterization of the new Zintl triad $[Ge_9\text{-}CH{=}CH\text{-}CH{=}CH\text{-}Ge_9]^{6-}$ by the reaction of $[Ge_9]^{4-}$ with 1,4-bis(trimethylsilyl)butadiyne in ethylenediamine is presented. Moreover, we shed light on the formation of the Zintl triads $[Ge_9\text{-}CH{=}CH\text{-}CH{=}CH\text{-}Ge_9]^{6-}$ and $[R\text{-}Ge_9\text{-}CH{=}CH\text{-}CH{=}CH\text{-}Ge_9\text{-}R]^{4-}$ by *in situ* studies. For the first time the postulated deprotonation of ethylenediamine upon additions of clusters to alkynes was indirectly verified by NMR spectroscopy.

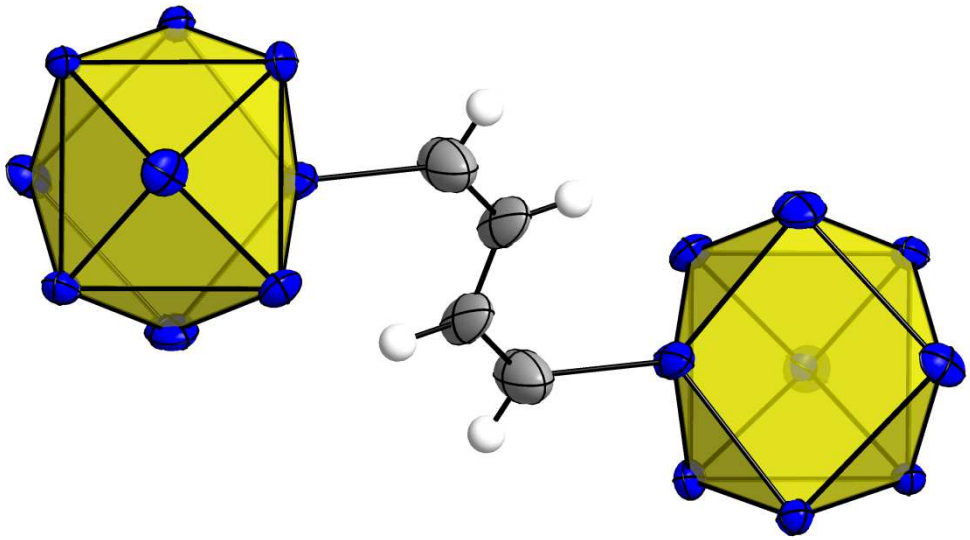

Supporting Information

On the formation of Ge_9-Linker-Ge_9 Zintl Triads - Syntheses and structures of $[Ge_9–CH=CH–CH=CH–Ge_9]^{6–}$ and $[R–Ge_9–CH=CH–CH=CH–Ge_9–R]^{4–}$

Manuel M. Bentlohner, Sabine Frischhut and Thomas F. Fässler*

Contents

Figures

1 Crystallographic details

Figure S1. Illustration of the unit cells of a) {K(222-crypt)]$_6$ **1a**}·(tol)$_2$·(en)$_2$, b) {Rb(222-crypt)]$_6$ **1a**}·(tol)$_2$·(en)$_2$ and c) {Rb(222-crypt)]$_4$ **2a**}·(tol). Only isomer **1a** is depicted and the minority components **1a^{II}** and **1a^{III}** are omitted for clarity. Ge_9 clusters are shown as dark-grey polyhedra. Atoms of the organic functionalities ^{ZZ}**B** and ^{Z}**R** are shown as empty spheres. Cryptand[2.2.2] and solvent molecules are shown schematically. Hydrogen atoms are omitted for clarity.

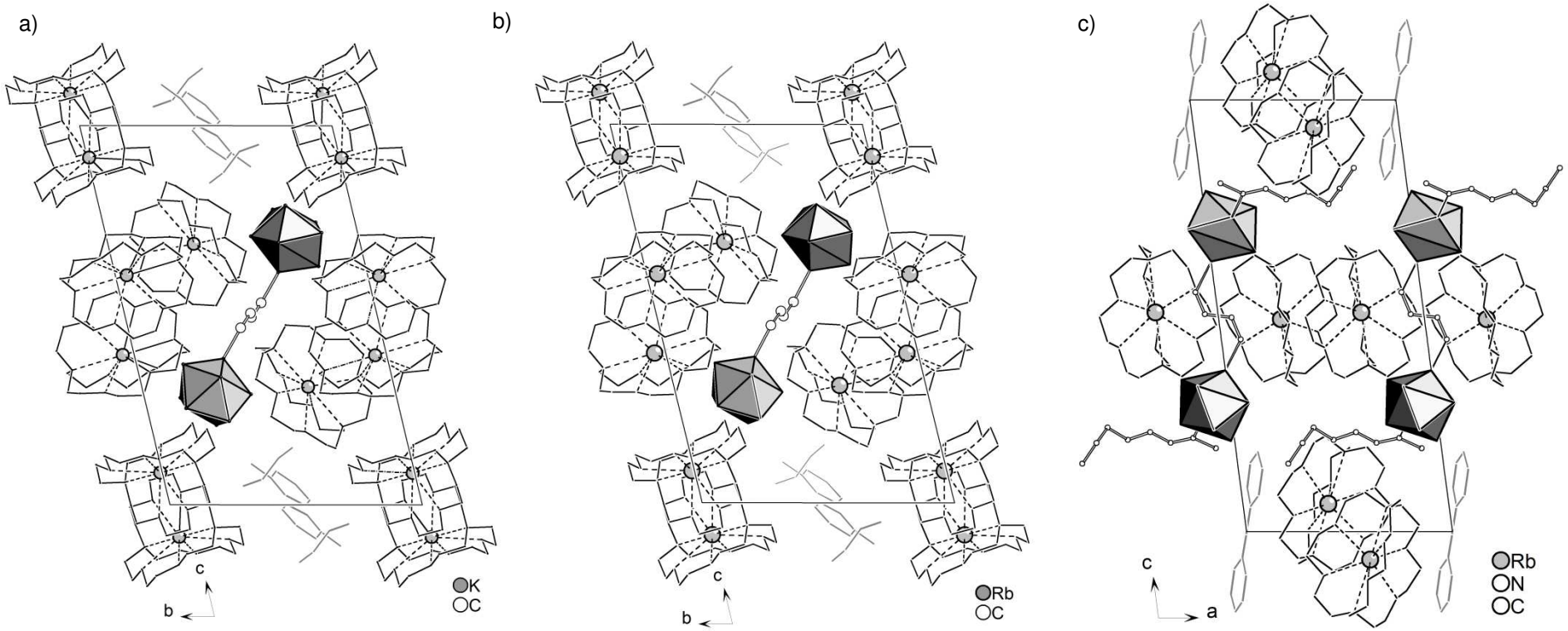

Figure S2. a) The disordered anion **1a**. The inversion center between C2 and C2^{i} is marked with *. The germanium atoms of the superimposing cluster components are depicted with different colors and shown individually in b). **I** (blue), **II** (green) and **III** (grey). The squares of the quadratic antiprism of the clusters are depicted by bold lines. Ellipsoids are shown at the probability level of 50%. c) Depiction of the C1/C2/C2^{i}/C1^{i} chain (red atoms) as well as Ge1/Ge1^{i} and Ge10/Ge10^{i}, which together result the *s-trans* [(Ge)-(**^{ZZ}B**)-(Ge)] building units of the conformers **1a^{I}** and **1a^{II}**, respectively. Planes through the atoms Ge1/C1/C2/C2^{i}/C1^{i}/Ge1^{i} (blue) and Ge10/C1/C2/C2^{i}/C1^{i}/Ge10^{i} (green) indicate the spatial orientations of **1a^{I}** and **1a^{II}** around the inversion center. Due to the almost identical spatial location of both **^{ZZ}B** functionalities of **1a^{I}** and **1a^{II}**, individual C_4-chains cannot be resolved by X-ray diffraction and solely a superposition of both chains appears in the crystal structures. As a consequence the occupancy of the C1/C2/C2^{i}/C1^{i} chain is 87% (sum **I** and **II**). d) Clusters **III**/**III**^{i} are not related to the C1/C2/C2^{i}/C1^{i} chain (see bond length and angles in Table S1). The shortest Ge-Ge^{i} distance of 6.572(8) Å (Ge19-Ge19^{i}), is indicative for another conformer **1a^{III}**, however due to low contribution of **III** (13%) it is unclear from X-ray data whether there is another differently orientated **^{ZZ}B** bridge, or if **III** is a $[Ge_9]^{3-}$ clusters. For the conformer **1a^{III}** the terminal carbon atoms of the C_4 chain are expected to be located in the grey plane.

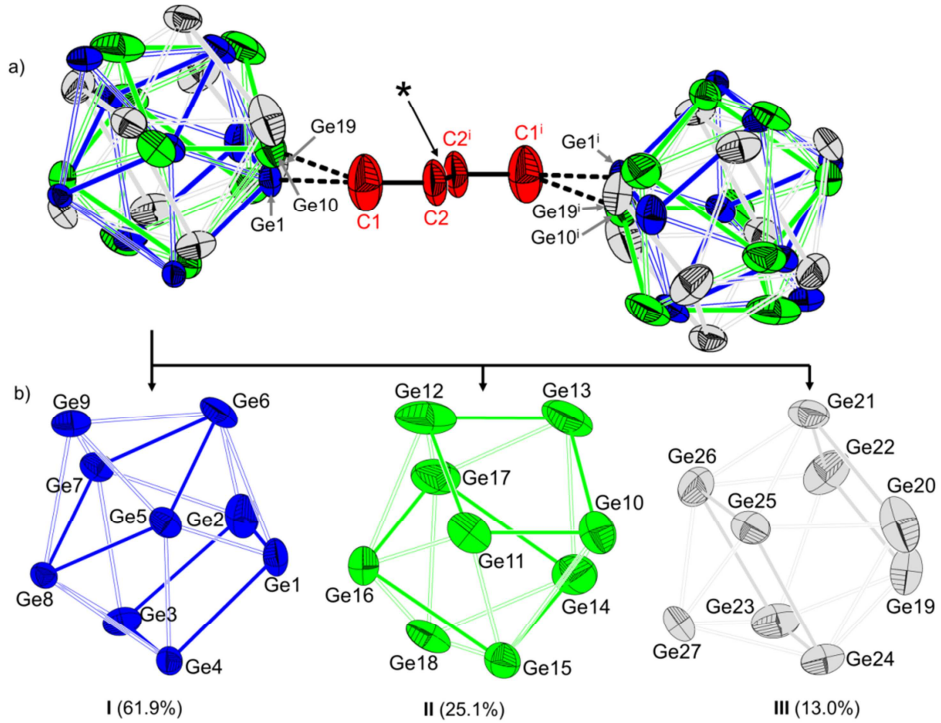

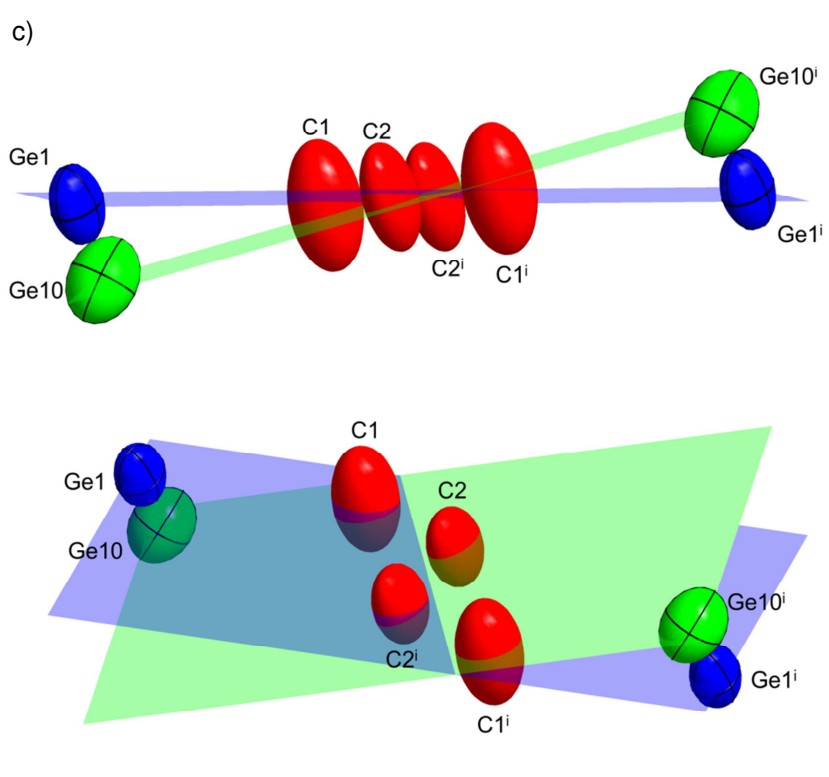
c)
Ge1
Ge10
C1
C2
C2i
C1i
Ge10i
Ge1i
C1
Ge1
Ge10
C2
C2i
C1i
Ge10i
Ge1i

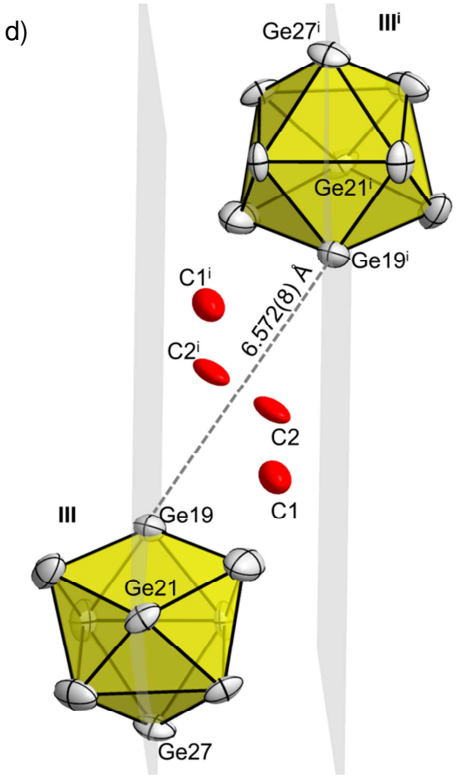
d)
Ge27i
IIIi
Ge21i
Ge19i
C1i
C2i
6.572(8) Å
C2
C1
III
Ge19
Ge21
Ge27

Figure S3. Illustration of conformers of **1a** differing by the orientation of the Ge_9 clusters with respect to the [(Ge)-(**B**)-(Ge)] plane. The shortest Ge-Ge^i distances are emphasized by a doted grey line and the corresponding distances are denoted, respectively.

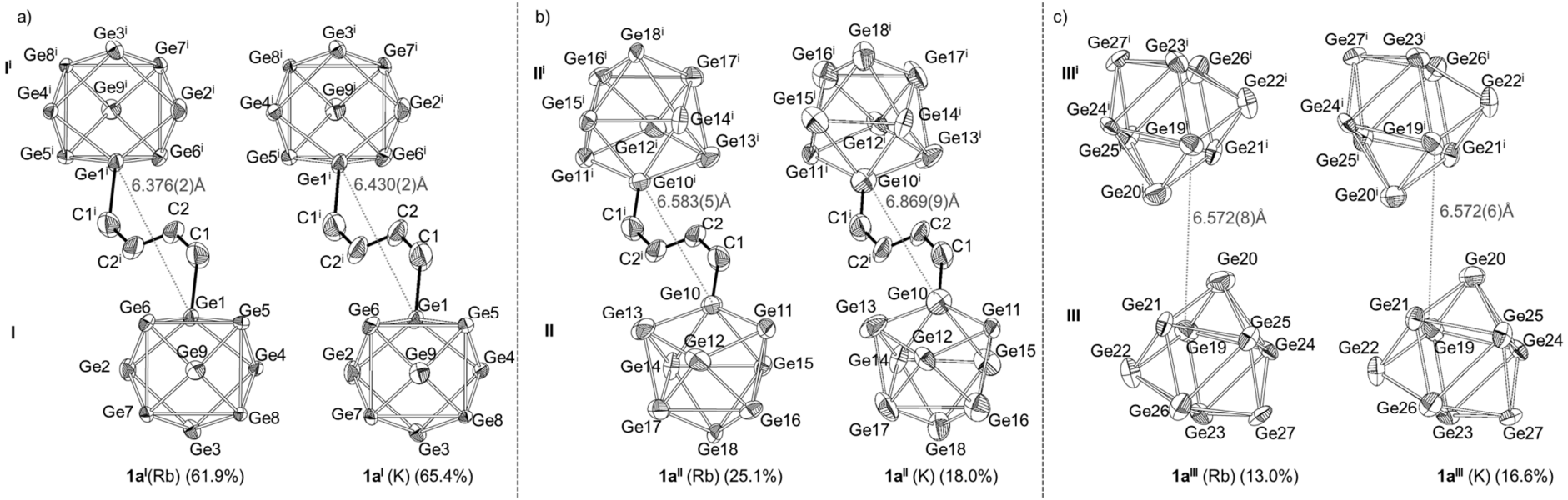

Figure S4. Illustration showing the absolut orientation of the Ge_9 clusters of **1a**^{I} and**1a**^{II}. The rotation angle of the clusters is defined by the angle between the face normals (dashed arrows) of the depicted planes. a) Conformer **1a**^{I}; blue plane: Ge1/C1/C2/C2^{i}/C1^{i}/Ge1^{i}; purple plane: Ge1/Ge3/Ge9. b) Conformer **1a**^{II}; green plane: Ge10/C1/C2/C2^{i}/C1^{i}/Ge10^{i}, purple plane: Ge10/Ge12/Ge18. The difference between the rotation angles of **1a**^{I} and**1a**^{II} is 165.4°. Thermal ellipsoids are shown at a probability level of 50%.

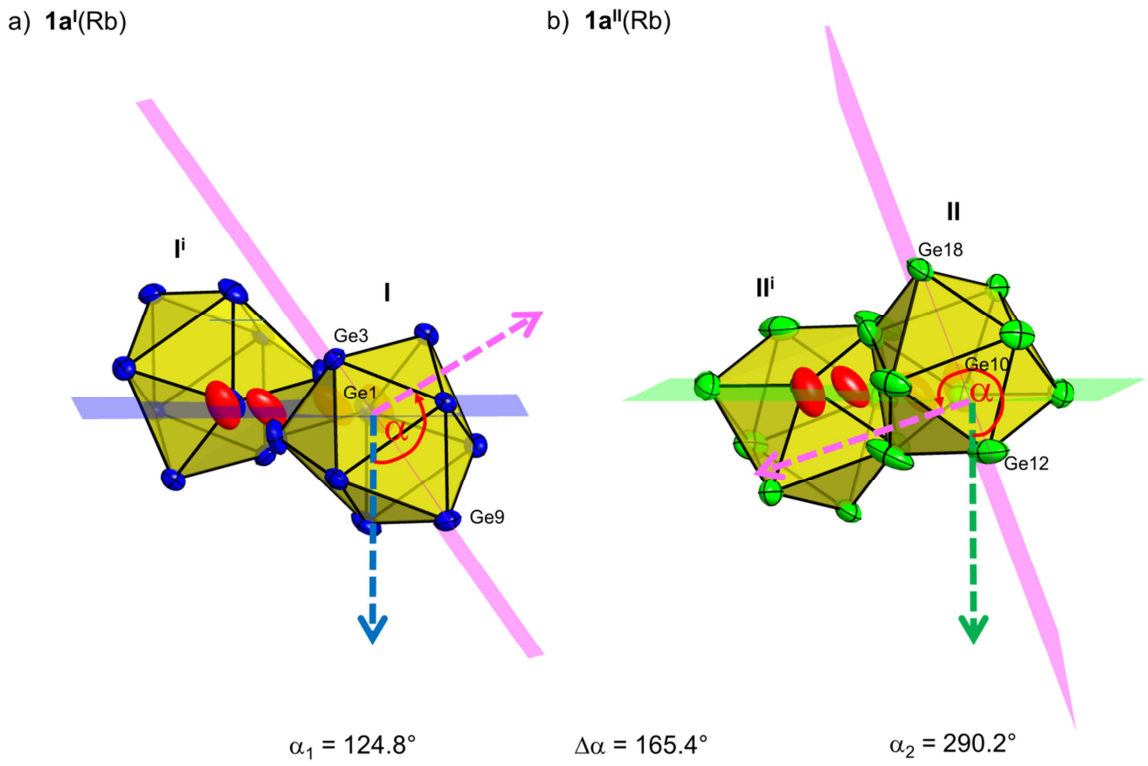

Table S1: Geometrical parameters of the clusters in the crystal structures of {A(222-crypt)]$_6$ **1a**}·(tol)$_2$·(en)$_2$ (A = K, Rb) and {A(222-crypt)]$_4$ **2a**}·(tol). The minority clusters **II** and **III** in the crystal structures of {A(222-crypt)]$_6$ **1a**}·(tol)$_2$·(en)$_2$ (A = K, Rb) was coupled to the geometrical parameters of the majority component **I** by applying the SAME instruction in shelxl97[1].

cluster	Symmetry	c[%][a]	α [°][b]	β [°][c]	ω [°][d]	c_1/c_2[e]	d_1/d_2[f]	h_1 [Å][g]	h_2 [Å][g]	h_3 [Å][g]	$(a_1+a_2)/(b_1+b_2)$
{[Rb(222-crypt)]$_6$ **1a**}·(tol)$_2$·(en)$_2$											
I	C_s	61.9	178.8	130.1	158.7	1.06	1.14	3.390	2.767	2.757	0.93
II	C_s	25.1	177.3	139.1	161.8	1.00	1.16	3.340	2.745	2.720	0.95
III	C_s	13.0	178.7	109.0	98.6	0.43	1.18	3.297	2.794	2.732	0.93
{[K(222-crypt)]$_6$ **1a**}·(tol)$_2$·(en)$_2$											
I	C_s	65.4	178.5	131.5	159.9	1.04	1.13	3.416	2.746	2.743	0.93
II	C_s	18.0	177.7	143.8	163.7	1.05	1.13	3.398	2.878	2.746	0.95
III	C_s	16.6	178.8	110.2	98.7	0.44	1.19	3.296	2.821	2.762	0.93
{[Rb(222-crypt)]$_4$ **2a**}·tol											
	C_{2v}	100	173.8	132.1	161.4	1.04	1.25	3.144	2.670	2.686	1.00
{[K(222-crypt)]$_4$ **2a**}·tol[2]											
	C_{2v}	100	174.0	131.3	160.3	1.04	1.26	3.149	2.676	2.690	1.00

a) occupancy

b) α is defined as the dihedral angle closest to 180° in the cluster.

c) is defined as the angle between 1/C1/C2

d) defines the out-of-plane angle ω of the *exo*-bonded ^{zz}**B** bridge

e) A c_1/c_2 ratio of 1 indicates that the C1 atom of ^{ZZ}**B** is located in the plane through 1/3/9. This is expected for the carbon atom of organic functionalities attached at the open square face of Ge_9 clusters[3]

f) d_1 and d_2 are the diagonals of the open square face that includes α.

g) h are the heights of the central trigonal prisms of the clusters. $h_1 = d_1$

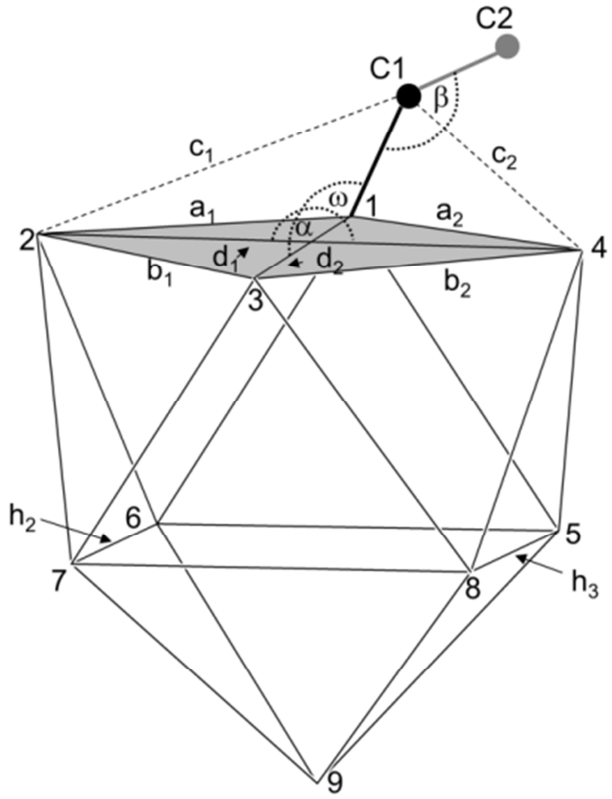

Table S2. Bond lengths [Å] of **1a** in {K(222-crypt)]$_6$ **1a**}·(tol)$_2$·(en)$_2$

1a^{I}		**1a**^{II}		**1a**^{III}	
Ge1—Ge2	2.480 (1)	Ge10—Ge13	2.457 (9)	Ge19—Ge20	2.463 (8)
Ge1—Ge4	2.492 (3)	Ge10—Ge11	2.530 (1)	Ge19—Ge22	2.488 (6)
Ge1—Ge6	2.575 (2)	Ge10—Ge14	2.549 (8)	Ge19—Ge23	2.563 (7)
Ge1—Ge5	2.615 (3)	Ge10—Ge15	2.599 (1)	Ge19—Ge24	2.614 (9)
Ge2—Ge7	2.532 (3)	Ge11—Ge16	2.564 (1)	Ge20—Ge25	2.535 (9)
Ge2—Ge3	2.674 (4)	Ge11—Ge12	2.611 (1)	Ge20—Ge21	2.680 (7)
Ge2—Ge6	2.700 (2)	Ge11—Ge15	2.724 (1)	Ge20—Ge24	2.733 (1)
Ge3—Ge8	2.579 (4)	Ge12—Ge17	2.571 (1)	Ge21—Ge26	2.551 (7)
Ge3—Ge7	2.589 (3)	Ge12—Ge16	2.620 (1)	Ge21—Ge25	2.591 (7)
Ge3—Ge4	2.669 (3)	Ge12—Ge13	2.646 (9)	Ge21—Ge22	2.625 (6)
Ge4—Ge8	2.562 (4)	Ge13—Ge17	2.602 (1)	Ge22—Ge26	2.537 (7)
Ge4—Ge5	2.642 (4)	Ge13—Ge14	2.643 (8)	Ge22—Ge23	2.663 (7)
Ge5—Ge9	2.570 (3)	Ge14—Ge18	2.559 (1)	Ge23—Ge27	2.549 (1)
Ge5—Ge8	2.742 (4)	Ge14—Ge15	2.853 (1)	Ge23—Ge24	2.817 (9)
Ge5—Ge6	2.852 (3)	Ge14—Ge17	2.878 (1)	Ge23—Ge26	2.822 (7)
Ge6—Ge9	2.571 (3)	Ge15—Ge18	2.560 (1)	Ge24—Ge27	2.563 (1)
Ge6—Ge7	2.746 (2)	Ge15—Ge16	2.747 (1)	Ge24—Ge25	2.762 (1)
Ge7—Ge9	2.609 (4)	Ge16—Ge18	2.591 (2)	Ge25—Ge27	2.613 (1)
Ge7—Ge8	2.844 (4)	Ge16—Ge17	2.896 (1)	Ge25—Ge26	2.906 (9)
Ge8—Ge9	2.572 (4)	Ge17—Ge18	2.566 (1)	Ge26—Ge27	2.564 (1)
Ge1—C1	2.007 (9)	Ge10—C1	1.989(1)		
C1—C2	1.337 (2)				
C2—C2^{i}	1.50 (2)				

Table S3. Bond lengths [Å] of **1a** in {Rb(222-crypt)]$_6$ **1a**}·(tol)$_2$·(en)$_2$

1a^{I}		**1a**^{II}		**1a**^{III}	
Ge1—Ge2	2.476 (2)	Ge10—Ge13	2.489 (5)	Ge19—Ge20	2.434 (1)
Ge1—Ge4	2.499 (4)	Ge10—Ge11	2.506 (1)	Ge19—Ge22	2.491 (7)
Ge1—Ge6	2.573 (2)	Ge10—Ge14	2.576 (6)	Ge19—Ge23	2.570 (1)
Ge1—Ge5	2.608 (5)	Ge10—Ge15	2.586 (1)	Ge19—Ge24	2.610 (1)
Ge2—Ge7	2.554 (3)	Ge11—Ge16	2.570 (1)	Ge20—Ge25	2.528 (9)
Ge2—Ge3	2.656 (6)	Ge11—Ge12	2.595 (1)	Ge20—Ge21	2.676 (9)
Ge2—Ge6	2.703 (2)	Ge11—Ge15	2.690 (1)	Ge20—Ge24	2.715 (1)
Ge3—Ge8	2.573 (5)	Ge12—Ge17	2.579 (1)	Ge21—Ge26	2.565 (9)
Ge3—Ge7	2.586 (5)	Ge12—Ge16	2.590 (1)	Ge21—Ge25	2.602 (8)
Ge3—Ge4	2.673 (5)	Ge12—Ge13	2.649 (7)	Ge21—Ge22	2.621 (7)
Ge4—Ge8	2.540 (5)	Ge13—Ge17	2.546 (1)	Ge22—Ge26	2.515 (9)
Ge4—Ge5	2.635 (5)	Ge13—Ge14	2.662 (5)	Ge22—Ge23	2.662 (9)
Ge5—Ge9	2.570 (5)	Ge14—Ge18	2.561 (1)	Ge23—Ge27	2.594 (2)
Ge5—Ge8	2.757 (5)	Ge14—Ge17	2.747 (1)	Ge23—Ge26	2.794 (1)
Ge5—Ge6	2.857 (5)	Ge14—Ge15	2.882 (9)	Ge23—Ge24	2.817 (1)
Ge6—Ge9	2.568 (2)	Ge15—Ge18	2.580 (1)	Ge24—Ge27	2.564 (2)
Ge6—Ge7	2.767 (4)	Ge15—Ge16	2.720 (1)	Ge24—Ge25	2.732 (1)
Ge7—Ge9	2.602 (3)	Ge16—Ge18	2.562 (1)	Ge25—Ge27	2.587 (1)
Ge7—Ge8	2.838 (4)	Ge16—Ge17	2.890 (1)	Ge26—Ge27	2.580 (1)
Ge8—Ge9	2.578 (6)	Ge17—Ge18	2.586 (1)		
Ge1—C1	2.001 (9)	Ge10—C1	1.918 (9)		
C1—C2	1.343 (1)				
C2—C2^{i}	1.447 (2)				

Table S4. Bond lengths [Å] of **2a** in {Rb(222-crypt)]$_6$ **2a**}·tol

Ge1—Ge2	2.515 (2)	Ge1—C1	1.933 (1)
Ge1—Ge4	2.533 (2)	C1—C2	1.351 (2)
Ge1—Ge5	2.553 (2)	C2—C2^{i}	1.50 (3)
Ge1—Ge6	2.592 (2)	Ge3—C4	2.004 (2)
Ge2—Ge3	2.514 (2)	C3—C4	1.56 (3)
Ge2—Ge6	2.666 (2)	C4—C5	1.31 (2)
Ge2—Ge7	2.677 (2)	C5—C6	1.40 (3)
Ge3—Ge4	2.542 (2)	C6—N1	1.31 (2)
Ge3—Ge7	2.577 (2)	N1—C7	1.47 (3)
Ge3—Ge8	2.591 (2)	C7—C8	1.51 (3)
Ge4—Ge8	2.629 (2)	C8—N2	1.49 (3)
Ge4—Ge5	2.650 (2)		
Ge5—Ge9	2.587 (2)		
Ge5—Ge8	2.686 (2)		
Ge6—Ge9	2.588 (2)		
Ge6—Ge7	2.670 (2)		
Ge7—Ge9	2.573 (2)		
Ge7—Ge8	2.930 (2)		
Ge8—Ge9	2.590 (2)		

2 *In situ* Studies

In order to shed light on the formation of the Zintl triads **1a** and **2a**, the reactivity of *en*, $KNH(CH_2)_2NHK$ and $[Ge_9]^{4-}$ towards 1,4-bis(trimethylsilyl)butadiyne (**3**) and 1-(trimethylsilyl)-7-amino-5-aza-hepta-3-en-1-yne (**4**) was tested. Therefore, test mixtures according to section 2.2 Scheme S1 were prepared. The reactions were investigated *in situ* by NMR-spectroscopy and ESI-MS. For methodologic details on NMR and ESI-MS experiments, see section 2.1. In section 2.3, an overview on all the species, which were identified by NMR, is given together with detailed descriptions of NMR-data. In Table S5-S7 the corresponding ^{1}H and ^{13}C NMR-data are summarized. In section 2.4 Table S8-S11 the outcomes of *in situ* NMR-investigations are broken down for the different types of test-mixtures. In section 2.5 Figure S5-S17 the NMR-spectra are shown together with experimental details on the preparation of the test mixtures. Section 2.6 shows the results of *in situ* ESI-MS experiments

2.1 General

NMR spectroscopy. ^{1}H, COSY, HSQC and HMBC NMR spectra were recorded on 500 MHz (Bruker AV-500) and 400 MHz (Bruker AV-400) NMR spectrometers, respectively. Aliquots of ca. 150 µl of the filtered test mixture (solvent: non-deuterated *en*) were filled into a Norell® NMR tube (outer diameter: 3 mm). The Norell® NMR tube was put into a NMR tube with a diameter of 4 mm (denoted as outer tube) and the outer NMR tube was filled with 0.4 ml of chloroform-d_1. Due to the application of non-deuterated *en* as solvent, the spectra show dominant signals at. 2.5-3.0 ppm (s, *en*, -C*H*$_2$-) and 1.3-1.9 ppm (s, *en*, -N*H*$_2$-), respectively. Samples for time-resolved ^{1}H-NMR-spectroscopy were taken immediately after the reactants entirely dissolved (ca. 15 min) and the NMR measurements immediately were started.

Electrospray Ionization Mass Spectrometry (ESI-MS) Investigation: ESI-MS was done on a HCT mass spectrometer (Bruker Daltronic) in the negative ion mode (-). Measurement conditions: capillary voltage: 2.5kV, capillary exit: -180 V, drying gas temperature: 125 °C, injection rate: 240 µL/h.

2.2 Test-mixtures

Scheme S1. Overview on test-mixtures, prepared for investigating the reactivity of a) *en*, $KNH(CH_2)_2NHK$ and b) $[Ge_9]^{4-}$ towards **3** and **4**. Reaction time and stoichiometry was varied. For experimental details on the preparation of each test mixtures as well as the NMR-spectra see section 2.5 Figures S5-S17. In the figure captions S5-S17 the preparation of each 2 ml reaction solutions is shown by default, even though in individual cases the actual volumes were 0.5 – 11 ml. Different types of mixtures are assigned with capital letters for distinction. For mixtures involving $[Ge_9]^{4-}$, the concentration of A_4Ge_9 (A = K, Rb) in *en* was set constant at 60 µmol/ml in order to provide comparability. Mixture type "A" and "B": **3** either was dissolved in water free *en* ("A") or *en* containing 0.5-1% water ("B"); Mixture type "C": 1 eq. $KNH(CH_2)_2NHK$ was dissolved in an *en*-solution containing 1 eq. **4**; Mixture type "D": The neat solids A_4Ge_9 and **3** (n = 0.25, 0.5, 2) were pre-mixed and dissolved in *en*; Mixture type "E": A mixture type "D" (0.5 eq. **3**, 1 eq. K_4Ge_9) was stirred for 20 h and subsequently an *en*-solution containing 4 eq. **4** was added; Mixture type "F": A_4Ge_9 (A = K, Rb) was dissolved in *en*-solutions containing **4** (m = 1, 2); Mixture type "G": Reaction solutions of type "F" (1-2 eq. **4**, 1 eq. A_4Ge_9) were stirred for 5 h and **3** (0.5 eq.) was added; Mixture type "H": A pre-mixture of the neat solids A_4Ge_9 and **3** (0.5 eq.) were dissolved in *en*-solutions containing **4** (m = 1, 2).

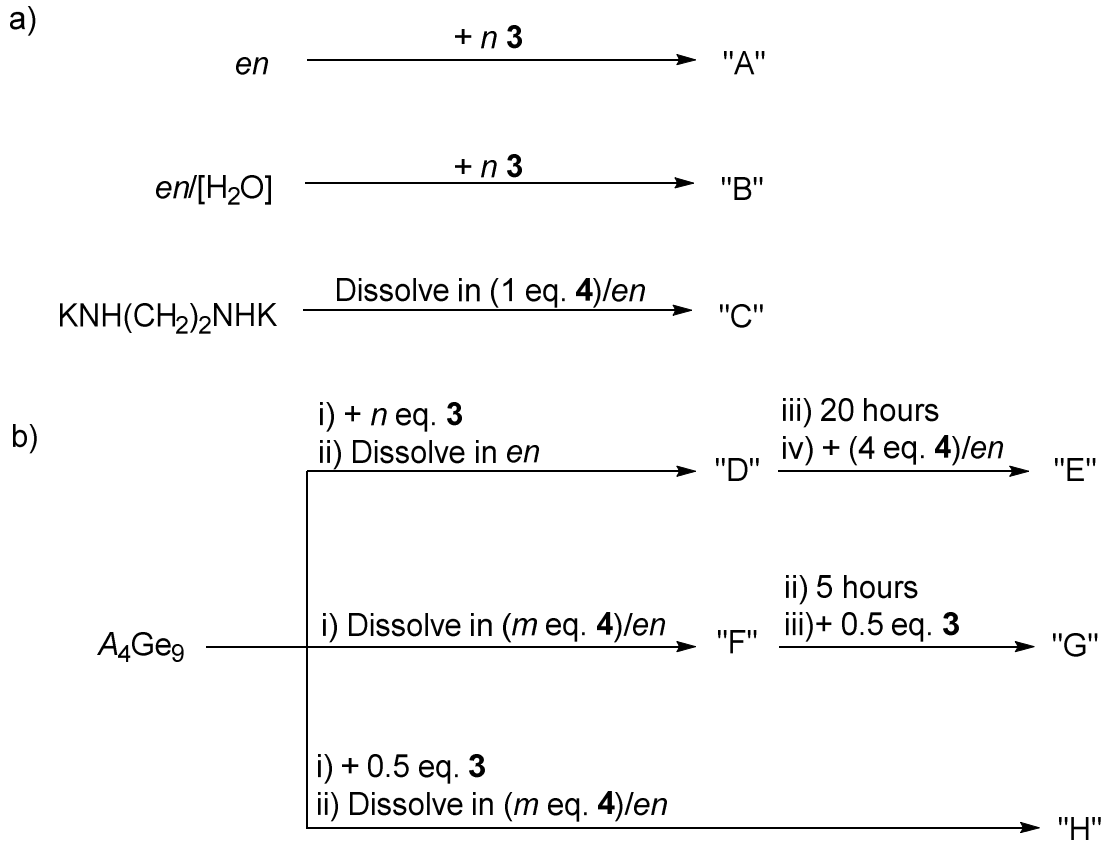

2.3 Identified organic molecules/functionalities and NMR-descriptions

In this chapter the NMR-data of organic molecules and functionalities which were identified in the test-mixtures by *in-situ* NMR are summarized and described in detail (Scheme S2 and Table S5-S7)

Scheme S2. a-f) Organic-molecules and functionalities identified by *in situ* NMR. a,c,d) Functionalities attached to NMR inactive nuclei and b,e,f) molecules are denoted with bold capital letters and bold numbers, respectively. Protons/carbons are labeled with greek-letters for distinction. Numbering see [4] Red: C_4-backbone originating from **3**, Blue: *en*-substituent.

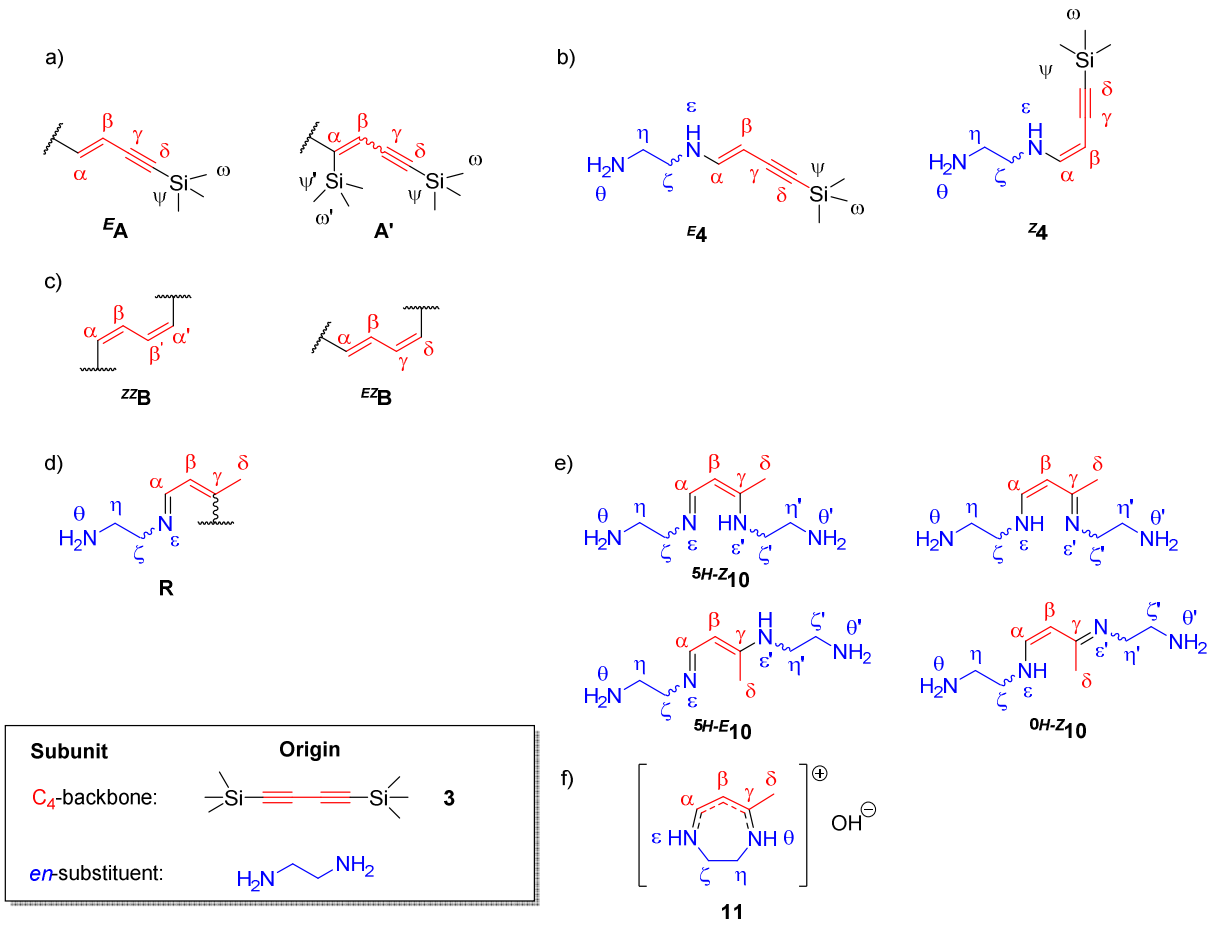

2.3.1 A, A' and ^{E}4/^{Z}4

Table S5. Summary of the ^{1}H (upper rows) and ^{13}C NMR (lower rows) chemical shifts (ppm) of ^{E}**A**, **A'** (^{E}**A**/**A'** = 80/20) and ^{E}**4**/^{Z}**4** (*E*/*Z* = 70/30). The ^{1}H NMR data are given together with the coupling pattern (s = singlet, d = doublet, dd = doublet of doublet, t = triplet, q = quartet), coupling constants (Hz) and integrals. Figures showing the NMR-spectra are referenced, respectively. Grey layered boxes: no signals are expected in ^{1}H and ^{13}C NMR for that atom positions.

	^{E}**A** (Figure S9)	**A'** (Figure S9)	^{E}**4** ([2] and Figure S5)	^{Z}**4** ([2] and Figure S5)
α	7.81 (d, *J* = 18.3 Hz, 1H)		6.91 (dd, *J* = 13.6 Hz/7.4 Hz, 1H)	6.40 (dd, *J* = 8.6 Hz/12.2 Hz, 1H)
	169.9	186.4	147.6	146.9
β	6.35 (d, *J* = 18.3 Hz, 1H)	7.97 (s 1H)	4.23 (d, *J* = 13.6 Hz, 1H)	3.96 (d, *J* = 8.6 Hz, 1H)
	116.5	124.5	70.7	70.1
γ				
	108.9	108.6	109.1	105.8
δ				
	86.8	89.4	86.1	93.9
ε			7.54 (s(broad), 1H)	6.67 (s(broad))
ζ			2.96 (pseudo q, *J* = 6.0 Hz, 2H)	3.21 (pseudo q, *J* = 6.0 Hz, 2H)
			46.3	49.7
η			2.79	2.76
			40.3	42.7
Θ			covered by *en*	covered by *en*
ω	0.13 (s)	0.14 (s)	0.19 (s, 9H)	0.23 (s, 9H)
	-0.7	-0.7	0	0
ω'		0.21 (s)		
		-0.7		

Functionality ^{E}A.

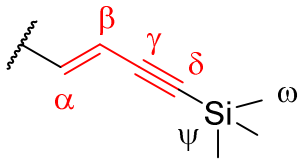

^{E}**A**

1D NMR data: see Table S5

2D NMR data: COSY (500 MHz, chloroform-d_1, 296 K), δ(ppm): 7.82/6.34 (^{3}J, ^{E}Aα/^{E}Aβ); HMBC (500 MHz, chloroform-d_1, 296 K), δ(ppm): 7.78/116.6 (^{2}J, ^{E}Aα/^{E}Aβ), 7.80/108.9 (^{3}J, ^{E}Aα/^{E}Aγ), 6.36/108.9 (^{2}J, ^{E}Aβ/^{E}Aγ), 6.35/86.8 (^{3}J, ^{E}Aβ/^{E}Aδ), 0.13/86.7 (^{3}J, ^{E}Aω/^{E}Aδ); HSQC (500 MHz, chloroform-d_1, 296 K), δ(ppm): 7.79/169.9 (^{1}J, ^{E}Aα/^{E}Aα), 6.33/116.5 (^{1}J, ^{E}Aβ/^{E}Aβ), 0.12/-0.73 (^{1}J, ^{E}Aω/^{E}Aω);

NMR description: In ^{1}H NMR (Figure S9a), ^{E}**A** generates three resonances, namely at 7.81 ppm (^{E}Aα), 6.35 ppm (^{E}Aβ) and 0.13 ppm (^{E}Aω). Both signals ^{E}Aα and ^{E}Aβ feature a doublet structure with a coupling constant of 18.3 Hz, being in the typical range for *trans*-orientated olefinic protons[5] and indicating a 1*E*[4] configuration for ^{E}**A**. The signal ^{E}Aω at 0.13 ppm is a singlet, which is expected for the methyl-protons of TMS connected to a carbon atom. From the HMBC and HSQC NMR spectra (Figure S9c/d) ^{13}C chemical shifts of 169.9 ppm (^{E}Aα), 116.5 ppm (^{E}Aβ), 108.9 ppm (^{E}Aγ), and 86.8 ppm (^{E}Aδ) were derived, respectively. In HMBC (Figure S9c) the -C≡C- unit is indicated by cross-peaks at 7.8 ppm/108.9 ppm and 6.35 ppm/86.8 ppm, corresponding to ^{3}J couplings of proton ^{E}Aα with carbon ^{E}Aγ and proton ^{E}Aβ with carbon ^{E}Aδ, respectively. Another, cross-peak at 0.13 ppm/86.7 ppm, corresponds to the ^{3}J coupling between proton ^{E}Aω and carbon ^{E}Aδ and indicates the connection of TMS group to the -C≡C- unit.

Functionality A'.

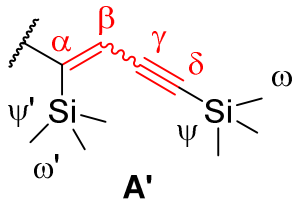

A'

1D NMR data: see Table S5

2D NMR data: HMBC (500 MHz, chloroform-d_1, 296 K), δ(ppm): 7.96/108.6 (^2J, A'β/A'γ), 7.97/89.4 (^3J, A'β/A'δ), 0.2/186.4 (^3J, A'ω/A'α), 0.13/86.7 (probably overlap of ^3J, Aω/Aδ and ^3J, A'ω/A'δ); HSQC (500 MHz, chloroform-d_1, 296 K), δ(ppm): 7.97/124.5 (^1J, A'β/ A'β), 0.14/-0.7 (^1J, A'ω/A'ω), 0.2/-0.7 (^1J, A'ω'/A'ω');

NMR description: In ^{1}H NMR (Figure S9a) functionality **A'** exhibits singlets at 7.97 ppm (A'β), 0.21 ppm (A'ω') and 0.14 ppm (A'ω), respectively. From the HMBC and HSQC spectra (Figure S9c/d) ^{13}C chemical shifts of 186.4 ppm (A'α), 124.5 ppm (A'β), 108.6 ppm (A'γ), and 89.4 ppm (A'δ) were derived. In HMBC, cross-peaks at 7.97 ppm/108.6 ppm and 7.97 ppm/89.4 ppm, correspond to ^2J and ^3J couplings of proton A'β with carbon A'γ and A'δ of the -C≡C- unit, respectively. Moreover, a cross-peak at 0.2 ppm/186.4 ppm is visible and originates from the ^3J coupling of proton A'ω' to carbon A'α. Due to similar ^{1}H and ^{13}C chemical shifts for the δ and ω protons/carbons of ^{E}**A** and **A'**, appears in HMBC at 0.13 ppm/86.7 ppm a superposition of ^3J couplings of proton A'ω with carbon A'δ and proton ^{E}Aω with carbon ^{E}Aδ, respectively. The configuration of the double bond of **A'** cannot be derived from the NMR data, as no couplings to proton A'α are visible due to non-hydrogen atoms at the neighboring β and ε positions.

Molecule ^{E}4 and ^{Z}4.

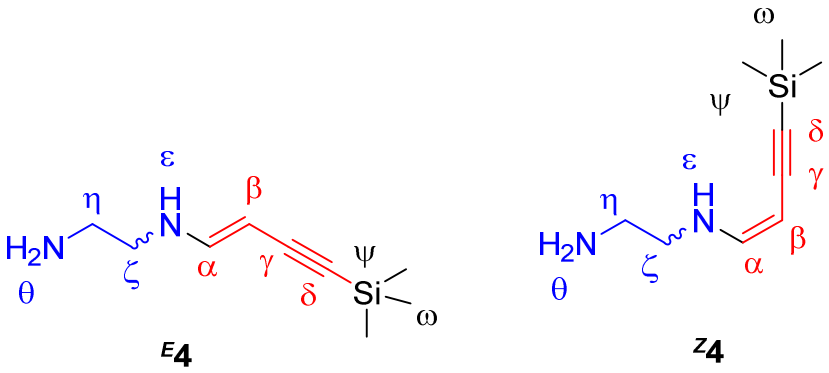

^{E}4 ^{Z}4

1D- and 2D-NMR data as well as detailed description of the data see [2].

2.3.2 ^{EZ}B and ^{ZZ}B

Table S6. Summary of the ^{1}H (upper rows) and ^{13}C NMR (lower rows) chemical shifts (ppm) of ^{EZ}**B** and ^{ZZ}**B** (*EZ*/*ZZ* = 80/20). The ^{1}H NMR data are given together with the coupling pattern (s = singlet, d = doublet, dd = doublet of doublet, t = triplet, q = quartet), coupling constants (Hz) and integrals. Figures showing NMR spectra are referenced, respectively. Grey layered boxes: no signals are expected in ^{1}H and ^{13}C NMR for that atom positions.

	^{EZ}**B** (Figure S10)	^{ZZ}**B** (Figure S10)
α	6.69 (d, *J* = 17.2 Hz, 1H)	7.71 (dd, *J* = 8.7/2.0 Hz, 1H)
	142.4	142.1
β	7.85 (dd, *J* = 17.3/10.0 Hz, 1H)	6.78 (dd, *J* = 8.6/2.1 Hz, 1H)
	143.6	142.8
γ	6.38 (dd, *J* = 11.1/10.1 Hz, 1H)	
	142.2	
δ	6.56 (d, *J* = 11.3 Hz, 1H)	
	139.0	

Functionality ^{ZZ}B.

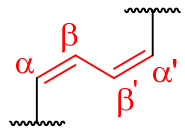

^{ZZ}**B**

1D NMR data: see Table S6

2D NMR data: COSY (500 MHz, chloroform-d_1, 296 K), δ(ppm): 7.71/6.79 (^3J, ^{ZZ}Bα/ ^{ZZ}Bβ); HMBC (500 MHz, chloroform-d_1, 296 K), δ(ppm): 6.78/142.8 (^2J, ^{ZZ}Bα/ ^{ZZ}Bβ); HSQC (500 MHz, chloroform-d_1, 296 K), δ(ppm): 7.72/142.1 (^1J, ^{ZZ}Bα/ ^{ZZ}Bα), 6.78/142.8 (^1J, ^{ZZ}Bα/ ^{ZZ}Bα);

NMR description: In ^{1}H NMR (Figure S10a), the C_4-backbone (red) of **^{ZZ}B** generates two resonances, namely 7.71 ppm (^{ZZ}Bα$^{(')}$) and 6.78 ppm (^{ZZ}Bβ$^{(')}$). Thereby, we assumed that proton ^{ZZ}Bα$^{(')}$, which is closest to the NMR inactive substituent (Ge_9 cluster), is largest deep field shifted, however an unambiguous assignment is not possible from NMR. Both signals ^{ZZ}Bα$^{(')}$ and ^{ZZ}Bβ$^{(')}$ feature a doublet of doublets structure with coupling constants of 8.6 and 2.1 Hz, respectively. Thereby, the chemical shifts and the 8.6 Hz coupling are indicative for *cis*-orientated olefinic protons.[5] Moreover, the 2.1 Hz fine structure is typical for *cis*,*cis*-buta-1,3-dienes, and originates from couplings between the magnetically non-equivalent protons ^{ZZ}Bα/^{ZZ}Bβ and ^{ZZ}Bα'/^{ZZ}Bβ'.[5] The ^3J coupling of ^{ZZ}Bα$^{(')}$ and ^{ZZ}Bβ$^{(')}$, can also be seen in COSY (Figure S10b) by cross-peaks at 7.71 ppm/6.79 ppm and 6.79 ppm/7.71 ppm, respectively. From the HSQC and HMBC spectra (Figure S10c/d) ^{13}C chemical shifts of 142.1 ppm (^{ZZ}Bα$^{(')}$) and 142.8 ppm (^{ZZ}Bβ$^{(')}$) were derived, which is in the typical region of olefinic carbons, respectively.[5]

Functionality ^{EZ}B.

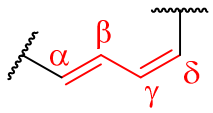

^{EZ}**B**

1D NMR data: see Table S6

2D NMR data: COSY (500 MHz, chloroform-d_1, 296 K), δ(ppm): 7.85/6.69 (^3J, ^{EZ}Bβ / ^{EZ}Bα), 7.85/6.36 (^3J, ^{EZ}Bβ / ^{EZ}Bγ), 6.34/6.55 (^3J, ^{EZ}Bγ / ^{EZ}Bδ); HMBC (500 MHz, chloroform-d_1, 296 K), δ(ppm): 7.86/142.7 (^2J, ^{EZ}Bβ/ ^{EZ}Bα), 6.68/143.1 (assumed overlap of ^2J, ^{EZ}Bα/ ^{EZ}Bβ and ^3J, ^{EZ}Bα/ ^{EZ}Bγ), 6.56/144.4 (^3J, ^{EZ}Bδ/^{EZ}Bβ), 6.38/143.8 (assumed overlap of ^3J, ^{EZ}Bγ/ ^{EZ}Bα and ^2J, ^{EZ}Bγ/ ^{EZ}Bβ); HSQC (500 MHz, chloroform-d_1, 296 K), δ(ppm): 7.86/143.6 (^1J, ^{EZ}Bβ / ^{EZ}Bβ), 6.68/142.4 (^1J, ^{EZ}Bα / ^{EZ}Bα), 6.56/139.0 (^1J, ^{EZ}Bδ / ^{EZ}Bδ), 6.38/142.2 (^1J, ^{EZ}Bγ / ^{EZ}B)

NMR description: In ^{1}H NMR (Figure S10a) the C_4-backbone (red) of ^{EZ}**B** exhibits four resonances, namely 6.69 ppm (^{EZ}Bα), 7.85 ppm (^{EZ}Bβ), 6.38 ppm (^{EZ}Bγ) and 6.56 ppm (^{EZ}Bδ). Thereby, ^{EZ}Bβ and ^{EZ}Bγ feature doublet of doublet structures with coupling constants of 17.3/10.0 Hz and 11.1/10.0 Hz, whereas the signals corresponding to ^{EZ}Bα and ^{EZ}Bδ are doublets with coupling constants of 17.3 and 10.0 Hz, respectively. The chemical shifts and coupling constants of 17.3 and 11.1/10.0 Hz are typical for *trans*- and *cis*-orientated olefinic protons, concluding an 1,4-disubstituted (1*E*,3*Z*)-buta-1,3-dien (for COSY see Figure S10b).[5] From the HSQC and HMBC spectra (Figure S10c/d) ^{13}C chemical shifts of 139.0 – 143.6 ppm were derived for the carbon atoms, being indicative for olefins.[5]

2.3.3 R, 10 and 11

Table S7. Summary of the ^{1}H (upper rows) and ^{13}C NMR (lower rows) chemical shifts (ppm) of a) **R** and **10** under water-free conditions and b) **10** and **11** in presence of water traces. Different isomers/tautomers of **R** and **10** appear in the NMR spectra by similar signal sets. NMR data do not reveal which signal set belongs to which isomer/tautomer and consequently the signal sets are distinguished by superscripted numbers. The signals $^{2\text{-}7}$10 severely interfere with *en* and consequently NMR-data are incomplete. Grey layered boxes: no signals are expected.

a)	**R**		**10**			
	^{1}R (90%) (Figure S13)	^{2}R (10%) (Figure S13)	^{1}10 (65%) (Figure S8/S13)	^{2}10 (35%) (Figure S8/S13)	^{3}10 (80%) (Figure S6)	^{4}10 (20%) (Figure S6)
α	9.37 (d, *J* = 8.8 Hz, 1H)	9.33 (d, *J* = 8.9 Hz, 1H)	7.79 (d, *J* = 11.6 Hz, 1H)	7.83 (d, *J* = 10.8 Hz, 1H)	7.46 (d, *J* = 11.5 Hz)	7.51 (d, *J* = 11.5 Hz)
	167.4	Intensity to low	157.9	161.5	161.7	Intensity to low
β	6.34 (d, *J* = 8.9 Hz, 1H)	6.32 (d)	4.24 (d, *J* = 11.6 Hz, 1H)	4.56 (d, *J* = 10.5 Hz, 1H)	3.11	3.33
	133.9	Intensity to low	79.5	82.0	ca. 64	ca. 64
γ						
	180.0	Intensity to low	163.0	161.5	169.6	Intensity to low
δ	2.18 (s 9H)	2.23 (s 9H)	2.05 (s)	2.00 (s)	2.05 or 2.0	2.05 or 2.0
	35.7	Intensity to low	22.3	22.3	22.3	22.3
ε			proton exchange	proton exchange	proton exchange	proton exchange
ζ	3.47 (t, *J* = 5.8 Hz, 1H)	3.44 (t, *J* = 5.8 Hz, 1H)	2.95 (t)	3.21 (t, *J* = 5.6 Hz, 1H)	covered by *en*	covered by *en*
	63.2	Intensity to low	53.3	64.1	covered by *en*	covered by *en*
η	2.8	covered by *en*	covered by *en*	covered by *en*	covered by *en*	covered by *en*
	43.5	Intensity to low	covered by *en*	covered by *en*	covered by *en*	covered by *en*
Θ	covered by *en*	covered by *en*	covered by *en*	covered by *en*	covered by *en*	covered by *en*
ε'			proton exchange	proton exchange	proton exchange	proton exchange
ζ'			2.98 (t)	covered by *en*	covered by *en*	covered by *en*
			53.2	covered by *en*	covered by *en*	covered by *en*
η'			covered by *en*	covered by *en*	covered by *en*	covered by *en*
			covered by *en*	covered by *en*	covered by *en*	covered by *en*
Θ'			proton exchange	proton exchange	proton exchange	proton exchange

b)	**10**			**11**
	^{5}10 (Figure S6)	^{6}10 (Figure S6)	^{7}10 (Figure S6)	11 (Figure S6)
α	7.88 (s, broad, variable)	7.88 (s, broad, variable)	7.5	6.87 (d, *J* = 7.4 Hz, 1H)
	in 2D NMR invisible	in 2D NMR invisible	in 2D NMR invisible	148.7
β	4.49 (s, broad, variable)	5.11 (s, broad, variable)	overlap with en, ca. 3	4.55 (d, *J* = 7.4 Hz, 1H)
	in 2D NMR invisible	in 2D NMR invisible	in 2D NMR invisible	91.9
γ				
	in 2D NMR invisible	in 2D NMR invisible	in 2D NMR invisible	161.6
δ	2.06 (s, broad, variable)	2.06 (s, broad, variable)	2.06 (s, broad, variable)	2.0 (s, 9H)
	in 2D NMR invisible	in 2D NMR invisible	in 2D NMR invisible	25.3
ε	fast proton exchange	fast proton exchange	fast proton exchange	fast proton exchange
ζ	3.32 (s, broad, variable)	3.13 (s, broad, variable)	covered by *en*	3.55 (s(broad))
	in 2D NMR invisible	in 2D NMR invisible	in 2D NMR invisible	52.3
η	covered by *en*	covered by *en*	covered by *en*	covered by *en*
	in 2D NMR invisible	in 2D NMR invisible	in 2D NMR invisible	covered by *en*
Θ	fast proton exchange	fast proton exchange	fast proton exchange	fast proton exchange
ε'	fast proton exchange	fast proton exchange	fast proton exchange	
ζ'	3.32 (s, broad, variable)	3.13 (s, broad, variable)	covered by *en*	
	in 2D NMR invisible	in 2D NMR invisible	in 2D NMR invisible	
η'	covered by *en*	covered by *en*	covered by *en*	
	in 2D NMR invisible	in 2D NMR invisible	in 2D NMR invisible	
Θ'	fast proton exchange	fast proton exchange	fast proton exchange	

Functionality R.

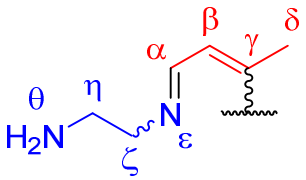

R

1D NMR data: see Table S7

2D NMR data: Signal set ^{1}R: COSY (500 MHz, chloroform-d$_1$, 296 K), δ(ppm): 9.37/6.34 (^{3}J, ^{1}Rα/^{1}Rβ), 9.37/3.46 (^{3}J, ^{1}Rα/^{1}Rζ), 6.34/2.17 (^{4}J, ^{1}Rβ/^{1}Rδ), 3.46/2.8 (^{3}J, ^{1}Rζ/^{1}Rη); HMBC (500 MHz, chloroform-d$_1$, 296 K), δ(ppm): 9.36/180.0 (^{3}J, ^{1}Rα/^{1}Rγ), 9.37/134.0 (^{2}J, ^{1}Rα/^{1}Rβ), 9.37/63.0 (^{3}J, ^{1}Rα/^{1}Rζ), 6.34/36.5 (^{3}J, ^{1}Rβ/^{1}Rδ), 3.47/168.1 (^{3}J, ^{1}Rζ/^{1}Rα), 3.47/43.5 (^{2}J, ^{1}Rζ/^{1}Rη), 2.18/179.9 (^{2}J, ^{1}Rδ/^{1}Rγ), 2.18/168.1 (^{4}J, ^{1}Rδ/^{1}Rα), 2.18/134.0 (^{3}J, ^{1}Rδ/^{1}Rβ); HSQC (500 MHz, chloroform-d$_1$, 296 K), δ(ppm): 9.36/167.4 (^{1}J, ^{1}Rα/^{1}Rα), 6.34/133.9 (^{1}J, ^{1}Rβ/^{1}Rβ), 3.47/63.2 (^{1}J, ^{1}Rζ/^{1}Rζ), 2.18/35.7 (^{1}J, ^{1}Rδ/^{1}Rδ);

NMR description: In the NMR spectrum two isomers of functionality **R** appear by two analogous signal sets $^{1/2}$R (^{1}R/^{2}R = 90/10), however their configuration cannot be derived from the data. Following the most intensive signal-set ^{1}R is discussed in detail. For signal set ^{2}R the 2D NMR-data are incomplete due to the low intensity. In the ^{1}H NMR spectrum (Figure S13a) the protons ^{1}Rα, ^{1}Rβ and ^{1}Rδ of the C$_4$-backbone (red) appear by two doublets (J = 8.9 Hz) at 9.37 ppm and 6.34 ppm as well as a singlet at 2.18 ppm, respectively. For protons ^{1}Rα and ^{1}Rβ, the chemical shifts and coupling constant of 8.9 Hz, are in the range for *cis*-orientated olefinic protons, concluding a *Z*-conformation of **R**.[5] In COSY (Figure S13b) a cross-peak at 9.37 ppm/3.46 ppm corresponds to a ^{4}J coupling between the protons ^{1}Rα and ^{1}Rζ and indicates the connection of the C$_4$-backbone to the *en*-substituent (blue). For the C$_4$-backbone ^{13}C chemical shifts of 167.4 ppm (^{1}Rα), 133.9 ppm (^{1}Rβ), 180.0 ppm (^{1}Rγ) and 35.7ppm (^{1}Rδ) were derived from the HSQC/HMBC-spectra (Figure S13d/e), respectively. In HMBC the C$_4$-backbone is indicated by ^{2}J and ^{3}J couplings between proton ^{1}Rα/carbon ^{1}Rβ (9.37 ppm/134.0 ppm), proton ^{1}Rδ/carbon ^{1}Rγ (2.18 ppm/179.9 ppm) and proton ^{1}Rδ/carbon ^{1}Rβ (2.18 ppm/134.0 ppm), respectively. Moreover, the connection of the C$_4$-backbone to the *en*-substituent (blue) is indicated by a cross-peak at 3.47 ppm/168.1 ppm, corresponding to a ^{3}J coupling of proton ^{1}Rζ

with carbon ^{1}Rα. In the ^{1}H NMR spectrum the signal of the proton ^{1}Rζ appears as a triplet (3.46 ppm, J = 5.6 Hz) due to the ^{3}J coupling with the proton ^{1}Rη, whereas ^{1}Rη and ^{1}Rθ are covered by the peaks of *en*. In COSY (Figure S13c) the cross-peaks at 3.46 ppm/2.8 ppm and 2.8 ppm/3.46 ppm correspond to the coupling of protons ^{1}Rζ and ^{1}Rη, pointing to a ^{1}H chemical shift of 2.8 ppm for ^{1}Rη.

Molecule 10 under water free conditions.

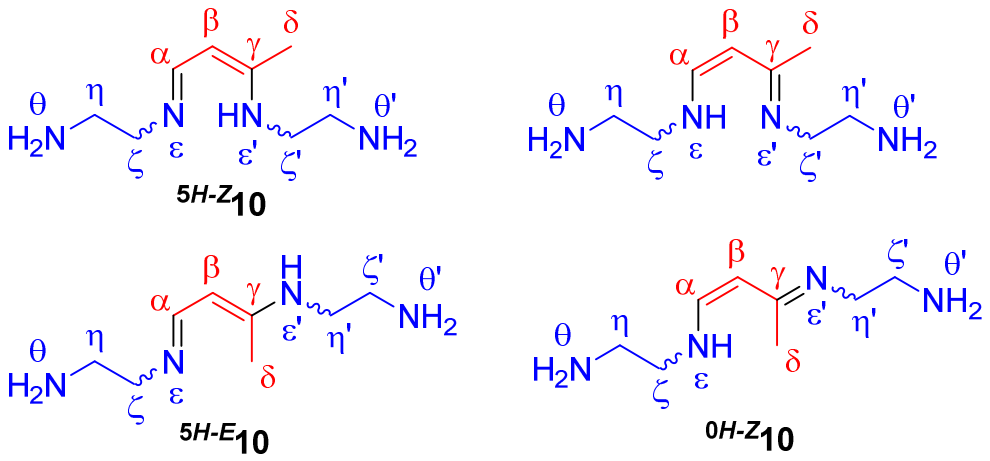

1D NMR data: see Table S7

2D NMR data:

Signal set ^{1}10: COSY (500 MHz, chloroform-d$_1$, 296 K), δ(ppm): 7.79/4.24 (^{3}J, ^{1}10α/^{1}10β), 7.79/2.94 (^{4}J, ^{1}10α/^{1}10ζ); HMBC (500 MHz, chloroform-d$_1$, 296 K), δ(ppm): 2.05/163.0 (^{2}J, ^{1}10δ/^{1}5γ), 2.05/79.8 (^{3}J, ^{1}10δ/^{1}10β), 4.25/22.3 (^{3}J, ^{1}10β/^{1}10δ), 7.79/79.5 (^{2}J, ^{1}10α/^{1}10β), 7.79/53.5 (^{3}J, ^{1}10α/^{1}10ζ), 2.98/162.9 (^{3}J, ^{1}10ζ'/^{1}10γ); HSQC (500 MHz, chloroform-d$_1$, 296 K), δ(ppm): 2.05/22.3 (^{1}J, ^{1}10δ/^{1}10δ), 4.24/79.5 (^{1}J, ^{1}10β/^{1}10β), 7.79/157.9 (^{1}J, ^{1}10α/^{1}10α), 2.92-3.00/53.3 (^{1}J, ^{1}10ζ/^{1}10ζ and ^{1}J, ^{1}10ζ'/^{1}10ζ');

Signal set ^{2}10: COSY (500 MHz, chloroform-d$_1$, 296 K), δ(ppm): 7.84/4.56 (^{3}J, ^{2}10α/^{2}10β), 7.84/3.25 (^{3}J, ^{2}10α/^{2}10ζ); HMBC (500 MHz, chloroform-d$_1$, 296 K), δ(ppm): 2.00/163.0 (^{2}J, ^{2}10δ/^{2}10γ), 2.00/82.2 (^{3}J, ^{2}10δ/^{2}10β), 7.83/82.0 (^{2}J, ^{2}10α/^{2}10β), 7.82/63.9 (^{3}J, ^{2}10α/^{2}10ζ), 3.21/161.5 (^{3}J, ^{2}10ζ/^{2}10α); HSQC (500 MHz, chloroform-d$_1$, 296 K), δ(ppm): 2.00/22.3 (^{1}J, ^{2}10δ/^{2}10δ), 4.57/82.0 (^{1}J, ^{2}10β/^{2}10β), 7.84/161.5 (^{1}J, ^{2}10α/^{2}10α), 3.21/63.8 (^{1}J, ^{2}10ζ/^{2}10ζ)

Signal set ^{3}10: COSY (500 MHz, chloroform-d_1, 296 K), δ(ppm): 7.46/3.11 (^{3}J, ^{3}10α/^{3}10β), HSQC (500 MHz, chloroform-d_1, 296 K), δ(ppm): 7.46/161.7 (^{1}J, ^{3}10α/^{3}10α), 3.11/64 (^{1}J, ^{3}10β/^{3}10β),

Signal set ^{4}10: COSY (500 MHz, chloroform-d_1, 296 K), δ(ppm): 7.51/3.33 (^{3}J, ^{3}10α/^{3}10β)

NMR description: In the NMR spectrum four different tautomers/isomers of molecule **10** appear by pairs of each two analogous signal sets, whereby it is unclear which signal-set corresponds to which isomer: $^{1/2}$10 (^{1}10/^{2}10 = 65/35), $^{3/4}$10 (^{3}10/^{4}10 = 80/20). According to coupling constants of 10-11.5 Hz for the doublets $^{1-4}$10α and $^{1-4}$10β we conclude that the bond between carbon α and β is in *Z*-configuration/conformation.[5] For signal sets $^{2-4}$10 the NMR data are incomplete due to the lower intensity and interferences with the peaks of *en*. As follows from the integral ratio between $^{1-4}$10α and $^{1-4}$10δ which is ca. 1:3, the methyl-protons δ of tautomeric pairs appear at almost identical chemical shifts, 2.05 and 2.0 ppm, respectively. In some spectra it can be seen that the singlets at 2.05 ppm and 2.0 ppm are each a superposition of two individual singlets (Figure S14). Moreover, the appearance of coupling patterns of signals $^{1-4}$10 points out that tautomerization/isomerization of **10** in water-free *en* is slow with respect to NMR time-scale. In the following the most intensive and ambiguous signal-set ^{1}10 is discussed in detail.

In the ^{1}H NMR spectrum (Figure S8a/S13a) the protons ^{1}10α, ^{1}10β and ^{1}10δ of the C_4-backbone appear by two doublets (J = 11.6 Hz) at 7.79 ppm and 4.24 ppm as well as a singlet at 2.05 ppm, respectively. For protons ^{1}10α and ^{1}10β, the chemical shifts and coupling constant of 11.6 Hz, are in the range for *cis*-orientated olefinic protons.[5] In COSY (Figure S8b/S13b) a cross-peak at 7.79 ppm/2.94 ppm is visible and indicates a ^{4}J coupling between the protons ^{1}10α and ^{1}10ζ. For the C_4-backbone ^{13}C chemical shifts of 157.9 (^{1}10α), 79.5 (^{1}10β), 163.0 (^{1}10γ), 22.3 (^{1}10δ) ppm were derived from the HSQC/HMBC-spectra (Figure S8c,d/S13c,d), respectively. In HMBC the C_4-backbone is indicated by ^{2}J and ^{3}J couplings between proton ^{1}10α/carbon ^{1}10β (7.79 ppm/79.5 ppm), proton ^{1}10δ/carbon ^{1}10γ (2.05 ppm/163.0 ppm) and proton ^{1}10δ/carbon ^{1}10β (2.05 ppm/79.5 ppm), respectively. Moreover, the

connection of the C_4-backbone to the *en*-substituents (blue) is indicated by cross-peaks at 2.95 ppm/157.9 ppm and 2.98 ppm/162.9 ppm, which are attributed to ^3J couplings of proton ^{1}10ζ with carbon ^{1}10α and proton ^{1}10ζ' with carbon ^{1}10γ, respectively. In the ^{1}H NMR spectrum the signals of the protons ^{1}10ζ (2.95 ppm) and ^{1}10ζ' (2.98 ppm) are very close to the *en* peak at 2.5-3 ppm, but just are recognizable. Thereby, a triplet structure is visible, which is due to the coupling of protons ^{1}10ζ and ^{1}10ζ' with ^{1}10η and ^{1}10η', respectively. In the NMR-spectra no signals/couplings of/with –N*H* appear. Due to the similarity of the protons ^{1}10η-^{1}10θ and ^{1}10η'-^{1}10θ' with *en*, the corresponding NMR signals are hidden under the *en* peaks, respectively.

Scheme S3. Supposed mechanism of a) water-triggered tautomerization/isomerization of **10** and b) tautomerization of **11**. Due to the open structure of **10**, the conformation of the C_4-backbone can change, whereas in case of **11** the conformation of the molecule is fixed because of its ring structure, and only tautomerization can occur. For the C_4-backbone both the configuration of the double bond as well as its conformation are given by superscripted prefixes.

a)

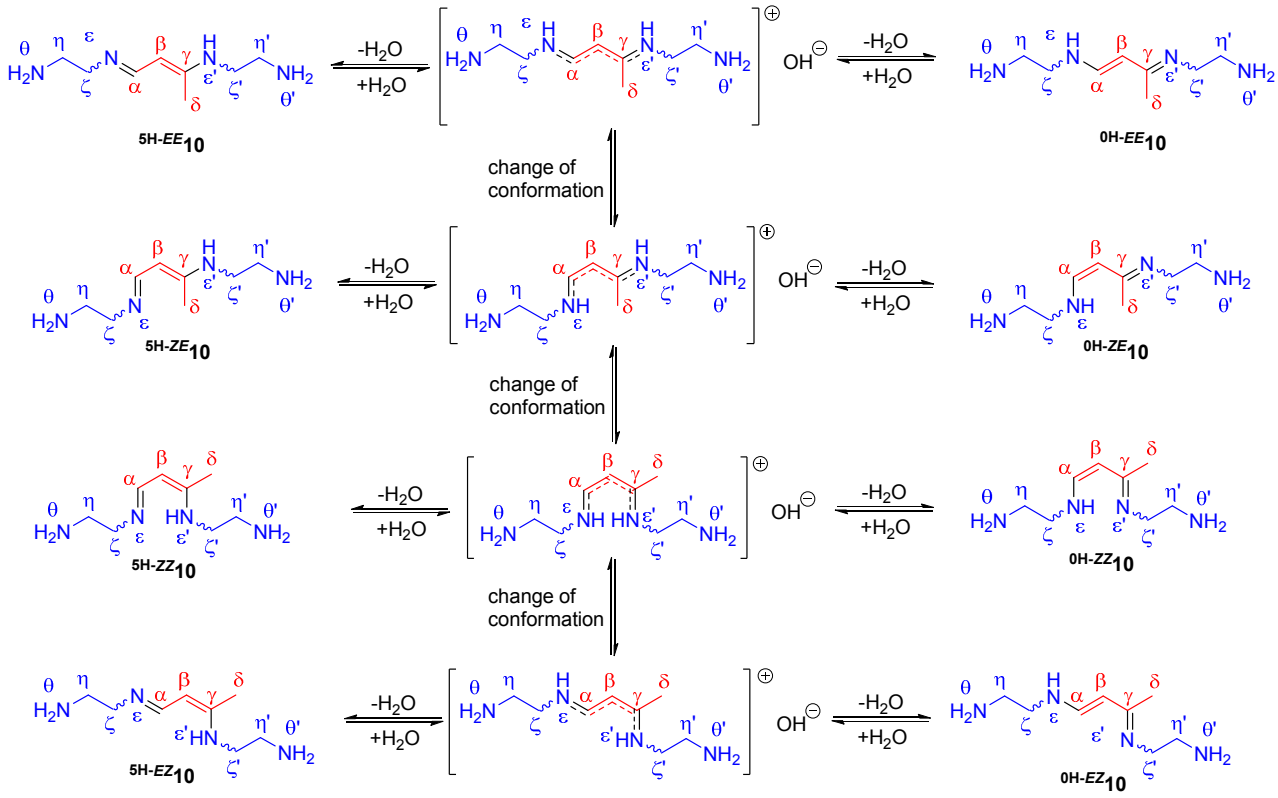

b)

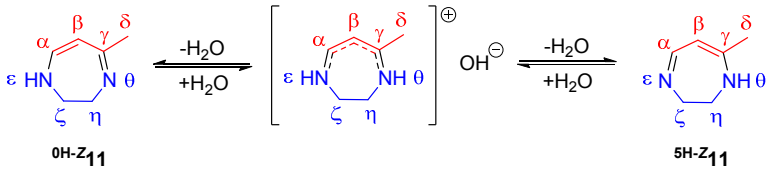

Molecule 10 in presence of water traces.

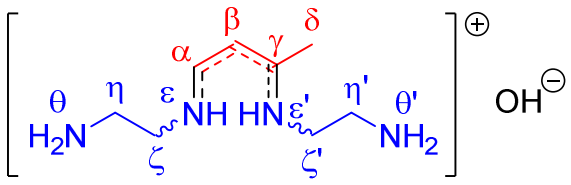

10

1D NMR data: see Table S7

2D NMR data: no couplings visible

NMR description: In water-free *en* the tautomerization/isomerization of **10** is slow, with respect to NMR time scale. However, in *en* containing water traces the signals of **10** broaden (signals denoted by $^{5\text{-}7}$10) and the coupling patterns disappear (Figure S15). We suppose that in presence of water molecule **10** tautomerizes/isomerizes fast according to the mechanism described in Scheme S3a. Due to the open structure of **10** the configuration/conformation of the C_4-backbone can change. As a further consequence of fast tautomerization the average chemical surroundings of the protons ζ and ζ' are almost identical (the only difference is the position of the methyl-group), and in ^{1}H NMR both protons appear at almost identical chemical shifts. The same argumentation is valid for protons η/η' and θ/θ', however these signals cannot be detected due to overlaps with *en*-peaks.

Molecule 11 in presence of water traces.

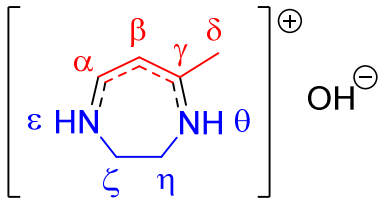

11

1D NMR data: see Table S7

2D NMR data: COSY (500 MHz, chloroform-d_1, 296 K), δ(ppm): 6.87/4.55 (^3J, 11α/11β); HMBC (500 MHz, chloroform-d_1, 296 K), δ(ppm): 6.87/161.6 (^3J, 11α/11γ), 4.54/161.6 (^2J, 11β/11γ), 2.01/161.6 (^2J, 11δ/11γ), 4.56/148.6 (^2J, 11β/11α), 6.87/91.9 (^2J, 11α/11β), 2.00/91.9 (^3J, 11δ/11β), 6.87/52.3 (^3J, 11α/11ζ), 4.56/25.3 (^3J, 11β/11δ); HSQC (500 MHz, chloroform-d_1, 296 K), δ(ppm): 6.87/148.7 (^1J, 11α/11α), 4.55/91.9 (^1J, 11β/11β), 3.55/52.4 (^1J, 11ζ,η/11ζ,η), 2.01/25.2 (^1J, 11δ/11δ)

NMR description: Analogously to **10**, molecule **11** can tautomerize fast in *en* containing water traces. In ^{1}H NMR (Figure S6a) the protons 11α, 11β and 11δ of the C_4-backbone appear by two doublets (J = 7.4 Hz) at 6.87 ppm and 4.55 ppm as well as a singlet at 2.0 ppm, respectively. Due to the ring structure, the configuration of the C_4-backbone is fixed and no isomerization can occur upon tautomerization (Scheme S3b). Consequently, the resonances of the protons of the C_4-backbone exhibit coupling patters. For 11α and 11β, the chemical shifts and coupling constant of 7.4 Hz are typical for *cis*-orientated olefinic protons. The tautomerization of **11** is associated with fast proton exchange at the nitrogen atoms 11ε/11θ, and delocalization of the double bonds among the nitrogen and carbon atoms 11ε/11α/11β/11γ/11θ, respectively. Due to fast proton exchange, no couplings of the -N*H* groups to the C_4-backbone and *en*-substituent are visible, respectively. As a further consequence of fast tautomerization, are the averaged chemical surroundings of the protons 11ζ and 11η of the *en*-substituent (blue) almost identical (the only difference is the position of methyl-group), and in ^{1}H NMR solely one signal (11ζ/11η: 3.55 ppm, superposition of two close laying triplets, integral 4H) appears, respectively. For the C_4-backbone and *en*-substituent, ^{13}C chemical shifts of 148.7

(11α), 91.9 (11β), 161.6 (11γ), 25.2 (11δ) ppm and 52.3 (6ζ/6η) ppm were derived from the HSQC/HMBC-spectra (Figure S6c/d), respectively. In HMBC the C_4-backbone is indicated by ^2J and ^3J couplings between proton 11α/carbon 11β (6.87 ppm/91.9 ppm), proton 11β/carbon 11γ (4.54 ppm/161.6 ppm) and proton 11β/carbon 11δ (4.56 ppm/25.3 ppm), respectively. Moreover, the connection of the C_4-backbone to the *en*-substituent is indicated by a cross-peak at 6.87 ppm/52.3 ppm, which is attributed to a ^3J coupling of proton 11α with carbon 11ζ.

2.4. Summary of *in situ* NMR

In Table S8-S11 the outcomes of *in situ* NMR investigations are broken down for the different mixtures and references to the figures, showing the corresponding NMRspectra are given.

Table S8. Molecules and functionalities identified in test mixtures A-C

Test mixture					Results: NMR	
Type	**Nucleophile**	**3**	**4**	**Reaction time [h]**	**Molecules/ Funct.**	**Figure S**
A	*en* 1ml	60-240 µmol	-	20	**4**	5a
	en 1ml	240 µmol	-	3-147	**4**	5b
B	*en*/[H_2O] 1ml	120 µmol	-	3-100	**4**, **10**, **11**	7
	en/[H_2O] 1ml	120 µmol	-	>20	**10**, **11**	6
C	$KNH(CH_2)_2NHK$ 1 eq.	-	1 eq.	0.5	**10**	8

Table S9. Molecules and functionalities identified in test mixtures D-E

Test mixture					Result: NMR	
Type	**Nucleophile**	**n 3 [eq.]**	**m 4 [eq.]**	**Reaction time [h]**	**Molecules/ Funct.**	**Figure S**
D	K_4Ge_9	0.5	-	<8	^{E}**A**, **A'**	9
	K_4Ge_9	0.25-0.5	-	>20	^{EZ}**B**/^{ZZ}**B**	10/11b
	Rb_4Ge_9	0.25-0.5	-	>20	^{EZ}**B**/^{ZZ}**B**	11b
	K_4Ge_9	2	-	>20	^{E}**A**	11b
E	K_4Ge_9	0.5	4	>20	**10**	12

Table S10. Molecules and functionalities identified in test mixtures F-G

Test mixture					Results: NMR	
Type	**Nucleophile**	**m 4 [eq.]**	**n 3 [eq.]**	**Reaction time [h]**	**Molecules/ Funct.**	**Figure S**
F	K_4Ge_9	1	-	>20	**R**, **10**	13
	K_4Ge_9	2	-	0.5-20	**R**, **10**	14a
	Rb_4Ge_9	1	-	>20	**R**, **10**	14b
	Rb_4Ge_9	2	-	>20	**R**, **10**	14b
G	K_4Ge_9	1	0.5	20	**R**, **10**	16a
	K_4Ge_9	2	0.5	20	**R**, **10**	16a
	Rb_4Ge_9	2	0.5	20	**R**, **10**	16a

Table S11. Molecules and functionalities identified in test mixture H

Test mixture				Results: NMR	
Type	**Nucleophile**	**n/m 3/4 [eq.]**	**Reaction time [h]**	**Molecules/ Funct.**	**Figure S**
H	K_4Ge_9	0.5/1	20	^{EZ}**B**/^{ZZ}**B**, **R**, **10**	16b
	Rb_4Ge_9	0.5/1	20	^{EZ}**B**/^{ZZ}**B**, **R**, **10**	16b
	K_4Ge_9	0.5/2	0.5-20	^{EZ}**B**/^{ZZ}**B**, **R**, **10**	17
	K_4Ge_9	0.5/2	20	^{EZ}**B**/^{ZZ}**B**, **R**, **10**	16b
	Rb_4Ge_9	0.5/2	20	^{EZ}**B**/^{ZZ}**B**, **R**, **10**	16b

2.5 NMR spectra and details on the preparation of test mixtures

In the following the NMR spectra of the test mixtures are shown. Experimental details on the preparation of the mixtures are given in the figure captions. In most cases only sections of the spectra are given and the intensity scales of different spectral regions were adjusted in a way that all relevant signals can be seen. r.t. = reaction time.

2.5.1 Reaction of *en* with 3

2.5.1.1 water-free *en* [2]

The following spectra correspond to test mixtures type A

Figure S5. a) ^{1}H NMR spectra of test mixtures prepared by reacting 23.4 mg (60 µmol), 46.7 mg (120 µmol) and 93.4 mg (240 µmol) of **3** with each 1 ml of water-free *en* (r.t. = 20 h). **3** dissolved in *en* within 1 h and transparent pale yellow solutions were obtained. The mixtures contain ^{Z}**4** and ^{E}**4**, and the overall concentration of **4** in the solution increases with the initial amount of **3**; b) ^{1}H NMR spectra of a mixture obtained by dissolving 93.4 mg (240 µmol) in 1 ml water-free *en* after reaction times of 3, 24 and 147 h. After a reaction time of 3 h the maximal concentration of $^{E/Z}$**4** is reached and remains constant.

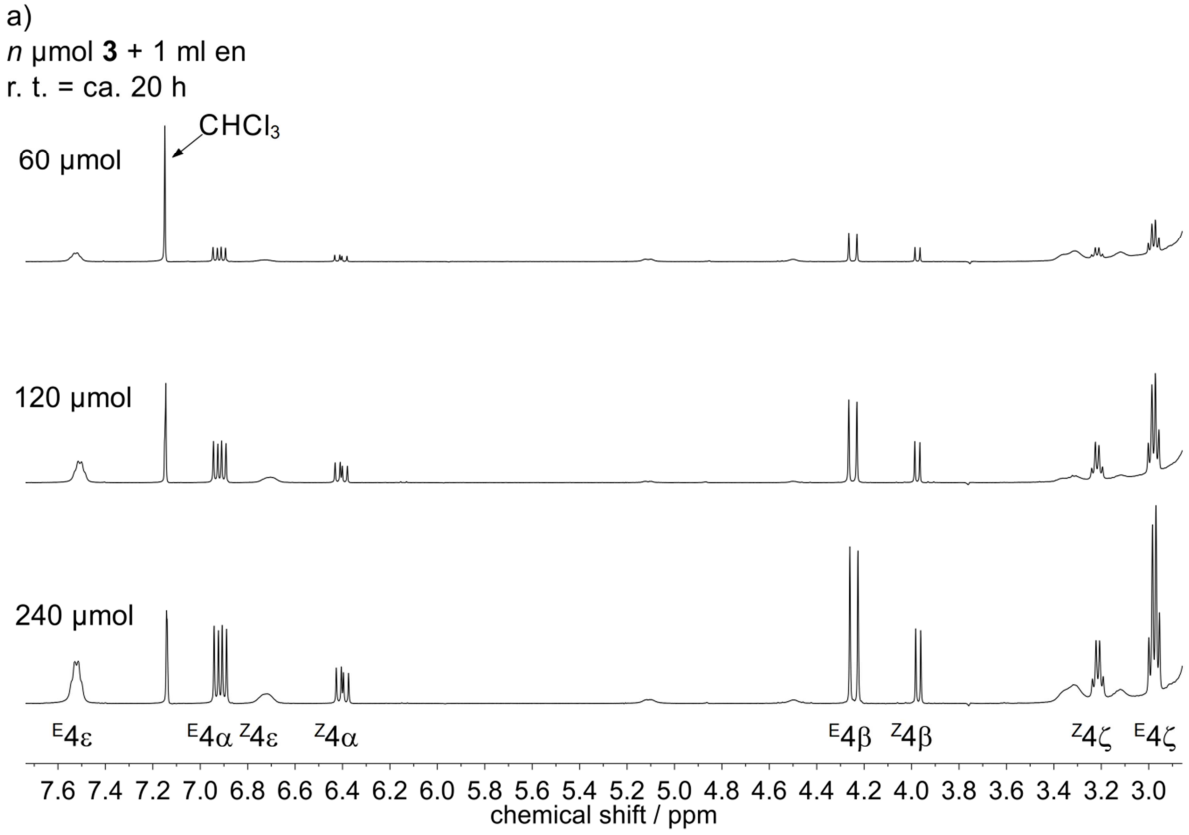

b) 240 µmol **3** + 1 ml *en*
r.t = variable

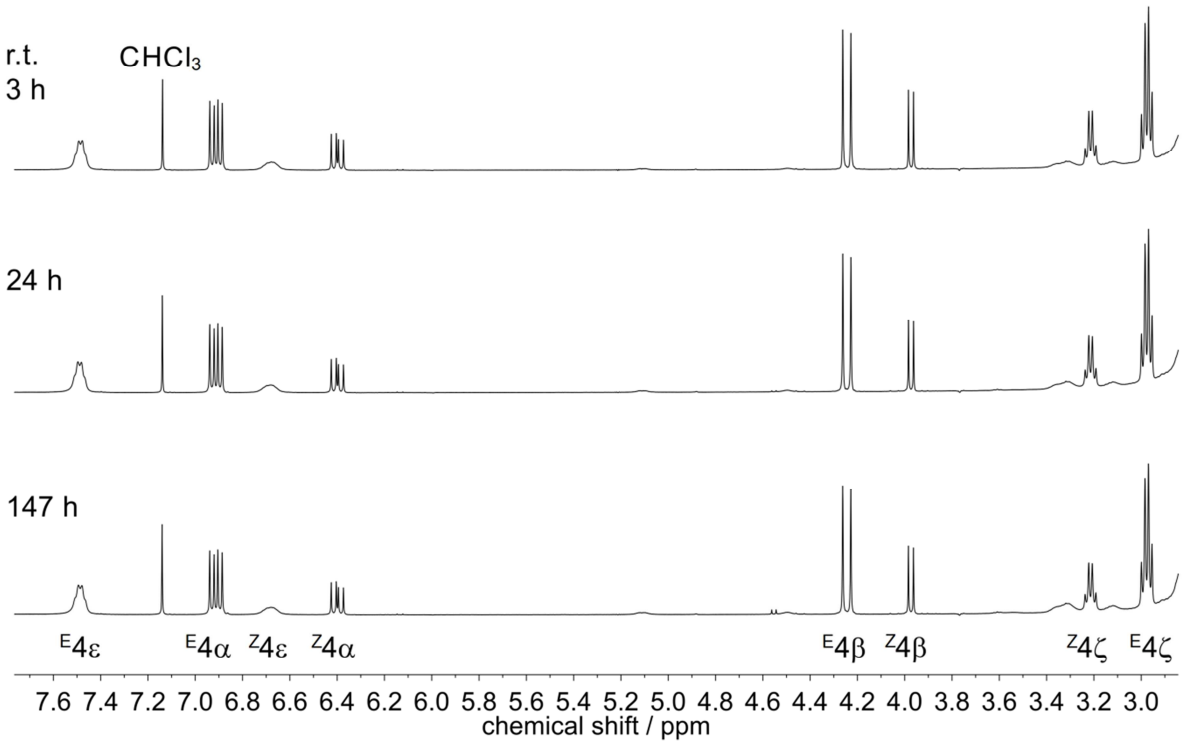

2.5.1.2 *en* containing water traces

The following spectra correspond to test mixtures type B

Figure S6. a) ^{1}H, b) COSY, c) HMBC and d) HSQC spectra of a test mixture, prepared by dissolving 46.7 mg (240 µmol) of **3** in 2 ml *en* containing ca. 0.5-1% water (r.t. > 20 h). Initially the colour of the mixture was pale yellow, but turned into intensive orange after 100 h. The NMR spectra exhibit signals of **10** and **11**, which both tautomerize/isomer fast in presence of water.

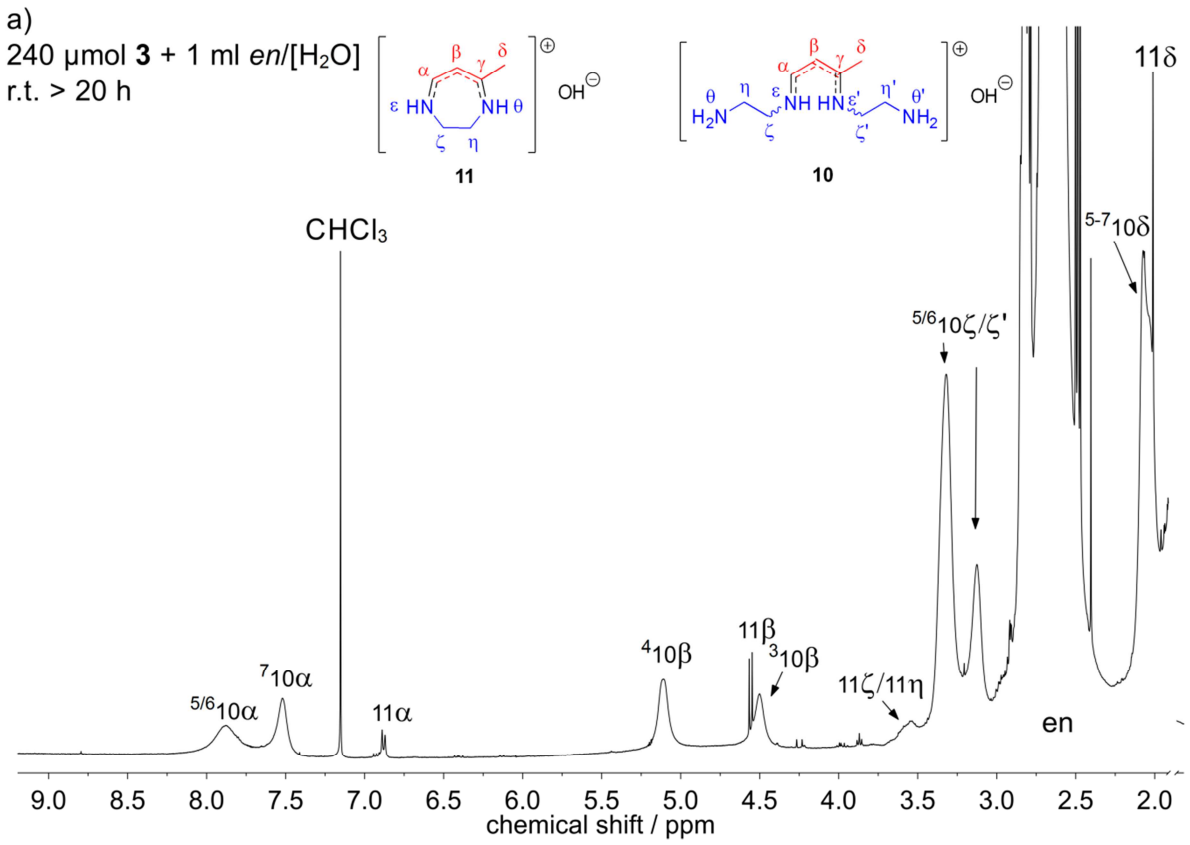

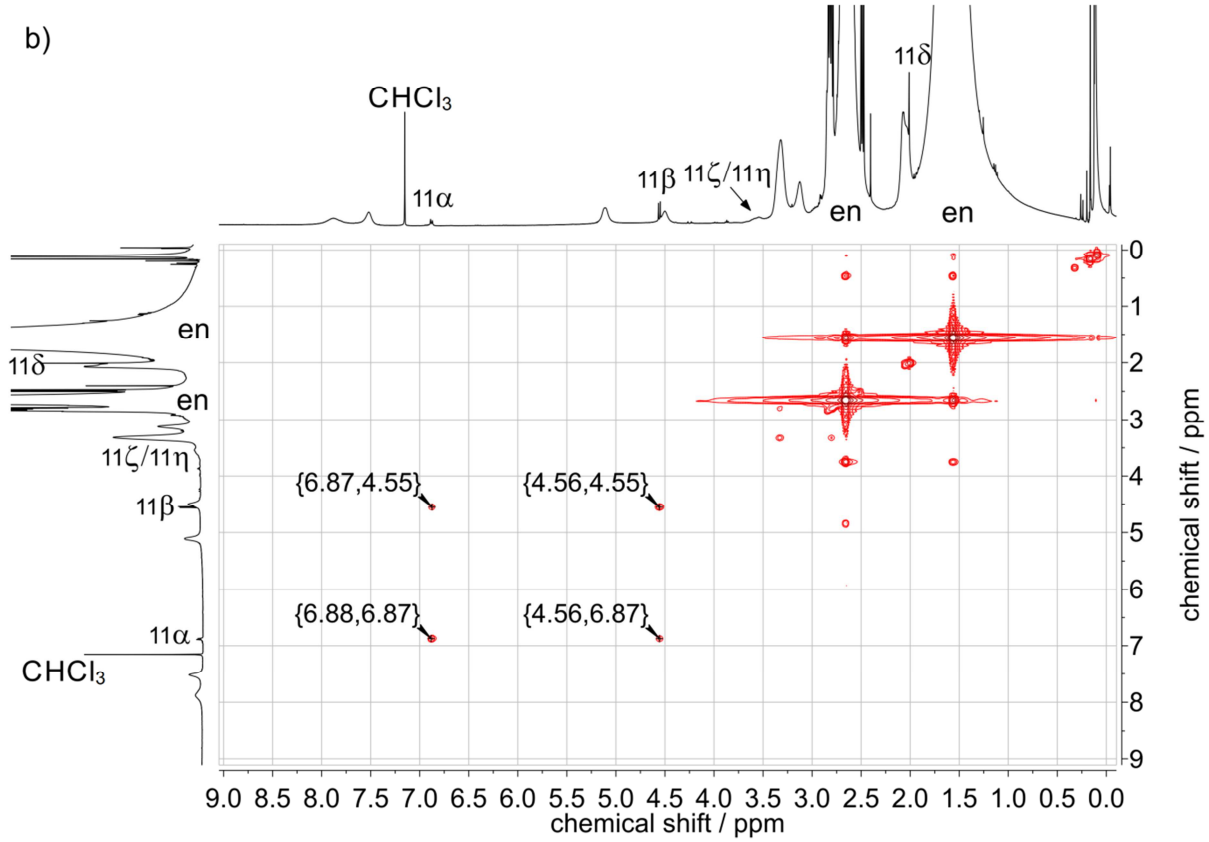
b)
CHCl3
11α
11β
11ζ/11η
11δ
en
en
en
11δ
en
11ζ/11η
11β
11α
CHCl3
{6.87,4.55}
{4.56,4.55}
{6.88,6.87}
{4.56,6.87}
chemical shift / ppm
chemical shift / ppm

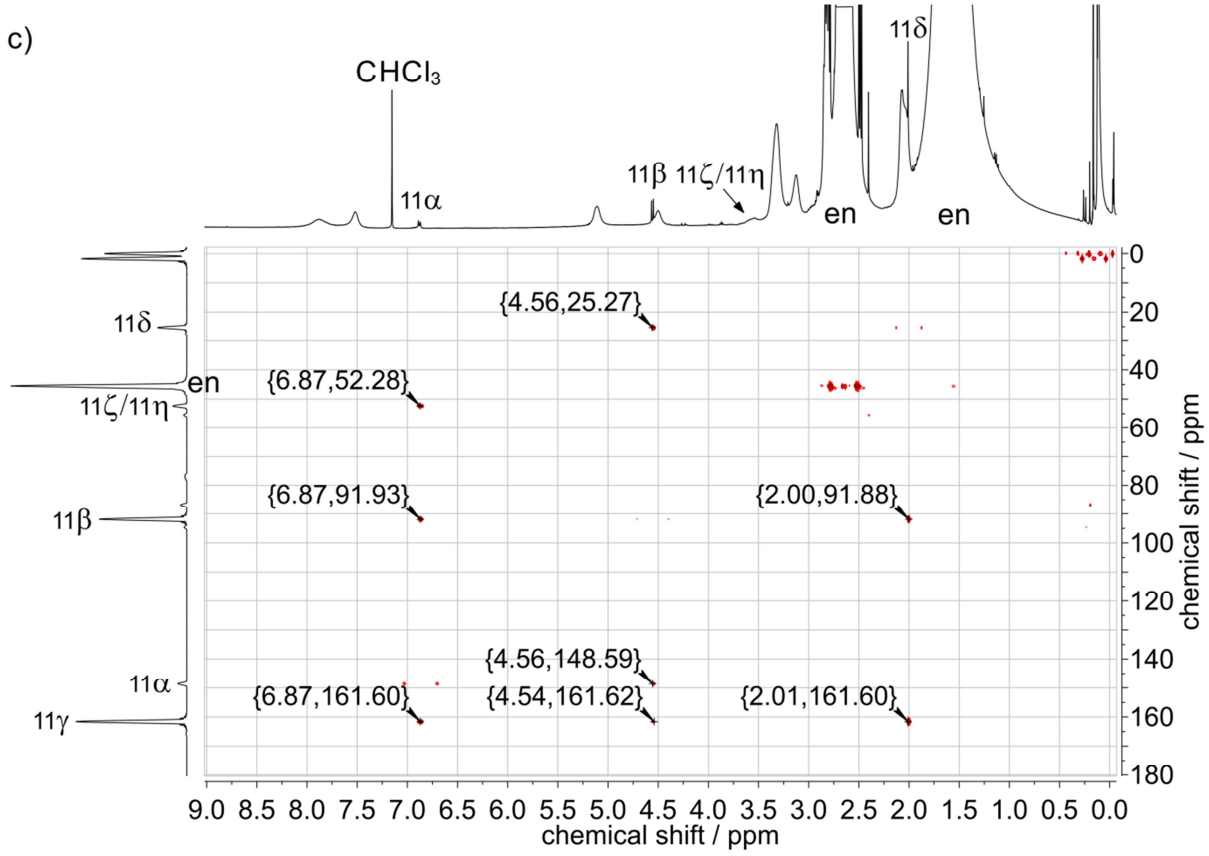
c)
CHCl3
11α
11β
11ζ/11η
11δ
en
en
11δ
en
11ζ/11η
11β
11α
11γ
{4.56,25.27}
{6.87,52.28}
{6.87,91.93}
{2.00,91.88}
{4.56,148.59}
{6.87,161.60}
{4.54,161.62}
{2.01,161.60}
chemical shift / ppm
chemical shift / ppm

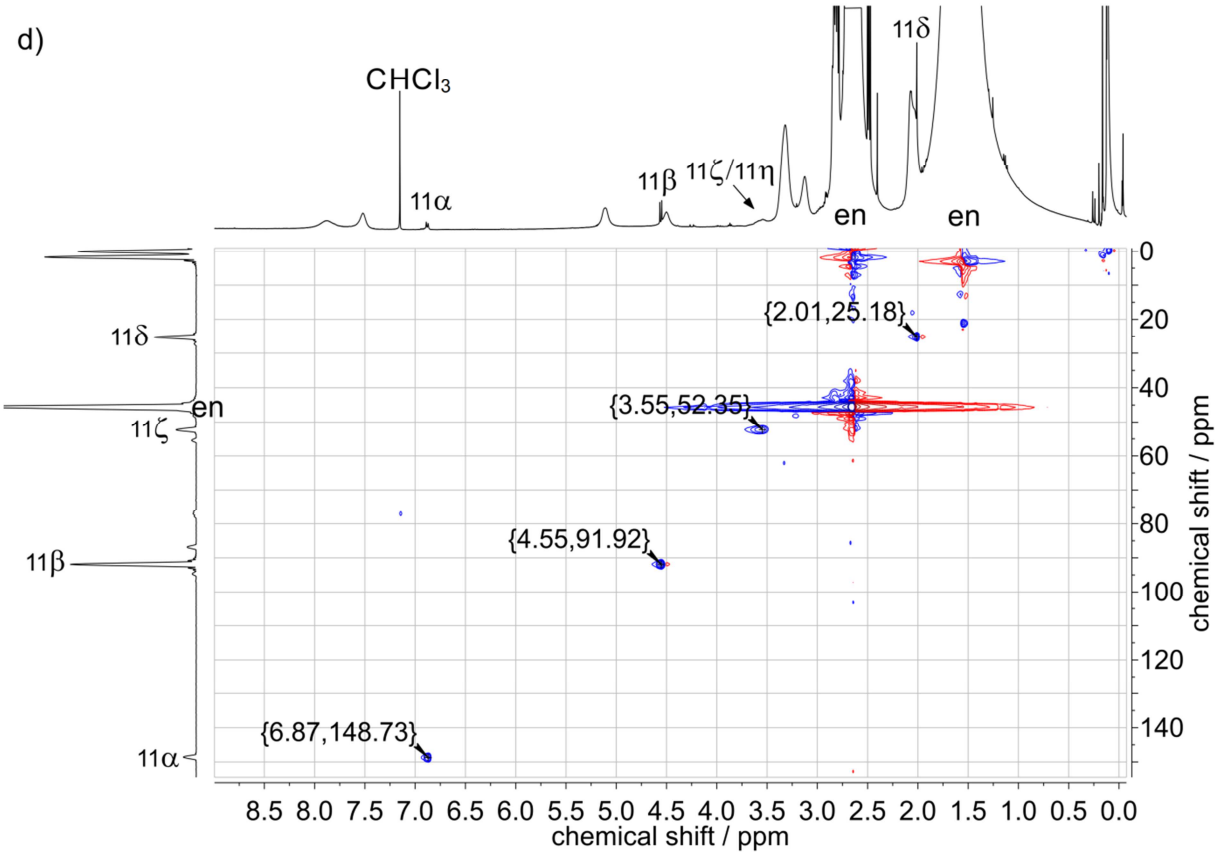
d)
CHCl3
11α
11β
11ζ/11η
en
en
11δ
{2.01,25.18}
{3.55,52.35}
{4.55,91.92}
{6.87,148.73}
11δ
en
11ζ
11β
11α
8.5 8.0 7.5 7.0 6.5 6.0 5.5 5.0 4.5 4.0 3.5 3.0 2.5 2.0 1.5 1.0 0.5 0.0
chemical shift / ppm
0 20 40 60 80 100 120 140
chemical shift / ppm

Figure S7. ^{1}H NMR spectra of a test mixture, prepared by dissolving 46.7 mg (240 µmol) of **3** in 2 ml *en* containing ca. 0.5-1% water, in dependence of reaction time (3, 20, 100 h). After reaction times of 3 h, signals of **4**, **10** and **11** are visible. With increasing reaction time the concentration of **4** decreases and after 100 h solely **10** and **11** are visible.

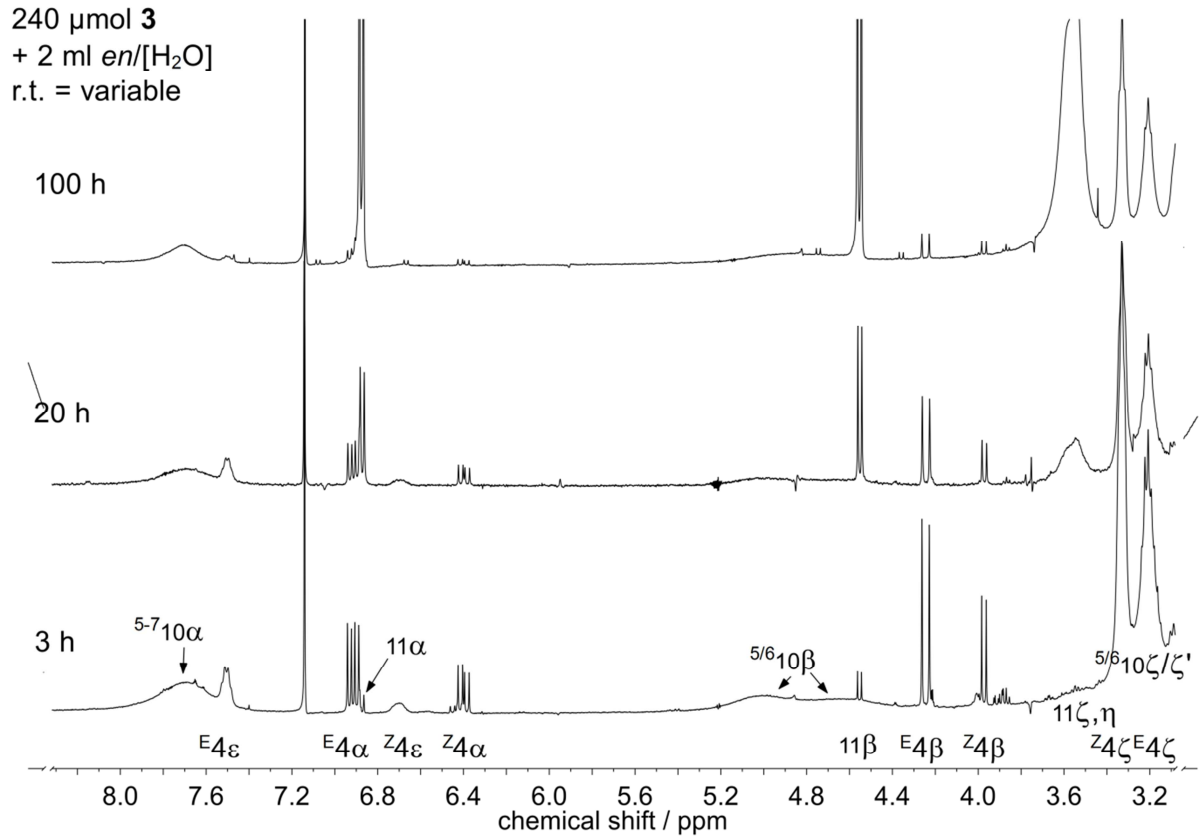

2.5.2 Reaction of $KNH(CH_2)_2NHK$ with 4 in water-free *en*

The following spectra correspond to test mixture type C

Figure S8. a) ^1H, b) COSY, c) HMBC and d) HSQC NMR spectra as well as e) a photography of a test mixture, prepared by dissolving $KNH(CH_2)_2NHK$ (6.1 mg , 45 µmol, 1 eq.) in 0.75 ml of an *en*-solution (water-free) containing 60 µmol/ml **4** (**4**: 45 µmol, 1 eq.). Immediately upon addition of $KNH(CH_2)_2NHK$ the color of the solution turned into intensive deep-orange. The mixture was stirred for 30 min, before a sample for NMR was taken. The NMR spectra show signals of **10**.

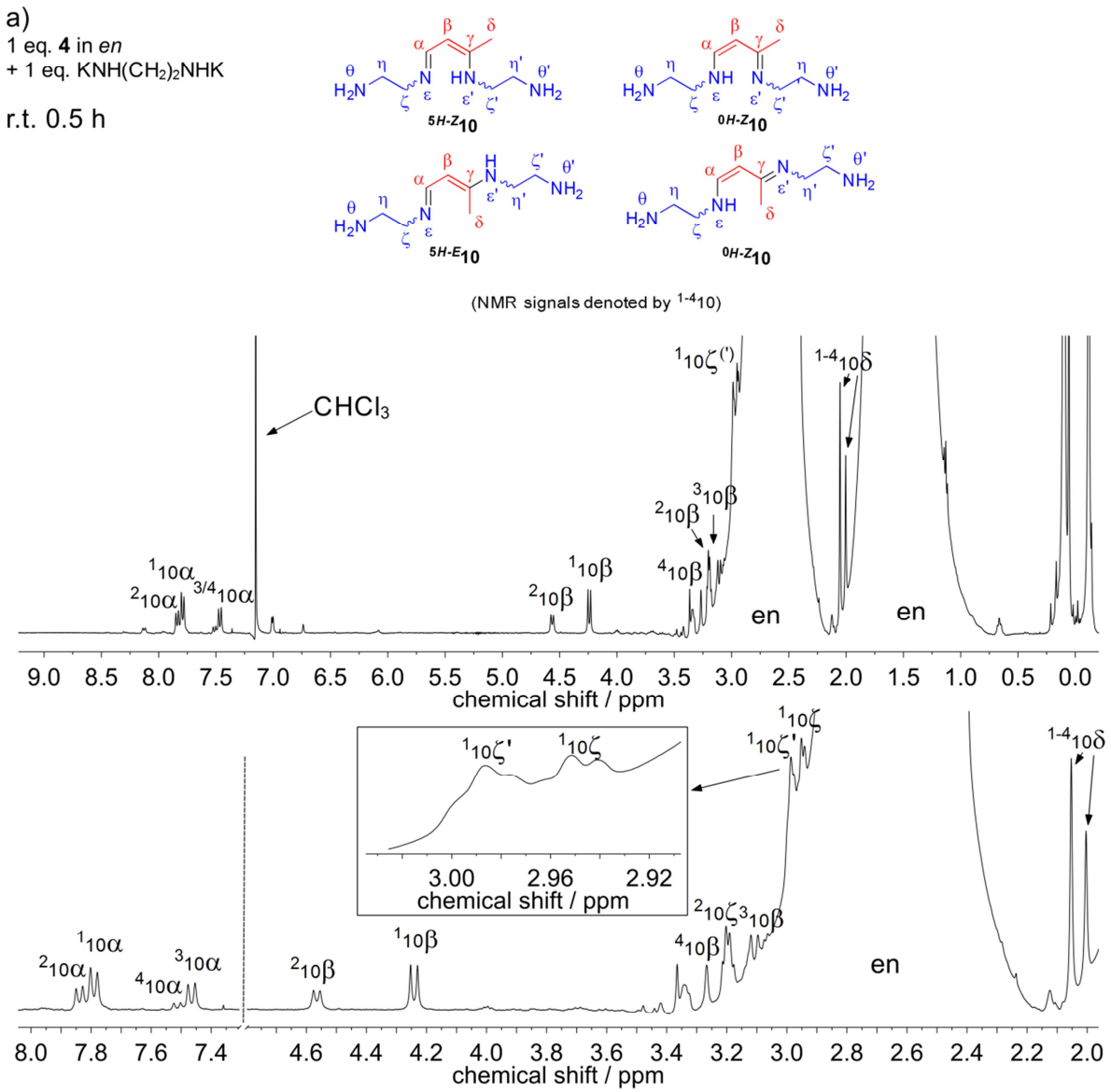

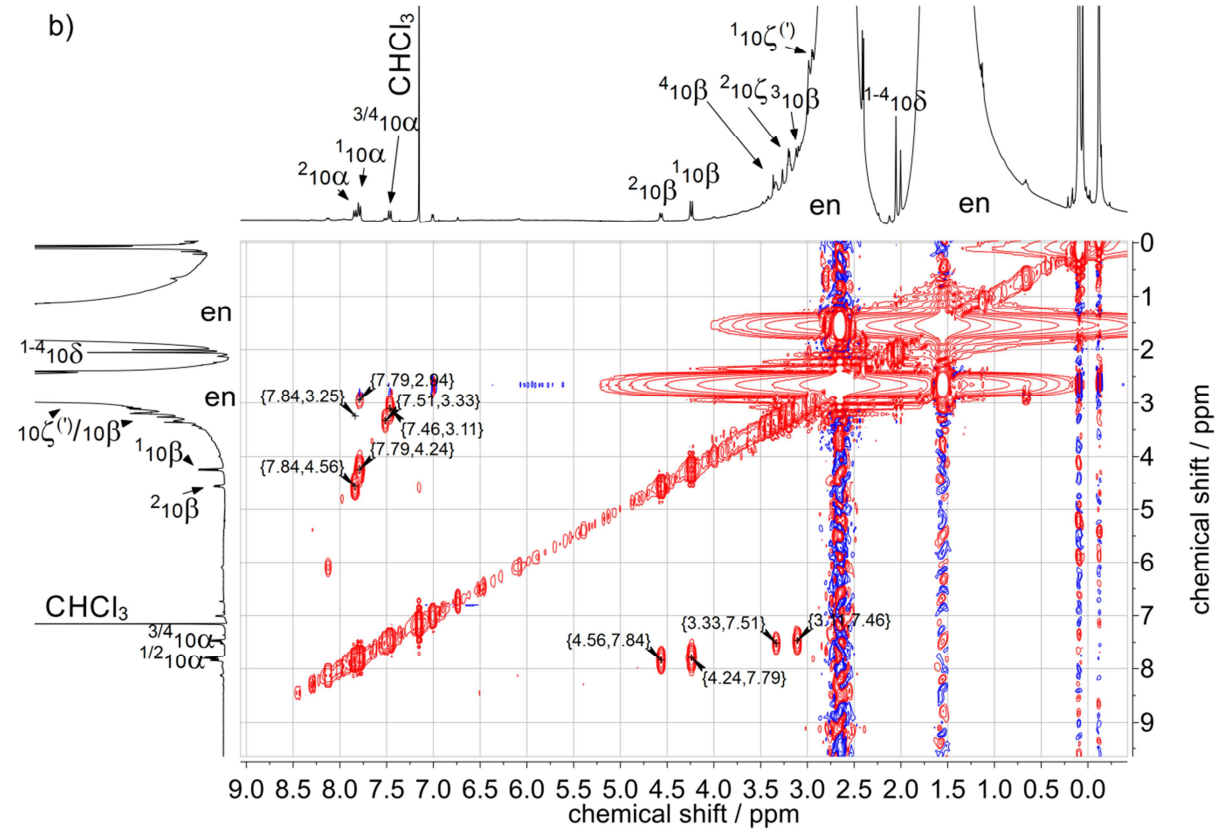
b)
CHCl3
3/4 10α
1 10α
2 10α
2 10β
1 10β
4 10β
2 10ζ 3 10β
1 10ζ(')
1-4 10δ
en
en
en
1-4 10δ
10ζ(')/10β
1 10β
2 10β
CHCl3
3/4 10α
1/2 10α
{7.84,3.25}
{7.79,2.94}
{7.51,3.33}
{7.46,3.11}
{7.84,4.56}
{7.79,4.24}
{4.56,7.84}
{3.33,7.51}
{3.11,7.46}
{4.24,7.79}
9.0 8.5 8.0 7.5 7.0 6.5 6.0 5.5 5.0 4.5 4.0 3.5 3.0 2.5 2.0 1.5 1.0 0.5 0.0
chemical shift / ppm
0 1 2 3 4 5 6 7 8 9
chemical shift / ppm

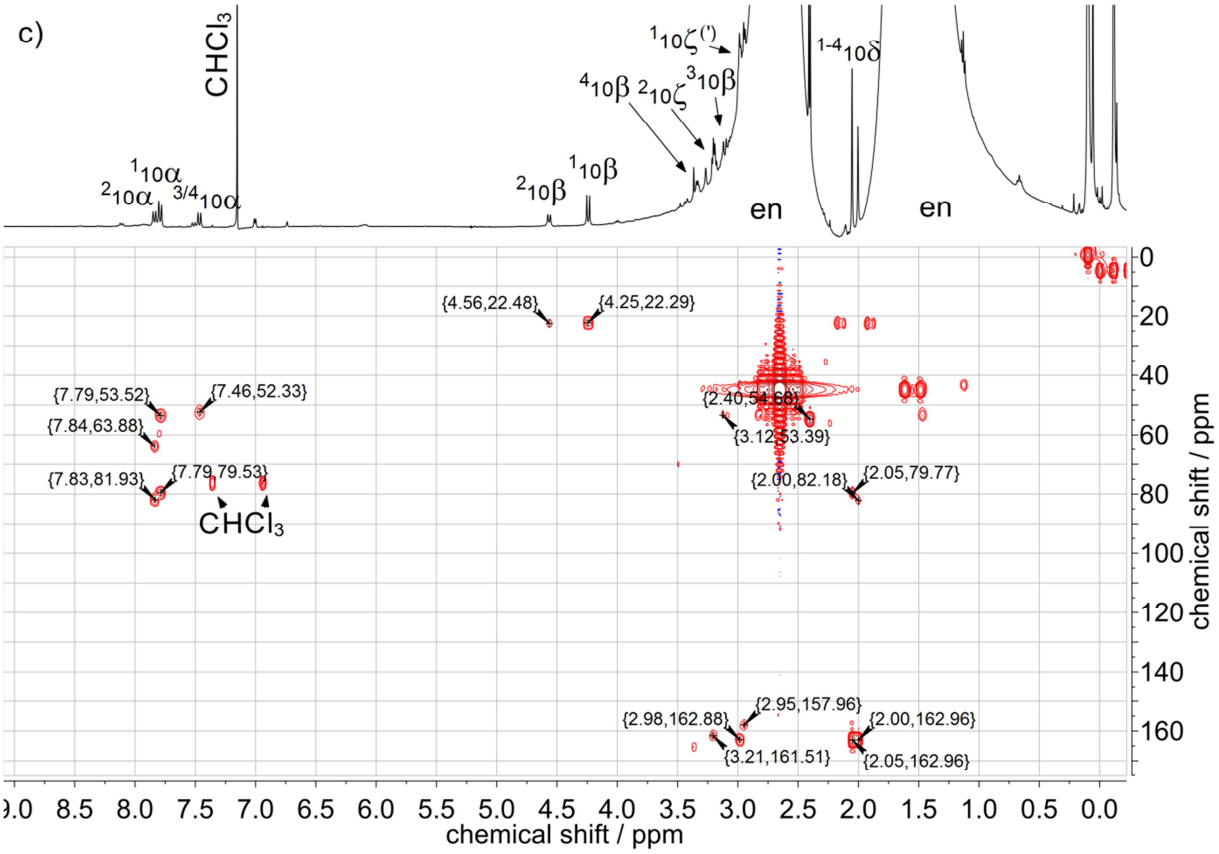
c)
CHCl3
1 10α
2 10α
3/4 10α
2 10β
1 10β
4 10β
2 10ζ 3 10β
1 10ζ(')
1-4 10δ
en
en
{4.56,22.48}
{4.25,22.29}
{7.79,53.52}
{7.46,52.33}
{7.84,63.88}
{7.83,81.93}
{7.79,79.53}
CHCl3
{2.40,54.68}
{3.12,53.39}
{2.00,82.18}
{2.05,79.77}
{2.98,162.88}
{2.95,157.96}
{3.21,161.51}
{2.00,162.96}
{2.05,162.96}
9.0 8.5 8.0 7.5 7.0 6.5 6.0 5.5 5.0 4.5 4.0 3.5 3.0 2.5 2.0 1.5 1.0 0.5 0.0
chemical shift / ppm
0 20 40 60 80 100 120 140 160
chemical shift / ppm

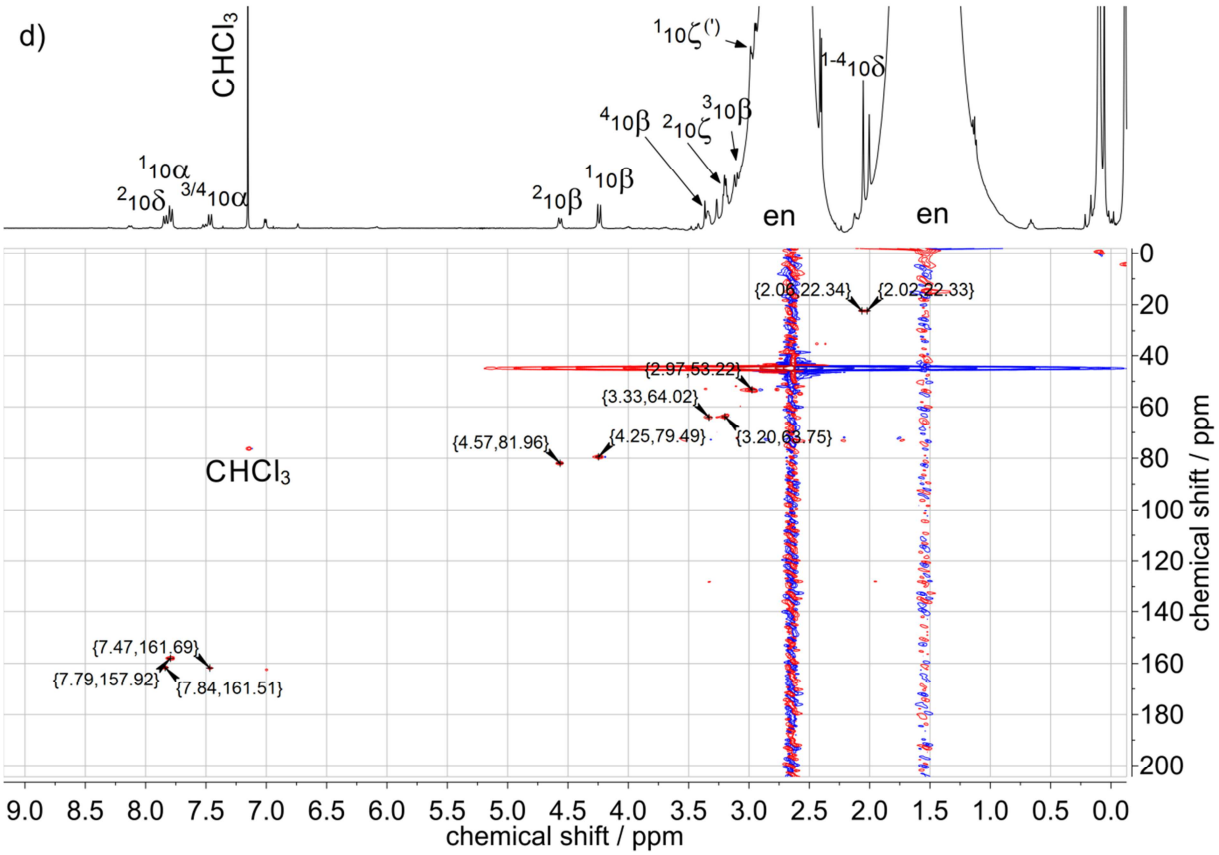
d)
CHCl3
1 10α
2 10δ
3/4 10α
2 10β
1 10β
4 10β
2 10ζ
3 10β
1 10ζ(')
1-4 10δ
en
en
{2.06,22.34}
{2.02,22.33}
{2.97,53.22}
{3.33,64.02}
{4.57,81.96}
{4.25,79.49}
{3.20,63.75}
CHCl3
{7.47,161.69}
{7.79,157.92}
{7.84,161.51}
chemical shift / ppm
chemical shift / ppm

e)

2.5.2 Reaction of $[Ge_9]^{4-}$ with 3 and 4 in water-free *en*

The following spectra correspond to test mixture type D

Figure S9. a) ^{1}H, b) COSY, c) HMBC and d) HSQC NMR spectra of a solution, prepared by dissolving a pre-mixture of the neat solids K_4Ge_9 (97.2 mg , 120 µmol, 1 eq.) and **3** (11.6 mg, 60 µmol, 0.5 eq.) in 2 ml *en*, after reaction times of < 8h. The reactants dissolved within 15 min and a homogenous dark-brown solution was obtained. In the NMR-spectra, signals corresponding to the organic functionalities ^{E}**A** and **A'** appear. Unknown signals are marked with ‡.

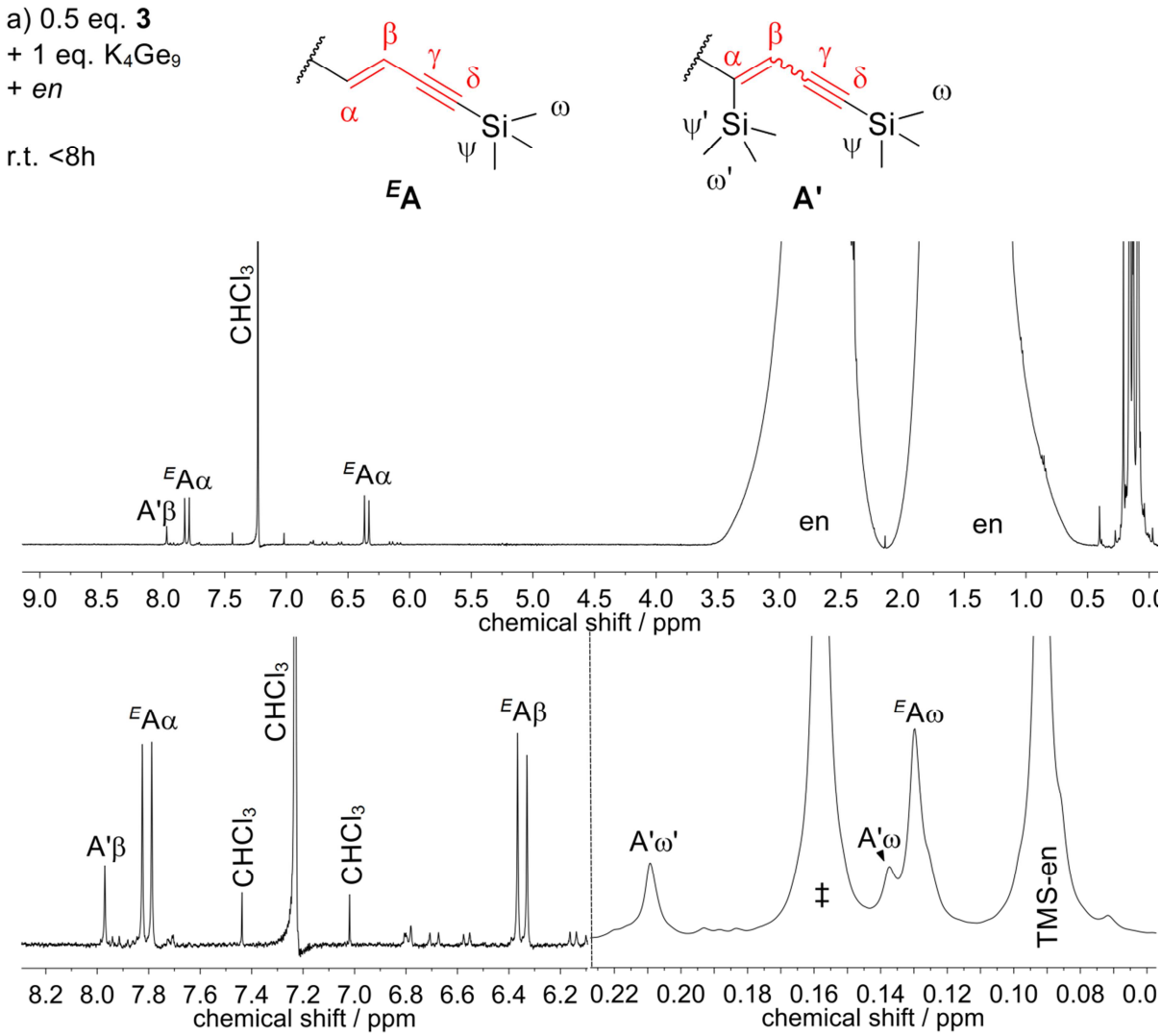

b)

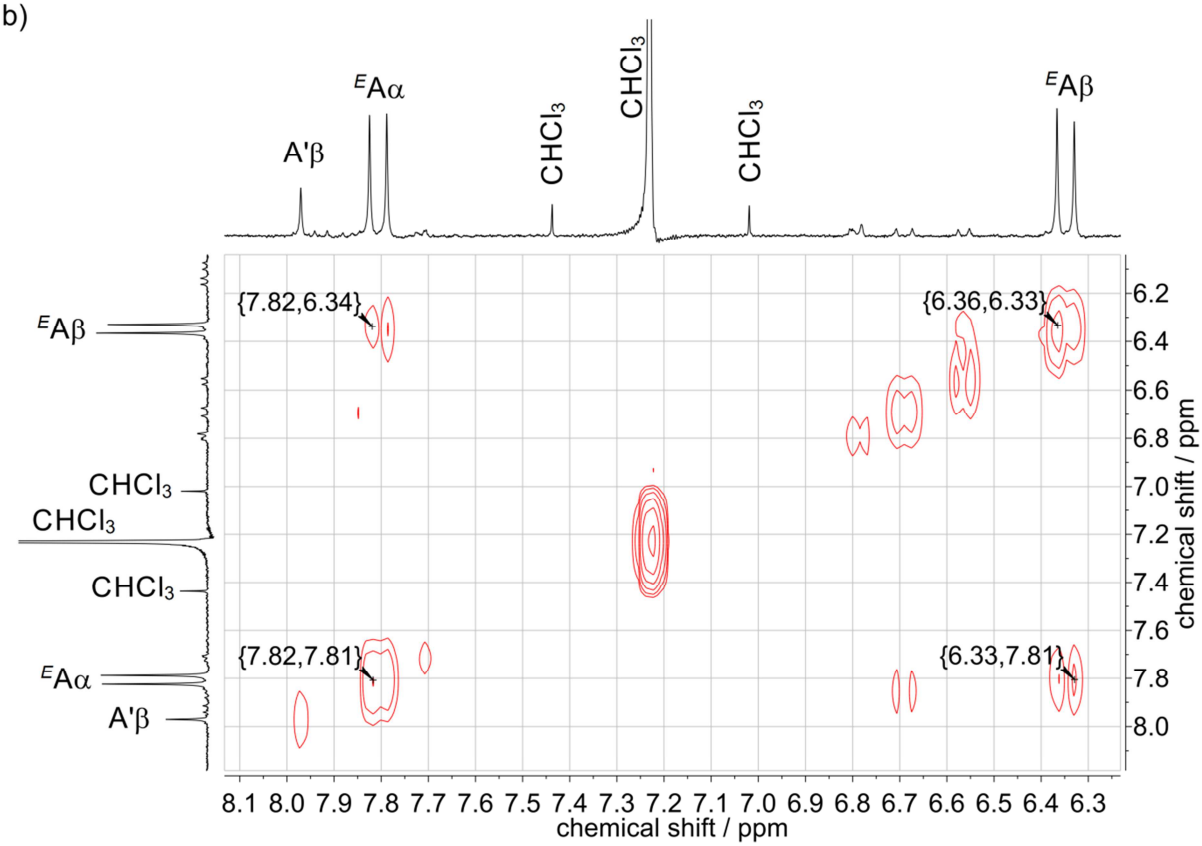
^{E}Aα
A'β
CHCl$_3$
CHCl$_3$
CHCl$_3$
^{E}Aβ
{7.82,6.34}
{6.36,6.33}
{7.82,7.81}
{6.33,7.81}
chemical shift / ppm
chemical shift / ppm

c)

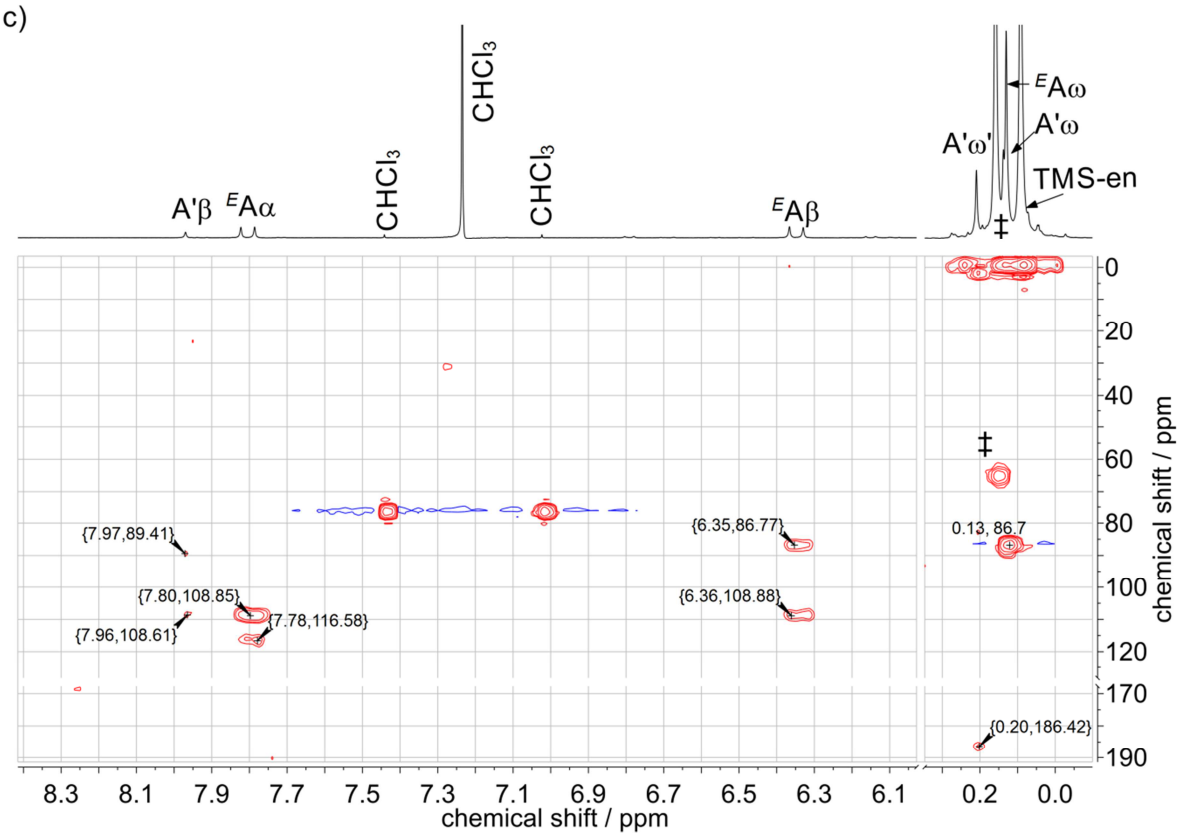
A'β
^{E}Aα
CHCl$_3$
CHCl$_3$
CHCl$_3$
^{E}Aβ
^{E}Aω
A'ω
A'ω'
TMS-en
‡
{7.97,89.41}
{7.80,108.85}
{7.96,108.61}
{7.78,116.58}
{6.35,86.77}
{6.36,108.88}
0.13, 86.7
{0.20,186.42}
chemical shift / ppm
chemical shift / ppm

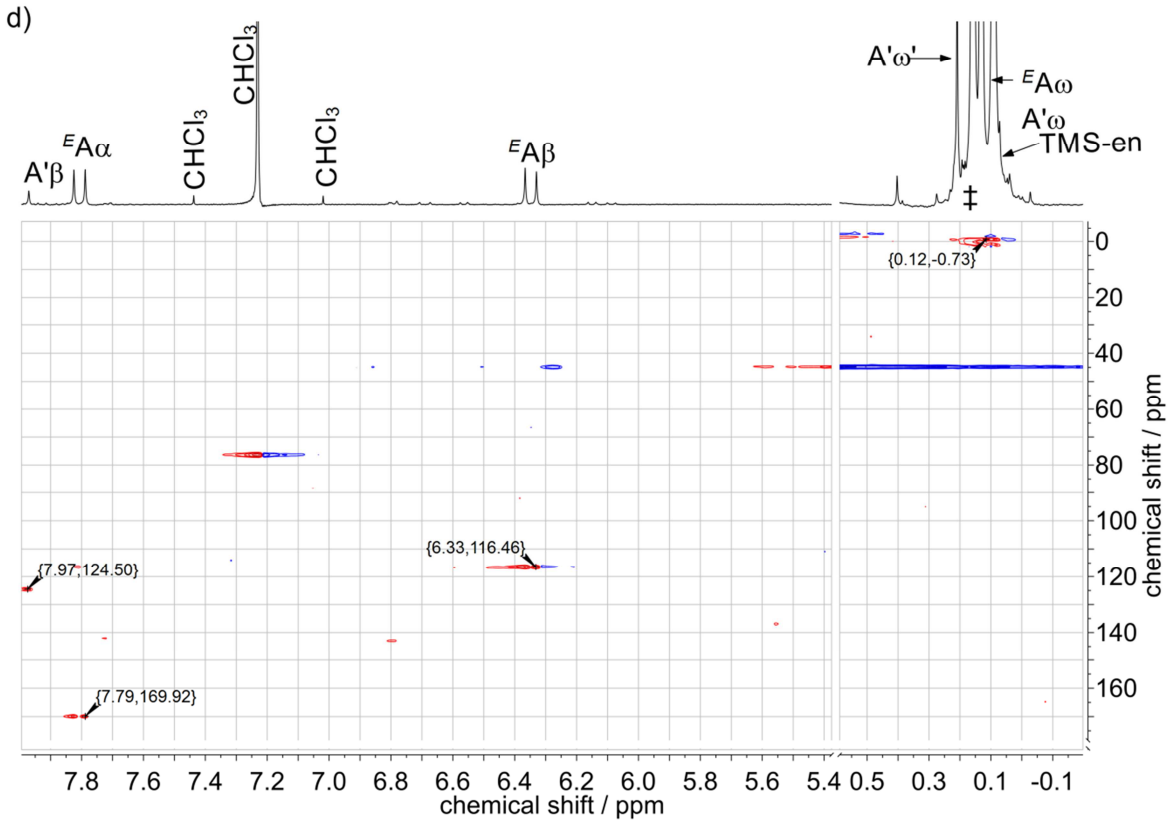
d)
A'β
EAα
CHCl3
CHCl3
CHCl3
EAβ
A'ω'
EAω
A'ω
TMS-en
‡
{0.12,-0.73}
{6.33,116.46}
{7.97,124.50}
{7.79,169.92}
chemical shift / ppm
chemical shift / ppm

Figure S10. a) ^{1}H, b) COSY, c) HMBC and d) HSQC spectra of a solution, prepared by dissolving a pre-mixture of the neat solids K_4Ge_9 (97.2 mg , 120 µmol, 1 eq.) and **3** (11.6 mg, 60 µmol, 0.5 eq.) in 2 ml *en*, after reaction times of > 17h. The reactants dissolved within 15 min and a homogenous dark-brown solution was obtained, which turned into deep-red after 17 h. In the NMR spectra, signals corresponding to the organic functionalities ^{ZZ}**B** and ^{EZ}**B** appear. Unknown signals are marked with ‡.

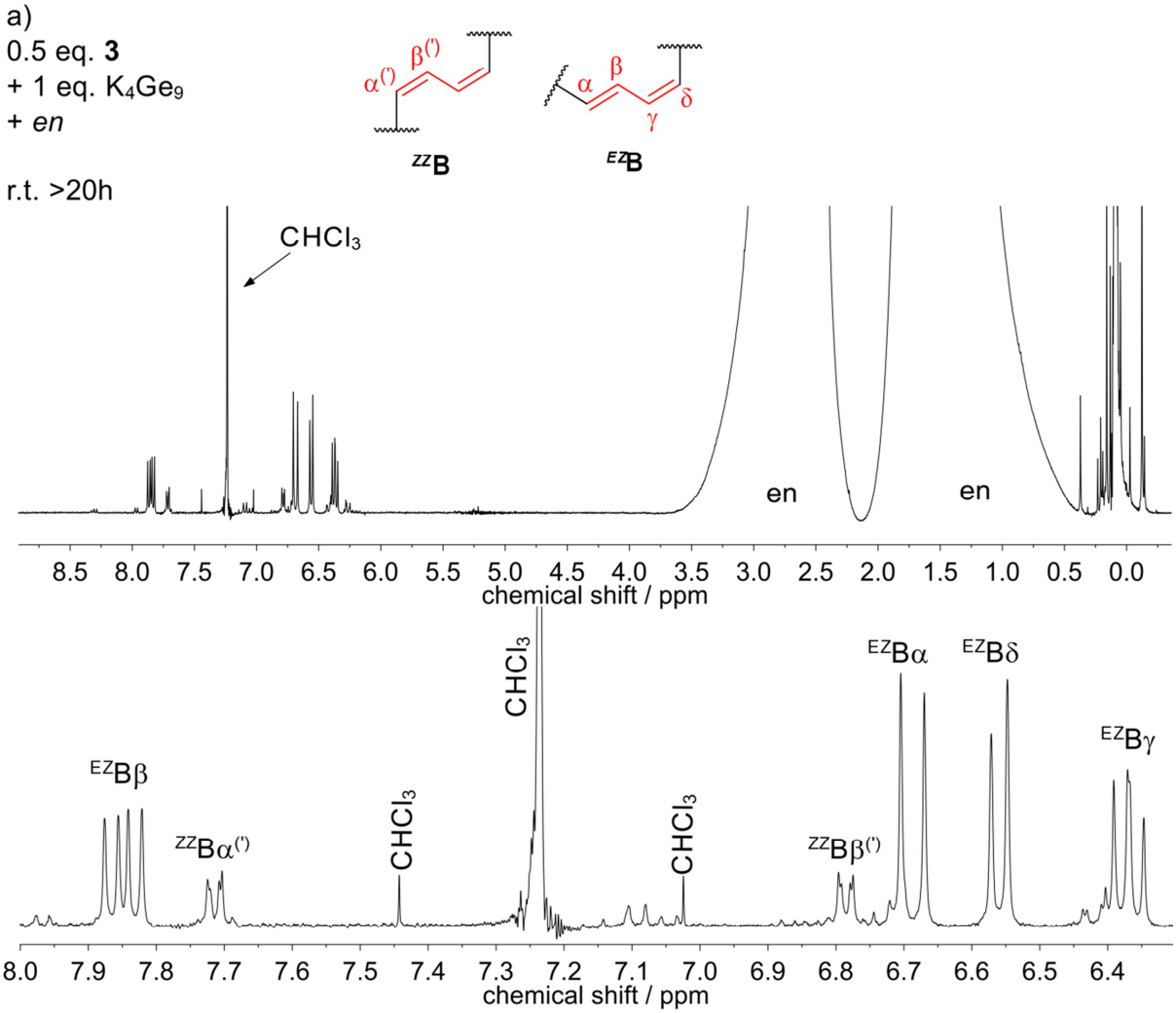

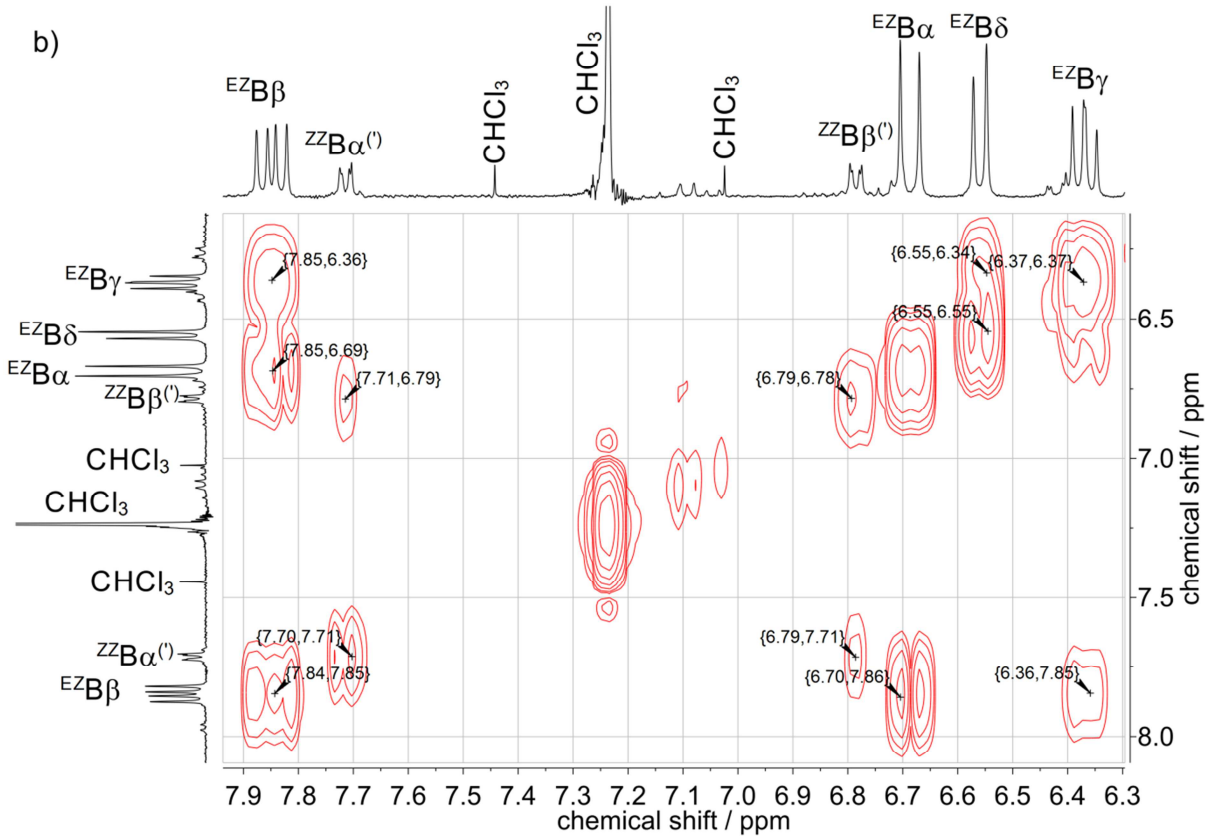
b)
EZBβ
ZZBα(')
CHCl3
CHCl3
CHCl3
ZZBβ(')
EZBα
EZBδ
EZBγ
{7.85,6.36}
{7.85,6.69}
{7.71,6.79}
{7.79,7.71}
{7.84,7.85}
{6.55,6.34}
{6.37,6.37}
{6.55,6.55}
{6.79,6.78}
{6.79,7.71}
{6.70,7.86}
{6.36,7.85}
chemical shift / ppm
chemical shift / ppm

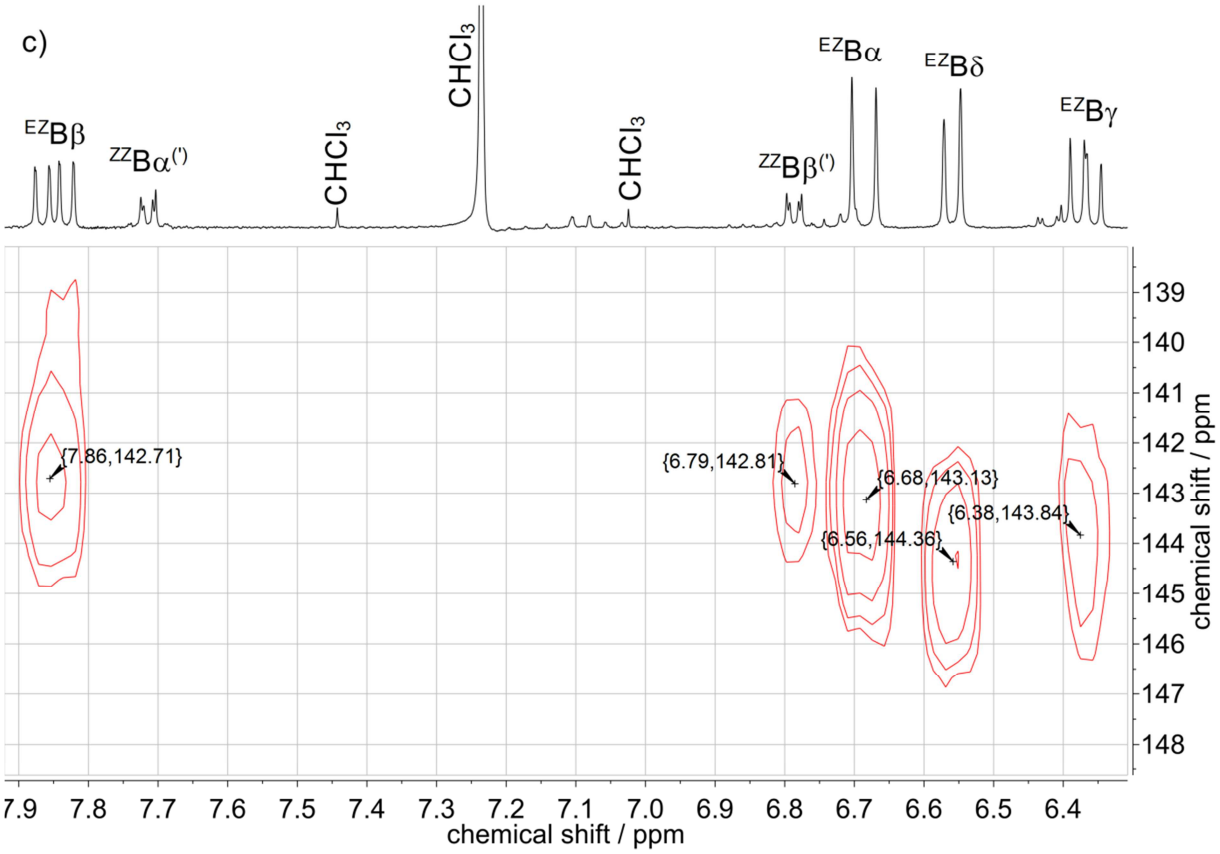
c)
EZBβ
ZZBα(')
CHCl3
CHCl3
CHCl3
ZZBβ(')
EZBα
EZBδ
EZBγ
{7.86,142.71}
{6.79,142.81}
{6.68,143.13}
{6.38,143.84}
{6.56,144.36}
chemical shift / ppm
chemical shift / ppm

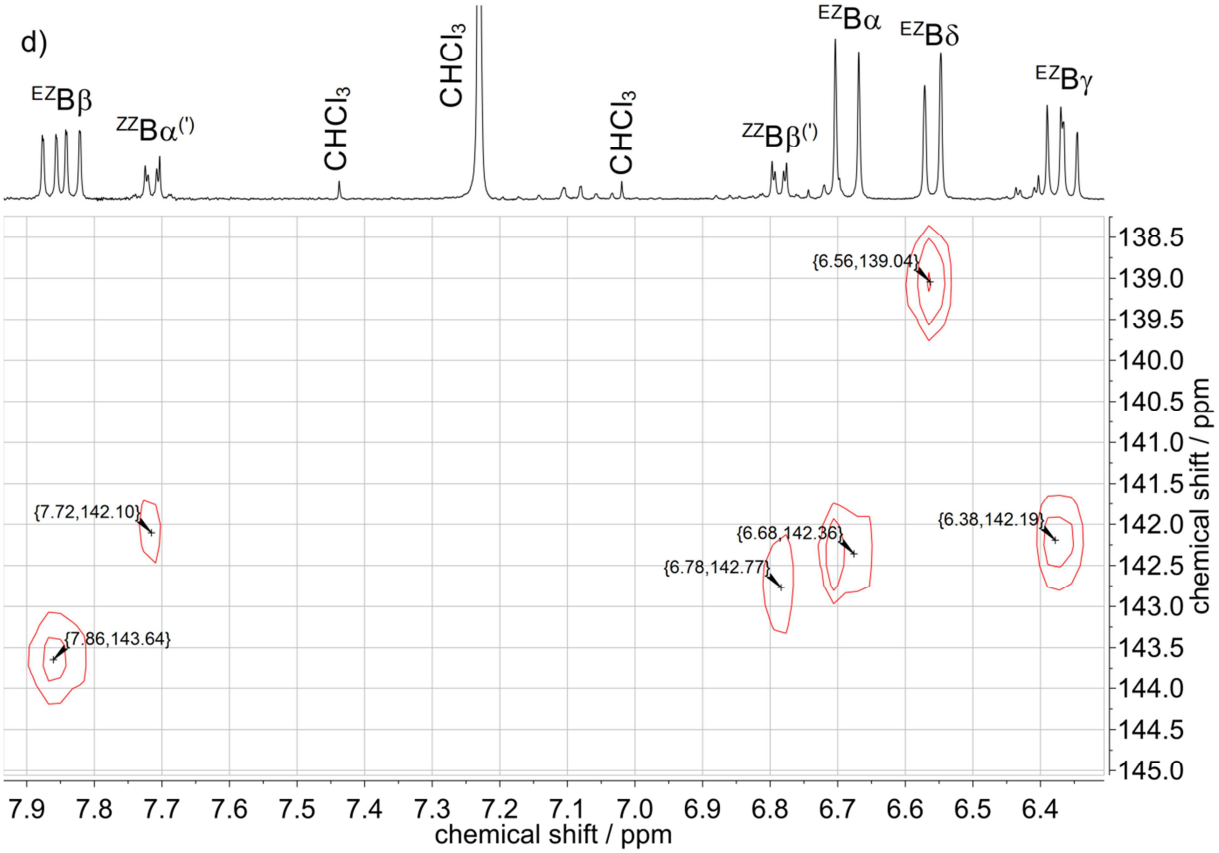
d)
EZBβ
ZZBα(')
CHCl3
CHCl3
CHCl3
ZZBβ(')
EZBα
EZBδ
EZBγ
{6.56,139.04}
{7.72,142.10}
{6.68,142.36}
{6.78,142.77}
{6.38,142.19}
{7.86,143.64}
7.9 7.8 7.7 7.6 7.5 7.4 7.3 7.2 7.1 7.0 6.9 6.8 6.7 6.6 6.5 6.4
chemical shift / ppm
138.5 139.0 139.5 140.0 140.5 141.0 141.5 142.0 142.5 143.0 143.5 144.0 144.5 145.0
chemical shift / ppm

Figure S11. a) Time dependent ^{1}H NMR spectra (r.t = 0.5 h - 20 h) of a solution, prepared by dissolving a pre-mixture of the neat solids K_4Ge_9 (97.2 mg , 120 µmol, 1 eq.) and **3** (11.6 mg, 60 µmol, 0.5 eq.) in 2 ml *en*. For reaction times of 0.5 h the signals corresponding to ^{E}**A**/**A'** are dominating. With increasing reaction time signals ^{E}**A**/**A'** decrease whereas signals of ^{ZZ}**B**/^{EZ}**B** increase. After 20 h signals of ^{E}**A**/**A'** vanished and ^{ZZ}**B**/ ^{EZ}**B** are dominating. In the Table below the absolute integrals of the signals corresponding to ^{E}**A**/**A'** and ^{ZZ}**B**/ ^{EZ}**B** are shown, respectively. b) ^{1}H NMR spectra of solutions, prepared by dissolving a pre-mixture of A_4Ge_9 (*A* = K: 97.2 mg , 120 µmol, 1 eq.; *A* = Rb: 119.4 mg, 120 µmol, 1 eq.) and different amounts of **3** (5.8 mg, 30 µmol, 0.25 eq.; 11.6 mg, 60 µmol, 0.5 eq.; 46.7 mg, 240 µmol, 2 eq) in 2 ml *en*. r.t. > 20 h. In the NMR spectra of mixtures containing ≤ 0.5 eq. of **3** signals corresponding to ^{ZZ}**B**/ ^{EZ}**B** appear. In case of the precursor being Rb_4Ge_9 the signals of ^{ZZ}**B**/ ^{EZ}**B** are slightly down-field shifted. For the mixture containing 2 eq. of **3** solely signals corresponding to functionality ^{E}**A** but no signals of ^{ZZ}**B**/ ^{EZ}**B** are visible.

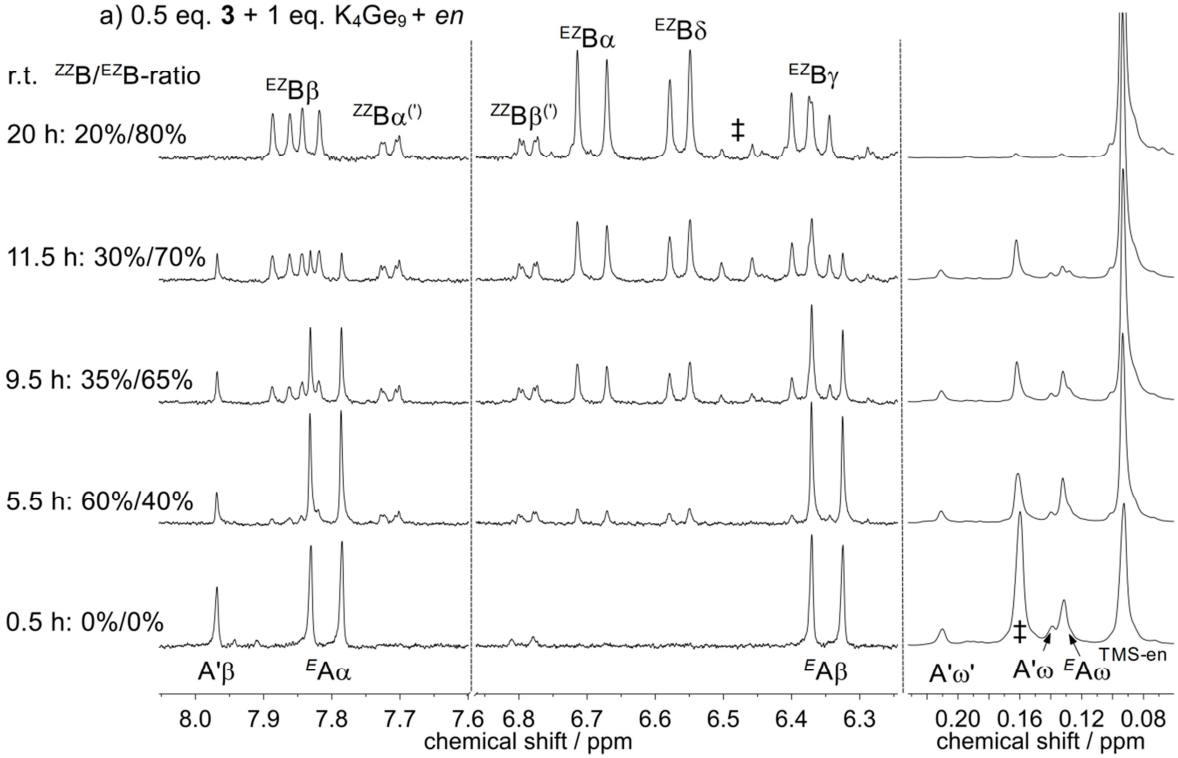

r.t. [h]	abs. Integral [a.u.] A'	abs. Integral [a.u.] ^{ZZ}B	abs. Integral [a.u.] ^{E}A	abs. Integral [a.u.] ^{EZ}B
0.5	0.20	0	0.75	0
20	0	0.22	0	0.74

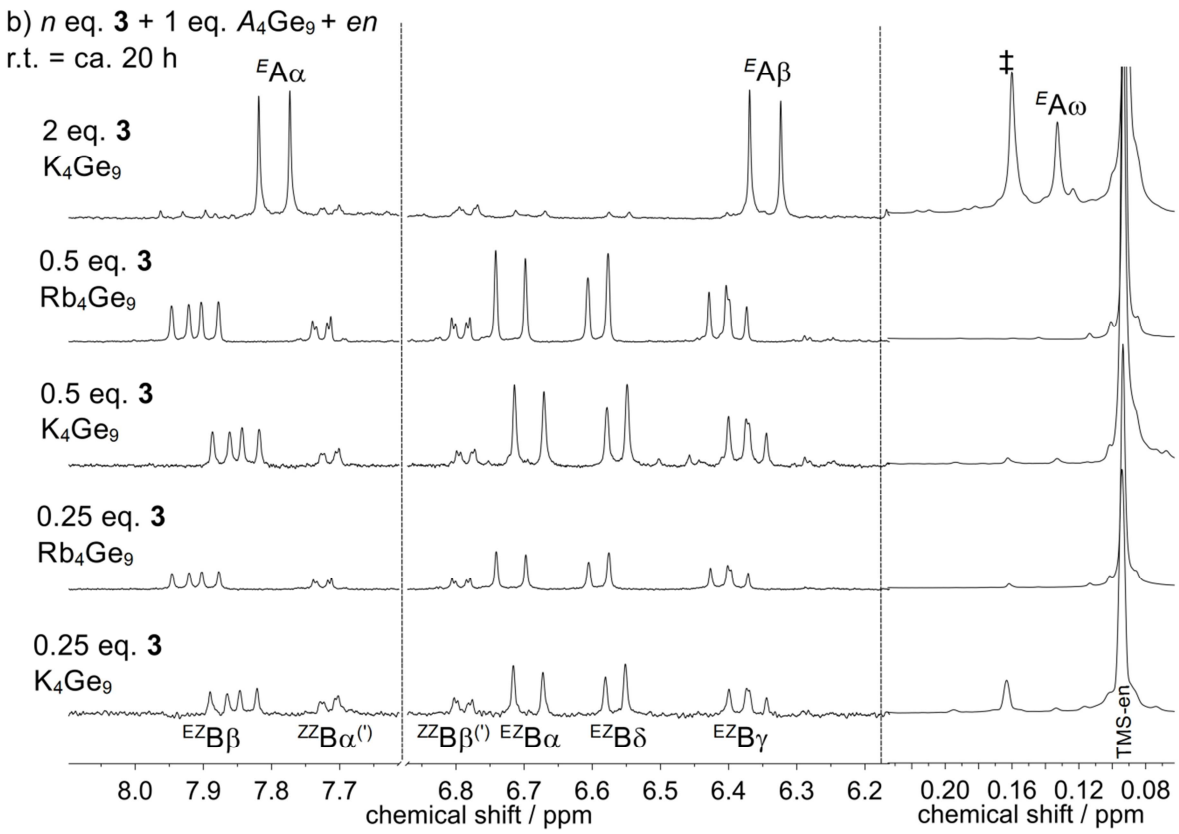
b) *n* eq. **3** + 1 eq. A_4Ge_9 + *en*
r.t. = ca. 20 h
$^{E}A\alpha$
$^{E}A\beta$
‡
$^{E}A\omega$
2 eq. **3**
K_4Ge_9
0.5 eq. **3**
Rb_4Ge_9
0.5 eq. **3**
K_4Ge_9
0.25 eq. **3**
Rb_4Ge_9
0.25 eq. **3**
K_4Ge_9
$^{EZ}B\beta$
$^{ZZ}B\alpha(')$
$^{ZZ}B\beta(')$
$^{EZ}B\alpha$
$^{EZ}B\delta$
$^{EZ}B\gamma$
TMS-en
8.0 7.9 7.8 7.7
6.8 6.7 6.6 6.5 6.4 6.3 6.2
0.20 0.16 0.12 0.08
chemical shift / ppm
chemical shift / ppm

The following spectrum corresponds to test mixture type E

Figure S12. ^{1}H NMR spectrum of a solution prepared by reacting a pre-mixture of the neat solids K_4Ge_9 (48.6 mg , 60 µmol, 1 eq.) and **3** (5.8 mg, 30 µmol, 0.5 eq.) with 1 ml *en*, for 20 h and adding 0.75 ml of an *en*-solution containing 240 µmol **4**/ml *en* (**4**: 180 µmol, 4 eq.).The colour of the obtained solution was intensive orange. r.t.= 15 h. In the NMR spectrum signals of **10** appear, but **B** and **R**, which are expected for the Zintl triad **2** are not visible. The formation of **10** is attributed to the reaction of the side product $^{-}$NHR' with **4**. $^{-}$NHR' arises from the formation of **1a** in the first synthetic step, "dissolution of A_4Ge_9/**3** in *en*".

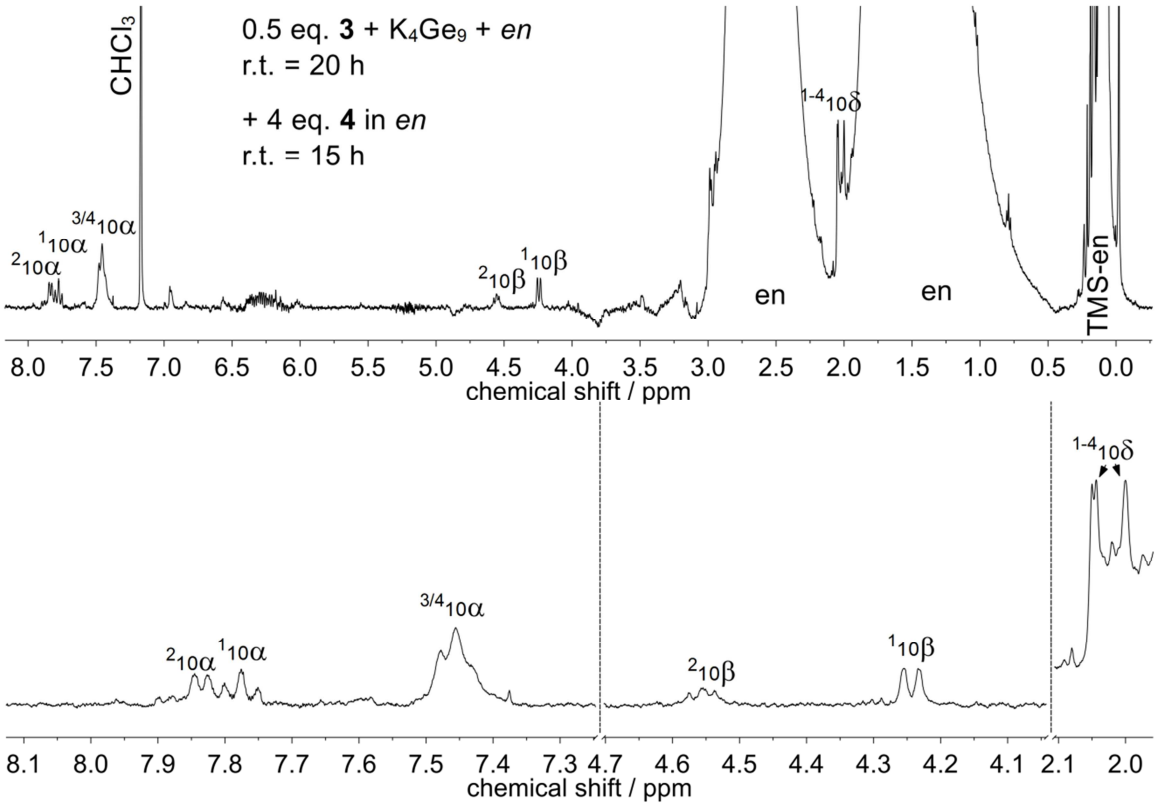

The following spectra correspond to test mixture type F

Figure S13. a) ^{1}H, b) COSY, c) HMBC and d) HSQC NMR spectra of a solution, prepared by dissolving K_4Ge_9 (97.2 mg , 120 µmol, 1 eq.) in 2 ml of an *en*-solution containing 60 µmol/ml **4** (120 µmol, 1 eq.), after a reaction time of > 20 h. The obtained solution was coloured red-brown. In the spectra signals corresponding to **R** and **10** appear. Unknown signals are marked with ‡.

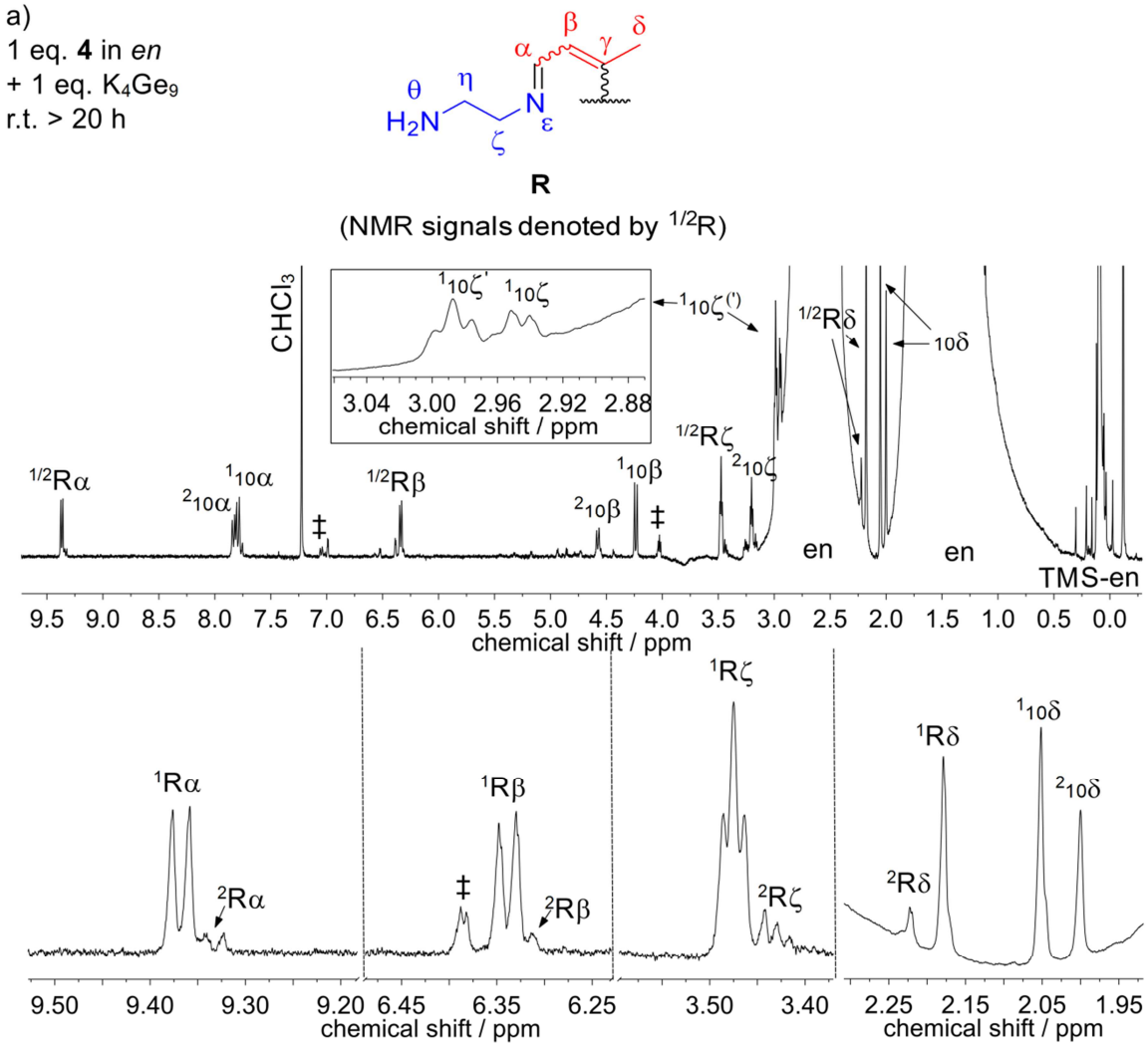

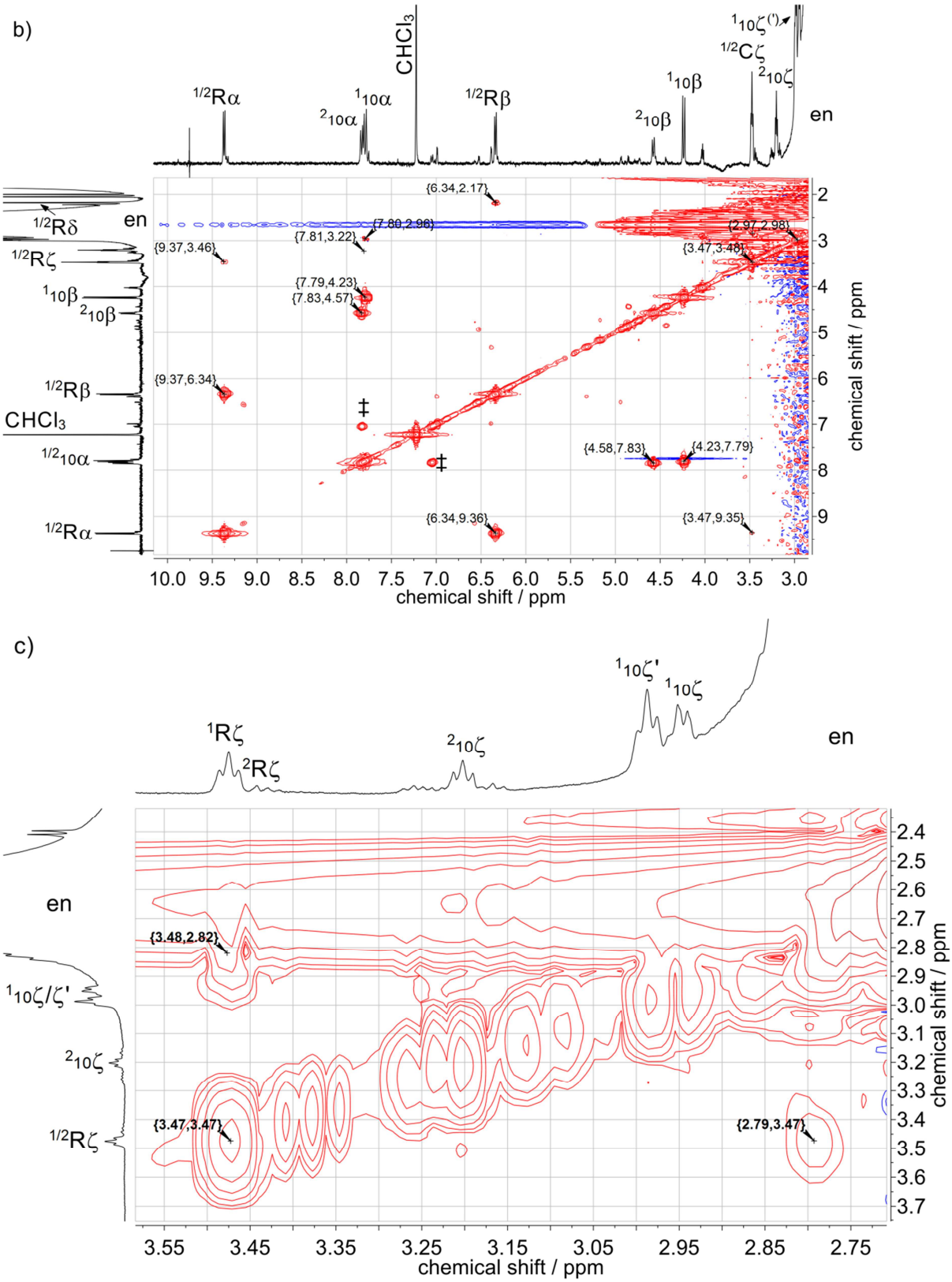
b)
$^{1/2}$Rα
^{2}10α
^{1}10α
CHCl$_3$
$^{1/2}$Rβ
^{2}10β
^{1}10β
$^{1/2}$Cζ
^{2}10ζ
^{1}10ζ(')
en
$^{1/2}$Rδ
$^{1/2}$Rζ
^{1}10β
^{2}10β
$^{1/2}$Rβ
CHCl$_3$
$^{1/2}$10α
$^{1/2}$Rα
{6.34,2.17}
{7.88,2.96}
{7.81,3.22}
{9.37,3.46}
{2.97,2.98}
{3.47,3.48}
{7.79,4.23}
{7.83,4.57}
{9.37,6.34}
{4.58,7.83}
{4.23,7.79}
{6.34,9.36}
{3.47,9.35}
chemical shift / ppm
chemical shift / ppm
c)
^{1}Rζ
^{2}Rζ
^{2}10ζ
^{1}10ζ'
^{1}10ζ
en
en
^{1}10ζ/ζ'
^{2}10ζ
$^{1/2}$Rζ
{3.48,2.82}
{3.47,3.47}
{2.79,3.47}
chemical shift / ppm
chemical shift / ppm

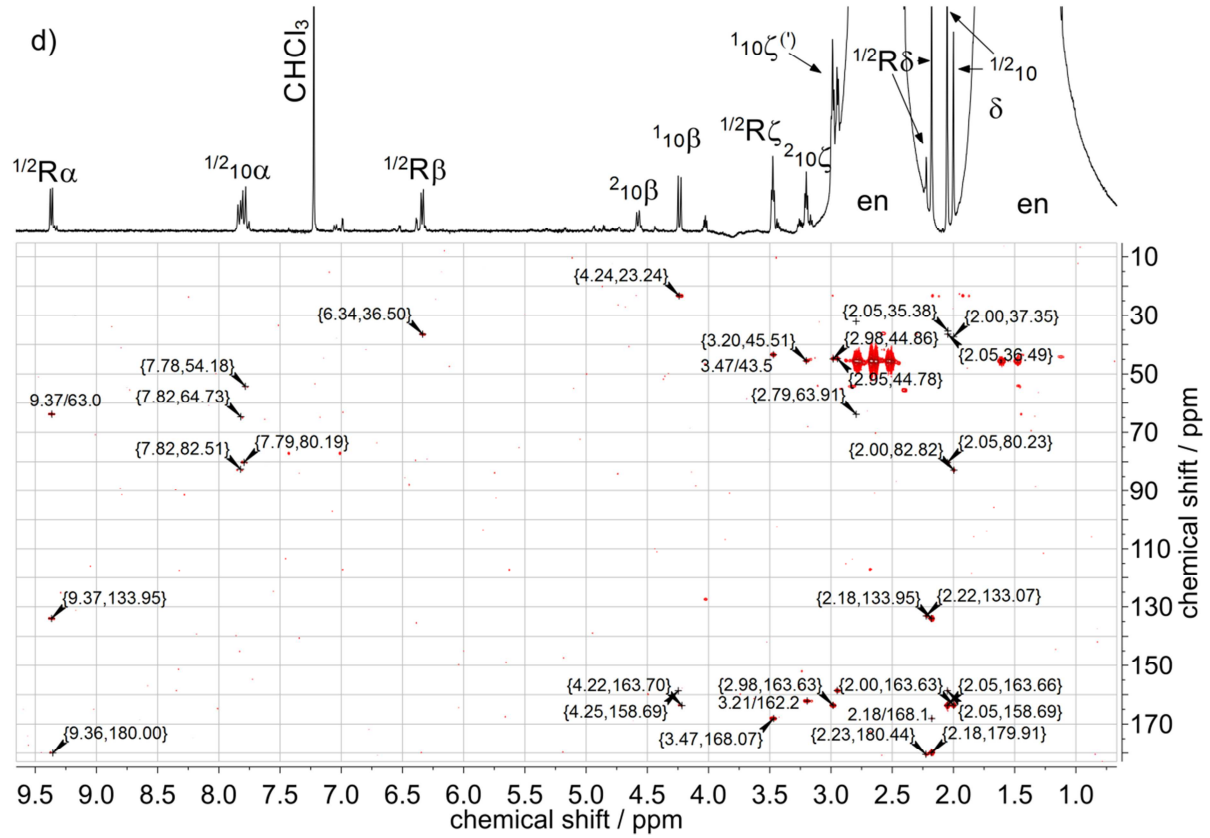
d)
CHCl3
1/2Rα
1/210α
1/2Rβ
210β
110β
1/2Rζ2
10ζ
10ζ(')
1/2Rδ
1/210
δ
en
en
{4.24,23.24}
{6.34,36.50}
{2.05,35.38}
{2.00,37.35}
{3.20,45.51}
{2.98,44.86}
3.47/43.5
{2.05,36.49}
{2.95,44.78}
{7.78,54.18}
9.37/63.0
{7.82,64.73}
{2.79,63.91}
{7.82,82.51}
{7.79,80.19}
{2.00,82.82}
{2.05,80.23}
{9.37,133.95}
{2.18,133.95}
{2.22,133.07}
{4.22,163.70}
{2.98,163.63}
{2.00,163.63}
{2.05,163.66}
{4.25,158.69}
3.21/162.2
2.18/168.1
{2.05,158.69}
{9.36,180.00}
{3.47,168.07}
{2.23,180.44}
{2.18,179.91}
chemical shift / ppm
chemical shift / ppm

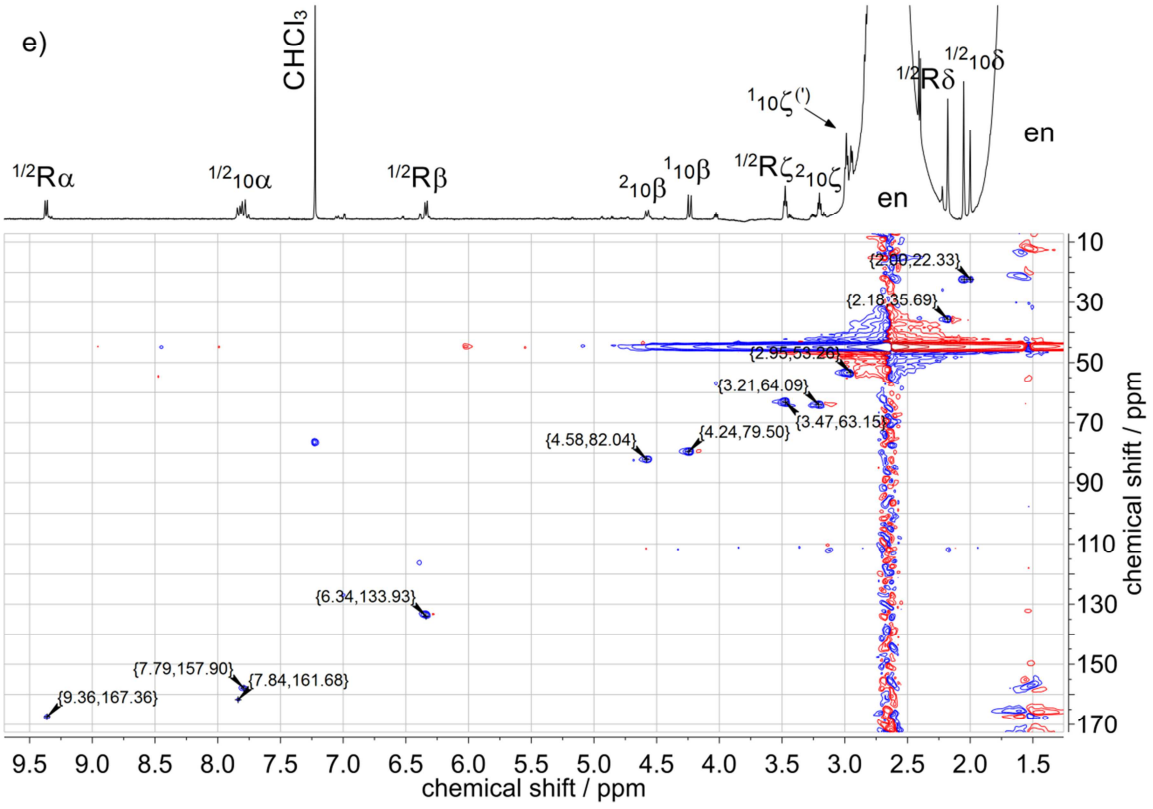
e)
CHCl3
1/2Rα
1/210α
1/2Rβ
210β
110β
1/2Rζ2
10ζ
10ζ(')
1/2Rδ
1/210δ
en
en
{2.00,22.33}
{2.18,35.69}
{2.95,53.26}
{3.21,64.09}
{3.47,63.15}
{4.58,82.04}
{4.24,79.50}
{6.34,133.93}
{7.79,157.90}
{7.84,161.68}
{9.36,167.36}
chemical shift / ppm
chemical shift / ppm

Figure S14. a) Time-dependent ^{1}H NMR spectra (r.t. = 0.5h–20h) of a solution, prepared by dissolving K_4Ge_9 (97.2 mg , 120 µmol, 1 eq.) in 2 ml of an *en*-solution containing 120 µmol/ml **4** (240 µmol, 2 eq.). After 0.5 h signals corresponding to functionality **R**, an unknown intermediate * and **10** are visible. With increasing reaction time the intensity of the signals of **R** increase, whereas the signals * decrease, respectively. After 20 h the signals * vanished. b) ^{1}H NMR spectra of solutions, prepared by dissolving A_4Ge_9 (*A* = K: 97.2 mg , 120 µmol, 1 eq.; *A* = Rb: 119.4 mg, 120 µmol, 1 eq.) in 2 ml of *en*-solutions containing different amounts of **4** (60 µmol **4**/ ml, 120 µmol, 1eq.; 120 µmol **4**/ml: 240 µmol, 2eq). r.t. = 10-20 h. In all spectra signals corresponding to **R** and **10** are visible. In case of the solutions involving the precursor Rb_4Ge_9 the signals of **R** are slightly down field shifted.

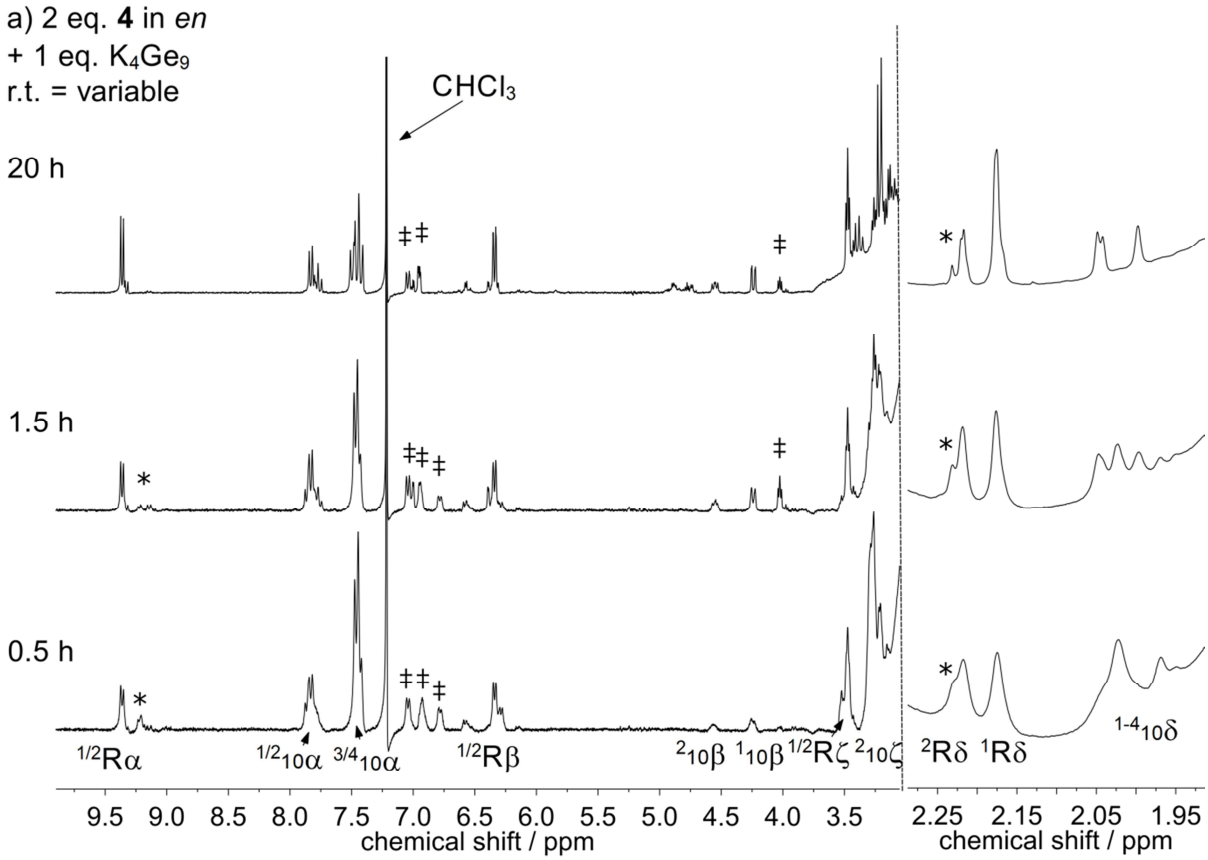

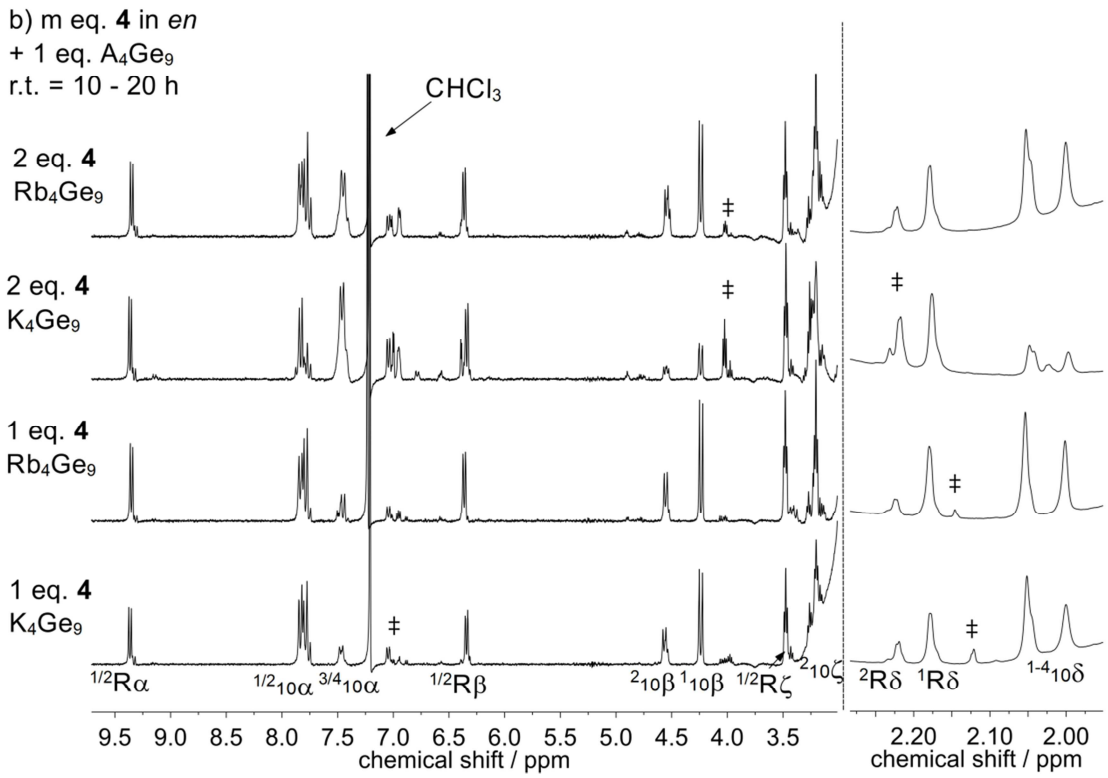
b) m eq. 4 in en
+ 1 eq. A4Ge9
r.t. = 10 - 20 h
2 eq. 4
Rb4Ge9
2 eq. 4
K4Ge9
1 eq. 4
Rb4Ge9
1 eq. 4
K4Ge9
CHCl3
‡
1/2Rα
1/210α
3/410α
1/2Rβ
210β
110β
1/2Rζ
210ζ
2Rδ
1Rδ
1-410δ
9.5 9.0 8.5 8.0 7.5 7.0 6.5 6.0 5.5 5.0 4.5 4.0 3.5
chemical shift / ppm
2.20 2.10 2.00
chemical shift / ppm

The following spectra correspond to test mixture type B, C and F

Figure S15. Stack of the ^{1}H NMR spectra a) Figure S8, b) Figure S6, c) Figure S13, d) a mixture prepared by dissolving K_4Ge_9 (97.2 mg , 120 µmol, 1 eq.) in 2 ml of an *en*-solution with water traces (ca.0.5-1%) and containing 240 µmol/ml **4** *en* (480 µmol, 4 eq.). Unknown signals are marked with ‡

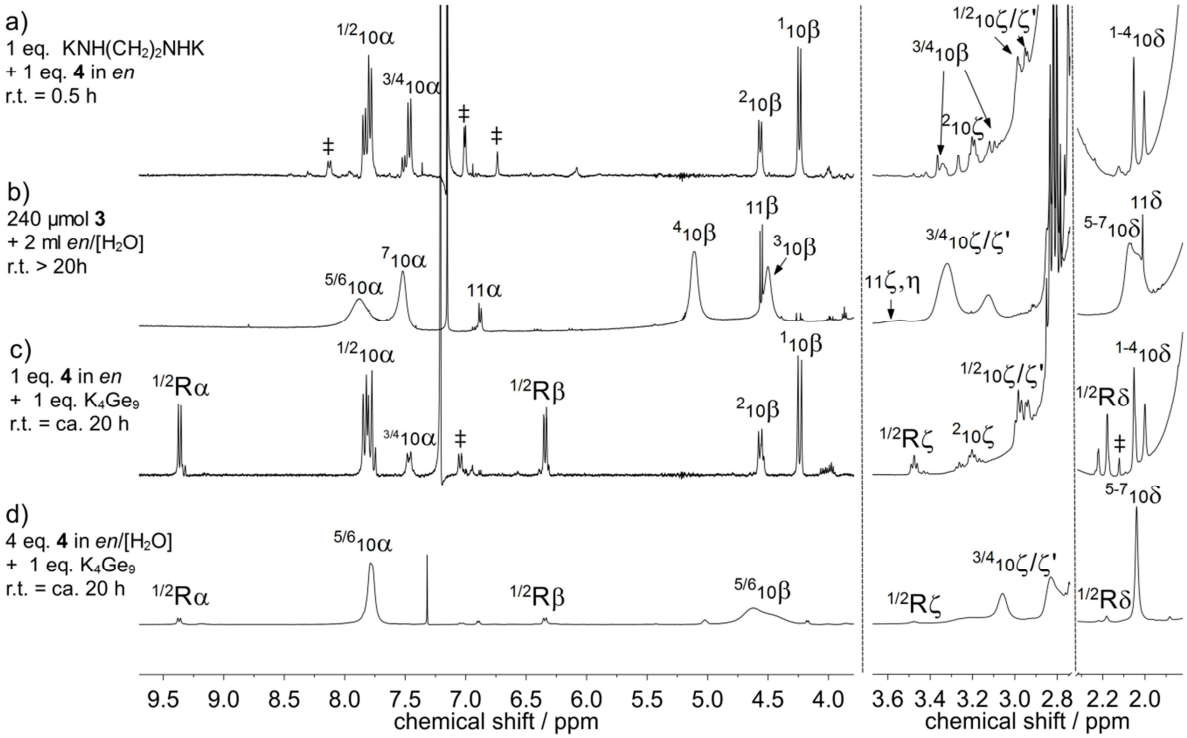

The following spectra correspond to mixtures type G and H

Figure S16. a) ^{1}H NMR spectra of test mixture G. First step: A_4Ge_9 (A=K: 97.2 mg , 120 µmol, 1 eq.; A=Rb: 119.4 mg, 120 µmol, 1 eq.) was dissolved in 2 ml of an *en*-solution containing different amounts of **4** (120 µmol, 1 eq.; 240 µmol, 2 eq.) and the solution was stirred for 5 h (= mixture type D). Second step: **3** (11.6 mg, 60 µmol, 0.5 eq.) was dissolved in mixture type D and an orange solution was obtained. r.t. ca. 20 h. In the spectra the dominating signals correspond to **R** and **10**. b) Mixture type H: Simultaneous reaction of **3**/**4** with A_4Ge_9 in water-free *en*. A pre-mixture of A_4Ge_9 (*A* = K: 97.2 mg, 120 µmol, 1 eq.; *A* = Rb: 119.4 mg, 120 µmol, 1 eq.) and **3** (11.6 mg, 60 µmol, 0.5 eq.) was dissolved in 2 ml of an *en*-solution containing different amounts of **4** (120 µmol, 1 eq.; 240 µmol, 2 eq.). Thereby orange coloured solutions were obtained. r.t. ca. 20 h. The NMR spectra show signals corresponding to **B**, **R** and **10**.

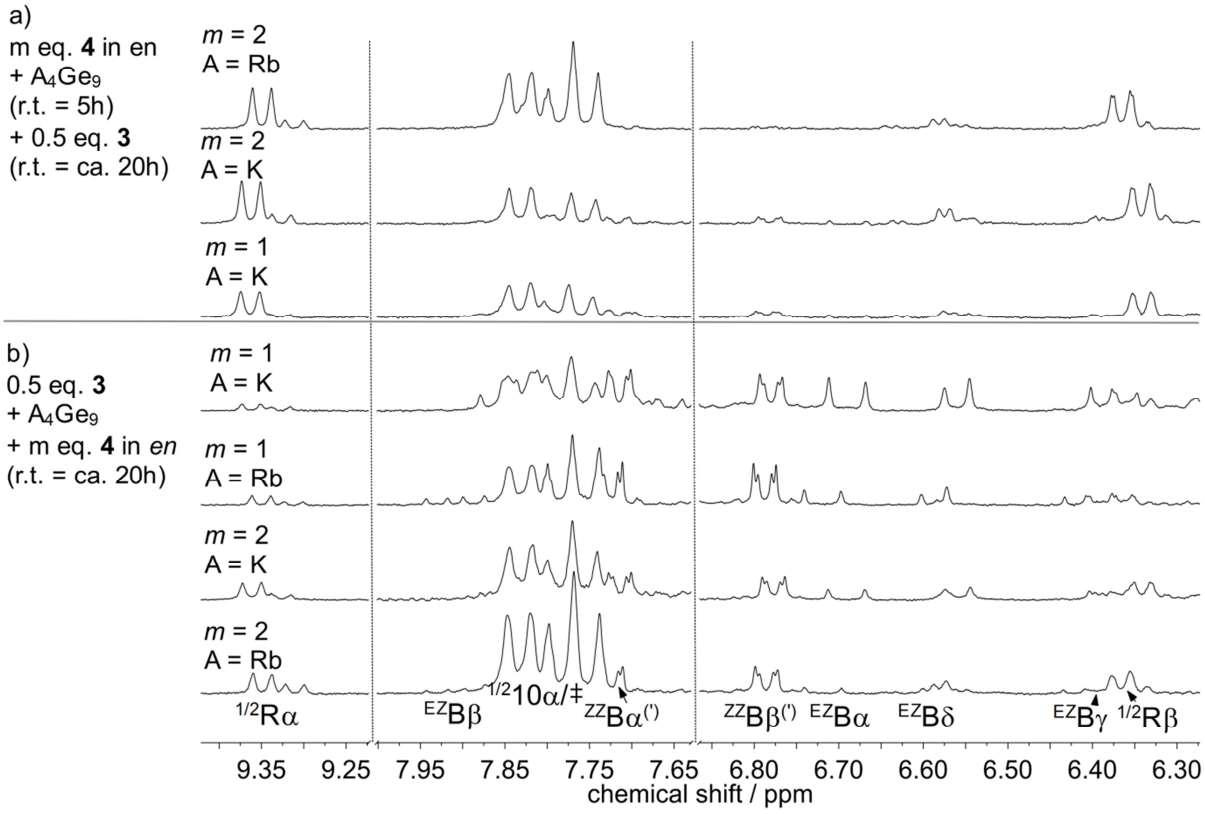

Figure S17. Time-dependent ^{1}H NMR spectra (r.t. =0.5h-16h) of test-mixtures H prepared by dissolving a pre-mixture of the neat solids K_4Ge_9 (97.2 mg, 120 µmol, 1 eq.) and **3** (11.6 mg, 60 µmol, 0.5 eq.) in 2 ml of an *en*-solution containing 120 µmol **4**/ ml *en* (**4**: 240 µmol, 2 eq.). The spectra show signals corresponding to **B**, **R** and **10**.

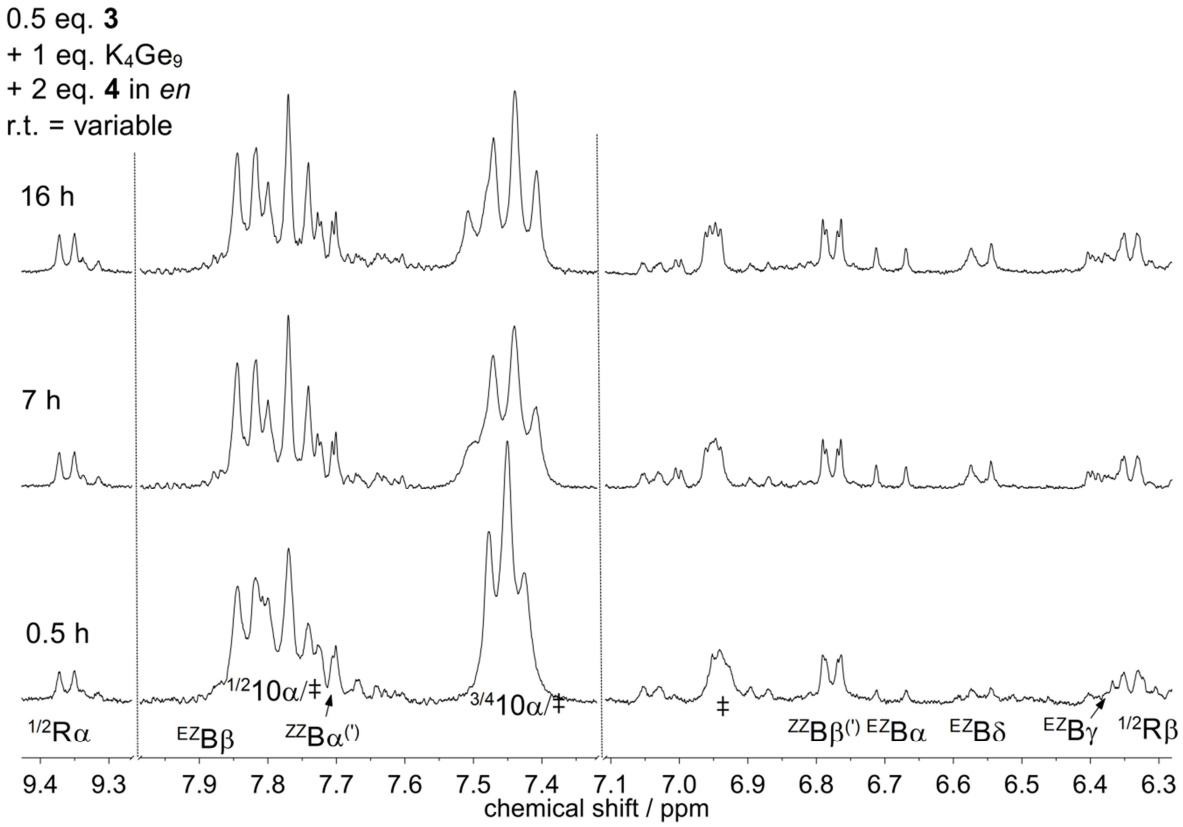

2.6 ESI-MS

Figure S18. ESI-MS investigation of a reaction solution (mixture type F) prepared by dissolving Rb_4Ge_9 (40 mg, 40 µmol, 1 eq.) in a **4**/*en* solution (60 µmol/ml, 40 µmol, 1 eq.). The spectrum was measured in negative ion mode. Prior to measurement the reaction solution was filtered over glass-fibres and diluted with *en* (1:100). In [6] the isolation of $[Ge_{10}]^{2-}$ is presented and the ESI-MS shown below is discussed in detail.

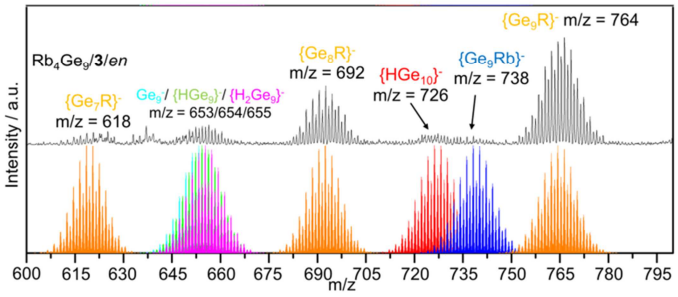

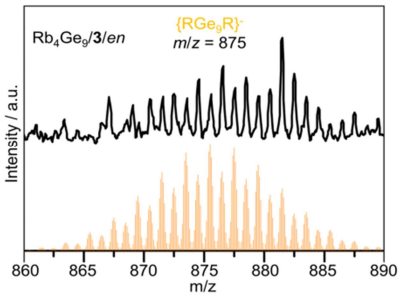

3 References

[1] G. M. Sheldrick, *Acta Crystallogr.* **2008**, *A64*, 112.
[2] M. M. Bentlohner, W. Klein, Z. H. Fard, L.-A. Jantke, T. F. Fässler, *Angew. Chem. Int. Ed.* **2015**, *54*, 3748-3753; *Angew. Chem.* **2015**, *127*, 3819-3824.
[3] C. B. Benda, J.-Q. Wang, B. Wahl, T. F. Fässler, *Eur. J. Inorg. Chem.* **2011**, 4262-4269.
[4] Numbering: In the text, the positions of the C=C double bonds are counted with respect to the C_4-backbone, whereby [Ge_9] and $H_2N(CH_2)_2N(H)$ are considered as autonomous subunits: α = 1, β = 2, γ = 3, δ = 4. For molecules **10** and **11** also the position of the –NH group is given: ε = 0, ε' = 5;
[5] M. Hesse, H. Meier, B. Zeeh, *Spektroskopische Methoden in der organischen Chemie*, Thieme, **2005**.
[6] M. M. Bentlohner, C. Fischer, T. F. Fässler, *Chem. Commun.* **2016**, *52*, 9841.

5.3 Synthesis and characterization of pristine *closo*-$[Ge_{10}]^{2-}$

Reproduced from M. M. Bentlohner, C. Fischer, T. F. Fässler, *Chem. Commun.* **2016**, *52*, 9841.with permission from The Royal Society of Chemistry

http://pubs.rsc.org/en/Content/ArticleLanding/2016/CC/c6cc04143d#!divAbstract

Contents and Contributions

In the scope of the publication the synthesis and structural characterization of the first *closo*-$[Ge_{10}]^{2-}$ Zintl anion, extending the series of homoatomic *closo*-$[E_{10}]^{2-}$ deltahedral clusters, is presented.

The publication was authored in the course of this thesis. The *closo*-$[Ge_{10}]^{2-}$ was crystallized as $[Rb(222\text{-crypt})]_2[Ge_{10}](en)_{1.5}$ salt, from a solution of Rb_4Ge_9 in *en*, containing additionally 7-amino-1-trimethylsilyl-5-aza-hepta-3-en-1-yne, by layering with *tol*/cryptand[2.2.2]. The synthesis and isolation of the compound was conducted in the course of this thesis. X-ray structure analysis of single crystals of $[Rb(222\text{-crypt})]_2[Ge_{10}](en)_{1.5}$ indicate a D_{4d} symmetric *closo*-deltahedron with 22 skeleton electrons for $[Ge_{10}]^{2-}$. Both X-ray data collection as well as solving of the crystal structure was done in this work. Moreover, in this publication the first Raman spectrum of a ten vertex deltahedral cluster is reported. Single crystals of $[Rb(222\text{-crypt})]_2[Ge_{10}](en)_{1.5}$ were collected and characterized with Raman spectroscopy by Herta Slavik. The Raman spectrum is dominated by one intensive mode at 209 cm^{-1}, which is characteristic for the “breathing” of the $[Ge_{10}]^{2-}$ Zintl anion. In the scope of this thesis data of Raman measurements were evaluated and interpreted in the context of existing literature. $[Rb(222\text{-crypt})]_2[Ge_{10}](en)_{1.5}$ was further characterized by ESI-MS. It turned out that *closo*-$[Ge_{10}]^{2-}$ is a rigid deltahedron which is stable under ESI-MS conditions as well as in *acn* solutions. For ESI-MS measurements single crystals of the compound were dissolved in *acn* and injected into the mass-spectrometer. Besides, also Rb_4Ge_9/*en* solutions, with and without 7-amino-1-trimethylsilyl-5-aza-hepta-3-en-1-yne, were investigated in ESI-MS in order to shed light on the formation of *closo*-$[Ge_{10}]^{2-}$. Thereby, it turned out that $[Ge_{10}]^{2-}$ readily forms upon simple dissolution of Rb_4Ge_9 in water-free ethylenediamine and also forms if 7-amino-1-trimethylsilyl-5-aza-hepta-3-en-1-yne is added to such a reaction solution. The investigations further revealed that Ge_9 clusters are derivatized by reaction with 7-amino-1-trimethylsilyl-5-aza-hepta-3-en-1-yne to $[Ge_9\text{-}R]^{3-}$ and $[R\text{-}Ge_9\text{-}R]^{2-}$ [*R* = 7-amino-5-aza-hepta-2,4-dien-2-yl], which do not crystallize by addition of cryptand[2.2.2]/*tol*, leading to crystallization of $[Ge_{10}]^{2-}$ ESI-MS measurements and sample preparation as well as data evaluation were done in this thesis by assistance of Christina Fischer

ChemComm

COMMUNICATION

View Article Online
View Journal | View Issue

Cite this: *Chem. Commun.*, 2016, 52, 9841

Received 17th May 2016,
Accepted 12th July 2016

DOI: 10.1039/c6cc04143d

www.rsc.org/chemcomm

Synthesis and characterization of pristine *closo*-$[Ge_{10}]^{2-}$†

Manuel M. Bentlohner, Christina Fischer and Thomas F. Fässler*

The first $[Ge_{10}]^{2-}$ Zintl anion, which is neither filled nor connected to another metal atom is presented in terms of X-ray structure, Raman-spectrum and ESI-MS. Pure $[Ge_{10}]^{2-}$, adapting a D_{4d} symmetric *closo*-structure, were crystallized from a Rb_4Ge_9/ethylendiamine solution, containing 7-amino-1-trimethylsilyl-5-aza-hepta-3-en-1-yne. The role of the latter on the formation of $[Rb(222\text{-crypt})]_2[Ge_{10}](en)_{1.5}$ is discussed.

The soft oxidation of *nido*-$[E_9]^{4-}$ Zintl anions (E = Ge, Sn, Pb) with 22 skeleton electrons (SE) is a powerful method for the synthesis of new types of the heavier representatives of group 14 clusters and led to a large variety of cage-like structures.[1–5] By that strategy new element allotropes[4–5] as well as ordered, (nano)porous forms of germanium have been obtained.[6–8] Although a comprehensive understanding of the cluster oxidation and thus a control over the reaction outcome is still lacking, a large number of investigations on the oxidation of $[E_9]^{4-}$ clusters in solution has been performed during the last couple of years,[1,2] and a broad variety of coupled clusters $\{[(Ge_9)_m]\}^{q-}$ (m = 2–4, ∞) has been obtained by soft oxidation of $[Ge_9]^{4-}$ in ethylenediamine (en), *N*,*N*-dimethylformamide (dmf) and liquid ammonia. Even though in most cases the reactions are not understood in detail,[9–16] mild oxidative properties have been ascribed to the involved solvents,[5,17–19] and recently we have shown that the solvent en indeed plays an important role in the cluster formation.[8]

It has been found that oxidative reaction conditions not only can trigger the coupling but also the growth of clusters.[20] Theoretical investigations showed that for E = Ge a full oxidation to novel germanium allotropes under retention of the polyhedral structure is reasonable.[21] The reaction of $[E_9]^{4-}$ with organometallic complexes ML_a (M = metal, L = ligand) in en, dmf and liquid ammonia yielded a broad variety of endohedrally filled clusters $[M@E_n]^{q-}$ ($n \geq 9$),[1–3] which in special cases adapt non-deltahedral structures and transition metal complexes of clusters with up to 45 covalently connected Ge atoms.[22–25] The formation of $[M@E_n]^{q-}$ ($n > 9$), from $[E_9]^{4-}$ cages, highlights the ability of these tetrel clusters to structurally reorganize in solution.[26,27]

The Zintl anions $[Pb_{10}]^{2-}$[28] and $[(Ge_{10})Mn(CO)_4]^{3-}$[29] are scarce examples of empty homoatomic ten-vertex tetrel clusters, and recently we extended the series of structurally characterized heteroatomic correspondents.[26,30,31] In $[Ge_9SnGe_9]^{4-}$ a formally *closo*-$[Ge_9Sn]^{2-}$ unit coordinates to a $[Ge_9]^{2-}$ cluster.[32] In case of $[M@E_n]^{q-}$ a stabilizing effect of the interstitial M atom on the surrounding $[E_n]$ cage has been evidenced by quantum-chemical calculations, indicating the preferred formation of endohedrally filled clusters with $n > 9$ instead of their empty correspondents.[1–3,20]

The formation of the empty pristine $[Pb_{10}]^{2-}$ unit on the one hand and of $[(Ge_{10})Mn(CO)_4]^{3-}$ on the other also suggests the existence of an unbound $[Ge_{10}]^{2-}$ Zintl anion. An earlier report on such a $[Ge_{10}]^{2-}$ cluster[33] turned out to be rather questionable because a disordered *closo*-$[Ge_9]^{2-}$ cluster (Fig. S1, ESI†) was unequivocally characterized in similar crystals.‡[34] Although the isolation of crystals containing the unbound and empty $[Ge_{10}]^{2-}$ Zintl anion has been unsuccessful so far, the latter is a frequently observed species in mass spectra obtained by laser desorption experiments or from solutions of Zintl phases in polar organic solvents.[29,32,35,36]

Herein we report on the synthesis and characterization of $[Rb(222\text{-crypt})]_2[Ge_{10}](en)_{1.5}$ (**1**) which contains such an empty and unbound $[Ge_{10}]^{2-}$ Zintl anion. Compound **1** was characterized by single crystal X-ray structure analysis, Raman-spectroscopy and electrospray ionization mass spectrometry (ESI-MS). Further, we present an ESI-MS investigation on the involved reaction solutions in order to shed some light on the formation of **1**.

Dark purple pillars of **1** were obtained (yield *ca.* 10–20%) from a solution of Rb_4Ge_9 (1 eq.) and 7-amino-1-trimethylsilyl-5-aza-hepta-3-en-1-yne (1 eq.)[37] in en after layering of the solution with toluene/cryptand[2.2.2] (4,7,13,16,21,24-hexaoxa-1,10-diazabicyclo[8.8.8]hexacosane; for experimental details see ESI†).

Crystals of **1** (Fig. S2, ESI†) contain two $[Rb(222\text{-crypt})]^+$ cations per cluster unit, and thus a formal charge of −2 can be assigned

Technische Universität München, Department Chemie, Lichtenbergstrasse 4, 85747 Garching, Germany. E-mail: Thomas.faessler@lrz.tum.de; Fax: +49 89 289 13186; Tel: +49 89 289 13131

† Electronic supplementary information (ESI) available: Experimental details, crystallographic details, ESI-MS spectra. CCDC 1479637. For ESI and crystallographic data in CIF or other electronic format see DOI: 10.1039/c6cc04143d

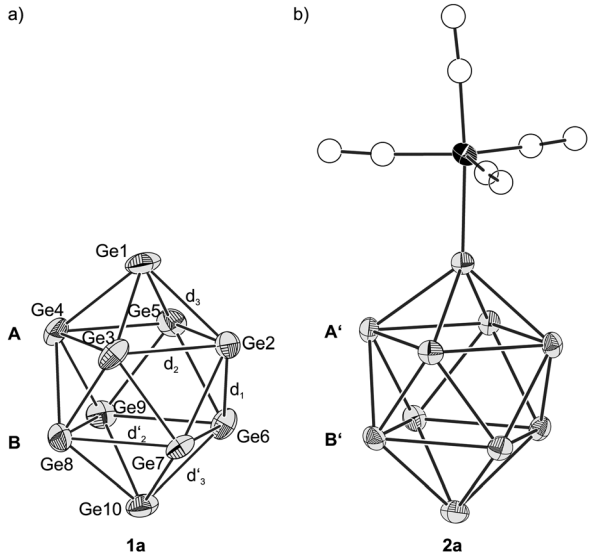

Fig. 1 (a) *closo*-$[Ge_{10}]^{2-}$ (**1a**) and (b) $[(Ge_{10})Mn(CO)_4]^{3-}$ (**2a**)[29] for comparison. Square planes of **1a** and **2a** are labeled with **A**/**B** and **A**′/**B**′, respectively. (a and b) Ge and Mn atoms are shown as grey and black ellipsoids, respectively, at a probability level of 50%. C and O atoms are shown as empty spheres.

to the anionic cluster entity (Fig. 1a). $[Ge_{10}]^{2-}$ (**1a**) consists of ten symmetry-independent germanium atoms and adapts the shape of a bi-capped square antiprism. The atoms of the planes **A** (Ge2 to Ge5) and **B** (Ge6 to Ge9) are nearly perfect squares with ratios of the face diagonals of 1.01 and 1.00 and torsion angles of 179.8° and 179.9°, respectively. The side lengths of **A** and **B** are in the narrow ranges of 2.760(1) Å (Ge2–Ge3) to 2.799(1) Å (Ge4–Ge5) and 2.780(1) Å (Ge7–Ge8) to 2.822(1) Å (Ge6–Ge9). Moreover, similar inter-square Ge–Ge distances from 2.535(1) Å (Ge3–Ge7) to 2.566(1) Å (Ge4–Ge9) indicate that **A** and **B** are in parallel. The mean inter-square Ge–Ge distance d_1(**1a**) = 2.55(1) Å is considerably shorter than the mean Ge–Ge distances within **A** and **B** [d_2(**1a**) = 2.79(2) Å, d_2'(**1a**) = 2.80(2) Å]. The two atoms Ge1 and Ge10 cap the quadratic antiprism, whereby d_3(**1a**) = 2.583(7) Å and d_3'(**1a**) = 2.59(2) Å are slightly longer than d_1(**1a**) = 2.55(1) Å. In summary **1a** adopts a nearly perfect D_{4d} symmetry.

The geometrical parameters of **1a** are very similar to those of $[(Ge_{10})Mn(CO)_4]^{3-}$ (**2a**) (Fig. 1b). Like for **1a**, the $[Ge_{10}]$ cluster in **2a** adapts D_{4d} symmetry. The mean Ge–Ge distances d_3(**2a**) and d_3'(**2a**) are both 2.58(1) Å, suggesting that d_3(**2a**) is not influenced by the coordination of the $Mn(CO)_4$ fragment. However, in contrast to the square planes in **1a**, **A**′ is significantly widened [d_2(**2a**) = 2.85(2) Å] compared to **B**′ [d_2'(**2a**) = 2.77(1) Å], which might be attributed to the neighboring $Mn(CO)_4$ fragment. The inter-square Ge–Ge distances are almost identical for **1a** and **2a** [d_1(**1a**) = 2.55(1) Å, d_1(**2a**) = 2.547(8) Å].[29]

According to Wade's rules, **1a** can be described as a *closo*-deltahedron with 22 skeleton electrons (SE), whereby each vertex atom contributes two electrons, plus two extra electrons due to the two-fold negative charge.[38]

In order to study the vibrational behavior of **1a**, single crystals of **1** were investigated by Raman spectroscopy. The

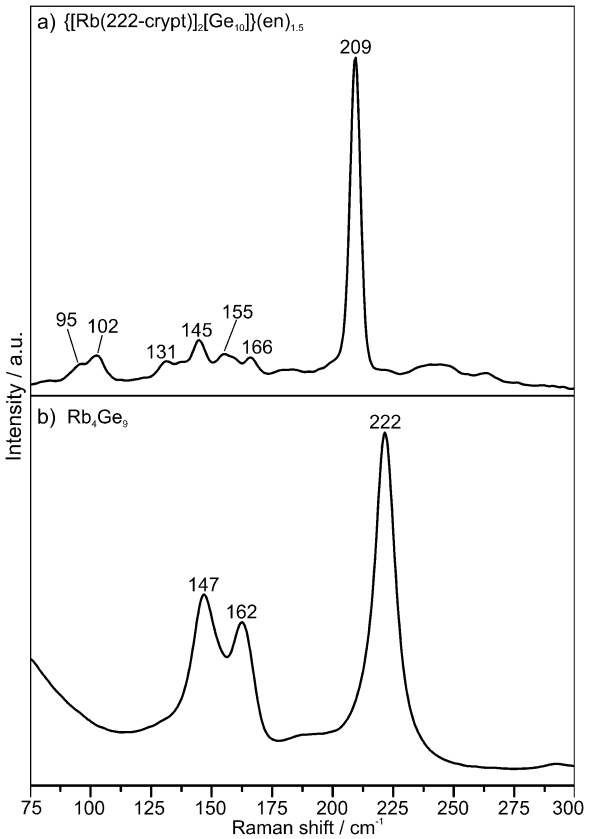

Fig. 2 Raman spectrum of (a) **1** and (b) Rb_4Ge_9. Characteristic modes are labeled with the corresponding Raman shifts.

spectrum (Fig. 2a) shows a very strong signal at 209 cm^{-1} and several very weak bands in the range from 95 to 166 cm^{-1}. In comparison, the Raman spectrum of the compound $[K(222\text{-crypt})]_2[Ge_9]$ exhibits one very intensive peak at 212 cm^{-1} and three signals below 200 cm^{-1} of medium intensity. Quantum-chemical calculations showed that the most intensive mode at 212 cm^{-1} corresponds to the "breathing" of the *closo*-$[Ge_9]^{2-}$ cluster. At least one of the medium intensive signals is attributed to vibrations of the central trigonal prism.[34] For *nido*-$[Ge_9]^{4-}$ clusters (Fig. 2b) the "breathing" mode appears at higher wavenumbers of *ca.* 222 cm^{-1}, and below 150 cm^{-1} medium-intensive signals are visible.[39–41] However, the latter appear in a neat solid with stronger alkaline metal–Ge interactions. In the spectrum of **1** the absence of intensive signals below 200 cm^{-1} evidences, that **1** does not contain $[Ge_9]^{2-}$ clusters, and thus we conclude that the mode at 209 cm^{-1} corresponds to the "breathing" vibration of **1a**.[34,39–41]

Crystals of **1** were obtained only from Rb_4Ge_9/en mixtures in the presence of 7-amino-1-trimethylsilyl-5-aza-hepta-3-en-1-yne (**3**), but not in the absence of **3**. Therefore we investigated several solutions by ESI-MS, namely **1** in acetonitrile (acn) (Fig. S3, ESI†) as well as Rb_4Ge_9/en and Rb_4Ge_9/en/**3** with a molar ratio Rb_4Ge_9/**3** = 1 : 1 at an equal concentration of Rb_4Ge_9 in en for both mixtures (Fig. S4, ESI†).

Crystals of **1** readily dissolve in acn (denoted as **1**/acn) giving a deep brown solution. Immediate injection of this solution into the mass spectrometer leads to peaks indicative for the presence of

Ge_{10}^- (m/z = 725), $\{Ge_{10}Rb\}^-$ (m/z = 812), and $\{Ge_{10}Rb(222\text{-crypt})\}^-$ (m/z = 1188), with the latter one as the most prominent species. The occurrence of solely Ge_{10} units hints for an enhanced stability of this cluster. By contrast, the ESI-MS of Rb_4Ge_9/en (Fig. S4a, ESI†) reveals the presence of $\{H_xGe_9\}^-$ (x = 0–2; m/z = 653, 654, 655), $\{HGe_{10}\}^-$ (m/z = 726) and $\{Ge_9Rb\}^-$ (m/z = 738) with an approximate ratio of intensities of 3 : 1 : 1. The high abundance of $\{HGe_{10}\}^-$ indicates that **1a** is readily formed upon solution of Rb_4Ge_9 in en, by a not yet understood fragmentation of the original $[Ge_9]^{4-}$ cluster.§¶

Interestingly, the mass spectrum of the solution of Rb_4Ge_9/**3**/en (Fig. S4b, ESI†), from which the crystals of **1a** were obtained, shows dominant signals of $\{Ge_9R\}^-$ (m/z = 764), $\{Ge_8R\}^-$ (m/z = 692) and $\{Ge_7R\}^-$ (m/z = 618) (R = 7-amino-5-aza-hepta-2,4-dien-2-yl) as well as the non-alkenylated species $\{H_xGe_9\}^-$ (x = 0–2), $\{Ge_9Rb\}^-$ ‖ [42] and $\{HGe_{10}\}^-$. The high abundance of clusters bearing organic ligands R, that arise from the nucleophilic addition of one and two molecules of **3** to the $[Ge_9]^{4-}$ unit, documents the higher reactivity of the $[Ge_9]^{4-}$ unit compared to that of $[Ge_{10}]^{2-}$.[37,42] The appearance of $\{HGe_{10}\}^-$ suggests that a fraction of the initial $[Ge_9]^{4-}$ clusters reacts to **1a** prior to the reaction with **3**. Thus, layering of a Rb_4Ge_9/**3**/en solution with cryptand[2.2.2] in toluene preferably produces crystals of **1** since the functionalized species $[Ge_9R]^{3-}$ obviously do not crystalize under these conditions. The binding mode of the organic group R to the cluster is shown in Fig. S5 (ESI†).

Our investigations shed some light onto the formation of the $[Ge_{10}]^{2-}$ Zintl anion. ESI-MS investigations revealed that the $[Ge_{10}]^{2-}$ unit is readily formed upon simple dissolution of Rb_4Ge_9 in en, highlighting the flexibility of the dissolved tetrel element $[Ge_9]^{4-}$ clusters which can grow and thereby change their shape. It turned out that the crystallization of the bare $[Ge_9]^{y-}$ (y = 2–4) clusters is favored over the crystallization of $[Ge_{10}]^{2-}$, both of which are present in Rb_4Ge_9/en solutions. Obviously, the $[Ge_{10}]^{2-}$ unit can only be obtained when the Ge_9 clusters are "masked" by the reaction with 7-amino-1-trimethylsilyl-5-aza-hepta-3-en-1-yne, leading to $[RGe_9]^{3-}$, which remains in solution and does not crystalize by layering with cryptand[2.2.2] in toluene. By adjusting the experimental conditions, it might be possible to obtain even larger empty germanium cages, and it also is feasible that other representatives of the $[E_{10}]^{2-}$ series can be synthesized by this method.

The authors are grateful to the SolTech (Solar Technologies go Hybrid) program of the State of Bavaria for financial support. Moreover, the authors thank Herta Slavik for Raman-spectroscopic measurements and Dr Wilhelm Klein for the help with the crystal structure analysis.

Notes and references

‡ Both Belin and Akerstedt isolated $[K(222\text{-crypt})]_2[Ge_9]$, which undergoes a disorder/order transition between 250 K and 100 K. Belin *et al.* performed single-crystal X-ray structure analysis at 250 K, and described the disordered $[Ge_9]^{2-}$ clusters as $[Ge_{10}]^{2-}$. Akerstedt *et al.* reinvestigated the same compound (identical unit cell and cell volume) at 100 K, and observed a fully ordered *closo*-$[Ge_9]^{2-}$ cluster.[33,34]

§ The formation of **1a** is an oxidative process (Scheme S1, ESI†), as the formal number of valence electrons per Ge atom, reduces from 22/9 in case of $[Ge_9]^{4-}$ to 22/10 for **1a**.

¶ Layering of such solutions with cryptand[2.2.2] or 18-crown-6 (1,4,7,10,13,16-hexaoxacyclooctadecane) in toluene has yielded a variety of crystals containing (connected) Ge_9 clusters, but none comprising **1a**.[17]

‖ The occurrence of also Ge_9^- and $(Ge_9Rb)^-$ in ESI-MS most likely is attributed to the cleavage of the Ge–C bonds of $[Ge_9R]^{3-}$ under ESI-MS conditions.[42]

1 T. F. Fässler and S. D. Hoffmann, *Angew. Chem., Int. Ed.*, 2004, **43**, 6242.
2 S. C. Sevov and J. M. Goicoechea, *Organometallics*, 2006, **25**, 5678.
3 S. Scharfe, F. Kraus, S. Stegmaier, A. Schier and T. F. Fässler, *Angew. Chem., Int. Ed.*, 2011, **50**, 3630–3670.
4 A. M. Guloy, R. Ramlau, Z. Tang, W. Schnelle, M. Baitinger and Y. Grin, *Nature*, 2006, **443**, 320.
5 T. F. Fässler, *Angew. Chem., Int. Ed.*, 2007, **46**, 2572.
6 D. Sun, A. E. Riley, A. J. Cadby, E. K. Richman, S. D. Korlann and S. H. Tolbert, *Nature*, 2006, **441**, 1126.
7 G. S. Armatas and M. G. Kanatzidis, *Science*, 2006, **313**, 817.
8 M. M. Bentlohner, M. Waibel, P. Zeller, K. Sarkar, P. Müller-Buschbaum, D. Fattakhova-Rohlfing and T. F. Fässler, *Angew. Chem., Int. Ed.*, 2016, **55**, 2441.
9 L. Xu and S. C. Sevov, *J. Am. Chem. Soc.*, 1999, **121**, 9245.
10 C. Downie, Z. J. Tang and A. M. Guloy, *Angew. Chem., Int. Ed.*, 2000, **39**, 337.
11 A. Ugrinov and S. C. Sevov, *J. Am. Chem. Soc.*, 2002, **124**, 10990.
12 R. Hauptmann and T. F. Fässler, *Z. Anorg. Allg. Chem.*, 2003, **629**, 2266.
13 A. Ugrinov and S. C. Sevov, *Inorg. Chem.*, 2003, **42**, 5789.
14 L. Yong, S. D. Hoffmann and T. F. Fässler, *Z. Anorg. Allg. Chem.*, 2004, **630**, 1977.
15 A. Nienhaus, S. D. Hoffmann and T. F. Fässler, *Z. Anorg. Allg. Chem.*, 2006, **632**, 1752.
16 S. Scharfe and T. F. Fässler, *Z. Anorg. Allg. Chem.*, 2011, **637**, 901.
17 A. Ugrinov and S. C. Sevov, *J. Am. Chem. Soc.*, 2003, **125**, 14059.
18 A. Ugrinov and S. C. Sevov, *Chem. – Eur. J.*, 2004, **10**, 3727.
19 C. Downie, J. G. Mao, H. Parmar and A. M. Guloy, *Inorg. Chem.*, 2004, **43**, 1992.
20 E. N. Esenturk, J. Fettinger, Y.-F. Lam and B. Eichhorn, *Angew. Chem., Int. Ed.*, 2004, **43**, 2132.
21 A. J. Karttunen, T. F. Fässler, M. Linnolahti and T. A. Pakkanen, *ChemPhysChem*, 2010, **11**, 1944.
22 A. Spiekermann, S. D. Hoffmann, T. F. Fässler, I. Krossing and U. Preiss, *Angew. Chem., Int. Ed.*, 2007, **46**, 5310.
23 J.-Q. Wang, S. Stegmaier and T. F. Fässler, *Angew. Chem., Int. Ed.*, 2009, **48**, 1998.
24 B. Zhou, M. S. Denning, D. L. Kays and J. M. Goicoechea, *J. Am. Chem. Soc.*, 2009, **131**, 2802.
25 G. Espinoza-Quintero, J. C. A. Duckworth, W. K. Myers, J. E. McGrady and J. M. Goicoechea, *J. Am. Chem. Soc.*, 2014, **136**, 1210.
26 M. M. Gillett-Kunnath, I. Petrov and S. C. Sevov, *Inorg. Chem.*, 2010, **49**, 721.
27 M. M. Gillett-Kunnath, A. G. Oliver and S. C. Sevov, *J. Am. Chem. Soc.*, 2011, **133**, 6560.
28 A. Spiekermann, S. D. Hoffmann and T. F. Fässler, *Angew. Chem., Int. Ed.*, 2006, **45**, 3459.
29 D. Rios and S. C. Sevov, *Inorg. Chem.*, 2010, **49**, 6396.
30 M. Waibel and T. F. Fässler, *Inorg. Chem.*, 2013, **52**, 5861.
31 D. Rios, M. M. Gillett-Kunnath, J. D. Taylor, A. G. Oliver and S. C. Sevov, *Inorg. Chem.*, 2011, **50**, 2373.
32 M. M. Bentlohner, L.-A. Jantke, T. Henneberger, C. Fischer, K. Mayer, W. Klein and T. F. Fässler, *Chem. – Eur. J.*, 2016, DOI: 10.1002/chem.201601706.
33 C. Belin, H. Mercier and V. Angilella, *New J. Chem.*, 1991, **15**, 931.
34 J. Åkerstedt, S. Ponou, L. Kloo and S. Lidin, *Eur. J. Inorg. Chem.*, 2011, 3999.
35 T. F. Fässler, H.-J. Muhr and M. Hunziker, *Eur. J. Inorg. Chem.*, 1998, 1433–1438.
36 S. Mitzinger, L. Broeckaert, W. Massa, F. Weigend and S. Dehnen, *Nat. Commun.*, 2016, **7**, 10480.
37 M. M. Bentlohner, W. Klein, Z. H. Fard, L.-A. Jantke and T. F. Fässler, *Angew. Chem., Int. Ed.*, 2015, **54**, 3748.
38 K. Wade, *Inorg. Nucl. Chem. Lett.*, 1972, **8**, 559.
39 H. G. Von Schnering, M. Baitinger, U. Bolle, W. Carrillo-Cabrera, J. Curda, Y. Grin, F. Heinemann, J. Llanos, K. Peters, A. Schmeding and M. Somer, *Z. Anorg. Allg. Chem.*, 1997, **623**, 1037.
40 M. Somer, W. Carrillo-Cabrera, E. M. Peters, K. Peters and H. G. v. Schnering, *Z. Anorg. Allg. Chem.*, 1998, **624**, 1915.
41 V. Hlukhyy, T. F. Fässler, S. Ponou, S. Lidin, N. P. Ivleva and R. Niessner, *Inorg. Chem.*, 2012, **51**, 4058.
42 M. W. Hull and S. C. Sevov, *J. Am. Chem. Soc.*, 2009, **131**, 9026.

Electronic Supplementary Material (ESI) for ChemComm.

Supplementary Information

Synthesis and characterization of pristine *closo* - $[Ge_{10}]^{2-}$

Manuel M. Bentlohner, Christina Fischer and Thomas F. Fässler*

Contents

Figures and Tables

1 Experimental Details

General Methods: All manipulations took place under a purified argon atmosphere using a glove box and standard Schlenk technique. The Zintl compound of the nominal composition Rb_4Ge_9 was synthesized by heating a stoichiometric mixture of the elements Rb and Ge (99.999% Chempur) at 650°C for 48 h in a tantalum ampoule.[1] *En* (Merck) was refluxed with calcium hydride (Merck) and immediately used after collection. The water-content of *en* was qualitatively checked according to a method described elsewhere.[2] 1,4-Bis(trimethylsilyl)butadiyne (Alfa Aesar 98%) was used as received. Toluene was dried over molecular sieve (4 Å) in a solvent purificator (MBraun MB-SPS). Cryptand[2.2.2] (Merck) was dried in a vacuum for 8 h.

Synthesis of $[Rb(222\text{-crypt})]_2[Ge_{10}](en)_{1.5}$: A solution of 7-amino-1-(trimethylsilyl)-5-aza-hepta-3-en-1-yne in *en* (60 µmol/mL) was prepared by dissolving bis(trimethylsilyl)butadiyne (15.2 mg, 78 µmol) in 1.3 ml *en*. [3] In a Schlenk tube 1.3 mL of the solution of 7-amino-1-(trimethylsilyl)-5-aza-hepta-3-en-1-yne (78 µmol, 1 eq.) in *en* was carefully dropped onto Rb_4Ge_9 (77.6 mg, 78 µmol, 1 eq.), and a dark red mixture was obtained. The reaction mixture was stirred for 20 h, whereby the color of the mixture became greenish, but no precipitate was formed. The reaction mixture was filtered over glass fibers and carefully layered with a solution of cryptand[2.2.2] (90.4 mg, 312 µmol, 4 eq.) in 4 mL toluene. After two weeks, dark purple, pillar-shaped crystals had formed (yield ca. 10-20%). Crystal size: 0.3 x 0.25 x 0.05 mm³; unit cell parameters: a = 10.8759(2), b = 13.4395(3), c = 21.2958(4) Å, α = 85.907(2)° , β = 88.885(2)°, γ = 88.995(2)°, V = 3104.2(11) Å^3, triclinic space group $P\bar{1}$; Z = 2, ρ_{calc} = 1.862 g cm^{-3}, μ = 6.38 mm^{-1}, θ_{max} = 26.00°, 65291 measured reflections, 11569 independent reflections, R_{int} = 0.081, R_1 = 0.041, wR_2 = 0.078 for reflections with $I > 2\sigma(I)$, R_1 = 0.095, wR_2 = 0.091 for all data. Min/max residual electron density: -0.87/1.12 e Å^{-3}. CCDC 1479637 contains the supplementary crystallographic data for this paper. These data can be obtained free of charge from The Cambridge Crystallographic Data Centre via www.ccdc.cam.ac.uk/data_request/cif. ESI-MS (negative ion mode): m/z (%): 1188 (85) $\{Ge_{10}Rb(222\text{-crypt})\}^-$, 812 (5) $\{Ge_{10}Rb\}^-$, 725

(3) Ge_{10}^{-}; Raman ν [cm^{-1}] = 95 (w), 102 (w), 131 (w), 138 (w), 145 (w), 155 (w), 166 (w), 209 (s);

X-Ray data collection and structure determination: A single crystal was fixed on the top of a glas fiber with perfluorinated ether and positioned in a cold N_2 stream at 123 K. The single crystal X-ray diffraction data were recorded on an Oxford-Diffraction Xcalibur3 diffractometer (Mo-K_α radiation). The crystal structure was solved by Direct Methods using the SHELX software.[4] The positions of the hydrogen atoms were calculated and refined using a riding model. All non-hydrogen atoms were treated with anisotropic displacement parameters.

Electrospray ionization mass spectrometry (ESI-MS) investigations: ESI-MS was done on a HCT mass spectrometer (Bruker Daltronic) in the negative ion mode (-); Preparation of **1**/*acn*: Several crystals of **1** were washed with toluene and dissolved in *acn*, giving an intensively brown, transparent solution. Prior to injection into the ESI-MS the solution was filtered; preparation of Rb_4Ge_9/*en* and Rb4Ge_9/**3**/*en*: The Rb_4Ge_9/**3**/*en* mixture was prepared according to the synthesis described for [Rb(222-crypt)]$_2$[Ge_{10}](en)$_{1.5}$. The Rb_4Ge_9/*en* mixture was prepared by dissolving Rb_4Ge_9 (40 mg, 0.04 mmol, 1 eq.) in 0.67 mL *en*. Upon addition of Rb_4Ge_9 to *en* a dark orange-green solution and a large amount of a yellow precipitate were obtained. The mixture was stirred for 20 h, where upon the color became deep-green, and the yellow precipitate dissolved; prior to the measurement both reaction mixtures were filtered and diluted with *en* (1:100). Measurement conditions: capillary voltage: 4.5 kV(*acn*)/2.5kV(*en*), capillary exit: -166(*acn*)/-180(*en*) V, drying gas temperature: 125 °C (*acn*/*en*), injection rate: 240 µL/h(*acn*/*en*).

Raman spectroscopy: Raman measurements were performed on single crystals sealed in glass capillaries with a Raman microscopy spectrometer (Senterra Raman spectrometer: Bruker Corporation; diode laser: 785 nm, 1 mW).

2 Crystallographic details

Figure S1. The *closo*-$[Ge_9]^{2-}$ Zintl cluster.[5] For a detailed discussion on the disorder see original publications.[5,6]

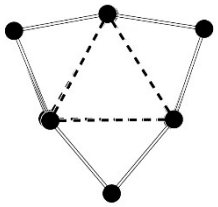

Table S1. Selected crystallographic data of **1**

Compound	**1**
Formula	$Ge_{10}Rb_2C_{39}H_{84}N_7O_{12}$
fw (g mol^{-1})	1739.97
space group (no.)	$P\bar{1}$ (2)
a (Å)	10.8759(2)
b (Å)	13.4395(3)
c (Å)	21.2985(4)
α (deg)	85.907(2)
β (deg)	88.885(2)
γ (deg)	88.995(2)
V (Å^3)	3104.2(1)
Z	2
T (K)	123(2)
λ (Å)	0.71073
ρ_{calcd} (g cm^{-3})	1.862
μ (mm^{-1})	6.38
collected reflections	65291
independent reflections	11569
R_{int}	0.081
parameters / restraints	631 / 6
R_1 [all data / $I > 2\,\sigma(I)$]	0.095 / 0.041
wR_2 [all data / $I > 2\,\sigma(I)$]	0.091 / 0.078
goodness of fit	0.855
max./min. diff. el. density (e Å^{-3})	1.12 / -0.87

Figure S2. Drawing of the unit cell of **1**. $[Ge_{10}]^{2-}$ clusters are shown as dark-grey polyhedra. Cryptand[2.2.2] is shown schematically, displacement ellipsoids of rubidium are shown at a probability level of 50% at 123 K. Solvent and hydrogen atoms are omitted for clarity.

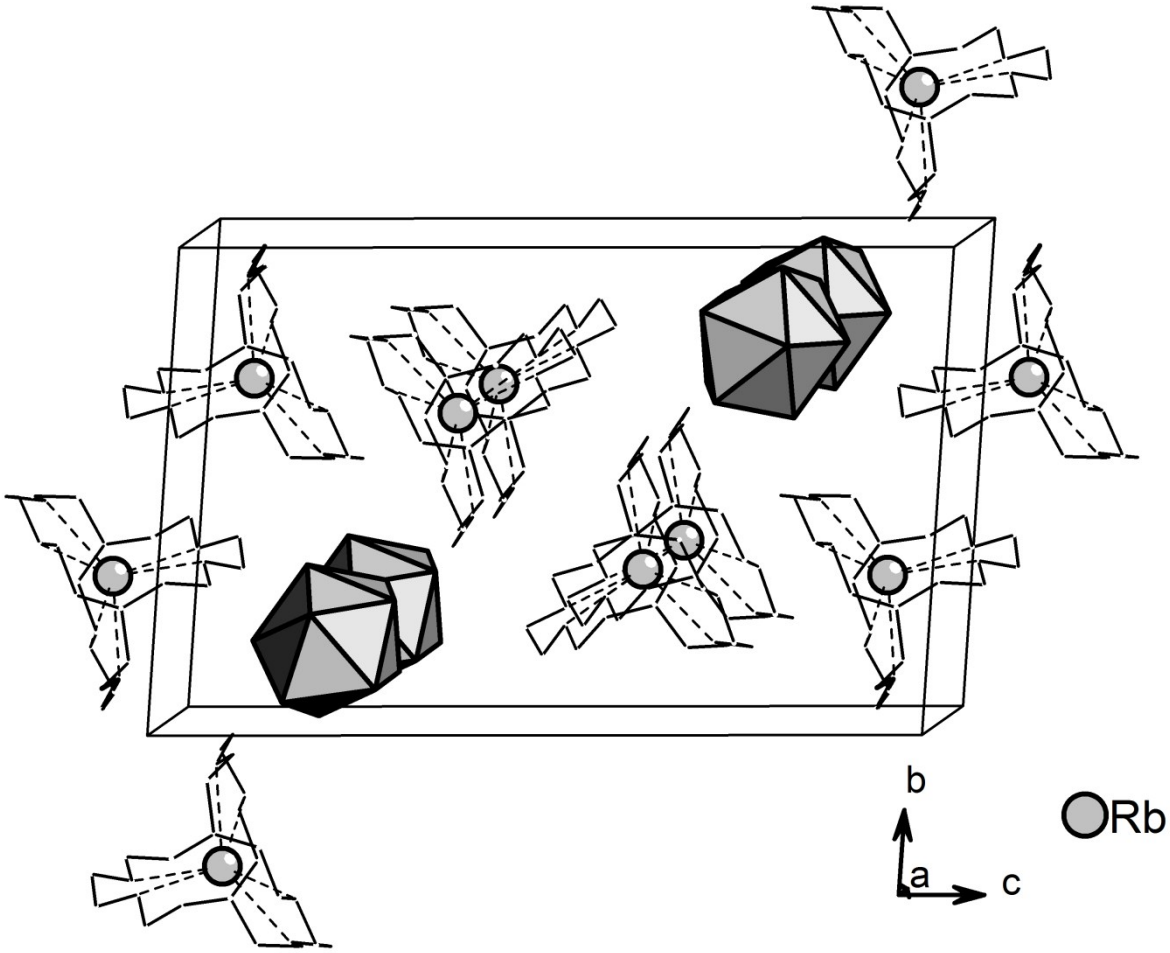

Table S2. Bond lengths [Å] in **1a**

Ge1—Ge5	2.573(1)	Ge4—Ge9	2.566(1)
Ge1—Ge4	2.584(1)	Ge4—Ge5	2.799(1)
Ge1—Ge3	2.587(1)	Ge5—Ge9	2.543(1)
Ge1—Ge2	2.588(1)	Ge5—Ge6	2.552(1)
Ge2—Ge6	2.546(1)	Ge6—Ge10	2.567(1)
Ge2—Ge7	2.559(1)	Ge6—Ge7	2.809(1)
Ge2—Ge3	2.760(1)	Ge6—Ge9	2.822(1)
Ge2—Ge5	2.792(1)	Ge7—Ge10	2.587(1)
Ge3—Ge7	2.535(1)	Ge7—Ge8	2.780(1)
Ge3—Ge8	2.564(1)	Ge8—Ge10	2.611(1)
Ge3—Ge4	2.797(1)	Ge8—Ge9	2.798(1)
Ge4—Ge8	2.551(1)	Ge9—Ge10	2.590(1)

Table S3. Bond angles [deg] in **1a**

Ge3—Ge1—Ge2	64.47 (3)	Ge1—Ge5—Ge4	57.33 (3)
Ge6—Ge2—Ge7	66.76 (3)	Ge2—Ge5—Ge4	90.00 (3)
Ge6—Ge2—Ge1	110.40 (4)	Ge2—Ge6—Ge5	66.42 (3)
Ge7—Ge2—Ge1	110.49 (4)	Ge2—Ge6—Ge10	110.36 (4)
Ge6—Ge2—Ge3	103.83 (4)	Ge5—Ge6—Ge10	109.72 (4)
Ge7—Ge2—Ge3	56.77 (3)	Ge2—Ge6—Ge7	56.84 (3)
Ge1—Ge2—Ge3	57.74 (3)	Ge5—Ge6—Ge7	102.68 (3)
Ge6—Ge2—Ge5	56.89 (3)	Ge10—Ge6—Ge7	57.32 (3)
Ge7—Ge2—Ge5	102.95 (3)	Ge2—Ge6—Ge9	102.70 (3)
Ge1—Ge2—Ge5	57.00 (3)	Ge5—Ge6—Ge9	56.20 (3)
Ge3—Ge2—Ge5	90.10 (3)	Ge10—Ge6—Ge9	57.21 (3)
Ge7—Ge3—Ge8	66.09 (3)	Ge7—Ge6—Ge9	89.51 (3)
Ge7—Ge3—Ge1	111.32 (4)	Ge3—Ge7—Ge2	65.62 (3)
Ge8—Ge3—Ge1	109.98 (4)	Ge3—Ge7—Ge10	111.17 (4)
Ge7—Ge3—Ge2	57.61 (3)	Ge2—Ge7—Ge10	109.30 (4)
Ge8—Ge3—Ge2	103.36 (3)	Ge3—Ge7—Ge8	57.46 (3)
Ge1—Ge3—Ge2	57.79 (3)	Ge2—Ge7—Ge8	102.94 (3)
Ge7—Ge3—Ge4	103.55 (3)	Ge10—Ge7—Ge8	58.09 (3)
Ge8—Ge3—Ge4	56.61 (3)	Ge3—Ge7—Ge6	102.76 (3)
Ge1—Ge3—Ge4	57.21 (3)	Ge2—Ge7—Ge6	56.39 (3)
Ge2—Ge3—Ge4	90.69 (3)	Ge10—Ge7—Ge6	56.63 (3)
Ge8—Ge4—Ge9	66.31 (3)	Ge8—Ge7—Ge6	90.27 (3)
Ge8—Ge4—Ge1	110.49 (4)	Ge4—Ge8—Ge3	66.31 (3)
Ge9—Ge4—Ge1	109.81 (4)	Ge4—Ge8—Ge10	110.17 (4)
Ge8—Ge4—Ge3	57.08 (3)	Ge3—Ge8—Ge10	109.45 (4)
Ge9—Ge4—Ge3	102.91 (3)	Ge4—Ge8—Ge7	103.60 (4)
Ge1—Ge4—Ge3	57.30 (3)	Ge3—Ge8—Ge7	56.45 (3)
Ge8—Ge4—Ge5	102.46 (4)	Ge10—Ge8—Ge7	57.24 (3)
Ge9—Ge4—Ge5	56.38 (3)	Ge4—Ge8—Ge9	57.10 (3)
Ge1—Ge4—Ge5	56.95 (3)	Ge3—Ge8—Ge9	102.92 (4)
Ge3—Ge4—Ge5	89.21 (3)	Ge10—Ge8—Ge9	57.08 (3)
Ge9—Ge5—Ge6	67.29 (3)	Ge7—Ge8—Ge9	90.59 (3)
Ge9—Ge5—Ge1	110.90 (4)	Ge5—Ge9—Ge4	66.44 (3)
Ge6—Ge5—Ge1	110.70 (4)	Ge5—Ge9—Ge10	109.27 (4)
Ge9—Ge5—Ge2	103.63 (3)	Ge4—Ge9—Ge10	110.39 (4)
Ge6—Ge5—Ge2	56.69 (3)	Ge5—Ge9—Ge8	102.68 (3)
Ge1—Ge5—Ge2	57.51 (3)	Ge4—Ge9—Ge8	56.59 (3)
Ge9—Ge5—Ge4	57.17 (3)	Ge10—Ge9—Ge8	57.83 (3)
Ge6—Ge5—Ge4	103.89 (4)	Ge5—Ge9—Ge6	56.51 (3)

Ge4—Ge9—Ge6	102.87 (3)	Ge7—Ge10—Ge9	99.97 (3)
Ge10—Ge9—Ge6	56.42 (3)	Ge6—Ge10—Ge8	99.82 (3)
Ge8—Ge9—Ge6	89.63 (3)	Ge7—Ge10—Ge8	64.67 (3)
Ge6—Ge10—Ge7	66.05 (3)	Ge9—Ge10—Ge8	65.09 (3)
Ge6—Ge10—Ge9	66.37 (3)		

3 Electrospray-ionization mass spectra (ESI-MS)

Figure S3. ESI-MS (-) of crystals of **1** dissolved in *acn*. a) Full spectrum and b) magnified sections, showing the most prominent fragments in detail. The measured spectrum and simulated pattern are depicted in black and as red columns, respectively. Unknown signals are marked with *.

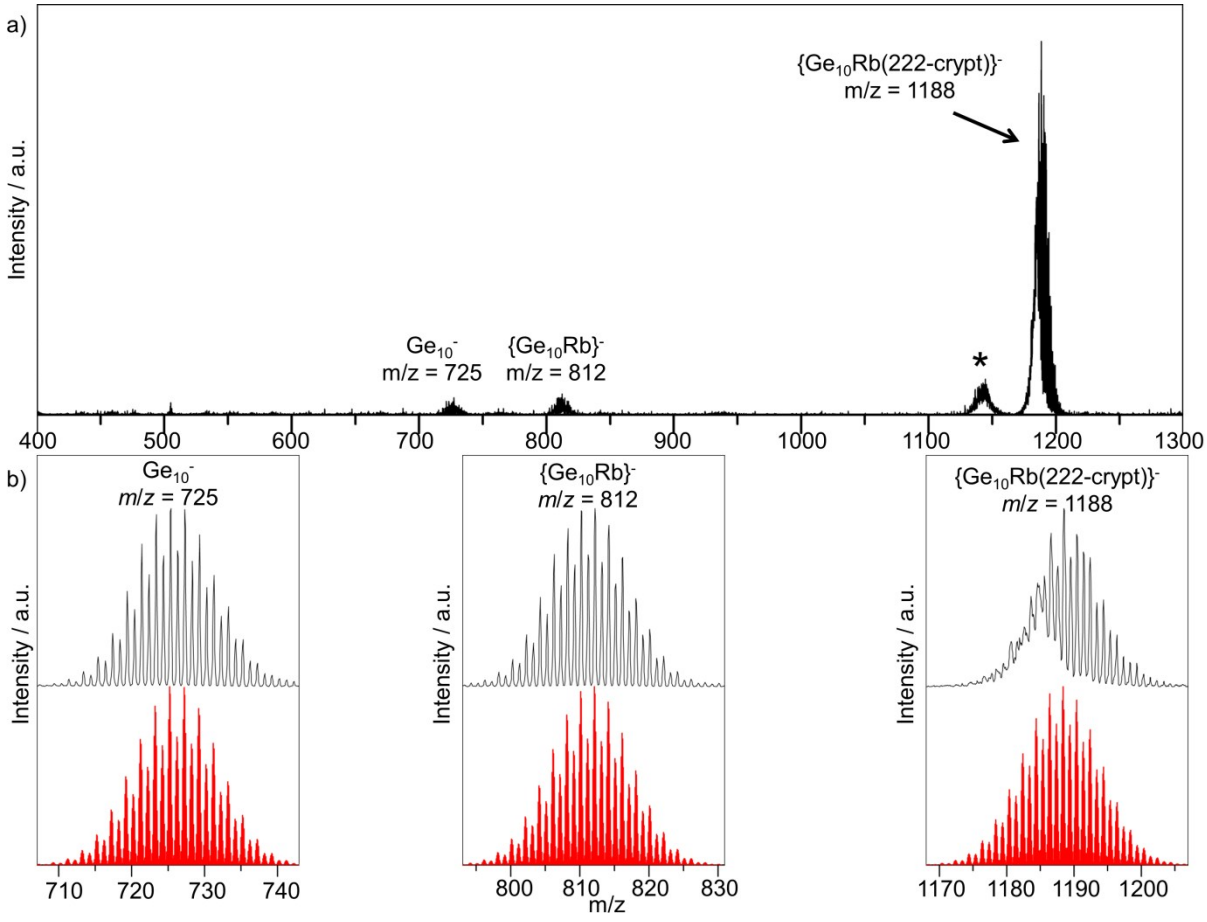

Figure S4. ESI-MS (-) of the reaction solutions a) Rb_4Ge_9/*en* and b) Rb_4Ge_9/**3**/*en*. The measured spectra (black) and simulated patterns (coloured), R = 7-amino-5-aza-hepta-2,4-dien-2-yl = $C_6H_{11}N_2$.

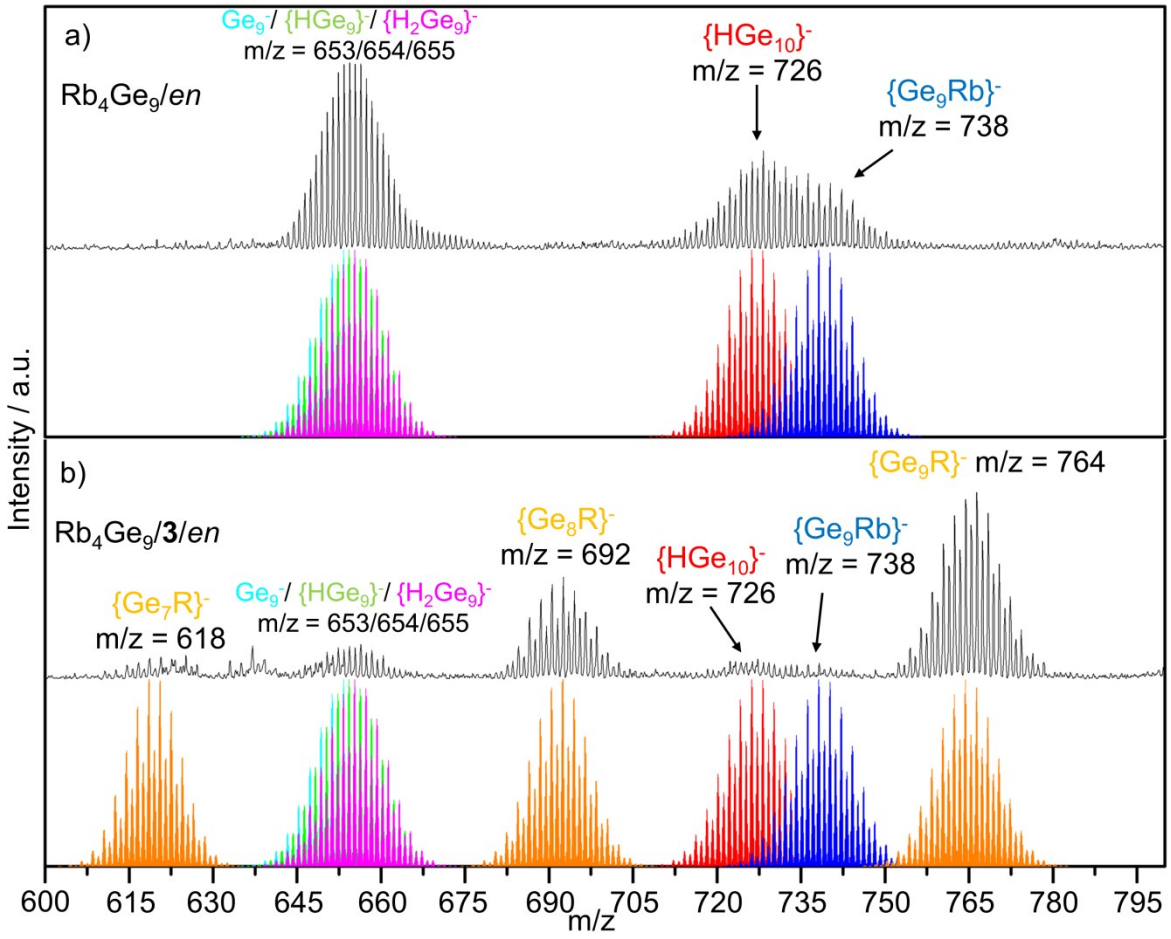

Figure S5. The $[R–Ge_9]^{3–}$ (R = 7-amino-5-aza-hepta-2,4-dien-2-yl) originating from the reaction of $[Ge_9]^{4–}$ with 7-amino-1-trimethylsilyl-5-aza-hepta-3-en-1-yne.

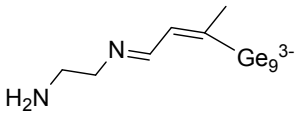

Scheme S1. Half reaction (oxidation) of the formation of $[Ge_{10}]^{2–}$ from $[Ge_9]^{4–}$ occurring upon dissolution of Rb_4Ge_9 in *en*.

$$Rb_4Ge_9 \xrightarrow{\text{Dissolve in } en} Ge_9^{4-} + 4\ Rb^+ \longrightarrow 9/10\ Ge_{10}^{2-} + 22/10\ e^- + 4\ Rb^+$$

4 References

1 C. Hoch, M. Wendorff, C. Röhr, *J. Alloys Compd.,* 2003, **361**, 206.

2 M. M. Bentlohner, M. Waibel, P. Zeller, K. Sarkar, P. Müller-Buschbaum, D. Fattakhova-Rohlfing and T. F. Fässler, *Angew. Chem. Int. Ed.,* 2016, **55**, 2441.

3 M. M. Bentlohner, W. Klein, Z. H. Fard, L.-A. Jantke, T. F. Fässler, *Angew. Chem. Int. Ed.,* 2015, **54**, 3748.

4 G. M. Sheldrick, *Acta Crystallogr.,* 2008, **A64**, 112.

5 J. Åkerstedt, S. Ponou, L. Kloo, S. Lidin, *Eur. J. Inorg. Chem.* **2011**, *2011*, 3999-4005.

6 C. Belin, H. Mercier, V. Angilella, *New J. Chem.,* **1991**, *15*, 931

5.4 On the nature of bridging metal atoms in intermetalloid clusters - Syntheses and Structure of the Metal Atom Bridged Zintl Clusters $[Sn(Ge_9)_2]^{4-}$ and $[Zn(Ge_9)_2)]^{6-}$

M. M. Bentlohner, L-A. Jantke, T. Henneberger, C. Fischer, K. Mayer, W. Klein, T. F. Fässler

published in:

Chem. Eur. J. **2016**, *22*, 13946.

Contents and Contributions

In the scope of the publication “On the nature of bridging metal atoms in intermetalloid clusters - Syntheses and Structure of the Metal Atom Bridged Zintl Clusters $[Sn(Ge_9)_2]^{4-}$ and $[Zn(Ge_9)_2)]^{6-}$ “, the addition of Sn and Zn ions to Ge_9 clusters upon the reaction of $[Ge_9]^{4-}$ with $SnPh_2Cl_2$ and $ZnCp^*_2$ as well as with $Zn_2[HC(Ph_2P{=}NPh)_2]_2$ (Cp* = 1,2,3,4,5-pentamethylcyclopentadienyl; Ph = phenyl) is reported. The reactivity of $[Ge_9]^{4-}$ Zintl anions towards organometal reagents is of special interest in understanding the formation of intermetalloid cluster species and defining a rational method for the stepwise extension of Zintl clusters.

Concretely, the compounds $[K(18\text{-crown-}6)]_4[Sn(Ge_9)_2)](en)_{4.5}$, $K_2[K(2.2.2\text{-crypt})]_4[Zn(Ge_9)_2)](NH_3)_{22}$ and $K_2[K(2.2.2\text{-crypt})]_4[Zn(Ge_9)_2)](NH_3)_{24}$ are presented in terms of syntheses and structural characterization as well as the bonding situations of their anionic entities. In the course of the present thesis the publication was authored. Text contributions to the description of the crystal structures and theoretical calculations were given by Christina Fischer, Kerstin Mayer and Thomas Henneberger as well as Laura-Alice Jantke, respectively. The compounds $K_2[K(2.2.2\text{-crypt})]_4[Zn(Ge_9)_2)](NH_3)_{22}$ and $K_2[K(2.2.2\text{-crypt})]_4[Zn(Ge_9)_2)](NH_3)_{24}$ were synthesized by Thomas Henneberger and Kerstin Mayer. In the scope of the Master thesis of Christina Fischer, which was supervised in the course of this thesis, the compound $[K(18\text{-crown-}6)]_4[Sn(Ge_9)_2)](en)_{4.5}$ was synthesized by the reaction of K_4Ge_9 with $SnPh_2Cl_2$ in presence of elemental potassium in *en*, and layering of the reaction solution with 18-crown-6/*tol*. The idea for bridging $[Ge_9]^{4-}$ clusters by reaction with $SnPh_2Cl_2$/K was given in the course of this thesis. X-ray structure analysis reveals that the anionic entity of $[K(18\text{-crown-}6)]_4[Sn(Ge_9)_2)](en)_{4.5}$ consists of two Ge_9 clusters bridged by tin atom, which coordinates in η^3 and η^4 mode to the clusters. ESI-MS investigations on reaction solutions from which $[K(18\text{-crown-}6)]_4[Sn(Ge_9)_2)](en)_{4.5}$ was isolated show that *closo*-$[Ge_9Sn]^{2-}$ is a rigid deltahedral clusters which is stable under the applied ESI-MS conditions and in *en* solutions. ESI-MS measurements and data evaluation was conducted by Christina Fischer. Evaluation of bond length as well as theoretical calculations revealed, that the anionic entity $[Sn(Ge_9)_2)]^{4-}$ is best described as an Lews acid/base pair of *closo*-$[Ge_9Sn]^{2-}$ and *closo*-$[Ge_9]^{2-}$. Theoretical calculations as well as evaluation of the results were conducted by Laura-Alice Jantke.

ChemPubSoc Europe

DOI: 10.1002/chem.201601706

CHEMISTRY A European Journal Full Paper

Metal–Metal Interactions

On the Nature of Bridging Metal Atoms in Intermetalloid Clusters: Synthesis and Structure of the Metal-Atom-Bridged Zintl Clusters $[Sn(Ge_9)_2]^{4-}$ and $[Zn(Ge_9)_2)]^{6-}$

Manuel M. Bentlohner, Laura-Alice Jantke, Thomas Henneberger, Christina Fischer, Kerstin Mayer, Wilhelm Klein, and Thomas F. Fässler*[a]

Dedicated to Professor Hansgeorg Schnöckel on the occasion of his 75th birthday

Abstract: The addition of Sn and Zn ions to $[Ge_9]$ clusters by reaction of $[Ge_9]^{4-}$ with $SnPh_2Cl_2$, $ZnCp^*_2$ (Cp^* = pentamethylcyclopentadienyl), or $Zn_2[HC(Ph_2P{=}NPh)_2]_2$ is reported. The resulting Sn- and Zn-bridged clusters $[(Ge_9)M(Ge_9)]^{q-}$ (M = Sn, $q=4$; M = Zn, $q=6$) display various coordination modes. The M atoms that coordinate to the open square of a C_{4v}-symmetric $[Ge_9]$ cluster form strong covalent multicenter M–Ge bonds, in contrast to the M atoms coordinating to triangular cluster faces. Molecular orbital analyses show that the M atoms of the Ge_9M fragments coordinate to a second $[Ge_9]$ cluster with similar orbitals but in different ways. The $[Ge_9Sn]^{2-}$unit donates two electrons to the triangular face of a second $[Ge_9]^{2-}$ cluster with D_{3h} symmetry, whereas $[Ge_9Zn]^{2-}$acts as an electron acceptor when interacting with the triangular face of a D_{3h}-symmetric $[Ge_9]^{4-}$ unit.

Introduction

Soluble homoatomic group 14 Zintl clusters[1] are excellent resources to construct larger homo- and heteroatomic clusters,[2] novel element allotropes, and nanomorphologies.[3] Even though homoatomic $[E_9]^{4-}$ clusters are easily accessible in alloys by a one-step reaction of the respective elements E = Si–Pb with alkali metals,[4] a rational and controlled synthesis of heterometallic clusters is less elaborated.[5] For the synthesis of intermetalloid clusters,[2,6] organometallic compounds of late transition metals have frequently been used, whereas corresponding early transition metal starting materials have more scarcely been applied for this purpose.[7] The basic synthetic approach involves the reaction of metal complexes MX_aL_b (M = transition metal, X = halogen, $a \geq 0$, L = two-electron donor ligand, $b > 0$) bearing weakly bonded ligands with $[E_9]^{4-}$ Zintl anions. Ligand-exchange reactions can lead to capped $[(E_9)(ML_a)]^{q-}$, bridged $\{[(E_9)M(E_9)]_m\}^{q-}$ ($m = 1-\infty$), and endohedrally filled $[M@E_n]^{q-}$($n \geq 9$) clusters.[2] The ability of $[E_9]$ cages to undergo oxidative coupling and/or fragmentation reactions,[3e,f,8] leads to intermetalloid clusters with different sizes and shapes. Notable examples are $[Au_3Ge_{45}]^{9-}$,[9] which to date is the largest known cluster of a heavier tetrel element, and $[Co@Ge_{10}]^{3-}$, which was the first one reported with a non-deltahedral structure.[10] Besides the bare $[E_9]^{4-}$ clusters, the silylated cluster $\{[Ge_9]Hyp_3\}^-$ [Hyp = $Si(SiMe_3)_3$][11] has been used as a starting material for the synthesis of low-charge or neutral intermetalloids with enhanced solubility in less polar solvents.[12,13]

The diverse intermetalloids[2] include several examples of mixed main group and main group/group 12 element clusters originating from bare homoatomic $[E_9]^{4-}$ and $[E'_7]^{3-}$ (E′ = P–Sb) Zintl anions.[14–16] The smaller representatives such as $[Sn_2Bi_2]^{2-}$[17] have been used in similar synthetic routes, and a whole series of bare heterometallic clusters comprising transition and rare earth metals has been obtained.[18] Studies on heterometallic clusters at the border between main group and group 12 elements are valuable for establishing a synthetic approach for the atom-by-atom extension of bare clusters.[14f,15b] Therefore, we studied the reactivity of Sn^{IV}, Zn^{II}, and Zn^{I} organyls towards $[Ge_9]^{4-}$ and looked for conditions that allow stepwise cluster extension.

Herein, we report on the synthesis, structure, and electronic situation of $[(Ge_9)Sn(Ge_9)]^{4-}$ and $[(Ge_9)Zn(Ge_9)]^{6-}$, which contain two $[Ge_9]$ clusters bridged by a Sn and a Zn atom, respectively. The bridging atoms have high coordination numbers (6 and 8, respectively). The cluster anions crystallize as $[K(18\text{-crown-}6)]_4[(Ge_9)Sn(Ge_9)]\cdot 4.5\,en$ (**1**; 18-crown-6 = 1,4,7,10,13,16-hexaoxacyclooctadecane, en = ethylenediamine), $K_2[K(2.2.2\text{-crypt})]_4[(Ge_9)Zn(Ge_9)]\cdot 21.6\,NH_3$ (**2**), and $K_2[K(2.2.2\text{-crypt})]_4[(Ge_9)Zn(Ge_9)](NH_3)_{24}$ (**3**; 2.2.2-crypt = 4,7,13,16,21,24-hexaoxa-1,10-diazabicyclo[8.8.8]hexacosane), which were characterized by X-ray structure analysis.

[a] M. M. Bentlohner, L.-A. Jantke, T. Henneberger, C. Fischer, K. Mayer, Dr. W. Klein, Prof. Dr. T. F. Fässler
Department Chemie, Technische Universität München
Lichtenbergstrasse 4, 85747 Garching (Germany)
E-mail: thomas.faessler@lrz.tum.de

Supporting information for this article (synthetic procedures and details of crystallography and computations) and ORCID(s) for the author(s) are available on the WWW under http://dx.doi.org/10.1002/chem.201601706.

Results and Discussion

The reaction of K_4Ge_9 and $SnPh_2Cl_2$ in the presence of elemental potassium and 18-crown-6 in ethylenediamine led to compound **1**. In the first step of the synthesis a suspension of $SnPh_2Cl_2$ in en (mixture A) and a mixture of K_4Ge_9, elemental K, and en (mixture B) were prepared. In the second step mixtures A and B were combined and stirred for 16 h. Afterwards the reaction mixture was heated for 1 h at 50 °C and layered with toluene/cryptand[2.2.2], whereby deep red blocks of **1** were obtained after 12 weeks. Sevov et al. used a similar procedure to synthesize the compounds [K(2.2.2-crypt)]$_3$[(Ge$_9$)(SnPh$_3$)]·en and [K(2.2.2-crypt)]$_3$[(Ge$_9$)(SnMe$_3$)],[14a] whereby SnR_3Cl (R = Ph, Me) was treated with elemental K prior to addition of K_4Ge_9, whereas in the current work Ph_2Cl_2Sn was treated with potassium in the presence of K_4Ge_9. Compounds **2** and **3** with similar anionic entities but with coordinated Zn instead of Sn were obtained by treating K_4Ge_9 with $Zn^{I}_2[HC(Ph_2PNPh)_2]_2$ and $ZnCp^*_2$ in the presence of cryptand[2.2.2] in liquid ammonia, respectively. K_4Ge_9, cryptand[2.2.2], and the Zn precursors were weighed out in a Schlenk tube and treated with liquid ammonia at −70 °C for 15 weeks, whereby dark red blocks were obtained. A more detailed description of the reactions is given in the Supporting Information.

In the crystal structure of **1**, four [K(18-crown-6)]$^+$ cations per cluster unit formally assign a charge of −4 to the cluster anion. [(Ge$_9$)Sn(Ge$_9$)]$^{4-}$ (**1a**) consists of two [Ge$_9$] clusters **1A** and **1B**, which are connected by a Sn atom (Figure 1a). Cluster **1A** has the shape of an idealized monocapped square antiprism (the ratio of the diagonal lengths of the open square is 1.0) and thus is C_{4v}-symmetric, whereas **1B** is an idealized D_{3h}-symmetric tricapped trigonal prism with three almost identical prism heights.[19] The bridging Sn atom is bonded to four atoms, Ge1–Ge4, of the open square of **1A**, with Sn–Ge distances of 2.630(1)–2.709(1) Å, which are slightly longer than the sum of the covalent radii (r_{Ge} = 1.20, r_{Sn} = 1.39 Å).[20] The Sn atom is further bonded to the three atoms Ge10–Ge12 of the triangular face of **1B**, with considerably longer Sn–Ge distances of 2.770(1), 2.975(1), and 3.151(1) Å. The distortion of the central trigonal prism of **1B** correlates with the coordination of the Sn atom to the triangular face Ge10/Ge11/Ge12, and the longest prism height of 2.960(1) Å (Ge10–Ge17) in **1B** corresponds to the shortest Ge–Sn distance of 2.770(1) Å (Ge10–Sn) and vice versa (2.806(1) Å for Ge12–Ge16 and 3.151(1) Å for Ge12–Sn). To designate the coordination modes of the bridging atoms, notations of the type η^4:η^3-**1a** are used throughout the paper.

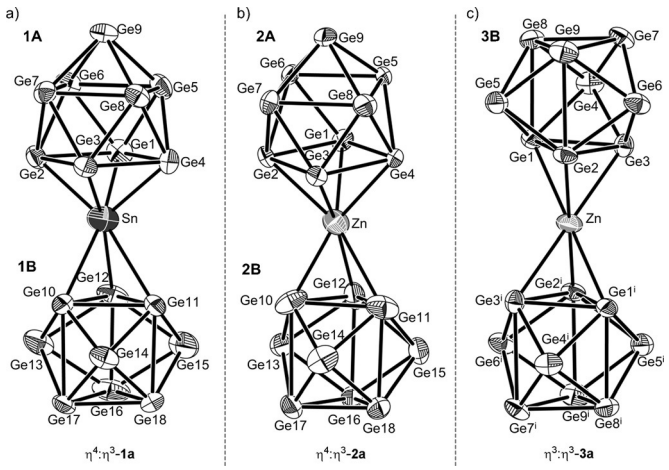

Figure 1. [Ge$_9$] clusters bridged by an M atom (M = Sn, Zn). a) [(η^4-Ge$_9$)Sn(η^3-Ge$_9$)]$^{4-}$ (η^4:η^3-**1a**), b) [(η^4-Ge$_9$)Zn(η^3-Ge$_9$)]$^{6-}$ (η^4:η^3-**2a**; 81.9%), and c) [(η^3-Ge$_9$)Zn(η^3-Ge$_9$)]$^{6-}$ (η^3:η^3-**3a**; 93%); for the minority components, see Supporting Information. Symmetry operation i: −*x*, −*y*, −*z*.. **A** and **B** denote C_{4v}- and D_{3h}- symmetric clusters, respectively. The ellipsoids are drawn at a probability of 70%.

The negative-ion ESI mass spectrum of the reaction solution (Figure 2) indicates strong bonds of the Sn atom to the nine-atom cluster units, since [Ge$_9$Sn]$^-$ (*m*/*z* = 771) is the only observed species of the reaction solution, and no other fragmentation of **1a** is observed. Besides, [Ge$_{10}$]$^-$ also appears as a prominent peak, and the isolation of crystals containing the first ordered [Ge$_{10}$]$^{2-}$ anions will be presented in a forthcoming paper.[21]

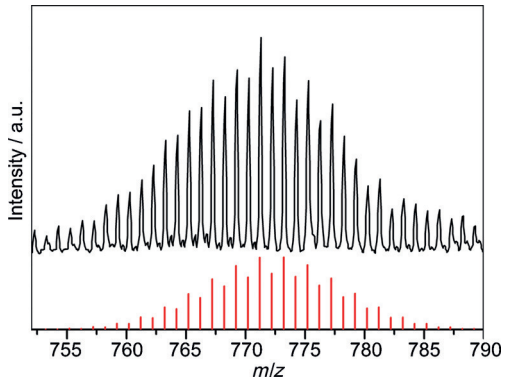

Figure 2. ESI(−) mass peak of [Ge$_9$Sn]$^-$. The experimental mass distribution is depicted in black, and the theoretical masses of the isotope distribution are shown in red.

In the crystal structure of **2**, six K^+ cations per formula unit, four of which are sequestered by cryptand[2.2.2], assign a sixfold negative charge to the anion. In analogy to **1a**, [(Ge$_9$)Zn(Ge$_9$)]$^{6-}$ (**2a**) is composed of two [Ge$_9$] clusters that coordinate to a Zn atom in η^4 and η^3 modes in the majority component η^4:η^3-**2a** (Figure 1b). Cluster **2A**, which has a slightly distorted C_{4v}-symmetric shape, coordinates through the atoms of the open square (Ge1–Ge4) to Zn with Zn–Ge distances in the range from 2.654(4) to 2.802(1) Å, whereas cluster **2B** has the shape of a slightly distorted tricapped trigonal prism and binds through its triangular face (Ge10–Ge12) to the Zn atom. The small distortion from D_{3h} symmetry is expressed by the different prism heights, which are in the narrow range from 2.968(1) to 3.085(1) Å, but the Zn–Ge distances are rather different (Ge10–Zn 2.685(1), Ge11–Zn 2.874(1), and Ge12–Zn 3.051(1) Å). Moreover, **2A** is superimposed by another nine-atom cluster, **2B**′.[19] This second cluster, similar to **2B**, has slightly distorted D_{3h} symmetry and coordinates to the Zn

atom in a η^3 mode. Owing to this disorder, the two structural isomers η^4:η^3-**2a** and η^3:η^3-**2a** occur with 81.9(2) and 18.1(2)% probability, respectively.

Compound **3** differs in chemical composition from compound **2** by additional NH_3 molecules. In $[(Ge_9)Zn(Ge_9)]^{6-}$ (**3a**) two $[Ge_9]$ clusters are also bridged by a Zn atom, which in this case is located on a crystallographic center of inversion. Therefore, both $[Ge_9]$ clusters coordinate in an η^3:η^3 fashion (Figure 1c) to the Zn atom through their triangular face (Ge1–Ge3) with Zn–Ge distances in the narrow range from 2.720(1) (Ge2–Zn) to 2.756(1) Å (Ge3–Zn). Major component **3B** (92.9%) is best described as a slightly distorted tricapped trigonal prism with prism heights of 2.917(1) (Ge1–Ge8), 3.007(2) (Ge2–Ge9), and 3.152(2) Å (Ge3–Ge7). Cluster **3A** (minor component, 7.1%) adopts the shape of a monocapped square antiprism with distorted C_{4v} symmetry and coordinates through the four atoms of the open square (Ge1–Ge4) to the Zn atom (η^4:η^4-**3a**).

Compounds **1**–**3** contain four- or sixfold negatively charged anions, formally composed of two $[Ge_9]$ clusters bridged by an Sn or Zn atom. The open questions are the charges of the anions and the nature of the bonding between the (ionic) metal atoms and the cluster atoms in these anions. At a first glance one might assume the presence of Sn^{IV} and Zn^{II} ions, each of which coordinate to two $[Ge_9]^{4-}$ clusters, but the presence of Sn in the high oxidation state of +4 in the highly reducing reaction environment is rather unlikely.[22] The structural parameters of the C_{4v}-symmetric clusters **1A** and **2A** are in full agreement with a 22-skeletal-electron (SE) *nido* cluster,[23] but the D_{3h}-symmetric clusters **1B**, **2B**, and **3B** show significantly different average prism heights h_m. Cluster **1B** has the shortest h_m of 2.88 Å, which is closest to the observed value of 2.72 Å for the 20-SE *closo* cluster $[Ge_9]^{2-}$,[24] whereas for **2B** and **3B** significantly larger h_m values of 3.02 and 3.03 Å, respectively, are observed (see also Table S1 in the Supporting Information). Hence, the latter two values indicate 22-SE clusters $[Ge_9]^{4-}$, with two extra electrons occupying the LUMO of the $[Ge_9]^{2-}$cluster, that is, antibonding along the prism heights.[25]

For η^4:η^3-**1a** shorter average Sn–Ge distances to the atoms of the η^4-coordinated cluster, which are typical for covalent bonds,[20] and widening of the open square face of **1A** (see Figure 4 and Tables 1–3) on the same order of magnitude as observed for $[Ge_{10}]^{2-}$,[21] allow the formulation of a ten-atom *closo* cluster $[Ge_9Sn]^{2-}$ with one lone pair at each vertex pointing radially to the outside of the cluster. According to the Wade rules this cluster has 22 SE, and thus η^4:η^3-**1a** can be interpreted as a combination of the fragments *closo*-$[Ge_9Sn]^{2-}$ (**1A**) and *closo*-$[Ge_9]^{2-}$ (**1B**) forming a Lewis base/Lewis acid pair. Coordinative interaction of the lone pair at the Sn atom of *closo*-$[Ge_9Sn]^{2-}$ (donor) with an acceptor orbital of D_{3h}-$[Ge_9]^{2-}$ (**1B**) can be seen in the considerably longer Ge–Sn distances and only slight widening of the coordinated triangular face of **1B**.

The Zn-containing cluster compound η^4:η^3-**2a** can similarly be regarded as being composed of a $[Ge_9Zn]^{2-}$ *closo* cluster having 22 SE, nine lone pairs (18 electrons), and a Zn atom with an acceptor orbital. The last-named interacts with a filled orbital of D_{3h}-$[Ge_9]^{4-}$ (**2B**). For η^4:η^3-**2a** the bonding between the Zn^{II} atom and cluster **2A** can be regarded as analogous to that in *closo*-$[Ge_9Zn(C_6H_5)]^{3-}$[15b] with a covalent interaction between Zn and the open square of the η^4-$[Ge_9]^{4-}$ cluster. Nonetheless, the Ge atoms that are situated at the open square of **2A** (η^4:η^3-**2a**) show shorter interatomic distances (2.68–2.75 Å) than cluster **1A** of η^4:η^3-**1a** (2.81 and 2.86 Å), which indicate less pronounced bond widening on coordination of Zn and thus a higher degree of electrostatic contribution for the adduct η^4:η^3-**2a**. The shortest Zn–Ge bonds [η^4:η^3-**2a**: 2.654(4) Å (Ge3–Zn) and η^3:η^3-**3a**: 2.720(1) Å (Ge3–Zn)] are considerably longer than typical covalent Zn–Ge bonds (r_{Ge} = 1.20, r_{Zn} = 1.22 Å),[20] and this again indicates a stronger electro-

Table 1. Influence on bond lengths of η^4 coordination of an additional atom M. Average bond lengths [Å] for a) bare *nido*-$[Ge_9]^{4-}$[4c] (no further atom), b) $[Ge_{10}]^{2-}$, formally $[(\eta^4\text{-}Ge_9)Ge]^{2-}$,[21] c) $[(\eta^4\text{-}Ge_9)Cu(\eta^1\text{-}Ge_9)]^{7-}$,[26] d) η^4:η^4-**3a**, e) η^4:η^3-**2a**, f) $[(\eta^4\text{-}Ge_9)Zn(C_6H_5)]^{3-}$,[15b] and g) η^4:η^3-**1a**. For bond types, see Figure 3.

	a	b	c	d	e	f	g
M	–	Ge	Cu	Zn (**3a**)	Zn (**2a**)	ZnPh	Sn (**1a**)
I	2.57	2.80	2.73	2.72	2.71	2.78	2.84
II	2.58	2.55	2.56	2.54	2.57	2.55	2.56
III	2.83	2.79	2.82	2.85	2.82	2.83	2.79
IV	2.57	2.58	2.57	2.59	2.58	2.56	2.59
V	–	2.59	2.50	2.88	2.73	2.59	2.67

Table 2. Influence on bond lengths of η^3coordination of an additional atom. Average bond lengths [Å] for a) η^4:η^3-**1a**, b) η^4:η^3-**2a**, c) η^3:η^3-**3a**, d) η^3:η^3-**2a**, e) $_\infty^1\{Zn[trans\text{-}\mu^2(\eta^3\text{:}\eta^3\text{-}Ge_9)]\}^{2-}$,[15g] f) $[(\eta^3\text{-}Ge_9Hyp_3)Zn(\eta^3\text{-}Ge_9Hyp_3)]^0$,[13a] g) $_\infty^1\{Hg[(\eta^3\text{:}\eta^1\text{-}Ge_9)]\}^{2-}$,[15a] and h) $[(\eta^3\text{-}Ge_9)In(\eta^3\text{-}Ge_9)]^{5-}$.[14f] For bond types, see Figure 3.

	a	b	c	d	e	f	g	h
M	Sn (**1a**)	Zn (**2a**)	Zn (**3a**)	Zn (**2a**)	Zn	Zn	Hg	In
I	2.73	2.70	2.73	2.75	2.69	2.89	2.79	2.73
II	2.55	2.55	2.56	2.56	2.57	2.51	2.56	2.54
III	2.88	3.02	3.03	2.98	2.93	3.29	2.88	2.95
IV	2.65	2.64	2.63	2.64	2.71	2.65	2.66	2.63
V	2.97	2.87	2.74	2.61	2.72	2.70	2.93	2.90

Table 3. Influence on bond lengths of η^3 coordination of an additional atom. Average bond lengths [Å] in η^3-coordinated Ge_9 clusters of a) $[K(222\text{-crypt})]_3[(\eta^3\text{-}Ge_9)(SnMe_3)]^-$;[14a] b) $[K(18\text{-crown-}6)]_3[(\eta^3\text{-}Ge_9)(SnMe_3)]\cdot thf\cdot 2\,en$;[14a] c) $[K(222\text{-crypt})]_3[(\eta^3\text{-}Ge_9)(SnPh_3)]\cdot en$;[14a] d) $[K(222\text{-crypt})]_3[(\eta^3\text{-}Ge_9)(SnPh_3)]\cdot 7\,NH_3$;[14g] and e) $[K(18\text{-crown-}6)(NH_3)_2]_2K[(\eta^3\text{-}Ge_9)(SnPh_3)]\cdot 15\,NH_3$.[14g] For bond types, see Figure 3.

	a	b	c	d	e
M	$SnMe_3$	$SnMe_3$	$SnPh_3$	$SnPh_3$	$SnPh_3$
I	2.74	2.71	2.73	2.74	2.76
II	2.57	2.59	2.60	2.57	2.57
III	2.97	2.98	2.93	2.92	2.93
IV	2.68	2.70	2.64	2.65	2.64
V	3.32	3.18	3.07	3.04	3.01

static interaction between Zn^{II} and the $[Ge_9]^{4-}$ clusters for η^4:η^3-**2a** and η^3:η^3-**3a**.

A molecular orbital analysis at the PBE0/def2-TZVPP/PCM level of theory revealed that the bonding between the two fragments of each intermetalloid cluster **1a** and **2a** can be described as a classical HOMO–LUMO interaction, as occurs in Lewis base/Lewis acid pairs. The lone pair at the Sn atom is part of the HOMO of *closo*-$[Ge_9Sn]^{2-}$ (**I** in Figure 3). This p_z orbital points radially to the outside of the cluster and interacts with the LUMO of *closo*-$[Ge_9]^{2-}$ (**III**), which corresponds to bonding interactions of p orbitals within the coordinating triangular face. The bonding combination forms the HOMO (**II**) of η^4:η^3-**1a**. The corresponding antibonding interaction of these two fragment orbitals results in LUMO+2. Vice versa the interaction of two π-type HOMO orbitals of *closo*-$[Ge_9]^{2-}$ (schematic view in Figure 3), which are very close in energy, with the LUMO p_x and p_y orbitals of the Sn atom of *closo*-$[Ge_9Sn]^{2-}$results in the almost degenerate HOMO−1 and HOMO−2 of η^4:η^3-**1a** (isosurfaces are shown in the Supporting Information). The two fragments *closo*-$[Ge_9]^{2-}$ and *closo*-$[Ge_9Sn]^{2-}$ of this intermetalloid cluster correspond to stable molecular anions.

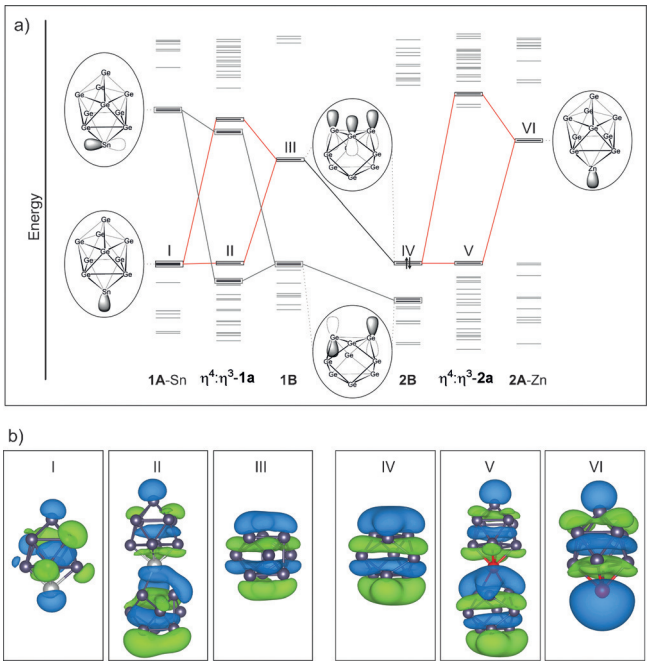

Figure 3. a) MO diagram of the two fragments $[Ge_9Sn]^{2-}$(**1A-Sn**) and $[Ge_9]^{2-}$(**1B**) as well as $[Ge_9Zn]^{2-}$(**2A-Zn**) and $[Ge_9]^{4-}$(**2B**) resulting in η^4:η^3-**1a** and η^4:η^3-**2a**, respectively. Schematic representation of the relevant contributions of the MOs to describe the interactions. The energies of the HOMOs of all species are put on the same energy level. To emphasize the difference between **1B** and **2B**, the additional electrons of the latter are shown. Solid lines correspond either to interactions or identical orbital contributions between **1B** and **2B**. b) Wave functions of the various MOs: HOMO of $[Ge_9Sn]^{2-}$ (**I**), HOMO of η^4:η^3-**1a** (**II**), LUMO of $[Ge_9]^{2-}$ (**III**), HOMO of $[Ge_9]^{4-}$ (**IV**), HOMO of η^4:η^3-**2a** (**V**), and LUMO of $[Ge_9Zn]^{2-}$(**VI**). Ge and Sn/Zn atoms are shown as dark gray and red spheres, respectively. All isovalues are shown at the level of 0.02. Further representations of MOs as well as the diagram without setting all HOMOs to the same energy level are shown in the Supporting Information.

The situation is reversed for the interaction of the fragments of the Zn analogue **2a**. The related fragment $[Ge_9Zn]^{2-}$ has an s orbital at the Zn atom, which is not occupied (**VI**, Figure 3) but is also oriented radially to the outside of the cluster, just like the free electron pair of Sn in **1A-Sn**. Thus, the LUMO of $[Ge_9Zn]^{2-}$ corresponds to the HOMO of $[Ge_9Sn]^{2-}$. Additionally, the LUMO of the D_{3h}-$[Ge_9]^{2-}$ (**1B**) fragment in **1a** with shorter prism heights is analogous to the HOMO of the fragment D_{3h}-$[Ge_9]^{4-}$(**2B**) in **2a**, of which the energy is lowered by elongation of the prism height (**IV**, Figure 3). In the Zn-containing cluster compound η^4:η^3-**2a** the predominant interaction occurs between the LUMO (**VI**) of the ten-atom cluster $[Ge_9Zn]^{2-}$and HOMO **VI** of the nine-atom cluster **2B**. The bonding combination forms the HOMO (**V**) of **2a**. Note that in Figure 3 all levels are shifted so that the HOMOs are equal in energy.

According to our computational analysis, the Zn^{II} and Sn^{II} ions act as an additional vertex that expands the nine-vertex *nido* to a ten-vertex *closo* cluster. Heteroatomic Sn–Zn deltahedral clusters have been observed in intermetallic compounds before.[27] The Sn atoms have a lone pair pointing radially to the outside of the cluster, which allows for interaction with an electron acceptor. In contrast, the corresponding orbital of the Zn atom remains empty. In consequence, the acceptor orbital at the Zn vertex allows coordination to an electron donor. Interestingly, the triangular face of a D_{3h}-*closo*-Ge_9 cluster serves both as an electron donor and as an electron acceptor, depending on its charge. Whereas the corresponding π-type orbital of the triangular face of a D_{3h}-$[Ge_9]^{2-}$ cluster is unfilled, the corresponding orbital in the D_{3h}-$[Ge_9]^{4-}$ cluster with strongly elongated prism heights is filled, and thus the triangular face switches from an electron acceptor to an electron donor (Figure 3).

The concept of cluster expansion to a ten-vertex *closo* cluster is supported by widening of the open square face of the Ge_9 cluster that is η^4-capped, whereas the triangular faces of the η^3-coordinated clusters are less affected, as shown by analysis of a series of structurally characterized clusters that exhibit

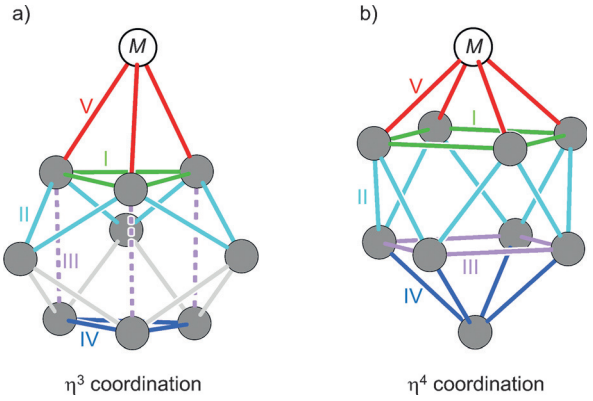

Figure 4. a) η^3- and b) η^4 coordinated Ge_9 clusters. Different classes of bonds are depicted in different colors and denoted by roman numbers. In Tables 1–3 the average bond lengths for each bond class are shown.

comparable coordination modes (Figure 4 and Tables 1–3). Accordingly, related species such as $[(\eta^3\text{-}Ge_9)\text{-}SnR_3]^{3-}$ (R = Me, Ph) can be explained by coordination of the tin atom of the $[SnR_3]^-$ fragment (donor) to the triangular face of a 20-SE *closo*-$[Ge_9]^{2-}$ cluster (acceptor).[14a] The situation is reversed for $[(\eta^3\text{-}Ge_9)In(\eta^3\text{-}Ge_9)]^{5-}$, in which two 22-SE *nido*-$[Ge_9]^{4-}$ clusters (donor) coordinate through a triangular face to an In^{3+} center (acceptor).[14f] A similar situation is also present in $^1_\infty[Zn\{trans\text{-}\mu_2(\eta^3\text{:}\eta^3\text{-}Ge_9)\}]^{2-}$,[15g] which can be described as adduct between Zn^{II} (acceptor) and *nido*-$[Ge_9]^{4-}$ (donor).

Conclusion

Recently, several reactions of Zintl ions of the tetrel elements showed their high synthetic potential. Beside vinylation[28] and silylation reactions,[11] electronic coupling of the clusters by forming Zintl triads[29] became available, and ideas on cluster expansion and cluster growth reactions in solution have been put forward.[7,30] We have provided a systematic view on the addition of a single metal ion and the subsequent coordination to a second cluster forming metal-ion-bridged units, which might be interpreted as a possible initial step for the formation of larger intermetalloid clusters. In a formalistic description both ions, Sn and Zn, add to the nine atom *nido* cluster to become part of a ten-atom deltahedral *closo* cluster and are able to dock to second $[Ge_9]$ cluster, as an electron donor and electron acceptor, respectively.

Experimental Section

Syntheses

All manipulations were performed under a purified argon atmosphere by using a glove box and standard Schlenk techniques. The Zintl compound of nominal composition K_4Ge_9 was synthesized by heating a stoichiometric mixture of the elements K and Ge (99.999% Chempur) at 650 °C for 20 h in a stainless steel tube.[4c] K was purified by liquation. Ethylenediamine (Merck) was heated to reflux with calcium hydride (Merck) and immediately used after collection. Toluene was dried with molecular sieves (4 Å) in a solvent purifier (MBraun MB-SPS). 18-Crown-6 was purified by vacuum sublimation at 80 °C. 2.2.2-Crypt (Merck) was dried under vacuum for 8 h. The Zn complexes $ZnCp^*_2$ and $Zn_2[HC(Ph_2P{=}NPh)_2]_2$ were synthesized according to literature methods.[31] Liquid ammonia was stored over sodium metal and freshly distilled before use. $SnPh_2Cl_2$ (Aldrich, 96%) was used as received.

$[K(18\text{-crown-}6)]_4[Sn(Ge_9)_2](en)_{4.5}$ (1)

In a Schlenk tube K_4Ge_9 (211 mg, 260 μmol) and K (15.6 mg, 400 μmol) were mixed with ethylenediamine (1 mL), and a suspension of $SnPh_2Cl_2$ (34.4 mg, 100 μmol) in ethylenediamine (1 mL) was added dropwise. Thereupon, a deep brown suspension was formed, which was stirred for 16 h at room temperature. Subsequently, the reaction mixture was held for 1 h at 50 °C and filtered through glass wool. The obtained deep brown filtrate was layered with a solution of 18-crown-6 (328 mg, 1.24 mmol) in toluene (8 mL). After 12 weeks deep red, block-shaped single crystals were isolated from the reaction mixture and used for single-crystal structure determination (yield ca. 10%). EDX (%) found (calcd): K 17.3 (17.4), Zn 4.7 (4.3), Ge 78.0 (78.3).

$K_2[K(2.2.2\text{-crypt})]_4[Zn(Ge_9)_2](NH_3)_{21.6}$ (2)

K_4Ge_9 (122 mg, 150 μmol), $Zn_2[HC(Ph_2P{=}NPh)_2]_2$ (95 mg, 75 μmol), and cryptand[2.2.2] (51 mg, 135 μmol) were weighed out in a Schlenk tube inside a glovebox. Sodium-dried ammonia (1 mL) was condensed into the Schlenk tube, and a dark orange suspension formed. The Schlenk tube was stored at −70 °C. After 15 weeks several dark red, blocklike crystals of **2** were isolated for single crystal X-ray diffraction, beside crystals of the known solvates $[K(2.2.2\text{-crypt})]_3[Ge_9]\cdot 8\,NH_3$[14g] and $[K_5(OH)][Ge_9]\cdot 11\,NH_3$[32]. EDX (%) found (calcd): K 14.7 (24.0), Zn 3.9 (4.0), Ge 81.4 (72.0%).

$K_2[K(2.2.2\text{-crypt})]_4[Zn(Ge_9)_2](NH_3)_{24}$ (3)

In a Schlenk tube K_4Ge_9 (122 mg, 150 μmol), $ZnCp^*_2$(25 mg, 75 μmol) and cryptand[2.2.2] (51 mg, 135 μmol) were weighed out and mixed with liquid ammonia (1 mL) to give a dark orange suspension. The Schlenk tube was stored at −70 °C. After 15 weeks dark red, block-shaped crystals were obtained for single-crystal X-ray diffraction. Besides several crystals of compound **3** (ca. yield 5%), crystals of the known solvates $K_4Ge_9(NH_3)_9$[33] and $[K(2.2.2\text{-crypt})]_3[Ge_9](NH_3)_8$[14g] were isolated from the reaction mixture. EDX (%) found (calcd): K 15.8 (24.0), Zn 3.6 (4.0), Ge 80.6 (72.0).

Single-crystal structure determination

Single crystals were fixed on top of a glass fiber with perfluorinated ether and positioned in a cold N_2 stream at 120 K. The single-crystal X-ray diffraction data were recorded with an Oxford Diffraction Xcalibur3 diffractometer ($Mo_{K\alpha}$ radiation). All crystal structures were solved by direct methods by using the SHELX software.[34] The positions of the hydrogen atoms were geometrically calculated and refined with a riding model. All non-hydrogen atoms were treated with anisotropic displacement parameters. In compound **1**, one CH_2 group of a solvent molecule showed partial disorder and was refined with restrained C–N distances. In **2**, some NH_3 molecules were refined at split positions with partial occupations. In **3**, atom Ge11 of the minor isomer had to be refined with restrained anisotropic displacement parameters. Selected crystallographic data of **1**–**3** arelisted in Table 4.

CCDC 1447119 (**1**), 1447118 (**2**), and 1447117 (**3**) contain the supplementary crystallographic data for this paper. These data are provided free of charge by The Cambridge Crystallographic Data Centre.

Electron-dispersive X-ray (EDX) analysis

Several single crystals of all compounds were analyzed with a scanning electron microscope (JEOL 5900LV) equipped with an energy dispersive X-ray analyzer (Oxford Instruments).

ESI mass spectrometry

ESI mass spectrometry was performed with a Bruker Daltonics HCT mass spectrometer in negative-ion mode (spray shield voltage: −3.5 kV, capillary voltage: −4 kV, capillary exit: −166 V, drying gas temperature: 125 °C). For the measurement, the sample of compound **1** was taken before setting this aside for crystallization and introduced by direct infusion with a syringe pump at 240 μL h^{-1}.

Table 4. Selected crystallographic data of **1**, **2**, and **3**.

Compound	**1**	**2**	**3**
formula	$C_{57}H_{132}Ge_{18}K_4N_9O_{24}Sn$	$C_{72}H_{210}Ge_{18}K_6N_{29.59(1)}O_{24}Zn$	$C_{72}H_{216}Ge_{18}K_6N_{32}O_{24}Zn$
formula weight [g mol^{-1}]	2909.43	3487.29	3521.36
space group	$P\bar{1}$ (no. 2)	$P\bar{1}$ (no. 2)	$P\bar{1}$ (no. 2)
a [Å]	15.3303(2)	16.6288(3)	13.6073(3)
b [Å]	18.5270(2)	18.3847(4)	15.8461(3)
c [Å]	19.4237(3)	24.2907(4)	18.5107(4)
α [°]	91.138(1)	91.871(2)	96.355(2)
β [°]	111.854(2)	101.270(2)	102.699(2)
γ [°]	90.240(1)	106.275(2)	111.738(2)
V [Å^3]	5118.9(1)	6960.8(2)	3534.6(1)
Z	2	2	1
T [K]	150(2)	120(2)	120(2)
λ [Å]	0.71073	0.71073	0.71073
ρ_{calcd} [g cm^{-3}]	1.888	1.664	1.654
μ [mm^{-1}]	5.66	4.23	4.17
collected reflections	109924	136157	65475
independent reflections	19036	25883	13145
R_{int}	0.0693	0.0937	0.0462
parameters/restraints	1026/4	1475/30	786/6
R_1 [all data/$I > 2\sigma(I)$]	0.091/0.051	0.109/0.050	0.075/0.051
wR_2 [all data/$I > 2\sigma(I)$]	0.146/0.134	0.110/0.100	0.113/0.108
goodness of fit	0.953	0.838	1.078
max./min. residual electron density [e Å^{-3}]	2.07/−3.69	1.44/−1.29	1.52/−1.08

Computations

All DFT calculations were performed with the Gaussian 09 program package[35] by using the Perdew–Burke–Ernzerhof hybrid functional (PBE0)[36] and def2-TZVPP basis sets for Ge[37] and Sn.[38] For Sn, a pseudopotential (ESP) was estimated.[39] The charge was compensated with a solvation model (polarizable continuum model, PCM).[40] The experimental structure of the anions in compounds **1**, **2**, and **3** and their fragments *closo*-$[Ge_9Sn]^{2-}$ and *closo*-$[Ge_9]^{2-}$ or *closo*-$[Ge_9Zn]^{2-}$ and *nido*-$[Ge_9]^{2-}$, respectively, were investigated by single-point calculations.

Acknowledgements

The authors thank Dr. Christian Benda for assistance during structure refinement and fruitful discussions. L.-A. J. is thankful to the Technische Universität München for the Laura-Bassi Preis. This work was funded within the research network "Solar Technologies go Hybrid" (State of Bavaria) via TUM.solar.

Keywords: germanium · metal–metal interactions · tin · zinc · Zintl anions

[1] J. D. Corbett, *Chem. Rev.* **1985**, *85*, 383 – 397.

[2] a) T. F. Fässler, S. D. Hoffmann, *Angew. Chem. Int. Ed.* **2004**, *43*, 6242 – 6247; *Angew. Chem.* **2004**, *116*, 6400 – 6406; b) S. C. Sevov, J. M. Goicoechea, *Organometallics* **2006**, *25*, 5678 – 5692; c) S. Scharfe, T. F. Fässler, *Phil. Trans. A Math. Phys. Eng. Sci.* **2010**, *368*, 1265 – 1284; d) S. Scharfe, F. Kraus, S. Stegmaier, A. Schier, T. F. Fässler, *Angew. Chem. Int. Ed.* **2011**, *50*, 3630 – 3670; *Angew. Chem.* **2011**, *123*, 3712 – 3754.

[3] a) A. M. Guloy, R. Ramlau, Z. Tang, W. Schnelle, M. Baitinger, Y. Grin, *Nature* **2006**, *443*, 320 – 323; b) G. S. Armatas, M. G. Kanatzidis, *Science* **2006**, *313*, 817 – 820; c) D. Sun, A. E. Riley, A. J. Cadby, E. K. Richman, S. D. Korlann, S. H. Tolbert, *Nature* **2006**, *441*, 1126 – 1130; d) T. F. Fässler, *Angew. Chem. Int. Ed.* **2007**, *46*, 2572 – 2575; *Angew. Chem.* **2007**, *119*, 2624 – 2628; e) A. J. Karttunen, T. F. Fässler, M. Linnolahti, T. A. Pakkanen, *ChemPhysChem* **2010**, *11*, 1944 – 1950; f) M. M. Bentlohner, M. Waibel, P. Zeller, K. Sarkar, P. Müller-Buschbaum, D. Fattakhova-Rohlfing, T. F. Fässler, *Angew. Chem. Int. Ed.* **2016**, *55*, 2441 – 2445; *Angew. Chem.* **2016**, *128*, 2487 – 2491.

[4] a) H. G. Von Schnering, M. Baitinger, U. Bolle, W. Carrillo-Cabrera, J. Curda, Y. Grin, F. Heinemann, J. Llanos, K. Peters, A. Schmeding, M. Somer, *Z. Anorg. Allg. Chem.* **1997**, *623*, 1037 – 1039; b) C. Hoch, M. Wendorff, C. Röhr, *J. Alloys Compd.* **2003**, *361*, 206 – 221; c) S. Ponou, T. F. Fässler, *Z. Anorg. Allg. Chem.* **2007**, *633*, 393 – 397.

[5] a) M. Waibel, C. B. Benda, B. Wahl, T. F. Fässler, *Chem-Eur. J.* **2011**, *17*, 12928 – 12931; b) M. Waibel, T. F. Fässler, *Inorg. Chem.* **2013**, *52*, 5861 – 5866.

[6] S. Stegmaier, T. F. Fässler, *J. Am. Chem. Soc.* **2011**, *133*, 19758 – 19768.

[7] C. B. Benda, M. Waibel, T. F. Fässler, *Angew. Chem. Int. Ed.* **2015**, *54*, 522 – 526; *Angew. Chem.* **2015**, *127*, 532 – 536.

[8] a) C. Downie, Z. J. Tang, A. M. Guloy, *Angew. Chem. Int. Ed.* **2000**, *39*, 337 – 340; *Angew. Chem.* **2000**, *112*, 346 – 348; b) A. Ugrinov, S. C. Sevov, *J. Am. Chem. Soc.* **2002**, *124*, 10990 – 10991; c) A. Ugrinov, S. C. Sevov, *Inorg. Chem.* **2003**, *42*, 5789 – 5791; d) L. Yong, S. D. Hoffmann, T. F. Fässler, *Z. Anorg. Allg. Chem.* **2004**, *630*, 1977 – 1981.

[9] A. Spiekermann, S. D. Hoffmann, T. F. Fässler, I. Krossing, U. Preiss, *Angew. Chem. Int. Ed.* **2007**, *46*, 5310 – 5313; *Angew. Chem.* **2007**, *119*, 5404 – 5407.

[10] a) J.-Q. Wang, S. Stegmaier, T. F. Fässler, *Angew. Chem. Int. Ed.* **2009**, *48*, 1998 – 2002; *Angew. Chem.* **2009**, *121*, 2032 – 2036; b) B. Zhou, M. S. Denning, D. L. Kays, J. M. Goicoechea, *J. Am. Chem. Soc.* **2009**, *131*, 2802 – 2803.

[11] F. Li, S. C. Sevov, *Inorg. Chem.* **2012**, *51*, 2706 – 2708.

[12] a) C. Schenk, A. Schnepf, *Angew. Chem. Int. Ed.* **2007**, *46*, 5314 – 5316; *Angew. Chem.* **2007**, *119*, 5408 – 5410; b) F. Li, S. C. Sevov, *Inorg. Chem.* **2015**, *54*, 8121 – 8125.

[13] a) F. Henke, C. Schenk, A. Schnepf, *Dalton Trans.* **2009**, 9141 – 9145; b) F. Li, A. Munoz-Castro, S. C. Sevov, *Angew. Chem. Int. Ed.* **2012**, *51*, 8581 – 8584; *Angew. Chem.* **2012**, *124*, 8709 – 8712; c) F. Li, S. C. Sevov, *J. Am. Chem. Soc.* **2014**, *136*, 12056 – 12063.

[14] a) A. Ugrinov, S. C. Sevov, *Chem. Eur. J.* **2004**, *10*, 3727 – 3733; b) M. M. Gillett-Kunnath, I. Petrov, S. C. Sevov, *Inorg. Chem.* **2010**, *49*, 721 – 729; c) M. M. Gillett-Kunnath, A. G. Oliver, S. C. Sevov, *J. Am. Chem. Soc.* **2011**, *133*, 6560 – 6562; d) D. Rios, M. M. Gillett-Kunnath, J. D. Taylor, A. G. Oliver, S. C. Sevov, *Inorg. Chem.* **2011**, *50*, 2373 – 2377; e) M. M. Gillett-Kunnath, A. Muñoz-Castro, S. C. Sevov, *Chem. Commun.* **2012**, *48*, 3524 –

3526; f) D. F. Hansen, B. Zhou, J. M. Goicoechea, *J. Organomet. Chem.* **2012**, *721 – 722*, 53 – 61; g) C. B. Benda, Doctoral Thesis, Technische Universität München, Verlag Dr. Hut, **2013**, ISBN 978-3-8439-1443-7.

[15] a) A. Nienhaus, R. Hauptmann, T. F. Fässler, *Angew. Chem. Int. Ed.* **2002**, *41*, 3213 – 3215; *Angew. Chem.* **2002**, *114*, 3352 – 3355; b) J. M. Goicoechea, S. C. Sevov, *Organometallics* **2006**, *25*, 4530 – 4536; c) M. B. Boeddinghaus, S. D. Hoffmann, T. F. Fässler, *Z. Anorg. Allg. Chem.* **2007**, *633*, 2338 – 2341; d) M. S. Denning, J. M. Goicoechea, *Dalton Trans.* **2008**, *43*, 5882 – 5885; e) B. Zhou, M. S. Denning, T. A. D. Chapman, J. E. McGrady, J. M. Goicoechea, *Chem. Commun.* **2009**, *46*, 7221 – 7223; f) L. Yong, M. B. Boeddinghaus, T. F. Fässler, *Z. Anorg. Allg. Chem.* **2010**, *636*, 1293 – 1296; g) C. B. Benda, R. Schäper, S. Schulz, T. F. Fässler, *Eur. J. Inorg. Chem.* **2013**, *2013*, 5964 – 5968.

[16] a) R. C. Haushalter, B. W. Eichhorn, A. L. Rheingold, S. J. Geib, *J. Chem. Soc. Chem. Commun.* **1988**, *15*, 1027 – 1028; b) C. Knapp, B. Zhou, M. S. Denning, N. H. Rees, J. M. Goicoechea, *Dalton Trans.* **2010**, *39*, 426 – 436.

[17] S. C. Critchlow, J. D. Corbett, *Inorg. Chem.* **1982**, *21*, 3286 – 3290.

[18] a) F. Lips, S. Dehnen, *Angew. Chem. Int. Ed.* **2009**, *48*, 6435 – 6438; *Angew. Chem.* **2009**, *121*, 6557 – 6560; b) F. Lips, R. Clérac, S. Dehnen, *J. Am. Chem. Soc.* **2011**, *133*, 14168; c) F. Lips, S. Dehnen, *Angew. Chem. Int. Ed.* **2011**, *50*, 955 – 959; *Angew. Chem.* **2011**, *123*, 986 – 990; d) F. Lips, M. Hołyńska, R. Clérac, U. Linne, I. Schellenberg, R. Pöttgen, F. Weigend, S. Dehnen, *J. Am. Chem. Soc.* **2012**, *134*, 1181.

[19] In the manuscript **A** and **B** are used to denote $[E_9]$ clusters with C_{4v} and D_{3h} symmetry, respectively. For geometrical parameters of all clusters see Table S1 and for details on the minority components of **2** and **3** see Figure S2 in the Supplementary Information.

[20] B. Cordero, V. Gomez, A. E. Platero-Prats, M. Reves, J. Echeverria, E. Cremades, F. Barragan, S. Alvarez, *Dalton Trans.* **2008**, *21*, 2832 – 2838.

[21] M. M. Bentlohner, C. Fischer, T. F. Fässler, *Chem. Commun.* **2016**, *52*, 9841 – 9843.

[22] R. E. Dessy, W. Kitching, T. Chivers, *J. Am. Chem. Soc.* **1966**, *88*, 453 – 459.

[23] K. Wade, *Inorg. Nucl. Chem. Lett.* **1972**, *8*, 559 – 562.

[24] J. Åkerstedt, S. Ponou, L. Kloo, S. Lidin, *Eur. J. Inorg. Chem.* **2011**, *2011*, 3999 – 4005.

[25] T. F. Fässler, *Coord. Chem. Rev.* **2001**, *215*, 347 – 377.

[26] S. Scharfe, T. F. Fässler, *Eur. J. Inorg. Chem.* **2010**, 1207 – 1213.

[27] S.-J. Kim, S. D. Hoffman, T. F. Fässler, *Angew. Chem. Int. Ed.* **2007**, *46*, 3144 – 3148; *Angew. Chem.* **2007**, *119*, 3205 – 3209.

[28] M. W. Hull, S. C. Sevov, *J. Am. Chem. Soc.* **2009**, *131*, 9026 – 9037.

[29] M. M. Bentlohner, W. Klein, Z. H. Fard, L.-A. Jantke, T. F. Fässler, *Angew. Chem. Int. Ed.* **2015**, *54*, 3748 – 3753; *Angew. Chem.* **2015**, *127*, 3819 – 3824.

[30] S. Mitzinger, L. Broeckaert, W. Massa, F. Weigend, S. Dehnen, *Nat. Commun.* **2016**, *7*, 10480.

[31] a) J. B. R. Bloom, P. H. M. Budzelaar, B. Fischer, A. Haaland, H. V. Volden, J. Weidlein, *Acta Chem. Scand. Ser. A* **1986**, *40*, 113 – 120; b) S. Schulz, S. Gondzik, D. Schuchmann, U. Westphal, L. Dobrzycki, R. Boese, S. Harder, *Chem. Commun.* **2010**, *46*, 7757 – 7759.

[32] C. B. Benda, H. He, W. Klein, M. Somer, T. F. Fässler, *Z. Anorg. Allg. Chem.* **2015**, *641*, 1080 – 1086.

[33] C. Suchentrunk, J. Daniels, M. Somer, W. Carrillo-Cabrera, N. Korber, *Z. Naturforsch. B* **2005**, *60*, 277 – 283.

[34] G. M. Sheldrick, *Acta Crystallogr. Sect. A* **2008**, *64*, 112 – 122.

[35] Gaussian 09, Revision B.01, M. J. Frisch, G. W. Trucks, H. B. Schlegel, G. E. Scuseria, M. A. Robb, J. R. Cheeseman, G. Scalmani, V. Barone, B. Mennucci, G. A. Petersson, H. Nakatsuji, M. Caricato, X. Li, H. P. Hratchian, A. F. Izmaylov, J. Bloino, G. Zheng, J. L. Sonnenberg, M. Hada, M. Ehara, K. Toyota, R. Fukuda, J. Hasegawa, M. Ishida, T. Nakajima, Y. Honda, O. Kitao, H. Nakai, T. Vreven, J. A. Montgomery, Jr., J. E. Peralta, F. Ogliaro, M. Bearpark, J. J. Heyd, E. Brothers, K. N. Kudin, V. N. Staroverov, R. Kobayashi, J. Normand, K. Raghavachari, A. Rendell, J. C. Burant, S. S. Iyengar, J. Tomasi, M. Cossi, N. Rega, N. J. Millam, M. Klene, J. E. Knox, J. B. Cross, V. Bakken, C. Adamo, J. Jaramillo, R. Gomperts, R. E. Stratmann, O. Yazyev, A. J. Austin, R. Cammi, C. Pomelli, J. W. Ochterski, R. L. Martin, K. Morokuma, V. G. Zakrzewski, G. A. Voth, P. Salvador, J. J. Dannenberg, S. Dapprich, A. D. Daniels, O. Farkas, J. B. Foresman, J. V. Ortiz, J. Cioslowski, D. J. Fox, Gaussian 09, revision A.02; Gaussian, Inc.: Wallingford, CT, **2009**; Gaussian, Inc., Wallingford CT, **2010**.

[36] a) J. P. Perdew, K. Burke, M. Ernzerhof, *Phys. Rev. Lett.* **1996**, *77*, 3865 – 3868; b) C. Adamo, V. Barone, *J. Chem. Phys.* **1999**, *110*, 6158 – 6170.

[37] F. Weigend, M. Häser, H. Patzelt, R. Ahlrichs, *Chem. Phys. Lett.* **1998**, *294*, 143 – 152.

[38] F. Weigend, R. Ahlrichs, *Phys. Chem. Chem. Phys.* **2005**, *7*, 3297 – 3305.

[39] S. Miertus, E. Scorcco, J. Tomasi, *Chem. Phys.* **1981**, *55*, 117 – 129.

[40] V. Barone, M. Cossi, *J. Phys. Chem. A* **1998**, *102*, 1995 – 2001.

Received: April 12, 2016
Published online on August 18, 2016

CHEMISTRY
A European Journal

Supporting Information

On the Nature of Bridging Metal Atoms in Intermetalloid Clusters: Synthesis and Structure of the Metal-Atom-Bridged Zintl Clusters $[Sn(Ge_9)_2]^{4-}$ and $[Zn(Ge_9)_2)]^{6-}$

Manuel M. Bentlohner, Laura-Alice Jantke, Thomas Henneberger, Christina Fischer, Kerstin Mayer, Wilhelm Klein, and Thomas F. Fässler*[a]

chem_201601706_sm_miscellaneous_information.pdf

Supporting Information

Contents

Figures and Tables

1. Overview on synthetic details

a)

Step 1:

$SnPh_2Cl_2 \xrightarrow[RT]{en}$ "Mixture A"

$K_4Ge_9/K \xrightarrow[RT]{en}$ "Mixture B"

Step 2:

"Mixture A" + "Mixture B" $\xrightarrow{\text{i) } en\text{/16 h/RT; ii) en/1h/50°C; iii) tol/18-crown-6}$ $[K(18\text{-crown-6})]_4[Sn(Ge_9)_2](en)_{4.5}$

1

b)

Step 1:

$SnPh_3Cl/K \xrightarrow[RT,\ -KCl]{en}$ "Mixture A"

Step 2:

"Mixture A" $\xrightarrow{\text{i) } K_4Ge_9\text{/cryptand[2.2.2]; ii) } en\text{/1 h/50°C; iii) tol}}$ $[K(222\text{-crypt})]_3[(Ge_9)\text{-}SnPh_3](en)$

c)

$K_4Ge_9/Zn_2[HC(Ph_2P{=}NPH)_2]_2$ /cryptand[2.2.2] $\xrightarrow[-70°C/15\ weeks]{NH_3\ (liq)}$ $K_2[K(2.2.2\text{-crypt})]_4[Zn(Ge_9)_2](NH_3)_{21.6}$

2

d)

$K_4Ge_9/ZnCp^*_2$ /cryptand[2.2.2] $\xrightarrow[-70°C/15\ weeks]{NH_3\ (liq)}$ $K_2[K(2.2.2\text{-crypt})]_4[Zn(Ge_9)_2](NH_3)_{24}$

3

Scheme 1. Overview on synthetic details. Syntheses of a) $[K(18\text{-crown-6})]_4[(Ge_9)Sn(Ge_9)](en)_{4.5}$ (**1**) b) $[K(2.2.2\text{-crypt})]_3[(Ge_9)(SnPh_3)]\cdot en$, [14a] c) $K_2[K(2.2.2\text{-crypt})]_4[(Ge_9)Zn(Ge_9)]\ (NH_3)_{21.6}$ (**2**) and d) $K_2[K(2.2.2\text{-crypt})]_4[(Ge_9)Zn(Ge_9)]\ (NH_3)_{24}$ (**3**). Stochiometric ratios: a) 1 eq. K_4Ge_9, 1.5 eq. K, 0.4 eq. $SnPh_2Cl_2$, 4.8 eq. 18-crown-6; b) 1 eq. K_4Ge_9, 0.8 eq. K, 0.4 eq. $SnPh_3Cl$, 4.8 eq. 2.2.2-crypt; c) 1 eq. K_4Ge_9, 0.5 eq. $Zn_2[HC(Ph_2P{=}NPH)_2]_2$, 0.9 eq. 2.2.2-crypt; d) 1 eq. K_4Ge_9, 0.5 eq. $ZnCp^*_2$, 0.9 eq. 2.2.2-crypt.

2. Additional crystallographic data and description of minority components

Structural details of $K_2[K(2.2.2\text{-crypt})]_4[Zn(Ge_9)_2](NH_3)_{21.6}$ (2) and $K_2[K(2.2.2\text{-crypt})]_4[Zn(Ge_9)_2](NH_3)_{24}$ (3)

For compound **2** the anion $[(Ge_9)Zn(Ge_9)]^{6-}$ (**2a**) was found in two different bonding modes: $[Zn(\eta^4\text{-}Ge_9)(\eta^3\text{-}Ge_9)]^{6-}$ (82%) (η^4:η^3-**2a**) and $[Zn(\eta^3\text{-}Ge_9)(\eta^3\text{-}Ge_9)]^{6-}$ (18%) (η^3:η^3-**2a**). Both clusters **2B** and **2B'** are close to D_{3h} symmetry, as the prism heights of 2.968(1)–3.085(1) Å (**2B**) and 2.927(9)–3.05(2) Å (**2B'**) are quite similar, as well as the minimal ratios of face diagonals differ significantly from one [d_1/d_2 = 1.31 (**2B**), 1.34 (**2B'**)], respectively. In η^4:η^3-**2a** the mean Zn–Ge distance to cluster **2A** is 2.73 Å, and slightly longer compared to the Zn–Ge distance to cluster **2B'** ($d_{m\ \text{Zn-Ge}}$ = 2.61 Å) in η^3:η^3-**2a**, respectively. The η^3-coordinated clusters **2B** and **2B'** have one elongated Zn–Ge bond with Zn-Ge12 = 3.051(1) Å and Zn-Ge21 = 2.81(2) Å, respectively.

For the anion $[(Ge_9)Zn(Ge_9)]^{6-}$ (**3a**) in compound **3**, zinc is located on a crystallographic center of inversion. Besides, the main η^3-coordination (93%) a superposition with η^4-coordination (7%) is observed. We assume at least a partial mixed η^3:η^4 coordination beside possibly a minor contribution of a η^4:η^4 species. Cluster **3A** coordinates with its open square face Ge10/Ge11/Ge12/Ge13 to the Zn atom, showing a dihedral angle for the open square face of 172° and a ratio of face diagonals of 1.10. Although the dihedral angle and the ratio of face diagonals slightly differs from the ideal values 180° and 1, respectively, cluster **3A** can be best described as a C_{4v}-symmetric monocapped square antiprism. The mean Zn–Ge distance to the η^4-coordinated cluster **3A** is 2.88 Å, and thus longer compared to 2.74 Å for the η^3-coordinated cluster **3B**.

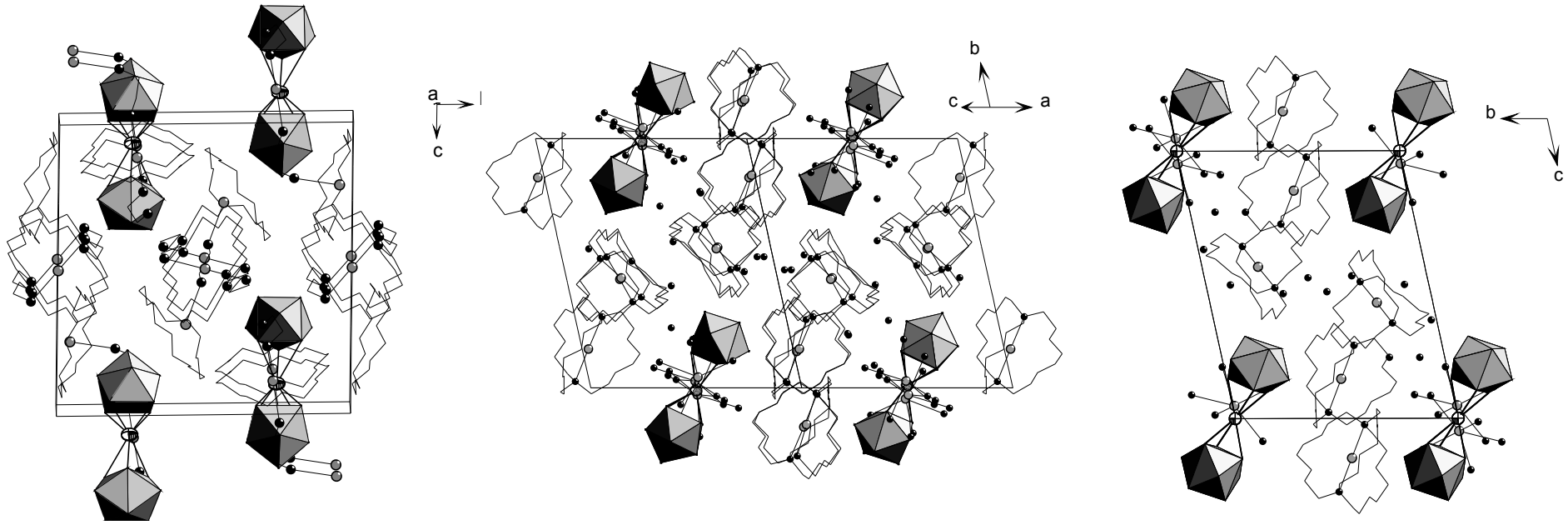

Figure S1. Unit cells of $[K(18\text{-crown-6})]_4[Sn(Ge_9)_2](en)_{4.5}$ (**1**), $K_2[K(2.2.2\text{-crypt})]_4[Zn(Ge_9)_2](NH_3)_{21.6}$ (**2**) and $K_2[K(2.2.2\text{-crypt})]_4[Zn(Ge_9)_2)](NH_3)_{24}$ (**3**). For compounds **2** and **3** only the structural isomers of $[Zn(Ge_9)_2)]^{6-}$ with the highest occupation are shown. The sequestering agents cryptand[2.2.2] and 18-crown-6 are shown schematically.

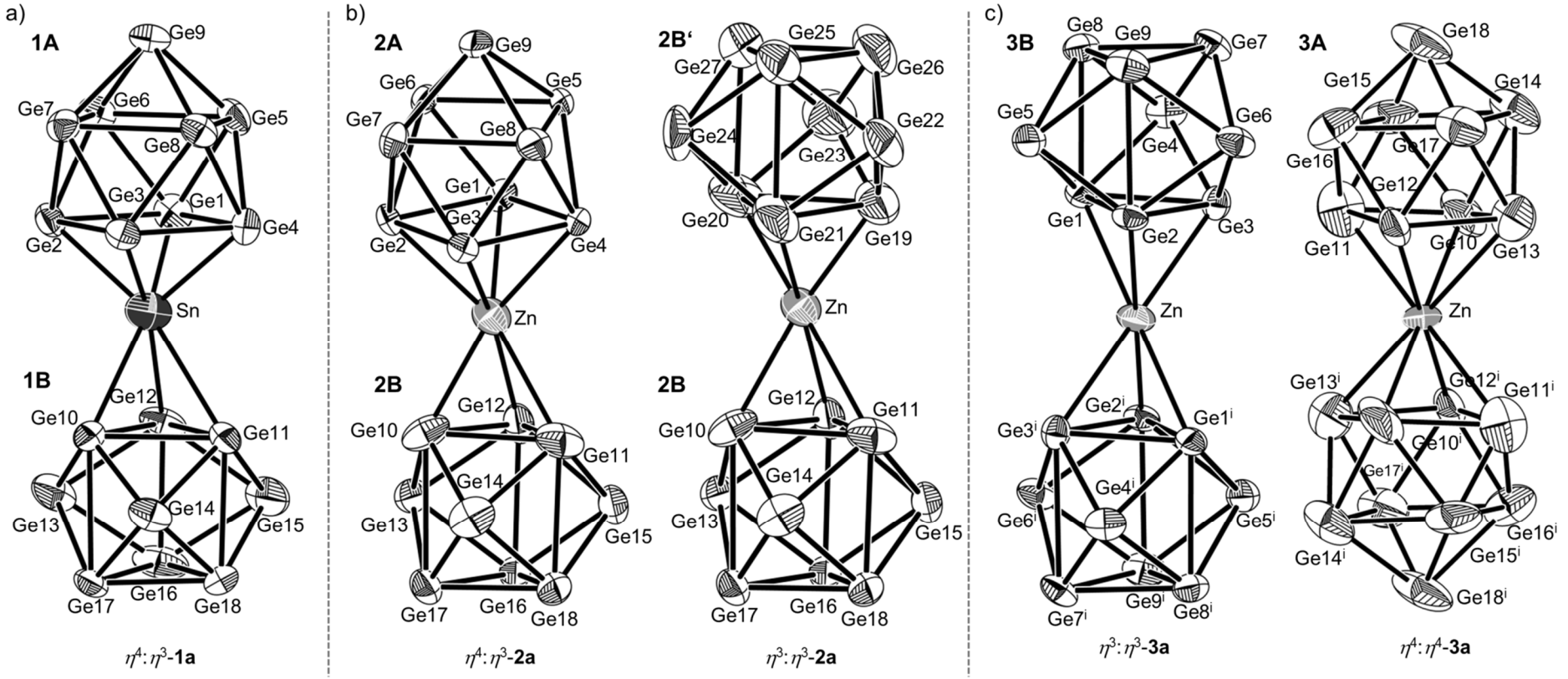

Figure S2. Anionic entities of [K(18-crown-6)][Sn(Ge_9)$_2$](en)$_{4.5}$ (**1**), K_2[K(2.2.2-crypt)]$_4$[Zn(Ge_9)$_2$](NH_3)$_{21.6}$ (**2**) and K_2[K(2.2.2-crypt)]$_4$[Zn(Ge_9)$_2$](NH_3)$_{24}$ (**3**). a) [Sn(η^4-Ge_9)(η^3-Ge_9)]$^{4-}$ (η^4:η^3-**1a**), b) [Zn(η^4-Ge_9)(η^3-Ge_9)]$^{6-}$ (η^4:η^3-**2a**) (82%), [Zn(η^3-Ge_9)(η^3-Ge_9)]$^{6-}$ (η^3:η^3-**2a**) (18%), c) [Zn(η^3-Ge_9)(η^3-Ge_9)]$^{6-}$ (η^3:η^3-**3a**) (93%), [Zn(η^4-Ge_9)(η^4-Ge_9)]$^{6-}$ (η^4:η^4-**3a**) (7%). C_{4v}- and D_{3h}-symmetric clusters are labeled with **A** and **B**, respectively. The atoms are shown as ellipsoids at a probability level of 70%, symmetry operation (i): -*x*, -*y*, -*z*.

The two unsequestered K atoms in the crystal structure of $K_2[K(2.2.2\text{-crypt})]_4[Zn(Ge_9)_2](NH_3)_{21.6}$ (**2**) are coordinated by NH_3 with K-N distances in the expected range from 2.594(1) Å (K6-N18) to 3.433(1) Å (K5-N13) (Figure S1). While K5 has five neighboring NH_3 molecules (N9-N13), K6 is coordinated to three fully occupied (N14-N16), one split (N17a and N17b) and one partially occupied NH_3 molecule (N18). Twelve more ammonia molecules do not coordinate a cation. The K–Ge distances are in the range of 3.432(1) Å (K6-Ge11) and 3.804(1) Å (K5-Ge1).

Similar to compound **2**, in $K_2[K(2.2.2\text{-crypt})]_4[Zn(Ge_9)_2](NH_3)_{24}$ (**3**) five NH_3 molecules coordinate to the unsequestered K atoms with typical bond lengths between 2.755(1) Å (K3-N5) and 3.149(1) Å (K3-N9) (Figure S1). Due to an inversion center at the Zn atom, the NH_3 surroundings of the K atoms are identical. The remaining 14 NH_3 molecules fill empty voids in the crystal structure. The K–Ge distances are in the range of 3.519(1) Å (K3-Ge3) and 3.749(1) Å (K3-Ge2)

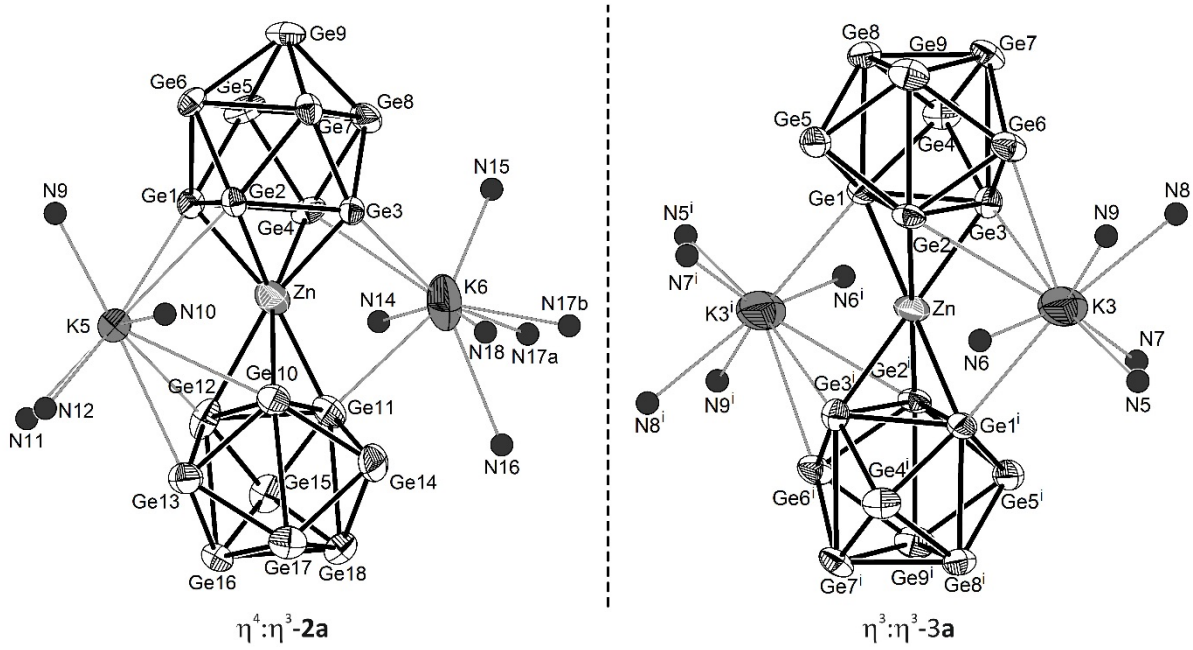

Figure S3. Coordinating NH_3 molecules in $K_2[K(2.2.2\text{-crypt})]_4[Zn(Ge_9)_2](NH_3)_{21.6}$ (**2**) and $K_2[K(2.2.2\text{-crypt})]_4[Zn(Ge_9)_2](NH_3)_{24}$ (**3**). Only the structural isomers of $[Zn(Ge_9)_2]^{6-}$ with the highest occupation (η^4:η^3-**2a** and η^3:η^3-**3a**) are shown. The atoms (except nitrogen) are shown as ellipsoids at a probability level of 70%, symmetry operation (i): *-x*, *-y*, *-z*.

Table S1: Geometrical parameters of all clusters in **1a**, **2a** and **3a**.

Cluster	Symmetry	h^*_1	h^*_2	h^*_3 [a]	h_m [Å]	h_m/e_m [b]	α_{min} [°][c]	d_1/d_2[d]	$d_{M\text{-}Ge}$ [Å][e]
	$[K(18\text{-crown-}6)]_6[Sn(Ge_9)_2](en)_{4.5}$ (**1**)								
1A	C_{4v}	1.47	1.02	1.03	3.19	1.21	179.7	1.00	2.67
1B	D_{3h}	1.03	1.09	1.05	2.88	1.07	165.3	1.41	2.97
	$K_2[K(2.2.2\text{-crypt})]_4[Zn(Ge_9)_2](NH_3)_{21.6}$ (**2**)								
2A	C_{4v}	1.40	1.06	1.03	3.16	1.19	179.0	1.01	2.73
2B	D_{3h}	1.10	1.13	1.09	3.02	1.13	161.4	1.31	2.87
2B'	D_{3h}	1.12	1.09	1.08	2.98	1.10	161.1	1.34	2.62
	$K_2[K(2.2.2\text{-crypt})]_4[Zn(Ge_9)_2)](NH_3)_{24}$ (**3**)								
3A	C_{4v}	1.33	1.04	1.02	3.07	1.13	171.5	1.11	2.89
3B	D_{3h}	1.16	1.07	1.11	3.03	1.13	164.0	1.28	2.74

a) h^* is defined as prism height normalized to the prism height 2.72 Å in the ideal *closo*-$[Ge_9]^{2-}$ in $[K[2.2.2\text{-crypt}]_2Ge_9$ [1]

b) ratio of mean prism height and mean length of basal edges

c) α_{min} is defined as the dihedral angle closest to 180° in the cluster.

d) d_1 and d_2 are the diagonals in square face that includes α_{min}.

e) mean M-Ge distance

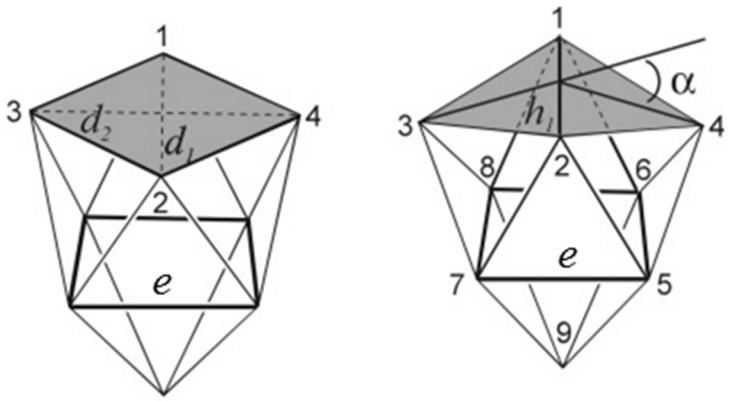

A **B**

C_{4v} symmetry D_{3h} symmetry

Table S2: Selected bond lengths (Å) in **1a**.

Cluster **1A**		Cluster **1B**	
Ge1-Ge2	2.860(1)	Ge10-Ge11	2.711(1)
Ge2-Ge3	2.807(1)	Ge11-Ge12	2.751(1)
Ge3-Ge4	2.834(1)	Ge12-Ge10	2.727(1)
Ge4-Ge1	2.846(1)	Ge10-Ge13	2.518(1)
Ge1-Ge3	4.008(1)	Ge10-Ge14	2.515(1)
Ge2-Ge4	4.016(1)	Ge11-Ge14	2.552(1)
Ge1-Ge5	2.556(1)	Ge11-Ge15	2.540(1)
Ge1-Ge6	2.562(1)	Ge12-Ge15	2.572(2)
Ge2-Ge6	2.542(1)	Ge12-Ge13	2.586(1)
Ge2-Ge7	2.558(1)	Ge13-Ge16	2.582(2)
Ge3-Ge7	2.564(1)	Ge13-Ge17	2.633(1)
Ge3-Ge8	2.571(1)	Ge14-Ge17	2.628(1)
Ge4-Ge8	2.562(1)	Ge14-Ge18	2.588(1)
Ge4-Ge5	2.555(1)	Ge15-Ge18	2.588(1)
Ge5-Ge6	2.820(1)	Ge15-Ge16	2.589(2)
Ge6-Ge7	2.788(1)	Ge16-Ge17	2.640(1)
Ge7-Ge8	2.781(1)	Ge17-Ge18	2.598(1)
Ge8-Ge5	2.788(1)	Ge18-Ge16	2.697(1)
Ge5-Ge9	2.556(1)	Ge10-Ge17	2.960(1)
Ge6-Ge9	2.580(1)	Ge11-Ge18	2.861(1)
Ge7-Ge9	2.605(1)	Ge12-Ge16	2.806(1)
Ge8-Ge9	2.599(1)		
Ge1-Sn	2.630(1)	Ge10-Sn	2.770(1)
Ge2-Sn	2.679(1)	Ge11-Sn	2.975(1)
Ge3-Sn	2.709(1)	Ge12-Sn	3.151(1)
Ge4-Sn	2.675(1)		

Table S3: Selected bond lengths (Å) in **2a**.

Cluster **2A**		Cluster **2B**		Cluster **2B'**	
Ge1-Ge2	2.684(1)	Ge10-Ge11	2.735(1)	Ge19-Ge20	2.80(2)
Ge2-Ge3	2.694(4)	Ge11-Ge12	2.677(1)	Ge20-Ge21	2.71(2)
Ge3-Ge4	2.746(5)	Ge12-Ge10	2.693(1)	Ge21-Ge19	2.73(3)
Ge4-Ge1	2.705(2)	Ge10-Ge13	2.522(1)	Ge19-Ge22	2.52(1)
Ge1-Ge3	3.813(3)	Ge10-Ge14	2.548(1)	Ge19-Ge23	2.54(1)
Ge2-Ge4	3.843(3)	Ge11-Ge14	2.565(1)	Ge20-Ge23	2.57(1)
Ge1-Ge5	2.583(1)	Ge11-Ge15	2.550(1)	Ge20-Ge24	2.58(1)
Ge1-Ge6	2.582(1)	Ge12-Ge15	2.552(1)	Ge21-Ge24	2.57(3)
Ge2-Ge6	2.583(1)	Ge12-Ge13	2.584(1)	Ge21-Ge22	2.56(2)
Ge2-Ge7	2.554(2)	Ge13-Ge16	2.572(1)	Ge22-Ge25	2.54(1)
Ge3-Ge7	2.568(4)	Ge13-Ge17	2.607(1)	Ge22-Ge26	2.54(1)
Ge3-Ge8	2.546(4)	Ge14-Ge17	2.587(1)	Ge23-Ge26	2.572(9)
Ge4-Ge8	2.554(3)	Ge14-Ge18	2.590(1)	Ge23-Ge27	2.607(9)
Ge5-Ge4	2.570(2)	Ge15-Ge18	2.593(1)	Ge24-Ge27	2.57(1)
Ge5-Ge6	2.781(1)	Ge15-Ge16	2.559(1)	Ge24-Ge25	2.560(9)
Ge6-Ge7	2.789(2)	Ge16-Ge17	2.650(1)	Ge25-Ge26	2.649(9)
Ge7-Ge8	2.854(2)	Ge17-Ge18	2.618(1)	Ge26-Ge27	2.649(9)
Ge8-Ge5	2.871(2)	Ge18-Ge16	2.660(1)	Ge27-Ge25	2.628(9)
Ge5-Ge9	2.590(1)	Ge10-Ge17	3.085(1)	Ge19-Ge26	2.97(2)
Ge6-Ge9	2.583(1)	Ge11-Ge18	2.968(1)	Ge20-Ge27	2.928(9)
Ge7-Ge9	2.568(2)	Ge12-Ge16	3.001(1)	Ge21-Ge25	3.04(2)
Ge8-Ge9	2.564(2)				
Ge1-Zn	2.779(1)	Ge10-Zn	2.685(1)	Ge19-Zn	2.51(1)
Ge2-Zn	2.801(1)	Ge11-Zn	2.874(1)	Ge20-Zn	2.519(7)
Ge3-Zn	2.654(4)	Ge12-Zn	3.051(1)	Ge21-Zn	2.81(2)
Ge4-Zn	2.673(3)				

Table S4: Selected bond lengths (Å) in **3a**.

Cluster **3B**		Cluster **3A**	
Ge1-Ge2	2.779(2)	Ge10-Ge11	2.64(5)
Ge2-Ge3	2.706(2)	Ge11-Ge12	2.93(3)
Ge3-Ge1	2.694(2)	Ge12-Ge13	2.64(2)
Ge1-Ge4	2.558(1)	Ge13-Ge10	2.69(4)
Ge1-Ge5	2.556(1)	Ge10-Ge12	3.62(4)
Ge2-Ge5	2.543(2)	Ge11-Ge13	4.06(3)
Ge2-Ge6	2.550(2)	Ge10-Ge14	2.67(3)
Ge3-Ge6	2.584(2)	Ge10-Ge15	2.54(4)
Ge3-Ge4	2.546(2)	Ge11-Ge15	2.31(4)
Ge4-Ge7	2.600(1)	Ge11-Ge16	2.51(4)
Ge4-Ge8	2.608(1)	Ge12-Ge16	2.56(2)
Ge5-Ge8	2.598(1)	Ge12-Ge17	2.56(2)
Ge5-Ge9	2.581(1)	Ge13-Ge17	2.53(2)
Ge6-Ge9	2.599(1)	Ge13-Ge14	2.59(2)
Ge6-Ge7	2.581(1)	Ge14-Ge15	2.88(3)
Ge7-Ge9	2.610(1)	Ge15-Ge16	2.81(3)
Ge7-Ge8	2.626(1)	Ge16-Ge17	2.91(3)
Ge8-Ge9	2.641(1)	Ge14-Ge17	2.77(2)
Ge1-Ge8	2.917(1)	Ge14-Ge18	2.53(2)
Ge2-Ge9	3.007(2)	Ge15-Ge18	2.60(3)
Ge3-Ge7	3.152(2)	Ge16-Ge18	2.62(2)
		Ge17-Ge18	2.59(3)
Ge1-Zn	2.7489(7)	Ge10-Zn	2.62(4)
Ge2-Zn	2.720(1)	Ge11-Zn	2.89(3)
Ge3-Zn	2.756(1)	Ge12-Zn	2.91(1)
		Ge13-Zn	3.11(1)

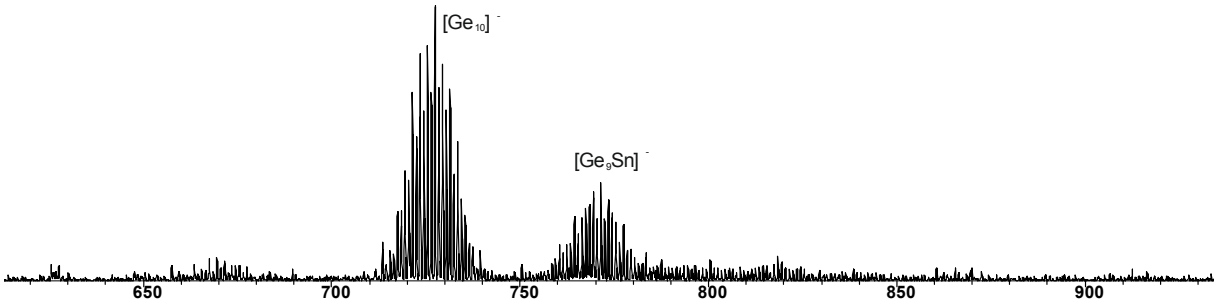

Figure S4. ESI(-) spectrum in the range from m/z = 600 to 950 of the reaction mixture. Beside the mass peak of $[Ge_9Sn]^-$ the most frequent peak is $[Ge_{10}]^-$ (m/z = 725). The isolation of crystals containing the well ordered $[Ge_{10}]^-$ anion will be presented in a forthcoming paper.

3. Computational details

The HOMO-LUMO gap of **1a** is with 2.90 eV between the gaps of the *closo*-$[Ge_9Sn]^{2-}$ cluster with 3.38 eV and the *closo*-$[Ge_9]^{2-}$ cluster (**1B**) with a HOMO-LUMO gap of 2.29 eV. A Hirshfeld partitioning of the charge density indicates that the character of this species is best described by two coordinating *closo*-clusters. The total charges of *closo*-$[Ge_9Sn]^{2-}$ and **1B** sum up to −1.98 electrons and the $[Ge_9Sn]^{2-}$ closo-cluster has an allover charge of −2.03.

The MO-interaction diagram as well as the isosurfaces of the HOMO are shown in the manuscript (Figure 3), in Figure S3 the molecular orbitals of the fragments and the corresponding LUMO (MO no. 302) and LUMO+1 (MO no. 303) are shown.

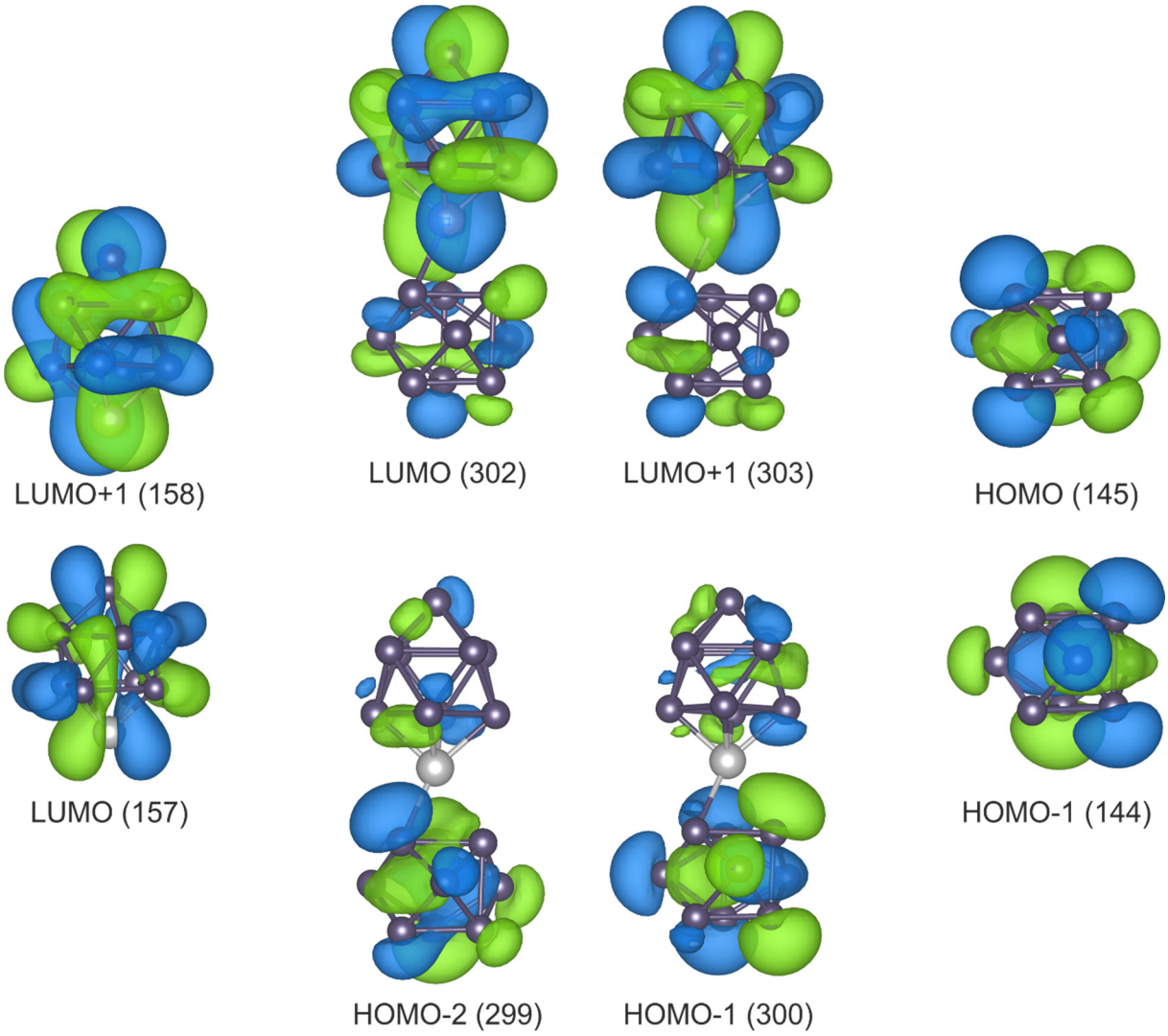

Figure S5. The wave functions for the interaction between the LUMO of closo-$[Ge_9Sn]^{2-}$ (left) and the HOMO of *closo*-$[Ge_9]^{2-}$ (right) resulting in η^4: η^3-**1a** (middle) are shown. The LUMO and LUMO+1 of the ten atomic cluster show a contribution of p_x and p_y of the heteroatom that interacts with the almost degenerated HOMO and HOMO-1 of the *closo*-$[Ge_9]^{2-}$. Schematically, these orbitals are shown in Figure 3 in the main text. The wave functions are shown with iso-values of 0.02.

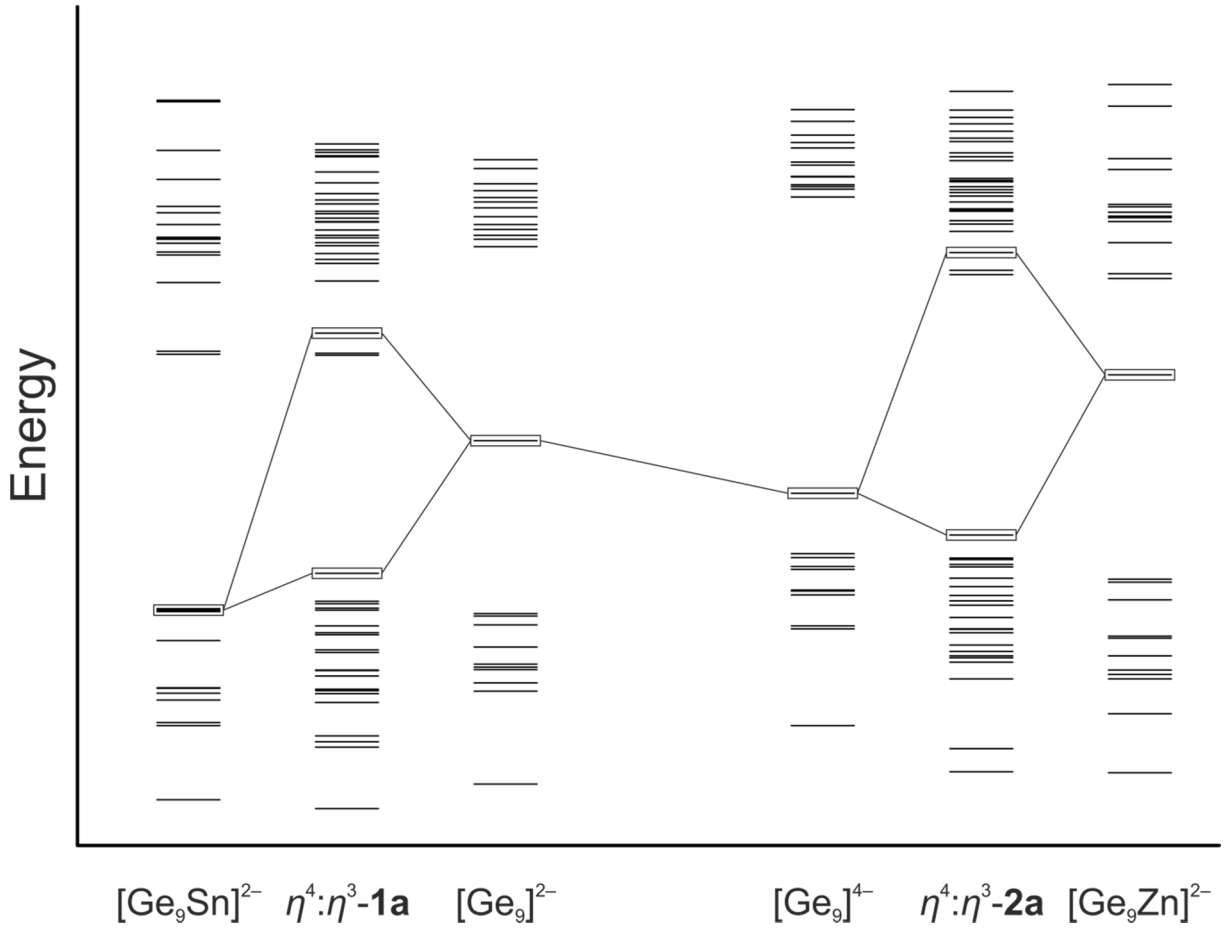

Figure S6. Energy level diagram for two fragments $[Ge_9Sn]^{2-}$ and $[Ge_9]^{2-}$ as well as $[Ge_9Zn]^{2-}$ and $[Ge_9]^{4-}$ resulting in η^4: η^3-**1a** and η^4: η^3-**2a**. The interactions resulting in HOMOs are highlighted. For comparison, in Figure 3 the energy level are shifted and the HOMOs are set to zero energy for clarity

HOMO-LUMO gaps: η^4: η^3-**2a**: 3.46 eV; η^3: η^3-**3a**: 2.82 eV; η^3: η^3-**2a**: 2.81 eV; η^4: η^4-**3a**: 3.25 eV

Table S5: Population analysis of the single-point calculation of the experimental structure of **1a** with the two methods Hirshfeld analysis and natural population analysis.[2,3] For evaluation of the type of interaction between the fragments, also the two *closo*-clusters are calculated on their own.

Position	Hirshfeld			NPA		
	1a	*closo*-$[Ge_9Sn]^{2-}$	*closo*-$[Ge_9]^{2-}$ **1B**	**1a**	*closo*-$[Ge_9Sn]^{2-}$	*closo*-$[Ge_9]^{2-}$ **1B**
Sn	0.17	0.11		-1.82	-0.6092	
Ge1	-0.30	-0.28		0.06	-0.0681	
Ge2	-0.26	-0.28		0.10	-0.0990	
Ge3	-0.27	-0.27		0.07	-0.1106	
Ge4	-0.29	-0.28		0.04	-0.0921	
Ge5	-0.20	-0.18		-0.19	-0.1741	
Ge6	-0.21	-0.18		-0.20	-0.1688	
Ge7	-0.20	-0.18		-0.18	-0.1722	
Ge8	-0.18	-0.18		-0.14	-0.1744	
Ge9	-0.28	-0.27		-0.32	-0.3316	
Ge10	-0.19		-0.21	-0.10		-0.20
Ge11	-0.21		-0.19	0.03		-0.17
Ge12	-0.20		-0.20	-0.06		-0.18
Ge13	-0.19		-0.20	-0.16		-0.20
Ge14	-0.21		-0.20	-0.18		-0.17
Ge15	-0.19		-0.20	-0.15		-0.19
Ge16	-0.26		-0.27	-0.26		-0.29
Ge17	-0.27		-0.27	-0.26		-0.29
Ge18	-0.27		-0.27	-0.28		-0.31

4. References

[2] Hirshfeld, F. L.; *Theor. Chim. Acta* **1977**, *44*, 129-138.

[3] Reed, A. E.; R. B. Weinstock, R. B.; Weinhold, F.; *J. Chem. Phys.***1985**, *83,* 735-746.

5.5 Zintl Clusters as Wet-Chemical Precursors for Germanium Nanomorphologies with Tunable Composition

M. M. Bentlohner, M. Waibel, P. Zeller, K. Sarkar, P. Müller-Buschbaum, D. Fattakhova-Rohlfing, T. F. Fässler

published in:

Angew. Chem. Int. Ed. **2016***, 55, 2441-2445; Angew. Chem.* **2016***, 128, 2487-2491.*

Contents and Contributions

In the scope of the publication “Zintl Clusters as Wet-Chemical Precursors for Germanium Nanomorphologies with Tunable Composition“, $[Ge_9]^{4-}$ Zintl clusters are used as soluble Ge source for a bottom-up fabrication of Ge nanomorphologies such as inverse opal structures with tunable composition. The method grounds on the transfer and oxidation of $[Ge_9]^{4-}$ Zintl anions to a solid germanium phase in a template mold.

The publication was authored in the course of this thesis. Fundamental *ex situ* investigations on the oxidation of $[Ge_9]^{4-}$ Zintl anions to a solid germanium phase with tunable composition were conducted. Raman spectroscopy and powder X-ray diffractometry indicate that $[Ge_9]^{4-}$ clusters are retained using *en* as a transfer medium to a mold after removal of the solvent if water is thoroughly excluded, but are oxidized to *a*-Ge in presence of water traces. ^{1}H NMR spectroscopy reveals the oxidative deprotonation of *en* by $[Ge_9]^{4-}$. The *a*-Ge phase can be transferred to a crystalline form by annealing for one hour at 600°C. Moreover, reaction of $GeCl_4$, $SiCl_4$ and PCl_3 with K_4Ge_9 leads to $Ge_{1-x}E_x$ phases and potassium chloride as follows from Raman and powder X-ray diffractometry. In the scope of the present work these *ex situ* experiments were conducted and the obtained data were evaluated. As an example for wet chemical synthesis of complex germanium nanomorphologies, the fabrication of undoped and phosphorus doped inverse opal structured germanium films is described in the present publication. In the course of this thesis a reproducible method for fabrication of inverse opal structured germanium films with tunable composition was developed. Monodisperse PMMA beads were obtained from PD Dr. Dina Fattakhova Rohlfing. Initial investigations on the utilization of $[Ge_9]^{4-}$ Zintl clusters for fabrication of germanium inverse opals were conducted by Dr. Markus Waibel. The morphology of films with regular volume-porosity is characterized by REM, TEM and grazing incidence small angle X-ray scattering (GISAXS). In the course of this thesis REM and TEM results were evaluated. GISAXS measurements were performed and evaluated by Dr. Kuhu Sarkar at the Elettra Sincrotrone Trieste. X-ray photoelectron spectroscopy shows a rather low oxygen content for the germanium inverse opal films, and was performed and evaluated by Patrick Zeller

Zintl Clusters

International Edition: DOI: 10.1002/anie.201508246
German Edition: DOI: 10.1002/ange.201508246

Zintl Clusters as Wet-Chemical Precursors for Germanium Nanomorphologies with Tunable Composition

Manuel M. Bentlohner, Markus Waibel, Patrick Zeller, Kuhu Sarkar, Peter Müller-Buschbaum, Dina Fattakhova-Rohlfing, and Thomas F. Fässler**

Abstract: *$[Ge_9]^{4-}$ Zintl clusters are used as soluble germanium source for a bottom–up fabrication of Ge nanomorphologies such as inverse opal structures with tunable composition. The method is based on the assembly and oxidation of $[Ge_9]^{4-}$ clusters in a template mold using $SiCl_4$, $GeCl_4$, and PCl_3 leading to Si and P-containing Ge phases as shown by X-ray diffraction, Raman spectroscopy, and energy-dispersive X-ray analysis. $[Ge_9]^{4-}$ clusters are retained using ethylenediamine (en) as a transfer medium to a mold after removal of the solvent if water is thoroughly excluded, but are oxidized to amorphous Ge in presence of water traces. ^1H NMR spectroscopy reveals the oxidative deprotonation of en by $[Ge_9]^{4-}$. Subsequent annealing leads to crystalline Ge. As an example for wet-chemical synthesis of complex Ge nanomorphologies, we describe the fabrication of undoped and P-doped inverse opal-structured Ge films with a rather low oxygen contents. The morphology of the films with regular volume porosity is characterized by SEM, TEM, and grazing incidence small-angle X-ray scattering.*

Group 14 element semiconductors such as Si and Ge are important materials in optoelectronic industry with a mature fabrication technology. Commercially available morphologies are dominated by bulk, thin film, and nanocrystalline forms, but the needs of emerging applications boost interest in other types of nanoarchitectures. Particularly, nanoparticles, nanowires and porous forms of Group 14 semiconductors attract significant attention because of a broad range of potential applications such as electrochemical energy storage, sensing, photovoltaics, microelectronics, and photonics.[1]

Synthetic approaches to manufacture Group 14 nanoparticles[2] and nanowires[3] are well-established, but the routes to the periodic porous materials are much more scarce. Porous Si or Ge layers are mainly obtained by chemical or electrochemical etching of corresponding dense materials providing a good control over the composition and crystallinity, but only a limited control over the porous structure and the surface chemistry.[1f,4] In this respect, bottom–up approaches based on the solidification of molecular precursors are more beneficial for fabricating periodic porous materials with an unprecedented control over the shape, size, and spatial arrangement of the pores. Numerous bottom–up approaches have been developed for metal oxides resulting in a large library of periodic porous morphologies.[5] However, an extension of these methods to the fabrication of non-oxide materials faces serious challenges and is mainly limited by the availability of suitable precursors capable of solidification to porous scaffolds in a controllable way. So far only a limited number of techniques to fabricate non-oxide porous semiconductors has been reported, such as chemical vapor deposition (CVD) involving silanes/germanes,[6] electrochemical reduction of Group 14 halides[7] and reduction of Ge^{IV} oxide with hydrogen or alkali metals.[8]

Several years ago germanium Zintl clusters have been introduced as precursors for nanostructured non-oxide semiconductors.[9,13a,g] Zintl clusters are polyanionic cages, which emerge in intermetallic compounds between alkaline or alkaline-earth metals and p-block (semi)metals. The solubility of Zintl phases in selected solvents, a rich library of compositions, and the possibility of coupling those units[10] make Zintl clusters attractive, versatile precursors for fabrication of non-oxide nanostructures with tunable composition and electronic properties.[11] Soluble Zintl clusters were used for electrodeposition of dense Ge layers[12] as well as for fabrication of mesoporous powders[13] and films[14] of Group 14–16 elements using surfactant-templating approaches. Despite of the expected potential of Zintl clusters as nanostructure precursors, today the number of reported applications is still rather low. The key problem is that the chemistry of the involved reactions is largely unclear, thereby restricting the generalization of these methods to diverse template morphologies and fabrication scales.

Here we present the application of $[Ge_9]^{4-}$ Zintl clusters as Ge source for the fabrication of Ge nanomorphologies with tunable composition by their controlled solidification to a solid phase, which is compatible with the controlled formation of complex morphologies (Figure 1). Specifically, our approach involves the transfer and homogenous distribution of the Zintl phase K_4Ge_9 in a template mold and the purposefully initiated oxidation of the $[Ge_9]^{4-}$ clusters. In order to gain control over this process we have additionally

[*] M. M. Bentlohner, Dr. M. Waibel, Prof. Dr. T. F. Fässler
Department Chemie, Technische Universität München
Lichtenbergstraße 4, 85747 Garching (Germany)
E-mail: thomas.faessler@lrz.tu-muenchen.de
P. Zeller, Priv.-Doz. Dr. D. Fattakhova-Rohlfing
University of Munich (LMU) and Center for NanoScience (CeNS)
Butenandtstrasse 5–13 (Haus E), 81377 München (Germany)
E-mail: dina.fattakhova@cup.uni-muenchen.de
Dr. K. Sarkar, Prof. Dr. P. Müller-Buschbaum
Physik-Department, Lehrstuhl für Funktionelle Materialien
Technische Universität München
James-Franck-Straße 1, 85748 Garching (Germany)

Supporting information for this article including all experimental details as well as extensive descriptions of the experimental data is available on the WWW under http://dx.doi.org/10.1002/anie.201508246. Video material is available under https://vimeo.com/76125397.

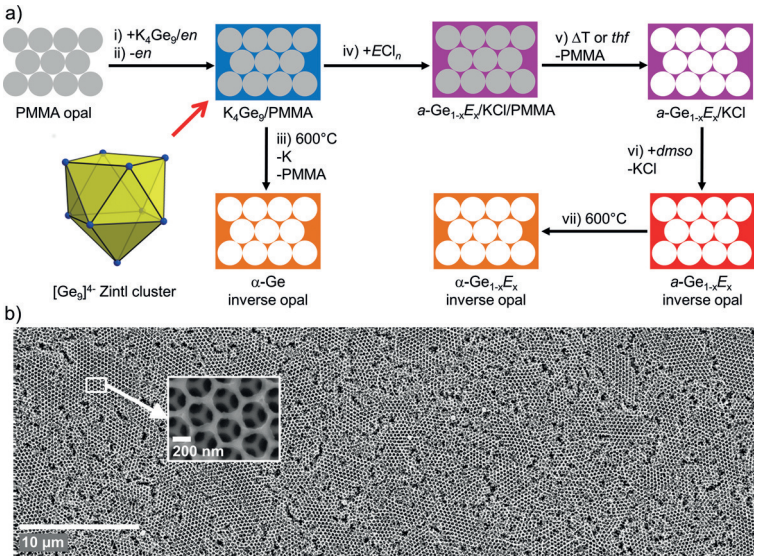

Figure 1. a) Fabrication of Ge inverse opals (INOP) by controlled oxidation of $[Ge_9]^{4-}$ Zintl clusters, (i) Infiltration of a polymethylmethacrylate (PMMA) opal (grey spheres) with K_4Ge_9/en, ii) evaporation of en, iii) annealing of the K_4Ge_9/PMMA composite at 600 °C and formation of crystalline α-Ge INOP and K vapor, iv) impregnation of K_4Ge_9/PMMA composite with ECl_n (E = Si, Ge, P) and formation of amorphous a-$Ge_{1-x}E_x$ (purple), v) removal of PMMA by flash-annealing or dissolution in tetrahydrofuran (thf), vi) removal of KCl with dimethylsulfoxid (dmso), vii) annealing of a-$Ge_{1-x}E_x$-INOP and formation of α-$Ge_{1-x}E_x$ INOP (orange). b) Scanning electron micrographs of a-$Ge_{1-x}Ge_x$ INOP and magnified section of the film as inlay.

conducted a series of ex situ experiments to investigate the transfer of $[Ge_9]^{4-}$ Zintl clusters into the templates and the cluster oxidation chemistry.

As transfer medium en, a common solvent for $[Ge_9]^{4-}$, was used.[11] Even though the previous publications hypothesize the possible role of en as an oxidant for K_4Ge_9,[10–11,13d–f] the experimental evidences for such a process have never been provided. We found that removal of en from a K_4Ge_9/en solution leads directly to amorphous Ge (a-Ge) through the oxidation of dissolved $[Ge_9]^{4-}$ Zintl clusters by en (Figure 2b). However, this reaction only takes place in the presence of traces of water,[15] which triggers the oxidation of the Zintl anions. For the first time deprotonation of en was confirmed using ^{1}H NMR spectroscopy (see Figure S4 in the Supporting Information), evidencing an oxidizing potential of en towards $[Ge_9]^{4-}$ clusters. Such a process has been previously proposed for the formation of Ge_9 dimers, oligomers, and polymers such as $[Ge_9=Ge_9=Ge_9=Ge_9]^{8-}$.[10,16] In contrast to that, removal of en from completely water-free K_4Ge/en-solutions (see the Supporting Information for the details of the en distillation) leads to the conservation of the polyhedral clusters as demonstrated by Raman spectroscopy (Figure 2a).

Thus, under meticulous exclusion of water, en is a suitable medium for the non-destructive transfer of K_4Ge_9 into the template molds, offering possibilities of their further transformations to solid Ge phase. One of such transformations is the oxidation of $[Ge_9]^{4-}$ Zintl clusters through thermal annealing (Figure 2c). Therefore, K_4Ge_9 recovered from a water-free en solution by the removal of solvent was annealed for 5 minutes at 500 °C in vacuo and subsequently for 1 h at 600 °C in argon resulting in crystalline Ge (α-Ge).[17] This process is accompanied by the release of elemental potassium visible as a metal mirror deposited on the colder parts of the recipient (Figure S2). Furthermore, the presence of intact Zintl clusters enables their cross-linking with ECl_n (E = Si, Ge, $n=4$; E = P, $n=3$; Figure 2d). Because of the high Lewis acidity of the positively polarized E atom in ECl_n, such halides react readily with the highly Lewis basic $[Ge_9]^{4-}$ clusters. This route is particularly attractive for nanostructure assembly as it proceeds at ambient conditions and, more importantly, enables tuning of composition and controllable doping by introducing different elements.[13a–c,f,14] Because of a vigorous reaction of ECl_n with en the latter should be thoroughly removed prior to the contact with ECl_n. In the ex situ experiments the cross-linking between the K_4Ge_9 and ECl_n (E = Si, Ge, $n=4$; E = P, $n=3$) was investigated in toluene, which is inert towards both compounds. The relevant XRD patterns of the obtained reaction products point to the formation of potassium chloride and an amorphous phase (see the powder diffractograms in Figures S5–S7, the Raman spectra in Figure S5, and the results of EDX in Table S1). The presence of potassium chloride is indicative for

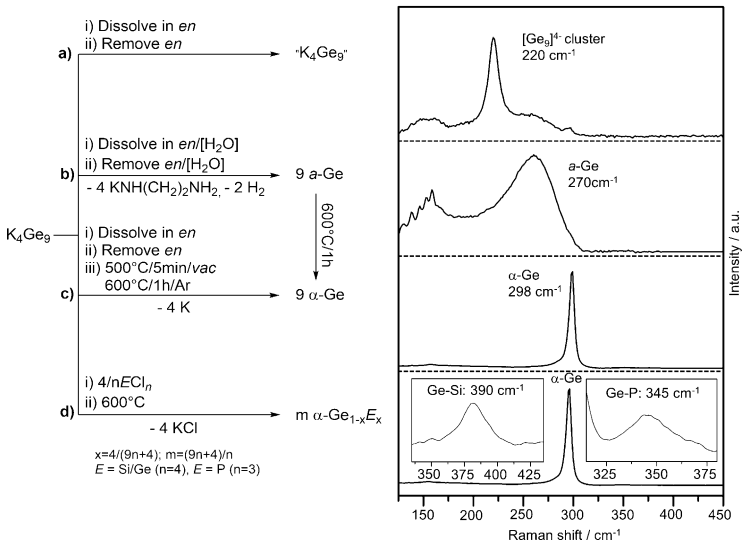

Figure 2. Ex situ investigations on the oxidation of $[Ge_9]^{4-}$ Zintl clusters (left: reaction schemes, right: Raman spectra, reference data see refs. [18–21]). Evaporating solutions of K_4Ge_9 in a) water-free en retains $[Ge_9]^{4-}$ clusters, but the same procedure in b) en containing water traces forms a-Ge which transforms to α-Ge at 600 °C; c) as a) and subsequent annealing forms α-Ge and K vapor, d) reaction of K_4Ge_9 with ECl_n (E = Si, Ge; $n=4$; E = P, $n=3$). KCl is removed with dmso, α-$Ge_{1-x}E_x$ forms at 600 °C. For details see Figures S2–S7.

the successful cross-linking reaction according to the reaction scheme in Figure 2d. The amorphous phase crystallizes by annealing at 600 °C, as follows from the XRD patterns as well as the Raman spectra. The use of heteroatomic linkers, different from Ge, enables incorporation of silicon or phosphorous into the Ge structure. When $SiCl_4$ is used as linker, the XRD reflections of the crystalline product are shifted to higher angles,[22] and in Raman spectra an additional signal at 390 cm^{-1} is detected corresponding to the Ge–Si vibrational mode.[20] For the product cross-linked with PCl_3, the Ge–P mode at 345 cm^{-1}[21] is visible in the Raman spectra. K/Cl/Ge/*E* (*E* = Si, P) atomic ratios obtained by energy-dispersive X-ray analysis (EDX) of the amorphous and crystallized products are in a good agreement with the expected stoichiometry of the cross-linking reactions.

Nanostructured materials are inherently fragile and thus the minimization of mechanical stress during fabrication is required. Generally, the application of gaseous reagents comes along with less mechanical stress compared to the application of solutions. Hence, representative for other volatile cross-linkers, we investigated the gas-phase reaction of $GeCl_4$ vapors with the bulk K_4Ge_9. Similar to the reaction in toluene described above, potassium chloride and Ge was formed, pointing to the applicability of the gas-phase oxidation method for the film fabrication.

As an example of the suitability of Zintl clusters for wet-chemical synthesis of complex Ge nanomorphologies using the oxidation reactions discussed above, we describe the fabrication of undoped and phosphorous-doped inverse opal-structured Ge films (Figure 1 and Figure S8). In contrast to the recently reported electrodeposition method for inverse opal structures,[7] the wet-chemical impregnation protocol followed by a controlled solidification described in this work is not limited to the conducting substrates, leads to nanostructured compounds with tunable composition and with lower oxygen content, and is universally applicable to any kind of morphologies with different shapes and dimensions. Ge films with an inverse opal structure are prepared by colloidal crystal templating using periodic arrays of polymethylmethacrylate (PMMA) beads as the templates for porosity. Dried composite films obtained after infiltration of PMMA opal template with a solution of K_4Ge_9 in en contain $[Ge_9]^{4-}$ clusters as follows from the Raman spectra. Zintl clusters periodically distributed in template voids can be transformed to a solid Ge phase with similar nanomorphology using either thermal treatment or cross-linking reaction routes described above. In a thermal procedure, the dried films are annealed for 5 minutes at 500 °C in vacuo and for one hour at 600 °C in Ar, resulting in the pyrolysis of PMMA,[23] release of elemental potassium and formation of mechanically stable crystalline macroporous Ge films (α-Ge-INOP). Alternatively, $[Ge_9]^{4-}$ Zintl clusters distributed in template voids can be cross-linked to form the solid phase. Treatment of the dried $[Ge_9]^{4-}$/PMMA composites in $GeCl_4$ vapor results in the formation of 3D-Ge network distributed in the PMMA bead matrix. PMMA can be removed by a gentle dissolution in thf, although the resulting macroporous films are rather fragile. Mechanical stability of the Ge networks is significantly improved after flash-annealing (5 minutes at 500 °C) in vacuo. Raman spectra of the resulting films show a broad signal at 270 cm^{-1} typical for the amorphous Ge (*a*-$Ge_{1-x}Ge_x$ INOP).[19b] KCl formed as a side product of this reaction is washed out by extracting the films with dmso. EDX analysis of such films proves that the framework consists entirely of Ge and that KCl is efficiently removed.

Scanning electron microscopy (SEM) images of the films obtained by both methods show the same inverse opal structure. In addition, perfect ordering of the inverse opal films is confirmed by grazing incidence small-angle X-ray scattering (GISAXS) experiments that gives insights into the volume morphology of the porous frameworks (detailed description of GISAXS data see Figure S11).[24] GISAXS scattering patterns show two types of periodicity with a d-spacing of 203 nm (called further pore A) and 151 nm (called pore B), which gives an evidence of a long-range periodicity in the bulk of the macroporous film. The porous structure parameters obtained by SEM and GISAXS are in a good agreement with the TEM results (Figure 3), which show uniformly sized periodic pores with the diameter of 150 nm and 200–250 nm corresponding to B pores and A pores, respectively.

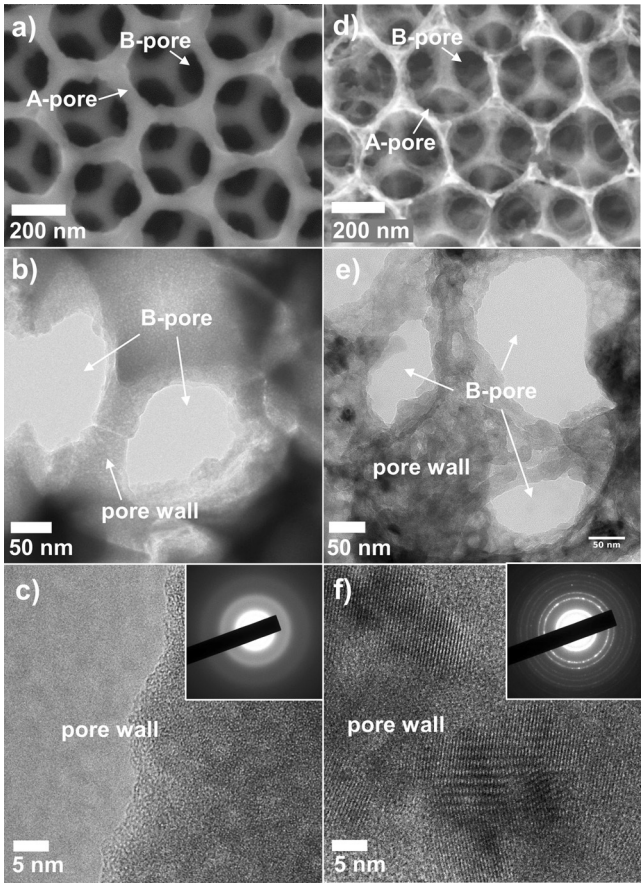

Figure 3. SEM and TEM images of a–c) *a*-$Ge_{1-x}Ge_x$-INOP and d–f) α-$Ge_{1-x}Ge_x$-INOP; a) and d) SEM (pore types A and B are depicted); b) and e) low-magnification TEM; c) and f) high-resolution TEM; insets c) and f) selected-area electron diffraction pattern.

The macroporous Ge scaffolds obtained by the low-temperature cross-linking of Zintl clusters are amorphous up to 500 °C, as follows from the Raman spectroscopy measurements, high-resolution TEM images (HR-TEM, Figure 3c) and selected-area electron diffraction (SAED) measurements in TEM. Aiming for the same inverse opal-structured Ge but with the enhanced crystallinity, the amorphous films were annealed for one hour at 600 °C in argon atmosphere (α-$Ge_{1-x}Ge_x$-INOP). SEM images of this film (Figure 3d) show that the inverse opal structure withstands annealing at 600 °C. The pore wall thickness decreases after annealing because of the densification of the Ge scaffold. TEM images (Figure 3e–f) as well as the SAED pattern (Figure 3f inset) of the film annealed at 600 °C reveal that the pore walls consist of crystalline Ge nanoparticles with the size of around 10–20 nm embedded in an amorphous matrix. Consequently, in the Raman spectrum a sharp peak at 298 cm^{-1} appears, corresponding to the optical phonon mode of crystalline Ge. Powder XRD patterns of the films scraped off the substrate display reflections of α-Ge (Figure S9). The size of the crystalline domains calculated from the broadening of individual lines using the Scherrer equation corresponds to 10–15 nm, in good agreement with the TEM analysis.

X-ray photoelectron spectra (XPS) of the annealed films (Figure 4) display signals of Ge^0 (binding energy Ge^0 3d orbital: 29.7 eV) and much lower signals of GeO and GeO_2 (binding energies: +1.8 eV and +3.4 eV with respect to Ge^0 3d, respectively).[25] Contributions from GeO and GeO_2 to both the $2p_{3/2}$ and 3d signals are significantly reduced by sputtering the films with Ar^+ ions, indicating that Ge oxides are present only at the surface of the porous framework (for details on the interpretation of the XPS spectra see Figures S12/S13). Therefore, the macroporous Ge scaffolds obtained from the Zintl clusters consist of Ge^0 and only little GeO and GeO_2, in contrast to electrodeposited Ge morphologies.[7d]

For the application of Ge in electronic devices doping is required.[26] To demonstrate the possibility of incorporating dopants into the porous Ge scaffold by our cross-linking method, we have treated $[Ge_9]^{4-}$/PMMA composite with PCl_3 vapor and annealed the film (600 °C/1 h) to remove PMMA and enhance the crystallinity (α-$Ge_{1-x}P_x$-INOP). SEM images of the washed films display the same regular porosity as the films obtained by cross-linking with $GeCl_4$, but the EDX analysis reveals the presence of phosphorous (Figure S8). Similar to the ex situ experiments with PCl_3 described above, the Raman spectra of the films show an additional signal at 345 cm^{-1} corresponding to the Ge–P vibration (Figure S10),[21] which indicates that phosphorous was incorporated into the porous Ge scaffold by PCl_3 cross-linking. The possibility to solidify clusters both by thermal annealing and cross-linking gives the possibility to control the amount of introduced dopants.

The presented results highlight the large potential of $[Ge_9]^{4-}$ Zintl clusters as Ge source for the versatile and controlled chemical fabrication of Ge morphologies. The detailed ex situ investigations on the transfer and controlled oxidation of $[Ge_9]^{4-}$ Zintl clusters and step-by-step monitoring of the transfer reactions provide the basis for a rational and general fabrication method for complex Ge nanomorphologies and the possibility of targeted composition tuning, as it is shown for the formation of highly ordered inverse opal structures. Currently we are running tests to apply the PMMA and K_4Ge_9/en solution by spin- and spray-coating on different types of substrates in order to achieve large-area inverse opal-structured films. The as-obtained inverse opal-structured films are tested for applications in hybrid solar cells and as thin film anodes. Moreover, our investigations outline that our method can be transferred to other types of Zintl compounds such as soluble $[Ge_{9-x}Si_x]^{4-}$ Zintl anions providing a versatile fabrication technique for nanostructured silicon films.

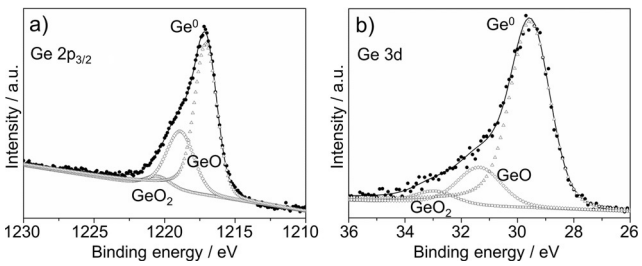

Figure 4. XPS spectra of *a*-$Ge_{1-x}Ge_x$-INOP after 20 min of sputtering with Ar^+ ions. a) Ge $2p_{3/2}$ and b) Ge 3d signal. Data points (circles), fitted curve (solid line). Contributions of Ge (triangles), GeO (rhombs), GeO_2 (squares).

Experimental Section

Fabrication of Ge INOP films: A PMMA opal (for the fabrication see the Supporting Information) was infiltrated with a solution of K_4Ge_9 in en grade A (concentration 50 mg mL^{-1}) by drop casting. The dried K_4Ge_9/PMMA composite was either annealed: 5 min/500 °C/in vacuo, 1 h/600 °C/Ar or treated with $GeCl_4$ or PCl_3 vapor at room temperature for one week or longer in a glass vessel, respectively. PMMA was removed either by dissolution in thf or flash-annealing (5 minutes at 500 °C in vacuo). KCl was removed by extracting the films for 1 h with dmso. The films were crystallized at 600 °C/1 h.

Acknowledgements

The authors thank for funding this work the research network "Solar Technologies go Hybrid" (State of Bavaria) via TUM.solar and LMU Center Materials for Renewable Energies, the NIM cluster (DFG) and the Center for Nano-Science (CeNS). We thank M.Sc. Michael Giebel, M.Sc. Sebastian Geier, and M.Sc. Kristina Peters for help with the preparation of the Ge INOP films and PMMA. The authors are grateful to Dr. Sigrid Bernstorff from the Elettra-Sincrotrone Trieste S.C.p.A for help during the setting-up of the GISAXS experiment, to Dr. Steffen Schmidt and Dr. Benjamin Mandlmeier, University of Munich (LMU), for electron microscopy, as well as to Dipl.-Phys. Benedikt Stoib and Prof. Dr. Martin Brandt, Walter Schottky Institute, for fruitful discussions. We also thank M.Sc. Marius Loch and Prof. Dr. Paolo Lugli, Technical University of Munich, for first tests on applying spin- and spray-coating methods.

Keywords: composition tuning · germanium · inverse opals · nanostructuring · zintl clusters

How to cite: *Angew. Chem. Int. Ed.* **2016**, *55*, 2441 – 2445
Angew. Chem. **2016**, *128*, 2487 – 2491

[1] a) M.-H. Park, K. Kim, J. Kim, J. Cho, *Adv. Mater.* **2010**, *22*, 415 – 418; b) D. D. Vaughn II, R. E. Schaak, *Chem. Soc. Rev.* **2013**, *42*, 2861 – 2879; c) R. Pillarisetty, *Nature* **2011**, *479*, 324 – 328; d) K. Ramasamy, P. G. Kotula, A. F. Fidler, M. T. Brumbach, J. M. Pietryga, S. A. Ivanov, *Chem. Mater.* **2015**, *27*, 4640 – 4649; e) M. G. Kanatzidis, *Adv. Mater.* **2007**, *19*, 1165 – 1181; f) A. Stein, *Nature* **2006**, *441*, 1055 – 1056.

[2] a) X. D. Pi, U. Kortshagen, *Nanotechnology* **2009**, *20*, 295602; b) A. Fojtik, M. Giersig, A. Henglein, *Ber. Bunsen-Ges. Phys. Chem.* **1993**, *97*, 1493 – 1496; c) A. Dowd, R. G. Elliman, B. Luther-Davies, *Appl. Phys. Lett.* **2001**, *79*, 2327 – 2329; d) J. A. Kelly, E. J. Henderson, J. G. C. Veinot, *Chem. Commun.* **2010**, *46*, 8704 – 8718.

[3] M. Amato, M. Palummo, R. Rurali, S. Ossicini, *Chem. Rev.* **2014**, *114*, 1371 – 1412.

[4] H. C. Choi, J. M. Buriak, *Chem. Commun.* **2000**, 1669 – 1670.

[5] D. Fattakhova-Rohlfing, A. Zaleska, T. Bein, *Chem. Rev.* **2014**, *114*, 9487 – 9558.

[6] a) M. Seino, E. J. Henderson, D. P. Puzzo, N. Kadota, G. A. Ozin, *J. Mater. Chem.* **2011**, *21*, 15895 – 15898; b) H. Míguez, E. Chomski, F. Garcia-Santamaría, M. Ibisate, S. John, C. López, F. Meseguer, J. P. Mondia, G. A. Ozin, O. Toader, H. M. van Driel, *Adv. Mater.* **2001**, *13*, 1634 – 1637.

[7] a) R. Al-Salman, X. Meng, J. Zhao, Y. Li, U. Kynast, M. M. Lezhnina, F. Endres, *Pure Appl. Chem.* **2010**, *82*, 1673 – 1689; b) L. K. van Vugt, A. F. van Driel, R. W. Tjerkstra, L. Bechger, W. L. Vos, D. Vanmaekelbergh, J. J. Kelly, *Chem. Commun.* **2002**, 2054 – 2055; c) W. Xin, J. Zhao, D. Ge, Y. Ding, Y. Li, F. Endres, *Phys. Chem. Chem. Phys.* **2013**, *15*, 2421 – 2426; d) X. Meng, R. Al-Salman, J. Zhao, N. Borissenko, Y. Li, F. Endres, *Angew. Chem. Int. Ed.* **2009**, *48*, 2703 – 2707; *Angew. Chem.* **2009**, *121*, 2741 – 2745.

[8] a) H. Míguez, F. Meseguer, C. López, M. Holgado, G. Andreasen, A. Mifsud, V. Fornés, *Langmuir* **2000**, *16*, 4405 – 4408; b) J. Hwang, C. Jo, M. G. Kim, J. Chun, E. Lim, S. Kim, S. Jeong, Y. Kim, J. Lee, *ACS Nano* **2015**, *9*, 5299 – 5309; c) J. Liang, X. Li, Z. Hou, T. Zhang, Y. Zhu, X. Yan, Y. Qian, *Chem. Mater.* **2015**, *27*, 4156 – 4164; d) C. Zhang, Z. Lin, Z. Yang, D. Xiao, P. Hu, H. Xu, Y. Duan, S. Pang, L. Gu, G. Cui, *Chem. Mater.* **2015**, *27*, 2189 – 2194; e) H. Jia, R. Kloepsch, X. He, J. P. Badillo, P. Gao, O. Fromm, T. Placke, M. Winter, *Chem. Mater.* **2014**, *26*, 5683 – 5688.

[9] A. M. Guloy, R. Ramlau, Z. Tang, W. Schnelle, M. Baitinger, Y. Grin, *Nature* **2006**, *443*, 320 – 323.

[10] a) T. F. Fässler, *Angew. Chem. Int. Ed.* **2007**, *46*, 2572 – 2575; *Angew. Chem.* **2007**, *119*, 2624 – 2628; b) A. J. Karttunen, T. F. Fässler, M. Linnolahti, T. A. Pakkanen, *ChemPhysChem* **2010**, *11*, 1944 – 1950.

[11] S. Scharfe, F. Kraus, S. Stegmaier, A. Schier, T. F. Fässler, *Angew. Chem. Int. Ed.* **2011**, *50*, 3630 – 3670; *Angew. Chem.* **2011**, *123*, 3712 – 3754.

[12] N. Chandrasekharan, S. C. Sevov, *J. Electrochem. Soc.* **2010**, *157*, C140 – C145.

[13] a) G. S. Armatas, M. G. Kanatzidis, *Science* **2006**, *313*, 817 – 820; b) S. D. Korlann, A. E. Riley, B. L. Kirsch, B. S. Mun, S. H. Tolbert, *J. Am. Chem. Soc.* **2005**, *127*, 12516 – 12527; c) P. N. Trikalitis, K. K. Rangan, T. Bakas, M. G. Kanatzidis, *Nature* **2001**, *410*, 671 – 675; d) G. S. Armatas, M. G. Kanatzidis, *Adv. Mater.* **2008**, *20*, 546 – 550; e) G. S. Armatas, M. G. Kanatzidis, *Nano Lett.* **2010**, *10*, 3330 – 3336; f) G. S. Armatas, M. G. Kanatzidis, *J. Am. Chem. Soc.* **2008**, *130*, 11430 – 11436; g) S. Dong, A. E. Riley, A. J. Cadby, E. K. Richman, S. D. Korlann, S. H. Tolbert, *Nature* **2006**, *441*, 1126 – 1130.

[14] a) A. E. Riley, S. D. Korlann, E. K. Richman, S. H. Tolbert, *Angew. Chem. Int. Ed.* **2006**, *45*, 235 – 241; *Angew. Chem.* **2006**, *118*, 241 – 247; b) S. D. Korlann, A. E. Riley, B. S. Mun, S. H. Tolbert, *J. Phys. Chem. C* **2009**, *113*, 7697 – 7705.

[15] A detailed section on the purification and quality check of en is shown in the Supporting Information. We exploited the reaction of 7-amino-1-(trimethylsilyl)-5-aza-hepta-3-en – 1-yne[27] to 2,3-dihydro-5-methyl-1*H*-1,4-diazepine in en, which is triggered by water, to qualitatively check the water content of the solvent.

[16] a) C. Downie, Z. J. Tang, A. M. Guloy, *Angew. Chem. Int. Ed.* **2000**, *39*, 337 – 340; *Angew. Chem.* **2000**, *112*, 346 – 348; b) L. Yong, S. D. Hoffmann, T. F. Fässler, *Z. Anorg. Allg. Chem.* **2004**, *630*, 1977 – 1981.

[17] An identical annealing procedure as for en treated K_4Ge_9, was applied to neat crystalline K_4Ge_9. Thereby a mixture of K_8Ge_{44} and α-Ge was obtained.

[18] H. G. Von Schnering, M. Baitinger, U. Bolle, W. Carrillo-Cabrera, J. Curda, Y. Grin, F. Heinemann, J. Llanos, K. Peters, A. Schmeding, M. Somer, *Z. Anorg. Allg. Chem.* **1997**, *623*, 1037 – 1039.

[19] a) S. Schlecht, M. Yosef, M. Froba, *Z. Anorg. Allg. Chem.* **2004**, *630*, 864 – 868; b) J. Fortner, R. Q. Yu, J. S. Lannin, *J. Vac. Sci. Technol. A* **1990**, *8*, 3493 – 3495.

[20] H. H. Burke, I. P. Herman, *Phys. Rev. B* **1993**, *48*, 15016 – 15024.

[21] N. Fukata, K. Sato, M. Mitome, Y. Bando, T. Sekiguchi, M. Kirkham, J.-i. Hong, Z. L. Wang, R. L. Snyder, *ACS Nano* **2010**, *4*, 3807 – 3816.

[22] L. Vegard, *Z. Kristallogr.* **1928**, *67*, 239.

[23] S. M. Al-Salem, P. Lettieri, J. Baeyens, *Waste Manage.* **2009**, *29*, 2625 – 2643.

[24] a) P. Müller-Buschbaum, *Anal. Bioanal. Chem.* **2003**, *376*, 3 – 10; b) G. Renaud, R. Lazzari, F. Leroy, *Surf. Sci. Rep.* **2009**, *64*, 255 – 380.

[25] D. Schmeisser, R. D. Schnell, A. Bogen, F. J. Himpsel, D. Rieger, G. Landgren, J. F. Morar, *Surf. Sci.* **1986**, *172*, 455 – 465.

[26] C. Claeys, E. Simoen, *Germanium-Based Technologies: From Materials to Devices*, Elsevier Science, Amsterdam, **2011**.

[27] M. M. Bentlohner, W. Klein, Z. H. Fard, L.-A. Jantke, T. F. Fässler, *Angew. Chem. Int. Ed.* **2015**, *54*, 3748 – 3753; *Angew. Chem.* **2015**, *127*, 3819 – 3824.

Received: September 3, 2015
Revised: October 4, 2015
Published online: December 3, 2015

Angewandte Chemie
Eine Zeitschrift der Gesellschaft Deutscher Chemiker

Supporting Information

Zintl Clusters as Wet-Chemical Precursors for Germanium Nanomorphologies with Tunable Composition

Manuel M. Bentlohner, Markus Waibel, Patrick Zeller, Kuhu Sarkar, Peter Müller-Buschbaum, Dina Fattakhova-Rohlfing, and Thomas F. Fässler**

anie_201508246_sm_miscellaneous_information.pdf
anie_201508246_sm_SD_Movie.mp4

Supporting Information

Contents

Figures and Tables

1 Experimental Details

1.1 Materials characterization

Raman spectroscopy was carried out using a LabRAM HR UV-Vis (HORIBA JOBIN YVON) Raman Microscope (OLYMPUS BX41) with a SYMPHONY CCD detection system and a He-Ne laser (λ = 633 nm) (spot size 4.5 µm) (laser power during measurement: 0.17mW).
X-ray powder diffractograms (XRD) were recorded on a STOE STADI P (Cu-$K_{\alpha 1}$ radiation, Ge monochromator, detector: IP-PSD) in transmission mode. Samples were prepared by scratching the films from the substrate onto a Scotch tape.
^{1}H NMR spectra were recorded on Bruker a 400 MHz spectrometer (Bruker AV-400). Acetonitrile-d_3 (Deutero GmbH 99.8%) was dried over molecular sieve (4 Å) for at least one day and stored in a glove box.
Scanning electron microscopy (SEM) measurements were carried out using a JEOL JSM-6500F scanning electron microscope equipped with field emission gun operated at 5-30 kV. Energy dispersive X-ray analysis was performed with an Oxford analysis system (Oxford Instruments) with a cross section of 10 mm² and an ATW2 window.
Transmission electron microscopy (TEM) was carried out using a JEOL JEM-2010 with a high resolution pole piece at an operation voltage of 200 kV. For the sample preparation material was scraped from the substrate and deposited on a holey carbon coated copper grid. The EDX system was an Apollo XLT SUTW (Co. AMETEK/EDAX) with a cross section of 30 mm².

1. 2 Materials preparation

All manipulations involving Zintl compounds were carried out under a purified argon atmosphere using a glove box and standard Schlenk techniques. Tetrahydrofuran was dried over molecular sieve (4 Å) in a solvent purificator (MBraun MB-SPS). Dimethylsulfoxid (Sigma Aldrich, water content < 0.005%) was used as received. Bidistilled water (Milipore Q) was used for substrate cleaning and the preparation of the PMMA dispersion.

1. 2. 1 Purification of ethylenediamine (*en*)

Ethylenediamine (*en*) (Merck) with an initial water content of ≤ 1% was refluxed over calcium hydride (Merck) and freshly collected prior to use. *En* containing trace amounts of water (denoted as grade B) was obtained after refluxing for 2-6 hours. The sample tubes for grade B *en* were stored under ambient conditions. Water free *en* (denoted as grade A) was obtained after refluxing for 72 hours. The sample tubes for grade A *en* were thoroughly cleaned and dried at 120°C immediately before the *en* collection. Analysis of water content was performed using reaction with bis(trimethylsilyl)butadiyne (**1**) developed in our group. We found that **1** readily reacts with *en* to form different reaction products depending on the water content. This reaction in water-free conditions results in formation of 7-amino-1-(trimethylsilyl)-5-aza-hepta-3-en-1-yne (**2**) [1] In presence of even trace amounts of water this product undergoes an intramolecular ring-closure to 2,3-dihydro-5-methyl-1H-1,4-diazepine (**3**). The rate of the **2** formation increases with the increasing water content. This reaction was utilized to analyze the water content in *en*, using ^{1}H NMR spectroscopy to determine the amount of **3**. In a typical procedure, **1** (34.9 mg) was dissolved in 3 ml *en*, and ^{1}H NMR spectra were recorded from the obtained solutions (in non-deuterated *en*) after different reaction times.[1] For the grade A *en*, the formation of **3** was not detected even after more than 150 hours of reaction, whereas for the grade B *en* the **1** entirely transformed to **2** within 100 hours.

1. 2. 2 Synthesis of K_4Ge_9

K_4Ge_9 was synthesized by heating a stoichiometric mixture of the elements K and Ge (Chempur, 99.999%) at 650 °C for 20 h in a stainless-steel tube.[2] K was purified by liquation. The purity of the product was analyzed using powder X-ray diffraction (Figure S1).

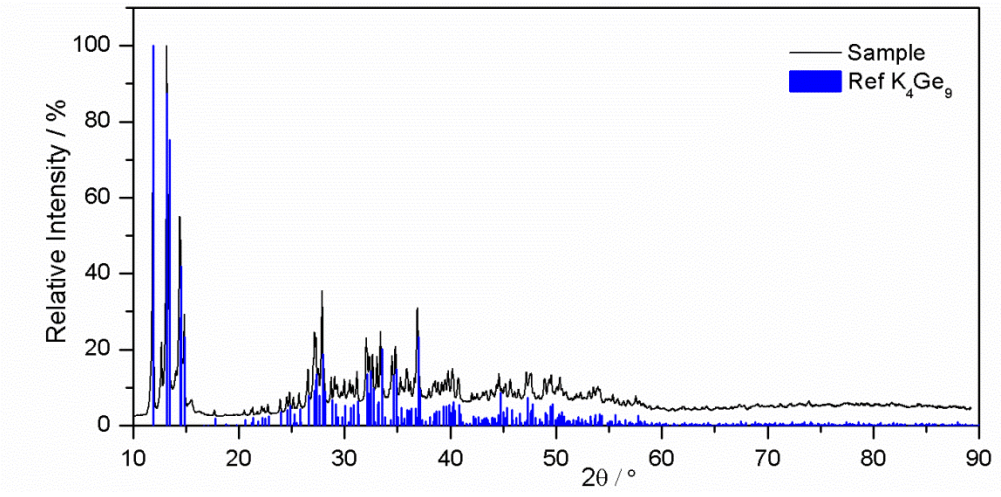

Figure S1. Powder X-ray diffractogram of phase-pure K_4Ge_9. The measurements were performed on a sample placed in Ar-sealed glass capillary.

2 *Ex situ* investigations on the oxidation of $[Ge_9]^{4-}$ Zintl clusters

2. 1 Reaction of K_4Ge_9 with ethylenediamine

In a typical procedure, K_4Ge_9 (50 mg, 0.062 mmol) were dissolved in 1 ml *en* in Schlenk tubes. Color of resulting solutions strongly depends on the water content in the *en*, being intensively red in grade A *en* and deep-green in grade B *en*, respectively. After stirring solutions for two hours the solvent was entirely removed *in vacuo*. The obtained drying-residues are denoted as A-RT and B-RT for the products prepared with grade A and grade B en, respectively. A part of these products was additionally annealed for 5min/500°C in vacuum and 1h/600°C in Ar. For the sample A-RT this process was accompanied by deposition of a metal mirror on the cold parts of the recipient (Figure S2). No metal mirror deposition was observed for the B-RT. The resulting products are denoted as A-600°C and B-600°C, respectively. The reaction products were analyzed using powder XRD (Figure S3) and ^{1}H NMR spectroscopy (Figure S4).

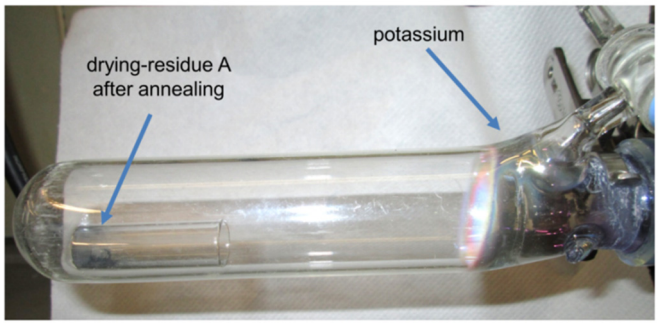

Figure S2. Annealing of drying residue A and deposition of potassium at the colder parts of the recipient.

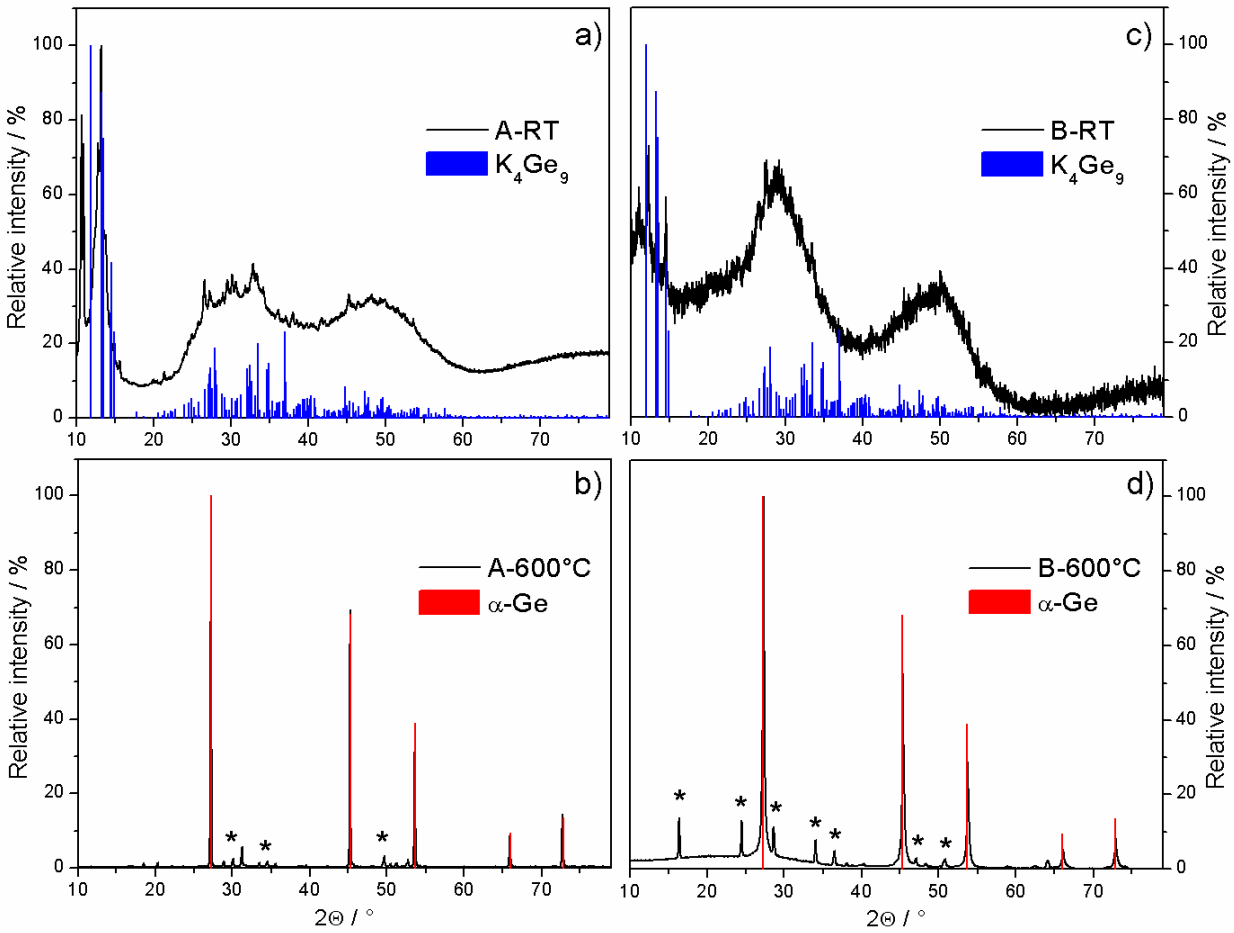

Figure S3. Powder X-ray diffractograms of the drying residues obtained from solutions of K_4Ge_9 in *en*: a) A-RT, b) A-600°C, c) B-RT, d) B-600°C. Unidentified reflections are labeled with asterisk. The measurements were performed on the samples placed in Ar-sealed glass capillaries.

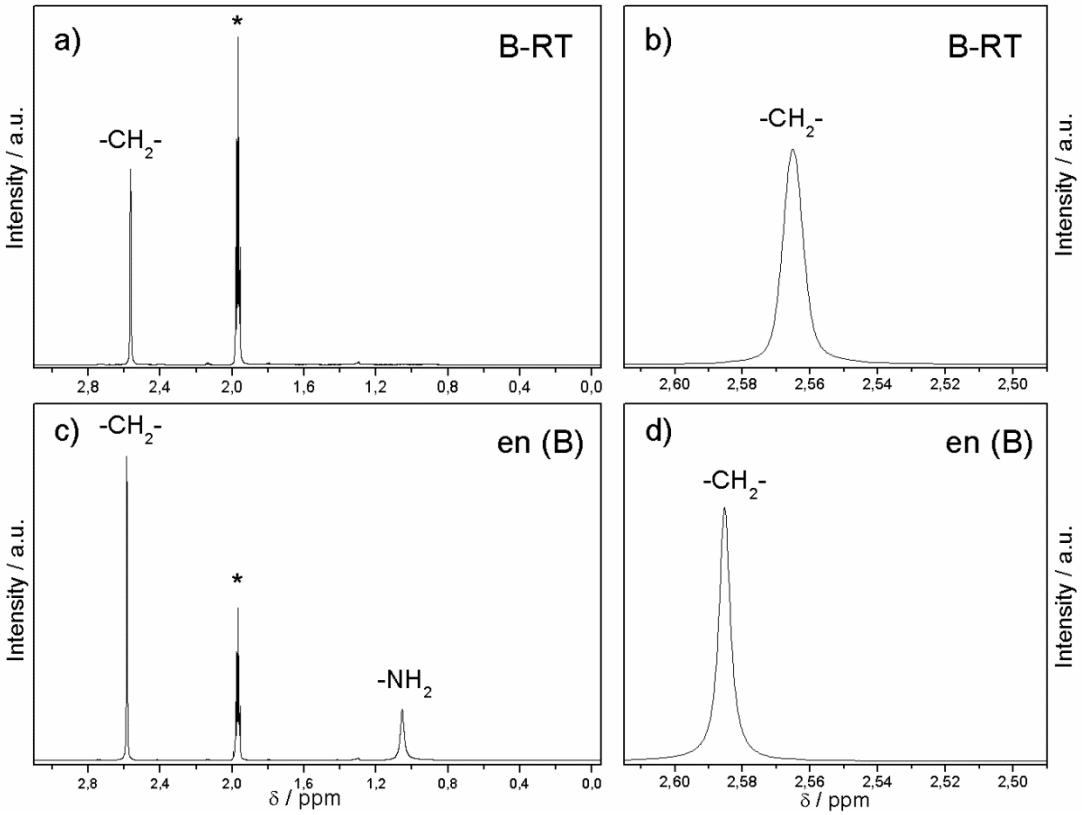

Figure S4. a/b) ^{1}H-NMR spectruma of the extract obtained by stirring sample B-RT for one hour with acetonitrile-d3 and subsequent filtration over glass-wool. c/d) ^{1}H-NMR spectrum of *en* grade B dissolved in acetontrilie-d3. Figure S4b shows a magnified section of the spectrum a) Figure S4d shows a magnified section of the spectrum c) Residues of CH_3CN are labelled with asterisk. The ^{1}H NMR spectrum of *en* in acetonitrile-d_3 shows two signals, corresponding to the methylene groups (2.555 ppm) and the amino functionality (1.02 ppm). For the extract the signal for the amino functionality is absent and exclusively a signal corresponding to methylene groups appears, indicating deprotonated *en*. As expected for a deprotonated *en*, the signal of the methylene groups is high field shifted due to a shielding effect of the negatively charged –NH^- functionalities.

2. 2 Reaction of K_4Ge_9 with ECl_n in toluene

In a typical procedure, K_4Ge_9 (194.4 mg, 0.24 mmol) was mixed in a Schlenk tube with solutions of ECl_n (E = Si, Ge, n = 4; E = P, n = 3) in 8 ml toluene. The sample denoted as $Ge_{1-x}Ge_x$-RT was prepared with $GeCl_4$ (30.7 µl, 0.26 mmol, 1.1 eq), the sample denoted as $Ge_{1-x}Si_x$-RT with $SiCl_4$ (30.2 µl, 0.26 mmol, 1.1 eq), the sample denoted as $Ge_{1-x}P_x$-RT with PCl_3 (30.6 µl, 0.35 mmol, 1.46 eq), respectively (eq denotes the molar ratio of ECl_n to K_4Ge_9). In the main text $Ge_{1-x}Ge_x$-RT corresponds to *a*-$Ge_{1-x}E_x$ and $Ge_{1-x}E_x$-600°C corresponds to α-$Ge_{1-x}E_x$, respectively. The obtained suspensions were stirred for four weeks, afterwards the toluene was pumped down resulting in grey solids. A part of the obtained products was additionally annealed for one hour at 600°C *in vacuo.* The obtained samples are denoted as $Ge_{1-x}P_x$-600°C, $Ge_{1-x}Si_x$-600°C and $Ge_{1-x}P_x$-600°C, respectively. The products were characterized by Raman spectroscopy (Figure S5), powder X-ray diffraction (Figure S6) and EDX (Table S1).

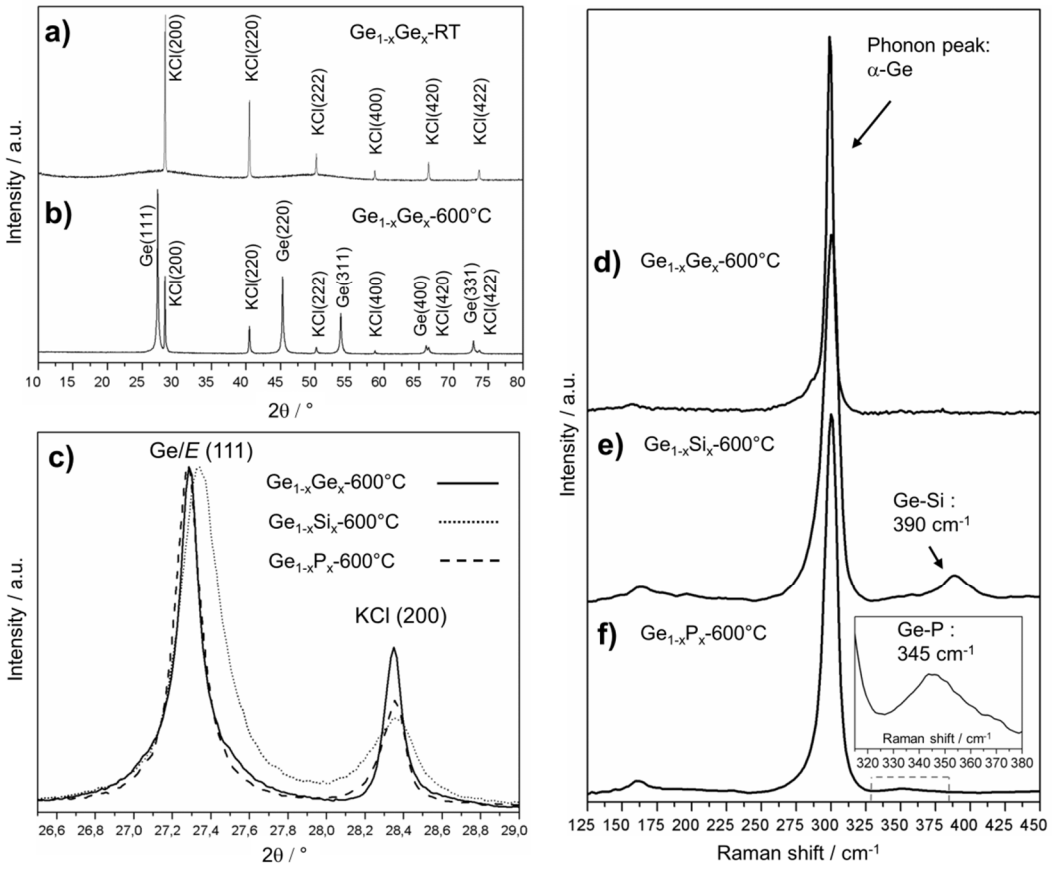

Figure S5. Powder X-ray diffractograms and Raman spectra of the products obtained by reacting K_4Ge_9 with ECl_n in toluene (reaction 2. 2): a/b) Powder XRD of the a) $Ge_{1-x}Ge_x$-RT and b) $Ge_{1-x}Ge_x$-600°C. The reflections of potassium chloride and α-Ge are labelled with the corresponding *hkl* indices. c) Magnified section of the diffractograms recorded from $Ge_{1-x}Ge_x$-600°C (solid line), $Ge_{1-x}Si_x$-600°C (dotted line) and $Ge_{1-x}P_x$-600°C (dashed line), respectively. Potassium chloride formed as a side product was used as internal standard. The (111) reflection is shown and a shift to higher diffraction angles can be observed in case of $Ge_{1-x}Si_x$-600°C d-f) Raman spectra of the crystallized products obtained with ECl_n. The optical phonon peak of α-Ge is visible at 298 cm^{-1}. d) $Ge_{1-x}Ge_x$-600°C: exclusively the phonon peak of α-Ge at 298 cm^{-1} appears, e) $Ge_{1-x}Si_x$-600°C: additionally to the phonon peak a signal at ~ 390 cm^{-1} corresponding to Ge-Si vibration mode appears;[3] f) $Ge_{1-x}P_x$-600°C: additionally to the phonon peak a signal at ~ 350 cm^{-1} corresponding to Ge-P vibration mode appears.[4]

Table S1. Composition (in at. %) of $Ge_{1-x}E_x$-RT and $Ge_{1-x}E_x$-600°C (*E* = Si, P) determined by EDX. All values are given in atomic percent (at%). *The calculated values (rounded to integers) refer to the stoichiometry of the reactions shown below the table and in general terms in the main paper in Figure 2, respectively.

Elements	$SiCl_4$			PCl_3		
	calculated* [at%]	$Ge_{1-x}Si_x$-RT [at%]	$Ge_{1-x}Si_x$-600°C [at%]	calculated* [at%]	$Ge_{1-x}P_x$-RT [at%]	$Ge_{1-x}P_x$-600°C [at%]
Ge	50	52	49	49	49	45
Si	6	7	9	0	0	0
P	0	0	0	7	6	3
K	22	21	21	22	24	27
Cl	22	20	21	22	21	25

$$K_4Ge_9 + SiCl_4 \longrightarrow 4KCl + 9Ge + Si$$

$$3K_4Ge_9 + 4PCl_3 \longrightarrow 12KCl + 27Ge + 4P$$

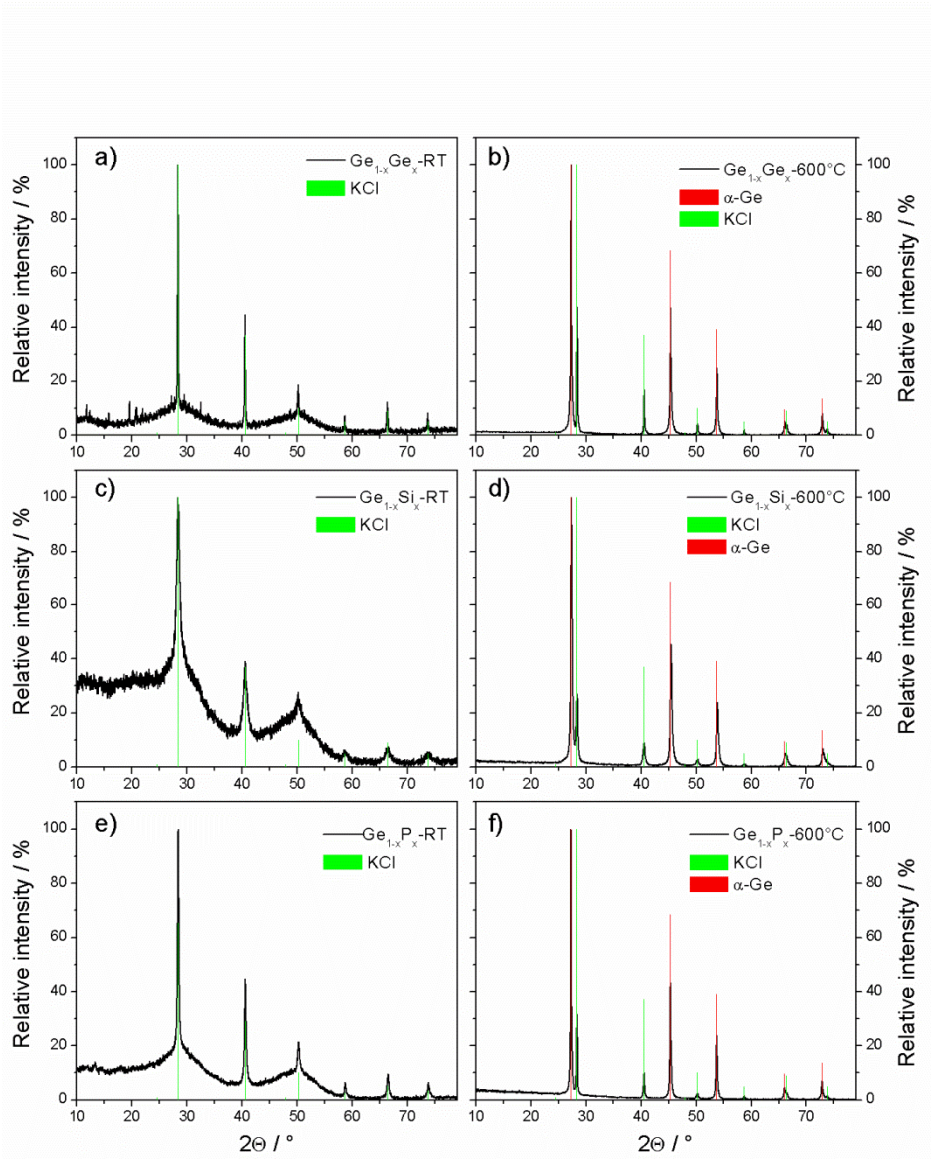

Figure S6. Powder X-ray diffractograms of reaction products of K_4Ge_9 with ECl_n in toluene as prepared (left column) and after annealing at 600°C for one hour (right column): a) $Ge_{1-x}Ge_x$-RT; b) $Ge_{1-x}Ge_x$-600°C; c) $Ge_{1-x}Si_x$-RT; d) $Ge_{1-x}Si_x$-600°C; e) $Ge_{1-x}P_x$-RT ; f) $Ge_{1-x}P_x$-600°C.

2. 3 Reaction of K_4Ge_9 with *E*Cl_n in gas phase

In another series of experiments the gas phase reactions of bulk K_4Ge_9 with $GeCl_4$ were investigated. In a typical procedure, solid K_4Ge_9 (50 mg, 0.062 mmol) and a small glass tube containing $GeCl_4$ (542 µl, 75 eq) were placed into a Schlenk tube. The sealed Schlenk tube was kept at room temperature for two weeks resulting in a black reaction product after partial evaporation of $GeCl_4$. The obtained product is denoted as gas-$Ge_{1-x}Ge_x$-RT. A portion of the product was annealed for one hour at 600°C; the obtained product is denoted as gas-$Ge_{1-x}Ge_x$-600°C. The products were characterized using powder X-ray diffraction (Figure S7).

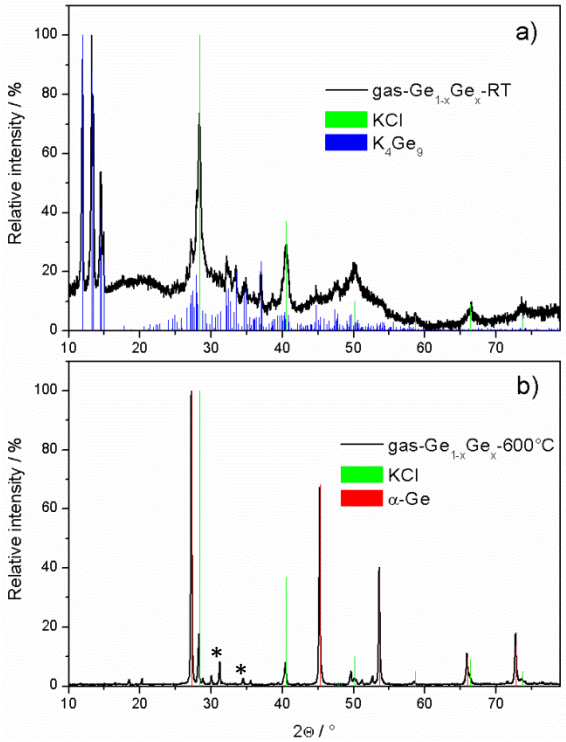

Figure S7. Powder X-ray diffractogram of the reaction product of K_4Ge_9 with ECl_n in gas phase (reaction 2.3): a) before annealing, gas-$Ge_{1-x}Ge_x$-RT, and b) after annealing for one hour at 600°C, gas-$Ge_{1-x}Ge_x$-600°C. As visible from the difractograms, potassium chloride and germanium are formed, however only a fraction of the bulk K_4Ge_9 reacted with $GeCl_4$. After annealing, not reacted clusters are thermally coupled to a solid germanium phase. Unknown reflections are labelled with asterisk.

3 Fabrication and characterization of inverse opal structured germanium films

3. 1 Fabrication of the PMMA opal template

Monodisperse PMMA beads were synthesized according to a method described elsewhere.[5] Thereby, methylmethacrylate (35.5 g, 0.35 mol) was stirred in 98 mL water at 90 °C for 1 h. Afterwards, $K_2S_2O_8$ (56.0 mg, 0.21 mmol) solved in 2 mL water was added, and the mixture was stirred at 90 °C for 2 h. After cooling down to room temperature the formed PMMA beads were centrifuged, washed with water several times and finally dried at 100°C. Dry PMMA beads (1.5 g) were stirred for one week in 8.5 ml water and daily ultrasonicated for 15 min to break up agglomerates. Average size of PMMA beads determined by dynamic light scattering (DLS) was 200 nm. The opal templates were fabricated by dip- or spin-coating 15 wt% PMMA dispersion on desirable substrates and dried for 4 hours at 100°C *in vacuo*. The substrates (silicon, silica, sapphire, ITO or FTO) were cleaned with water/surfactant, ethanol and acetone by ultrasonication for 15 min, respectively, then treated with an oxygen-plasma.

3. 2 Fabrication of inverse opal structured germanium films

PMMA opal template described in 3.1 was infiltrated with a solution of K_4Ge_9 in *en* grade A (concentration 50 mg/ml) by drop casting. For film fabrication via thermal solidification of clusters, the dried K_4Ge_9/PMMA composite was annealed *in vacuo* at 5min/500°C and 1h/600°C in Ar (films as-prepared denoted with α-Ge-INOP: INOP = inverse opal). Film fabrication via cluster cross-linking was done by treating the dried K_4Ge_9/PMMA composite with $GeCl_4$ or PCl_3 vapor at room temperature, respectively. Therefore, the K_4Ge_9/PMMA composite was stored within a glass vessel containing vaporous $GeCl_4$ or PCl_3 for at least one week at room temperature, respectively. PMMA was removed either by dissolution in tetrahydrofurane (*thf*) or flash-annealing (5 min at 500°C) *in vacuo*. Potassium chloride was washed out by extracting the films for one hour with dimethylsulfoxide (*dmso*) (films as-prepared denoted with *a*-$Ge_{1-x}E_x$-INOP). To enhance the crystallinity of the germanium morphologies the films were additionally annealed for one hour at 600°C (films as-prepared denoted with α-$Ge_{1-x}E_x$-INOP). The SEM images and EDX characterization of the obtained films is shown in Figure S8, XRD patterns and estimated crystalline domain size in Figure S9 and Table S2, respectively; and Raman spectra of films with different dopands in Figure S10.

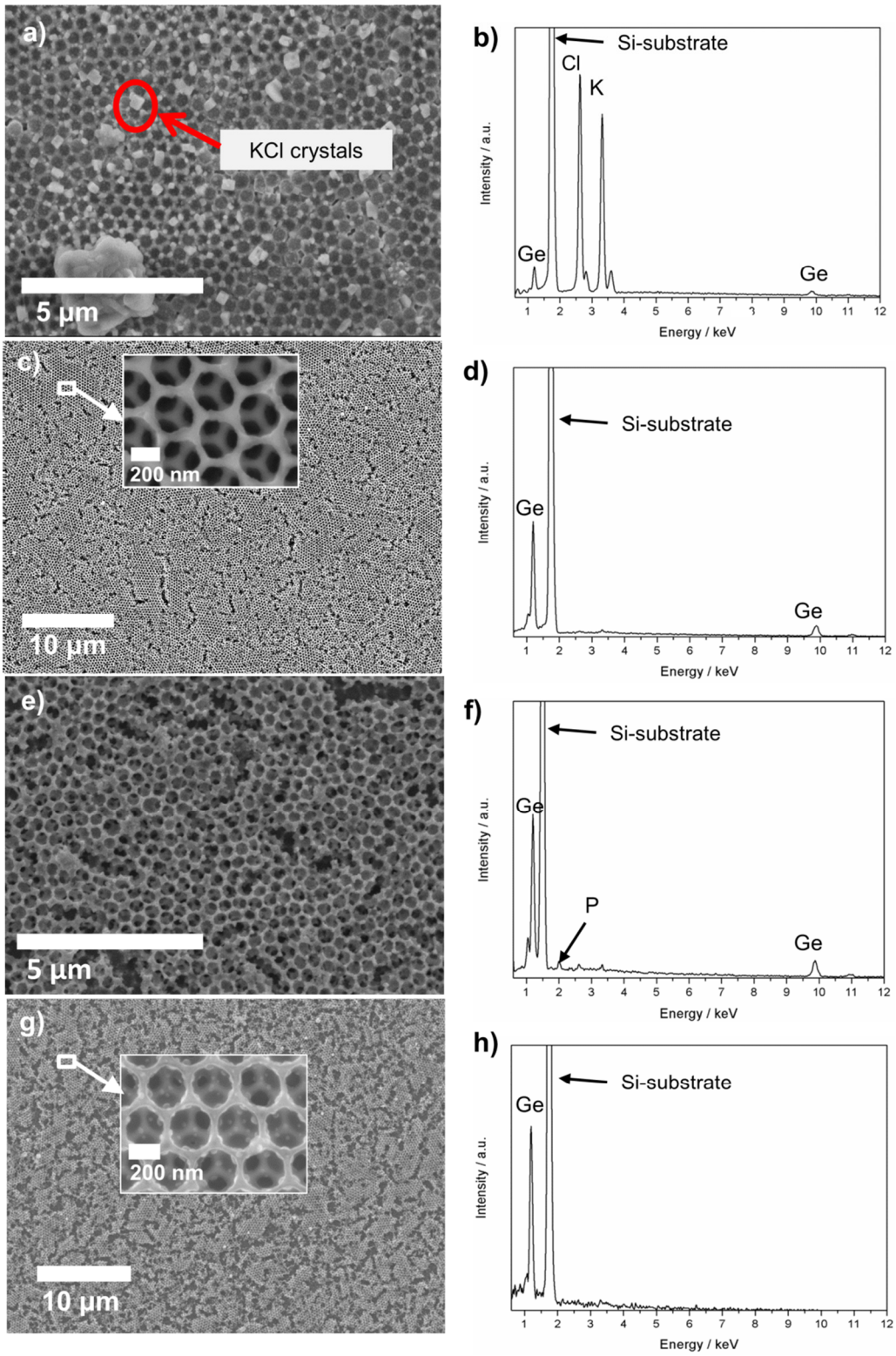

Figure S8. SEM micrographs (left column) and EDX spectra (right column), of a/b) a film after cross-linking with vaporous $GeCl_4$ and before washing with *dmso* (*a*-$Ge_{1-x}Ge_x$/KCl/PMMA) : cubic shaped crystals consist of potassium chloride as confirmed by EDX, c/d) a film after flash-annealing (5min/500°C) and washing with *dmso* (*a*-$Ge_{1-x}Ge_x$-INOP): PMMA and potassium chloride are removed as indicated by EDX, e/f) a phosphorous doped germanium film fabricated via cross-linking with PCl_3 (*a*-$Ge_{1-x}P_x$-INOP). In EDX phosphorous is visible, g/h) a film fabricated by thermal solidification of clusters (α-Ge-INOP).

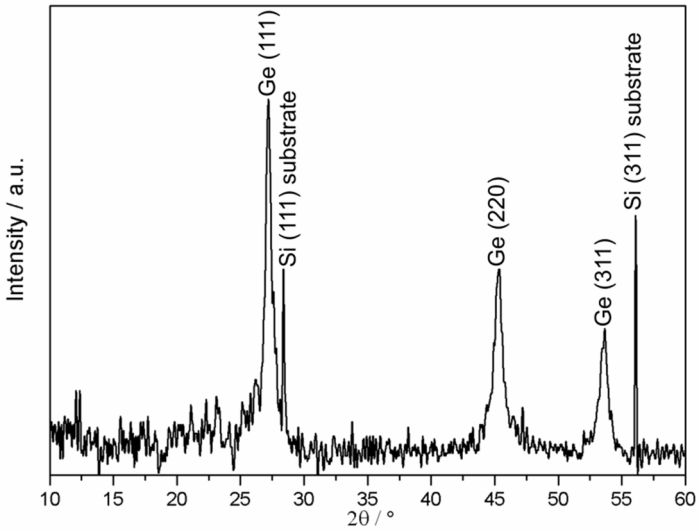

Figure S9. X-ray diffractogram (Cu) of α-$Ge_{1-x}Ge_x$-INOP. The diffractogram was used to estimate the crystallite sizes with the Scherer Equation (see Table S2).

Table S2. XRD data used to evaluate the crystallite sizes for α-$Ge_{1-x}Ge_x$-INOP with the Scherrer Equation.

	hkl	Reflex 2Theta [°]	half width [°]	corrected half width [°]	Crystallite Size [nm]
Ge	111	27,19	0,5	0,5	17
	220	45,33	0,8	0,8	11
	311	53,65	0,7	0,7	13
Si Standard	111	28,38	0,1		
	311	56,09	0,1		

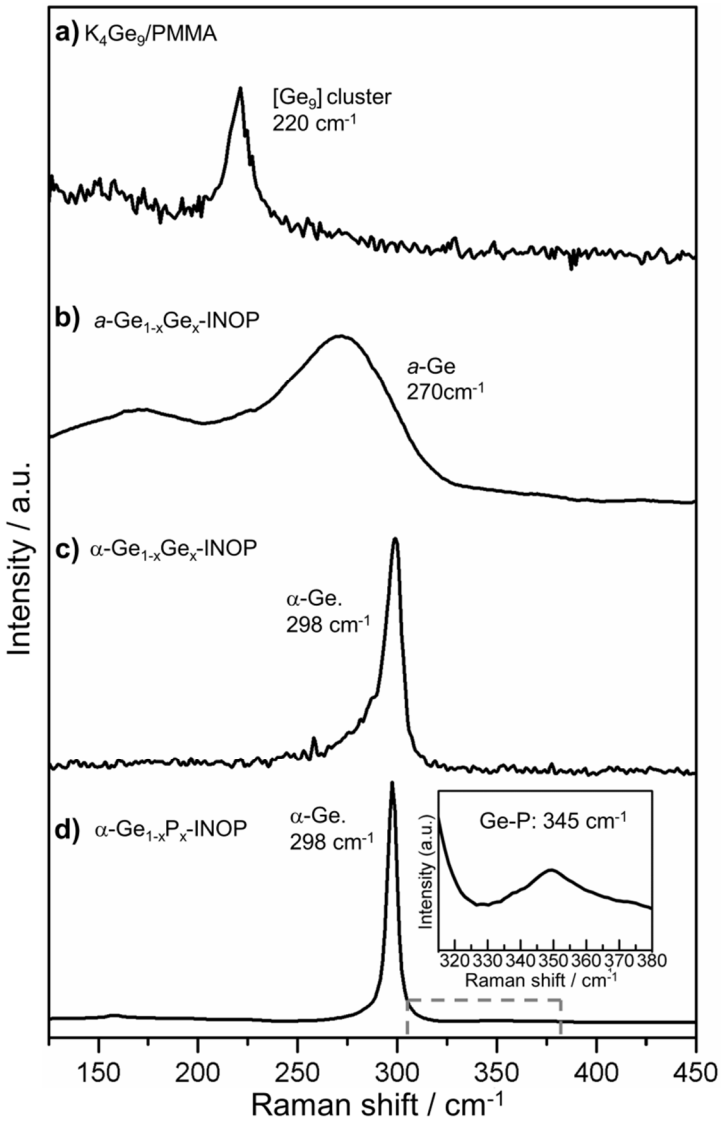

Figure S10: Raman spectra of a) K_4Ge_9/PMMA composite and b-d) inverse opal structured germanium films: b) *a*-$Ge_{1-x}Ge_x$-INOP, c) α-$Ge_{1-x}Ge_x$-INOP, d) α-$Ge_{1-x}P_x$-INOP. Inlay: magnified section of Raman spectrum d) to emphasize the Ge-P vibration mode.

3. 3 Characterization of inverse opal structured germanium films using grazing incidence small angle X-ray scattering (GISAXS)

GISAXS experiments were performed at the SAXS beamline of the Elettra synchrotron at Trieste, Italy. The incident angle for the measurements was chosen well-above the critical angle of the material (0.3°), thereby ensuring penetration of the x-ray beam into the film volume and decoupling of the specular and the Yoneda peak positions in the scattering signal. The wavelength of the synchrotron radiation used was 1.5 Å (x-ray energy of 8.26 keV). A sample-detector distance of 2.047 m was fixed for the measurements using vertical horizontal beam dimensions of 200 µm x 3 mm. The scattered signal was detected by a Pilatus 1M detector with pixel dimensions of (172 x 172) μm^2. It is a noise-free detector with a signal readout time of 2.3 ms. A semi-transparent beamstop was used for the data acquisition in order to shield the detector from high intensity specular and off-specular scattering. Careful adjustment of the counting time was done in order to prevent beam damage to the film. The horizontal line cut from the 2d GISAXS data is performed by averaging over seven pixels along the q_z direction (from 0.53 – 0.58 nm^{-1}).

For *a*-$Ge_{1-x}Ge_x$-INOP, grazing small angle X-ray scattering measurements were conducted in order to investigate the volume-morphology. The corresponding two dimensional (2d) GISAXS data of the film is shown in Figure S11. The highest intensity in the signal is observed at the Yoneda peak position, which is located at the critical angle of the material and thus materials specific.[6] In case of smooth films, the highest intensity in the 2d GISAXS data would be expected at the position of the specular peak. Due to the high surface roughness of the film under investigation, which was confirmed by profilometric measurements, and the resulting enhanced diffuse scattering this is not the case in the present data. The rectangular feature observed in the 2d GISAXS data in the Yoneda region (from q_y = -0.08 nm^{-1} to 0.04 nm^{-1}) originates

from the used semi-transparent beamstop. Additionally, lateral scattering signals are observed along the q_y direction, indicating the presence of lateral structures in the volume of the film. Quantitative information from the 2d GISAXS data is obtained by analyzing the horizontal line cut (along the q_y direction) as indicated by the dashed arrow in Figure S11a. The horizontal line cut along with the fit to the data is plotted in Figure S11b. The two peaks observed in the horizontal line cut correspond to two prominent lateral structural length scales. Modeling is performed in the framework of distorted wave Born approximation (DWBA).[7, 8] The model chosen for fitting the horizontal line cut comprises of 1d paracrystalline lattice (structure factor) decorated with cylindrically shaped objects (form factor). To fit the data, three structure and form factors are used together with a Lorentzian-shaped resolution function. Both, the structure and the form factors, are considered to follow a Gaussian distribution function. All parameters obtained from the fit are listed in Table S3. The form factor corresponds to the Ge nanoparticles or clusters of nanoparticles, whereas the structure factor represents the average centre-to-centre distances between these nanoparticles or clusters of nanoparticles. Hence, the average pore size of the film is calculated using the equation:[9]

Pore size = Structure factor – 2 ˣ radius of form factor (Equation 1)

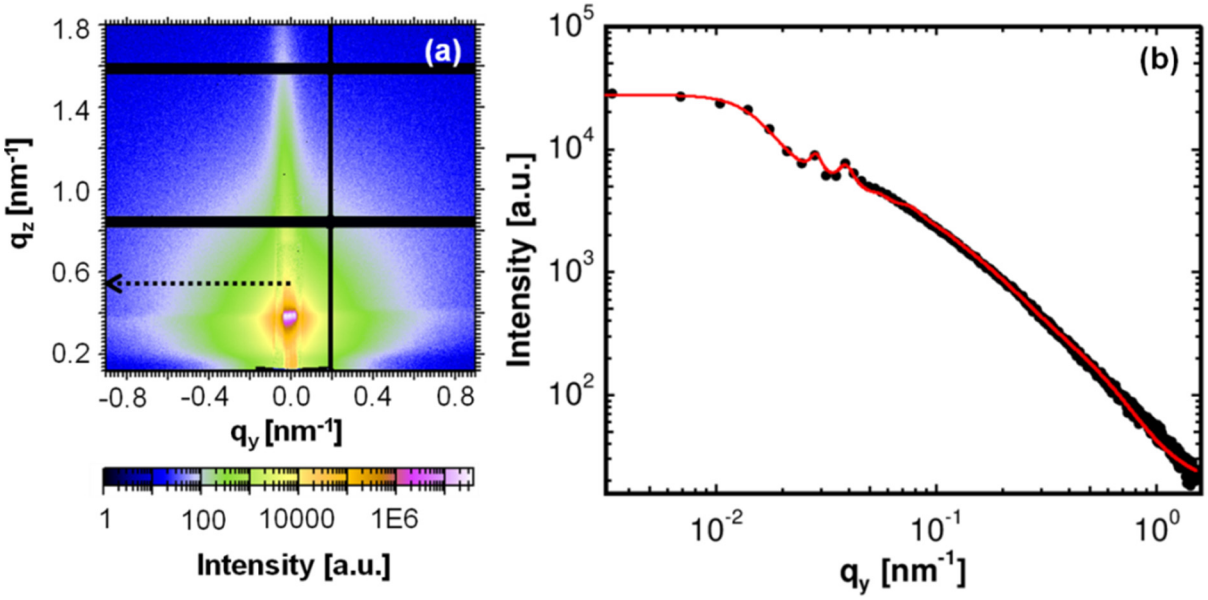

Figure S11. a) 2d GISAXS data of *a*-$Ge_{1-x}Ge_x$-INOP. The high intensity Yoneda peak is visible behind the corrected semi-transparent beamstop. The horizontal dashed arrow represents the cut position for quantitative analysis of the data. The horizontal and the vertical black stripes are the inter-module gaps of the detector. The intensity bar is shown at the bottom of the image. b) Horizontal line cut (symbols) along with a fit (solid red line) as described in the text.

Table S3: Summary of different structural length scales in the film volume as obtained from the fit to the GISAXS data, shown in Figure S11b. The corresponding Gaussian size distribution for all length scales are also extracted from the fit.

structure factor [nm]	distribution [nm]	Form factor radius [nm]	distribution [nm]
220 ± 5	14	8.5 ± 1	8.1
160 ± 4	12	4.4 ± 0.6	4.3
40 ± 10	19	2.1 ± 0.3	1.3

3. 4 Characterization of inverse opal structured germanium films using X-ray photoelectron spectroscopy (XPS)

XPS spectra have been recorded from *a*-$Ge_{1-x}Ge_x$-INOP of which the PMMA either was removed by flash-annealing or dissolution in *thf*, respectively. XPS spectra are shown in Figures S12 and S13. XPS analysis was performed using a VSW HA 100 hemispherical analyzer and a VSW TA10 X-ray source providing non monochromatized Al K_α radiation (Al K_α = 1486.6 eV). Germanium films were cleaned by argon sputtering using a VSW AS10 ion source (E = 1 keV). XPS peaks were fitted with Gaussians convoluted with Doniach-Sunjic functions.[10] Shadowed areas in the porous network are not reached by the Ar^+-ions. Hence, even at very long sputtering times, contributions of germanium oxides are visible in the XPS spectra. Moreover, due to a higher inelastic mean free path for XPS 3d electrons than for XPS 2p electrons the 3d

electrons probe deeper into the framework's surface. As, independently of sputtering times, generally higher contributions of Ge^0 to the 3d signals than to the 2p signals were found, this is another evidence of surficial germanium oxides. Surface oxides most likely occur as the films have been exposed to air for a short time during transfer into the XPS chamber. XPS spectra of films of which the PMMA was removed by dissolution show analogous results.

Figure S12. XPS spectra of *a*-$Ge_{1-x}Ge_x$-INOP (PMMA removed by dissolution in *thf*) in dependence of sputtering times. Left: $2p_{3/2}$- and right Ge 3d signals.

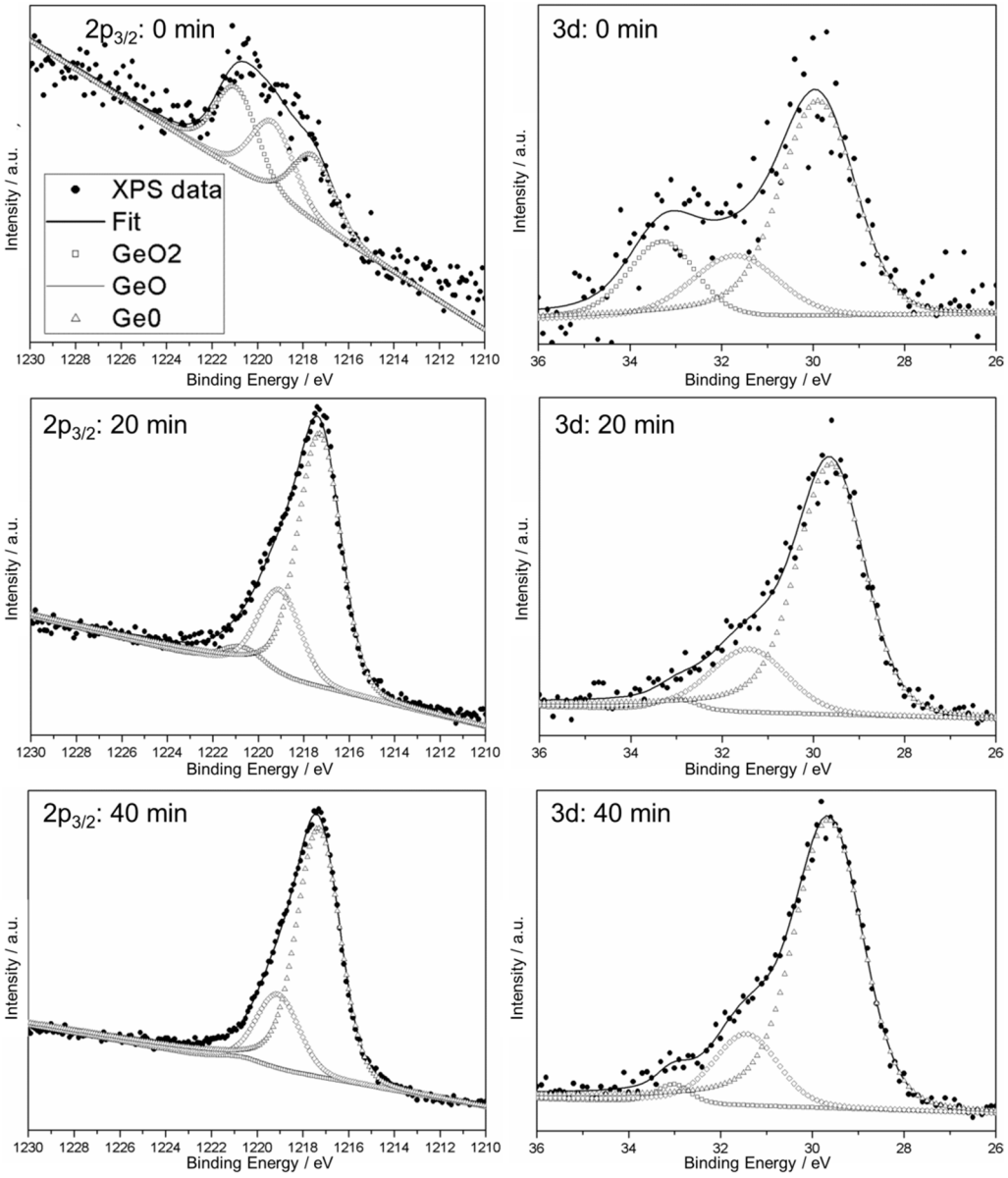

Figure S13. XPS spectra of *a*-$Ge_{1-x}Ge_x$ inverse opal film (PMMA removed by flash-annealing 500°C/5min) in dependence of sputtering times. Left: $2p_{3/2}$- and right Ge 3d signals.

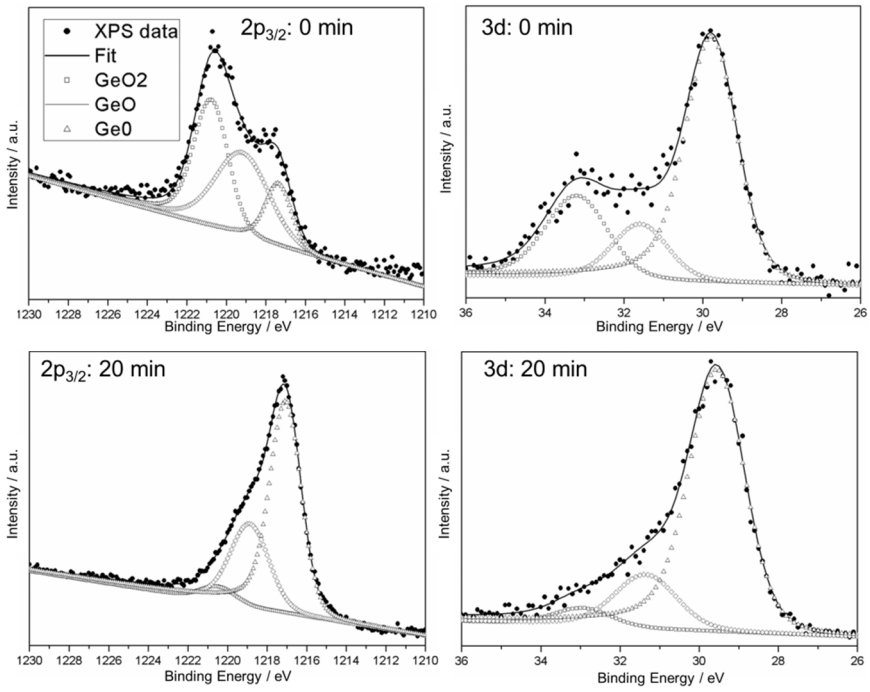

Table 4. Contributions of Ge^0 in dependence of sputter time and probed orbital. a) XPS spectra in Figure S12, b) XPS spectra in Figure S13

a)

Sputter Time [min]	3d: Ge^0 [%]	$2p_{3/2}$: Ge^0 [%]
0	60.8	29.8
20	76.4	70.4
40	78.8	75.6

b)

Sputter Time [min]	3d: Ge^0 [%]	$2p_{3/2}$: Ge^0 [%]
0	61.5	16.7
20	77.2	64.6

4 References

[1] M. M. Bentlohner, W. Klein, Z. H. Fard, L.-A. Jantke, T. F. Fässler, *Angew. Chem. Int. Ed.* **2015**, 54, 3748-3753; *Angew. Chem.* **2015**, 127, 3819-3824.

[2] T. F. Fässler, *Coord. Chem. Rev.* **2001**, *215*, 347-377.

[3] H. H. Burke, I. P. Herman, *Phys. Rev. B* **1993**, *48*, 15016-15024.

[4] N. Fukata, K. Sato, M. Mitome, Y. Bando, T. Sekiguchi, M. Kirkham, J.-i. Hong, Z. L. Wang, R. L. Snyder, *ACS Nano* **2010**, *4*, 3807-3816.

[5] T. Wang, O. Sel, I. Djerdj, B. Smarsly, *Colloid. Polym. Sci.* **2006**, *285*, 1-9.

[6] Y. Yoneda, *Phys. Rev.* **1963**, *131*, 2010-2013.

[7] P. Müller-Buschbaum, in *Polymer Surfaces and Interfaces* (Ed.: M. Stamm), Springer Berlin Heidelberg, **2008**, pp. 17-46.

[8] R. Lazzari, *J. Appl. Crystallogr.* **2002**, *35*, 406-421.

[9] K. Sarkar, C. J. Schaffer, D. M. Gonzalez, A. Naumann, J. Perlich, P. Muller-Buschbaum, *J. Mater. Chem. A* **2014**, *2*, 6945-6951.

[10] S. Doniach, M. Sunjic, *J. Phys. C* **1970**, *3*, 285.

5.6 Fabrication of inverse opal structured germanium films and their application in hybrid solar cells with P3HT

M. M. Bentlohner, S. Geier, M. A. Giebel, M. Loch, L. Song, P. Lugli, P. Müller-Buschbaum, D. Fattakhova-Rohlfing, T. F. Fässler *

Manuscript for publication

5.6.1 Contents and Contributions

In the scope of the publication “Fabrication of inverse opal structured germanium films and their application in P3HT hybrid solar cells“, the wet chemical fabrication of inverse opal structured germanium films over extensive areas on transparent substrates as well as their application in hybrid solar cells are presented.

The present publication was authored in the course of this Ph. D. thesis. The inverse opal structured films were fabricated by infiltration of a poly(methylmethacrylat) opal with solutions of $[Ge_9]^{4-}$ Zintl anions in water-free *en* and controlled oxidation of the clusters to an undoped and phosphorus containing germanium phase, by reaction with $GeCl_4$, PCl_3 and PPh_3, respectively. Spray- and spin-coating techniques were applied to fabricate optically homogenous inverse opal films across extensive areas on different substrates such as fluorine doped tin oxide/titanium dioxide (FTO/TiO_2) and glass. Except of spin- and spray-coating all preparation steps for the germanium inverse opals were done in the course of the present work. Spin- and spray coating was conducted in the group of Prof. Dr. Paolo Lugli (Technical University of Munich) by Marius Loch. Initial investigations on the phosphorus doping of the films with PPh_3 were conducted in a practical training and master thesis by Sebastian Geier, which were both supervised in the course of the present work. UV-Vis spectra of the films indicate that the optical properties of the germanium inverse opals can be tuned by doping and annealing. The UV-Vis spectra were recorded in the group of Prof. Dr. Thomas Bein (University of Munich) by Enrico Greul and the data were evaluated in the scope of this thesis. For fabrication of hybrid solar cells, germanium inverse opals were deposited on FTO/TiO_2. The pores of the germanium inverse opals were filled with P3HT by spin-coating the films with a solution of P3HT in chlorobenzene. The successful filling of the pores with P3HT was proven by scanning electron microscopy. For extraction of the photo-generated charges from the solar cell, gold contacts were deposited on top of the P3HT/Ge/TiO_2/FTO composite. Efficiency tests with the Au/P3HT/Ge/TiO_2/FTO prototypes in a solar simulator indicate that working photovoltaic cells were obtained by the presented method. The filling of the pores with P3HT and the deposition of gold contacts as well as efficiency tests on the resulting Au/P3HT/Ge/TiO_2/FTO hybrid solar cells were done at the chair of Prof. Dr. Peter Müller-Buschbaum (Technical University of Munich) by Lin Song.

5.6.2 Manuscript for Publication

Fabrication of inverse opal structured germanium films and their application in hybrid solar cells with P3HT

Manuel M. Bentlohner, Sebastian Geier, Michael A. Giebel, Marius Loch, Lin Song, Paolo Lugli[#], Peter Müller-Buschbaum[¬], Dina Fattakhova-Rohlfing[†], Thomas F. Fässler [*]

[*]
Manuel M. Bentlohner, Sebastian Geier, Michael A. Giebel, Prof. Dr. Thomas F. Fässler
Department Chemie, Technische Universität München
Lichtenbergstraße 4, 85747 Garching, Germany
E-mail: thomas.faessler@lrz.tu-muenchen.de

[¬]
Lin Song, Prof. Dr. Peter Müller-Buschbaum
Physik-Department, Lehrstuhl für Funktionelle Materialien Technische Universität München
James-Franck-Straße 1, 85747 Garching
Email: muellerb@ph.tum.de

[#]
Marius Loch, Prof. Dr. Paolo Lugli
Institut für Nanoelektronik, Technische Universität München
Theresienstrasse 90, 80333 München
Email: lugli@tum.de

[†]
PD Dr. Dina Fattakhova-Rohlfing
Ludwig Maximilian Universität München
Butenandtstrasse 11 (Haus E), 81377 München
Email: dina.fattakhova@cup.uni-muenchen.de

Key Words

Zintl clusters, photovoltaic, hybrid solar-cell, band gap, doping

Abstract

Inverse opal structured inorganic non-oxide semiconductor films exhibit valuable characteristics for application in electronic devices, such as photovoltaics and batteries. In this context germanium and silicon are in particular interesting due to their broad adjustability of optoelectronic properties and high charge carrier mobility. We present the wet chemical fabrication of inverse opal structured germanium films, utilizing $[Ge_9]^{4-}$ Zintl anions as Ge precursor, for the application in Au/P3HT/Ge/TiO_2/FTO hybrid solar cells. The inverse opal structured films were fabricated by infiltration of a poly(methylmethacrylat) opal with solutions of $[Ge_9]^{4-}$ Zintl anions in ethylenediamine and controlled oxidation of the clusters to elemental germanium. Spray- and spin-coating techniques were applied to fabricate optically homogeneous inverse opal films across extensive areas on transparent and conductive substrates. By the oxidation of clusters with PCl_3 or PPh_3, phosphorus doped germanium inverse opals were obtained. UV-VIS spectra indicate that the optical properties of the germanium inverse opals can be tuned by doping and annealing. For fabrication of hybrid solar cells, (doped) germanium inverse opals were deposited on TiO_2 coated fluorine doped tin oxide (FTO). The pores of the inverse opals were filled with P3HT by spin- coating, which was proven by scanning electron microscopy. Gold contacts were deposited on top of the P3HT/Ge/TiO_2/FTO composite, and working Au/P3HT/Ge/TiO_2/FTO hybrid solar cells were demonstrated.

Introduction

The world's increasing need for energy triggers the search for low cost and efficient photovoltaic devices. So far, solar cells based on inorganic bulk-materials, such as silicon, hold the majority of commercially applied photovoltaics due to their relatively high efficiency, but energy expensive production and rigidity make alternative approaches interesting for the future.[1] Organic photovoltaics, with its key advantage of cheap and easy roll-to-roll production, are one focus of research, but rather low efficiencies and in particular short life times, have hindered a large scale commercialization, so far.[2] To tackle these problems the idea of combining the advantages of organic and inorganic materials in hybrid solar cells has emerged.[1, 3] A prominent design concept for hybrid solar cells is the combination of nanostructured inorganic film morphologies with organic semiconducting polymers. It is necessary to establish continuous and well-ordered interpenetrating substructures with harmonized optoelectronic properties, so that electron-hole pairs formed by the incoming light can be efficiently separated at the materials' interfaces. [1]

A key step for the fabrication of efficient and sustainable hybrid solar cells is the development of scale- and controllable fabrication methods for the nanostructured inorganic frameworks.[1] In particular, wet chemical bottom-up methods, based on the assembly of molecular precursors, are in high demand due to their general potential of simplicity, scalability and applicability, e.g. in printing or spray processes. [4] So far, primarily metal oxides have been applied in inorganic-organic hybrid cells, however, due to broadly tunable optoelectronic properties and high charge carrier mobility of silicon and germanium, the attention was drawn to these materials, too.[5]

Synthetic protocols for germanium/silicon nanoparticles and nanowires are well established, but the fabrication of film morphologies with three dimensionally ordered porous structures are less pronounced [5-7

Recently, we presented a facile and flexible wet chemical method utilizing soluble $[Ge_9]^{4-}$ Zintl clusters as precursors for the wet chemical fabrication of inverse opal structured germanium films (Ge-*INOP*) with tunable composition.[8] Germanium is an interesting material for application in photovoltaics (PV) as it exhibits a lower band gap compared to silicon, leading to light absorption already in the near infrared region and enhancing the harvesting of low energy photons.[9] Compared to

conventional flat materials, inverse opal structured materials exhibit both, high interface areas for efficient exciton dissociation and better light absorption due to their photonic band structure.[10] Besides the intrinsic properties of germanium, it is mandatory to fabricate continuous and homogeneous germanium frameworks of several square centimeters, to avoid short cuts and to enable extraction of the photo-generated charges at the electrodes. Consequently, one milestone is the development of coating techniques allowing the fabrication of homogeneous germanium inverse opals across extensive areas.

In this study we present the wet chemical fabrication of inverse opal structured germanium films (Ge-*INOP*), utilizing $[Ge_9]^{4-}$ Zintl anions as Ge precursor [8], by spray- and spin-coating techniques and their application in Au/P3HT/Ge/TiO_2/FTO hybrid solar cells. Different methods for controlled oxidation of clusters and introduction of phosphorus into the film morphologies are shown. The influence of doping and thermal annealing on the optical properties of the inverse opal structured films was investigated by UV-Vis-spectroscopy.

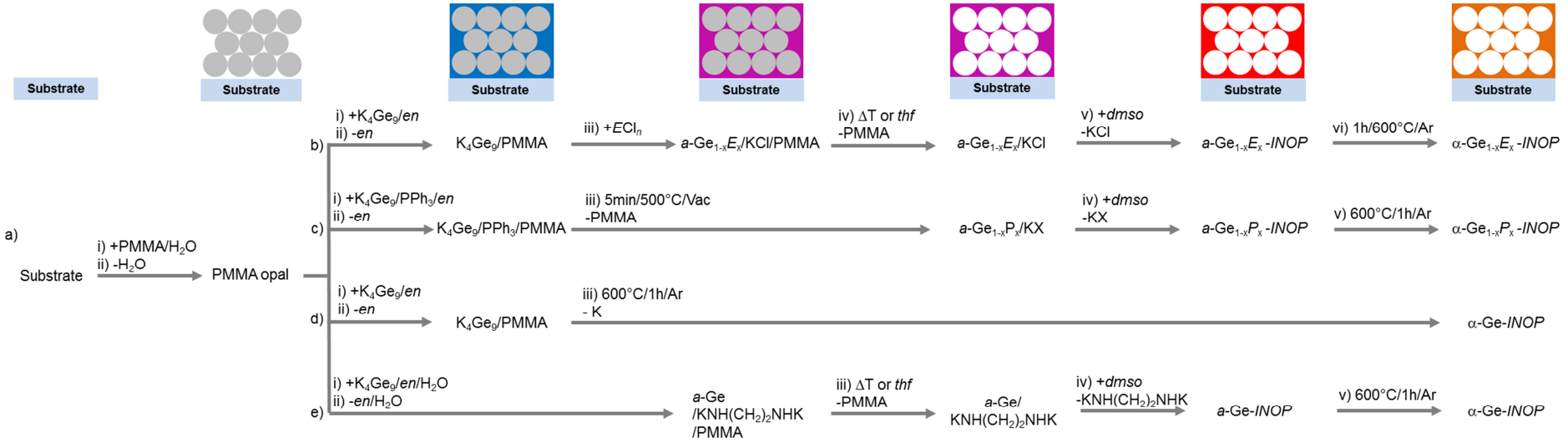

Figure 1. a) Fabrication of PMMA opals by coating a substrate with a suspension of monodisperse PMMA beads in water. b-e) Fabrication of inverse opal structured germanium films by transfer of $[Ge_9]^{4-}$ clusters into the voids of a PMMA opal and oxidation of the clusters to elemental germanium. b) *E*Cl*n*-method (*E* = P, *n* = 3; *E* = Ge, *n* = 4), c) PPh_3-method, d) annealing-method and e) *en*/H_2O-method. In all methods PMMA is removed either by pyrolysis or dissolution in *thf*. Side products are removed by washing the films with *dmso*.

Results and Discussion

For the fabrication of germanium inverse opals films, a poly(methylmethacrylate) (PMMA) opal template was assembled on a substrate (Si, SiO_2, TiO_2/FTO, Al_2O_3; area = 1-4 cm^2), by coating the substrate with a suspension of monodisperse PMMA beads (250-300 nm) in water (Figure 1a). The PMMA was applied either by dip-, spin- or spray-coating (experimental details see SI chapter 2.1). By dip-coating continuous and thick PMMA opals with an extension of several square millimeters, but inhomogeneous film thickness are obtained (Figure S1). In contrast, spin-coating of PMMA leads to very thin (0-2 PMMA bead layers) and broken opals which are interfused by PMMA agglomerates (Figure S4). Spray-coating of PMMA leads to optically homogeneous films and the formation of agglomerates can be avoided (Figure S1). However, SEM investigations reveal covered regions with several (1-4) PMMA layers appear, beside non covered sections of the substrate.

The PMMA opals were dried for 4 h at 100 °C in fine vacuum in order to thoroughly remove water. Subsequently, the voids of the template structure were infiltrated with the Ge precursor solution by drop-casting or spin-coating and the Ge_9 clusters were oxidized to elemental germanium (Figure 1b-e, SI chapter 2.2.1 and 2.2.2). Apart from the annealing-method (Figure 1d), the PMMA opal was preferably removed by flash-annealing (5 min at 500°C in vacuum)[8, 11], whereby amorphous (denoted with prefix *a*) and mechanically stable films were obtained. Alternatively to pyrolysis, PMMA can be removed by dissolution in tetrahydrofuran (*thf*), either before or after cluster oxidation, but the mechanical stability of such films is worse. Finally, side products were washed out by extracting the films with dimethylsulfoxide (*dmso*). By annealing of the amorphous films for 1h at 600°C the crystallinity can be enhanced (films denoted with prefix α).[8]

SEM investigations show that the homogeneity of the PMMA opals directly transfers to the homogeneity of the obtained inverse opal structured films. In case of films prepared by dip-coating of PMMA and drop-casting of the Ge precursor solution, thick germanium inverse opal with an extension of several square millimeters are obtained (Figure 2 and Figure S2/S3). Profilometry shows that the thickness of such germanium inverse opals is 5-10 µm. In particular for drop-casting it is important to avoid an excess of the Ge precursor, as otherwise the porous framework is covered

by germanium crusts. In contrast, by spin-coating of both PMMA and the Ge precursor, very thin (monolayer) and inhomogeneous films are obtained, which are interfused by germanium particles with diameters of several micrometers (Figure S4). On the other hand films prepared by spray-coating of PMMA and spin-coating of the Ge precursor exhibit no particulate agglomerates and the films are macroscopically homogeneous across extensive areas (Figure 2b). In SEM thin and isolated regions with inverse opal structure are visible (Figure S5).

In particular, phosphorus doped germanium inverse opals are interesting for application in hybrid solar cells, due to their expectedly higher electrical conductivity, facilitating the extraction of negative charges from the device. Previously, we showed that the oxidation of clusters with strong Lewis acidic halides like $SiCl_4$ or PCl_3 allows composition tuning and doping of the inverse opal structured films ($Ge_{1-x}E_x$-*INOP*: E = Ge, Si, P) (Figure 1b). Thereby EDX (Figure S3) and Raman measurements show that *E* is implemented in the germanium framework.[8] In addition, the less Lewis acidic PPh_3 was applied for the fabrication of phosphorus doped films ($Ge_{1-x}P_x$-*INOP*) (Figure 1c). Previous investigations of *Belin* show that addition of PPh_3 to K_4Ge_9/*en*, forms stable solutions with intact Ge_9 clusters.[12] For film preparation we dissolved a mixture of PPh_3 and K_4Ge_9 in *en* and infused a PMMA opal with it. After evaporation of *en* a PMMA/K_4Ge_9/PPh_3 composite was obtained, which was annealed for 5 min at 500°C *in vacuo* and washed with *dmso* for 1h. SEM and EDX show inverse opal structured germanium containing only trace amounts of potassium. By annealing such films for 1 h at 600°C the inverse opal structure collapses and a porous material consisting of agglomerated particles (diameter 10-20 nm) emerges.

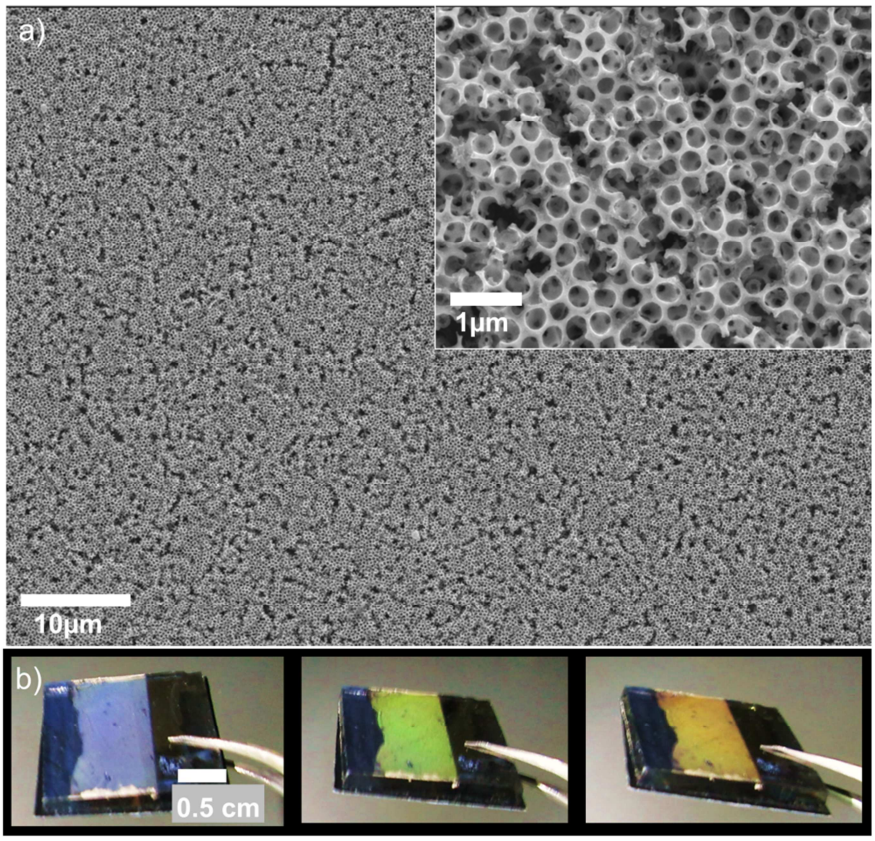

Figure 2. a) SEM micrograph of *a*-$Ge_{1-x}Ge_x$-*INOP*, fabricated by the *E*Cl*n*-method (Oxidizer: $GeCl_4$). Coating: dip (PMMA)/drop (K_4Ge_9). Inset: magnified sections of the films. b) Photography of *a*-$Ge_{1-x}Ge_x$-*INOP*, fabricated by the *E*Cl$_n$-method (Oxidizer: $GeCl_4$). Coating: spray (PMMA)/spin (K_4Ge_9). The film was illuminated with white light at different incident angles.

The tunable morphology, composition and crystallinity of inverse opal germanium films raise the question about the optical properties of such films. For clarification, we prepared amorphous and crystalline $Ge_{1-x}Ge_x$-*INOP* and $Ge_{1-x}P_x$-*INOP* by oxidation of clusters with $GeCl_4$, PCl_3 and PPh_3 and investigated the films by UV-VIS spectroscopy. PMMA/H_2O and the Ge precursor solutions were applied at glass-substrates by dip-coating and drop-casting, respectively. In UV-Vis the transmission (T) and reflectance (R) of the films were measured in the spectral range of 500-2400 nm. Therefrom, the absorption coefficients α and the band gaps of the films were evaluated (details see SI chapter 4)

The *a*-$Ge_{1-x}Ge_x$-INOP exhibits a band gap of approx. 1.1-1.2 eV which is close to literature reported values for *a*-Ge films.[13] In case of α-$Ge_{1-x}Ge_x$-*INOP* the band gap is 0.94 eV, whereas for monocrystalline germanium an indirect band gap of 0.6 eV is expected.[14] Our previous investigations show that annealing of *a*-$Ge_{1-x}Ge_x$-INOP films at 600°C for 1 h in Ar atmosphere leads to pore walls comprising nanocrystals

(diameter ca. 10 nm) embedded in an *a*-Ge matrix.[8] Consequently, the observed band gap of 0.94 eV for α-$Ge_{1-x}Ge_x$-*INOP* might be interpreted as a superposition of the band gaps of *a*-Ge and α-Ge. For the *a*-$Ge_{1-x}P_x$-INOP films the indirect band gap is 1.03 eV (oxidizer: PCl_3) and 0.95 eV (oxidizer: PPh_3), respectively. These lower values point for the successful doping of the Ge framework with phosphorus. [15]

With the germanium inverse opals, Au/P3HT/Ge/TiO_2/FTO hybrid solar cells were assembled (experimental details see SI chapter 5). For evaluation of the influence of the inverse opal structure on the solar cell efficiency, also flat germanium films (Ge-*FL*) were tested. For fabrication of Ge-*FL* (Figure S6), a thin inverse opal structured Ge layer was deposited on a FTO substrate by spray-coating of PMMA and spin-coating of the Ge precursor solution. The porous structure was filled with Ge precursor solution and the clusters were either reacted with ECl_n (E = P, n = 3; E = Ge, n = 4) or PPh_3. In this case the thin inverse opal structure acts as a bonding agent and allows the fabrication of thicker flat Ge films which do not delaminate from the substrate.

A poly(3-hexylthiophene-2,5-diyl) (P3HT) solution was spin cast on both, Ge-*INOP* and Ge-*FL*, using chlorobenzene as a solvent to establish the active layer of the solar cells. Gold contacts were deposited by physical vapor deposition to finalize the devices (Figure 3 and Figure S13). The efficiency of the obtained solar cells was tested in a solar simulator using AM1.5 test conditions.

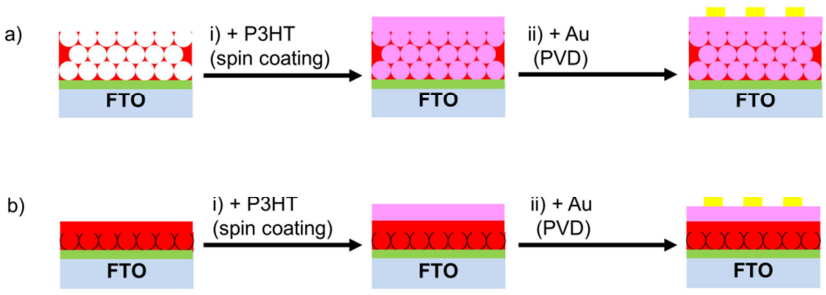

Figure 3. Assembly of Au/P3HT/Ge/TiO_2/FTO solar cells. a) Infiltration of an inverse opal germanium film with a solution of P3HT in chlorobenzene by spin-coating and deposition of gold contacts by physical vapor deposition (PVD). b) Coating of a flat germanium film with a solution of P3HT in chlorobenzene by spin coating and deposition of gold contacts.

The J-U curves (Figure 4 and SI Figure S16/Table S2) demonstrate that it is possible to assemble working hybrid solar cells both, with Ge-*INOP* and Ge-*FL* films, although the efficiency is low at this stage. As can be seen from SEM (Figure S14) is it possible to fill the pores of the Ge-*INOP* by spin-coating with P3HT/chlorobenzene. However, SEM also shows that only a fraction of the available pores is filled with P3HT. Moreover, in some areas P3HT only covers the walls of the porous framework. In order to enhance the efficiency of the hybrid solar cells both, the homogeneity of the Ge-*INOP* films as well as the filling of the pores with P3HT has to be improved.

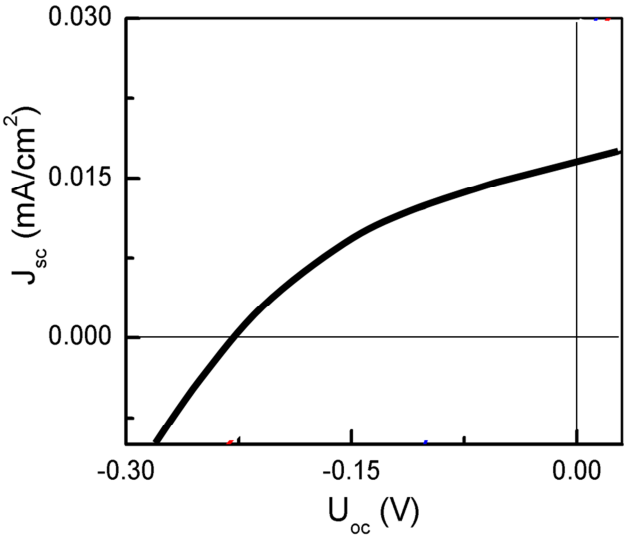

Figure S4. J-U curve of an Au/P3HT/*a*-Ge-*INOP*/TiO_2/FTO hybrid solar cell. The *a*-Ge-*INOP* was fabricated by the *en*/H_2O method. Coating: spin (PMMA)/spin (K_4Ge_9).

Conclusion

The presented results highlight the huge potential of $[Ge_9]^{4-}$ Zintl clusters as flexible building blocks for versatile wet chemical fabrication of undoped and doped inverse opal structured germanium films. Moreover, first tests on the application of germanium inverse opals in hybrid solar cells were successful, even though further improvements concerning the film homogeneity and filling of the pores with P3HT have to be done to enhance efficiencies. Morphological investigations with SEM indicate regular porosity for the films and hold out the prospect of advantageous application not only in photovoltaics but also in batteries, due to high interface areas.

Additionally, optoelectronic properties of such films were found to be tunable by annealing and doping, giving the opportunity to adapt the properties of the germanium frameworks to the organic counterpart of the hybrid solar cells. Preliminary results on the application of our wet chemical precursors in spray- and spin-coating processes indicate that the production of larger areas of the porous films is possible. It is also a subject of our research to apply other group III – V halogenides for cluster-crosslinking and fabricate undoped and doped inverse opal structured germanium/silicon films by this method.

Experimental section

Fabrication of Au/P3HT/Ge/TiO2/FTO hybrid solar cells. Germanium films (flat or inverse opal structured) were deposited on FTO substrates, which were covered with a thin layer of TiO_2, according to the methods shown in Figure 1 and Figure S6, respectively. Subsequently, the germanium films were coated/infiltrated with P3HT/chlorobenzene (20 mg/ml) by spin-coating (Delta 6 RC TT, Süss MicroTec Lithography GmbH, 2000 rpm / 60 s). After evaporation of chlorobenzene, gold contacts were deposited (physical vapor deposition) on the P3HT/Ge composites. Some of the as prepared hybrid solar cells were characterized by SEM and tested in solar simulator.

Testing of Au/P3HT/Ge/TiO2/FTO hybrid solar cells. The efficiency of the Ge/P3HT solar cells was tested with a solar simulator (SolarConstant, K. H. Steuernagel Lichttechnik GmbH). The light intensity was calibrated to be 1000 W/cm^2 (AM1.5 solar illumination) by using a silicon-based calibration solar cell (WPVS Reference Solar Cell Type RS-ID-3k Fraunhofer ISE). The J-U-curves were probed with a Keithley 2400 sourcemeter and the bias was varied from -1 V to 0.1 V.

References

[1] M. D. McGehee, *MRS Bull.* **2009**, *34*, 95-100.

[2] S. Günes, H. Neugebauer, N. S. Sariciftci, *Chem. Rev.* **2007**, *107*, 1324-1338.

[3] S. Günes, N. S. Sariciftci, *Inorg. Chim. Acta* **2008**, *361*, 581-588.

[4] B. Weintraub, Z. Zhou, Y. Li, Y. Deng, *Nanoscale* **2010**, *2*, 1573-1587.

[5] a) M. Seino, E. J. Henderson, D. P. Puzzo, N. Kadota, G. A. Ozin, *J. Mater. Chem.* **2011**, 21, 15895-15898. b) H. Miguez, E. Chomski, F. Garcia-Santamaria, M. Ibisate, S. John, C. Lopez, F. Meseguer, J. P. Mondia, G. A. Ozin, O. Toader, H. M. van Driel, *Adv. Mater.* **2001**, *13*, 1634-1637.

[6] a) R. Al-Salman, X. Meng, J. Zhao, Y. Li, U. Kynast, M. M. Lezhnina, F. Endres, *Pure Appl. Chem.* **2010**, *82*, 1673-1689; b) L. K. van Vugt, A. F. van Driel, R. W. Tjerkstra, L. Bechger, W. L. Vos, D. Vanmaekelbergh, J. J. Kelly, *Chem. Commun.* **2002**, 2054-2055; c) W. Xin, J. Zhao, D. Ge, Y. Ding, Y. Li, F. Endres, *Phys. Chem.* **2013**, *15*, 2421-2426; d) X. Meng, R. Al-Salman, J. Zhao, N. Borissenko, Y. Li, F. Endres, *Angew. Chem. Int. Ed.* **2009**, *48*, 2703-2707; *Angew. Chem.* **2009**, 121, 2741-2745.

[7] a) H. Miguez, F. Meseguer, C. Lopez, M. Holgado, G. Andreasen, A. Mifsud, V. Fornes, *Langmuir* **2000**, *16*, 4405-4408; b) J. Hwang, C. Jo, M. G. Kim, J. Chun, E. Lim, S. Kim, S. Jeong, Y. Kim, J. Lee, *ACS Nano* **2015**, *9*, 5299-5309; c) J. Liang, X. Li, Z. Hou, T. Zhang, Y. Zhu, X. Yan, Y. Qian, *Chem. Mater.* **2015**, *27*, 4156-4164; d) C. Zhang, Z. Lin, Z. Yang, D. Xiao, P. Hu, H. Xu, Y. Duan, S. Pang, L. Gu, G. Cui, *Chem. Mater.* **2015**, *27*, 2189-2194; e) H. Jia, R. Kloepsch, X. He, J. P. Badillo, P. Gao, O. Fromm, T. Placke, M. Winter, *Chem. Mater.* **2014**, *26*, 5683-5688. [8] M. M. Bentlohner, M. Waibel, P. Zeller, K. Sarkar, P. Müller-Buschbaum, D. Fattakhova-Rohlfing, T. F. Fässler, *Angew. Chem. Int. Ed.* **2016**, *55*, 2441-2445; *Angew. Chem.* **2016**, *128*, 2487-2491.

[9] A. Du Pasquier, D. D. T. Mastrogiovanni, L. A. Klein, T. Wang, E. Garfunkel, *Appl. Phys. Lett.* **2007**, *91*, 183501.

[10] S. Guldin, S. Hüttner, M. Kolle, M. E. Welland, P. Müller-Buschbaum, R. H. Friend, U. Steiner, N. Tétreault, *Nano Lett.* **2010**, *10*, 2303-2309.

[11] S. M. Al-Salem, P. Lettieri, J. Baeyens, *Waste Management* **2009**, *29*, 2625-2643.

[12] C. Belin, H. Mercier, V. Angilella, *New. J. Chem.* **1991**, 15, 931-938.

[13] A. Y. Mkrtchyan, *Int. J. Mod. Phys.: Conference Series* **2012**, *15*, 219-223.

[14] C. F. O. Graeff, M. Stutzmann, K. Eberhardt, *Philos. Mag. B* **1994**, *69*, 387-396.

[15] R. W. Lechner, *Dissertation*, Technical University Munich, **2009**

Acknowledgments

This work was financially supported by the Bavarian Collaborative Research Project “Solar technologies go Hybrid" (SolTech). L.S. acknowledges funding by the China Scholarship Council (CSC). The authors are grateful M. Sc. Enrico Greul for measuring the UV-VIS spectra.

TOC

The fabrication of undoped and doped germanium inverse opal films and their application in P3HT based hybrid solar cells is presented. Germanium inverse opals were fabricated by a wet chemical method utilizing soluble $[Ge_9]^{4-}$ Zintl clusters as germanium precursors. Spray- and spin-coating techniques were used to fabricate the films across extensive areas.

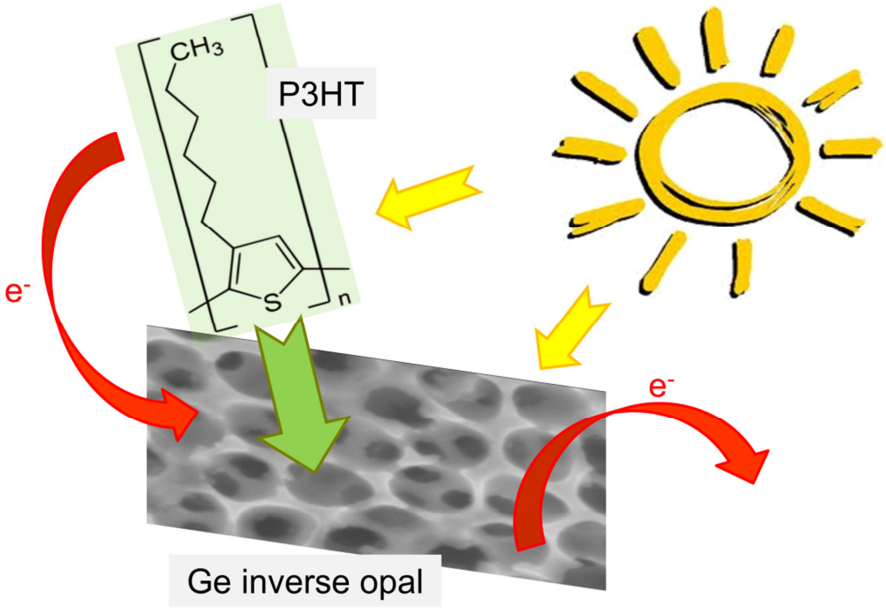

Supporting Information

Fabrication of inverse opal structured germanium films and their application in hybrid solar cells with P3HT

Manuel M. Bentlohner, Sebastian Geier, Michael Giebel, Marius Loch, Lin Song, Paolo Lugli, Peter Müller-Buschbaum¬, Dina Fattakhova-Rohlfing†, Thomas F. Fässler *

Contents

Figures and Tables

Table S1: Band gaps of inverse opal structured germanium films determined from the Tauc plots.

1 Experimental details

1.1 Characterization techniques

Scanning electron microscopy (SEM) measurements were carried out using JEOL JSM-6500F and JSM-7500F scanning electron microscopes equipped with field emission guns operated at 1-30 kV. Energy dispersive X-ray analysis was performed with an Oxford analysis system (Oxford Instruments).
UV/VIS spectra were recorded at a Lambda 1050 UV/VIS-spectrometer (*PerkinElmer*) equipped with GaInAs integrating sphere detector.
Dynamic light scattering (*DLS*) was used to determine the particle size of PMMA. Measurements were carried out on a Malvern Zetasizer Nanoseries.

1.2 Preparation of precursors

1.2.1 General

All manipulations involving Zintl compounds were carried out under a purified argon atmosphere using a glove box and standard Schlenk techniques. Tetrahydrofuran was dried over molecular sieve (4 Å) in a solvent purificator (MBraun MB-SPS). Dimethylsulfoxide (Sigma Aldrich, water content < 0.005 %) was used as received. Bidistilled water (Milipore Q) was used for substrate cleaning and the preparation of the PMMA dispersion.

1.2.2 PMMA-Dispersion

Synthesis of monodisperse PMMA. PMMA beads (250 nm) were obtained from PD Dr. Dina Fattakhova-Rohlfing University of Munich (LMU) and prepared according to literature procedures.[1] In a typical procedure, 35.5 g (0.35 mol) methylmethacrylate was stirred in 98 mL water at 90 °C for 1 h. 56.0 mg (0.21 mmol) $K_2S_2O_8$ dissolved in 2 mL water was added to the solution. Subsequently, the solution was stirred at 90 °C for 2 h. After cooling down to room temperature the PMMA beads were centrifuged and washed with water several times. The centrifuged beads were dried at 100 °C. 1.5 g monodisperse PMMA beads were dispersed in 8.5 ml water by intensive stirring. To break up agglomerates, the mixture was stirred for one week and daily treated in an ultrasonicator for at least 15 min. The dispersity and the average PMMA bead size of the dispersion were determined by dynamic light

scattering. The obtained 15 wt% PMMA dispersion was used for fabrication of PMMA opal templates. In order to avoid agglomeration upon storage, the dispersion was continuously stirred.

1.2.3 Synthesis of K_4Ge_9

K_4Ge_9 was synthesized by heating a stoichiometric mixture of the elements K and Ge (Chempur, 99.999 %) at 650 °C for 20 h in a stainless-steel tube.[2] K was purified by liquation. The purity of the product was analyzed using powder X-ray diffraction.

1.2.4 Purification of ethylenediamine

Ethylenediamine (*en*) (Merck) with an initial water content of ≤ 1 % was refluxed over calcium hydride (Merck) and freshly collected prior to use. *En* containing trace amounts of water (denoted as grade B) was obtained after refluxing for 2-6 h. The sample tubes for grade B *en* were stored under ambient conditions. Water free *en* (denoted as grade A) was obtained after refluxing for 72 h. The sample tubes for grade A *en* were thoroughly cleaned and dried at 120 °C immediately before the *en* collection. Analysis of water content was performed using reaction with bis(trimethylsilyl)butadiyne (**1**).[3]

2 Fabrication of inverse opal structured germanium films

2.1 Fabrication of PMMA opals

2.1.1 General

Substrates (silicon, silica, sapphire, ITO or FTO) were cleaned with water/surfactant, ethanol and acetone by ultrasonication for 15 min. Silicon, silica and sapphire substrates were additionally treated with an oxygen-plasma to remove rest impurities on the surface and improve the wettability. Immediately after plasma treatment, the substrates were coated (chapter 2.1.2) with a suspension of monodisperse PMMA beads in water and the substrates were dried for 4 h at 100°C in vacuum. PMMA was applied by different coating techniques.

2.1.2 Application of PMMA

Dip coating was done at the chair of Prof. Dr. Thomas Bein (University of Munich, LMU) with a self-constructed dip-coater. Thereby, the substrate was clamped vertically at the dip-coater and dipped once (ca. 0.5 cm/s) into the PMMA dispersion. The coated substrate was stored vertically for ca. 10 min in ambient air, in order to remove the majority of water. SEM image of dip-coated PMMA opal see Figure S1a.

Spin-coating was done with a SCC-200 spin coater (NOVOCONTROL Technologies GmbH Co KG) at the chair of Nanoelectronics Prof. Dr. Paolo Lugli (Technical University of Munich). In a typical procedure, 100 µl of PMMA/H_2O dispersion were dropped onto the stationary substrate, which was subsequently rotated at 1500 rpm for 45 s. For a SEM image of spin-coated PMMA after infiltration with Ge precursor solution see Figure S4.

Spray-coating was done at the chair of Nanoelectronics Prof. Dr. Paolo Lugli (Technical University of Munich) with a self-constructed setup. The deposition setup is composed of a commercially available spray gun (Krautzberger GmbH, Germany) connected to a semi-automated pneumatic controller. The atomizing gas is pressurized N_2 and the pressure was always kept below 2 bar in order to obtain smoother depositions. The samples were placed on a hotplate 15 cm below the spray gun and heated at 80 °C during the spray process. An aqueous PMMA dispersion

(0.4 wt%, bead diameter: 250-300 nm) was used for spray-coating and the spray time was 5-15 s: For a SEM image of spray-coated PMMA opal see Figure S1b.

Figure S1. SEM micrographs of PMMA opals fabricated by different coating methods. a) PMMA dip-coating, substrate: silicon; b) PMMA spray-coating, substrate FTO/TiO_2. Films fabricated by spin-coating of PMMA were investigated in SEM solely after infiltration with the Ge precursor (see below).

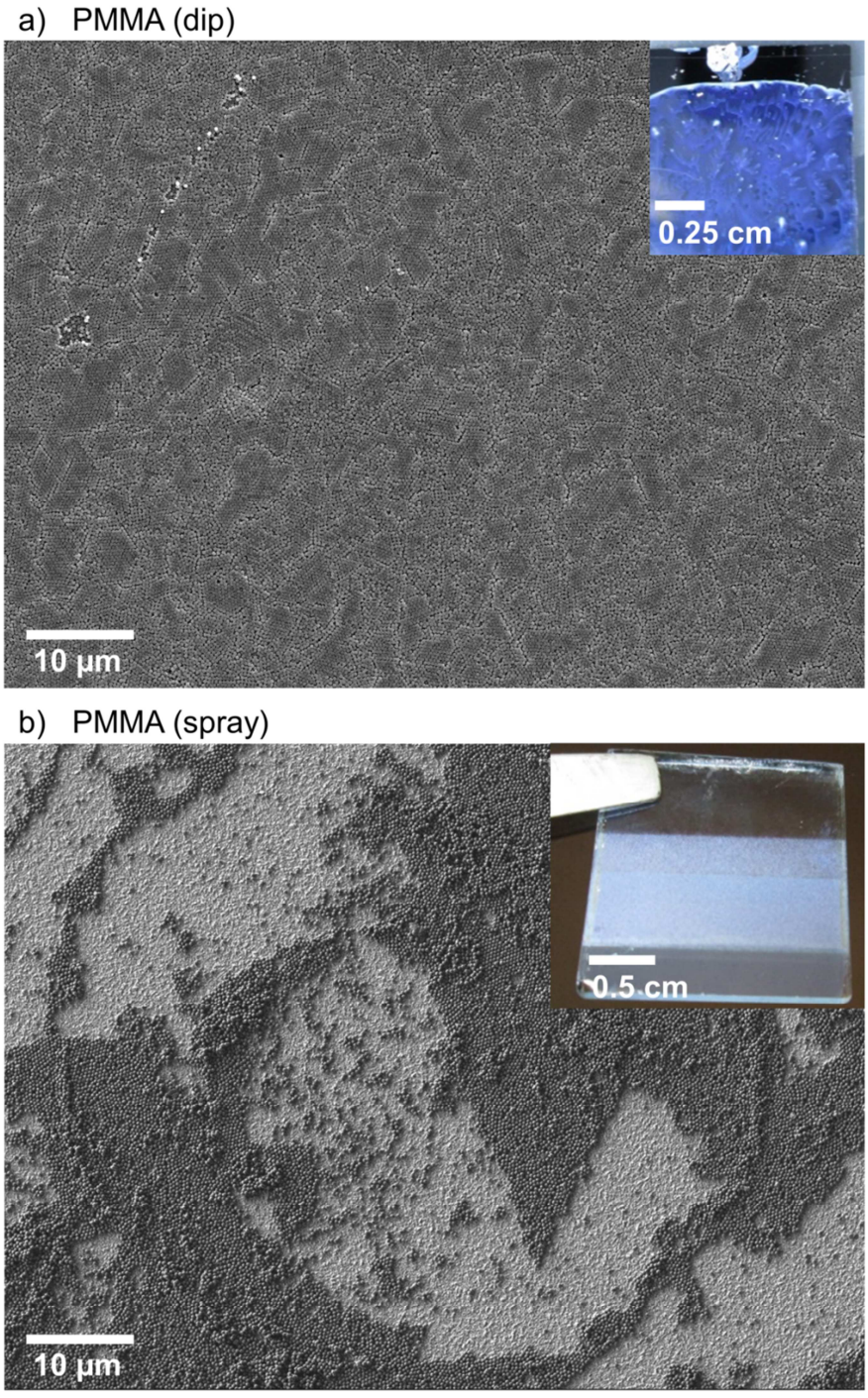

2.2 Infiltration of PMMA opal with Ge precursor and cluster oxidation

In chapter 2.2.1 different methods for the fabrication of inverse opal Ge films are presented. The methods differ by the way of cluster oxidation. In chapter 2.2.2 different application methods for the Ge precursor at the PMMA opal are shown. The methods shown in 2.2.1 can be optionally combined with the application techniques for the Ge precursor shown in 2.2.2.

2.2.1 Methods in general

***E*Cl$_n$-Method**[4]**.** In a Schlenk tube K_4Ge_9 (50 mg, 62 µmol) was dissolved in 1 ml *en* grade A. Thereby, an orange-red solution was obtained, which was stirred for maximal 1 h and filtered over glass fibers immediately before use. For film fabrication, a PMMA opal template was coated (chapter 2.2.2) with the K_4Ge_9/*en* solution (50 mg/ml) and *en* was evaporated at room temperature in an argon atmosphere. Thereby an orange colored film (K_4Ge_9/PMMA/substrate) is obtained. The K_4Ge_9/PMMA/substrate composite was treated with *E*Cl$_n$ vapor for at least 12 h in a glass container, whereby the color of the films changed into dark-violet (Figure S2). Subsequently, the film was annealed for 5 min at 500 °C in vacuum to remove the PMMA template. Alternatively the PMMA was removed by dissolution in tetrahydrofuran. To remove side products, the film was washed with dimethylsulfoxide (1 h) as well as tetrahydrofuran (0.5 h) and dried for 0.5 h in vacuum. Porous frameworks with enhanced crystallinity were obtained by additional annealing of the films for 1 h at 600 °C in an argon atmosphere. The films prepared by that method are denoted by Ge$_{1-x}$*E*$_x$-*INOP* or Ge$_{1-x}$*E*$_x$-*FL* (prefix *a* = amorphous, α = crystalline)

PPh$_3$-Method. In a Schlenk tube a mixture of the neat solids K_4Ge_9 (50 mg, 62 µmol, 1 eq.) and PPh_3 (21.7 mg, 83 µmol, 1.33 eq.) was dissolved in 1 ml *en*, whereby an orange-red solution was obtained. For film fabrication a PMMA opal was coated (chapter 2.2.2) with the K_4Ge_9/PPh_3/*en* solution and the *en* was evaporated at room temperature in an argon atmosphere. Thereby, a brownish red colored film (= K_4Ge_9/ PPh_3/PMMA/substrate) was obtained. The K_4Ge_9/PPh_3/PMMA composite was annealed for 5 min at 500 °C in vacuum, whereby a brownish black colored film was

obtained. Finally, the film was washed with dimethylsulfoxide (1 h) as well as tetrahydrofuran (0.5 h) and dried for 0.5 h in vacuum. Porous frameworks with enhanced crystallinity were obtained by additional annealing of the films for 1 h at 600 °C in an argon atmosphere. The films prepared by that method are denoted by $Ge_{1-x}P_x$-*INOP* or $Ge_{1-x}P_x$-*FL* (prefix *a* = amorphous, α = crystalline)

Annealing-Method[4]**.** A PMMA opal template was coated (chapter 2.2.2) with a solution of K_4Ge_9 in *en* grade A (50 mg/ml). Thereby an orange colored film (K_4Ge_9/PMMA/substrate) was obtained, which was annealed in argon for 1 h at 600 °C. Thereby, very thin crystalline inverse opal structured germanium films are formed. The films prepared by that method are denoted by α-Ge-*INOP*

***en*/H_2O-Method**[4]**.** In a Schlenk tube K_4Ge_9 (50 mg, 62 µmol) was dissolved in 1 ml *en* grade B. Thereby, an deep green solution was obtained, which was stirred for maximal 1 h and filtered over glass fibers immediately before use. For film fabrication, a PMMA opal template was coated (chapter 2.2.2) with the K_4Ge_9/*en* solution (50 mg/ml) and *en* was evaporated at room temperature in an argon atmosphere. Thereby a dark violet colored film (*a*-Ge/PMMA/substrate) was obtained. The *a*-Ge/PMMA/substrate composite was annealed for 5 min at 500 °C in vacuum to remove the PMMA template. To remove side products, the film was washed with dimethylsulfoxide (1 h) as well as tetrahydrofuran (0.5 h) and dried for 0.5 h in vacuum, respectively. Porous frameworks with enhanced crystallinity were obtained by additional annealing of the films for 1 h at 600 °C in an argon atmosphere. The films prepared by that method are denoted by *a*-Ge-*INOP*

2.2.2 Application of germanium precursor

Drop Casting. A thoroughly dried PMMA opal was horizontally placed in a glove box and by a syringe ca. 50-100 µl of Ge precursor solution (K_4Ge_9/*en* containing optionally PPh_3) was dropped onto the PMMA opal. Instantaneously the substrate was carefully tilted in order to homogeneously distribute the Ge precursor solution over the PMMA opal. The excess of precursor solution was removed by holding the

substrate inclined. Subsequently, the substrate was placed again horizontally in the glove box, whereby *en* evaporated within ca. 10 min. In areas with shiny crusts an excess of K_4Ge_9 is present and the porous structure is covered. Non covered parts appear matt (Figure S2)

Spin-coating was done with a Delta6 RC spin coater (Süss MicroTec Lithography GmbH) at the Chair of Nanoelectronics Prof. Dr. Paolo Lugli (Technical University of Munich). The spin coater was placed in a nitrogen filled glove box (MBraun). In a typical procedure, 100 µl of precursor solution was dropped onto the stationary substrate, which was subsequently rotated at 1500 rpm for 40 s (Figure S4/5).

Figure S2. a) Photography of an *a*-$Ge_{1-x}Ge_x$/KCl/PMMA composite (substrate: Si-wafer) and b) profilometry of *a*-$Ge_{1-x}Ge_x$-*INOP* obtained by the *E*Cl_n-method (Oxidizer: $GeCl_4$). Coating: dip (PMMA)/drop (K_4Ge_9). a) Violet regions: porous structure, Shiny metallic regions: excess of germanium covers porous structure (crusts), White regions: pure PMMA opal. The appearance of *a*-$Ge_{1-x}P_x$/KCl/PMMA and *a*-$Ge_{1-x}Si_x$/KCl/PMMA is similar. b) The strong deflections are attributed to crusts on the films.

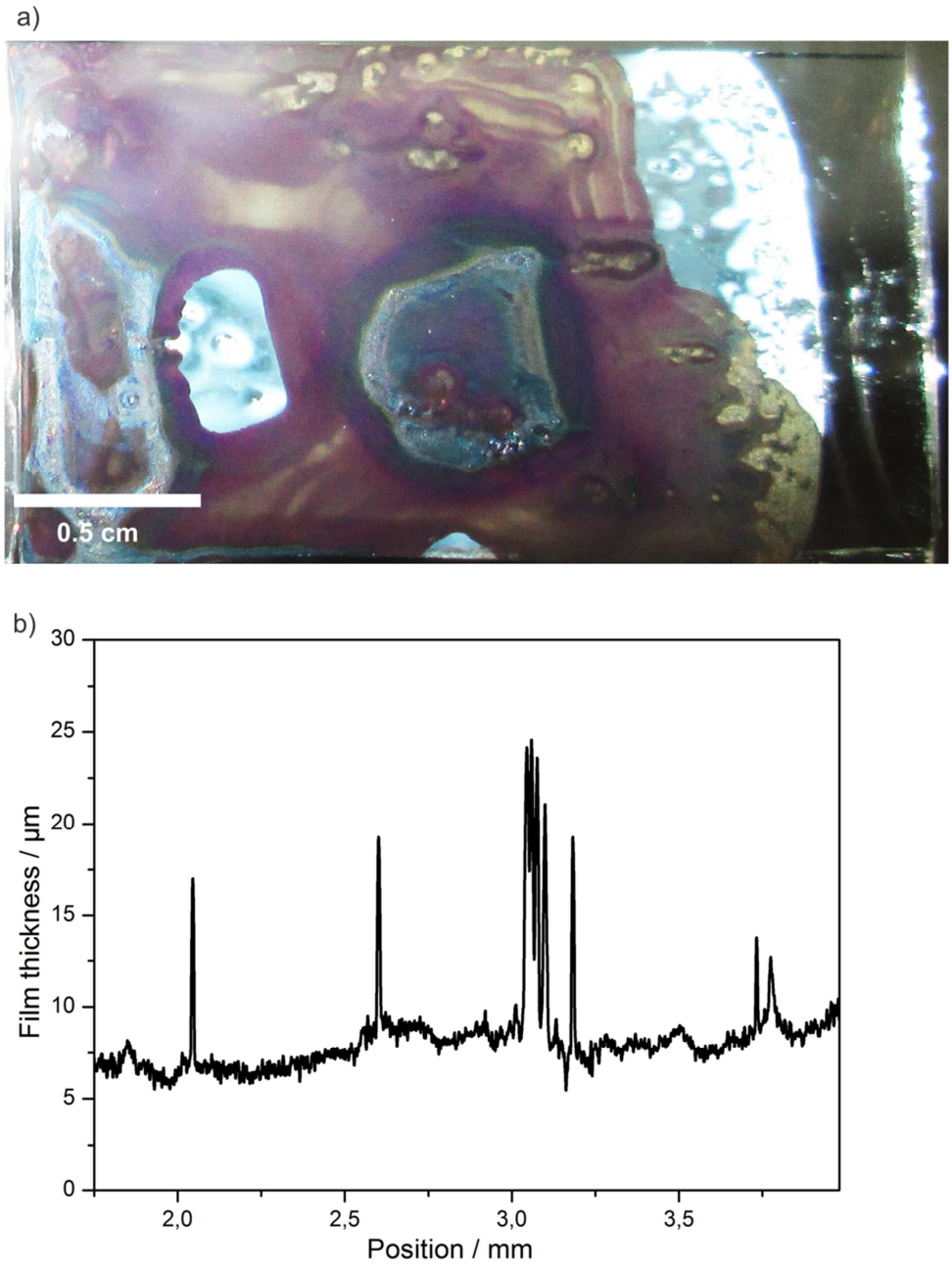

Figure S3. SEM micrographs and EDX spectra of a,c,e) amorphous and b,d,f,g) crystalline inverse opal structured germanium fabricated by a-d) *E*Cl$_n$-method, e-f) PPh_3-method and g) annealing method. Substrates: a-f) glass (EDX: Si, Na, Ca), g) Si. Coating: dip (PMMA)/drop (K_4Ge_9). Insets: magnified sections of the films.

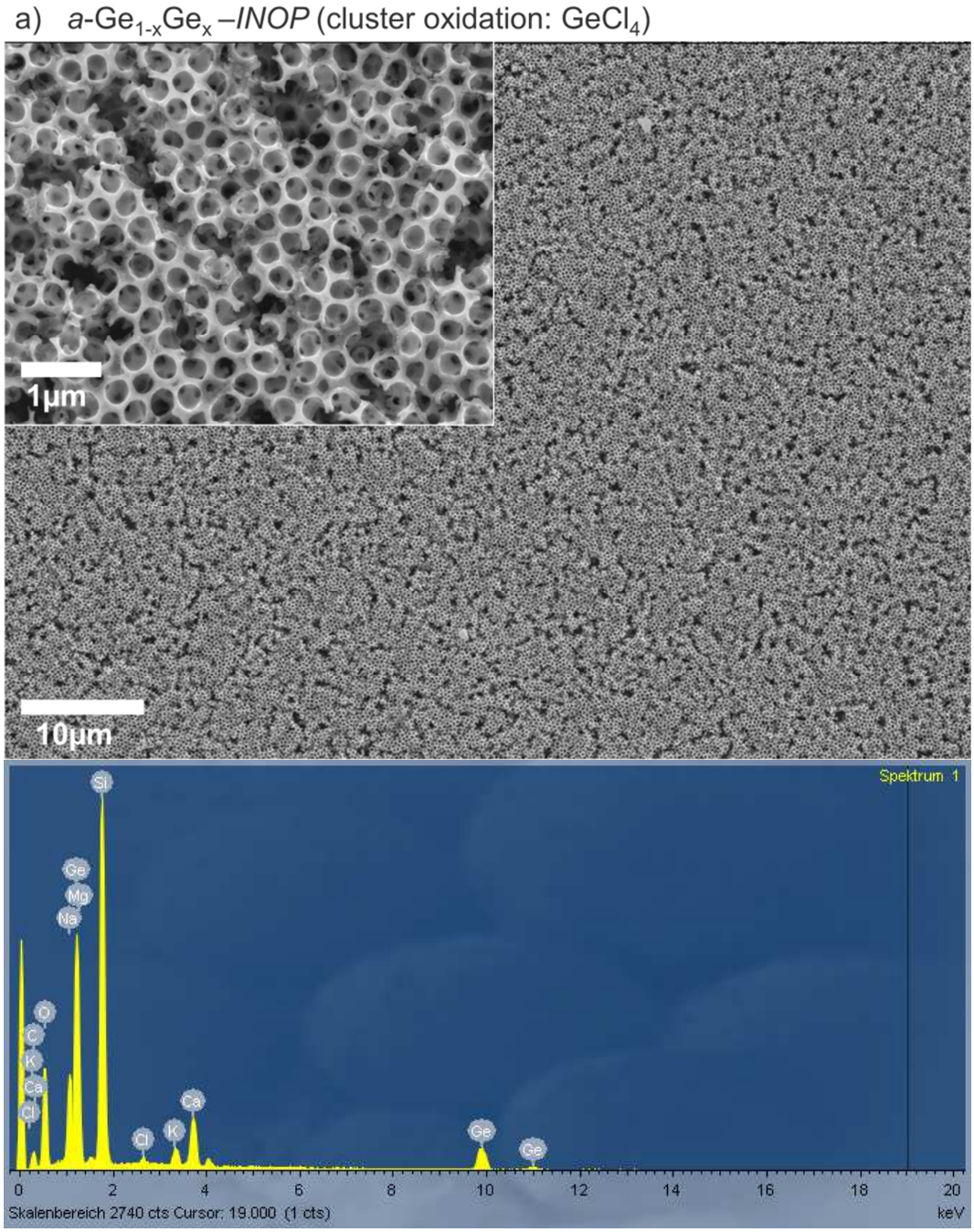

b) α-$Ge_{1-x}Ge_x$ –*INOP* (cluster oxidation: $GeCl_4$)

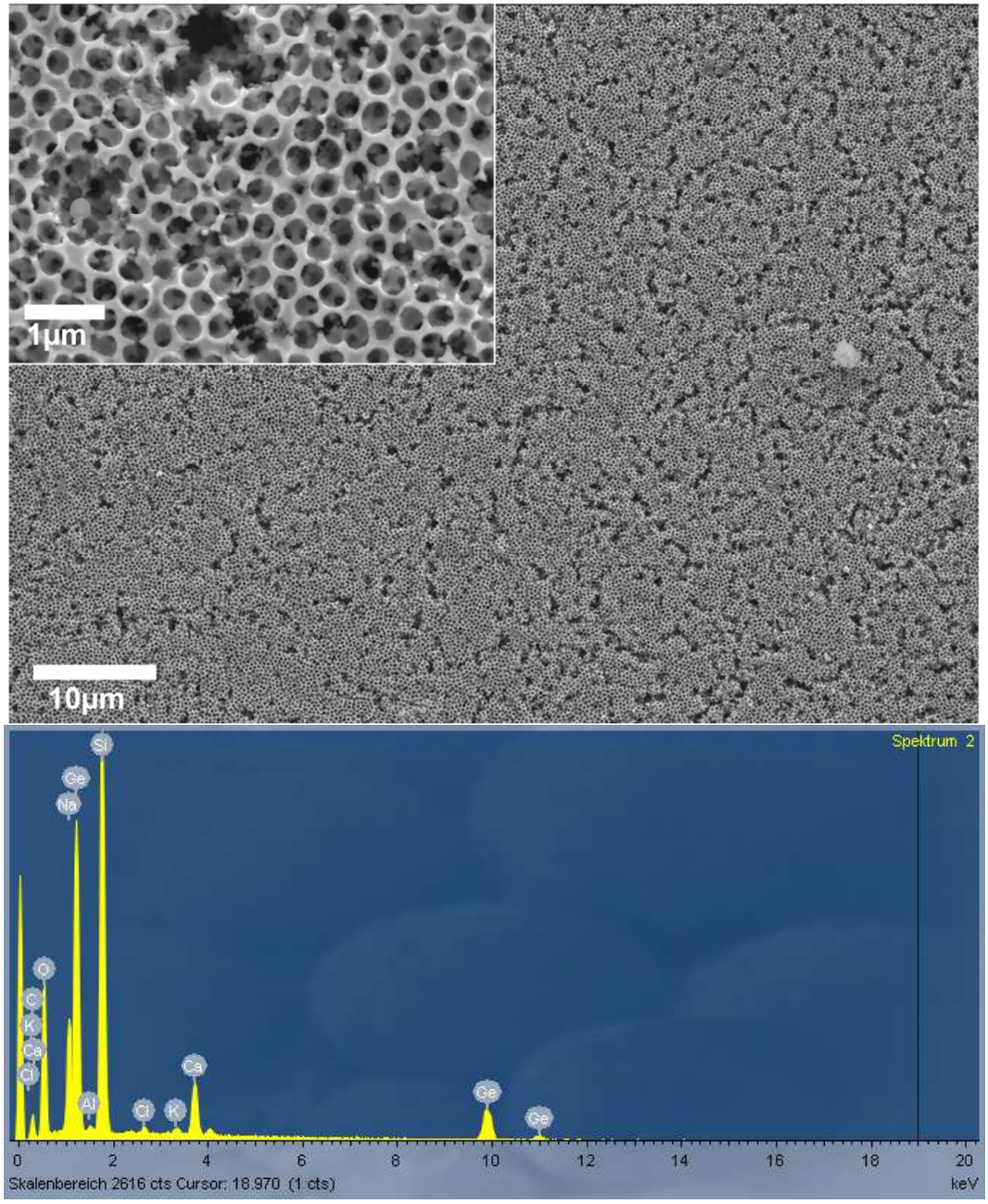

c) *a*-$Ge_{1-x}P_x$ –*INOP* (cluster oxidation: PCl_3)

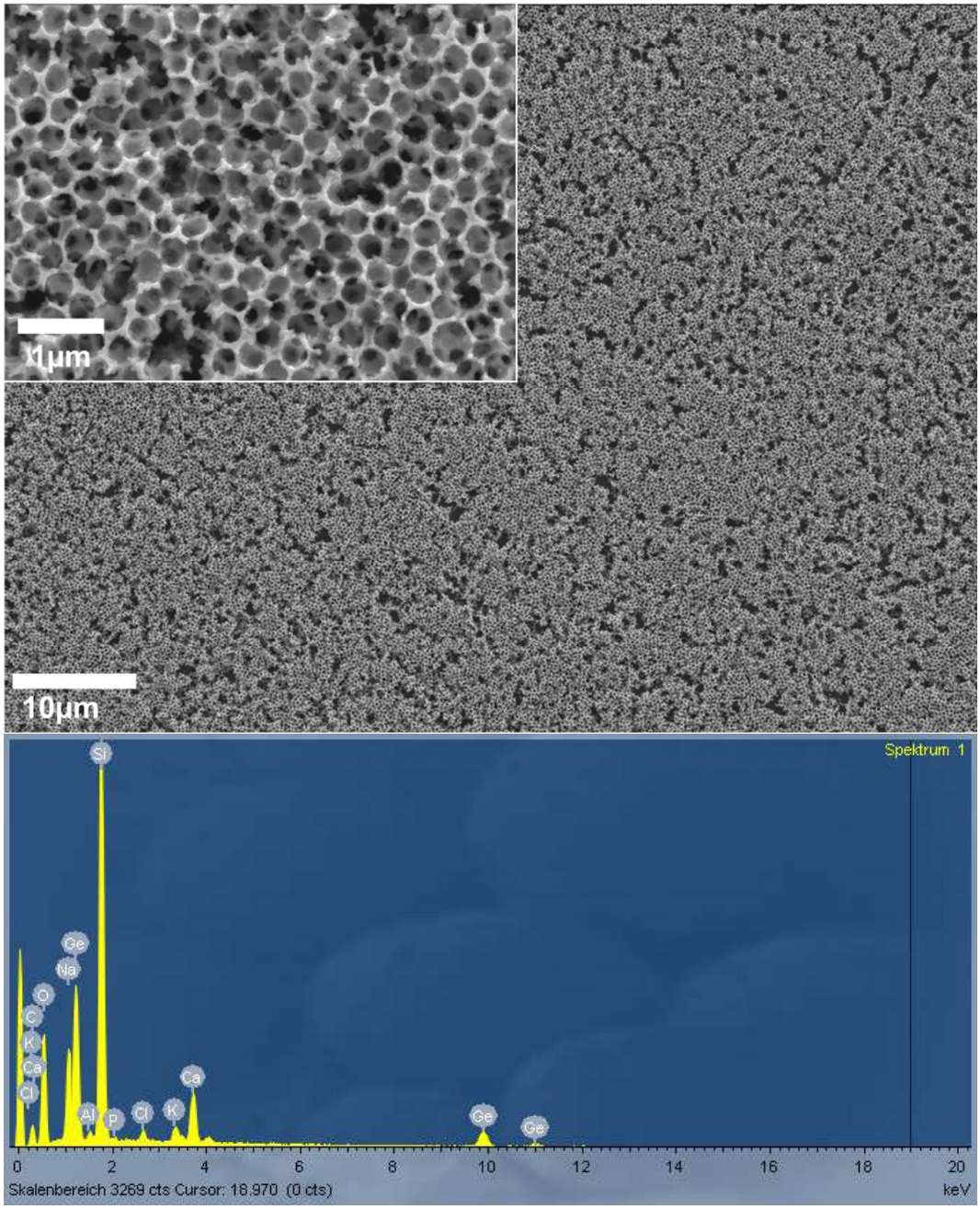

d) α-$Ge_{1-x}P_x$ –*INOP* (cluster oxidation: PCl_3)

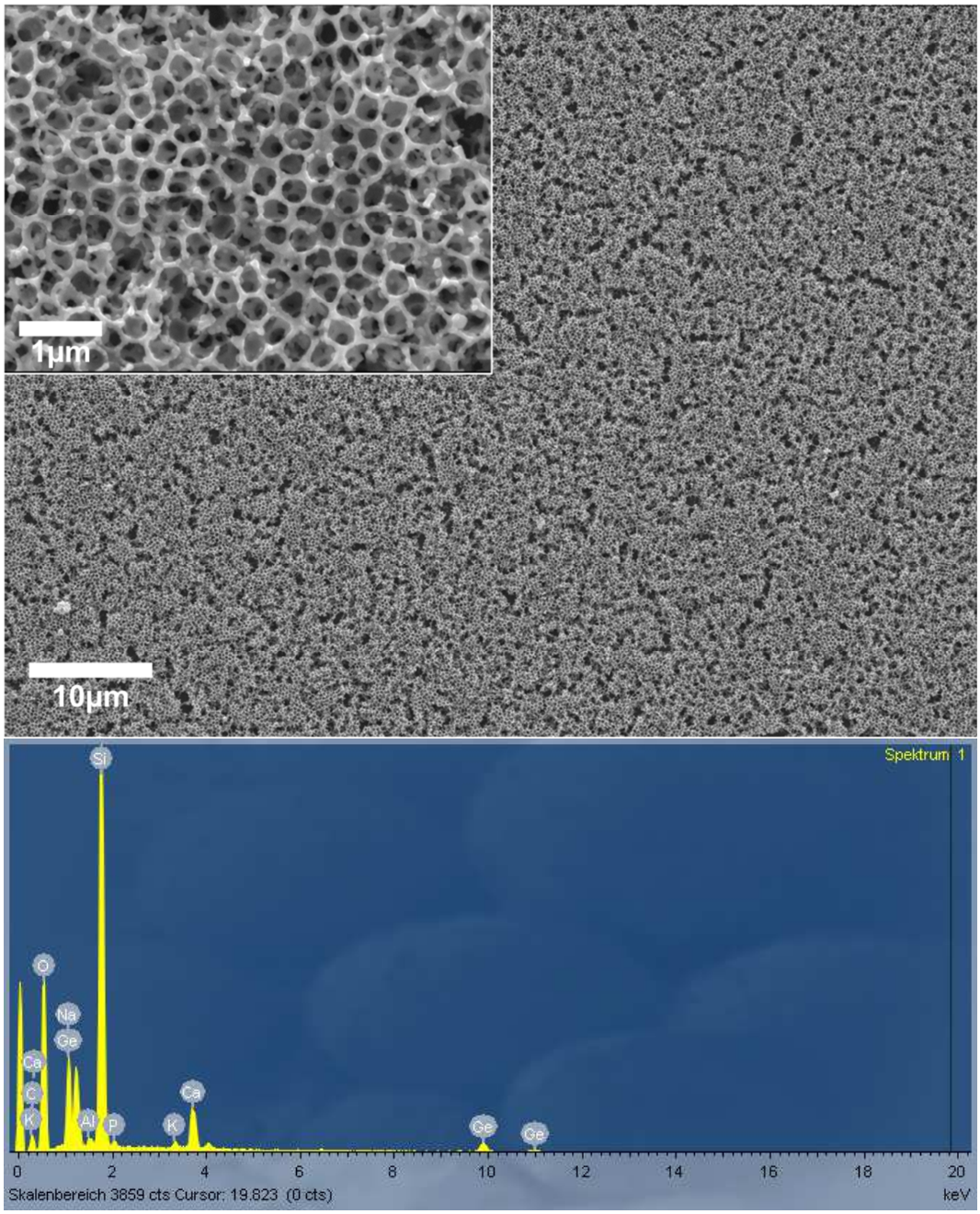

e) *a*-$Ge_{1-x}P_x$ –*INOP* (cluster oxidation: PPh_3)

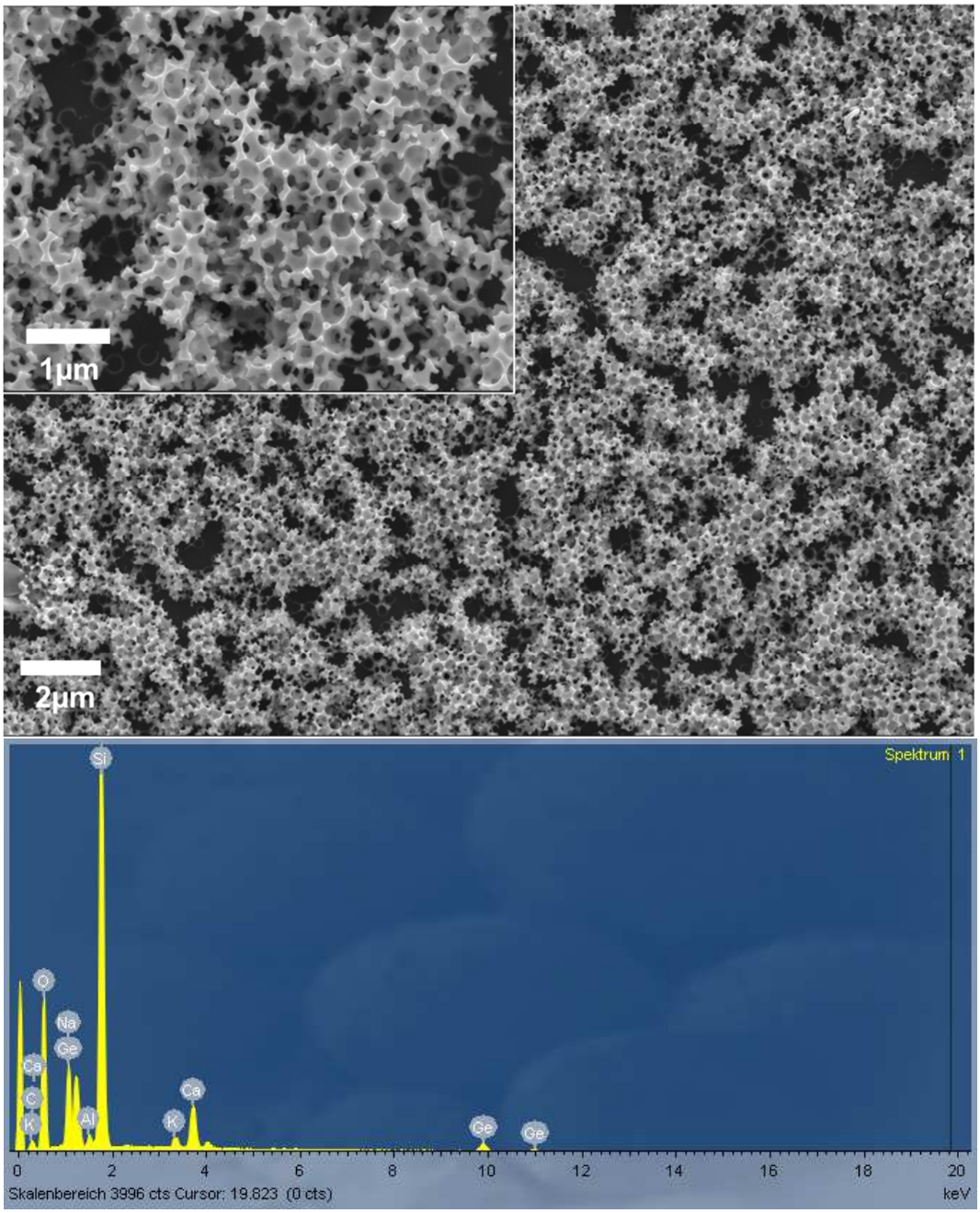

f) α-$Ge_{1-x}P_x$ –*INOP* (cluster oxidation: PPh_3)

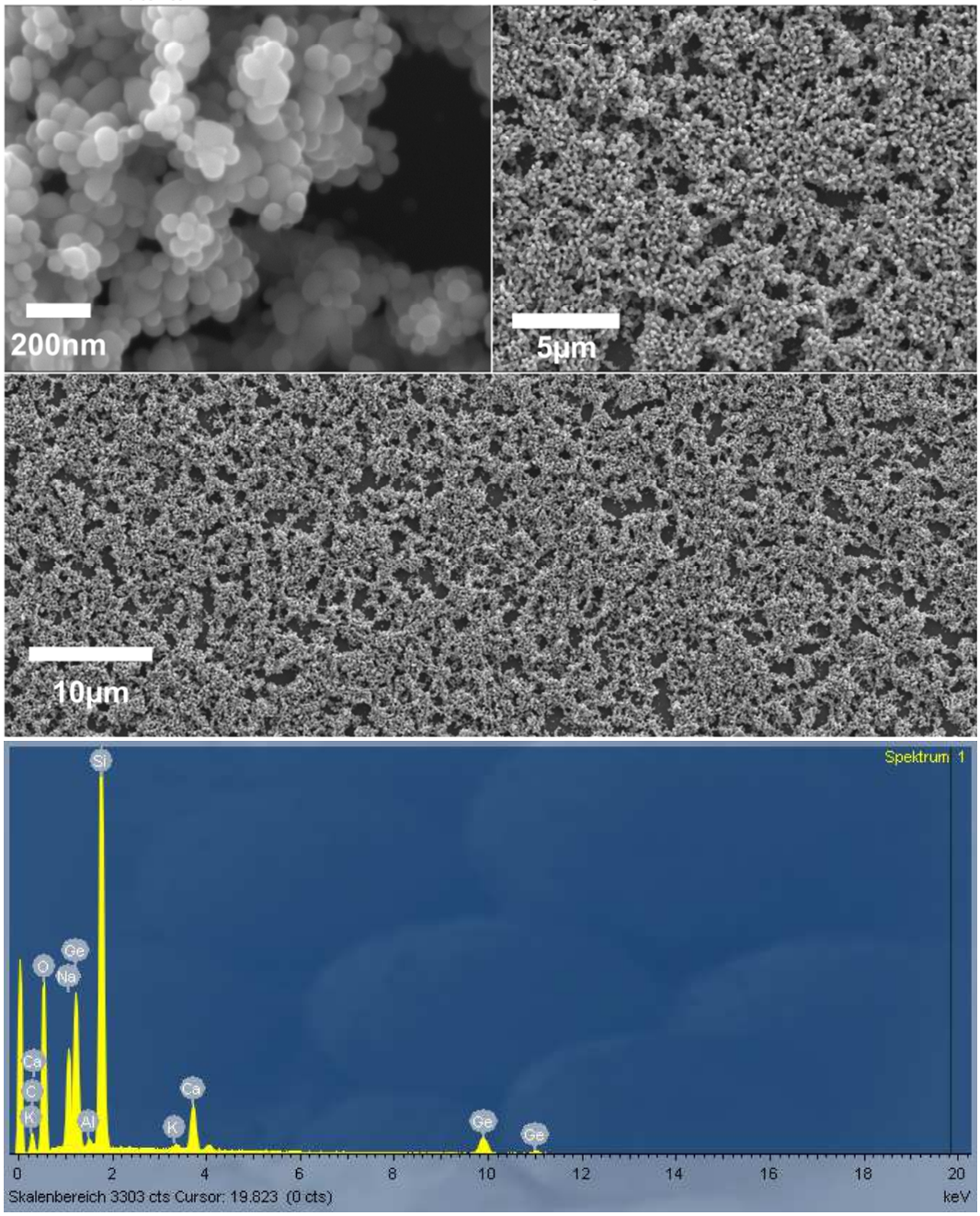

g) α-Ge –*INOP* (cluster oxidation: thermal-annealing)

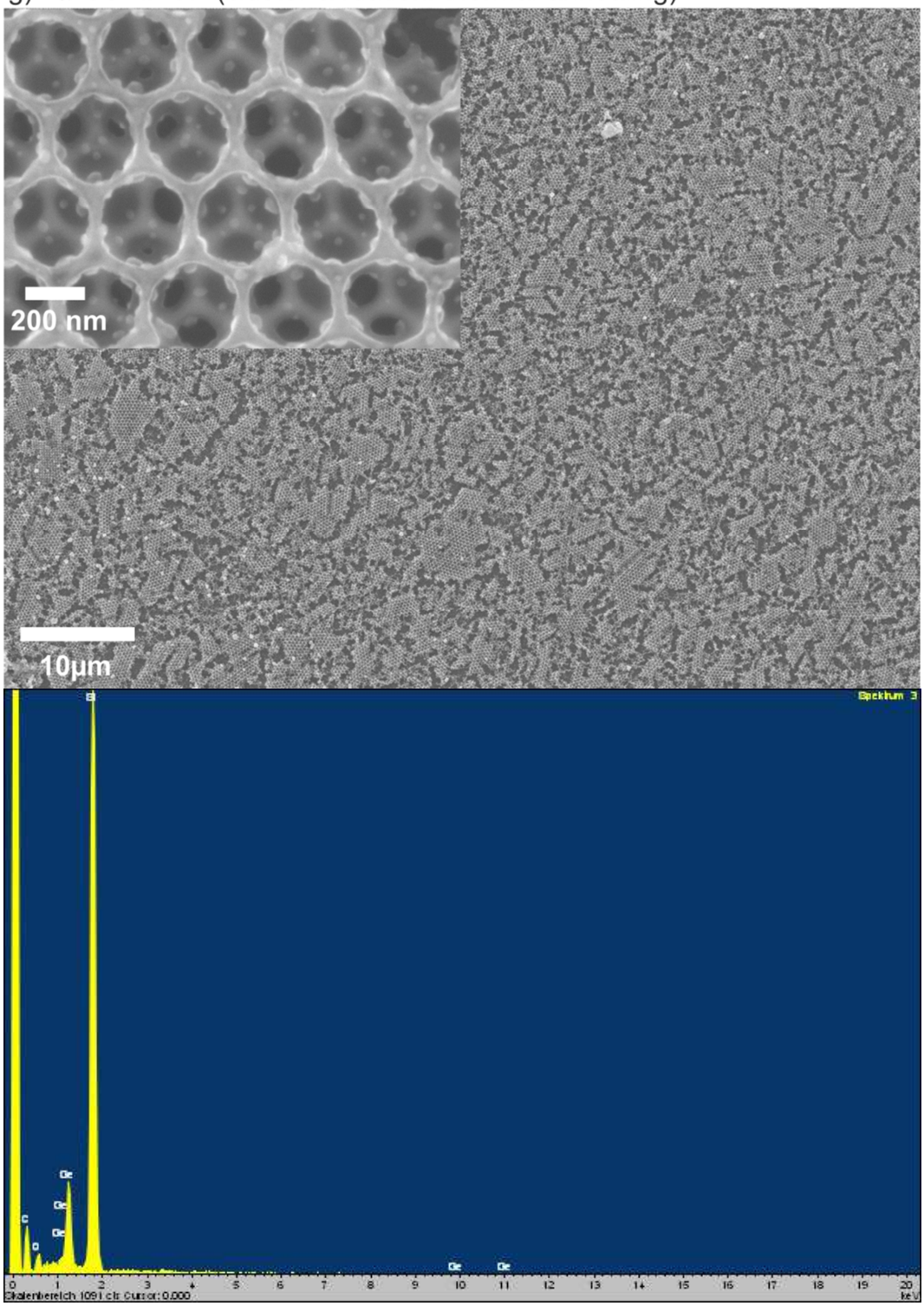

Figure S4. SEM micrograph of *a*-Ge-*INOP*, fabricated by the *en*/H_2O-method. Substrate: FTO/TiO_2. Coating: spin (PMMA)/spin (K_4Ge_9). Inset (left): magnified sections of the films, Inset (right): photography of the film.

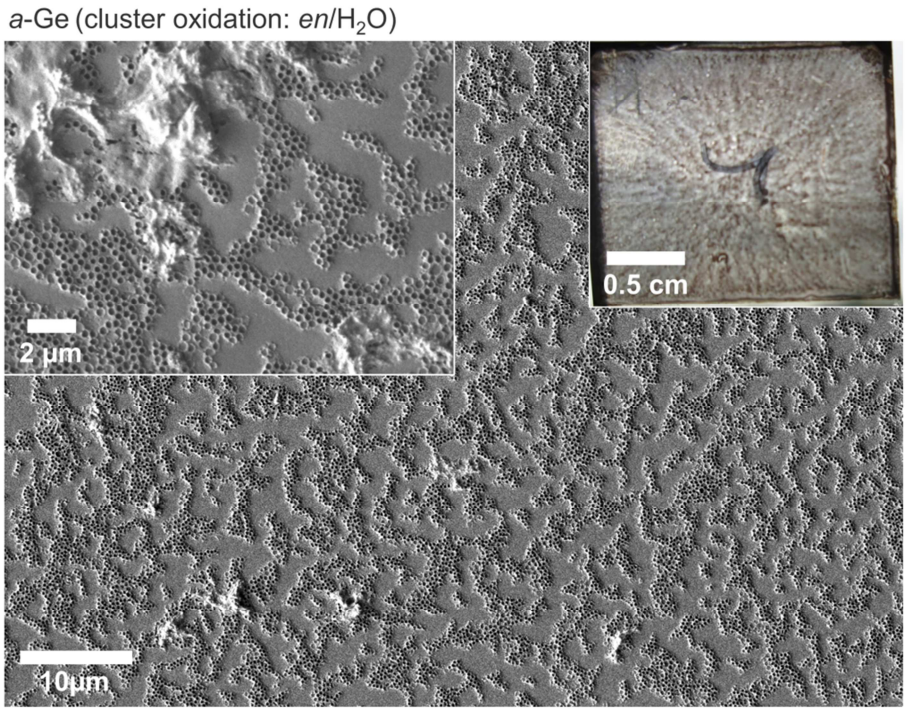

Figure S5. SEM micrograph and b) photography of *a*-$Ge_{1-x}Ge_x$-*INOP*, fabricated by the *E*Cl_n-method. Coating: spray (PMMA)/spin (K_4Ge_9). Inset (left): magnified sections of the films. Inset (right): photography of the film.

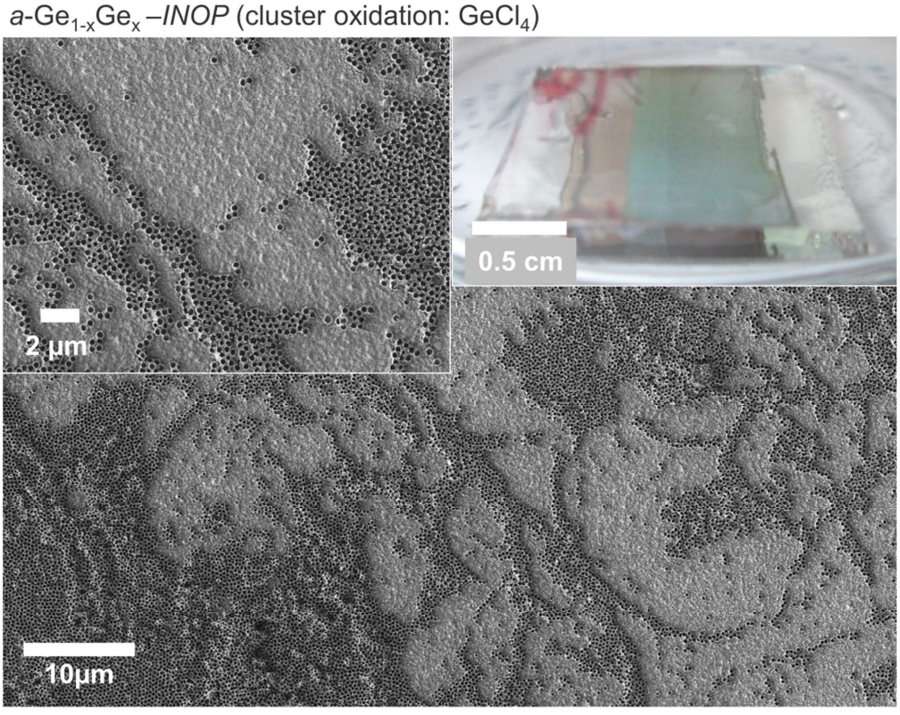

3 Fabrication of flat germanium films

Figure S6. Fabrication of flat germanium films (Ge-*FL*). The clusters are oxidized either by ECl_n or PPh_3. A PMMA bead monolayer is deposited on a FTO substrate by spray-coating and the template voids are filled with the germanium precursor solutions by spin-coating. After oxidation of clusters and removal of PMMA the porous germanium monolayer is filled with the germanium-precursor by drop-casting. The clusters are analogously oxidized as in the first oxidation step. The porous Ge layer acts as bonding agent and enables the fabrication of thicker germanium layers on FTO substrates, which do not flake off.

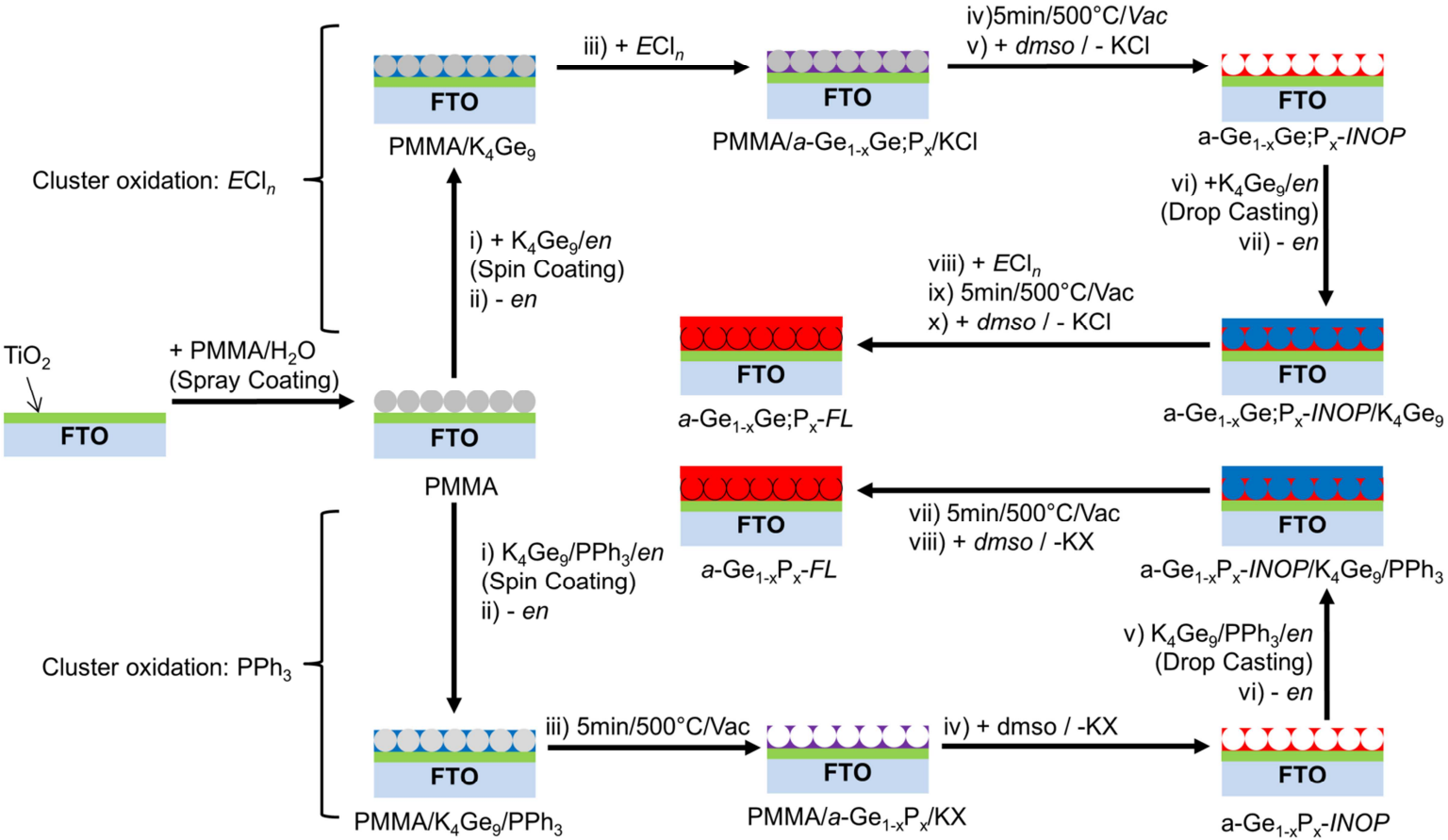

Figure S7. Photos of a) *a*-$Ge_{1-x}Ge_x$-*FL* and b) *a*-$Ge_{1-x}P_x$-*FL* fabricated by *E*Cl*n*- and PPh_3-method, respectively. Substrates: FTO/TiO_2. Coating: spray (PMMA)/spin (K_4Ge_9)/drop (K_4Ge_9). SEM micrographs of corresponding P3HT hybrid solar cells see Figure S14.

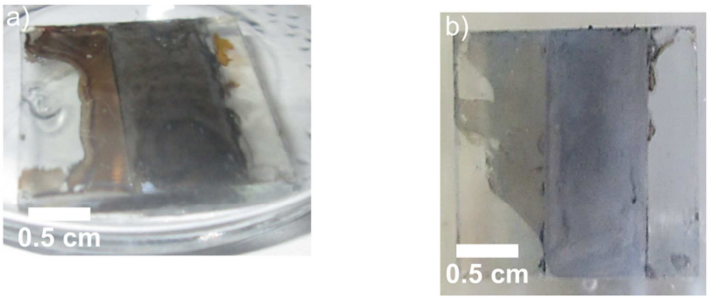

4 Band gap determination

4.1 General

The band gap of inverse opal structured germanium films was determined by UV-VIS spectroscopy. Therefore, amorphous and crystalline $Ge_{1-x}E_x$-*INOP* films were prepared by the *E*Cl$_n$- and PPh_3-method (Coating: dip (PMMA)/drop (Ge-precursor). In UV-Vis the transmission (T), reflectance (R) and absorbance (Ext) of the films were measured in the spectral range of 500-2400 nm. The spot size was ca. 2x2 mm. The absorption (A) of the films was calculated according to equation 1. By that calculation, intensity losses due to absorption of the glass substrate and light scattering are considered and the actual absorption of the film is obtained. From the absorbance (Ext.) the non-corrected absorption can be obtained by equation 2. In Figure S9 the A-E plots for both the corrected absorption and the non-corrected absorption are given, respectively. From absorption A the absorption coefficient (α) was calculated by equation 3 (α-E plot see Figure S10).[5] As the film thickness (d) of the samples is inhomogeneous and unknown, d was set arbitrarily to 1. Tauc-plots (Figure S8 and Equation 4/5) for indirect (Figure S11: $(\alpha E)^2$-E plot) and direct (Figure S12: $(\alpha E)^{0.5}$-E plot) semiconductors were used to evaluate the band gaps from the UV-Vis data.[6] In Table S1 a summarization of the results is given.

$A_{corr} = 1 - R - T$ (Equ. 1)

$A_{non\text{-}corr} = 1 - 10^{-Ext}$ (Equ. 2)

$$\alpha = -\ln\left[\frac{T}{(1-R)^2}\right] d^{-1} \quad \text{(Equ. 3)}$$

indirect band gap: $\sqrt{\alpha \cdot E} \sim E - E_{gap}$ (Equ. 4)

direct band gap: $(\alpha \cdot E)^2 \sim E - E_{gap}$ (Equ. 5)

Figure S8. The determination of band gaps by the Tauc plot

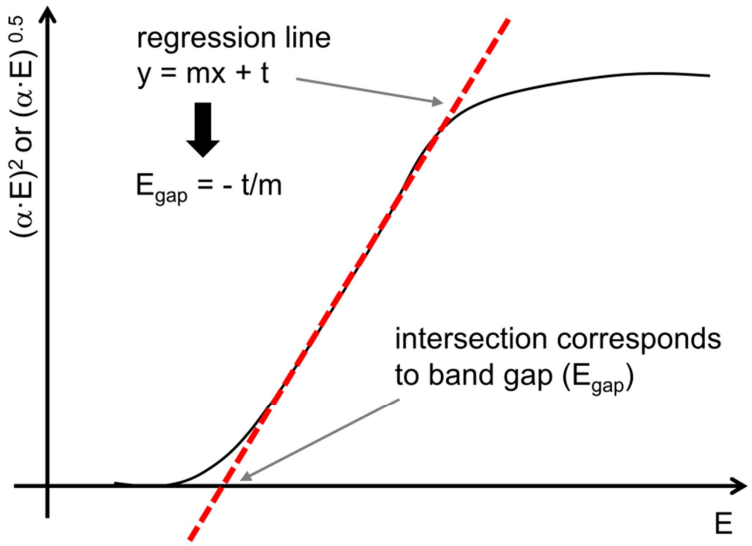

4.2 Summarization of results

Table S1. Band gaps of amorphous and crystalline $Ge_{1-x}Ge$, P_x-*INOP* determined from by Tauc plots. The colors indicate the linearity of the curve and give an impression on the reliability of the values.

	Band gap / eV	
	indirect	direct
a-$Ge_{1-x}Ge_x$–*INOP* ($GeCl_4$)	1.13 / 1.20	1.35 / 1.39
α-$Ge_{1-x}Ge_x$–*INOP* ($GeCl_4$)	0.94	1.26
a-$Ge_{1-x}P_x$–*INOP* (PCl_3)	1.03	1.16
α-$Ge_{1-x}P_x$–*INOP* (PCl_3)	1.32	1.66
a-$Ge_{1-x}P_x$–*INOP* (PPh_3)	0.95	1.16
α-$Ge_{1-x}P_x$–*INOP* (PPh_3)	0.87	1.13

4.3 Absorption spectra (A-E plot)

Figure S9. A-E plots of amorphous (left column) and crystalline (right column) of $Ge_{1-x}Ge$, P_x-*INOP* fabricated by the a-d) ECl_n- and e-f) PPh_3-method. Substrate: glass. Coating: dip (PMMA)/drop (K_4Ge_9). Black lines: corrected absorption (Equ.1), green lines: not corrected absorption (Equ. 2)

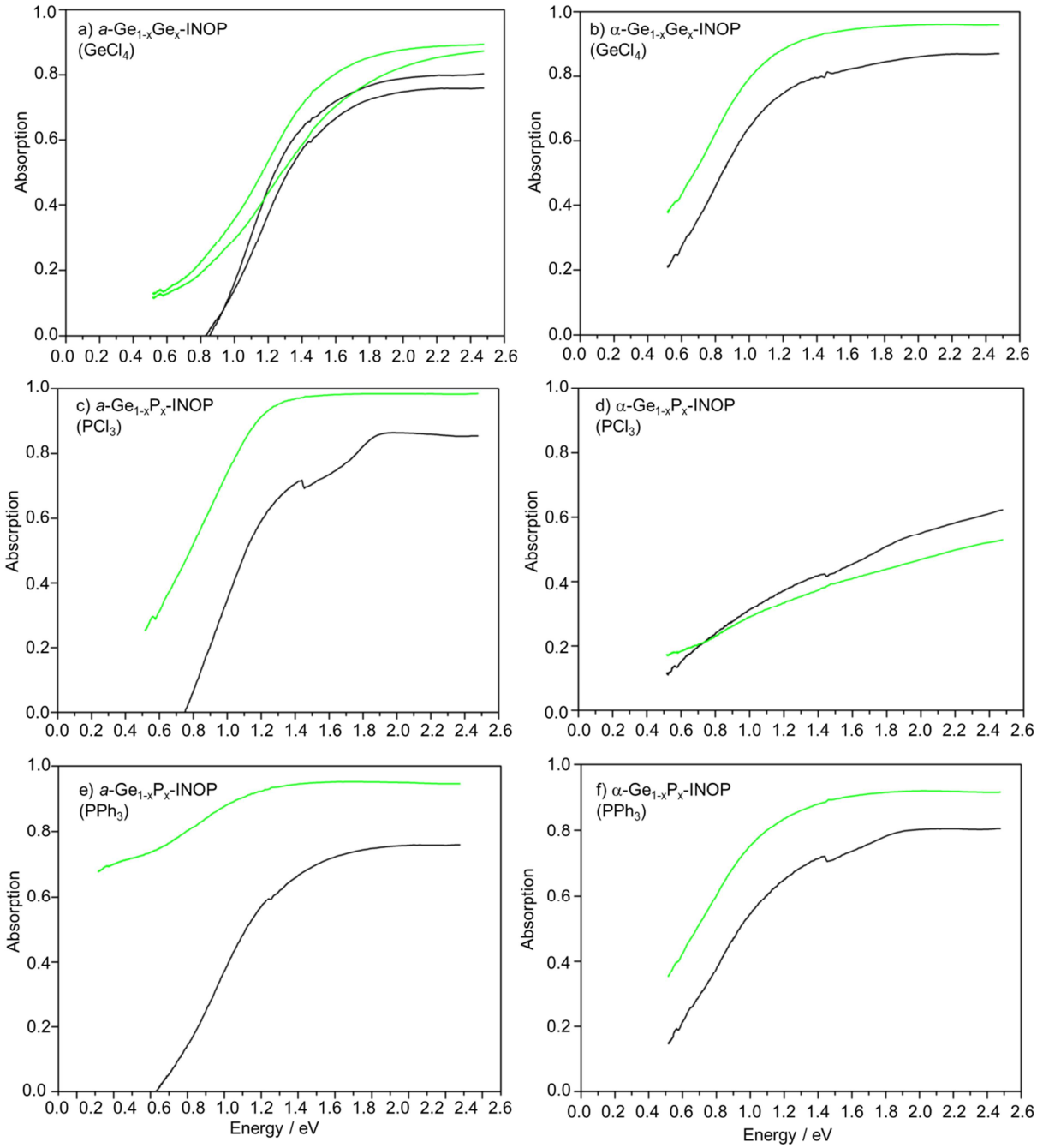

Figure S10. α-E plots (α calculated by Equ. 3) of amorphous (left column) and crystalline (right column) $Ge_{1-x}Ge$, P_x-*INOP* fabricated by the a-d) *E*Cl_n- and e-f) PPh_3-method. Substrate: glass. Coating: dip (PMMA)/drop (K_4Ge_9).

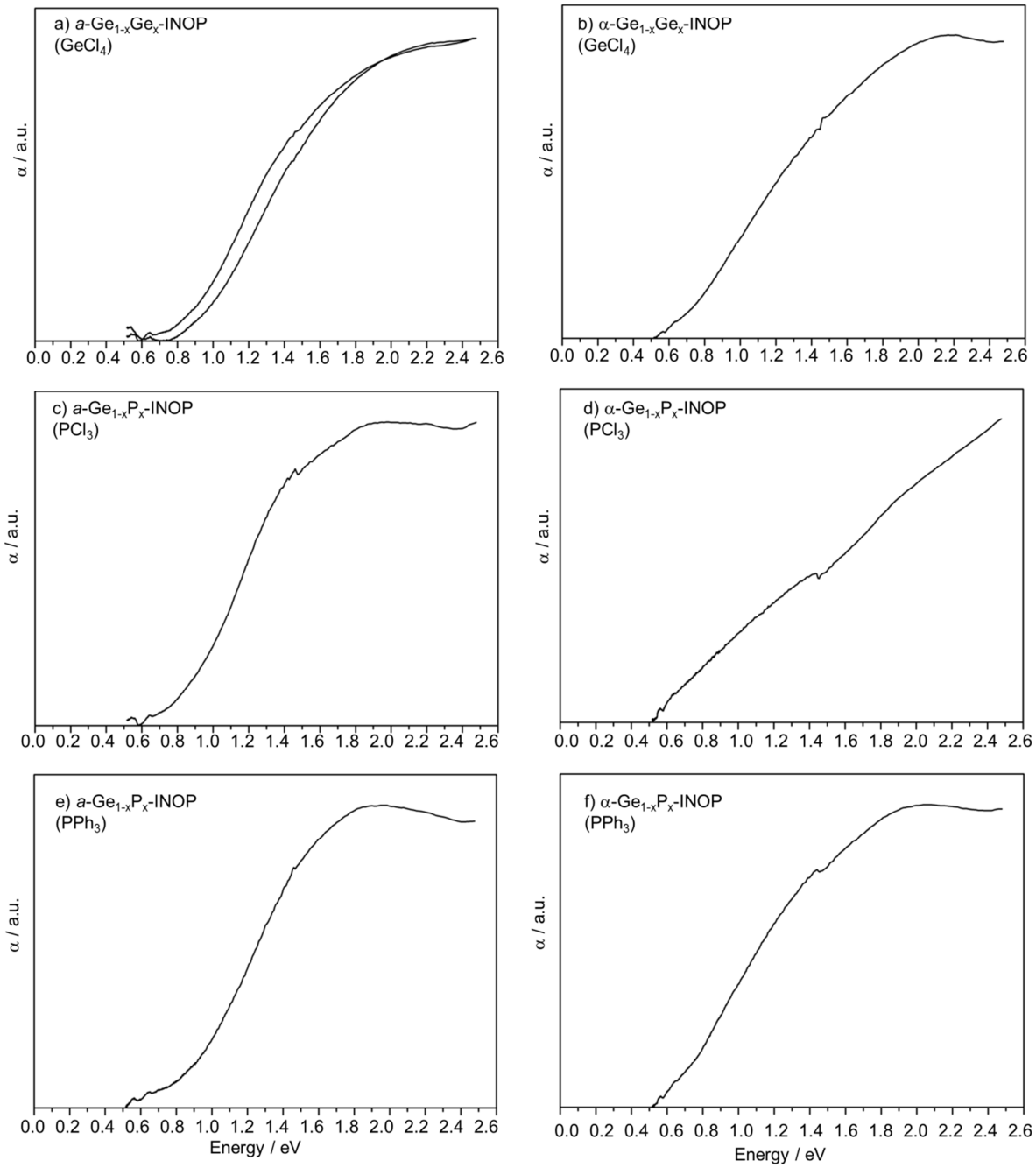

4.4 Tauc Plots

Figure S11. Tauc plots (direct band gap: $(\alpha E)^2$-E plot) of amorphous (left column) and crystalline (right column) $Ge_{1-x}Ge$, P_x-*INOP* fabricated by the a-d) *E*Cl_n- and e-f) PPh_3-method. Substrate: glass. Coating: dip (PMMA)/drop (K_4Ge_9). Red lines: linear regression line (intercept and slope see boxes). E_{gap} = –intercept/slope

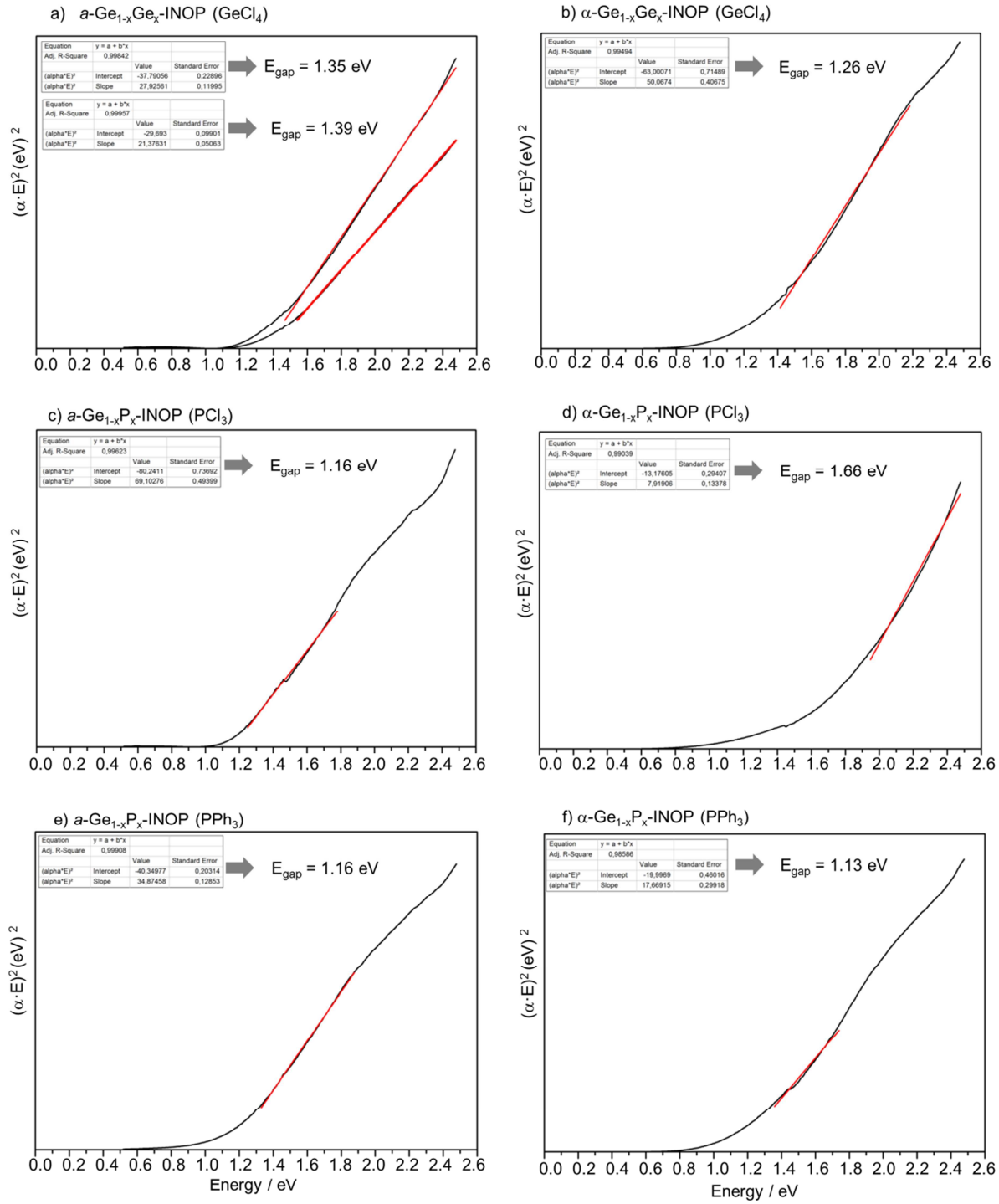

Figure S12. Tauc plots (direct band gap: $(\alpha E)^{0.5}$-E plot) of amorphous (left column) and crystalline (right column) $Ge_{1-x}Ge$, P_x-*INOP* fabricated by the a-d) *E*Cl_n- and e-f) PPh_3-method. Substrate: glass. Coating: dip (PMMA)/drop (K_4Ge_9). Red lines: linear regression line (intercept and slope see boxes). E_{gap} = –intercept/slope

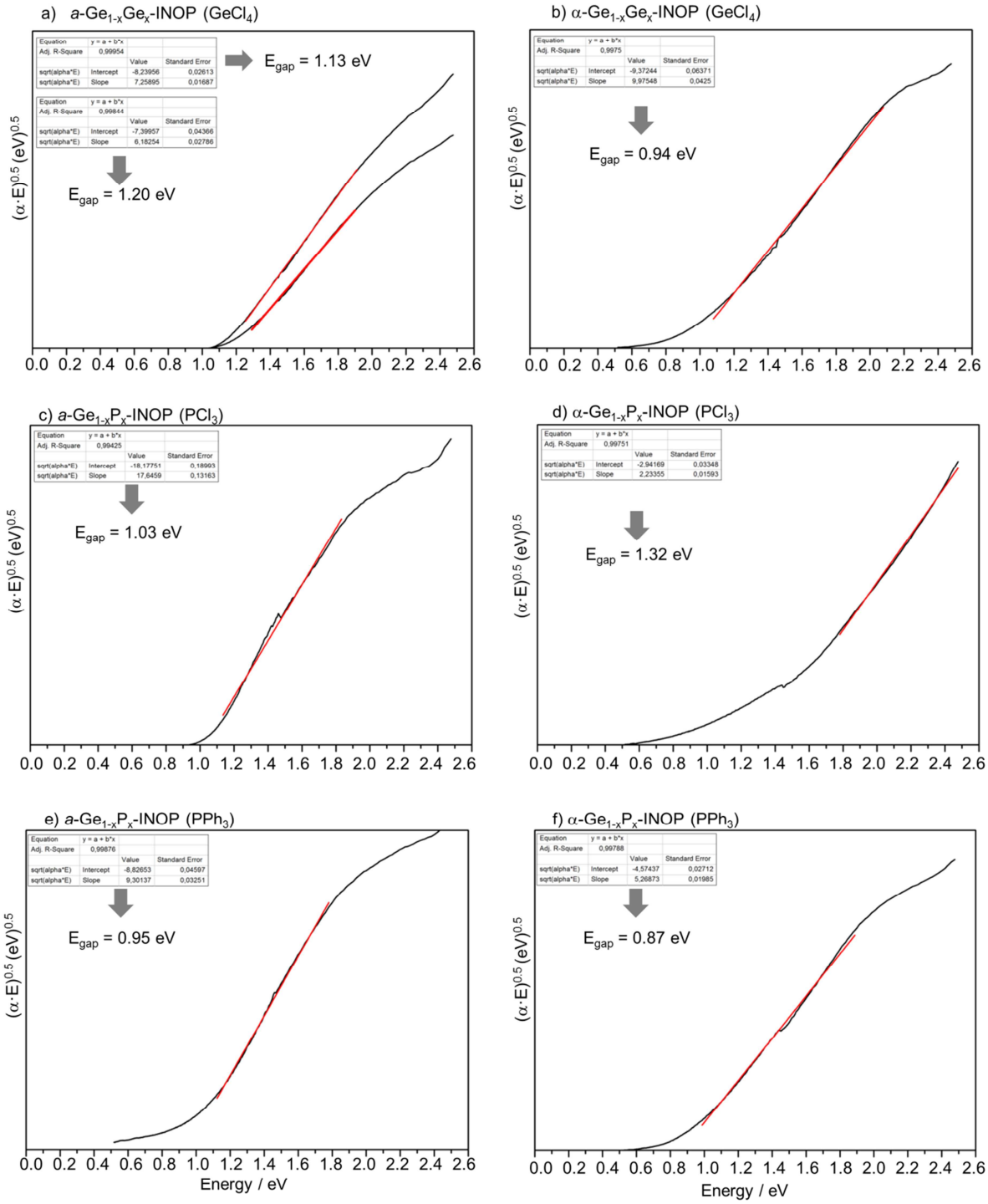

5 Application of germanium films in P3HT hybrid solar cells

5.1 Assembly of P3HT/Ge solar cells

Flat and inverse opal structured germanium films were deposited on FTO substrates, covered with a thin layer of TiO_2. Subsequently, the germanium films were coated/infiltrated with P3HT solution (20 mg/ml in chlorobenzene) by spin-coating (Delta 6 RC TT, Süss MicroTec Lithography GmbH, 2000 rpm, 60 s). After P3HT deposition, a mask was placed on top of the P3HT/Ge/TiO_2/FTO composites and then gold contacts were deposited by physical vapor deposition. The as prepared hybrid solar cells (Figure S13) were characterized by SEM (Figure S14) and tested in a solar simulator (Figure S15 and Table S2) at the chair for .functional materials (Prof. Dr. P. Müller-Buschbaum, Technical University of Munich).

Figure S13. Photography of an Au/P3HT/Ge/TiO_2/FTO hybrid solar cell. P3HT shows purple color.

5.2 SEM investigations

Figure S14. a/b) SEM micrographs of Au/*a*-$Ge_{1-x}Ge_x$-*INOP*/P3HT/TiO_2/FTO solar cell. Insets: magnified section of the film. P3HT filled and not-filled pores are marked with blue arrows, respectively. The germanium films were fabricated by the *E*Cl_n-method. Substrate: FTO/TiO_2. Coating: spray (PMMA)/spin (K_4Ge_9).

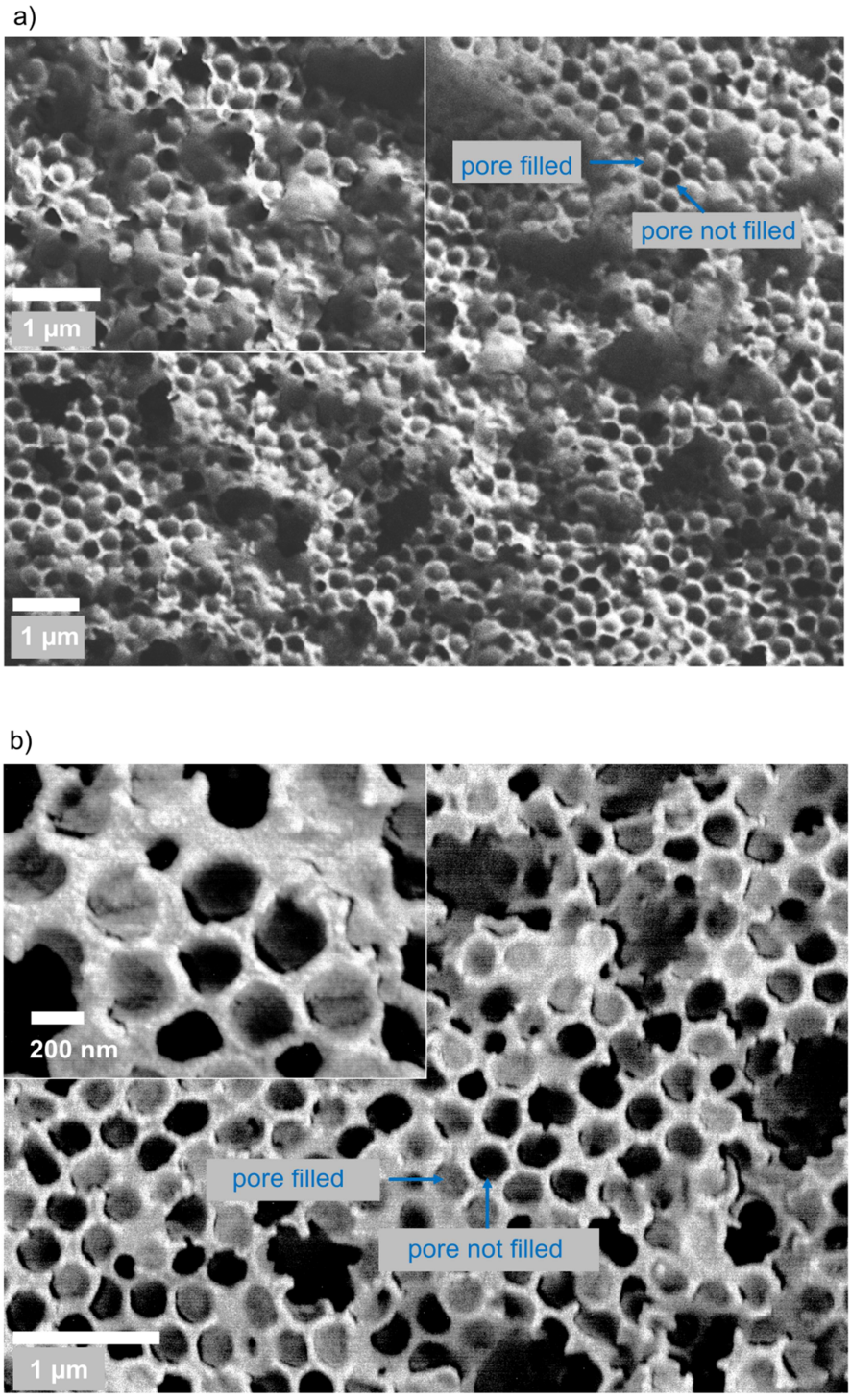

Figure S15. SEM micrographs of a) Au/*a*-$Ge_{1-x}Ge_x$-*FL*/P3HT/TiO_2/FTO and b) Au/*a*-$Ge_{1-x}P_x$-*FL*/P3HT/TiO_2/FTO solar cells. Insets: magnified section of the films. P3HT (EDX: S) appears as a smooth layer on top of the germanium flat films. The germanium films were fabricated by the a) *E*Cl_n- and b) PPh_3-method. Substrate: FTO/TiO_2 (EDX: Si, Na, Ca, Sn, Ti). Coating: spray (PMMA)/spin (K_4Ge_9)/drop (K_4Ge_9).

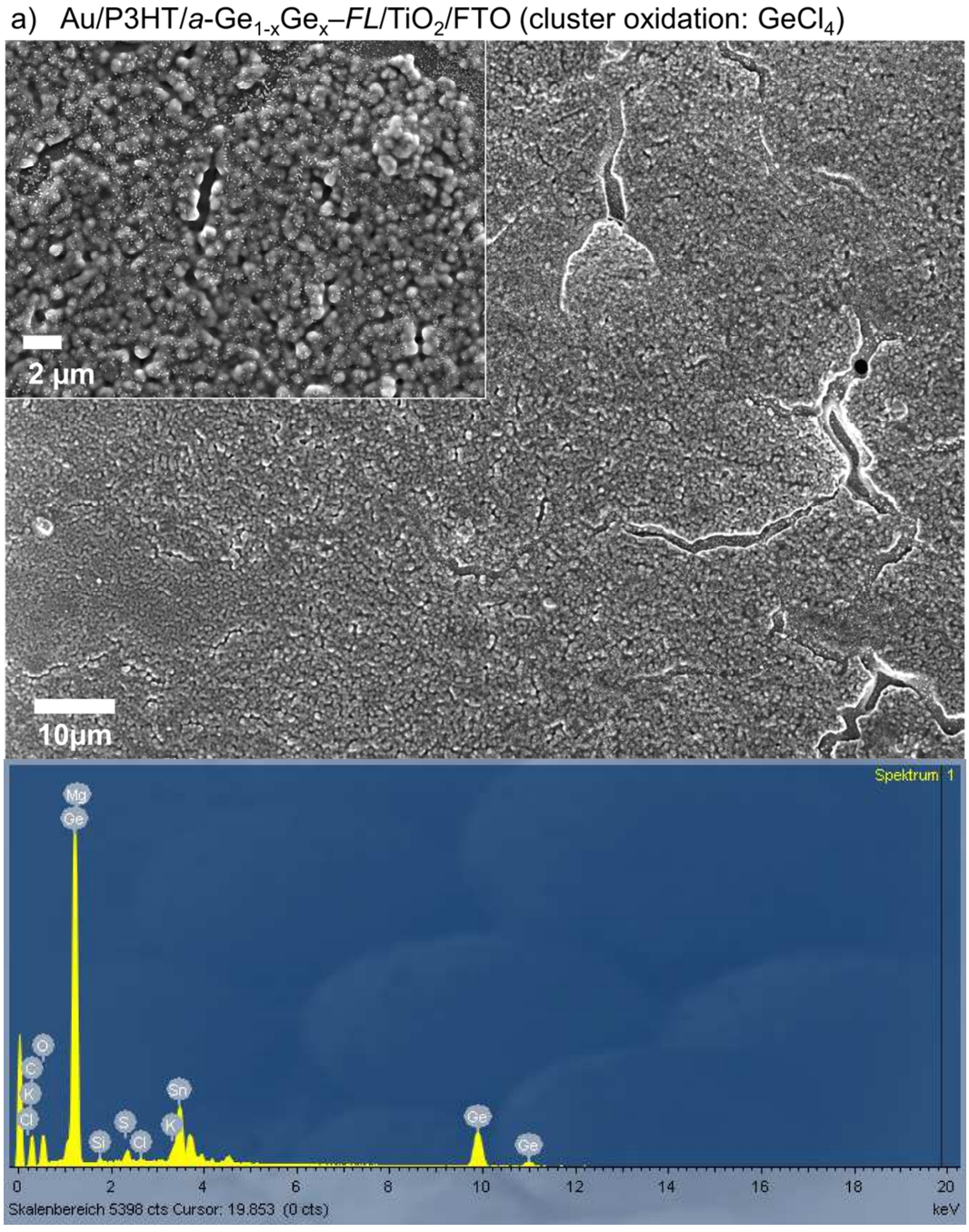

b) Au/P3HT/*a*-$Ge_{1-x}P_x$–*FL*/TiO_2/FTO (cluster oxidation: $GeCl_4$)

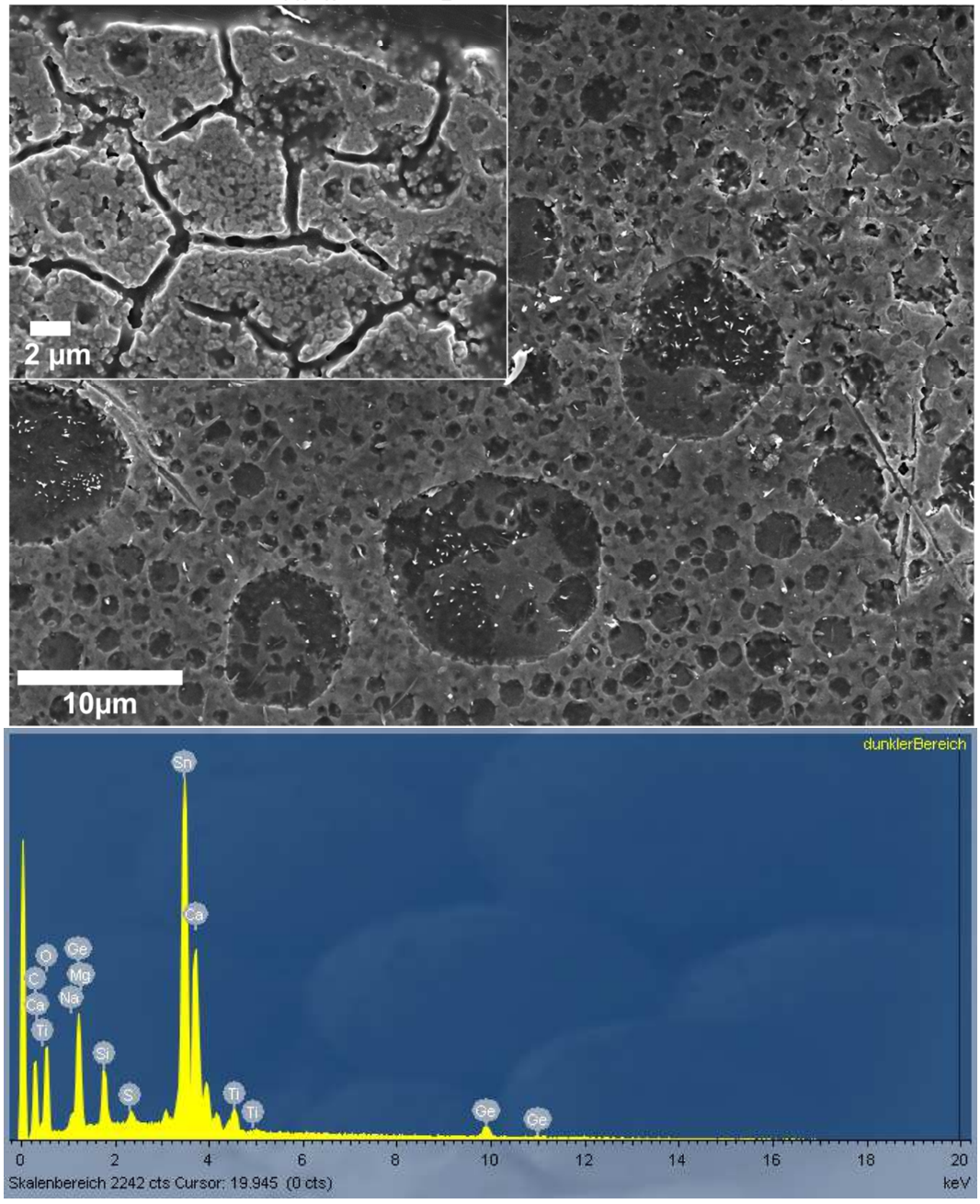

5.3 Efficiency tests

The efficiency of the Ge/P3HT solar cells was tested with a solar simulator (SolarConstant, K. H. Steuernagel Lichttechnik GmbH). The light intensity was calibrated to be 1000 W/cm^2 (AM1.5 solar illumination) by using a silicon-based calibration solar cell (WPVS Reference Solar Cell Type RS-ID-3k Fraunhofer ISE). The IV-curves were recorded with a Keithley 2400 sourcemeter and the bias was -1 V to 0.1 V.

Figure S16. U-I curves of Au/P3HT/*a*-$Ge_{1-x}Ge_x$-*FL*/TiO_2/FTO and Au/P3HT/*a*-$Ge_{1-x}P_x$-*FL*/TiO_2/FTO hybrid solar cells. b) two identical cells were tested.

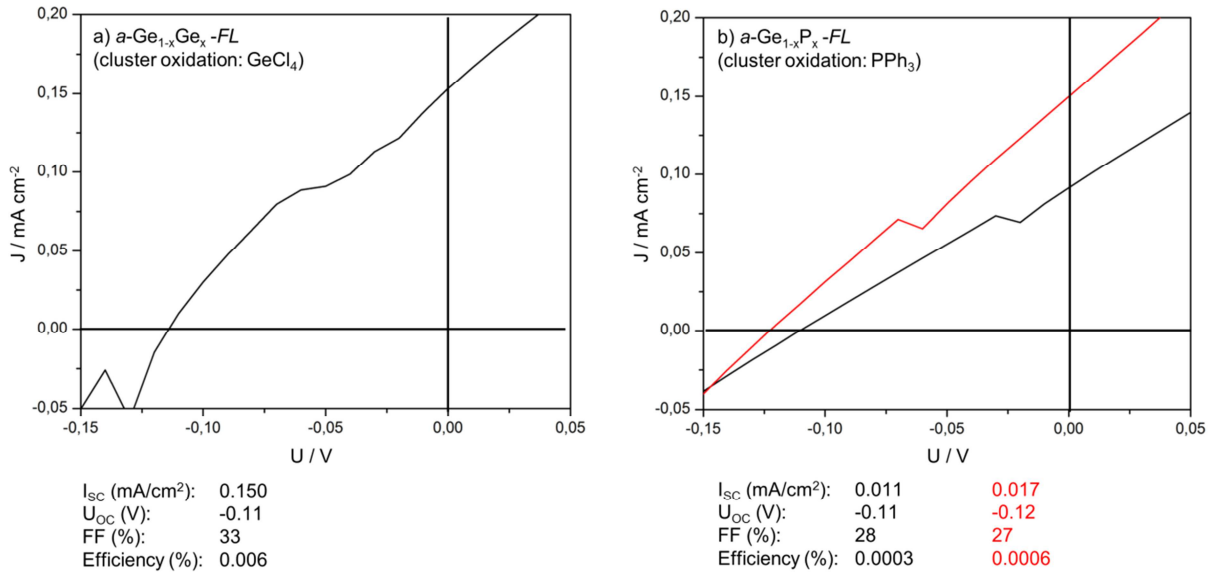

6 References

[1] T. Wang, O. Sel, I. Djerdj, B. Smarsly, *Colloid Polym Sci* **2006**, *285*, 1-9.

[2] T. F. Fässler, *Coordin. Chem. Rev.* **2001**, *215*, 347-377.

[3] M. M. Bentlohner, S. Frischhut, T. F. Fässler, unpublished work.

[4] M. M. Bentlohner, M. Waibel, P. Zeller, K. Sarkar, P. Müller-Buschbaum, D. Fattakhova-Rohlfing, T. F. Fässler, *Angew. Chem. Int. Ed.* **2016**, *55*, 2441-2445; *Angew. Chem.* **2016**, *128*, 2487-2491.

[5] J. I. Pankove, *Optical Processes in Semiconductors*, Dover, New York, **1975**

[6] J. Tauc, R. Grigorovici, A. Vancu, *Phys. Status Solidi B*, **1966**, *15*, 627-637.